The Magma Ocean of Mercury and the Role of Sulfur on the Early Evolution of the Innermost Terrestrial Planet

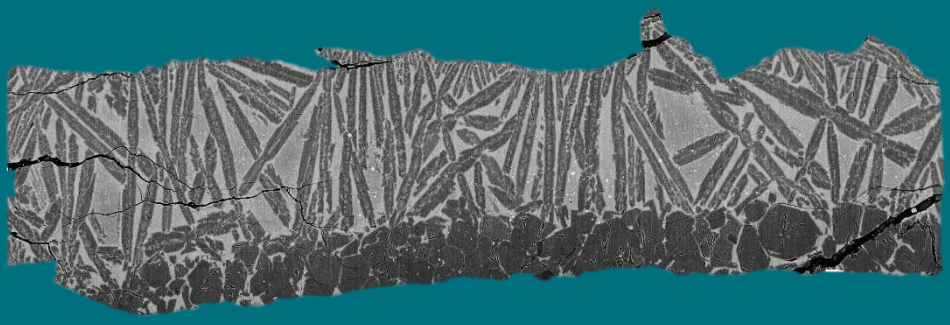

Fabrizio Saracino

PhD Advisor

Dr. Bernard Charlier

PhD dissertation submitted in partial fulfilment of the requirements for the degree of Doctor of Sciences from the University of Liège

2025

Jury

Prof. Jacqueline Vander Auwera	Université de Liège, Belgium	President
Dr. Bernard Charlier	Université de Liège, Belgium	PhD Advisor
Prof. Max Collinet	Université de Namur, Belgium	External Examiner
Prof. Tahar Hammouda	Université Clermont Auvergne, France	External Examiner
Prof. Stephan Klemme	Universität Münster, Germany	External Examiner
Prof. Olivier Namur	Katholieke Universiteit Leuven, Belgium	External Examiner

To Henzina, Marflabbo, Biba

Table of Contents

Acknowledgements

First and foremost, I would like to thank my supervisor Bernard Charlier for placing his trust in me and giving me the opportunity to pursue this doctoral project without prior background in experimental petrology. Thank you, Bernard, for your great patience in always answering my many questions and for pushing me to do more. I am also deeply thankful to Olivier Namur, Yishen Zhang, and Manon Lécaille for the precious discussions, helpful suggestions, comments, and corrections that greatly improved the quality of this doctoral work.

I must also thank all the people who have assisted me in the use of the different analytical instruments over the course of this doctoral project. I am extremely grateful to Jean-Luc Devidal for his unmatched expertise in the use of the EPMA at Université Clermont Auvergne, and to Roman Klinghardt for his generous help with the SEM at the University of Aachen. Huge thanks also to Yishen Zhang, and Thomas Van Gerve for their help with the EPMA and SEM at KU Leuven.

Ringrazio i miei amici Nicoló, Gianluca e Raffaele che non si sono ancora stufati di me.

Last but *definitely* not least, I am forever grateful to Fleet Foxes, Real Estate, Sam Amidon, The War on Drugs, King Creosote, Talk Talk, Haley Heynderickx, Luluc, and Michael Kiwanuka. Music has indeed been my faithful yet discreet companion. Like an old friend that you always cherish spending time with. Thank you for healing me from the sorrows of this world.

Sans la *Biba*, je ne sais pas si j'aurais pu atteindre ce but. Merci.

Abstract

Planet Mercury exhibits unique geochemical features and physical properties among the planets in our solar system. Mercury is the smallest terrestrial planet and is characterized by a large metallic core. As the planet accreted, the heat originated from early accretional impacts, core-mantle differentiation, and radiogenic decay was sufficient to melt Mercury. This early period, known as the "Magma Ocean" stage, has been first invoked for the Moon and is thought to have occurred in most terrestrial planets. As the silicate and metal portions separated, the crystallization of the silicate part resulted in the formation of the primordial mantle. What occurs during this critical period sets the stage for all subsequent events that shaped Mercury as we see it today. This includes mantle remelting and the production of a secondary magmatic crust, as well as the stability and storage of volatile elements that are crucial for planetary dynamics and building of an atmosphere. The data returned by NASA's MErcury Surface, Space ENvironment, GEochemistry, and Ranging (MESSENGER) spacecraft revealed an unusually high concentration of sulfur of surface volcanic units coupled with the paucity of iron. This indicates highly reduced conditions (or low oxygen availability) of formation of surface lavas. Sulfur is thus a major mantle volatile, and its occurrence has profound implications for melting temperatures, phase equilibria and, consequently, the vertical structure of the mantle. The goal of this doctoral thesis is to investigate the structure of the primordial mantle of Mercury as the direct result of the crystallization of its magma ocean, to provide a revised standard model for the evolution of the planet in its early history. Piston-cylinder experiments were performed on compositions that span Mercury's magma ocean's evolving silicate liquid, over a vast range of temperature (1125 – 1950 °C), pressures (0.5 – 3.0 GPa), and oxygen fugacity (from IW-3.0 to IW-8.5, with IW being the iron-wüstite solid buffer). Experimental results (phase equilibria, major element distribution) were then combined with petrologic modelling to simulate the fractional crystallization of Mercury's magma ocean (MMO), to reconstruct the stratigraphic sequence of Mercury's primordial mantle. Our results show that the structure of the primordial mantle of Mercury relies heavily on the Bulk Silicate Mercury (BSMe) composition and the presence of sulfur. Starting compositions with a low Mg/Si plus sulfur favour enstatite over forsterite, stabilize quartz, and delay the formation of clinopyroxene and plagioclase. In addition, Mg-, Ca-rich sulfides may segregate from the magma ocean, and their abundance will depend on the initial S content of BSMe. The mantle of Mercury is dominated by either orthopyroxene or olivine depending on the BSMe composition. Based on our modelled crystallization sequences, we identify both refractory and fertile mantle reservoirs. The former feature either olivine, orthopyroxene, or both coexisting phases in the lower cumulus, while the latter are defined by the appearance of clinopyroxene. Sulfur strongly influences the composition of the residual MMO liquid, leading to SiO_2 enrichment in S-bearing melts, whereas S-free liquids become SiO_2-depleted. We demonstrate that

sulfur behaves like other common volatiles, as it lowers the liquidus temperature and the density of Mercury-like silicate melts. Finally, we show that the storage of heat-producing elements (HPE) in Mercury's mantle is affected by sulfur. Indeed, the presence of sulfides segregated from the magma ocean, coupled with trapped liquid in the early cumulates will enhance HPE storage in the upper primordial mantle of Mercury, which is hypothesized to host a Moon-like KREEP layer.

Chapters Overview

Chapter 1 - *Introduction on Mercury and the magma ocean concept* - gives a general outlook on what we know about Mercury and how the concept of magma oceans developed and evolved in the science community. A general introduction on Mercury is proposed (1.1.), specifically about Mercury's major features (1.1.1.), the exploration of the planet (1.1.2.), Mercury's surface geochemical heterogeneity (1.1.3.), the bulk silicate composition of the planet (1.1.4.), and formational scenarios (1.1.5.). The second part of this chapter is dedicated to magma oceans (1.2.), particularly on the very concept of magma ocean and how it was introduced and how it took roots in the science community (1.2.1.). A discussion on magma ocean processes then follows (1.2.2.), and the role of viscosity in the evolution of magma oceans is also presented (1.2.3.). A short paragraph is dedicated to basal magma oceans and how they could originate (1.2.4.), followed by a discussion on magma ocean cooling timescales (1.2.5.). Finally, an introduction on Mercury's Magma Ocean tackles the current constraints on the early existence of a putative magma ocean on Mercury (1.2.6.). This chapter ends with a paragraph defining the goal of the doctoral thesis (1.3.).

Chapter 2 – *Methodology* - describes the array of experimental, and analytical techniques employed over the course of this PhD. The starting paragraph is dedicated to the preparation of the starting powders (2.1.). This is followed by a section that tackles the experimental strategy (2.2.), with details on the principles and functioning of the piston cylinder, and sample treatment (2.2.1.). Next is the turn of the analytical strategy (2.3.), with information on the principles of scanning electron microscopy (2.3.1.) and electron probe micro-analysis (2.3.2.). Two final digressions of this chapter concern the calculation of the relative phase proportions in our experiments through mass balance (2.4) and the determination of oxygen fugacity (2.5.).

Chapter 3 - *The role of sulfur on the liquidus temperature and olivine-orthopyroxene equilibria in highly reduced magmas* - is the first published article, where we delve into the influence of sulfur on the liquidus temperature and silicate phase equilibria of Mg-rich silicate melts under low oxygen fugacity conditions, and the implications for the magma ocean differentiation.

Chapter 4 - *The crystallization of Mercury's magma ocean and the formation of its primordial mantle structure* - represents the second scientific article currently under review. We explore the crystallization products of Mercury's S-bearing magma ocean under reduced conditions, by considering a range of potential BSMe compositions. We then investigate the several major implications for the magma ocean crystallization, spanning from the definition of mantle refractory and fertile reservoirs to the influence of sulfur on silicate liquid density and HPE storage.

Chapter 5 – *Perspectives for BepiColombo* – reviews the major contributions that the upcoming ESA BepiColombo mission will provide to the characterization of Mercury (5.1.). This chapter also shows how the results of this doctoral thesis can help place tighter constraints on the compositional features found on the surface of the planet (5.2.). Some concluding thoughts end this final chapter (5.3.).

At the end of the thesis, additional information is also provided. First, the supplementary materials of the first published article (Chapter 3) are shown (*Appendices A, B)*. Next, supplementary information related to the second article under review (Chapter 4) is provided (*Appendices C, D).* A list of each experimental run describing the experimental conditions, compositions, and relative phase assemblages is added at the end of the manuscript (*Appendix E*).

Chapter 1: Introduction to Planet Mercury and the Magma Ocean Concept

1.1.Mercury

1.1.1. Mercury's Major Features

Mercury is one of the most interesting planetary bodies to investigate in the field of planetary sciences. Although no single individual is credited for the discovery of the planet as it is visible with the naked eye, Mercury's appearance is often recorded as morning or evening star in Babylonian clay tablets dating around the first half of the second millennium before common era (BCE) (Sachs, 1974). The planet owes its name to the swift wing-footed Roman messenger of gods (Hermes in the Greek mythology), probably due to the rapidity of the planet's brief appearances just before dawn or after sunset (Dunne and Burgess, 1978). Mercury has a mean spherical radius of 2439 km and is the smallest amongst the four terrestrial planets (Table 1.1.). The planet orbits around the Sun with a mean heliocentric distance of 0.39 Astronomical Units (AU) and is characterized by a high orbital eccentricity ε (0.2). Mercury is also known for its 3:2 spin-orbit resonance (Colombo, 1965; Colombo and Shapiro, 1966), meaning that for every three rotations around its axis, the planet revolves twice about the Sun. Except for Earth, Mercury is the only terrestrial planet that hosts a global magnetic field, resulting from a dominantly dipolar core dynamo (Johnson et al., 2018). Mercury does not possess an atmosphere, but a neutral gas exospheric envelope surrounds the planet (McClintock et al., 2018).

Table 1.1. *Major physical properties of the terrestrial planets of our solar system (De Pater and Lissauer, 2015; McDonough, 2025).*

	Mercury	Venus	Earth	Moon	Mars
Distance from Sun (AU)	0.39	0.72	1.00	1.00	1.52
Radius (km)	2439	6052	6371	1738	3390
Mass (10^{24} kg)	0.33	4.87	5.97	0.07	0.64
Uncompressed density (kg m^{-3})	5300	4400	4400	3300	3800
Surface Gravity (m s^{-2})	3.7	8.9	9.8	1.6	3.7

Mercury's internal configuration follows that of the other terrestrial planets Venus, Earth, and Mars (Fig. 1.1.). A metallic core, a silicate mantle and crust form the planet. Similarities end here though. Mercury's most enigmatic feature is indeed its high uncompressed density (the density calculated

without considering the effect of gravity, Table 1.1.), which is the result of its high core-to-mantle ratio (Fig. 1.1.).

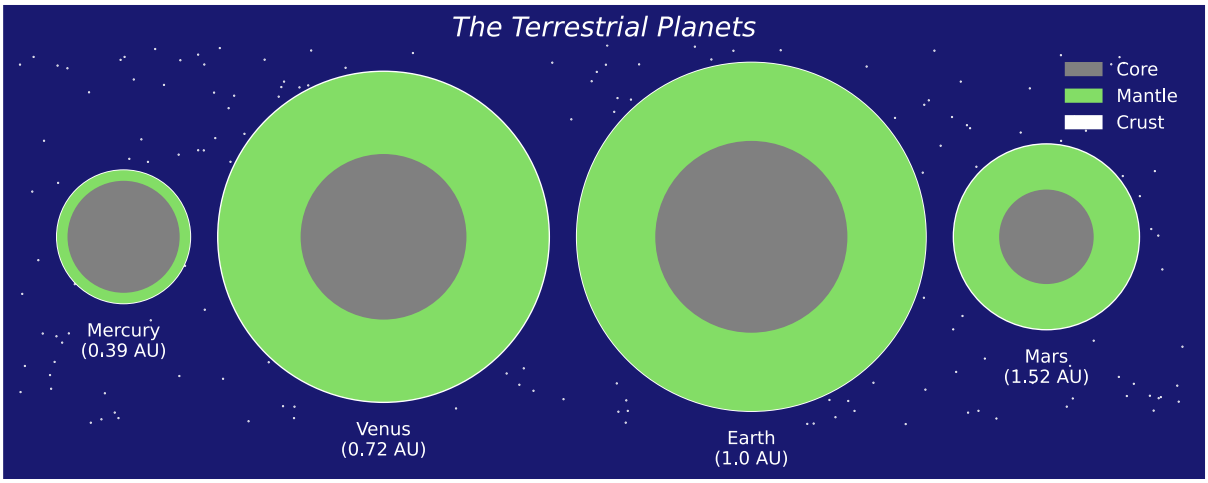

Figure 1.1. *Internal configuration of the four terrestrial planets (numbers in parentheses refer to the heliocentric distance expressed in astronomical units AU).*

Mercury's metallic core is ~ 85 % of the planetary radius and is divided into an outer and inner core. Magnetic and geodetic data suggest that the outer part might be partially molten and rich in light elements (Si, S, C), while the solid inner core (up to 1500 km in size) is nearly pure metallic Fe (Margot et al., 2007; Johnson et al., 2018; Knibbe and van Westrenen, 2018; Genova et al., 2019; Wardinski et al., 2019; Steinbrügge et al., 2021). The possibility for the existence of a FeS layer at the core-mantle boundary has also been considered (Cartier et al., 2020; Pirotte et al, 2023; Davies et al., 2024). Mercury's outer silicate shell (~ 420 km in thickness) comprises a heterogenous mafic mantle (about 400 km thick) and a relatively thick secondary crust (~ 35 ± 18 km) (Padovan et al., 2015; Namur et al., 2016a; McCoy et al., 2018; Wang et al., 2022; Beuthe et al., 2020; Goossens et al., 2022). Mercury's mantle is presently considered to be the product of the primordial differentiation caused by the crystallization of a global scale, silicate magma ocean (MMO) early in the planet's history. Early differentiation processes within the mantle may have caused density-driven instability, which triggered mantle overturn, eventually leading to a stable mantle configuration (Mouser et al., 2021; Mouser and Dygert, 2023). The crust of Mercury is volcanic in origin with reprocessing caused by surface impacts (McCoy et al., 2018). The magma erupting on the surface of the planet was produced by generally low-pressure batch decompression melting of the mantle (Charlier et al., 2013; Namur et al., 2016a; McCoy et al., 2018).

1.1.2. Mercury Exploration

The fascination around Mercury and its characterization is partly due to the difficulty of its exploration. The planet is located in the Sun potential well and cannot be investigated by telescope observations, given the elevated risk of optics damage from the exposure to direct electromagnetic radiation (Solomon, 2003; Solomon and Anderson, 2018). The innermost planet was first visited by NASA's Mariner 10 spacecraft (Fig. 1.2.a), which performed three fly-bys between 1974 and 1975 (Cremonese et al., 2007 and references therein). During these close approaches, Mariner 10 could obtain images of the apparent Moon-like surface of Mercury (Fig. 1.2.b), detect a handful of neutral exosphere constituents, and discover the presence of a global magnetic field (Shirley, 2003; Solomon and Anderson, 2018). In addition to Mariner 10's findings, Earth-based observations confirmed the presence of volatile elements in the exosphere (Vander Kaaden et al., 2019 and references therein).

The first in-depth mission designed to target the 'Iron Planet' (Solomon et al., 2001; Strom and Sprague, 2003) was NASA's MErcury Surface, Space ENvironment, GEochemistry, and Ranging (MESSENGER) mission (Fig. 1.2.c). The spacecraft was launched in August 2004 on a Delta II rocket. After performing several flybys around Earth, Venus, and Mercury, the probe entered the orbit of Mercury in March 2011. MESSENGER major scientific objectives involved investigating the surface chemical composition, the geologic history of Mercury, the characterization of the core and the nature of its exosphere, magnetic field, and the distribution of volatiles at the poles (Solomon et al., 2001; Solomon and Anderson, 2018).The MESSENGER spacecraft was capable of meeting all the goals set by the primary mission, as it allowed the planetary science community to obtain unprecedented insights into the least studied terrestrial planet. After completing its primary mission, and two mission extensions, the probe was left crushing on Mercury's surface on the 30$^{th\ of}$ April 2015. During its 4-year operative regime (2011-2015), MESSENGER was able to provide the first global view of Mercury, coupled with the surprising composition and heterogeneity of its surface (Weider et al., 2015). Only the southern hemisphere was not as resolved as the northern, due to the ellipticity of MESSENGER orbit. This caused elemental maps to be at a relatively low spatial resolution (McNutt et al., 2018; Benkhoff et al., 2021). MESSENGER first unveiled the extent of effusive volcanism on the surface of the planet and its importance in building Mercury's crust, revealing different volcanic processes other than purely effusive (Blewett et al., 2013; Byrne et al., 2018). MESSENGER observations also helped place constraints on the size of the metallic core (~2000 km), although large uncertainties regarding the size of the inner core still exist (Benkhoff et al., 2021). A renewed effort to explore Mercury is underway through the BepiColombo mission (Fig. 1.2.d), a joint venture between the European Space Agency (ESA) and the Japan Aerospace Exploration Agency (JAXA). Led by ESA, the mission is named after the Italian scientist Giuseppe "Bepi" Colombo, who made significant contributions to the understanding of Mercury's orbit (Colombo, 1965). BepiColombo consists of two spacecrafts: ESA's Mercury Planetary Orbiter (MPO), and JAXA's Mercury Magnetospheric Orbiter (Mio, formerly known as

MMO). The first spacecraft is led by ESA, and will provide a global characterization of the planet, focusing on the interior structure, surface, exosphere, and magnetosphere. Mio is led by JAXA and will devote itself to the study of Mercury's exosphere and magnetosphere, including the interactions between the solar wind and Mercury's surface (Benkhoff et al., 2021). BepiColombo officially began its long journey on the 20th of October 2018. The spacecraft is expected to enter the orbit of Mercury in November 2026, and to start routine science operations in early 2027 (at the time of writing).

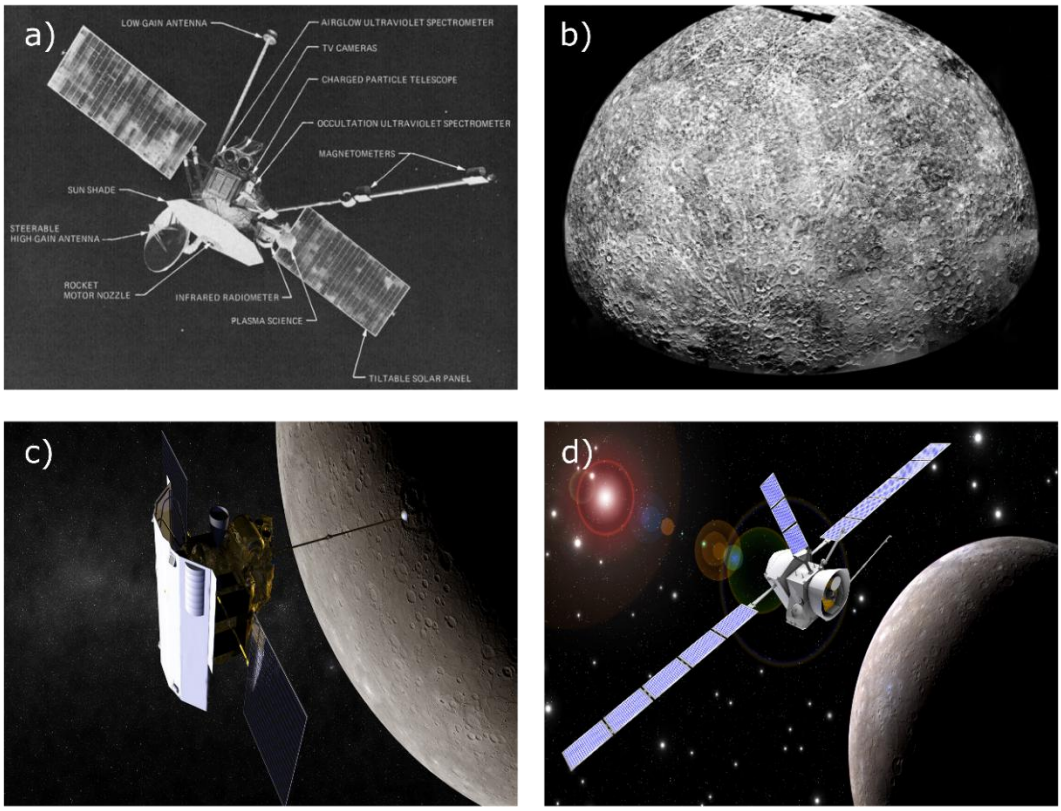

Figure 1.2. *(a) The Mariner 10 spacecraft and its science instruments (NASA / JPL) (b) Mercury's southern hemisphere as seen by Mariner 10 (Credit: NASA/JPL). (c) 3D artist rendition of the MESSENGER spacecraft orbiting Mercury (NASA/JHUAPL). (d) 3D artist rendition of the BepiColombo spacecraft on the way to Mercury (ESA/JAXA).*

1.1.3. Mercury's Geochemical Heterogeneity

MESSENGER spectroscopic data showed that the volcanic material covering Mercury's surface has unusual characteristics. Surface lavas were generally found to be enriched in both SiO_2 and MgO, but also FeO-depleted, sulfur and alkali-rich (Nittler et al., 2018). Mercury's surface composition was also found to be spatially heterogenous, and several geochemical regions have been identified (Fig. 1.3.). Depending on the criteria and methods utilized to discriminate Mercury's geochemical regions, a

differing number of terranes have been identified in the literature (Weider et al., 2015; McCoy et al., 2018; Vander Kaaden et al., 2017; Peplowski and Stockstill-Cahill, 2019). Here, for simplicity, we only refer to the geochemical regions present in McCoy et al. (2018).

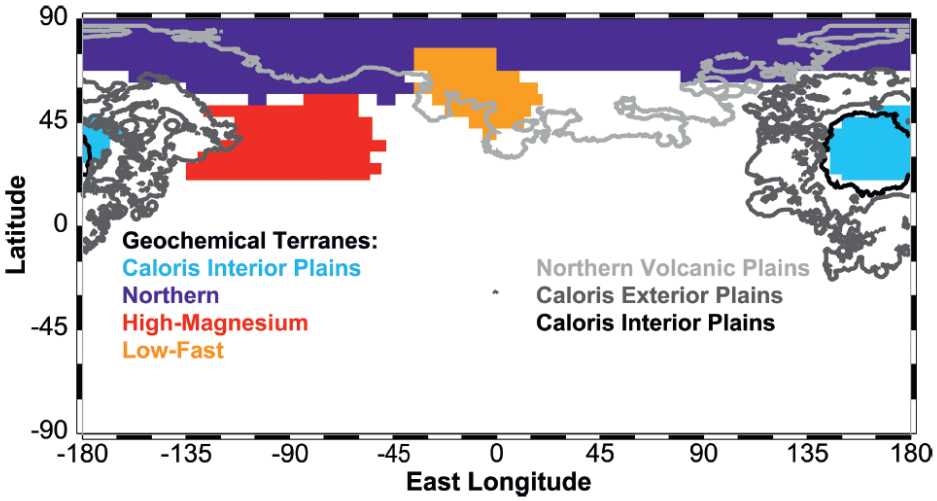

Figure 1.3. *Map of Mercury showing the geochemical terranes of Mercury (McCoy et al., 2018).*

The *High-Magnesium Terrane* (red region in Fig. 1.3.) is the largest geochemical region and is characterized by the highest surface Mg/Si (up to ~ 0.8), Ca/Si (~ 0.2 – 0.3), and S/Si (0.1 – 0.2) coupled with the lowest Al/Si. The *Caloris Interior Plains Terrane* (light blue region in Fig. 1.3.) is the only geochemical terrane that almost perfectly overlaps with the ~ 1550 km-wide impact basin geomorphic unit. This unit is characterized by low Mg/Si (~ 0.4) and the highest Al/Si (up to ~ 0.3) on the surface of the planet. The *Northern Terrane* (violet region in Fig. 1.3.) is partly associated with the smooth plains' unit, which is a geomorphic unit considered to be an ancient emplacement of lavas erupted via flood volcanism (Head et al., 2011). It exhibits low Mg/Si (< 0.5), Ca/Si (< 0.2), S/Si (< 0.1), and high Al/Si (0.2 – 0.3). Finally, the *Low Fast Terrane* represents a portion of the northern smooth plains. Its name derives from the low count rates for fast neutrons detected by the Neutron Spectrometer (NS) onboard MESSENGER (Lawrence et al., 2017), which are sensible to the average atomic mass of surface elements, particularly regarding the relative concentrations of high-mass and low-mass elements. This unit has an intermediate Mg/Si (0.4 – 0.5), with lower Ca/Si and Na/Si as compared to the Northern Terrane.

1.1.4. Bulk Silicate Mercury (BSMe)

FeO depletion combined with the positive correlation between S and normally lithophile elements (e.g., Mg, Ca, Na) on surface volcanic units point to parental magmas formed under highly reduced conditions (e.g., Namur et al., 2016a). Planetary scientists have then attempted to investigate

mantle sources, and as a consequence, Bulk Silicate Mercury (BSMe), starting from the surface compositional data through both petrology modelling and laboratory experiments (Charlier et al., 2013; Namur et al., 2016a; Wang et al., 2022; Anzures et al., 2020; Fischer and Parman, 2025; Saracino et al., 2025). Importantly, investigating BSMe implies exploring the compositional array that the potential Mercury's building blocks might cover. Terrestrial planets unlikely accreted from a single meteorite composition (Brown and Elkins-Tanton, 2009). Isotopic analyses tell us that the contribution from different compositions is expected, as has been shown for Earth and Mars (Dauphas, 2017; Sanloup et al., 1999; Tang and Dauphas, 2014). The scarcity of data on Mercury's surface and the resulting large uncertainties in the composition of the Bulk Silicate Mercury (BSMe) make it reasonable to assess a single meteoritic composition. In the case of Mercury, EC enstatite chondrites have been considered close analogues of BSMe, as they show similar geochemical features like FeO-free silicate phases, a relative abundance of S, and alkali metals (McCoy et al., 1999; Malavergne et al., 2010; Brown and Elkins-Tanton, 2009; Nittler et al., 2018; Charlier and Namur, 2019). BSMe has been investigated by both combining data from surface volcanic materials with melting experiments (Namur et al., 2016a; Nittler et al., 2018) and by defining magmatic fractionation lines of surface and mantle compositions (Anzures et al., 2020; Fischer and Parman, 2025). Nittler et al. (2018) calculated the mantle sources of the high-Mg region and the North Volcanic Plains by considering the phase proportions and compositions of enstatite and forsterite reported by Namur et al. (2016a) (see Table 1.2.). Their results were similar to the silicate portion of ECs, adjusted to account for silica reduction to Si stored in the core under low fO_2 (e.g., Malavergne et al., 2010; Chabot et al., 2014). Fischer and Parman (2025) calculated a BSMe composition (Table 1.2.) based on a new Mercury Fractionation Line (MFL) obtained by recalculating the Mg/Si and Al/Si ratios of X-Ray Spectrometer (XRS) data in McCoy et al. (2018). Because ECs are enriched in silica, they calculated the amount of Si being reduced and removed to the core for each published EC composition until the Si-depleted compositions fell along the MFL. Anzures et al. (2020) proposed a modified CH3 chondrite composition (ALH 85085) as the best approximation of the BSMe, due to its similar Mg/Si, Al/Si, Fe/Si, and Ni/Si ratios.

The BSMe compositions considered in this doctoral thesis are inspired by the silicate fraction of ECs (Table 1.2.; Xu et al., 2024; Saracino et al., 2025). An average composition was obtained from published analyses of high-iron (EH) and low-iron (EL) enstatite chondrites (Jarosewich, 1990; Berthet et al., 2009). We decreased the P_2O_5 content to account for the markedly siderophile behaviour of P (Gu et al., 2019; Steenstra et al., 2020; Pirotte et al., 2023). Some Si was also removed from the original chondritic composition: two compositions with different Mg/Si ratios were selected, corresponding to the segregation of 8 wt% and 15 wt% Si from the silicate fraction into the core (named Mer8 and Mer15, respectively; Xu et al., 2024; Saracino et al., 2025). Assuming that the core of Mercury represents 67% of the planet's bulk mass (Hauck et al., 2013), these values imply core Si contents of 2.9 wt% (Mer8)

and 5.5 wt% Si (Mer15), spanning the lower range of estimated Si concentrations in Mercury's core (Nittler et al., 2018). All BSMe and mantle compositions are reported in Table 1.2.

Table 1.2. *Compositions of the starting materials used in this doctoral thesis (expressed in wt%). Also shown are (a) Mercury's pre-melting mantle compositions of the Northern Smooth Plains and Intercrater Highly cratered Terrains, respectively (Nittler et al., 2018), (b) Primitive Mantle Mercury (Anzures et al., 2020), (c) Bulk Silicate Mercury from Fischer and Parman (2025), (d) EH4 Indarch (Berthet et al., 2009), and Bulk Silicate Earth (McDonough, 2025). Abbreviations: n.d. – not determined.*

	BSMe (this thesis)		**Pre-melting mantle (NSP)[a]**	**Pre-melting mantle (IcP HCT)[a]**	**Primitive Mantle Mercury[b]**	**Bulk Silicate Mercury[c]**	**Bulk Silicate Earth[d]**
	Mer8	**Mer15**					
SiO_2	54.82	47.91	53.67	51.98	51.32	52.06	44.92
TiO_2	0.14	0.16	0.24	0.21	0.21	0.13	0.20
Al_2O_3	3.70	4.26	4.57	4.24	3.78	3.38	4.19
Cr_2O_3	0.52	0.60	n.d.	n.d.	0.41	0.54	0.33
FeO_{tot}	n.d.	n.d.	0.02	0.03	0.54	0.20	8.05
MnO	0.28	0.33	n.d.	n.d.	0.09	0.31	0.14
MgO	37.32	43.04	36.89	37.64	40.72	39.84	37.81
CaO	1.62	1.87	2.26	3.84	2.73	1.75	3.27
Na_2O	1.37	1.58	1.97	1.29	0.08	1.62	0.36
K_2O	0.13	0.15	0.05	0.04	0.02	0.17	0.03
P_2O_5	0.10	0.10	n.d.	n.d.	n.d.	n.d	0.02
NiO	n.d.	n.d.	n.d.	n.d.	0.11	n.d	0.22
Total	100.00	100.00	99.67	99.27	100.01	100.00	99.54
Mg/Si	0.88	1.16	0.89	0.93	1.02	0.99	1.09
Ca/Al	1.18	1.18	1.34	2.45	1.95	1.40	2.11

1.1.5. Mercury's Formational Scenarios

Mercury's unusual features, mainly its large metal-to-silicate ratio (Fig. 1.1.), have led planetary scientists to propose different mechanisms regarding the formation of the planet. These scenarios are usually divided into two classes or endmembers: orderly and chaotic processes (Fig. 1.4.; Ebel and Stewart, 2018; Charlier and Namur, 2019). *Orderly processes* are defined as those processes that characterize the inner region of the solar nebula in the initial stages of planetary formation. A number of mechanisms have been brought up to explain Mercury's signatures including differing condensation temperatures of metals and silicates (Lewis, 1973), aerodynamic fractionation (Weidenschilling, 1978), solar wind-driven mantle evaporation (Fegley and Cameron, 1987), photophoresis (Wurm et al., 2013; Wurm, 2018), magnetic erosion (Hubbard, 2014), electromagnetic processes in the protoplanetary disc (McDonough and Yoshizaki, 2021), and accretion from unequilibrated, organic interplanetary dust particles (C-IDP) (Ebel and Alexander, 2011). Early condensation models explain the peculiar nature of Mercury by either the differing condensation temperatures of metals and silicates (Lewis, 1973) or by the fact that an energetic Sun was hot enough to vaporize part of the mantle of Mercury (Fegley and Cameron, 1987). Condensation models and partial mantle evaporation both imply significant depletion of volatiles in the mantle and are not consistent with the recent observations performed by MESSENGER showing volatile amounts (e.g., Na, Cl, K, S) comparable to those of other rocky bodies (Nittler et al., 2018; Lewis, 1973; Brown and Elkins-Tanton, 2009). Weidenschilling (1978) suggested that the separation of metals and silicates in Mercury would occur through aerodynamic fractionation where silicates are more preferentially removed than metals because of gas drag in a centrally condensed nebula with non-Keplerian rotation. Photophoretic processes have also been proposed to account for Mercury's features. Photophoresis is an astrophysical process that can separate highly thermally conducting material (metals) from low thermally conductive silicates. This process would be capable of reproducing Mercury's features and other exoplanets sharing similar characteristics (Wurm et al., 2013; Wurm, 2018). To explain Mercury's large metal / silicate ratio, Hubbard (2014) called on magnetic-induced collisions that would have favored the build-up of metallic materials at the expense of the loosely bound silicate portion during planetesimal formation. The aerodynamic fractionation, magnetic erosion, and photophoretic processes (Weidenschilling, 1978; Hubbard, 2014; Wurm et al., 2013; Wurm, 2018) can recreate Mercury's high density and metal enrichment, but they do not provide an explanation for the reducing conditions of differentiation of the planet (Ebel and Stewart, 2018). Ebel and Alexander (2011) investigated condensation models with a high abundance of unequilibrated, anhydrous, and organic interplanetary dust particles, or C-IDPs. Their results show similarities in mineralogy and petrology with enstatite chondrite material, which would have later accreted to form Mercury. Recently, McDonough and Yoshizaki (2021) developed a compositional model of the inner solar system where they suggest that the core mass fractions (thus the metal-to-silicate ratios) of the

terrestrial planets depend on the varying electromagnetic separation capability of magnetized metallic alloys and silicates.

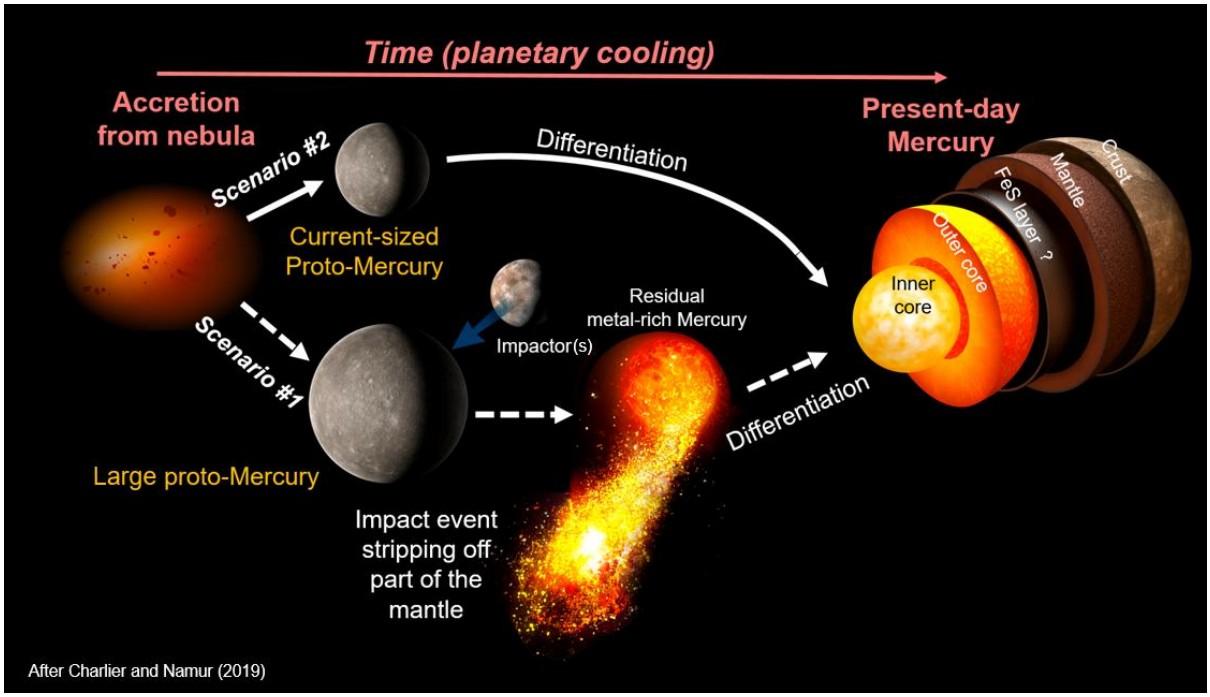

Figure 1.4. *End member scenarios for the formation of Mercury (modified after Charlier and Namur, 2019; illustrations courtesy of M. Garlick).*

Chaotic processes, on the other hand, require external 'input,' like the collision of one or more impactors of differing sizes onto a putative primordial Mercury, also called proto-Mercury. One of the most recurring hypotheses about Mercury's origin is that a giant impact stripped off part of the silicate portion of a large chondritic proto-Mercury. Benz et al. (2007) showed that a large impact on a proto-Mercury with 2.25 times the mass of current-sized Mercury could have caused a long-term compositional differentiation of the planet. In a recent work investigating Ni and Co distribution between metal and silicate in aubrite meteorites (reduced enstatite-rich achondrites), Cartier et al. (2024) proposed that the Aubrite Parent Body (AuPB) might represent a fraction of the mantle of a large proto-Mercury which was partly stripped off by a large collision, thus supporting the giant impact hypothesis. On the other hand, Asphaug and Reufer (2014) hypothesized that Mercury (as well as other iron-rich bodies) could have been formed by inefficient accretion. They indeed show that one or more events of hit-and-run collisions (HRC, oblique collision between two bodies that later gravitationally separate) could have been able to produce Mercury. Chau et al. (2018) investigated the possibility of a single giant impact, a hit-and-run, and multiple collisions, respectively, capable of producing Mercury as we see it now. In order to create modern Mercury, a single giant impact is expected to be head-on and relatively fast (circa 30 km/s). The hit-and-run scenario, with proto-Mercury as the smaller body targeting a larger body, must consider a large proto-Mercury (about 4.5 M_{Mercury}) given the high probability of proto-Mercury

disruption upon impact. Lastly, multiple collisions can effectively form today's Mercury especially if the number of impacts is limited to two and the associated velocities are moderate (~ 20 km/s).

1.2.Magma Oceans

1.2.1. The Concept of Magma Ocean (MO)

Following accretional processes, terrestrial planets are thought to have been characterized by local or global scale magma oceans in their early stages of evolution. In order to have such an extensive melting, a substantial amount of thermal energy is required. Depending on the size of the planetary body, magma oceans are considered to have formed thanks to the supply of multiple heat sources. For planetesimals and proto-planets, an inner source of heat could be provided by the presence of radioactive elements like ^{26}Al and ^{60}Fe (which are now extinct) with short half-lives (~ 0.7 and 2.6 Myrs, respectively) called Short-Lived Radioisotopes (SLRs), whose decay is thought to have released a significant amount of heat in the first million years of the solar system (a few million years after the formation of Calcium-Aluminium-rich Inclusions, CAIs). ^{26}Al for example is produced in supernovas, when nuclides are ejected following the explosion of large, short-lived stars (Christiansen et al., 2022). The presence of ^{26}Al (the most abundant SLR) is evidenced by the measured ^{26}Mg, a daughter product of ^{26}Al, in chondritic samples. Other radioactive isotopes with longer half-lives and that are still active today like ^{238}U, ^{40}K, ^{232}Th might have also played a non-negligible part in the heat budget, although with a lesser extent (Salvador et al., 2023). For larger bodies, the heat released by SLRs alone wouldn't have been enough to melt them (Schaefer and Elkins-Tanton, 2018). In this latter case, local or global melting could have been achieved as the kinetic energy of colliding objects is converted into thermal energy during planet-building accretionary impacts (Elkins-Tanton, 2012; Tronnes et al., 2018; Brown and Elkins-Tanton, 2009; Salvador et al., 2023; Solomatov, 2015). The extent of melting is controlled by the size and mass of the colliding bodies, the impact angle, the velocity, and the frequency of impacts (Salvador et al., 2023 and references therein). Accretionary impacts would have also likely released volatiles from the impacted silicate bodies. This would have created steam atmospheres capable of lengthening the lifetime of surface MOs by raising the surface temperature above the solidus (Hamano et al. 2013; Chao et al., 2021). Metal-silicate differentiation is another class of processes that would add an additional source of heat for MOs. During the early stages of planetary formation, protoplanets would warm up through radioactive decay and accretionary heating. Within these bodies, Fe-rich material would have then separated from the silicate portion (owing to their lower solidus temperature) and coalesced, forming a metallic core (Christiansen et al., 2022). Specifically, the separation of the metallic core from the silicate portion would have caused the release of gravitational potential energy, which is dissipated through friction in both the silicate liquid and metallic core (Christiansen et al., 2022). Metal-silicate differentiation could be caused by different processes (liquid metal percolating through solid

silicates, liquid metal sinking through liquid silicates), occurring over different timescales, but it would likely provide with enough thermal energy to melt the overlying silicate layers (Salvador et al., 2023 and references therein).

It is common in specialized journals, conferences, and books to stumble upon the term magma ocean as indicating large bodies of silicate liquid produced through extensive melting. As for the terminology, though, the very expression 'magma ocean' was questioned by Warren (1985) who suggested that a magma ocean would have theoretically meant a 'virtually 100 % liquid, with a mainly gas/liquid upper surface and a water-like viscosity of the order of 10^{-2} poise (1 poise = 0.1 Pa s)' and preferring the term *magmasphere*. A detailed definition of magma ocean is found in Solomatov (2015), which we borrow and extend to all planetary bodies, thus defining a magma ocean as a 'partially or completely molten layer within a planetary body's deep interior whose motions are controlled largely by liquid viscosity'. According to Taylor and Norman (1992), magma oceans can be defined by two factors: (1) the magma behaves rheologically as a fluid, with suspended crystals being less than 50 % in volume: (2) the magma ocean represents a consistent fraction (more than 10%) of a planetary body. The modern concept of MO was established following the recovery of more than a thousand rock samples by the Apollo 11 mission by Wood et al. (1970), and Smith et al. (1970). They indeed suggested that the global distribution of anorthosites on the lunar surface (plagioclase-rich rocks) could have been the result of the flotation of plagioclase in a denser global silicate magma ocean. Large scale melting was later confirmed by studying trace elements through experimental petrology (Schnetzler and Philpotts, 1971; Shervais and Taylor, 1986). Since then, the lunar magma ocean (LMO) hypothesis has garnered general acceptance. Over the last decades, geochemical evidence in combination with geophysical models and numerical simulations of the evolution of the solar system have thus led planetary scientists to apply the MO concept to Mercury (Brown and Elkins-Tanton, 2009; Vander Kaaden and McCubbin, 2015; Mouser et al., 2021; Xu et al., 2024), Venus (Trønnes et al., 2019, Hamano et al., 2015), Earth (Trønnes et al., 2019; Solomatov, 2015), Mars (Elkins-Tanton et al., 2003; Elkins-Tanton, 2012), Vesta (Elkins-Tanton, 2012; Greenwood et al., 2005; Mandler and Elkins-Tanton, 2013), and Io (Khurana et al., 2011). Major advancements in detection techniques in exoplanetary science have also revealed a class of rocky exoplanets characterized by surface magma oceans which are sometimes termed as *lava worlds* (Chao et al., 2021; Leger et al., 2011), demonstrating the importance of the magma ocean stage as a crucial period for planetary evolution.

1.2.2. Magma Ocean Processes

The process of solidification in magma oceans mainly follows two steps (Brown and Elkins-Tanton, 2009): (1) assuming that a young planetary body is hot enough to be entirely above the liquidus temperature (the highest temperature where both liquid and solid phases are in thermodynamic

equilibrium), a strong convective regime begins, causing initial liquid homogenization (no chemical gradient) and allowing heat to flow upwards. Simple convection can be quantified by using the Rayleigh number, an a-dimensional ratio between buoyant and viscous forces, as shown below:

$$Ra = \frac{\rho\, g\, \alpha\, \Delta T\, D^3}{\eta\, \kappa} \qquad \text{(Eq. 1.1)}$$

Where ρ is liquid density, g is gravity, α is the thermal expansivity coefficient, ΔT is the temperature range across the liquid, D is liquid depth, η is dynamic viscosity, and κ is thermal diffusivity. As the liquid cools, the adiabat curve (i.e., the temperature gradient within the cooling magma ocean) intersects the solidus at depth, enabling the magma ocean to crystallize starting from the bottom upwards (Walker et al., 1975; Elkins-Tanton et al., 2003; Brown and Elkins-Tanton, 2009). The solidification of a magma ocean can follow two paths: fractional or equilibrium crystallization. In order for the former to happen, it's necessary that the velocity of crystal settling exceeds the convection velocity, allowing the crystals to create a chemical differentiation (Elkins-Tanton, 2012; Solomatov, 2015). On the contrary, equilibrium crystallization is expected to occur when crystal sedimentation, or settling, time is smaller than crystallization time (Solomatov, 2015 and references therein). This can happen if the crystal size doesn't exceed a critical value (d_{critical}) considered as the threshold between equilibrium and fractional crystallization which Solomatov (2015) suggests is about 1 mm for Earth. (2) Crystallization models mimicking the solidification of MOs usually produce unstable density structures (Schaefer and Elkins-Tanton, 2018). According to Elkins-Tanton (2012) such instabilities may cause mantle overturn which may be produced by the following processes: MO enrichment in heavy elements (Elkins-Tanton et al., 2011); formation of crystals at different temperatures with different compressibilities (Elkins-Tanton et al., 2003); Fe enrichment in residual liquids following Mg-Fe exchange in mafic minerals (Schaefer and Elkins-Tanton, 2018). A gravitationally unstable mantle can result in overturn via Rayleigh-Taylor instabilities. Assuming a liquid with constant dynamic viscosity η, the overturn time scale of unstable mantle cumulates with thickness D can be quantified as follows (Hess and Parmentier, 1995):

$$t_{\text{overturn}} = \frac{4\ \pi^2\, \eta}{\gamma\, \text{g}\, D^2} \qquad \text{(Eq. 1.2)}$$

Where g is the gravity acceleration, γ is the density gradient (in this model, liquid density is thought to vary linearly with depth). High viscosities will lengthen overturn time, while mantle thickening and the rise in g (depending on the internal mass distribution) are expected to lead to a decrease of t_{overturn}. Various phases of overturn are considered to have taken place in the primordial mantle of Venus and Earth (Elkins-Tanton, 2012; Rolf et al., 2018), the Moon (Grove and Krawczynski, 2009; Prissel et al., 2023; Maurice et al., 2024), and Mars (Elkins-Tanton et al., 2003, Elkins-Tanton, 2012). The inferred unusual composition of Mercury's silicates presumably prevented overturn from occurring (Vander Kaaden and McCubbin, 2015), although a recent study posits that it might have occurred within 100 Myr of MMO solidification (Mouser and Dygert, 2023).

1.2.3. The Importance of Viscosity on the Behaviour of Silicate Melts

Although this doctoral thesis is not centered on investigating the rheological properties of the silicate melts produced during the course of the experimental series, for which specific experimental designs and instruments are necessary, it is nonetheless important to discuss about the relevance of viscosity in the study of melts and magma oceans. As also shown in the definition of magma ocean in Solomatov (2015), viscosity is a major variable to consider when approaching the study of MO behaviour.

Peridotite liquids at near-liquidus temperatures are characterized by viscosities in the order of 10^{-1} Pa s at low pressure (Dingwell et al., 2004; Solomatov, 2015). Viscosity of ultramafic silicates generally decreases sensibly with temperature (Solomatov, 2015). As for pressure dependency, differences arise whether melts are polymerized (non-bridging oxygens versus tetrahedrally coordinated cations, NBO/T < 1) or depolymerized (NBO/T > 2) (Russell et al., 2024). Viscosity of polymerized melts decreases with pressure between 1 and 13 GPa (Wang et al., 2014; Sakamaki and Ohtani, 2022), while depolymerized melts exhibit an increase with pressure. Liebske et al. (2005) found that the viscosity of peridotite liquids increases to ~ 8.5 GPa and decreases at higher pressure. Cochain et al. (2017) showed that (a) viscosity of pyroxene melts decreases with pressure, and (b) two viscosity trends can be found, with a first marked drop in viscosity below 5 GPa and a second more softened decrease above 5 GPa. Russell et al. (2024) developed a viscosity model for ultramafic melts where viscosity is seen to significantly increase with pressure at mantle conditions. If we now consider a global scale crystallizing body of magma on a planet, we may expect the evolving residual liquid to vary significantly in composition, which in turn may seriously affect the physical and rheological properties of the very magma ocean. Over the course of the MO lifetime, the variation in viscosity can be indeed of several orders of magnitude (Salvador et al., 2023). As for the volatile control on viscosity, H_2O for example decreases the viscosity of silicate melts at low pressure and temperature conditions (Russell et al., 2024; Solomatov, 2015), although differences in viscosities between anhydrous and hydrous melts seem to be negligible at high temperatures (Solomatov, 2015; Salvador et al., 2023). The viscosity model of Russell et al. (2024), on the other hand, predicts a 0.5 log units monotonous decrease in viscosity for Earth's mantle melts when 5 mol% H_2O are added. Recently, Mouser et al. (2021) showed the negative dependency of dissolved sulfur on viscosity in reduced Mg-rich melts relevant to Mercury's magma ocean. The viscosity of silicate melts is crucially controlled by the solid fraction in the melt (Solomatov, 2015). The influence of the solid fraction on the viscosity can be shown in the following expression (Roscoe, 1952):

$$\eta = \frac{\eta_l}{(1-\frac{\phi}{\phi_m})^{2.5}} \qquad \text{(Eq. 1.3)}$$

Where η is viscosity of the suspension, η_l is the viscosity of the liquid, ϕ is the solid volume fraction, and ϕ_{m} is the maximum packing crystal fraction (Solomatov, 2015) and is the critical solid fraction separating a melt-dominated rheology from a solid-dominated rheology (Salvador et al., 2023). The rheological shift from melt-dominated behaviour to crystal-dominated behaviour makes the magma rheologically 'locked,' where crystal shape is hypothesized to play a major role (Mangler et al., 2024).

1.2.4. Basal Magma Oceans (BMOs)

Although magma oceans are believed to develop mainly on the outermost part of planetary bodies, some of them like Venus, Earth, the Moon might have hosted inner, basal magma oceans (BMOs). BMOs could be produced by means of the following processes (Elkins-Tanton, 2012): (i) planetesimal melting from the interior (accretional heating); (ii) density inversion between solids and liquids, with the latter sinking downwards (especially in large planets, Trønnes et al., 2019); (iii) conversion of potential energy of core formation to thermal energy, which would be stored in the planetary interior; (iv) radiogenic heating from radio-isotopes-enriched layers forming as a consequence of fractionation and subsequent overturn. Labrosse et al. (2007) hypothesized that a deep, ~100 km-thick layer of dense melt may have formed early in Earth's history (Fig. 1.5.), representing a geochemical reservoir, particularly for heat producing elements (HPEs). The dense Fe-rich BMO would have slowly frozen through fractional crystallization, depositing the Fe-rich solids upwards on the bottom of the solid mantle. Boukaré et al. (2025) recently suggested that on Earth, an iron-oxide-rich BMO would have formed and that it represents the last residue of the magma ocean solidification.

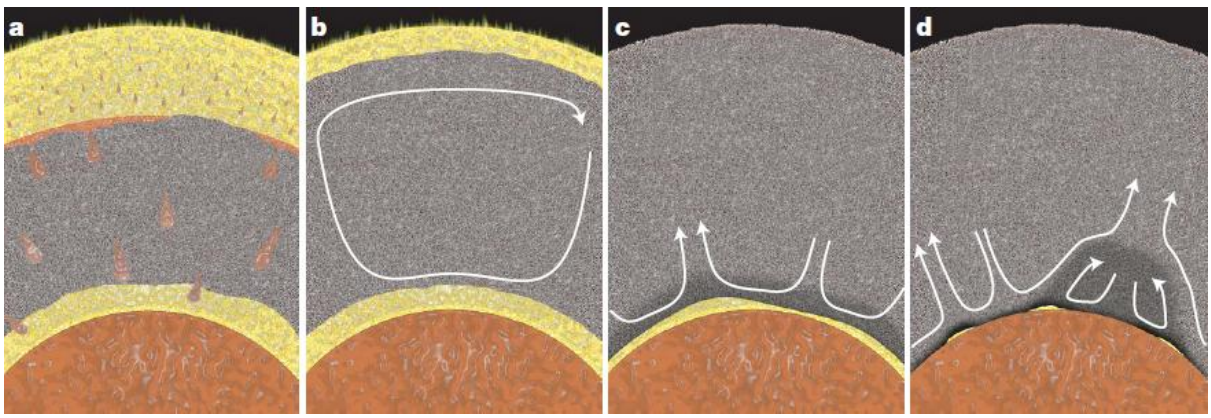

Figure 1.5. *Evolution of Earth's magma ocean with the formation of a surficial and a basal magma ocean (yellow areas) and the crystallization of mantle minerals (grey areas) (Labrosse et al., 2007).*

Kraettli et al. (2022) investigated the possibility for the formation of a BMO on the Moon (Fig. 1.6.). They suggested that in the crystallizing LMO, neutrally buoyant olivine would have stalled in the middle of the magma ocean creating a barrier that would have separated the residual magma ocean into

a surface magma ocean, and a ~ 220 km-thick basal magma ocean. The lunar BMO would have then crystallized dense garnet-rich layers and would have produced a highly evolved residual liquid that might still exist at the present time. They found that the existence of the lunar BMO is dependent on many factors, mainly the initial depth of the LMO, the initial composition of Bulk Silicate Moon (mostly the starting Mg/Fe ratio), and the compressibility of the magma ocean. Given the similarity between Earth's and Venus' sizes, O'Rourke (2020) extended the possibility of BMO formation also the sister planet of Earth. As Venus has no plate tectonics, the lifetime for a BMO would be extended significantly as more heat would be still stored in the interior. A 200-400 km-thick BMO would be still present today, representing a potential reservoir for incompatible elements.

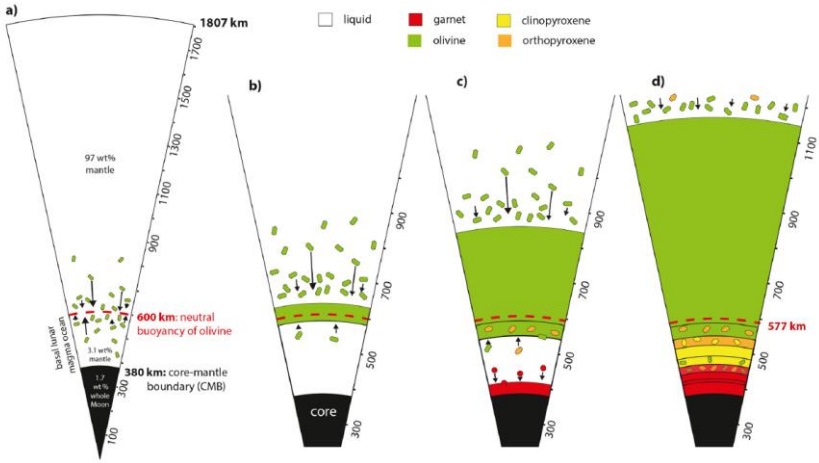

Figure 1.6. *Schematic evolution of the 220 km-thick lunar basal magma ocean (Kraettli et al., 2022).*

1.2.5. Magma Ocean Cooling

MO cooling timescale depends on the heat flux within the magma ocean, which is controlled by turbulent convection regimes (Maurice, 2020). This in turn depends on MO viscosity, which, as we have seen, can be rather low for primitive compositions. This would create strong turbulent heat fluxes (Solomatov, 2015). In general, the time required for a MO to solidify can be expressed as such (Chao et al., 2021):

$$t_{MO} = \frac{\rho D L}{q} \qquad \text{(Eq. 1.4)}$$

Where ρ is the magma ocean density, D is the magma ocean depth, L is the latent heat of crystallization, and q is the heat flux. End-member scenarios leading to three considerably different cooling timescales are now presented (Chao et al., 2021): (a) in the case of the formation of a stable surficial lid, the magma ocean cooling time will depend on the lid thickness, with timescale ranges being a considerable fraction of a planetary body's age; (b) during the MO crystallization, a secondary atmosphere might made of

volatiles (usually H_2O or CO_2) might develop (Abe, 1997). In this case, the heat flux at the surface is partly suppressed, leading a typical terrestrial magma ocean hundreds of km thick to cool in the order of several hundred thousands of years (if not millions) (Maurice, 2020); (c) in the absence of both a stable crust and/or a thick atmosphere, the heat escape towards the outer space would be extremely effective (unless there's an equal amount of heat produced from the interior), thus leading a magma ocean to crystallize in a very short time (decades).

1.2.6. Mercury's Magma Ocean

Independently from the formational scenarios that shaped planet Mercury early in its history (e.g., Ebel and Stewart, 2018), the combination of accretionary impacts, metal–silicate segregation, and decay of short-lived radioisotopes would have produced enough heat to completely melt the planet (Schubert et al., 1988; Schaefer and Elkins–Tanton, 2018). This inference is supported by the large size of the core of the planet (Hauck et al., 2013), meaning that a high degree of differentiation capable of effectively segregating nearly all the metal in the core must have been reached in its early history. This would have created a global Mercury Magma Ocean (MMO). Layering would have developed within the crystallizing magma ocean to form the primordial mantle of Mercury. The segregation of olivine- and pyroxene-rich cumulates denser than the residual liquid probably resulted in the formation of a vertically heterogeneous mantle composed of increasingly ultramafic lithologies towards the core-mantle boundary (McCoy et al., 2018, Brown and Elkins-Tanton, 2009). The inferred bulk mantle S content (Namur et al., 2016a) led authors to suggest that also sulfide phases would have segregated from the MMO, with major implications for potential mantle overturn (Boukaré et al., 2019; Mouser and Dygert, 2023). Also, following interpretations of MESSENGER's spectroscopic data, the expected paucity of FeO in Mercury's magma ocean presumably prevented flotation of plagioclase as a result of the low-density residual liquid (Vander Kaaden and McCubbin, 2015). A recent study from Mouser and Dygert (2023) nonetheless suggested that overturn could have been possible within 100 Myrs of magma ocean solidification, caused by density instabilities of dense pyroxenite layers on underlying less dense harzburgite layers. In any case, according to Vander Kaaden and McCubbin (2015), graphite would have been the only low-density, buoyant phase in a FeO-depleted MMO, whose flotation likely contributed to forming Mercury's primary flotation crust, with its thickness depending on the bulk C content of the MMO.

1.3.Goal of the Thesis

This introduction briefly explained the peculiar character of Mercury amongst the planetary bodies in our solar system. Mercury is unique both in its interior makeup and in its composition. The amount of data in our possession as obtained by Mariner 10, MESSENGER, and Earth-based observations is not comparable to that of Mars, or the Moon. Nevertheless, substantial advancements have been made in the understanding of Mercury's configuration, formation, and evolution. We know very little about the early magma ocean stage, and the few scientific efforts are mostly based on modelling. This doctoral endeavour serves as a first revised model of the interior of Mercury based on experimental petrology.

The goal of the thesis is therefore to reconstruct the primordial structure of the mantle of Mercury via an experimentally driven approach capable of retrieving the silicate phase equilibria and the sequence of crystallization of a global magma ocean on Mercury under reducing conditions (Fig. 1.7.). The experimental approach is combined with petrological modelling (Namur et al., 2012; Charlier et al., 2018; Zhang et al., 2024), which is employed with the scope of tracking the compositional evolution of a silicate magma ocean, as new crystals form and segregate from the silicate liquid. Our combined approach has the ultimate scope of reconstructing the internal layering of Mercury's silicate shell from the core-mantle boundary up to the crust. Thanks to our modelled crystallization sequence, we will be able to define mantle fertile and refractory reservoirs, which are paramount to investigating the petrogenesis of surface lavas. In parallel, we investigate the role of sulfur in affecting silicate phase equilibria, the liquidus temperatures, and density of Mercury's magma ocean. We indeed aim to use the experimental dataset developed throughout the project to quantify the shifts in phase boundaries induced by sulfur dissolved in silicate melts, and to empirically parameterize the depression of the liquidus temperature as a function of sulfur content in reduced, Mg-rich silicate systems. Moreover, we investigate the role of sulfur on the density of the magma ocean of Mercury, as this has major consequences on the possibility for solid phases to be able to float and thus contributing to the buildup of the primary crust of the planet. Lastly, we explore the impact of sulfur on the storage of HPE, which is crucial to study the thermal evolution of the planet. Our study will provide the most up-to-date model for the evolution of the silicate portion of Mercury's interior.

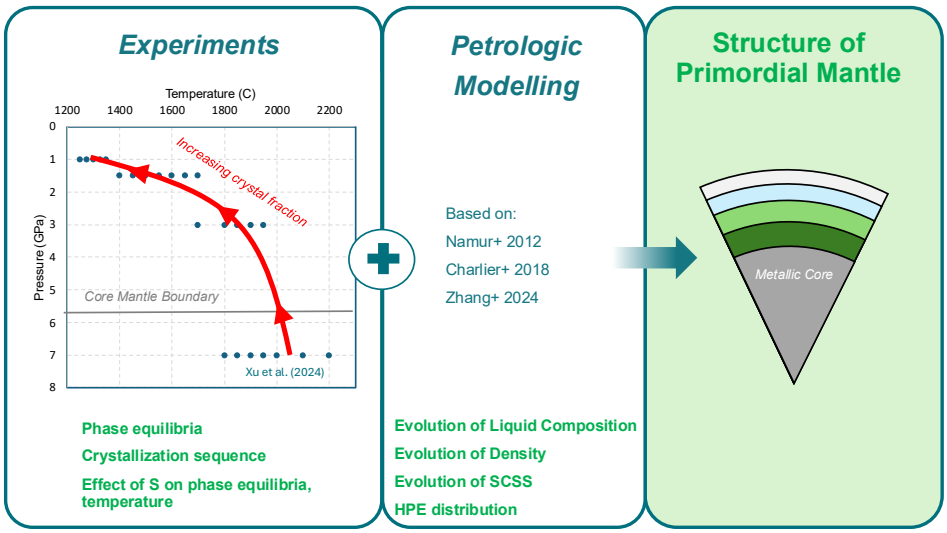

Figure 1.7. Schematic concept showing the approach undertaken by this doctoral thesis

References

Abe, Y., 1997. Thermal and chemical evolution of the terrestrial magma ocean. Phys. Earth Planet. Inter. Interiors 100, 27–39. https://doi.org/10.1016/S0031-9201(96)03229-3

Anzures, B.A., Parman, S.W., Milliken, R.E., Namur, O., Cartier, C., Wang, S., 2020. Effect of sulfur speciation on chemical and physical properties of very reduced mercurian melts. Geochim. Cosmochim. Acta 286, 1–18. https://doi.org/10.1016/j.gca.2020.07.024

Asphaug, E., Reufer, A., 2014. Mercury and other iron-rich planetary bodies as relics of inefficient accretion. Nat. Geosci. 7, 564–568. https://doi.org/10.1038/ngeo2189

Benkhoff, J., Murakami, G., Baumjohann, W., Besse, S., Bunce, E., Casale, M., Cremosese, G., Glassmeier, K.-H., Hayakawa, H., Heyner, D., Hiesinger, H., Huovelin, J., Hussmann, H., Iafolla, V., Iess, L., Kasaba, Y., Kobayashi, M., Milillo, A., Mitrofanov, I.G., Montagnon, E., Novara, M., Orsini, S., Quemerais, E., Reininghaus, U., Saito, Y., Santoli, F., Stramaccioni, D., Sutherland, O., Thomas, N., Yoshikawa, I., Zender, J., 2021. BepiColombo - Mission overview and science goals. Space Sci. Rev. 217, 90. https://doi.org/10.1007/s11214-021-00861-4

Benz, W., Anic, A., Horner, J., Whitby, J.A., 2007. The origin of Mercury. Space Sci. Rev. 132, 189–202. https://doi.org/10.1007/s11214-007-9284-1

Berthet, S., Malavergne, V., Righter, K., 2009. Melting of the Indarch meteorite (EH4 chondrite) at 1GPa and variable oxygen fugacity: implications for early planetary differentiation processes. Geochim. Cosmochim. Acta 73, 6402–6420. https://doi.org/10.1016/j.gca.2009.07.030

Beuthe, M., Charlier, B., Namur, O., Rivoldini, A., Van Hoolst, T., 2020. Mercury's crustal thickness correlates with lateral variations in mantle melt production. Geophys. Res. Lett. 47, e2020GL087261. https://doi.org/10.1029/2020GL087261

Blewett, D.T., Vaughan, W.M., Xiao, Z., Chabot, N.L., Denevi, B.W., Ernst, C.M., Helbert, J., D'Amore, M., Maturilli, A., Head, J.W., Solomon, S.C., 2013. Mercury's hollows: constraints on formation and composition from analysis of geological setting and spectral reflectance. J. Geophys. Res. Planets 118, 1013–1032. https://doi.org/10.1029/2012JE004174

Boukaré, C.-E., Badro, J., Samuel, H., 2025. Solidification of Earth's mantle led inevitably to a basal magma ocean. Nat. 640, 114–119. https://doi.org/10.1038/s41586-025-08701-z

Boukaré, C.-E., Parman, S.W., Parmentier, E.M., Anzures, B.A., 2019. Production and preservation of sulfide layering in Mercury's mantle. J. Geophys. Res. Planets 124, 3354–3372. https://doi.org/10.1029/2019JE005942

Brown, S.M., Elkins-Tanton, L.T., 2009. Compositions of Mercury's earliest crust from magma ocean models. Earth Planet Sci. Lett. 286, 446–455. https://doi.org/10.1016/j.epsl.2009.07.010

Byrne, P.K., Whitten, J.L., Klimczak, C., McCubbin, F.M., Ostrach, L.R., 2018. The volcanic character of Mercury, in: Solomon, S.C., Nittler, L.R., Anderson, B.J. (Eds.), Mercury. Cambridge University Press, pp. 287–323. https://doi.org/10.1017/9781316650684.012

Cartier, C., Llado, L., Pirotte, H., Tissandier, L., Namur, O., Collinet, M., Wang, S.-J., Charlier, B., 2024. Partitioning of nickel and cobalt between metal and silicate melts: expanding the oxybarometer to reducing conditions. Geochim. Cosmochim. Acta 367, 142–164. https://doi.org/10.1016/j.gca.2023.12.020

Cartier, C., Namur, O., Nittler, L.R., Weider, S.Z., Crapster-Pregont, E., Vorburger, A., Frank, E.A., Charlier, B., 2020. No FeS layer in Mercury? Evidence from Ti/Al measured by MESSENGER. Earth Planet. Sci. Lett. 534, 116108. https://doi.org/10.1016/j.epsl.2020.116108

Chabot, N.L., Wollack, E.A., Klima, R.L., Minitti, M.E., 2014. Experimental constraints on Mercury's core composition. Earth Planet. Sci. Lett. 390, 199–208. https://doi.org/10.1016/j.epsl.2014.01.004

Chao, K.-H., deGraffenried, R., Lach, M., Nelson, W., Truax, K., Gaidos, E., 2021. Lava worlds: from early Earth to exoplanets. Geochemistry 81, 125735. https://doi.org/10.1016/j.chemer.2020.125735

Charlier, B., Grove, T.L., Namur, O., Holtz, F., 2018. Crystallization of the lunar magma ocean and the primordial mantle-crust differentiation of the Moon. Geochim. Cosmochim. Acta 234, 50–69. https://doi.org/10.1016/j.gca.2018.05.006

Charlier, B., Grove, T.L., Zuber, M.T., 2013. Phase equilibria of ultramafic compositions on Mercury and the origin of the compositional dichotomy. Earth Planet Sci. Lett. 363, 50–60. https://doi.org/10.1016/j.epsl.2012.12.021

Charlier, B., Namur, O., 2019. The origin and differentiation of planet Mercury. Elements 15, 9–14. https://doi.org/10.2138/gselements.15.1.9

Chau, A., Reinhardt, C., Helled, R., Stadel, J., 2018. Forming Mercury by giant impacts. Astrophys. J. 865, 35. https://doi.org/10.3847/1538-4357/aad8b0

Christiansen, E.H., Best, M.G., Radebaugh, J., 2022. The origin of magma on planetary bodies, in: Planetary volcanism across the solar system. Elsevier, pp. 235–270. https://doi.org/10.1016/B978-0-12-813987-5.00006-7

Cochain, B., Sanloup, C., Leroy, C., Kono, Y., 2017. Viscosity of mafic magmas at high pressures. Geophys. Res. Lett. 44, 818–826. https://doi.org/10.1002/2016GL071600

Colombo, G., 1965. Rotational period of the planet Mercury. Nat. 208, 575.

Colombo, G., Shapiro, I.I., 1966. The rotation of the planet Mercury. Astrophys. J. 145, 296. https://doi.org/10.1086/148762

Cremonese, G., Sprague, A., Warell, J., Thomas, N., Ksamfomality, L., 2007. The surface of Mercury as seen by Mariner 10. Space Sci. Rev. 132, 291–306. https://doi.org/10.1007/s11214-007-9231-1

Dauphas, N., 2017. The isotopic nature of the Earth's accreting material through time. Nat. 541, 521–524. https://doi.org/10.1038/nature20830

Davies, C.J., Pommier, A., Greenwood, S., Wilson, A., 2024. Thermal and magnetic evolution of Mercury with a layered Fe-Si(-S) core. Earth Planet Sci. Lett. 641, 118812. https://doi.org/10.1016/j.epsl.2024.118812

De Pater, I., Lissauer, J.J., 2015. Planetary Sciences, 2nd ed. Cambridge University Press. https://doi.org/10.1017/CBO9781316165270

Dingwell, D.B., Courtial, P., Giordano, D., Nichols, A.R.L., 2004. Viscosity of peridotite liquid. Earth Planet Sci. Lett. 226, 127–138. https://doi.org/10.1016/j.epsl.2004.07.017

Dunne, J.A., Burgess, E., 1978. The Voyage of Mariner 10. NASA / Jet Propulsion Laboratory California Institute of Technology.

Ebel, D.S., Alexander, C.M.O., 2011. Equilibrium condensation from chondritic porous IDP enriched vapor: Implications for Mercury and enstatite chondrite origins. Planet. Space Sci. 59, 1888–1894. https://doi.org/10.1016/j.pss.2011.07.017

Ebel, D.S., Stewart, S.T., 2018. The Elusive Origin of Mercury, in: Solomon, S.C., Nittler, L.R., Anderson, B.J. (Eds.), Mercury. Cambridge University Press, pp. 497–515. https://doi.org/10.1017/9781316650684.019

Elkins-Tanton, L.T., 2012. Magma oceans in the inner solar system. Annu. Rev. Earth Planet. Sci. 40, 113–139. https://doi.org/10.1146/annurev-Earth-042711-105503

Elkins-Tanton, L.T., Burgess, S., Yin, Q.-Z., 2011. The lunar magma ocean: Reconciling the solidification process with lunar petrology and geochronology. Earth Planet. Sci. Lett. 304, 326–336. https://doi.org/10.1016/j.epsl.2011.02.004

Elkins-Tanton, L.T., Parmentier, E.M., Hess, P.C., 2003. Magma ocean fractional crystallization and cumulate overturn in terrestrial planets: Implications for Mars. Meteorit. Planet. Sci. 38, 1753–1771. https://doi.org/10.1111/j.1945-5100.2003.tb00013.x

Fegley, B., Cameron, A.G.W., 1987. A vaporization model for iron/silicate fractionation in the Mercury protoplanet. Earth Planet Sci. Lett. 82, 207–222. https://doi.org/10.1016/0012-821X(87)90196-8

Fischer, E.L., Parman, S.W., 2025. The bulk composition and initial size of Mercury. Icarus 439, 116664. https://doi.org/10.1016/j.icarus.2025.116664

Genova, A., Goossens, S., Mazarico, E., Lemoine, F.G., Neumann, G.A., Kuang, W., Sabaka, T.J., Hauck, S.A., Smith, D.E., Solomon, S.C., Zuber, M.T., 2019. Geodetic Evidence That Mercury Has A Solid Inner Core. Geophys. Res. Lett. 46, 3625–3633. https://doi.org/10.1029/2018GL081135

Goossens, S., Renaud, J.P., Henning, W.G., Mazarico, E., Bertone, S., Genova, A., 2022. Evaluation of recent measurements of Mercury's moments of inertia and tides using a comprehensive Markov Chain Monte Carlo method. Planet. Sci. J. 3, 37. https://doi.org/10.3847/PSJ/ac4bb8

Greenwood, R.C., Franchi, I.A., Jambon, A., Buchanan, P.C., 2005. Widespread magma oceans on asteroidal bodies in the early Solar System. Nat. 435, 916–918. https://doi.org/10.1038/nature03612

Grove, T.L., Krawczynski, M.J., 2009. Lunar mare volcanism: where did the magmas come from? Elements 5, 29–34. https://doi.org/10.2113/gselements.5.1.29

Gu, T., Stagno, V., Fei, Y., 2019. Partition coefficient of phosphorus between liquid metal and silicate melt with implications for the Martian magma ocean. Phys. Earth Planet. Inter. 295, 106298. https://doi.org/10.1016/j.pepi.2019.106298

Hamano, K., Abe, Y., Genda, H., 2013. Emergence of two types of terrestrial planet on solidification of magma ocean. Nat. 497, 607–610. https://doi.org/10.1038/nature12163

Hamano, K., Kawahara, H., Abe, Y., Onishi, M., Hashimoto, G.L., 2015. Lifetime and spectral evolution of a magma ocean with a steam atmosphere: its detectability by future direct imaging. Astrophys. J. 806, 216. https://doi.org/10.1088/0004-637X/806/2/216

Hauck, S.A., Margot, J., Solomon, S.C., Phillips, R.J., Johnson, C.L., Lemoine, F.G., Mazarico, E., McCoy, T.J., Padovan, S., Peale, S.J., Perry, M.E., Smith, D.E., Zuber, M.T., 2013. The curious case of Mercury's internal structure. J. Geophys. Res. Planets 118, 1204–1220. https://doi.org/10.1002/jgre.20091

Head, J.W., Chapman, C.R., Strom, R.G., Fassett, C.I., Denevi, B.W., Blewett, D.T., Ernst, C.M., Watters, T.R., Solomon, S.C., Murchie, S.L., Prockter, L.M., Chabot, N.L., Gillis-Davis, J.J., Whitten, J.L., Goudge, T.A., Baker, D.M.H., Hurwitz, D.M., Ostrach, L.R., Xiao, Z., Merline, W.J., Kerber, L., Dickson, J.L., Oberst, J., Byrne, P.K., Klimczak, C., Nittler, L.R., 2011. Flood volcanism in the northern high latitudes of Mercury revealed by MESSENGER. Science 333, 1853–1856. https://doi.org/10.1126/science.1211997

Hess, P.C., Parmentier, E.M., 1995. A model for the thermal and chemical evolution of the Moon's interior: implications for the onset of mare volcanism. Earth Planet Sci. Lett. 134, 501–514. https://doi.org/10.1016/0012-821X(95)00138-3

Hubbard, A., 2014. Explaining Mercury's density through magnetic erosion. Icarus 241, 329–335. https://doi.org/10.1016/j.icarus.2014.06.032

Jarosewich, E., 1990. Chemical analyses of meteorites: a compilation of stony and iron meteorite analyses. Meteoritics 25, 323-337.

Johnson, C.L., Anderson, B.J., Korth, H., Phillips, R.J., Philpott, L.C., 2018. Mercury's internal magnetic field, in: Solomon, S.C., Nittler, L.R., Anderson, B.J. (Eds.), Mercury. Cambridge University Press, pp. 114–143. https://doi.org/10.1017/9781316650684.006

Khurana, K.K., Jia, X., Kivelson, M.G., Nimmo, F., Schubert, G., Russell, C.T., 2011. Evidence of a global magma ocean in Io's interior. Science 332, 1186–1189. https://doi.org/10.1126/science.1201425

Knibbe, J.S., Van Westrenen, W., 2018. The thermal evolution of Mercury's Fe–Si core. Earth Planet Sci. Lett. 482, 147–159. https://doi.org/10.1016/j.epsl.2017.11.006

Kraettli, G., Schmidt, M.W., Liebske, C., 2022. Fractional crystallization of a basal lunar magma ocean: A dense melt-bearing garnetite layer above the core? Icarus 371, 114699. https://doi.org/10.1016/j.icarus.2021.114699

Labrosse, S., Hernlund, J.W., Coltice, N., 2007. A crystallizing dense magma ocean at the base of the Earth's mantle. Nat. 450, 866–869. https://doi.org/10.1038/nature06355

Lawrence, D.J., Peplowski, P.N., Beck, A.W., Feldman, W.C., Frank, E.A., McCoy, T.J., Nittler, L.R., Solomon, S.C., 2017. Compositional terranes on Mercury: information from fast neutrons. Icarus 281, 32–45. https://doi.org/10.1016/j.icarus.2016.07.018

Leger, A., Grasset, O., Fegley, B., Codron, F., Albarede, A.F., Barge, P., Barnes, R., Cance, P., Carpy, S., Catalano, F., Cavarroc, C., Demangeon, O., Ferraz-Mello, S., Gabor, P., Grießmeier, J.M., Leibacher, J., Libourel, G., Maurin, A.S., Raymond, S.N., Rouan, D., Samuel, B., Schaefer, L., Schneider, J., Schuller, P.A., Selsis, F., Sotin, C., 2011. The extreme physical properties of the CoRoT-7b super-Earth. Icarus 213, 1–11. https://doi.org/10.1016/j.icarus.2011.02.004.

Lewis, J.S., 1973. Chemistry of the planets. Annu. Rev. Phys. Chem. 24, 339–351. https://doi.org/10.1146/annurev.pc.24.100173.002011

Liebske, C., Schmickler, B., Terasaki, H., Poe, B., Suzuki, A., Funakoshi, K., Ando, R., Rubie, D., 2005. Viscosity of peridotite liquid up to 13 GPa: Implications for magma ocean viscosities. Earth Planet Sci. Lett. 240, 589–604. https://doi.org/10.1016/j.epsl.2005.10.004

Malavergne, V., Toplis, M.J., Berthet, S., Jones, J., 2010. Highly reducing conditions during core formation on Mercury: Implications for internal structure and the origin of a magnetic field. Icarus 206, 199–209. https://doi.org/10.1016/j.icarus.2009.09.001

Mandler, B.E., Elkins-Tanton, L.T., 2013. The origin of eucrites, diogenites, and olivine diogenites: magma ocean crystallization and shallow magma chamber processes on Vesta. Meteorit. Planet. Sci. 48, 2333–2349. https://doi.org/10.1111/maps.12135

Mangler, M.F., Humphreys, M.C.S., Iveson, A.A., Cooper, K.M., Clynne, M.A., Lindoo, A., Brooker, R.A., Wadsworth, F.B., 2024. Crystal resorption as a driver for mush maturation: an experimental investigation. J. Petrol. 65, egae088. https://doi.org/10.1093/petrology/egae088

Margot, J.L., Peale, S.J., Jurgens, R.F., Slade, M.A., Holin, I.V., 2007. Large longitude libration of Mercury reveals a molten core. Science 316, 710–714. https://doi.org/10.1126/science.1140514

Maurice, M.O., 2020. The influence of magma ocean crystallization on mantle dynamics: investigating the Martian and lunar magma oceans. Doctoral thesis, Technischen Universität Berlin.

Maurice, M.O., Dasgupta, R., Hassanzadeh, P., 2024. Volatile atmospheres of lava worlds. Astron. Astrophys. 688, A47. https://doi.org/10.1051/0004-6361/202347749

McClintock, W.E., Cassidy, T.A., Merkel, A.W., Killen, R.M., Burger, M.H., Vervack, R.J., 2018. Observations of Mercury's exosphere: composition and structure, in: Solomon, S.C., Nittler, L.R., Anderson, B.J. (Eds.), Mercury. Cambridge University Press, pp. 371–406. https://doi.org/10.1017/9781316650684.015

McCoy, T.J., Dickinson, T.L., Lofgren, G.E., 1999. Partial melting of the indarch (EH4) meteorite: a textural, chemical, and phase relations view of melting and melt migration. Meteorit. Planet. Sci. 34 (5), 735–746. https://doi.org/10.1111/j.1945- 5100.1999.tb01386.x.

McCoy, T.J., Peplowski, P.N., McCubbin, F.M., Weider, S.Z., 2018. The Geochemical and Mineralogical Diversity of Mercury, in: Solomon, S.C., Nittler, L.R., Anderson, B.J. (Eds.), Mercury. Cambridge University Press, pp. 176–190. https://doi.org/10.1017/9781316650684.008

McDonough, W.F., 2025. Earths composition: origin, evolution, and energy budget. https://doi.org/10.48550/arXiv.2505.02641

McDonough, W.F., Yoshizaki, T., 2021. Terrestrial planet compositions controlled by accretion disk magnetic field. Prog. Earth Planet. Sci. 8. https://doi.org/10.1186/s40645-021-00429-4

McNutt, R.L. Jr., Benkhoff, J., Fujimoto, M., Anderson, B.J., 2018. Future Missions: Mercury after MESSENGER, 2018., in: Mercury. Cambridge University Press, pp. 544–569. https://doi.org/10.1017/9781316650684.021

Mouser, M.D., Dygert, N., 2023. On the potential for cumulate mantle overturn in Mercury. J. Geophys. Res. Planets 128, e2023JE007739. https://doi.org/10.1029/2023JE007739

Mouser, M.D., Dygert, N., Anzures, B.A., Grambling, N.L., Hrubiak, R., Kono, Y., Shen, G., Parman, S.W., 2021. Experimental investigation of Mercury's magma ocean viscosity: implications for the formation of Mercury's cumulate mantle, its subsequent dynamic evolution, and crustal petrogenesis. J. Geophys. Res. Planets 126, e2021JE006946. https://doi.org/10.1029/2021JE006946

Namur, O., Charlier, B., Holness, M.B., 2012. Dual origin of Fe-Ti-P gabbros by immiscibility and fractional crystallization of evolved tholeiitic basalts in the Sept Iles layered intrusion. Lithos, 154, 100-114. https://doi.org/10.1016/j.lithos.2012.06.034

Namur, O., Charlier, B., Holtz, F., Cartier, C., McCammon, C., 2016a. Sulfur solubility in reduced mafic silicate melts: implications for the speciation and distribution of sulfur on Mercury. Earth Planet Sci. Lett. 448, 102–114. https://doi.org/10.1016/j.epsl.2016.05.024

Nittler, L.R., Chabot, N.L., Grove, T.L., Peplowski, P.N., 2018. The chemical composition of Mercury, in: Solomon, S.C., Nittler, L.R., Anderson, B.J. (Eds.), Mercury. Cambridge University Press, pp. 30–51. https://doi.org/10.1017/9781316650684.003

O'Rourke, J.G., 2020. Venus: a thick basal magma ocean may exist today. Geophys. Res. Lett. 47, e2019GL086126. https://doi.org/10.1029/2019GL086126

Padovan, S., Wieczorek, M.A., Margot, J., Tosi, N., Solomon, S.C., 2015. Thickness of the crust of Mercury from geoid-to-topography ratios. Geophys. Res. Lett. 42, 1029–1038. https://doi.org/10.1002/2014GL062487

Peplowski, P.N., Stockstill-Cahill, K., 2019. Analytical identification and characterization of the major geochemical terranes of Mercury's northern hemisphere. J. Geophys. Res. Planets 124, 2414–2429. https://doi.org/10.1029/2019JE005997

Pirotte, H., Cartier, C., Namur, O., Pommier, A., Zhang, Y., Berndt, J., Klemme, S., Charlier, B., 2023. Internal differentiation and volatile budget of Mercury inferred from the partitioning of heat-producing elements at highly reduced conditions. Icarus 405, 115699. https://doi.org/10.1016/j.icarus.2023.115699

Prissel, T.C., Zhang, N., Jackson, C.R.M., Li, H., 2023. Rapid transition from primary to secondary crust building on the Moon explained by mantle overturn. Nat. Commun. 14, 5002. https://doi.org/10.1038/s41467-023-40751-7

Rolf, T., Steinberger, B., Sruthi, U., Werner, S.C., 2018. Inferences on the mantle viscosity structure and the post-overturn evolutionary state of Venus. Icarus 313, 107–123. https://doi.org/10.1016/j.icarus.2018.05.014

Roscoe, R., 1952. The viscosity of suspensions of rigid spheres. Br. J. Appl. Phys. 3, 267–269. https://doi.org/10.1088/0508-3443/3/8/306

Russell, J.K., Hess, K.-U., Dingwell, D.B., 2024. Ultramafic melt viscosity: A model. Earth Planet Sci. Lett. 643, 118899. https://doi.org/10.1016/j.epsl.2024.118899

Sachs, A., 1974. Babylonian observational astronomy. Phil. Trans. R. Soc. Lond. A. 276, 43-50.

Sakamaki, T., Ohtani, E., 2022. High pressure melts. Rev. Mineral. Geochem. 87, 557–574. https://doi.org/10.2138/rmg.2022.87.11

Salvador, A., Avice, G., Breuer, D., Gillmann, C., Lammer, H., Marcq, E., Raymond, S.N., Sakuraba, H., Scherf, M., Way, M.J., 2023. Magma ocean, water, and the early atmosphere of Venus. Space Sci. Rev. 219, 51. https://doi.org/10.1007/s11214-023-00995-7

Sanloup, C., Jambon, A., Gillet, P., 1999. A simple chondritic model of Mars. Phys. Earth Planet. Inter. 112, 43–54. https://doi.org/10.1016/S0031-9201(98)00175-7

Saracino, F., Charlier, B., Zhang, Y., Lécaille, M., Lin, Y., Namur, O., 2025. The role of sulfur on the liquidus temperature and olivine-orthopyroxene equilibria in highly reduced magmas. Chem. Geol. 683, 122777. https://doi.org/10.1016/j.chemgeo.2025.122777

Schaefer, L., Elkins-Tanton, L.T., 2018. Magma oceans as a critical stage in the tectonic development of rocky planets. Phil. Trans. R. Soc. A. 376, 20180109. https://doi.org/10.1098/rsta.2018.0109

Schnetzler, C.C., Philpotts, J.A., 1971. Alkali, alkaline Earth, and rare-Earth element concentrations in some Apollo 12 soils, rocks, and separated phases. Proc. Lunar Sci. Conf. 2, 1101-1122.

Schubert, G., Ross, M.N., Stevenson, D.J., Spohn, T., 1988. Mercury's thermal history and the generation of its magnetic field. In Mercury, ed. F. Vilas, C. R. Chapman, and M. S. Matthews. Tucson, AZ: University of Arizona Press, pp. 429–460.

Shervais, J.W., Taylor, L.A., 1986. Petrologic constraints on the origin of the Moon. In Origin of the Moon (Eds. Hartmann, W.K., Phillips, R.J., Taylor, G.J.): Proc. Conf., Kona, HI, October 13-16, 1984.

Shirley, D.L., 2003. The Mariner 10 mission to Venus and Mercury. Acta Astronaut. 53, 375–385. https://doi.org/10.1016/S0094-5765(03)00155-3

Smith, J.V., Anderson, A.T., Newton, R.C., Olsen, E.J., Wyllie, P.J., 1970. Petrologic history of the moon inferred from petrography, mineralogy, and petrogenesis of Apollo 11 rocks. Proc. Apollo11 Lunar Sci. Conf. 1, 897-925.

Solomatov, V., 2015. Magma oceans and primordial mantle differentiation, in: Treatise on Geophysics. Elsevier, pp. 81–104. https://doi.org/10.1016/B978-0-444-53802-4.00155-X

Solomon, S.C., 2003. Mercury: the enigmatic innermost planet. Earth Planet Sci. Lett. 216, 441–455. https://doi.org/10.1016/S0012-821X(03)00546-6

Solomon, S.C., Anderson, B.J., 2018. The MESSENGER mission: science and implementation overview, in: Solomon, S.C., Nittler, L.R., Anderson, B.J. (Eds.), Mercury. Cambridge University Press, pp. 1–29. https://doi.org/10.1017/9781316650684.002

Solomon, S.C., Jr, R.L.M., Gold, R.E., Acuna, M.H., Baker, D.N., Boynton, W.V., Chapman, C.R., Cheng, A.F., Gloeckler, G., Peale, S.J., Phillips, R.J., Robinson, M.S., Slavin, J.A., Smith, D.E., Strom, R.G., Trombka, J.I., Zuber, M.T., 2001. The MESSENGER mission to Mercury: scientific objectives and implementation. Planet. Space Sci.

Steenstra, E.S., Seegers, A.X., Putter, R., Berndt, J., Klemme, S., Matveev, S., Bullock, E.S., Van Westrenen, W., 2020. Metal-silicate partitioning systematics of siderophile elements at reducing conditions: A new experimental database. Icarus 335, 113391. https://doi.org/10.1016/j.icarus.2019.113391

Steinbrügge, G., Dumberry, M., Rivoldini, A., Schubert, G., Cao, H., Schroeder, D.M., Soderlund, K.M., 2021. Challenges on Mercury's interior structure posed by the new measurements of its obliquity and tides. Geophys. Res. Lett. 48, e2020GL089895. https://doi.org/10.1029/2020GL089895

Strom, R.G., Sprague, A.L., 2003. Exploring Mercury: The Iron Planet. Springer / Praxis.

Tang, H., Dauphas, N., 2014. 60Fe–60Ni chronology of core formation in Mars. Earth Planet Sci. Lett. 390, 264–274. https://doi.org/10.1016/j.epsl.2014.01.005

Taylor, G.J., Norman, M.D., 1992. Evidence for magma oceans on asteroids, the Moon, and Earth. Workshop on the Physics and Chemistry of Magma Oceans from 1 Bar to 4 Mbar p 58-65, LPI.

Trønnes, R.G., Baron, M.A., Eigenmann, K.R., Guren, M.G., Heyn, B.H., Løken, A., Mohn, C.E., 2019. Core formation, mantle differentiation and core-mantle interaction within Earth and the terrestrial planets. Tectonophysics 760, 165–198. https://doi.org/10.1016/j.tecto.2018.10.021

Vander Kaaden, K.E., McCubbin, F.M., 2015. Exotic crust formation on Mercury: consequences of a shallow, FeO-poor mantle. J. Geophys. Res. Planets 120, 195–209. https://doi.org/10.1002/2014JE004733

Vander Kaaden, K.E., McCubbin, F.M., Byrne, P.K., Chabot, N.L., Ernst, C.M., Johnson, C.L., Thompson, M.S., 2019. Revolutionizing our understanding of the solar system via sample return from Mercury. Space Sci. Rev. 215, 49. https://doi.org/10.1007/s11214-019-0614-x

Vander Kaaden, K.E., McCubbin, F.M., Nittler, L.R., N. Peplowski, P.N., Weider, S.Z., Frank, E.A., McCoy, T.J., 2017. Geochemistry, mineralogy, and petrology of boninitic and komatiitic rocks on the Mercurian surface: insights into the Mercurian mantle. Icarus 285, 155–168. https://doi.org/10.1016/j.icarus.2016.11.041

Walker, D., Longhi, J., Hays, J.F., 1975. Differentiation of a very thick magma body and implications for the source regions of mare basalts. Proc. Lunar Sci. Conf. 6, 1103-1120.

Wang, Y., Sakamaki, T., Skinner, L.B., Jing, Z., Yu, T., Kono, Y., Park, C., Shen, G., Rivers, M.L., Sutton, S.R., 2014. Atomistic insight into viscosity and density of silicate melts under pressure. Nat. Commun. 5, 3241. https://doi.org/10.1038/ncomms4241

Wang, Y., Xiao, Z., Xu, R., 2022. Multiple mantle sources of high-magnesium terranes on Mercury. J. Geophys. Res. Planets 127, e2022JE007218. https://doi.org/10.1029/2022JE007218

Wardinski, I., Langlais, B., Thébault, E., 2019. Correlated time-varying magnetic fields and the core size of Mercury. J. Geophys. Res. Planets 124, 2178–2197. https://doi.org/10.1029/2018JE005835

Warren, P.H., 1985. The magma ocean concept and Lunar evolution. Ann. Rev. Earth Planet. Sci. 13, 201 – 240. 10.1146/annurev.ea.13.050185.001221

Weidenschilling, S.J., 1978. Iron/silicate fractionation and the origin of Mercury. Icarus 35, 99–111. https://doi.org/10.1016/0019-1035(78)90064-7

Weider, S.Z., Nittler, L.R., Starr, R.D., Crapster-Pregont, E.J., Peplowski, P.N., Denevi, B.W., Head, J.W., Byrne, P.K., Hauck, S.A., Ebel, D.S., Solomon, S.C., 2015. Evidence for geochemical terranes on Mercury: global

mapping of major elements with MESSENGER's x-ray spectrometer. Earth Planet Sci. Lett. 416, 109–120. https://doi.org/10.1016/j.epsl.2015.01.023

Wood, J.A., Dickey, J.S., Marvin, U.B., Powell, B.N., 1970. Lunar anorthosites and a geophysical model of the moon. Proc. Apollo 11 Lun. Sci. Conf. 1, 965-988.

Wurm, G., 2018. Selective aggregation experiments on planetesimal formation and Mercury-like planets. Geosci. 8, 310. https://doi.org/10.3390/Geosci.8090310

Wurm, G., Trieloff, M., Rauer, H., 2013. Photophoretic separation of metals and silicates: the formation of mercury-like planets and metal depletion in chondrites. Astrophys. J. 769, 78. https://doi.org/10.1088/0004-637X/769/1/78

Xu, Y., Lin, Y., Wu, P., Namur, O., Zhang, Y., Charlier, B., 2024. A diamond-bearing core-mantle boundary on Mercury. Nat. Commun. 15, 5061. https://doi.org/10.1038/s41467-024-49305-x

Zhang, Y., Charlier, B., Krein, S.B., Grove, T.L., Namur, O., Holtz, F., 2024. The very late-stage crystallization of the lunar magma ocean and the composition of immiscible urKREEP. Earth Planet Sci. Lett. 646, 118989.

Zolotov, M.Yu., Sprague, A.L., Hauck, S.A., Nittler, L.R., Solomon, S.C., Weider, S.Z., 2013. The redox state, FeO content, and origin of sulfur-rich magmas on Mercury. J. Geophys. Res. Planets 118, 138–146. https://doi.org/10.1029/2012JE004274

Chapter 2: Methodology

2.1. Preparation of Starting Materials

The composition of a magma ocean is expected to vary significantly from the beginning right to the end of crystallization. As this doctoral project aims at investigating the chemical evolution of a global scale magma ocean on planet Mercury, multiple starting materials are needed to recreate the evolving composition of the silicate liquid. This approach is inspired by Charlier et al. (2018) who investigated the crystallization products of the lunar magma ocean. For the first part of this doctoral project (Chapter 3), the first compositions that we consider need to represent the average composition of the silicate portion of the planet, or Bulk Silicate Mercury (BSMe) as it formed after the separation of the metallic core from the silicate component. The starting composition Mer8 and Mer15 are reported in Table 1.2. and a discussion on how they were determined can be found in Section 1.1.4. (Chapter 1). Testing starting compositions with a range of different Mg/Si proves indeed important as this has been shown to deeply affect the layering of Mercury's primordial mantle (Anzures et al., 2020; Saracino et al., 2025). For the second part of the project (Chapter 4), we prepared starting powders that represent the residual liquid of the MMO as the cumulus thickens with decreasing melt fraction *F*. Mer_1, Mer_2, and Mer_3 were then prepared. A detailed explanation of how they were determined is proposed in Section 4.1. (Chapter 4). The compositions of all starting materials are shown in Table 2.1.

Table 2.1. *Chemical composition of the silicate starting materials used throughout the doctoral project. n.d. – not determined.*

	Mer8	Mer15	Mer_1	Mer_2	Mer_3
SiO_2	54.82	47.91	56.53	62.91	66.48
TiO_2	0.14	0.16	0.38	0.17	0.16
Al_2O_3	3.70	4.26	9.46	13.85	16.62
Cr_2O_3	0.52	0.60	0.56	0.11	0.02
MnO	0.28	0.33	0.37	0.31	0.04
MgO	37.32	43.04	24.01	11.95	4.39
CaO	1.62	1.87	4.33	5.12	5.68
Na_2O	1.37	1.58	3.75	5.10	6.00
K_2O	0.13	0.15	0.36	0.49	0.60
P_2O_5	0.10	0.10	0.26	n.d.	n.d.
Total	100.00	100.00	100.00	100.00	100.00

The starting powders were produced from high-purity oxide powders: SiO_2, TiO_2, Al_2O_3, Cr_2O_3, MnO, MgO, $CaSiO_3$, Na_2SiO_3, $K_2Si_4O_9$, and $AlPO_4$. $CaSiO_3$ and Na_2SiO_3 were produced following simple reactions of decarbonation, as shown below:

$$CaCO_3 + SiO_2 = CaSiO_3 + CO_2 \quad \text{(Eq. 2.1)}$$

$$Na_2CO_3 + SiO_2 = Na_2SiO_3 + CO_2 \quad \text{(Eq. 2.2)}$$

All the settings for the preparation of the powders are reported in Table 2.2. To obtain reducing conditions for our experimental runs, a strongly reducing agent like metallic Si is needed (Cartier and Wood, 2019). We therefore prepared our powders with different metallic Si/SiO_2 ratios in the starting materials to obtain a range of oxygen fugacity consistent with the average fO_2 estimated for the silicate interior of Mercury. Once the powders were prepared, they were mixed in an agate mortar with methanol. Both S-free and S-bearing compositions were prepared, with FeS, S, or a mixture of FeS+S being added to the starting materials to ensure sulfide saturation. All the powder mixtures were stored in oven at 120 °C.

Table 2.2. *List of oxide components produced at the laboratory in Liege.*

Oxide Powders	Reaction	Drying settings reactants	Drying settings products
MgO			1400 ℃ for 96 h
SiO_2			1100 ℃ for 72 h
$CaCO_3$			400 ℃ for 12 h
$CaSiO_3$	$SiO_2 + CaCO_3 = CaSiO_3 + CO_2$	$CaCO_3$ – 400 ℃ for 4 h SiO_2 – See above	750 ℃ for 12 h / After / 1100 ℃ for 96 h
Na_2SiO_3	$SiO_2 + Na_2CO_3 = Na_2SiO_3 + CO_2$	Na_2CO_3 – 750 ℃ for 48 h SiO_2 – See above	750 ℃ for for 12 h / After / 750 ℃ for 96 h
$K_2Si_4O_9$	$4\ SiO_2 + K_2CO_3 = K_2Si_4O_9 + CO_2$	K_2CO_3 – 700 ℃ for 116 h SiO_2 – See above	

2.2. Experimental Strategy

Our entire project has been revolving around the use of the piston cylinder. The piston-cylinder apparatus is a device able to investigate phase equilibria at high pressures and high temperatures, usually 0.2 – 5.0 GPa and 600 to 2000 ˚C (Boyd and England, 1960; Dunn, 1993; McDade et al., 2002). The first person to design an instrument capable of applying both high pressure and temperature to a solid

substance was the English engineer C. A. Parsons (Parsons, 1888). Parsons' original design was later improved by Bridgman (1940). The basis for the modern piston cylinder designs is after the work of Boyd and England (1960), who were the first to use a device of this sort to investigate the interior structure of Earth. The pressure and temperature ranges attained by piston-cylinder apparatuses make them indeed well suited for investigating crustal and upper mantle conditions on Earth, or even core conditions on smaller bodies (Condamine et al., 2022). The modern concept of the piston-cylinder is to exert pressure on a sample assembly in a tungsten carbide (WC) vessel supported by a steel ring (Boyd and England, 1960) (Fig. 2.1.).

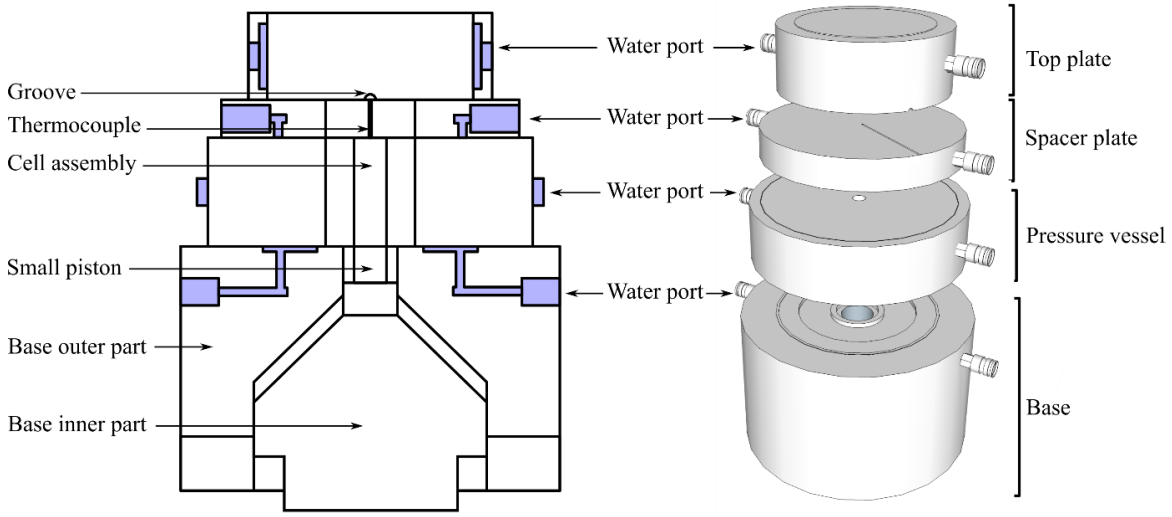

Figure 2.1. *Two-dimensional (left) and three-dimensional (right) model of an end-loaded piston-cylinder (Pirotte, 2023). The assembly containing the sample is placed in the pressure vessel.*

Pressure transfer to the sample via a solid pressure medium is achieved by means of pressure amplification. A small load of a large steel piston is converted into a large load on a small piston (Dunn, 1993). Pressure amplification can be expressed as follows:

$$p_{\mathrm{nom}}(kbar) = 10^{-3}\frac{\pi r_{\mathrm{ram}}^2}{\pi r_{\mathrm{piston}}^2}p_{oil}(bar) \qquad \text{(Eq. 2.3)}$$

Where r_{ram} is the radius of the upper ram, r_{piston} is the radius of the piston, p_{oil} is the hydraulic pressure of the oil. It is clear from this relation that small pistons will be able to achieve higher pressure than larger pistons. This translates into different cell assembly sizes (expressed in inches, ½ ", ¾ ", 1"), based on the pressure range investigated. Piston cylinders are usually divided into two types: *non-end-loaded* piston cylinders possess one hydraulic pump, and the pressure attained cannot exceed 2.2 GPa, which corresponds to the strength of WC in the core vessel. *End-loaded* piston cylinders, on the other hand, are equipped with two hydraulic pumps allowing them to attain higher pressures (3 – 6 GPa), which can vary depending on the type of steel alloy employed for the vessel (Vetere, 2024). Temperature is

applied by setting a regulated voltage to the furnace and is monitored with a thermocouple (Dunn, 1993). Thermocouples can be of different materials (like Pt-Rh or W-Re) and of different types (according to the relative metal proportions) (Dunn, 1993). Attaining the entire spectrum of temperature and pressure conditions also depends on the properties of the materials making up the different cell assemblies (McDade et al., 2002). The more widely used materials for cell assemblies are NaCl, talc+pyrex, and $BaCO_3$. NaCl cells are suited for low T (< 1600 °C), low-to-high pressure runs, and for short and long durations. $BaCO_3$ are more suited for high temperature (> 1600 °C), low-to-high pressure, and for all durations. Talc assemblies behave well at high temperature (T > 1600 °C), although their use at high pressure should be avoided, given their high frictional correction factor (as too much pressure would be applied to the WC core) (Condamine et al., 2022 and references therein). Capsules are also a major component in piston cylinders cell assemblies, as they contain the samples to study. They can be made of different materials like Au, Pt, graphite, and AgPd alloys. Importantly, capsules need to be weak in order not to interfere with the pressure transmission and be quite inert to not react with the sample (Dunn, 1993). As for this doctoral project, low-to-high pressure (0.5 – 3.0 GPa) and high temperature (1125 – 1950 ˚C) experiments featured in this thesis were conducted by employing the Voggenreiter Mavo LPC 250-300/50 end-loaded piston-cylinder located in the Laboratory of Petrology, Geochemistry, and Petrophysics of the University of Liege (Fig. 2.2.). All experiments here featured were conducting using graphite capsules. These were chosen for several reasons. First, they buffer the oxygen fugacity at the C-CO equilibrium. Graphite is also quite inert as a material and reacts little with the silicate phases. Also, Mercury likely differentiated in C-saturated conditions (Steenstra and van Westrenen, 2020). For experiments conducted at pressures between 1.0 and 3.0 GPa, half an inch assemblies were employed coupled with $BaCO_3$ cells (Fig. 2.3.a). The latter were produced by sintering $BaCO_3$ powder mixed with toner ink at room temperature and later fired in a muffle furnace at T = 700 °C for 25 minutes. For experiments conducted at 0.5 GPa, three quarters inch assemblies in combination with talc+pyrex cells were used (Fig. 2.3.b).

Figure 2.2. *End-loaded Voggenreiter Mavo LPC 250-300/50 piston-cylinder model at the Department of Geology, University of Liege (Belgium).*

The starting powders (~10 mg) were packed into graphite capsules and dried in the oven at 120 ℃. The capsule is surrounded by a Al_2O_3 sleeve and MgO spacers and inserted into a graphite furnace. $BaCO_3$ cells were used as the pressure medium. Assembled cells are eventually wrapped in a polytetrafluoroethylene (PTFE) sheet. Details on the cell assembly are shown in Fig. 2.3. Assemblies are first pressurized at room temperature up to 0.7 GPa for half inch assemblies, or 0.4 GPa for three quarters inch assemblies. Next, temperature is increased to 865 ℃ at 100 ℃/min. A temperature dwell is then followed during which the target pressure is attained. The duration of the dwell can vary depending on the target pressure. After the dwell, a new increase in temperature is followed (at 50 ℃/min) up to the target temperature. The difference in temperature between the tip of the thermocouple and the centre of the capsule is ~ 25 ℃. During the course of the doctoral project, 'spontaneous' pressure increase was observed particularly in S-bearing runs at temperatures higher than 1300 ˚C. Lower ram pressure was therefore kept 10-to-20 bars below the target pressure to compensate for such an effect. Experiments were eventually quenched by switching off the power supply. A list comprising all experimental runs featured in this doctoral thesis can be found in the supplementary information (Appendix E).

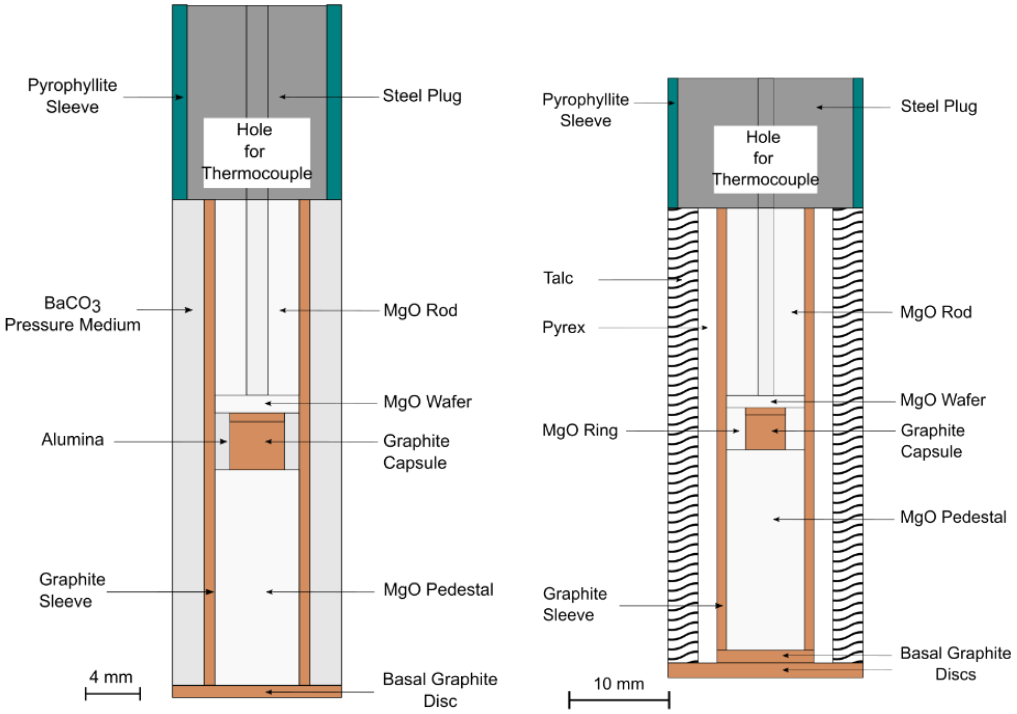

Figure 2.3. *Two dimensional sketches of the (left) 1/2" assembly and (right) 3/4" inch assembly employed during this doctoral project. Both assemblies were wrapped in PTFE prior to insertion into the pressure vessel of the piston–cylinder.*

2.2.1. Sample Recovery and Mounting

After quenching the experiments, the samples are extracted from the experimental assembly (Fig. 2.4.). The extracted capsules are later glued into a thin section, mounted on a diamond wafer saw apparatus and cut into two halves. The two halves are then detached from the thin section and placed in a silicone mold and eventually mounted in epoxy. The epoxy is later left solidifying for ~ 14 hours. Samples are later polished with increasingly fine SiC polishing pads (800, 1200, 2400, 4000 P# grits), and finally with a 1 µm diamond pads. They are now ready to be analyzed.

Figure 2.4. *Freshly extracted 3/4" assembly after quenching an experimental run. The assembly is wrapped in PTFE (greyish film) and covered in a mixture of mineral oil and MoS_2 (or molikote, dark stains on the PTFE sheet) to facilitate the assembly extraction from the pressure vessel of the piston-cylinder. The steel plug for the thermocouple insertion can be seen on the top of the image (the pyrophyllite ring encircling the steel plug is missing).*

2.3. Analytical Strategy

Sample characterization was performed through non-destructive qualitative and quantitative analytical techniques. Qualitative analyses were performed via Scanning Electron Microscopy (SEM) to identify the silicate phases (crystals and glass), metals, and sulfides and for illustrative purposes. On the other hand, quantitative analyses were conducted via Electron Probe Micro-Analysis (EPMA) to retrieve the chemical composition of all the identified phases. A review of the two analytical techniques employed over the course of this doctoral project is now presented.

2.3.1. Scanning Electron Microscopy

Scanning Electron Microscopy (SEM) is an analytical technique designed for micro elemental analysis and for imaging of solid samples in a wide range of physical sciences (Newbury and Ritchie, 2013; Goldstein et al., 2003). The principles of the SEM were first outlined by Knoll (1935), and the first microscope was built by von Ardenne (1938). The basic idea of the SEM is to target a sample with an energetic source to characterize it. The volume of the specimen is irradiated by an electron beam with energy in the range 5 – 30 keV (Reed, 2005), originated from an electron source (or gun), which is focussed thanks to the use of apertures and electromagnetic coils (Goldstein et al., 2003). When the electrons impinge on the targeted sample, both elastic – meaning that they involve little energy loss -

and inelastic - with high energy loss - scattering processes occur (Wenk, 1976). Electrons are particularly slowed down during inelastic interactions, which are defined as interactions between the impinging electrons and the bound electrons or the lattice of the specimen. The amount of energy loss is called *stopping power* and is dependent on the density of the targeted sample (Reed, 2005). Elastic scattering occurs when the incident electron gets deflected by the specimen's atomic nuclei (Fig. 2.5.). This type of interaction implies almost no loss of energy, due to the large mass of the nucleus as compared to that of the electron (Reed, 2005).

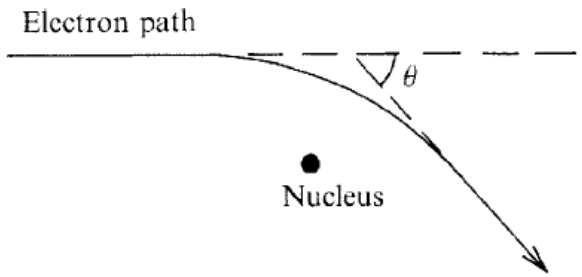

Figure 2.5. *Schematic view of elastic scattering (Reed, 2005).*

As inelastic interactions imply the transfer of energy from the targeting electrons to the specimen's atoms, the excited atoms also release secondary electrons (SE). A fraction of the incident electrons is scattered with an angle larger than 90° and emerge from the interface of the sample. These are referred to as backscattered electrons (BSE). Secondary electrons are characterized by lower energies (a few eV only) as compared to backscattered electrons. Secondary electrons and backscattered electrons are both used for sample imaging. SE images are usually useful to highlight the topography of the sample, while BSE images are mostly used to show the compositional variations of the specimen.

Another type of signal produced by the targeted sample is the emission of x-rays. X-rays are usually produced through two distinct mechanisms (Reed, 2005). A continuous x-ray spectrum is the result of energetic electrons interacting with atomic nuclei. This can cause a change of energy state which takes the form of an x-ray. A characteristic x-ray spectrum is the consequence of the electrons transitioning between different energy levels and they are specific to each elemental species (Fig. 2.6.; Reed, 2005). In this latter case, x-rays are produced when the bombarding electrons excite the electrons of an inner shell of the specimen, which are later ejected. The electron hole created by the incident radiation causes another electron from the outer shell to fill the hole. The difference in energy between the two energy levels is released in the form of an x-ray. Because x-rays are characteristic of each elemental species, x-rays provide compositional information of the sample (Zhou et al., 2006). SEMs are typically equipped with semiconductor Energy Dispersive Spectrometers (EDS), which detect the characteristic x-rays emitted by the sample and convert them into electrical signals. These detectors measure the energy and intensity of the x-rays, producing spectra that allow both qualitative and quantitative analysis

of the sample's composition (Reed, 2005). The energy of the x-rays identifies the elements present, while their intensity reflects the relative abundance. The lowest element concentration that can be detected is referred to as detection limits and is usually expressed in parts per million (ppm). For EDS, detection limits are usually around 1000 ppm or 0.1 wt% for heavier elements (Chew et al., 2021), although recent technological advancements allowed lower detection limits to be attained (Newbury and Ritchie, 2015).

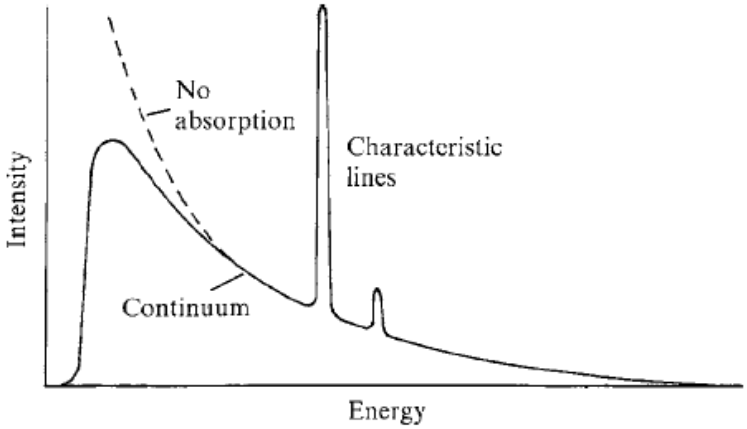

Figure 2.6. *Difference between continuous and characteristic spectra (Reed, 2005).*

Qualitative analysis of our samples, including imaging and phase identification, was performed with the FEI QEMSCAN at RWTH Aachen (Germany), and with the TESCAN MIRA (4th Gen) at the Department of Geology at KU Leuven (Belgium). Backscattered images (BSE) were captured to analyze the different phases present and to show phase textures. Both general and close-up images were taken to highlight textural features and to compare results with mass balance calculations. In RWTH Aachen, BSE images were taken with an accelerating voltage of 15 keV, a 1 nA beam current, and a 10 mm working distance. BSE images in KU Leuven were taken with an accelerating voltage of 15-20 keV, a 1 nA beam current, and a working distance of 15 mm. Selected EDS spectra analyses were also performed to help identify phases, and to retrieve their chemical composition.

2.3.2. Electron Probe Micro-Analysis

The Electron Probe Micro-Analyzer (or EPMA) is an instrument that allows for chemical analyses of selected volumes of solid samples which are hit by a focused beam of electromagnetic radiation of charged particles (Reed, 2005; Potts et al., 1995). The principles for the functioning of the first EPMA were delineated in the doctoral thesis of Castaing in 1951 (Castaing, 1951). The physical principles behind of EPMAs are identical to what has been shown for SEMs. EPMAs generally feature two types of X-ray spectrometers: Energy Diffusive Spectrometers (EDS) and Wavelength-Dispersive

Spectrometers (WDS). While EDS detectors categorize the incident x-ray radiation based on its energy, WDSs sort x-rays based on wavelength thanks to Bragg diffraction from a crystal, which is crucially dependent on measured angles, as shown here:

$$n\lambda = 2d\ sin\theta \qquad \text{(Eq. 2.4)}$$

Where n is the diffraction order, d is the interplanar spacing of θ is the Bragg angle (Fig. 2.7.a). Different diffracting crystals with different d values are used to cover the broad λ range of typical rock-forming elements, so that multiple diffracting crystals are used in an EPMA. Also, the geometry of the crystal is slightly convex rather than flat to obtain an approximately constant Bragg angle (Fig. 2.7.b). Sorting x-rays by wavelength rather than by energy allows WDS measurements to be much accurate than EDS measurements. WDS detectors have detection limits in the order of 10s ppm and possess a spectral resolution that is an order of magnitude higher than that of EDS detectors (Chew et al., 2021). For WDS measurements, a crucial role is played by the interplay between the positioning of the electron source, the angle of the diffracting crystals, and the positioning of the x-ray detector (Ritchie and Newbury, 2013).

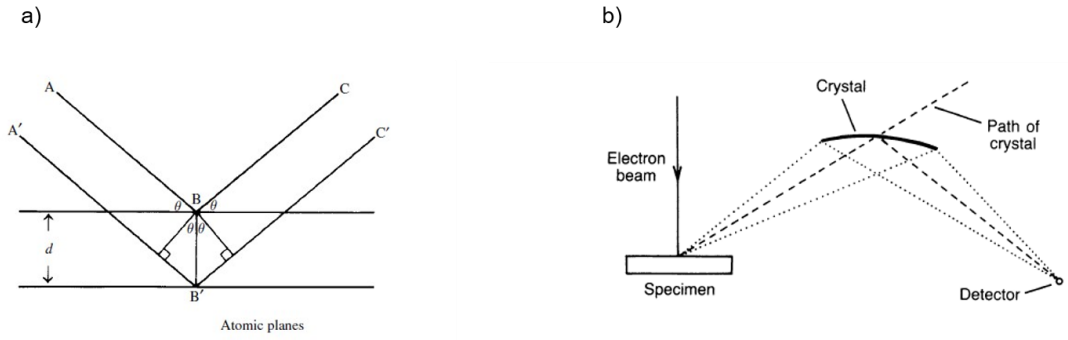

Figure 2.7. *(a) Bragg diffraction (Reed, 2005). (b) Schematic geometry of a Wavelength Dispersive Spectrometer (Potts et al., 1995).*

As for what pertains to our project, quantitative analyses were performed by employing the CAMECA SX Five Tactis at Laboratoire Magmas et Volcans, Université Clermont Auvergne (Clermont-Ferrand, France), and with the JEOL JXA-8530F at the Department of Material Engineering at KU Leuven (Belgium).

In Clermont-Ferrand, silicate crystals, sulfide, and metallic phases were measured with a 15 kV accelerating voltage and 15 nA beam current. Silicate glasses were measured with a 15 kV accelerating voltage and a 4 to 15 nA beam current (depending on the melt fraction). Silicate crystals were analyzed with a focused beam, whereas glasses with a defocused beam (the spot size being 2-20 µm depending on the size of the glass pocket and/or quench textures). Sulfides were measured with a focused beam

and metals with a focused or defocused beam (5-10 μm), depending on the size of the metallic phases and on the presence of heterogeneities and quenched textures. Counting times of 10-30 s were used for each element. Both natural and synthetic calibration standards were employed. The standards for crystals are albite for Na, orthoclase for K and Al, wollastonite for Ca, San Carlos olivine for Si, forsterite for Mg, $TiMnO_3$ for Ti and Mn, Cr_2O_3 for Cr, fayalite for Fe. For the glass we used: albite for Na, orthoclase for K and Al, forsterite for Mg, $TiMnO_3$ for Ti and Mn, Cr_2O_3 for Cr, fayalite for Fe. The same standards were used for the glass phases, except that wollastonite was employed for both Si and Ca, and $BaSO_4$ was used for S. Details on how S was measured in the silicate glass are reported in Chapter 3 (Section 3.2.3.). The calibration standards for the sulfide phases are albite for Na, Si metal for Si, wollastonite for Ca, forsterite for Mg, orthoclase for Al, $TiMnO_3$ for Ti, Cr metal for Cr, chalcopyrite for Fe and S, Mn metal for Mn, Fe_2P for P. The same standards were used for metallic phases, except that Fe metal was used for Fe. A ZAF (Z, atomic number; A, absorption; F, fluorescence) correction was applied to account for inter-elemental (matrix) effects.

In Leuven, silicate crystals and sulfide and metallic phases were measured with a 15 kV accelerating voltage and 10 nA beam current. Silicate glasses were measured with a 15 kV accelerating voltage and a 15 nA beam current. Crystals were analyzed with a focused beam and glasses with a beam defocused to 5–20 μm depending on the size of the glass pool. Sulfides were measured with a focused beam and metals with either a focused or a defocused beam (5–10 μm) depending on the size of the metallic phase and the presence of heterogeneities and quench textures. Peak counting times were 10–30 s and background counting times on each side of the peak were 5–15 s for each element. The standards for crystals are albite for Na, orthoclase for K and Al, diopside for Ca, olivine for Si and Mg, rutile for Ti, MnO for Mn, Cr_2O_3 for Cr, fayalite for Fe. For the glass we used albite for Na, obsidian for K and Al, olivine for Mg, diopside for Ca, rutile for Ti, rhodonite for Mn, Cr_2O_3 for Cr, hematite for Fe, and $BaSO_4$ was used for S. The standards we used for metals and sulfides are albite for Na, Si metal for Si, diopside for Ca, olivine for Mg, obsidian for Al, rutile for Ti, Cr metal for Cr, Fe metal for Fe, Mn metal for Mn, pyrite for S. A CITZAF (Armstrong, 1988) correction was applied to account for the matrix effect.

2.4. Mass Balance Calculations

Mass balance is a major tool in petrology and geochemistry to assess a variety of processes. In igneous petrology, mass balance is employed to investigate fractional crystallization trends, magma mixing, and mantle melting (Li et al., 2020; Janousek et al., 2016). In particular, calculating the balance of masses proves extremely useful to check the quality of compositional data (EDS or WDS data, for example), and to assess the attainment of equilibrium. In a magmatic system, mass balance can be described by the following equation:

$$C_0 = F\ C_{\mathrm{L}} + (1 - F)C_{\mathrm{S}} \qquad \text{(Eq. 2.5)}$$

Where C_0 is the concentration of a component in the system, F is the liquid fraction, C_{L} is the concentration of a component in the liquid fraction, and C_S is the concentration of a component in the solid fraction. For the purpose of this project, mass balance calculations were performed in order to retrieve the relative phase proportions of our experimental runs. A macro-enabled Visual Basic for Application (VBA) Excel program developed by Li et al. (2020) was employed. The composition of the melt, combined with those of the coexisting solid phases (and relative 1σ errors) are needed for the calculation procedure. The starting composition is also needed for the balance of masses to be calculated. The resulting relative proportions (Table 2.3.) are then shown in a separate table together with the associated error (sum of the square error estimate, SSE). Standard deviation estimates of phase proportions are also computed. Mass balance determination was not possible only in the case of the impossibility to retrieve data for very small, solid phases.

Table 2.3. *Example of mass balance determination on run A468.*

Unconstrained Result for A468					
Phases	Prop.(%)	Norm-Prop.(%)	Std.	Comp.	Residual
Gl	79.100	77.349	4.229	SiO2	0.000
Opx	6.467	6.324	5.735	Al2O3	-0.085
Ol	16.697	16.327	2.903	MgO	0.000
SUM	***102.263***	***100.000***		CaO	0.232
				SSE	***0.061***

2.5. Oxygen Fugacity

The oxidation state of a system is a major concept in petrology. It corresponds to the hypothetical charge that an atom would possess if all its bonds with other atoms would be ionic (Cicconi et al., 2020). The concept of oxidation states is intricately linked to redox, or oxidation-reduction, reactions. These are defined as reactions involving changes in the oxidation states of the participating chemical species (Cicconi et al, 2020). The availability of electrons is what controls the oxidation state of an element. In extremely simple terms, oxidation can be considered as the loss of electrons, and reduction is the gain of electrons (White, 2013). The tendency of chemical species of gaining electrons can be approximated as redox (electron) potential. To measure the potential for redox exchange in high temperature geological systems, Earth scientists use molecular oxygen transfer (Moretti and Neuville, 2021). Igneous petrologists use oxygen fugacity (fO_2) to describe the oxidation state of magmatic systems. fO_2 is defined as the partial pressure of oxygen in a non-ideal mixture. Fugacity is a variable that is defined as pressure adjusted to account for the non-ideal behaviour of magmatic systems

(McSween et al., 2003). In Earth-based magmatic systems, fO_2 is relative to the valence state of Fe. In oxidizing conditions, Fe is present as Fe^{2+}, following this reaction (Frost, 1991; Carmichael and Ghiorso, 1990):

$$Fe_2SiO_4 \leftrightharpoons 2\,Fe_0 + SiO_2 + O_2 \qquad \text{Fayalite – Iron – Quartz (FIQ)} \quad \text{(Eq. 2.6)}$$

At higher fO_2, Fe will be present as both Fe^{2+} and Fe^{3+} according to this reaction:

$$2\,Fe_3O_4 + 3\,SiO_2 \leftrightharpoons 3\,Fe_2SiO_4 + O_2 \qquad \text{Fayalite – Quartz – Magnetite (FMQ)} \quad \text{(Eq. 2.7)}$$

At exceedingly high fO_2, Fe will only occur as trivalent Fe, according to the following reaction:

$$6\,Fe_2O_3 \leftrightharpoons 4\,Fe_3O_4 + O_2 \text{ Magnetite – Haematite (MH)} \qquad \text{(Eq. 2.8)}$$

In more reducing conditions, such as those present in Earth's mantle, or in Mercury, iron will be present as both Fe^{2+} and Fe^0 (Corgne et al., 2008):

$$Fe + \frac{1}{2}O_2 \leftrightharpoons FeO \text{ Iron – Wüstite (IW)} \qquad \text{(Eq. 2.9)}$$

At the conditions below the IW buffer, Fe will occur only in its metallic form Fe^0. All reactions shown above where component atoms are in more than one oxidation state are therefore called redox reactions (McSween et al., 2003). Although all the presented reactions include oxygen, it is important to point out that it is misleading to talk about redox reactions as an exchange of oxygen, where in reality the exchange between reactants and products involves electrons (Cicconi et al., 2020; McSween et al., 2003). An important point to make when looking at the redox reactions is that the thermodynamic coexistence of an atom in two different valence states, for example Fe^{3+} and Fe^{2+}, will fix the oxygen fugacity. fO_2 will change only when one of the phases will be completely consumed (White, 2013). This is the reason these reactions are defined as solid buffers (Fig. 2.8.).

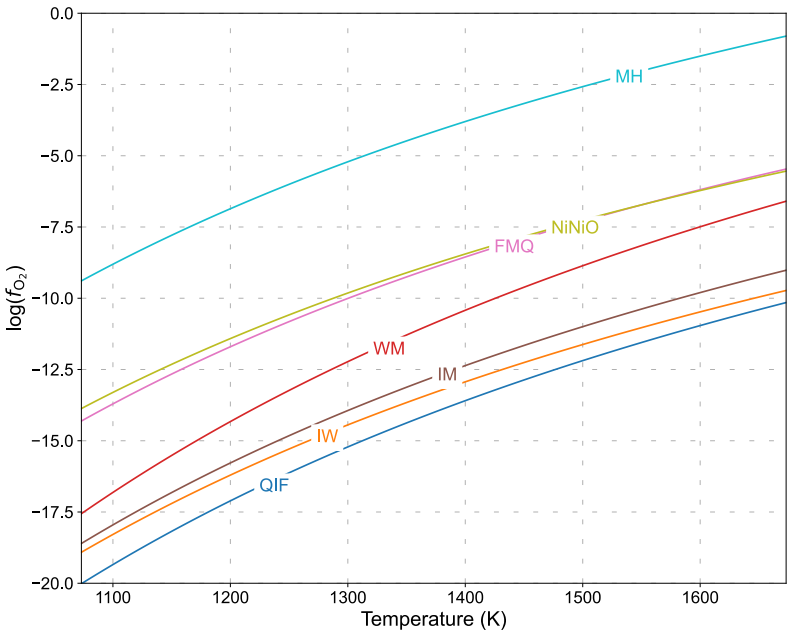

Figure 2.8. *Common oxygen buffers used in petrology. Data are compiled from Frost (1991). MH, NiNiO, FMQ, WM, IW, QIF refer to magnetite-hematite, nickel-nickel oxide, fayalite-magnetite-quartz, wüstite-magnetite, iron-wüstite, and quartz-iron-fayalite redox solid buffers, respectively (curves are extrapolated over the displayed temperature range).*

Studying redox conditions on Mercury is of particular importance. As we have already seen, Mercury's lavas originated from a mantle that differentiated under low fO_2 (Cartier and Wood, 2019; Namur et al., 2016a). Oxygen fugacity is therefore expressed relative to the IW buffer. Also, Mercury's primordial mantle likely differentiated in FeO-poor conditions, so that the fO_2 determination cannot rely on the concentration of FeO. In detail, the activity coefficients calculated for FeO in Mercury-like systems are poorly constrained (Namur et al., 2016b; Anzures et al., 2020; Wykes et al., 2015, Pirotte et al., 2023). fO_2 can thus be calculated using the equilibrium between Si-rich metal and SiO_2 in the silicate melt (Cartier et al., 2014):

$$SiO_{2\,\mathrm{Melt}} = Si_{\mathrm{Metal}} + O_2 \qquad \text{(Eq. 2.10)}$$

Where $SiO_{2\,\mathrm{melt}}$ is the concentration of SiO_2 in the silicate melt, and Si_{met} is the concentration of Si in the metal. The activity of SiO_2 in the melt (a_{SiO_2}) is assumed to be ~ 1 as SiO_2 is the main component of the melt that can also saturate solid SiO_2 phases (Cartier et al., 2014). Conversely, the activity of Si in the metal is given by:

$$a_{\mathrm{Si}} = X_{\mathrm{Si}}\,\gamma_{\mathrm{Si}} \qquad \text{(Eq. 2.11)}$$

Where X_{Si} is the molar Si content in the metal and γ_{Si} is the activity coefficient of Si as determined following the thermodynamic formalism of Ma (2001). Since in the first part of the project (Chapter 3)

we obtained several experimental assemblages constituted by silicate melt + olivine + orthopyroxene, a_{SiO_2} can be calculated from the following reaction:

$$Mg_2SiO_4 + SiO_2 = Mg_2Si_2O_6 \qquad \text{(Eq. 2.12)}$$

In the first part of the part of the project, we therefore determined the oxygen fugacity by revising the method of Cartier et al. (2014). More details are discussed in Chapter 3 and in Appendix A. For the second part of the project (Chapter 4), we obtain more evolved melts with a higher SiO_2 content that also saturate quartz. In this latter case, we could therefore assume $a_{SiO_2} \sim 1$.

References

Anzures, B.A., Parman, S.W., Milliken, R.E., Namur, O., Cartier, C., Wang, S., 2020. Effect of sulfur speciation on chemical and physical properties of very reduced Mercurian melts. Geochim. Cosmochim. Acta 286, 1–18. https://doi.org/10.1016/j.gca.2020.07.024

Armstrong, J.T., 1988. Quantitative analysis of silicate and oxide materials: comparison of Monte Carlo, ZAF, and φ(ρz) procedures, in Microbeam Analysis (1988) (Ed. Newbury, D.E.), San Franscisco Press.

Boyd, F.R., England, J.L., 1960. Apparatus for phase-equilibrium measurements at pressures up to 50 kilobars and temperatures up to 1750°C. J. Geophys. Res. 65, 741–748. https://doi.org/10.1029/JZ065i002p00741

Bridgman, P.W., 1940. New high pressures reached with multiple apparatus. Phys. Rev. 57, 342–343. https://doi.org/10.1103/PhysRev.57.342

Carmichael, I.S.E., Ghiorso, M.S., 1990. The effect of oxygen fugacity om the redox state of natural liquids and their crystallizing phases, in Modern methods of igneous petrology (1990) (Eds. Nicholls, J., Russell, K.), De Gruyter.

Cartier, C., Hammouda, T., Doucelance, R., Boyet, M., Devidal, J.-L., Moine, B., 2014. Experimental study of trace element partitioning between enstatite and melt in enstatite chondrites at low oxygen fugacities and 5GPa. Geochim. Cosmochim. Acta 130, 167–187. https://doi.org/10.1016/j.gca.2014.01.002

Cartier, C., Wood, B.J., 2019. The role of reducing conditions in building Mercury. Elements 15, 39–45. https://doi.org/10.2138/gselements.15.1.39

Castaing, R., 1951. Application of electron probes to local chemical and crystallographic analysis, Doctoral thesis, University of Paris.

Charlier, B., Grove, T.L., Namur, O., Holtz, F., 2018. Crystallization of the lunar magma ocean and the primordial mantle-crust differentiation of the Moon. Geochim. Cosmochim. Acta 234, 50–69. https://doi.org/10.1016/j.gca.2018.05.006

Chew, D., Drost, K., Marsh, J.H., Petrus, J.A., 2021. LA-ICP-MS imaging in the geoscience and its applications to geochronology. Chem. Geol. 559, 119917. https://doi.org/10.1016/j.chemgeo.2020.119917

Cicconi, M.R., Moretti, R., Neuville, D.R., 2020. Earth's electrodes. Elements 16, 157–160. https://doi.org/10.2138/gselements.16.3.157

Condamine, P., Tournier, S., Charlier, B., Médard, E., Triantafyllou, A., Dalou, C., Tissandier, L., Lequin, D., Cartier, C., Füri, E., Burnard, P.G., Demouchy, S., Marrocchi, Y., 2022. Influence of intensive parameters and assemblies on friction evolution during piston-cylinder experiments. Am. Min. 107, 1575–1581. https://doi.org/10.2138/am-2022-7958

Corgne, A., Keshav, S., Wood, B.J., McDonough, W.F., Fei, Y., 2008. Metal–silicate partitioning and constraints on core composition and oxygen fugacity during Earth accretion. Geochim. Cosmochim. Acta 72, 574–589. https://doi.org/10.1016/j.gca.2007.10.006

Dunn, T., 1993. The piston-cylinder apparatus. In R.W. Luth, Ed., Experiments at high pressure and applications to the Earth's mantle, 21, pp. 39–94. Mineralogical Association of Canada.

Frost, B.R., 1991. Introduction to oxygen fugacity and its petrological importance, in Oxide minerals: petrologic and magnetic importance (Ed. Lindsey, D.H.), Rev. Mineral., Vol. 25, Mineralogical Society of America, De Gruyter

Goldstein J.I., Newbury D.E, Joy D.C., Lyman C.E., Echlin P., Lifshin E., Sawyer L., Michael, J. 2003. Scanning electron microscopy and X-ray microanalysis (3rd edition), Springer, New York, NY, USA.

Janoušek, V., Moyen, J.-F., Martin, H., Erban, V., Farrow, C., 2016. Geochemical modelling of igneous processes – principles and recipes in r language: bringing the power of r to a geochemical community. Springer Berlin Heidelberg, Berlin, Heidelberg. https://doi.org/10.1007/978-3-662-46792-3

Knoll, M., 1935. Static potential and secondary emission of bodies under electron radiation. Z. techn. Phys., 16, 467.

Li, X., Zhang, C., Almeev, R.R., Holtz, F., 2020. GeoBalance: an excel VBA program for mass balance calculation in Geoscience. Geochemistry 80, 125629. https://doi.org/10.1016/j.chemer.2020.125629

Ma, Z., 2001. Thermodynamic description for concentrated metallic solutions using interaction parameters. Metall. Mater. Trans. 32B, 87-103. https://doi.org/10.1007/s11663-001-0011-0

McDade, P., Wood, B.J., Van Westrenen, W., Brooker, R., Gudmundsson, G., Soulard, H., Najorka, J., Blundy, J., 2002. Pressure corrections for a selection of piston-cylinder cell assemblies. Mineral. Mag. 66, 1021–1028. https://doi.org/10.1180/0026461026660074

McSween, H.Y., Richardson, S.M., Uhle, M.E., 2003. Geochemistry: pathways and processes, Second edition. ed. Columbia University Press, New York; Chichester, England.

Moretti, R., Neuville, D., 2021. Redox equilibria: from basic concepts to the magmatic realm. In Magma Redox Geochemistry: Geophysical Monograph (1st Ed.), 266. https://doi.org/10.1002/9781119473206.ch1

Namur, O., Charlier, B., Holtz, F., Cartier, C., McCammon, C., 2016a. Sulfur solubility in reduced mafic silicate melts: Implications for the speciation and distribution of sulfur on Mercury. Earth Planet Sci. Lett. 448, 102–114. https://doi.org/10.1016/j.epsl.2016.05.024

Namur, O., Collinet, M., Charlier, B., Grove, T.L., Holtz, F., McCammon, C., 2016b. Melting processes and mantle sources of lavas on Mercury. Earth Planet Sci. Lett. 439, 117–128. https://doi.org/10.1016/j.epsl.2016.01.030

Newbury, D.E., Ritchie, N.W.M., 2013. Is Scanning Electron Microscopy/Energy Dispersive X-ray Spectrometry (SEM/EDS) quantitative? Scanning 35, 141–168. https://doi.org/10.1002/sca.21041

Newbury, D.E., Ritchie, N.W.M., 2015. Performing elemental microanalysis with high accuracy and high precision by scanning electron microscopy/silicon drift detector energy-dispersive X-ray spectrometry (SEM/SDD-EDS). J. Mater. Sci. 50, 493–518. https://doi.org/10.1007/s10853-014-8685-2

Parsons, C.A., 1888. Experiments on carbon at high temperatures and under great pressures, and in contact with other substances. Proc. R. Soc. Lond. https://doi.org/10.1098/rspl.1888.0045

Pirotte, H., 2023. Planet Mercury and the behaviour of elements in reducing conditions, Doctoral thesis, University of Liege. https://hdl.handle.net/2268/308790

Pirotte, H., Cartier, C., Namur, O., Pommier, A., Zhang, Y., Berndt, J., Klemme, S., Charlier, B., 2023. Internal differentiation and volatile budget of Mercury inferred from the partitioning of heat-producing elements at highly reduced conditions. Icarus 405, 115699. https://doi.org/10.1016/j.icarus.2023.115699

Potts, P.J., Bowles, J.F.W., Reed, S.J.B., Cave, M.R., 1995. Microprobe techniques in the earth sciences. Mineralogical Society Series (Ed. Jones, A.P.).

Reed, S.J.B., 2005. Electron microprobe analysis and scanning electron microscopy in geology (2nd Ed.), Cambridge University Press.

Saracino, F., Charlier, B., Zhang, Y., Lécaille, M., Lin, Y., Namur, O., 2025. The role of sulfur on the liquidus temperature and olivine-orthopyroxene equilibria in highly reduced magmas. Chem. Geol. 683, 122777. https://doi.org/10.1016/j.chemgeo.2025.122777

Steenstra, E.S., van Westrenen, W., 2020. Geochemical constraints on core-mantle differentiation in Mercury and the aubrite parent body. Icarus 340, 113621. https://doi.org/10.1016/j.icarus.2020.113621

Vetere, F.P., 2024. Elementi di petrologia sperimentale. Firenze University Press / USiena Press. 10.36253/979-12-215-0247-3

von Ardenne, M., 1938. Das Elektronen-Rastermikroskop, Z. techn. Phys., 109, 553. https://doi.org/10.1007/BF01341584

Wenk, H.-R., 1976. Electron microscopy in mineralogy. Springer Berlin Heidelberg, Berlin, Heidelberg. https://doi.org/10.1007/978-3-642-66196-9

White, W.M., 2013. Geochemistry. John Wiley & Sons Inc, Hoboken, NJ.

Wykes, J.L., O'Neill, H.St.C., Mavrogenes, J.A., 2015. The effect of FeO on the sulfur content at sulfide saturation (SCSS) and the selenium content at selenide saturation of silicate melts. J. Petrol. 56, 1407–1424. https://doi.org/10.1093/petrology/egv041

Zhou, W., Apkarian, R.P., Wang, Z.L., Joy, D., 2006. Fundamentals of Scanning Electron Microscopy, in Scanning Microscopy for Nanotechnology (Eds. Zhou, W., and Wang, Z.L.), Springer New York, NY. https://doi.org/10.1007/978-0-387-39620-0_1

Chapter 3: The Role of Sulfur on the Liquidus Temperature and Olivine-Orthopyroxene Equilibria in Highly Reduced Magmas

Fabrizio Saracino [1] , Bernard Charlier [1], Yishen Zhang [2, 3], Manon Lécaille [1], Yanhao Lin [4], Olivier Namur [2]

[1] Department of Geology, University of Liege, 4000 Liege, Belgium

[2] Department of Earth and Environmental Sciences, KU Leuven, Celestijnenlaan 200E, 3001 Leuven, Belgium

[3] Department of Earth, Environmental, and Planetary Sciences, Rice University, 6100 Main Street, MS 126, Houston, TX 77005, USA

[4] Center for High Pressure Science and Technology Advanced Research, Beijing 100193, People's Republic of China

Manuscript published in *Chemical Geology*

Abstract

The geochemical data provided by the NASA MESSENGER spacecraft unveiled the geochemical heterogeneity of the volcanic crust of Mercury. Surprisingly, a high amount of sulfur was detected which combined with a low iron content, implies highly reduced conditions of parental magmas. Several variables (temperature, pressure, oxygen fugacity fO_2, and to a lesser extent, melt composition) affect the solubility of sulfur in silicate melts. In reduced silicate melts, sulfur has an oxidation state of S^{2-} and replaces anionic oxygen to form MgS and CaS complexes. Experimental studies have shown the high S solubility in silicate melts at low fO_2. As observed with other volatile elements, high S contents in silicate melts can deeply affect their properties such as (1) lowering the liquidus as compared to S-free compositions and (2) changing solid-liquid phase equilibria. In this study, we performed high temperature (1500 – 1950 °C) and high pressure (1.5 – 3.0 GPa) piston-cylinder experiments on Fe-poor compositions relevant to the petrogenesis of Mercury's volcanic crust with the aim of quantifying the effect of sulfur on depressing their liquidus temperature and understanding its role on phase equilibria. Several compositions were prepared to track the stability fields of olivine (high melt Mg/Si ratio) and orthopyroxene (low melt Mg/Si ratio) in both S-saturated melts and S-free melts. A range of reduced conditions were obtained by using different Si/SiO_2 ratios in the mixes. S-saturated experiments show increasing S abundances in the silicate melts (~ 1 – 9 wt%) as fO_2 decreases (from IW -2.9 to IW -6.2, IW representing the iron-wüstite thermodynamic equilibrium). Parameterizing our experimental results gives the liquidus depression as a function of the sulfur content in the melt (mol. fraction):

$$\Delta T_{liq}(°C) = -65208.22\,[S]_{melt}^{3} + 16595.32\,[S]_{melt}^{2} + 532.31\,[S]_{melt}$$

(MSWD = 3.24; SEE = 35 °C)

The range of sulfur concentration in our experimental melts would cause a liquidus depression of ca. 20 – 190 °C. Moreover, our experiments illustrate the role of sulfur in promoting the stability field of orthopyroxene over that of olivine which has major implications for the crystallization of the Mercurian magma ocean and the primordial mineralogical stratification of the mantle. In addition, the presence of sulfur lowers the pressure and temperature conditions of the olivine-orthopyroxene cotectic.

3.1.Introduction

Analysis of spectrometric data returned by NASA's MErcury Surface, Space ENvironment, GEochemistry, and Ranging (MESSENGER) spacecraft revealed peculiar features of planet Mercury. Specifically, the unusually high concentration of sulfur in surface volcanic units coupled with the paucity of iron pointed to highly reduced conditions for surface lavas (Nittler et al., 2011, 2020;

McCubbin et al., 2012; Zolotov et al., 2013; Weider et al., 2015). Such a high amount of sulfur at reducing conditions may bond with cations such as Si, Mg and Ca in silicate structures (Berthet et al., 2009; Namur et al., 2016a; Anzures et al., 2020; Pommier et al., 2023), which raises questions about its effects on the thermodynamic activities of major oxide components in the melt. As such, high-S concentrations are expected to severely affect silicate phase equilibria and melt properties (Namur et al., 2016b; Pommier et al., 2023), which in turn exert an influence on Mercury's differentiation processes of Mercury such as the crystallization of the magma ocean, mantle structure, mantle melting, and volcanism (Vander Kaaden et al., 2017; Boukaré et al., 2019; Mouser et al., 2021; Lark et al., 2022; Iacovino et al., 2023; Xu et al., 2024). Moreover, understanding the role of sulfur on the liquidus temperature of reduced silicate melts is necessary to investigate metal-silicate partitioning during the primordial differentiation as well as the thermal evolution of Mercury during its early history (Mouser et al., 2021; Mouser and Dygert, 2023).

For magmatic compositions relevant to Earth or more generally the terrestrial planets, it has been shown that volatile elements have important effects on magmatic liquidus temperature, phase equilibria, and fractionation trends. Although much effort has been made to characterize the influence of H_2O and CO_2 (e.g. Brey and Green, 1977; Médard and Grove, 2008; Dasgupta et al., 2013), more recent studies have investigated the role of other volatile species like Cl, F in terrestrial evolution and in planetary interiors (e.g. Filiberto et al., 2012, 2014; Farcy et al., 2016). All together, these studies point toward a strong effect of volatiles in depressing magmatic liquidus temperatures (Brey and Green, 1977; Médard and Grove, 2008; Dasgupta et al., 2013) and in changing the stability field of key silicate minerals such as olivine and orthopyroxene (Filiberto et al., 2012, 2016).

The behaviour of sulfur depends on the oxidation state of the system (e.g., O'Neill and Mavrogenes, 2002; Jugo et al., 2004; Nilsson and Peach, 1993; Boulliung and Wood, 2023). In reducing systems, sulfur has an oxidation state of S^{2-} in silicate melts while it is under the form of S^{6+} in more oxidizing conditions. The solubility of sulfur in silicate melts depends on several different variables, such as temperature, pressure, oxygen fugacity, and, to a lesser extent, melt composition (Wallace and Carmichael, 1992; Mavrogenes and O'Neill, 1999; O'Neill and Mavrogenes, 2002). In oxidizing conditions, S solubility in the melt is proportional to the melt FeO content (O'Neill, 2021) and can reach some thousands of ppm. Interestingly, several experimental studies have shown much higher S solubility in FeO-poor (or free) reduced melts (McCoy et al., 1999; Holzheid and Grove, 2002; Berthet et al., 2009; Chabot et al., 2014; Wykes et al., 2015; Namur et al., 2016a, b; Anzures et al., 2020). Namur et al. (2016a) showed that S concentration in reduced mafic melts significantly increases from < 1 wt% at oxygen fugacity (fO_2) IW -2 (IW being the iron-wüstite thermodynamic equilibrium) to > 10 wt% at IW -8. The solubility of S^{2-} is also affected by the bulk composition of silicate melts. Experiments performed at reducing conditions (IW -1 to IW -2) showed that S solubility decreases with a higher

degree of polymerization (i.e., bulk SiO_2 content; Holzheid and Grove, 2002). Previous experiments also demonstrated how sulfur deeply affects the equilibria of silicate phases, particularly those regarding the stability of olivine, orthopyroxene, and clinopyroxene (Berthet et al., 2009; Namur et al., 2016b, Anzures et al., 2020, Pommier et al., 2023), with increasingly reducing conditions favoring pyroxenes over olivine. However, so far, the effect of sulfur on phase equilibria has remained qualitative.

In this study we performed a series of high temperature (1500 – 1950 °C) and high pressure (1.5 – 3.0 GPa) piston-cylinder experiments on Mercury-like mantle compositions under reduced conditions in order to: (1) fully quantify the effect of sulfur in depressing the liquidi of Mercury-like mantle melts (2) quantify the role of sulfur on changing the size of olivine and pyroxene stability fields in melts with a range of starting Mg/Si ratios. Our results have significant implications for the crystallization of the magma ocean and mantle-derived lavas on Mercury as well as for understanding the conditions of mantle melting on Mercury.

3.2.Materials and Methods

3.2.1. Starting Materials

Our starting materials are inspired by the composition of the silicate fraction of enstatite chondrites, the likely building blocks of planet Mercury (Fig. 3.1.; Taylor and Scott, 2003; Malavergne et al., 2010; Cartier and Wood, 2019). An average composition (expressed in wt%) was obtained from data on EH and EL meteorite samples (Jarosewich, 1990; Berthet et al., 2009). The amount of P_2O_5 was decreased to 0.1 wt% to account for its markedly siderophile behaviour (Gu et al., 2019; Steenstra et al., 2020). As more Si can dissolve in metals at low fO_2 (Kilburn and Wood, 1997), part of Si was subtracted from the original chondritic composition to simulate Si partitioning in Mercury's core.

Two compositions with different Mg/Si ratios were then prepared, corresponding to 8 wt% and 15 wt% Si of the silicate fraction segregated into the metallic core (named Mer8 and Mer15, respectively) (Table 3.1.). This assumes that Mercury's core is 67 wt% of Mercury's bulk mass (Hauck et al., 2013) and contains 2.9 and 5.5 wt% Si, respectively. These values are in the range of the most recent estimates of the Si weight fraction in the core of Mercury (Goossens et al., 2022). Different reduced conditions were obtained by using different Si/SiO_2 ratios in the starting materials: 10 wt%, 20 wt%, and 30 wt% metallic Si (named Mer(10), Mer(20), Mer(30)). S-free and S-bearing compositions were prepared, with FeS being added to the starting materials as the sulfur source. 17 wt% FeS was added to Mer8(10) and to Mer15(10), 20 wt% FeS was added to Mer8(20) and Mer15(20), and 30 wt% FeS was added to Mer8(30) because more S is expected to partition into the silicate melt in the more reducing conditions (Mer(20), Mer(30)).

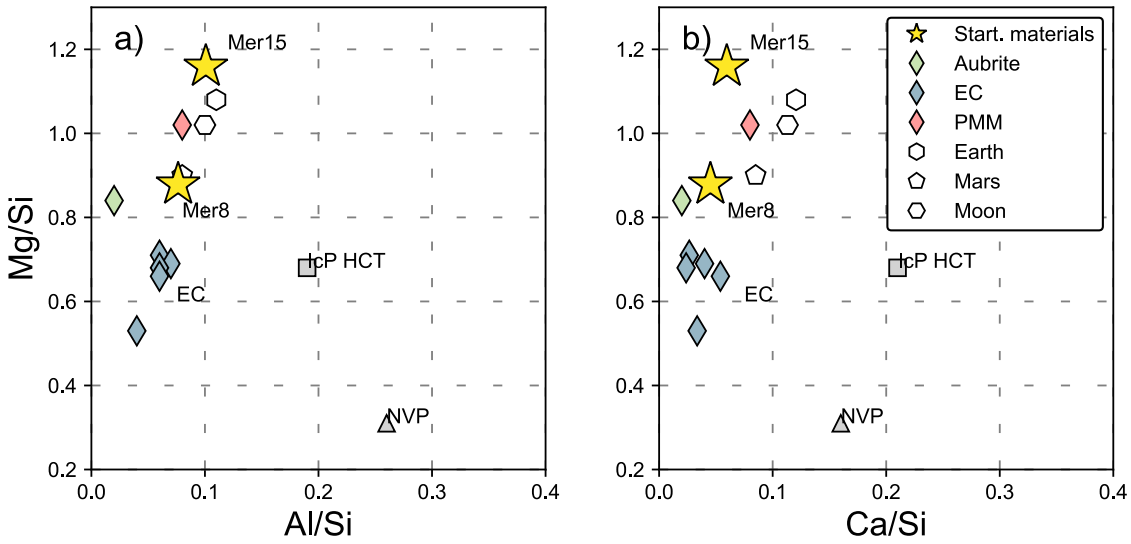

Figure 3.1. *(a) Mg/Si – Al/Si (in wt%) and (b) Mg/Si – Ca/Si plots showing our starting materials Mer8 and Mer15 compared to EC enstatite chondrites (Jarosewich, 1990; Berthet et al., 2009), average Aubrite (Keil, 2010), Primitive Mantle Mercury (Anzures et al., 2020 and based on CH ALH85085 in Weisberg et al., 1988), and Bulk Silicate Earth, Bulk Silicate Mars, and Bulk Silicate Moon (McDonough and Sun, 1995; Taylor, 2013; O'Neill, 1991). Also shown as comparison are the Intercrater Plains Highly Cratered Terrain (IcP HCT) and the Northern Volcanic Plains (NVP) compositions (Namur et al., 2016a).*

In total, seven different starting materials were produced, including two S-free compositions with 10 wt% Si added (Mer8(10), Mer15(10)), two S-saturated compositions with 10 wt% Si added (Mer8(10) + S, Mer15(10) + S), two S-saturated compositions with 20 wt% Si added (Mer8(20) + S, Mer15(20) + S), and one S-saturated composition with 30 wt% Si added (Mer8(30) + S). The starting materials were synthesized from high-purity oxide powders: SiO_2, TiO_2, Al_2O_3, Cr_2O_3, MnO, MgO, $CaSiO_3$, Na_2SiO_3, $K_2Si_4O_9$, and $AlPO_4$. $CaSiO_3$, Na_2SiO_3, and $K_2Si_4O_9$ were produced by decarbonation of mixtures with carbonates + SiO_2. Our powders were mixed in an agate mortar with methanol and then stored in oven at 120 °C.

Table 3.1. *Compositions of starting materials Mer8 and Mer15 (expressed in wt%). Also shown are the [a] Mercury's pre-melting mantle compositions of the Northern Smooth Plains and Intercrater Plains-Heavily Cratered Terrain, respectively (Nittler et al., 2018), [b] Primitive Mantle Mercury (Anzures et al., 2020), [c] Bulk Silicate Earth (McDonough and Sun, 1995), [d] Bulk Silicate Moon (O'Neill, 1991), [e] Bulk Silicate Mars (Taylor, 2013), and [f] renormalized average Ivuna meteorite (King et al., 2020). * FeOt = FeO + Fe_2O_3. n.d. – not determined.*

	Mer8	Mer15	Pre-melting mantle (NSP)[a]	Pre-melting mantle (IcP HCT)[a]	Primitive Mantle Mercury[b]	Bulk Silicate Earth[c]	Bulk Silicate Moon[d]	Bulk Silicate Mars[e]	Average Ivuna[f]
SiO_2	54.82	47.91	53.67	51.98	51.32	45.00	44.60	43.70	32.21
TiO_2	0.14	0.16	0.24	0.21	0.21	0.20	0.17	0.14	0.10
Al_2O_3	3.70	4.26	4.57	4.24	3.78	4.45	3.90	3.04	2.33
Cr_2O_3	0.52	0.60	n.d.	n.d.	0.41	0.38	0.47	0.73	0.51
FeOt*	n.d.	n.d.	0.02	0.03	0.54	8.05	12.40	18.10	36.78
MnO	0.28	0.33	n.d.	n.d.	0.09	0.14	0.17	0.44	0.44
MgO	37.32	43.04	36.89	37.64	40.72	37.80	35.10	30.50	22.30
CaO	1.62	1.87	2.26	3.84	2.73	3.55	3.30	2.43	1.88
Na_2O	1.37	1.58	1.97	1.29	0.08	0.36	0.05	0.53	1.03
K_2O	0.13	0.15	0.05	0.04	0.02	0.03	n.d.	0.04	0.09
P_2O_5	0.10	0.10	n.d.	n.d.	n.d.	0.02	n.d.	0.15	0.28
NiO	n.d.	n.d.	n.d.	n.d.	0.11	0.25	n.d.	n.d.	2.04
Total	100.00	100.00	99.67	99.27	100.01	99.99	100.16	99.80	100.00

3.2.2. Experimental Methods

Experiments were conducted with a Voggenreiter Mavo LPC 250-300/50 12.7 mm end-loaded piston-cylinder apparatus at the University of Liège (Belgium). Graphite capsules with MgO spacers were placed in a graphite furnace, and $BaCO_3$ cells were used as the pressure medium (see Fig. S3.1. in Appendix A). Temperature was monitored with a $W_{75}R_{25}/W_{97}Re_3$ thermocouple. The temperature gradient between the tip of the thermocouple and the center of the capsule is ~ 25 °C. Assemblies were first pressurized at room temperature up to 0.7 GPa. Then temperature was increased to 865 °C at 100 °C/min while keeping the pressure steady. Then temperature was held for 6 min in order to pressurize to the target pressure. A second temperature increase was followed up to the target temperature at 50 °C/min. A friction correction of 9.3% was applied (Condamine et al., 2022). Experiments were quenched by switching off the electric power. Experimental samples were cut in half with a diamond wafer saw, mounted in epoxy, and polished up to 1 µm.

3.2.3. Analytical Methods

Imaging and phase identification were performed with the FEI QEMSCAN 650F scanning electron microscope (SEM) at the Faculty of Georesources and Materials Engineering at RWTH Aachen (Germany). Quantitative analyses of our experimental products were conducted with the CAMECA SX Five Tactis electron probe micro-analyzer (EPMA) at Laboratoire Magmas et Volcans, Université Clermont Auvergne (Clermont-Ferrand, France). Silicate crystals, sulfide, and metallic phases were measured with a 15 kV accelerating voltage and 15 nA beam current. Silicate glasses were measured with a 15 kV accelerating voltage and a 4 to 15 nA beam current (depending on the melt fraction). Crystals were measured with a focused beam, whereas a defocused beam was used for glasses (2 – 20 µm depending on the size of the glass pool and quench textures). Although quenching is fast, some of the MgO-rich melt produced quench crystals, so that more points and a larger beam size were needed for better statistics. Nonetheless, calculated standard deviations are usually higher in quench-textured melts. Sulfides were measured with a focused beam and metals with a focused or defocused beam (5 – 10 µm), depending on the size of the metallic phases and on the presence of heterogeneities and quenched textures. Peak counting times of 10 – 30 s were used for each element and half on the background. The calibration standards for the silicate crystals are natural albite for Na, natural orthoclase for K and Al, natural wollastonite for Ca, San Carlos olivine for Si, synthetic forsterite for Mg, synthetic $TiMnO_3$ for Ti and Mn, synthetic Cr_2O_3 for Cr, synthetic fayalite for Fe. The same

standards were employed for the glass calibration except that wollastonite was used for both Si and Ca, with the addition of natural $BaSO_4$ for S. As for S measurements, a peak search was done on our experimental samples. Next, the peak position value was changed in the microprobe setup from $BaSO_4$ to the peak position value measured on our glasses, so as to obtain a more reliable S measurement at the peak sample position. The calibration standards used for sulfide phases are albite for Na, synthetic Si metal for Si, wollastonite for Ca, forsterite for Mg, $TiMnO_3$ for Ti, synthetic Cr metal for Cr, natural chalcopyrite for Fe and S, Mn metal for Mn, synthetic Fe_2P for P. The same set of standards were used for the metals, except that synthetic Fe metal was used for Fe.

3.2.4. Oxygen Fugacity Calculations

Under reduced conditions, the fO_2 of experimental products can be calculated considering the equilibrium between Fe-bearing metals and FeO-bearing silicate melts (Corgne et al., 2008), as shown below:

$$Fe_{\text{Metal}} + \frac{1}{2}O_2 = FeO_{\text{Melt}} \qquad \text{(Eq. 3.1)}$$

However, the typical Mercurian melts have extremely low FeO contents in the silicate melts (< 1 wt%) and are typically close or below the detection limit. The activity coefficient of FeO at low Fe^{2+} concentration is poorly constrained (Cartier et al., 2014; Wykes et al., 2015; Namur et al., 2016a; Anzures et al., 2020; Pirotte et al., 2023) which makes fO_2 estimates using Eq. (3.1) unreliable. In contrast, fO_2 can be calculated using the equilibrium between Si-rich metal and SiO_2 in the silicate melt (Cartier et al., 2014):

$$SiO_{2,\text{Melt}} = Si_{\text{Metal}} + O_2 \qquad \text{(Eq. 3.2)}$$

where $SiO_{2,\text{Melt}}$ is the SiO_2 concentration in the melt and Si_{Metal} is the Si concentration in the metal. The activity of Si in the metal is given by:

$$a_{\text{Si}} = X_{\text{Si}}\gamma_{\text{Si}} \qquad \text{(Eq. 3.3)}$$

With X_{Si} being the molar Si content in the metal and γ_{Si} the activity coefficient of Si. Here we use the Si activity coefficients as determined following the thermodynamic formalism of Ma (2001). Because many of our samples feature both olivine and orthopyroxene, we calculated the activity of SiO_2 in the silicate melt from the following reaction:

$$Mg_2SiO_4 + SiO_2 = Mg_2Si_2O_6 \qquad \text{(Eq. 3.4)}$$

More details are in Appendix A (Section S3.2.). The range of fO_2 attained in this work (IW -2.9 to IW -6.2) is consistent with the fO_2 range of Mercurian lavas (IW ~ -3 – 7, Cartier and Wood, 2019) and the average mantle fO_2 (IW -5.4) (Namur et al. 2016a).

3.3.Results

3.3.1. Textures and Phase Equilibria

Representative backscattered images of our experimental products are shown in Fig. 3.2. S-bearing experiments show a multi-phase assemblage composed of silicate melt ± olivine and/or orthopyroxene, metals, and sulfides (Figs. 3.2.a, c, d, f). S-free experiments show quenched silicate melt, crystals (olivine, orthopyroxene, ± clinopyroxene), and small metallic Cr-, P-, Si-bearing globules (Fig. 3.2.b, e). Olivine and orthopyroxene are euhedral with well-developed faces ranging in size from 5-300 μm. Clinopyroxene is only found in low-melt fraction, low-temperature S-free runs and appears as bright thin rims on orthopyroxene crystals (Fig. 3.2.e). As for the silicate melt, only a few experiments at high temperature show quench textures (Fig. 3.2.d). The evolution of the melt fraction F in our experiments is shown in Fig. S3.2. Olivine and orthopyroxene are usually located in the bottom part of the capsule in high melt fraction (F > 50 %) samples, whereas they are more evenly distributed in low melt fraction (F < 40 %) runs. Metals and sulfides are featured as spherical/sub-spherical metal+sulfide globules of differing size (5 – 250 μm depending on temperature), usually consisting of a Si-bearing metallic Fe core surrounded by an FeS rim, whose shape suggests that they were coexisting as two metallic and sulfide liquids right before quenching (Figs. 3.2.a, c, f). In some cases, smaller metallic globules are more irregularly interspersed in FeS. FeS is mostly homogeneous, appearing in some runs pervaded by bright veinlets (alternating tiny bright and dark round, elliptical features), presumably due to incomplete separation between Fe metal and FeS (Fig. 3.2.d). Troilite (FeS) produced by quenching of a FeS-bearing sulfide melt, is the main sulfide phase. Some experiments contain (Mg,Fe)S, which is preferentially found in the most reduced samples at T < 1700 °C. (Fe,Mg,Cr,Mn)S represents the third type of sulfide and is found in most of the S-bearing samples as thin veneers surrounding FeS or as small, isolated droplets (slightly darker than FeS, Figs. 3.2.c, f). The metal-sulfide textures described here have been reported in the literature (McCoy et al., 1999; Corgne et al., 2008; Cartier et al., 2014; Namur et al., 2016a, b; Cartier et al., 2020; Pitsch et al., 2025). All experimental conditions, and relative phase assemblages are reported in Table 3.2.

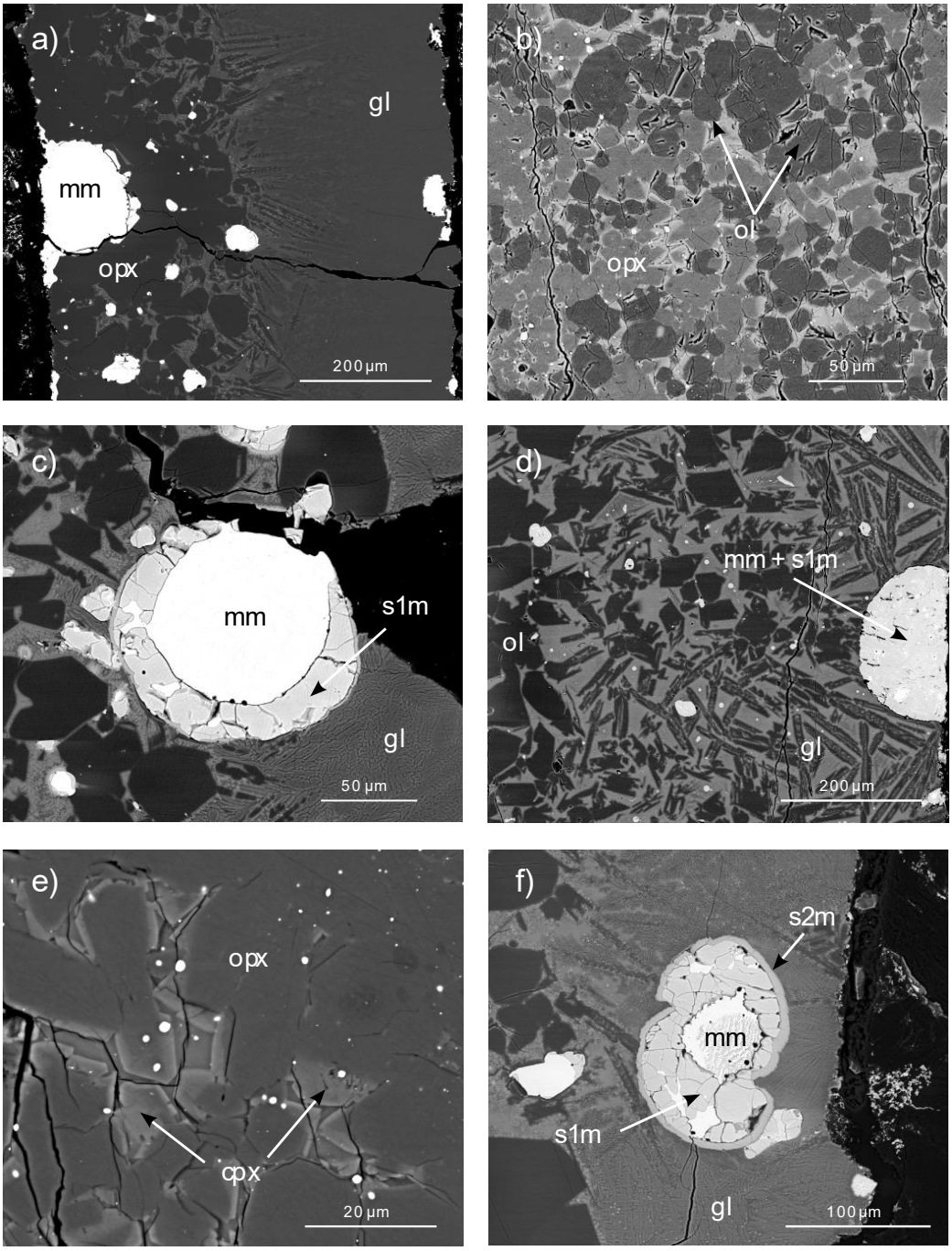

Figure 3.2. *Backscattered images of representative experimental products. (a) A328 (T = 1600 °C; P = 1.5 GPa) – Orthopyroxene crystals surrounding a metal-sulfide globule are shown on the left. Quenched silicate glass is shown on the right; (b) A304 (T = 1700 °C; P = 3.0 GPa) – Low melt fraction run exhibiting crystals of olivine (darker) and orthopyroxene (brighter); (c) A361 (T = 1550 °C; P = 1.5 GPa) – close-up on a metal-sulfide globule. The core is Si-bearing Fe metal, and the thick rim is*

FeS. A thin (Fe, Cr, Mn, Mg) S rim surrounds FeS; (d) A344 (T = 1750 °C; P = 1.5 GPa) – Olivine crystals (left and upper centre), quenched silicate glass (lower centre and right). Note the metal-sulfide globule texture described in 3.1. (e) A302 (T = 1700 °C; P = 3 GPa) Clinopyroxene rims (bright) surrounding orthopyroxene crystals (dark). (f) A329 (T = 1600 °C; P = 1.5 GPa) Sulfide-metal globule in the silicate melt. A metallic core is surrounded by a thick FeS rim and a thin (Fe, Cr, Mn, Mg) S rim. Abbreviations: gl – quenched silicate glass, ol – olivine, opx – orthopyroxene, mm – Si-bearing Fe metal, s1m – FeS, s2m – (Fe, Cr, Mn, Mg) S.

The inferred phase diagrams are shown in Fig. 3.3. We modelled our liquidus curves with Theriak-Domino (de Capitani and Brown, 1987; de Capitani and Petrakakis, 2010; details are in Appendix A, Section S3.3.), as it approximates more accurately the liquidus position of our S-free experiments as compared to other thermodynamic models (Fig. S3.3.).

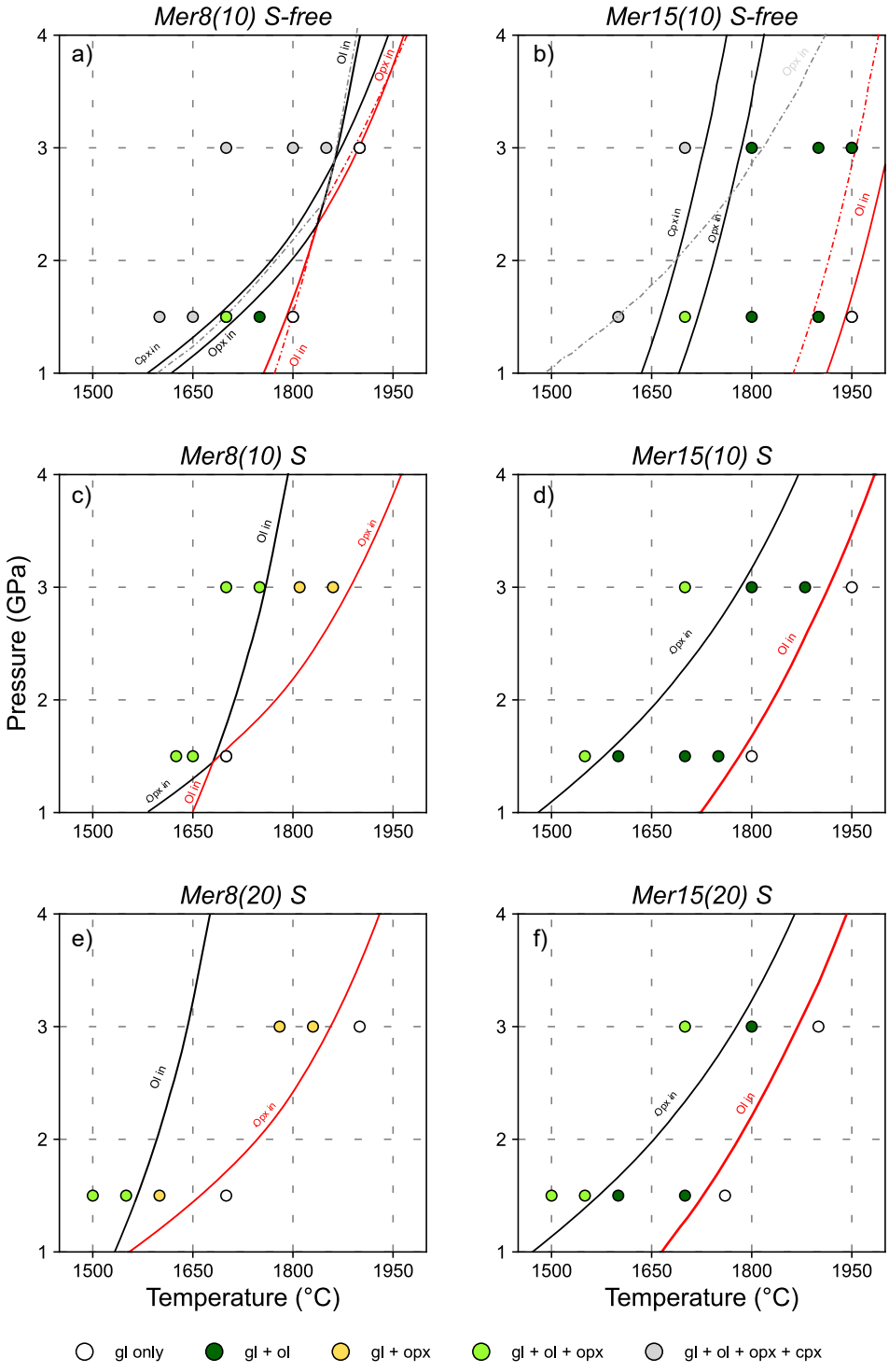

Figure 3.3 *Pressure, temperature conditions, and phase assemblages of our experimental runs. Inferred liquidi curves are shown in solid red lines and major phase boundaries in solid black lines. Also shown as comparison are liquidi (red dashed lines) and major phase boundaries (grey dashed lines) of S-free*

starting compositions as modelled by Theriak-Domino (de Capitani and Brown, 1987; de Capitani and Petrakakis, 2010). Details on the phase diagram modelling are shown Appendix A. Abbreviations: gl – silicate glass, ol – olivine, opx – orthopyroxene, cpx – clinopyroxene.

In composition S-free Mer8, olivine is the liquidus phase at 1.5 GPa, while olivine, orthopyroxene, and clinopyroxene first appear together at T = 1850 °C at 3 GPa (Fig. 3.3.a). The olivine-orthopyroxene cotectic is expected to be approximately at P ~ 2.3 GPa. In S-saturated conditions (Fig. 3.3.c), the cotectic shifts towards lower temperatures (> 100 °C) and pressures (> 0.5 GPa) for the most reduced S-bearing composition (Figs. 3.3.c, e), where orthopyroxene becomes the liquidus phase at the investigated pressure range. Interestingly, the orthopyroxene liquidus only appears to slightly decrease (< 50 °C) in the presence of sulfur (Figs, 3.3a, c, e). On the other hand, olivine is always the liquidus mineral for S-free and S-bearing Mer15 compositions, both at 1.5 GPa and 3 GPa (Figs. 3.3.b, d, f). The stability field of olivine at a given pressure nevertheless significantly contracts (~ 150 – 200 °C) as the melt becomes enriched in sulfur.

Table 3.2. *Experimental run conditions, phase assemblages, and results of mass balance calculations of silicate phases expressed in wt% (Li et al., 2020). All fO_2 values are relative to the IW (iron-wüstite) buffer. Some fO_2 values are missing because of incomplete separation between metals and FeS. Abbreviations: gl – silicate glass, ol – olivine, opx – orthopyroxene, cpx – clinopyroxene, pm – P-, Si-, Cr-bearing metal, mm – Si- and S-bearing metal, s1m – FeS, s2m – (Fe, Cr, Mg, Mn) S, s3m – (Mg, Fe) S. *Clinopyroxene couldn't be measured due to its small size. ** Revised after Cartier et al. (2014). *** Calculated liquidus temperature (in °C) on a S-free basis with Eq. (3.8). **** Calculated liquidus temperature depression (ΔT, °C) from Eq. (3.7).*

Run	T (˚C)	P (GPa)	Duration (hrs)	Silicate phases	Metals and sulfides	gl	ol	opx	cpx*	ΔIW**	Calc T_{liq} (℃)	ΔT_{liq} (℃)
Mer8(10)												
A307	1900	3.0	01:00	gl	pm	100						
A381	1850	3.0	01:10	gl, ol, opx, cpx	pm	60	10	30	x			
A305	1800	3.0	01:20	gl, ol, opx, cpx	pm	50	10	41	x			
A302	1700	3.0	01:50	gl, ol, opx, cpx	pm	<15			x			
A262	1800	1.5	00:30	gl	pm	100						
A290	1750	1.5	01:00	gl, ol	pm	93	7					
A263	1700	1.5	01:00	gl, ol, opx	pm	79	13	8				
A311	1650	1.5	02:00	gl, ol, opx, cpx	pm	15	16	69	x			
A296	1600	1.5	03:00	gl, ol, opx, cpx	pm	<15			x			
Mer8(10) S												
A380	1860	3.0	00:20	gl, opx	mm, s1m, s2m	90		10		-3.5	1901	41
A378	1810	3.0	01:10	gl, opx	mm, s1m, s2m	53		47		-3.6	1938	128
A359	1750	3.0	01:35	gl, ol, opx	mm, s1m, s2m	<20						
A297	1700	3.0	01:50	gl, ol, opx	mm, s1m, s2m	<20						
A247	1700	1.5	00:30	gl	mm, s1m, s2m	100				-3.8		
A268	1650	1.5	02:30	gl, ol, opx	mm, s1m, s2m	78	10	12		-3.6	1736	86
A309	1625	1.5	02:45	gl, ol, opx	mm, s1m, s2m	53	8	39		-3.9	1748	123
Mer8(20) S												
A322	1900	3.0	00:40	gl	mm, s1m, s2m	100				-4.7		
A379	1830	3.0	00:45	gl, opx	mm, s1m, s2m	69		31		-5.0	1929	99
A377	1780	3.0	01:00	gl, opx	mm, s1m, s2m	64		36		-5.0	1916	136
A334	1700	1.5	01:10	gl	mm, s1m, s2m	100				-4.9		
A328	1600	1.5	03:00	gl, opx	mm, s1m, s2m	74		26		-5.5	1781	181
A361	1550	1.5	03:30	gl, ol, opx	mm, s1m, s2m, s3m	45	7	47		-5.9	1756	206
A375	1500	1.5	04:00	gl, ol, opx	mm, s1m, s2m, s3m	30	15	55		-6.2	1673	173

Run	T (˚C)	P (GPa)	Duration (hrs)	Silicate phases	Metals and sulfides	gl	ol	opx	cpx*	ΔIW**	Calc T_{liq} (℃)	ΔT_{liq} (℃)
Mer8(30) S												
A456	1700	1.5	00:30	gl	mm, s1m, s2m	100				-5.4		
A466	1600	1.5	00:50	gl, opx	mm, s1m, s2m, s3m	99		1		-5.8	1759	159
A468	1550	1.5	00:55	gl, ol, opx	mm, s1m, s2m, s3m	77	16	6		-6.1	1711	161
Mer15(10)												
A351	1950	3.0	00:35	gl, ol	pm	72	28					
A308	1900	3.0	01:00	gl, ol	pm	39	61					
A303	1800	3.0	01:20	gl, ol	pm	35	65					
A304	1700	3.0	01:50	gl, ol, opx, cpx	pm	20	51	29	x			
A343	1950	1.5	00:20	gl	pm	100						
A273	1900	1.5	00:30	gl, ol	pm	58	42					
A257	1800	1.5	00:30	gl, ol	pm	45	55					
A265	1700	1.5	01:00	gl, ol, opx	pm	34	61	5				
A294	1600	1.5	06:00	gl, ol, opx, cpx	pm	24	61	15	x			
Mer15(10) S												
A349	1950	3.0	00:35	gl	mm, s1m, s2m	100						
A373	1880	3.0	01:00	gl, ol	mm, s1m, s2m	70	30				1950	70
A282	1800	3.0	01:20	gl, ol	mm, s1m, s2m	48	52				1828	28
A306	1700	3.0	01:55	gl, ol, opx	mm, s1m, s2m	35	54	12		-3.0	1785	85
A249	1800	1.5	00:30	gl	mm, s1m	100						
A344	1750	1.5	00:45	gl, ol	mm, s1m, s2m	62	38				1785	35
A259	1700	1.5	01:00	gl, ol	mm, s1m, s2m	57	43			-3.1	1751	51
A279	1600	1.5	03:00	gl, ol	mm, s1m, s2m	39	61			-3.6	1589	-11
A331	1550	1.5	03:30	gl, ol, opx	mm, s1m, s2m	28	56	17		-3.9	1617	67

Run	T (˚C)	P (GPa)	Duration (hrs)	Silicate phases	Metals and sulfides	gl	ol	opx	cpx*	ΔIW**	Calc T_{liq} (℃)	ΔT_{liq} (℃)
Mer15(20) S												
A323	1900	3.0	00:40	gl	mm, s1m	100				-3.9		
A364	1800	3.0	01:00	gl, ol	mm, s1m, s2m	63	37			-4.5	1922	122
A367	1700	3.0	01:30	gl, ol, opx	mm, s1m, s2m, s3m	50	37	13		-5.1	1927	227
A372	1760	1.5	00:40	gl	mm, s1m, s2m	100				-3.8		
A339	1700	1.5	01:10	gl, ol	mm, s1m, s2m	78	22			-4.4	1845	145
A329	1600	1.5	03:00	gl, ol	mm, s1m, s2m	64	36			-5.3	1800	200
A362	1550	1.5	03:30	gl, ol, opx	mm, s1m, s2m, s3m	57	39	4		-5.8	1767	217
A376	1500	1.5	04:00	gl, ol, opx	mm, s1m, s2m, s3m	42	46	11		-5.9	1733	233

3.3.2. Composition of Phases

Major element compositions of silicate glasses are presented in Table 3.3. The glass Si content in S-free runs varies from 23 to 29 wt%, Mg from 8 to 25 wt% (Fig. 3.4.), Al from 2 to 11 wt%. In S-saturated experiments, Si is in the range 21 – 27 wt%, Mg 11 – 27 wt%, Al 1.2 – 7.8 wt%. The sulfur content in S-saturated experiments for Mer8(10) and Mer15(10) compositions is in the range of 1.7 to 4.8 wt% (Fig. 3.5.); Mer8(20) and Mer15(20) compositions have S contents in the range of 5.1 to 8 wt%, whereas in Mer8(30) S is in the range 6.8 – 9.1 wt% (Table 3.3.), showing that more reduced experiments have a higher sulfur concentration (Fig.3.6.).

Table 3.3. *Average composition of silicate glasses expressed in wt%. No – number of analyses. * Melt pockets were too small to be accurately measured. ** Oxygen was calculated by stoichiometry.*

Run	T (˚C)	P (GPa)	No	Composition of silicate glasses (wt%)												
				Si	Ti	Al	Fe	Mn	Mg	Ca	Na	K	S	Cr	O**	Total
Mer8(10)																
A307	1900	3.0	7	26.6	0.12	2.27		0.20	22.8	1.35	0.38	0.08		< dl	48.2	102.0
A381	1850	3.0	5	26.9	0.16	2.99		0.15	21.1	1.56	0.17	0.07		< dl	48.1	101.3
A305	1800	3.0	8	26.0	0.14	3.16		0.21	20.6	1.99	0.57	0.14		0.10	47.4	100.4
A302*	1700	3.0														
A262	1800	1.5	10	26.0	0.11	2.16		0.21	22.5	1.31	0.57	0.11		< dl	47.3	100.3
A290	1750	1.5	7	26.6	0.12	2.19		0.20	22.3	1.31	0.33	0.10		0.20	47.9	101.2
A263	1700	1.5	11	27.0	0.14	2.45		0.22	20.9	1.57	0.39	0.12		0.19	47.8	100.7
A311	1650	1.5	7	24.3	< dl	10.5		0.09	8.16	8.79	1.32	0.87		< dl	46.8	100.9
A296*	1600	1.5														
Mer8(10) S																
A380	1860	3.0	7	25.3	0.08	2.09	0.58	0.16	21.7	1.32	0.74	0.10	2.62	0.10	46.2	100.9
A378	1810	3.0	7	23.3	0.14	3.03	0.44	0.24	21.0	2.31	1.40	0.21	4.76	< dl	45.0	101.9
A359*	1750	3.0														
A297*	1700	3.0														
A247	1700	1.5	12	26.2	0.09	2.01	0.29	0.18	21.8	1.20	0.81	0.10	3.14	< dl	47.0	102.8
A268	1650	1.5	8	26.2	0.12	2.51	0.56	0.18	20.9	1.40	0.85	0.13	2.66	< dl	47.2	102.7
A309	1625	1.5	9	25.0	0.09	3.18	0.42	0.15	20.1	1.96	1.12	0.18	3.79	< dl	46.1	102.0
Mer8(20) S																
A322	1900	3.0	13	25.5	0.12	1.95	0.39	0.19	22.0	1.17	0.58	0.08	5.12	< dl	46.2	103.3
A379	1830	3.0	7	23.7	0.12	2.46	0.46	0.21	21.4	1.77	0.99	0.14	7.28	< dl	44.8	103.4
A377	1780	3.0	6	24.0	0.09	2.78	0.40	0.21	21.0	1.76	1.08	0.14	7.18	< dl	45.2	103.8
A334	1700	1.5	11	25.0	0.09	1.92	0.37	0.17	21.8	1.22	0.65	0.09	5.71	< dl	45.5	102.5
A328	1600	1.5	10	24.4	< dl	2.53	0.47	0.21	21.8	1.50	0.64	0.12	6.92	< dl	45.6	104.2
A361	1550	1.5	11	23.8	< dl	3.81	0.43	0.08	19.0	2.56	0.97	0.22	8.00	< dl	44.7	103.6

Run	T (˚C)	P (GPa)	No	Composition of silicate glasses (wt%)												
				Si	Ti	Al	Fe	Mn	Mg	Ca	Na	K	S	Cr	O**	Total
A375	1500	1.5	9	24.4	< dl	5.30	0.31	< dl	14.5	4.10	2.45	0.36	7.50	< dl	45.1	104.1
Mer8(30) S																
A456	1700	1.5	10	24.1	< dl	1.89	0.64	0.17	21.5	1.09	0.61	0.10	9.01	< dl	44.3	103.5
A466	1600	1.5	10	24.7	< dl	1.90	0.54	0.14	21.1	1.12	0.62	0.10	8.61	< dl	44.7	103.5
A468	1550	1.5	13	26.0	< dl	2.51	0.53	< dl	19.3	1.24	1.07	0.15	6.86	< dl	45.8	103.4
Mer15(10)																
A351	1950	3.0	5	23.8	0.10	3.72		0.21	23.5	2.06	0.32	0.13		< dl	47.1	101.0
A308	1900	3.0	5	27.7	0.22	5.89		0.29	14.9	3.57	0.52	0.17		< dl	48.6	101.9
A303	1800	3.0	6	28.2	0.22	6.79		0.34	12.1	4.25	0.87	0.30		0.14	48.7	101.9
A304	1700	3.0	5	24.2	0.21	8.19		0.30	13.3	6.42	0.88	0.31		0.10	47.0	100.9
A343	1950	1.5	10	24.1	0.12	3.31		0.19	24.8	1.86	0.06	0.10		< dl	47.6	102.1
A273	1900	1.5	5	25.2	0.15	4.27		0.28	21.5	2.39	0.09	0.14		0.11	47.9	102.1
A257	1800	1.5	8	27.0	0.20	5.08		0.34	17.4	3.07	0.14	0.13		0.11	48.3	101.8
A265	1700	1.5	7	27.1	0.23	6.33		0.37	12.8	4.18	1.06	0.20		< dl	47.5	99.8
A294	1600	1.5	5	27.1	0.17	8.37		0.30	11.6	5.95	0.13	0.37		< dl	48.6	102.6
Mer15(10) S																
A349	1950	3.0	6	21.5	0.09	1.20	0.58	0.12	26.6	1.27	0.30	0.04	1.73	< dl	44.0	97.4
A373	1880	3.0	6	23.8	0.10	3.15	0.53	0.15	22.7	1.84	0.74	0.10	2.24	0.10	46.3	101.8
A282	1800	3.0	9	25.5	0.17	4.42	0.66	0.18	17.4	2.66	1.22	0.16	2.28	< dl	46.5	101.1
A306	1700	3.0	5	25.7	< dl	6.04	0.36	< dl	15.0	4.03	1.58	0.19	2.10	< dl	47.1	102.2
A249	1800	1.5	8	26.1	0.10	2.02	0.43	0.18	21.7	1.25	0.78	0.10	2.81	< dl	46.9	102.4
A344	1750	1.5	7	24.5	0.12	3.70	0.52	0.18	21.5	2.13	0.99	0.18	3.05	< dl	47.0	103.9
A259	1700	1.5	5	24.9	0.14	3.94	0.37	0.18	20.0	2.28	1.16	0.14	2.93	< dl	46.9	103.0

Run	T (˚C)	P (GPa)	No	Composition of silicate glasses (wt%)											
				Si	Ti	Al	Fe	Mn	Mg	Ca	Na	K	S	Cr	O**	Total
A279	1600	1.5	5	26.9	0.14	5.70	0.32	0.13	13.1	3.86	1.84	0.23	3.84	< dl	47.0	103.0
A331	1550	1.5	6	25.6	< dl	7.71	0.39	0.15	11.8	4.41	1.81	0.36	4.28	< dl	46.8	103.4
Mer15(20) S																
A323	1900	3.0	6	22.6	0.10	2.47	0.48	0.22	24.7	1.35	0.54	0.11	5.50	< dl	45.3	103.4
A364	1800	3.0	7	23.7	0.11	3.44	0.29	0.24	20.8	2.00	0.83	0.13	6.34	< dl	45.2	103.1
A367	1700	3.0	9	22.4	0.09	4.17	0.43	0.18	19.6	2.78	1.02	0.17	7.27	< dl	44.1	102.2
A372	1760	1.5	11	22.3	0.09	2.52	0.62	0.21	24.4	1.54	0.58	0.11	6.35	< dl	45.0	103.7
A339	1700	1.5	6	23.1	0.09	2.88	0.46	0.25	23.1	1.69	0.60	0.14	6.12	0.10	45.4	103.9
A329	1600	1.5	12	23.6	0.08	3.40	0.47	0.20	21.3	1.93	0.59	0.17	6.42	< dl	45.3	103.4
A362	1550	1.5	7	22.6	0.09	4.33	0.51	0.09	18.0	2.72	1.77	0.22	7.59	< dl	43.7	101.7
A376	1500	1.5	10	23.2	< dl	5.00	0.45	< dl	17.0	3.17	1.99	0.27	7.72	< dl	44.5	103.3

In all our experimental runs, olivine, and orthopyroxene feature Mg end-member compositions (forsterite and enstatite, respectively). In S-free experiments, CaO (ranging from 0.2 to 1.2 wt%) and Al_2O_3 (0.5 – 3.2 wt%) increase in orthopyroxene as temperature decreases. S-saturated experiments show orthopyroxene crystals with generally lower CaO (0.1 – 0.5 wt%) and Al_2O_3 (0.4 – 2.0 wt%) contents. Only a few analyses on clinopyroxene in S-free experiments could be performed due to the small size of the crystals.

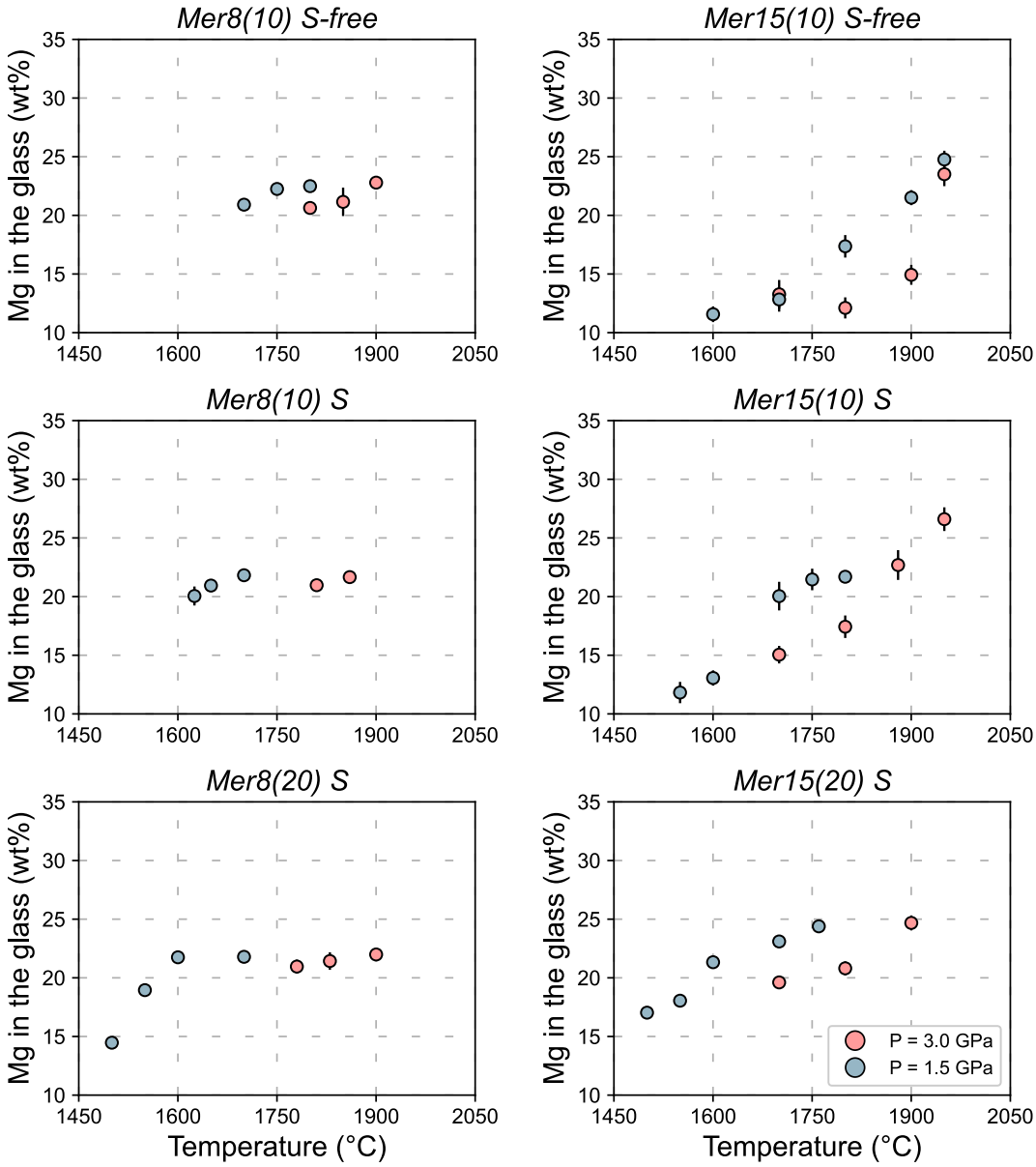

Figure 3.4. *Mg content in the silicate glass as a function of temperature (in °C). 1σ standard deviation is represented by the vertical bars (small 1σ values are hidden by the symbols).*

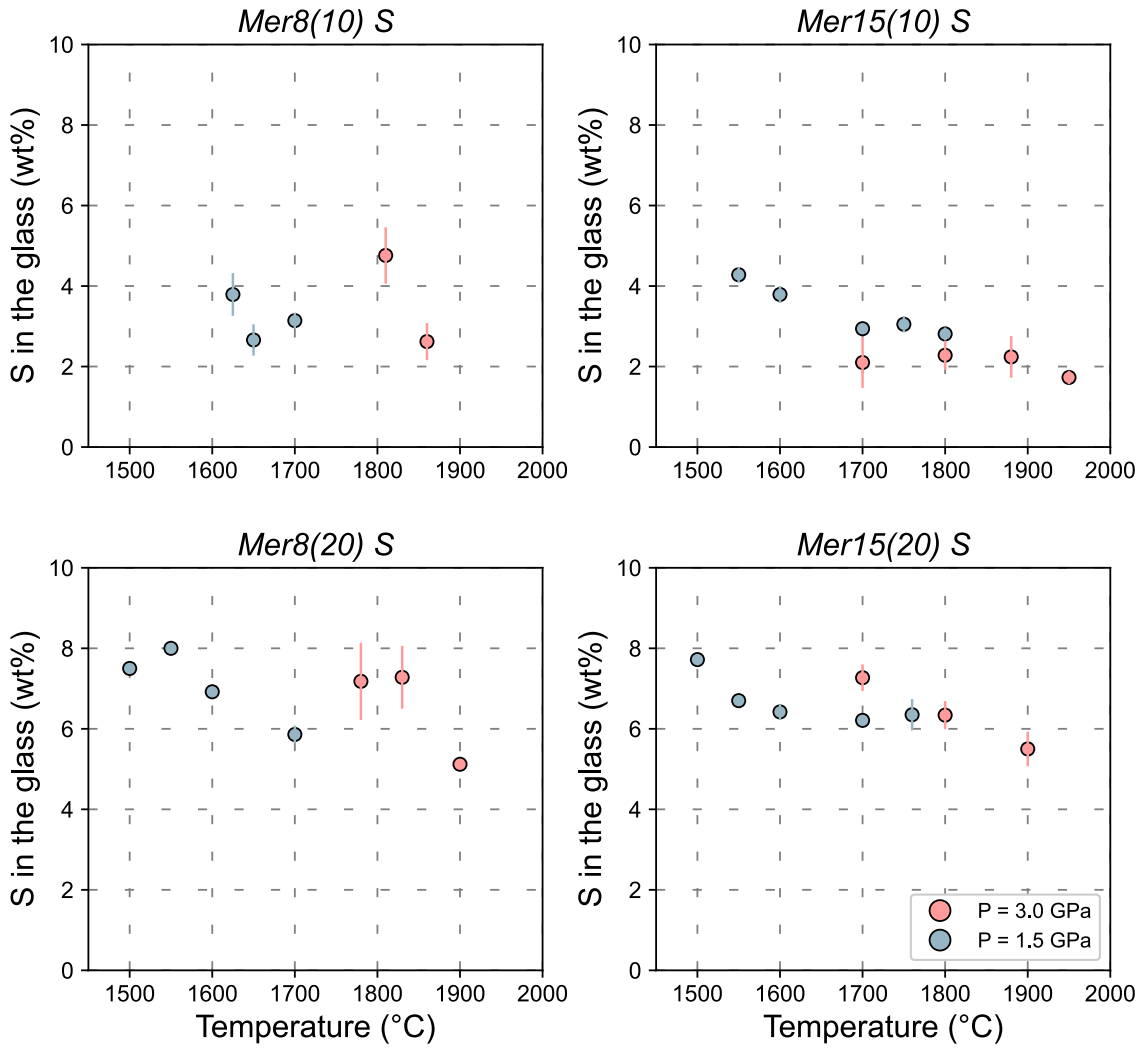

Figure 3.5. *Sulfur content in the silicate glass (in wt%) at sulfide saturation as a function of temperature (in °C). 1σ standard deviation is represented by vertical bars (small 1σ values are hidden by the symbols).*

The average clinopyroxene composition is $En_{73}Wo_{27}$ in the MgO-FeO-CaO -system. The compositions of metallic and sulfide phases in S-bearing experiments are reported in Appendix B. The small P-, Si-, Cr-bearing globules in S-free experiments could not be measured due to their small size (Fig. 3.2.e). Metallic alloys in S-saturated compositions (Mer8(10), Mer15(10)) display Fe ranging from 90 to 96 wt%, and Si ranging from 0.3 to 2.5 wt% (Figs. 3.7.; S3.4.). In more reduced experiments (Mer8(20), Mer15(20)), Fe is in the range 85.7 – 91.4 wt%, and Si in the range 2 – 11 wt%. Sulfide phases are FeS, (Mg,Fe)S (found at IW < -5, Appendix B), and (Fe,Cr,Mn)S. The latter could not be measured due to its small size. Compositions with 10% Si display FeS with a Fe content in the range 55.6 – 63.9 wt%, and S in the range 31.9 – 37.4 wt%. S-bearing Mer(20) melts show Fe ranging from 52 to 58 wt%, S

from 35.9 to 37.6 wt%. (Mg,Fe)S is only found in Mer8(20), Mer15(20), and Mer8(30) at IW < -5 at low temperature and display S in the range 45 – 49 wt%, Mg in the range 22 – 25 wt%, 15 – 20 wt% Fe.

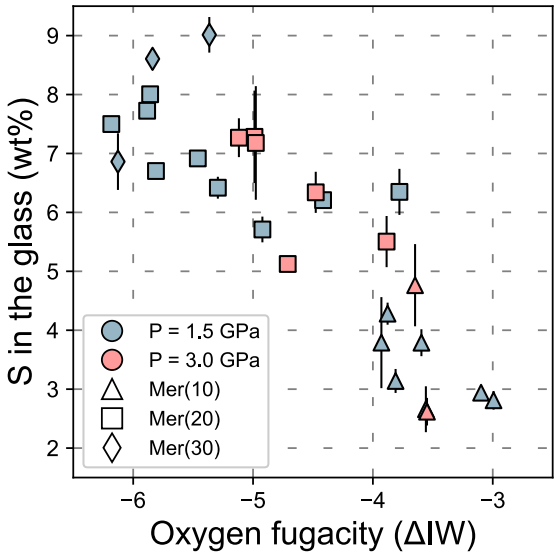

Figure 3.6. *Sulfur content in the silicate glass (wt%) as a function of the oxygen fugacity (ΔIW) from this study. fO_2 was calculated following the procedures of Cartier et al. (2014).*

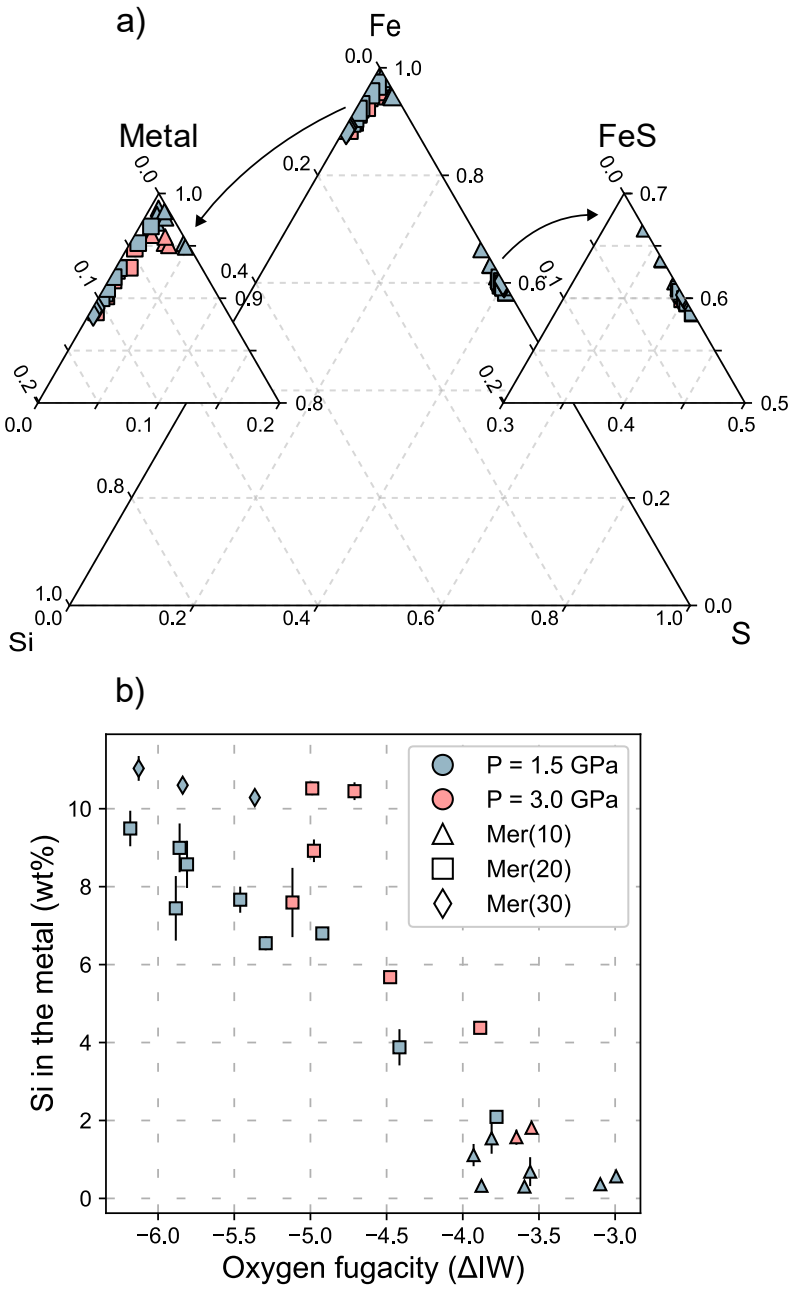

Figure 3.7. *(a) Fe – Si – S ternary diagram showing the composition (expressed in wt%) of Si-bearing Fe metal and FeS in our S-saturated experiments. (b) Si content in the metal as a function of the calculated oxygen fugacity (expressed in log units below the iron-wüstite buffer, IW).*

3.3.3. Attainment of Equilibrium and Time Series

Time series experiments were performed to test quantitatively the attainment of equilibrium and to check for potential escape of volatile species (mainly S and Na) during the runs. Five experiments were

run with starting composition Mer15(20), at 1700 °C and 1.5 GPa, and different durations (15 min, 30 min, 70 min, 3 hr, 6 hr; Fig S3.5.). Under these conditions, the silicate melt is saturated with olivine only. In all experiments, olivine displays a euhedral shape and homogeneous composition. Crystal size increases from short duration runs (less than 100 μm) to long duration runs (more than ~ 150 μm). The silicate glass does not display any remarkable differences in major element composition (e.g., Fig. S3.6.). Sulfur is readily incorporated in the silicate melt in the 15 min experiment, as shown by the little variation in S concentration at longer duration (Fig. S3.6.b). Only long duration experimental runs (> 1 hr) showed a significant Na loss (> ~ 40 %, Fig. S3.6.c). Based on these observations, we conclude that our experiments reached chemical equilibrium after less than 30 minutes, and that noticeable Na loss occurs after 1 hr. Additional information on the compositions and textures of our experiments (including the time series) can be found in Appendices A, B.

3.4.Discussion

3.4.1. The Effect of S on the Liquidus Temperature

Our experimental dataset clearly shows how the liquidus depresses in sulfur-saturated experiments as compared to sulfur-free systems (Fig. 3.3.). In such reducing conditions, sulfur bonds with crystal-forming cations, such as Mg and Ca (see section 3.4.2 for details). This process decreases the activities of the crystal forming elements bonded to oxygen (a_{MgO}, a_{CaO}) by the following reactions:

$$\frac{1}{2}S_{2,g} + MO_{Melt} = MS_{Melt} + \frac{1}{2}O_{2,g} \qquad \text{(Eq. 3.5)}$$

with M being a metal (e.g., Ca, Mg). This reaction also illustrates the strong effect of fO_2 on S solubility in the silicate melt (Fincham and Richardson, 1954; O'Neill and Mavrogenes, 2002).

The equilibrium constant of the above reaction can be written as:

$$K = \frac{(a_{O_{2,g}})^{1/2} a_{MS}}{(a_{S_{2,g}})^{1/2} a_{MO}} \qquad \text{(Eq. 3.6)}$$

and illustrates that S incorporation in the silicate melt decreases the melt degree of saturation of key silicate phases (olivine, orthopyroxene) at a given temperature (section 3.4.2).

The effect of sulfur on the liquidus temperature of a silicate phase is given by the temperature difference between the saturation temperatures of the phase in the S-free compositions and the corresponding S-bearing compositions, as shown below. Here, we parameterize our data for the liquidus depression by considering the liquidus temperatures of olivine and orthopyroxene together:

$$\Delta T_{Liq(ol,opx)} = T_{Liq,S-free(ol,opx)} - T_{Liq,S-bearing\ (ol,opx)} \qquad \text{(Eq. 3.7)}$$

Because we performed experiments over a range of temperatures, we produced a range of melt compositions. For each of these melt compositions, we can define a liquidus temperature. In the case of our S-bearing runs, this temperature corresponds to $T_{\text{Liq, S-bearing}}$ in Eq. (3.7). Defining $T_{\text{Liq, S-free}}$ from Eq. (3.7) for S-bearing experiments is more complicated as $T_{\text{liq, S-free}}$ would correspond to the liquidus temperature of our experimental melts if they were S-free. Importantly, our S-free experiments cannot be considered as direct analogue S-free melts of our S-bearing melts because early crystallizing phases in these S-free melts with high liquidus temperatures lead to significant changes in melt composition as compared to S-bearing melts at a given temperature. Compositional differences also result from the incorporation of Si in the iron alloy and from the formation of (Fe,Mg,Cr,Mn)S phases which also change the composition of the equilibrium silicate melts.

The S-free experiments are valuable to build a predictive liquid thermometer for S-free compositions which could be used for rather large compositional and temperature ranges. Here, we obtain $T_{\text{Liq, S-free}}$ by combining our S-free experimental melts, and published S-free experiments on Mercury-like melts (Charlier et al., 2013; Namur and Charlier, 2017; Namur et al., 2016a, b). In order to parameterize a liquid thermometer for Mercury-like compositions, we first expressed magma compositions in terms of mole percent of silicate components in the liquid. This approach is inspired by Lee et al. (2009), where silicate components are calculated based on the mole percent of oxides and normalized to an 8-oxygen basis (details provided in Appendix A of Lee et al., 2009). Using an F-test model (Zhang et al., 2023) and a compiled dataset from previous studies (N=89), we empirically derived the following expression to predict the temperature for S-free Mercury-like experiments:

$$T\,(^{\circ}\text{C}) = 899.6(64.2) + 9.9(3.0)Al_{\frac{16}{3}}O_8 + 10.6(1.0)Mg_4Si_2O_8 + 5.1(1.7)Na_2Al_2Si_2O_8 + 63.4(14.8)K_2Al_2Si_2O_8 + 0.0096(0.001)P \qquad \text{(Eq. 3.8)}$$

where the silicate components in Eq. (3.8) are given in mole percent (normalized to 100%), P is pressure in GPa, and numbers in parentheses represent the one standard error of the coefficients. All parameters have p-values less than 0.05, indicating they are statistically significant at the 95% confidence level.

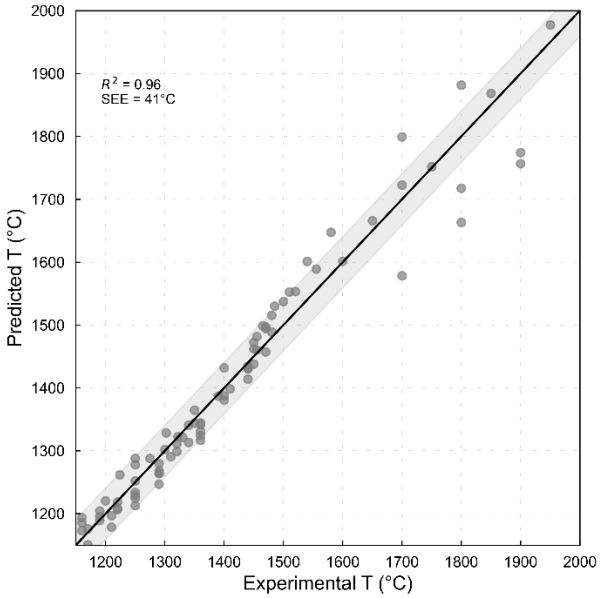

Figure 3.8. *Prediction of our experimental temperatures with liquid thermometry. The R^2 is 0.96 and the SEE is 41 °C. Grey areas represent the SEE of the fit.*

The fit achieves an R^2 value of 0.96, with a Standard Error of Estimate (SEE) of 41°C (Fig. 3.8.). To calculate the liquid temperature for our S-bearing experiments, we first renormalized the melt composition by excluding S. The normalized, S-free compositions were then used to calculate the silicate components as described above. This approach allows the calculation of the liquidus temperature on a S-free basis. Using the liquid thermometer, we then calculate the liquidus temperature of the silicate melt in our S-bearing experiments on a S-free basis (Table 3.2.), i.e. we determine what would be the temperature of a melt with the same elemental ratios for major elements if it was S-free. Finally, using Eq. (3.7) we calculate the temperature depression $\Delta T_{\mathrm{Liq(ol,\ opx)}}$ through a polynomial fit for the ΔT_{Liq} as a function of the S concentration in the melt (Fig. 3.9.).

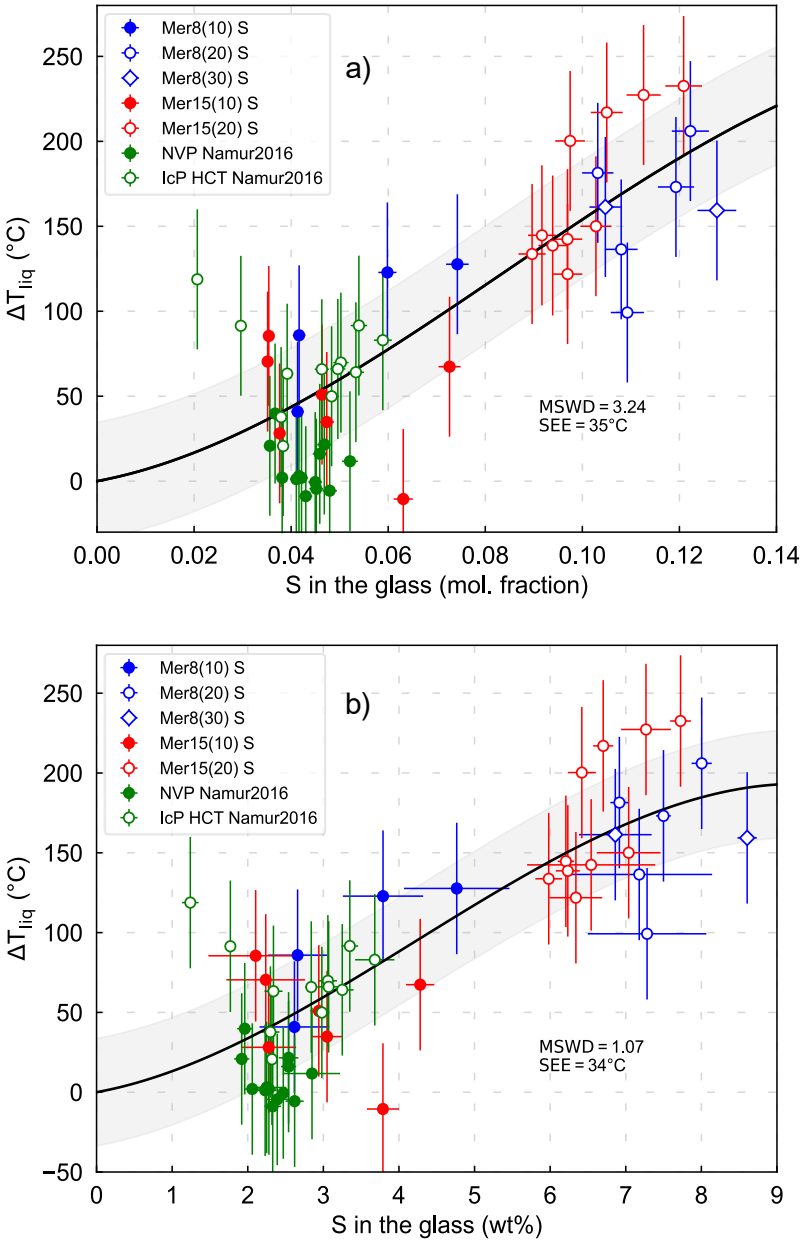

Figure 3.9. *Liquidus temperature depression (ΔT, °C) as a function of the sulfur content in the glass (expressed in (a) molar fraction and (b) in wt%). The fitted experimental data are from this study and from Namur et al. (2016a). Vertical bars represent the uncertainty of the thermometric model (more details are in section 3.4.1). Horizontal bars refer to the 1σ standard deviation of measurements. Grey areas represent the SEE of the polynomial fit.*

Multiple linear regression was performed to investigate the potential effect of pressure and major melt components (mainly Mg, Si, Ca, Al, Na) on the liquidus temperature, but returned p-values were too high to comprise them in our regression. Only sulfur was seen to be statistically relevant. In any case, we only include the S-bearing NVP and High-Mg IcP HCT glasses of Namur et al. (2016a) in our parameterization, as this enables us to use their compositional dataset in a manner similar to that used in this study. The S-free NVP and High-Mg IcP HCT experiments have been employed to build our liquid thermometer, while the S-bearing experiments have been used to parameterize the liquidus temperature depression as a function of the sulfur content in the melt. We used a polynomial similar to that described by Medard and Grove (2008) for H_2O:

$$\Delta T_{\mathrm{Liq}}(°\mathrm{C}) = -65208.22\,[S]^3_{\mathrm{Melt}} + 16595.32\,[S]^2_{\mathrm{Melt}} + 532.31\,[S]_{\mathrm{Melt}} \quad \text{(Eq. 3.9)}$$

$$\Delta T_{\mathrm{Liq}}(°\mathrm{C}) = -0.39\,[S]^3_{\mathrm{Melt}} + 4.89\,[S]^2_{\mathrm{Melt}} + 8.65\,[S]_{\mathrm{Melt}} \quad \text{(Eq. 3.10)}$$

where ΔT_{Liq} is the liquidus depression expressed in °C, and $[S]_{\mathrm{Melt}}$ is the concentration of sulfur in the silicate melt (in molar fraction in Eq. (3.9), and in wt% in Eq. (3.10)). The Mean Squared Weighted Deviation (MSWD) is 3.24 for Eq. (3.9) and 1.07 for Eq. (3.10), and the SEE is 35°C for Eq. (3.9) and 34 °C for Eq. (3.10).

Our experiments and modelling show that sulfur is as important as other volatiles in influencing the melt liquidus temperature (Fig. 3.10.). However, we note that for volatile concentrations below ca. 5 – 6 wt%, the degree of liquidus depression is less in S-bearing systems compared to systems with other volatiles such as H_2O and F (Médard and Grove, 2008; Almeev et al., 2007; Filiberto et al., 2012). For example, 4 wt% of H_2O in basaltic melts would depress the liquidus of about 110 – 120 °C (based on experiments performed at T = 1100 – 1350 °C, P = 0.0001 – 1 GPa; Medard and Grove, 2008; Almeev et al., 2007). Sulfur in the same concentration would decrease the liquidus by 100 °C. Chlorine in synthetic tholeiitic basalts however only causes a smaller degree of liquidus depression of about 40 °C for 4 wt% of Cl added (T ~ 1300 – 1500 °C, P = 0.7 – 1.5 GPa; Filiberto et al., 2014). At higher volatile concentrations (> 7 wt%), however, sulfur exerts a stronger effect. For instance, 9 wt% of S would depress the liquidus by ~ 193 °C whereas 9 wt% of dissolved H_2O would cause a liquidus drop of ca. 180 °C. Summarizing and considering the uncertainties related to each parameterization, we can see how the effect of sulfur on the liquidus temperature is as strong as the effect of H_2O and F, while it results to be more effective in lowering the liquidus temperature than Cl (Fig. 3.10.).

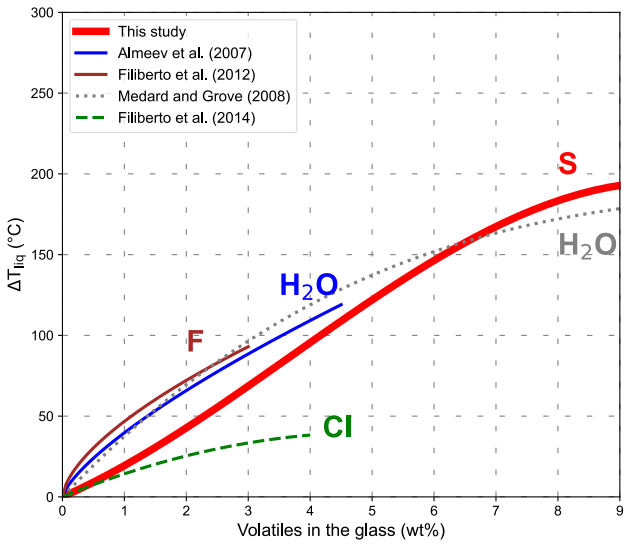

Figure 3.10. *Liquidus temperature depression (expressed in °C) as a function of the volatile content in the glass (in wt%). The effect of different volatiles (Cl, F, H2O) on the liquidus depression are shown as comparison (Almeev et al., 2007; Medard and Grove, 2008; Filiberto et al., 2012; Filiberto et al., 2014).*

3.4.2. The Role of Sulfur on the Olivine and Orthopyroxene Stability

The bulk silicate composition (Mg/Si) and the presence of sulfur have profound implications for silicate phase equilibria. By comparing S-free and S-saturated experimental runs, we show that olivine is the liquidus phase for Mer8 (at P = 1.5 GPa) and for Mer15 in S-free melts. S-saturated compositions, on the other hand, saturate orthopyroxene as the liquidus phase for Mer8, both at 1.5 GPa and 3 GPa. S-saturated Mer15 melts still saturate olivine as the liquidus mineral, although the stability field of olivine-only narrows significantly as more S is dissolved in the melt (Figs. 3.3.b, d, f).

We plot the compositions of our S-free and S-bearing silicate glasses on the olivine-Ca-tschermakite-quartz pseudoternary diagram (Fig. 3.11.). At low fO_2, the concentration of O^{2-} decreases, so that S^{2-} becomes an important anion in the melt (Anzures et al., 2020; Pommier et al., 2023). This is interpreted as S^{2-} replacing O^{2-} in $[SiO_4]^{4-}$ tetrahedra (Namur et al., 2016b). Sulfur can therefore bond with mineral-forming cations (e.g., Si, Mg, Ca, Mn, Na) forming S complexes (Eq. (3.5)). Indeed, MgS and CaS complexes have been thought to become stable below the IW buffer (Fogel, 2005). Raman spectra of MgS and CaS complexes in quenched silicate glasses at low fO_2 have been reported in the literature (Namur et al., 2016a). XANES spectra suggesting the presence of MgS, CaS in 1 atm silicate melts

have been also reported (Métrich et al., 2009). K-edge XANES spectra reporting MgS and CaS complexes in quenched glasses are shown in Anzures et al. (2020, 2025). Sulfur might therefore act as a network modifier, although it is also seen to bond with Si (Pommier et al., 2023), suggesting that sulfur might also display a structural role in the silicate melt. Viscosity of silicate melts indeed decreases in the presence of sulfur (Mouser et al., 2021). The nature of the cation with which S dominantly bonds is controlled by oxygen fugacity (Anzures et al., 2020, 2025). MgS is the dominant sulfide species at IW < -4.5 (plus minor CaS), while CaS is the main sulfide species at IW > -4.5 (Anzures et al., 2020, 2025). We therefore recalculated our S-bearing melts by considering the influence of the different sulfide species on the oxide fractions (e.g., X_{CaO}, X_{MgO}) of the melt as a function of fO_2. We show that the more reduced melts (that is, Mer + 20 wt% Si) move away from the olivine apex, whereas the relatively more oxidized melts (Mer + 10 wt% Si) move away from the Ca-Ts apex. In general, we observe that the plotted experimental melts in the presence of sulfur complexes cross the olivine-orthopyroxene phase boundary and move towards the orthopyroxene stability field.

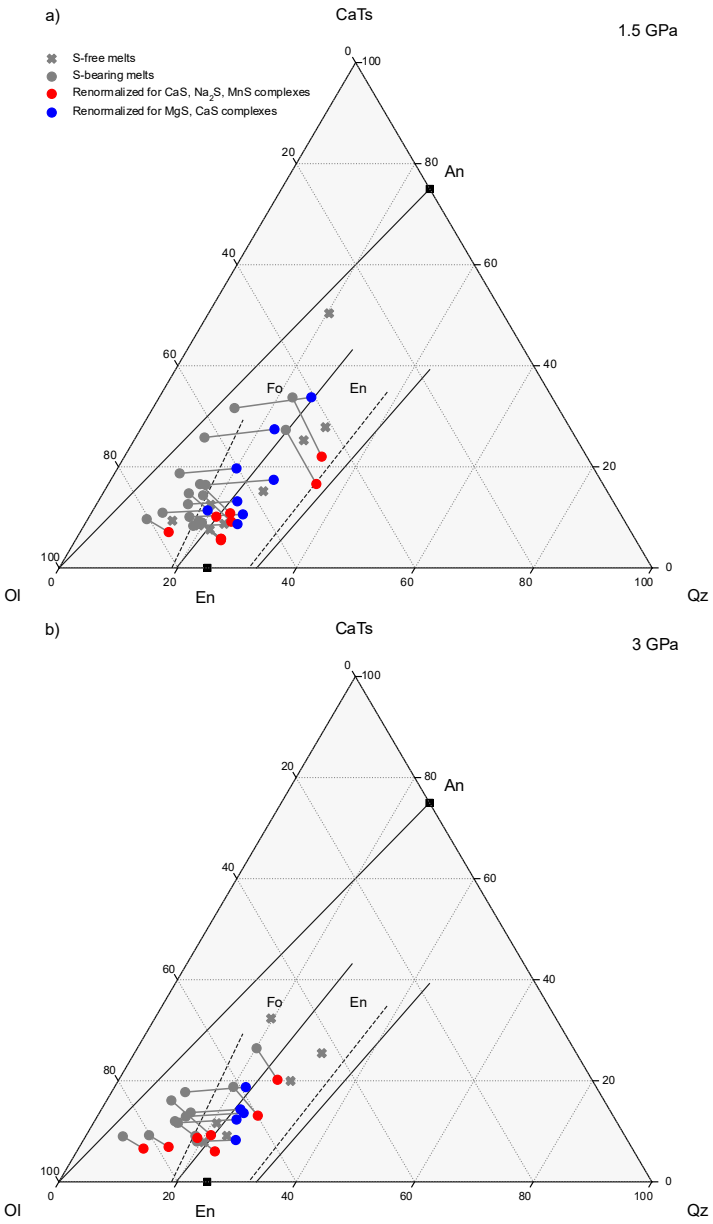

Figure 3.11. *Molecular normative projection from diopside of the major element compositions of our experimental glasses on the plane olivine-Ca-tschermak-quartz (Médard, 2004; Sorbadere et al., 2013). Cross symbols are S-free melts. Grey circles are S-bearing melts. Red circles are recalculated melt compositions by considering the formation of CaS, Na_2S, and MnS complexes. Blue circles represent recalculated melt compositions by considering the formation of MgS, CaS complexes (see also Fig. S8 Namur et al., 2016a; Anzures et al., 2020, 2025). Solid and dashed lines represent respectively 1 and 3 GPa phase boundaries in the CMAS system (Chen and Presnall, 1975; Milholland and Presnall, 1998; Sen & Presnall, 1984). Details on the calculation of the CMAS components are given in Appendix A (Section S3.6.).*

The bonding of S with silicate forming elements (e.g., Mg, Ca, Mn, Na) decreases the activity of the oxides of these elements in the silicate melt, affecting the saturation of the silicate crystals (Eq. (3.5)). Under less reducing conditions (IW > -4.5), S bonds with Ca forming CaS, which causes a decrease of the activity of CaO in the silicate melt. This affects the saturation of clinopyroxene, as compared to more reducing conditions (IW < -4.5). The lessened CaO activity (Ca^{2+} bonding with S^{2-}) would indeed delay the crystallization of clinopyroxene and plagioclase (Anzures et al., 2020). Our experiments also feature clinopyroxene only in S-free runs (Fig. 3.3.). The absence of clinopyroxene in our S-saturated runs could be caused by the decreased CaO activity, whereas the presence of clinopyroxene can be simply caused by the lower melt fraction in S-free experiments, which makes the residual melt richer in CaO. A combination of the two effects is also plausible. In more reducing systems, sulfur complexing with Mg would decrease the activity of MgO (and comparatively increase the activity of SiO_2) in the silicate melt, favoring orthopyroxene at the expense of olivine (Anzures et al., 2020, Eq. (3.4)). The expansion of the orthopyroxene stability field at the expense of olivine is also favored at increasing pressure (Chen and Presnall, 1975; Milholland and Presnall, 1998; Sen & Presnall, 1984). It needs to be pointed out, though, that the replacement of S^{2-} on the anion sublattice would also decrease the activity of SiO_2 (O'Neill, 2021), even if the effect on MgO is larger than that on SiO_2.

Our results are in accordance with Namur et al. (2016b) who showed the contraction of the olivine stability field in favour of orthopyroxene in the presence of sulfur. Using the same starting compositions as in this study, Xu et al. (2024) show that forsterite is still the liquidus phase for Mer15(20) + S at higher pressure (7 GPa), while olivine+orthopyroxene represents the first phases appearing for Mer8(20) + S, indicating that the effect of a_{SiO2} and a_{MgO} on phase stability observed in this study is valid over a large pressure range.

3.4.3. Implications for the Orthopyroxene-Olivine-Melt Cotectic

Sulfur has a major influence in lowering the pressure-temperature conditions of the orthopyroxene-olivine-melt cotectic. Our study confirms the lowering of the cotectic in the presence of sulfur for Mer8 (Figs. 3.3.a, c, e). As shown in Fig. 3.3.a, the cotectic is located at $T \sim 1840$ °C, $P \sim 2.3$ GPa in S-free Mer8. In Fig. 3.3.c, the cotectic of S-saturated Mer8(10) is located at $T \sim 1680$ °C, $P =$ 1.4 GPa. This means that for S-saturated Mer8(10), the temperature difference (ΔT) is ~ 160 °C, and the difference in pressure (ΔP) is ~ 0.9 GPa. The cotectic in S-saturated Mer8(20) is found even lower in the *T*-*P* diagram (Fig. 3.3.e), and is located at $T \sim 1520$ °C, $P \sim 0.9$ GPa. This would yield $\Delta T \sim 320$ °C, $\Delta P \sim 1.4$ GPa for S-saturated Mer8(20). It's clear from this comparison that the cotectic shift is larger for S-bearing Mer8(20) than for S-bearing Mer8(10), as more sulfur is dissolved in the silicate melt. The amount of dissolved S is caused by more reducing conditions in Mer8(20) than in Mer8(10).

We estimate a cotectic depression of $\Delta T \sim 50$ °C, $\Delta P \sim 0.3$ GPa for every 1 wt% S added in the silicate melt. Namur et al. (2016b) first showed how the olivine-orthopyroxene cotectic (or multi-saturation point, MSP) is shifted towards lower temperatures and pressures in the presence of sulfur. They found a $\Delta T = 85$ °C, $\Delta P = 0.95$ GPa for the more Mg-rich Intercrater Plains, Heavily cratered Terrains composition (IcP HCT). As for the North Volcanic Plains composition (NVP), $\Delta T = 65$ °C and $\Delta P = 0.55$ GPa. The difference in the cotectic pressure shift was found to be dependent on the nepheline and anorthite components, which are more impacted when CaS, and Na_2S complexes form (Namur et al. 2016b). The inferred pressure shifts of the cotectic obtained in this study are larger than those in Namur et al. (2016b) due to the lower anorthite and nepheline components in Mer8 and Mer15 mantle compositions than in IcP-HCT, and NVP crustal compositions (Fig. 3.11., this study; Fig.S3.8. in Namur et al. 2016b).

3.4.4. Implications for the Magma Ocean Differentiation

Although the exact bulk silicate composition of Mercury (BSMe) is under debate (Brown and Elkins-Tanton, 2009), our results are still indicative for the magma ocean differentiation of Mercury. Enstatite chondrites (EC) have been historically considered as the precursor material for building Mercury, although recent studies argued against a pure EC origin for the planet (Cartier and Wood, 2019; Anzures et al., 2020). Anzures et al. (2020) proposed as Mercury's precursory material the bulk silicate composition of a metal-rich carbonaceous chondrite (CH). In an attempt to explore what the BSMe can be, our SiO_2-depleted EC-like starting materials can be considered as end member compositions with respect to the CH-based primitive mantle (PMM) of Anzures et al. (2020) (see Fig. 3.1.). Magma ocean crystallization models generally assume a basal dunite layer (Mouser et al., 2021; Mouser and Dygert, 2023). Only Anzures et al. (2020) posit an orthopyroxene layer at the base of the primordial mantle. Magma oceans with a higher Mg/Si ratio (like PMM in Anzures et al. 2020, Mer15 of this study) would first crystallize olivine, while BSMes with a low Mg/Si ($< \sim 0.9$, Mer8) would be saturated in orthopyroxene first.

Our experimental results combined with studies in the literature allow us to better place constraints on the early differentiation of Mercury's magma ocean. If the mantle of Mercury is similar to Mer8 and is S-saturated, our experiments show that orthopyroxene is the liquidus mineral, which is also the case at high pressure ($P = 7$ GPa; Xu et al., 2024). This indicates that orthopyroxene is the liquidus phase at the core mantle boundary conditions of Mercury ($P \sim 5.8$ GPa; Goossens et al., 2022; Xu et al., 2024) and likely forms a basal layer. Also, once it reaches the saturation condition of olivine, orthopyroxene will still be the dominant crystallizing mineral. This would have major implications for the interior dynamics and thermal evolution history of the silicate mantle of Mercury. Pyroxenes display different

rheological properties as compared to olivine. Clinopyroxene and orthopyroxene are less viscous than olivine, which would make mantle convection on Mercury more vigorous and more lasting (Cioria et al., 2024). Thermal properties of orthopyroxene are also different from olivine. Because thermal conductivity in orthopyroxene is greater than in olivine, orthopyroxene-rich mantle geotherms would be colder than olivine-rich mantle geotherms (Guo et al., 2024; Zhang et al., 2019). On the contrary, if BSMe is more similar to Mer15, olivine would be the first silicate mineral to crystallize from the MMO. A dunite layer would be present at the base of the mantle of Mercury, and its thickness will depend on the bulk S content of the MMO.

3.5.Conclusions

We performed 56 experiments on compositions representative of Mercury's average silicate composition over a wide range of physical and chemical conditions with the aim of investigating the silicate phase equilibria and the influence of sulfur on the liquidus temperature. Sulfur is responsible for lowering the olivine and orthopyroxene liquidus temperature of Mercurian melts. We propose a model linking the liquidus depression with the sulfur concentration in the melt. We found that 1 wt% S in the silicate melt would decrease the liquidus of around 20 °C. Sulfur is also responsible for lowering the olivine-orthopyroxene cotectic. Finally, sulfur is also crucial for stabilizing orthopyroxene at the expense of olivine. This has profound implications for Mercury's primordial mantle and its mineralogical layering, as the Hermean planet would likely host an orthopyroxenite layer at the base of the mantle. Pyroxene-dominated mantles might display a sensibly different dynamics and evolution compared to olivine-dominated mantles. However, our approach was unable to discern additional variables, such as pressure and melt composition, which may influence the role of sulfur in lowering the liquidus temperature. Future studies are also needed to further investigate the thermodynamic behaviour of reduced S-rich melts in greater detail.

Acknowledgements

We thank Sonja Aulbach (Editor), Hugh O'Neill, and Yuan Li for the insightful comments that greatly improved this manuscript. FS also wishes to thank Roman Klinghardt and Jean-Luc Devidal for their help with the SEM and the EPMA, respectively. This research was funded by the National Fund of Scientific Research (FNRS, Belgium) grant FRIA 40009280 (Fund for Research Training in Industry and Agriculture). BC is a Research Associate of the Belgian Fund for Scientific Research-FNRS and acknowledges funding from the ESA PRODEX Program (Grant 4000142722). ON acknowledges

support from the European Research Council (ERC) for a Consolidator Grant (IronHeart) under the European Union's Horizon (grant agreement no. 101125126).

CRediT authorship contribution statement

Fabrizio Saracino: conceptualization, writing - original draft, investigation, data analysis, visualization **Bernard Charlier:** conceptualization, supervision, writing - reviewing and editing **Yishen Zhang:** data analysis, modelling, writing - reviewing and editing **Manon Lécaille:** data analysis, modelling, modelling, visualization, writing - reviewing and editing **Yanhao Lin:** writing - reviewing and editing **Olivier Namur:** conceptualization, modelling, writing - reviewing and editing

References

Almeev, R.R., Holtz, F., Koepke, J., Parat, F., Botcharnikov, R.E., 2007. The effect of H_2O on olivine crystallization in MORB: Experimental calibration at 200 MPa. Am. Mineral. 92, 670–674. https://doi.org/10.2138/am.2007.2484

Anzures, B.A., Parman, S.W., Milliken, R.E., Namur, O., Cartier, C., McCubbin, F.M., Vander Kaaden, K.E., Prissel, K., Iacovino, K., Lanzirotti, A., Newville, M., 2025. An oxygen fugacity-temperature-pressure-composition model for sulfide speciation in Mercurian magmas. Geochim. Cosmochim. Acta 388, 61–77. https://doi.org/10.1016/j.gca.2024.11.012

Anzures, B.A., Parman, S.W., Milliken, R.E., Namur, O., Cartier, C., Wang, S., 2020. Effect of sulfur speciation on chemical and physical properties of very reduced Mercurian melts. Geochim. Cosmochim. Acta 286, 1–18. https://doi.org/10.1016/j.gca.2020.07.024

Berthet, S., Malavergne, V., Righter, K., 2009. Melting of the Indarch meteorite (EH4 chondrite) at 1GPa and variable oxygen fugacity: Implications for early planetary differentiation processes. Geochim. Cosmochim. Acta 73, 6402–6420. https://doi.org/10.1016/j.gca.2009.07.030

Boukaré, C. E., Parman, S.W., Parmentier, E.M., Anzures, B.A., 2019. Production and preservation of sulfide layering in Mercury's mantle. J. Geophys. Res. Planets 124, 3354–3372. https://doi.org/10.1029/2019JE005942

Boulliung, J., Wood, B.J., 2023. Sulfur oxidation state and solubility in silicate melts. Contrib. Mineral. Petrol. 178, 56. https://doi.org/10.1007/s00410-023-02033-9

Brey, G., Green, D.H., 1977. Systematic study of liquidus phase relations in olivine melilitite $+H_2O$ $+CO_2$ at high pressures and petrogenesis of an olivine melilitite magma. Contrib. Mineral. Petrol. 61, 141–162. https://doi.org/10.1007/BF00374364

Brown, S.M., Elkins-Tanton, L.T., 2009. Compositions of Mercury's earliest crust from magma ocean models. Earth Planet. Sci. Lett. 286, 446–455. https://doi.org/10.1016/j.epsl.2009.07.010

Cartier, C., Hammouda, T., Doucelance, R., Boyet, M., Devidal, J.-L., Moine, B., 2014. Experimental study of trace element partitioning between enstatite and melt in enstatite chondrites at low oxygen fugacities and 5GPa. Geochim. Cosmochim. Acta 130, 167–187. https://doi.org/10.1016/j.gca.2014.01.002

Cartier, C., Namur, O., Nittler, L.R., Weider, S.Z., Crapster-Pregont, E., Vorburger, A., Frank, E.A. and Charlier, B., 2020. No FeS layer in Mercury? Evidence from Ti/Al measured by MESSENGER. Earth Planet. Sci. Lett. 534, 116108. https://doi.org/10.1016/j.epsl.2020.116108

Cartier, C., Wood, B.J., 2019. The role of reducing conditions in building Mercury. Elements 15, 39–45. https://doi.org/10.2138/gselements.15.1.39

Chabot, N.L., Wollack, E.A., Klima, R.L., Minitti, M.E., 2014. Experimental constraints on Mercury's core composition. Earth Planet. Sci. Lett. 390, 199–208. https://doi.org/10.1016/j.epsl.2014.01.004

Charlier, B., Grove, T.L., Zuber, M.T., 2013. Phase equilibria of ultramafic compositions on Mercury and the origin of the compositional dichotomy. Earth Planet. Sci. Lett. 363, 50–60. https://doi.org/10.1016/j.epsl.2012.12.021

Chen, C.-H., Presnall, D.C., 1975. The system Mg_2SiO_4-SiO_2 at pressures up to 25 kilobars. Am. Mineral. 60, 398–406.

Cioria, C., Mitri, G., Connolly, J.A.D., Perrillat, J., Saracino, F., 2024. Mantle mineralogy of reduced sub-Earths exoplanets and exo-Mercuries. J. Geophys. Res. Planets 129, e2023JE008234. https://doi.org/10.1029/2023JE008234

Condamine, P., Tournier, S., Charlier, B., Médard, E., Triantafyllou, A., Dalou, C., Tissandier, L., Lequin, D., Cartier, C., Füri, E., Burnard, P.G., Demouchy, S., Marrocchi, Y., 2022. Influence of intensive parameters and assemblies on friction evolution during piston-cylinder experiments. Am. Mineral. 107, 1575–1581. https://doi.org/10.2138/am-2022-7958

Corgne, A., Keshav, S., Wood, B.J., McDonough, W.F., Fei, Y., 2008. Metal–silicate partitioning and constraints on core composition and oxygen fugacity during Earth accretion. Geochim. Cosmochim. Acta 72, 574–589. https://doi.org/10.1016/j.gca.2007.10.006

Dasgupta, R., Mallik, A., Tsuno, K., Withers, A.C., Hirth, G., Hirschmann, M., 2013. Carbon-dioxide-rich silicate melt in the Earth's upper mantle. Nat. 493, 211–215. https://doi.org/10.1038/nature11731

de Capitani, C., Brown, T.H., 1987. The computation of chemical equilibrium in complex systems containing non-ideal solutions. Geochim. Cosmochim. Acta 51, 2639–2652. https://doi.org/10.1016/0016-7037(87)90145-1

de Capitani, C., Petrakakis, K., 2010. The computation of equilibrium assemblage diagrams with Theriak/Domino software. Am. Mineral. 95, 1006–1016. https://doi.org/10.2138/am.2010.3354

Farcy, B.J., Gross, J., Carpenter, P., Hicks, J., Filiberto, J., 2016. Effect of chlorine on near-liquidus crystallization of olivine-phyric shergottite NWA 6234 at 1 GP a: Implication for volatile-induced melting of the Martian mantle. Meteorit. Planet. Scien. 51, 2011–2022. https://doi.org/10.1111/maps.12662

Filiberto, J., Baratoux, D., Beaty, D., Breuer, D., Farcy, B.J., Grott, M., Jones, J.H., Kiefer, W.S., Mane, P., McCubbin, F.M., Schwenzer, S.P., 2016. A review of volatiles in the Martian interior. Meteorit. Planet. Sci. 51, 1935–1958. https://doi.org/10.1111/maps.12680

Filiberto, J., Chin, E., Day, J.M.D., Franchi, I.A., Greenwood, R.C., Gross, J., Penniston-Dorland, S.C., Schwenzer, S.P., Treiman, A.H., 2012. Geochemistry of intermediate olivine-phyric shergottite Northwest Africa 6234, with similarities to basaltic shergottite Northwest Africa 480 and olivine-phyric shergottite Northwest Africa 2990. Meteorit. Planet. Scien. 47, 1256–1273. https://doi.org/10.1111/j.1945-5100.2012.01382.x

Filiberto, J., Dasgupta, R., Gross, J., Treiman, A.H., 2014. Effect of chlorine on near-liquidus phase equilibria of an Fe–Mg-rich tholeiitic basalt. Contrib. Mineral. Petrol. 168, 1027. https://doi.org/10.1007/s00410-014-1027-1

Fincham, C.J.B., Richardson, F.D., 1954. The behaviour of sulphur in silicate and aluminate melts. Proc. Roy. Soc. Lond. Ser. A Math. Phys. Sci. 223, 40-62.

Fogel, R.A., 2005. Aubrite basalt vitrophyres: The missing basaltic component and high-sulfur silicate melts. Geochim. Cosmochim. Acta 69, 1633–1648. https://doi.org/10.1016/j.gca.2003.11.032

Goossens, S., Renaud J.P., Henning, W., G., Mazarico, E., Bertone, S., Genova, A., 2022. Evaluation of recent measurements of Mercury's moments of inertia and tides using a comprehensive Markov chain Monte Carlo method. Planet. Sci. J. 3, 37.

Gu, T., Stagno, V., Fei, Y., 2019. Partition coefficient of phosphorus between liquid metal and silicate melt with implications for the Martian magma ocean. Phys. Earth Planet. Inter. 295, 106298. https://doi.org/10.1016/j.pepi.2019.106298

Guo, X., Feng, B., Zhang, B., Zhai, S., Xue, W., Song, Yunke, Song, Yuping, Yan, X., 2024. Effect of iron content on the thermal conductivity and thermal diffusivity of orthopyroxene. Geochem. Geophys. Geosyst. 25, e2023GC011419. https://doi.org/10.1029/2023GC011419

Hauck, S.A., Margot, J., Solomon, S.C., Phillips, R.J., Johnson, C.L., Lemoine, F.G., Mazarico, E., McCoy, T.J., Padovan, S., Peale, S.J., Perry, M.E., Smith, D.E., Zuber, M.T., 2013. The curious case of Mercury's internal structure. J. Geophys. Res. Planets 118, 1204–1220. https://doi.org/10.1002/jgre.20091

Holzheid, A., Grove, T.L., 2002. Sulfur saturation limits in silicate melts and their implications for core formation scenarios for terrestrial planets. Am. Mineral. 87, 227–237. https://doi.org/10.2138/am-2002-2-304

Iacovino, K., McCubbin, F.M., Vander Kaaden, K.E., Clark, J., Wittmann, A., Jakubek, R.S., Moore, G.M., Fries, M.D., Archer, D., Boyce, J.W., 2023. Carbon as a key driver of super-reduced explosive volcanism on Mercury: Evidence from graphite-melt smelting experiments. Earth Planet. Sci. Lett. 602, 117908. https://doi.org/10.1016/j.epsl.2022.117908

Jarosewich, E., 1990. Chemical analyses of meteorites: A compilation of stony and iron meteorite analyses. Meteorit. Planet. Sci. 25, 323–337. https://doi.org/10.1111/j.1945-5100.1990.tb00717.x

Jugo, P.J., Luth, R.W., Richards, J.P., 2004. An experimental study of the sulfur content in basaltic melts saturated with immiscible sulfide or sulfate liquids at 1300 C and 1.0 GPa. J. Petrol. 46, 783–798. https://doi.org/10.1093/petrology/egh097

Keil, K., 2010. Enstatite achondrite meteorites (aubrites) and the histories of their asteroidal parent bodies. Geochem. J. 70, 295–317. https://doi.org/10.1016/j.chemer.2010.02.002

Kilburn, M.R., Wood, B.J., 1997. Metal–silicate partitioning and the incompatibility of S and Si during core formation. Earth Planet. Sci. Lett. 152, 139–148. https://doi.org/10.1016/S0012-821X(97)00125-8

King, A.J., Phillips, K.J.H., Strekopytov, S., Vita-Finzi, C., Russell, S.S., 2020. Terrestrial modification of the Ivuna meteorite and a reassessment of the chemical composition of the CI type specimen. Geochim. Cosmochim. Acta 268, 73–89. https://doi.org/10.1016/j.gca.2019.09.041

Lark, L.H., Parman, S., Huber, C., Parmentier, E.M., Head, J.W., 2022. Sulfides in Mercury's mantle: implications for Mercury's interior as interpreted from moment of inertia. Geophys. Res. Lett. 49, e2021GL096713. https://doi.org/10.1029/2021GL096713

Lee, C.-T.A., Luffi, P., Plank, T., Dalton, H., Leeman, W.P., 2009. Constraints on the depths and temperatures of basaltic magma generation on Earth and other terrestrial planets using new thermobarometers for mafic magmas. Earth Planet. Sci. Lett. 279, 20–33. https://doi.org/10.1016/j.epsl.2008.12.020

Li, X., Zhang, C., Almeev, R.R., Holtz, F., 2020. GeoBalance: an excel VBA program for mass balance calculation in Geoscience. Geochem. J. 80, 125629. https://doi.org/10.1016/j.chemer.2020.125629

Ma, C., Beckett, J.R., Rossman, G.R., 2011. Murchisite, Cr_5S_6, a new mineral from the Murchison meteorite. Am. Min. 96, 1905-1908. https://doi.org/10.2138/am.2011.3858

Malavergne, V., Toplis, M.J., Berthet, S., Jones, J., 2010. Highly reducing conditions during core formation on Mercury: implications for internal structure and the origin of a magnetic field. Icarus 206, 199–209. https://doi.org/10.1016/j.icarus.2009.09.001

Mavrogenes, J.A., O'Neill, H.St.C., 1999. The relative effects of pressure, temperature, and oxygen fugacity on the solubility of sulfide in mafic magmas. Geochim. Cosmochim. Acta 63, 1173–1180. https://doi.org/10.1016/S0016-7037(98)00289-0

McCoy, T.J., Dickinson, T.L., Lofgren, G.E., 1999. Partial melting of the Indarch (EH4) meteorite: a textural, chemical, and phase relations view of melting and melt migration, Meteorit. Planet. Sci 34(5), pp. 735–746. https://doi.org/10.1111/j.1945-5100.1999.tb01386.x

McCubbin, F.M., Riner, M.A., Vander Kaaden, K.E., Burkemper, L.K., 2012. Is Mercury a volatile-rich planet? Geophys. Res. Lett. 39, 2012GL051711. https://doi.org/10.1029/2012GL051711

McDonough, W.F. and Sun, S. -s., 1995. The composition of the Earth. Chem. Geol. 120(3–4), 223–253. https://doi.org/10.1016/0009-2541(94)00140-4

Médard, E., 2004. Genèse de magmas riches en calcium dans les zones de subduction et sous les rides médio-océaniques : approche expérimentale. Université Blaise Pascal - Clermont-Ferrand II, Français.

Médard, E., Grove, T.L., 2008. The effect of H2O on the olivine liquidus of basaltic melts: experiments and thermodynamic models. Contrib. Mineral. Petrol. 155, 417–432. https://doi.org/10.1007/s00410-007-0250-4

Métrich, N., Berry, A.J., O'Neill, H.St.C., Susini, J., 2009. The oxidation state of sulfur in synthetic and natural glasses determined by X-ray absorption spectroscopy. Geochim. Cosmochim. Acta 73, 2382–2399. https://doi.org/10.1016/j.gca.2009.01.025

Milholland, C.S., Presnall, D.C., 1998. Liquidus phase relations in the CaO–MgO–Al_2O_3–SiO_2 System at 3.0 GPa: the aluminous pyroxene thermal divide and high-pressure fractionation of picritic and komatiitic magmas. J. Petrol. 39(1), 3–27. https://doi.org/10.1093/petroj/39.1.3

Mouser, M.D., Dygert, N., 2023. On the potential for cumulate mantle overturn in Mercury. J. Geophys. Res. Planets 128, e2023JE007739. https://doi.org/10.1029/2023JE007739

Mouser, M.D., Dygert, N., Anzures, B.A., Grambling, N.L., Hrubiak, R., Kono, Y., Shen, G., Parman, S.W., 2021. Experimental investigation of Mercury's magma ocean viscosity: Implications for the formation of Mercury's cumulate mantle, its subsequent dynamic evolution, and crustal petrogenesis. J. Geophys. Res. Planets 126, e2021JE006946. https://doi.org/10.1029/2021JE006946

Namur, O., Charlier, B., 2017. Silicate mineralogy at the surface of Mercury. Nat. Geosci. 10, 9–13. https://doi.org/10.1038/ngeo2860

Namur, O., Charlier, B., Holtz, F., Cartier, C., McCammon, C., 2016a. Sulfur solubility in reduced mafic silicate melts: Implications for the speciation and distribution of sulfur on Mercury. Earth Planet. Sci. Lett. 448, 102–114. https://doi.org/10.1016/j.epsl.2016.05.024

Namur, O., Collinet, M., Charlier, B., Grove, T.L., Holtz, F., McCammon, C., 2016b. Melting processes and mantle sources of lavas on Mercury. Earth Planet. Sci. Lett. 439, 117–128. https://doi.org/10.1016/j.epsl.2016.01.030

Nilsson, K., Peach, C.L., 1993. Sulfur speciation, oxidation state, and sulfur concentration in backarc magmas. Geochim. Cosmochim. Acta 57, 3807–3813. https://doi.org/10.1016/0016-7037(93)90158-S

Nittler, L.R., Chabot, N.L., Grove, T.L., Peplowski, P.N., 2018. The chemical composition of Mercury, in: Solomon, S.C., Nittler, L.R., Anderson, B.J. (Eds.), Mercury. Cambridge University Press, pp. 30–51. https://doi.org/10.1017/9781316650684.003

Nittler, L.R., Frank, E.A., Weider, S.Z., Crapster-Pregont, E., Vorburger, A., Starr, R.D., Solomon, S.C., 2020. Global major-element maps of Mercury from four years of MESSENGER X-Ray Spectrometer observations. Icarus 345, 113716. https://doi.org/10.1016/j.icarus.2020.113716

Nittler, L.R., Starr, R.D., Weider, S.Z., McCoy, T.J., Boynton, W.V., Ebel, D.S., Ernst, C.M., Evans, L.G., Goldsten, J.O., Hamara, D.K., Lawrence, D.J., McNutt, R.L., Schlemm, C.E., Solomon, S.C., Sprague, A.L., 2011. The Major-Element Composition of Mercury's Surface from MESSENGER X-ray Spectrometry. Science 333, 1847–1850. https://doi.org/10.1126/science.1211567

O'Neill, H.S.C., Mavrogenes, J.A., 2002. The sulfide capacity and the sulfur content at sulfide saturation of silicate melts at 1400°C and 1 bar. J. Petrol. 43 (6), 1049-1087.

O'Neill, H.St.C., 1991. The origin of the Moon and the early history of the Earth—A chemical model. Part 1: The moon. Geochim. Cosmochim. Acta 55, 1135–1157. https://doi.org/10.1016/0016-7037(91)90168-5

O'Neill, H.S.C., 2021. The thermodynamic controls on sulfide saturation in silicate melts with application to ocean floor basalts, in: Moretti, R., Neuville, D.R. (Eds.), Magma Redox Geochemistry. John Wiley and Sons. https://doi.org/10.1002/9781119473206.ch10

Pirotte, H., Cartier, C., Namur, O., Pommier, A., Zhang, Y., Berndt, J., Klemme, S., Charlier, B., 2023. Internal differentiation and volatile budget of Mercury inferred from the partitioning of heat-producing elements at highly reduced conditions. Icarus 405, 115699. https://doi.org/10.1016/j.icarus.2023.115699

Pitsch, S, Connolly, J.A.D., Schmidt, M.W., Sossi, P.A., Liebske, C., 2025. Solids and liquids in the (Fe,Mg,Ca)S-system: experimentally determined and thermodynamically modelled phase relations. Phys. Chem. Miner. 52, 12. https://doi.org/10.1007/s00269-025-01313-z

Pommier, A., Tauber, M.J., Pirotte, H., Cody, G.D., Steele, A., Bullock, E.S., Charlier, B., Mysen, B.O., 2023. Experimental investigation of the bonding of sulfur in highly reduced silicate glasses and melts. Geochim. Cosmochim. Acta 363, 114–128. https://doi.org/10.1016/j.gca.2023.10.027

Sen, G., Presnall, D.C., 1984. Liquidus phase relationships on the join anorthite-forsterite-quartz at 10 kbar with applications to basalt petrogenesis. Contr. Mineral. Petrol. 85, 404–408. https://doi.org/10.1007/BF01150296

Sorbadere, F., Médard, E., Laporte, D., Schiano, P., 2013. Experimental melting of hydrous peridotite–pyroxenite mixed sources: Constraints on the genesis of silica-undersaturated magmas beneath volcanic arcs Earth Planet. Sci. Lett. 384, 42–56.

Steenstra, E.S., Seegers, A.X., Putter, R., Berndt, J., Klemme, S., Matveev, S., Bullock, E.S., Van Westrenen, W., 2020. Metal-silicate partitioning systematics of siderophile elements at reducing conditions: A new experimental database. Icarus 335, 113391. https://doi.org/10.1016/j.icarus.2019.113391

Taylor, G.J., 2013. The bulk composition of Mars. Geochemistry 73, 401–420. https://doi.org/10.1016/j.chemer.2013.09.006

Taylor, G.J., Scott, E.R.D., 2003. 1.18 - Mercury, in: Holland, H.D., Turekian, K.K. (Eds.), Treatise on Geochemistry. Pergamon, Oxford, pp. 477–485. https://doi.org/10.1016/B0-08-043751-6/01071-9

Vander Kaaden, K.E., McCubbin, F.M., Nittler, L.R., Peplowski, P.N., Weider, S.Z., Frank, E.A., McCoy, T.J., 2017. Geochemistry, mineralogy, and petrology of boninitic and komatiitic rocks on the Mercurian surface: insights into the Mercurian mantle. Icarus 285, 155–168. https://doi.org/10.1016/j.icarus.2016.11.041

Wallace, P., Carmichael, I.S.E., 1992. Sulfur in basaltic magmas. Geochim. Cosmochim. Acta 56, 1863–1874. https://doi.org/10.1016/0016-7037(92)90316-B

Weider, S.Z., Nittler, L.R., Starr, R.D., Crapster-Pregont, E.J., Peplowski, P.N., Denevi, B.W., Head, J.W., Byrne, P.K., Hauck, S.A., Ebel, D.S., Solomon, S.C., 2015. Evidence for geochemical terranes on Mercury: global mapping of major elements with MESSENGER's X-Ray Spectrometer. Earth Planet. Sci. Lett. 416, 109–120. https://doi.org/10.1016/j.epsl.2015.01.023

Weisberg, M., Prinz, M., Nehru, C., 1988. Petrology of ALH85085: a chondrite with unique characteristics. Earth Planet. Sci. Lett. 91, 19–32. https://doi.org/10.1016/0012-821X(88)90148-3

Wykes, J.L., O'Neill, H.St.C., Mavrogenes, J.A., 2015. The effect of FeO on the sulfur content at sulfide saturation (SCSS) and the selenium content at selenide saturation of silicate melts. J. Petrol. 56, 1407–1424. https://doi.org/10.1093/petrology/egv041

Xu, Y., Lin, Y., Wu, P., Namur, O., Zhang, Y., Charlier, B., 2024. A diamond-bearing core-mantle boundary on Mercury. Nat. Commun. 15, 5061. https://doi.org/10.1038/s41467-024-49305-x

Zhang, Y., Namur, O., Li, W., Shorttle, O., Gazel, E., Jennings, E., Thy, P., Grove, T.L., Charlier, B., 2023. An extended calibration of the olivine–spinel aluminum exchange thermometer: application to the melting conditions and mantle lithologies of large igneous provinces. J. Petrol. 64, egad077. https://doi.org/10.1093/petrology/egad077

Zhang, Y., Yoshino, T., Yoneda, A., Osako, M., 2019. Effect of iron content on thermal conductivity of olivine with implications for cooling history of rocky planets. Earth Planet. Sci. Lett. 519, 109–119. https://doi.org/10.1016/j.epsl.2019.04.048

Zolotov, M.Yu., Sprague, A.L., Hauck, S.A., Nittler, L.R., Solomon, S.C., Weider, S.Z., 2013. The redox state, FeO content, and origin of sulfur-rich magmas on Mercury. J. Geophys. Res. Planets 118, 138–146. https://doi.org/10.1029/2012JE004274

Chapter 4: The Crystallization of Mercury's Magma Ocean and the Formation of its Primordial Mantle Structure

Fabrizio Saracino [1], Bernard Charlier [1], Yishen Zhang [2,3], Olivier Namur [3]

[1] Department of Geology, University of Liege, 4000 Liege, Belgium

[2] Department of Earth, Environmental, and Planetary Sciences, Rice University, 6100 Main Street, MS 126, Houston, TX 77005, USA

[3] Department of Earth and Environmental Sciences, KU Leuven, Celestijnenlaan 200E, 3001 Leuven, Belgium

Manuscript under review in *Advances in Geochemistry and Cosmochemistry*

Abstract

Early in its history, Mercury underwent a magma ocean stage; its crystallization produced a primordial mantle and a flotation crust, setting the stage for early volcanism, crustal production, and thermochemical evolution. Here, we performed crystallization experiments on reduced, sulfur-rich silicate melt compositions relevant to Mercury's magma ocean and its solidification during cooling. Our approach aims to reconstruct the primordial mantle stratigraphy by combining a fractional crystallization model with phase equilibria experiments on a suite of residual melts at 1525–1125 °C and 1.5–0.5 GPa under low oxygen fugacity (−3.7 to −8.4 log units below iron-wüstite equilibrium) to investigate the crystallization sequence for two potential Bulk Silicate Mercury compositions: a low-Mg/Si melt in the enstatite stability field and a high-Mg/Si melt in the forsterite stability field. Residual melts become co-saturated in enstatite and forsterite, followed by the crystallization of clinopyroxene at melt fractions F = 0.40–0.35, quartz at F = 0.28–0.24, and plagioclase at F = 0.19–0.14. We define the evolution of the mantle cumulate pile and the thickness of the refractory and fertile reservoirs based on the appearance of clinopyroxene. We propose that Mercury's volcanic crust resulted from partial melting of the fertile mantle. Density calculations indicate that sulfur reduced the density of the silicate magma ocean, causing sulfides to become denser than the magma ocean, ultimately being stored in the mantle. We illustrate the influence of the magma ocean bulk composition ± sulfides on the storage and spatial distribution of heat-producing elements in Mercury's interior.

4.1. Introduction

Accretionary impacts, metal–silicate segregation, and the decay of short-lived radioisotopes would have produced enough thermal energy to completely melt Mercury during its very early evolution, forming a global silicate magma ocean (Schubert et al., 1988; Schaefer and Elkins-Tanton, 2018; Charlier and Namur, 2019). Subsequent crystallization of the magma ocean ultimately produced the primordial Mercurian mantle, whose vertical structure was determined by the crystallization regime and the initial composition of the bulk silicate Mercury (BSMe), although the latter remains debated (Brown and Elkins-Tanton, 2009; Nittler et al., 2018; Anzures et al., 2020; Xu et al., 2024; Fischer and Parman, 2025). Experimental studies of surface lavas indicate significant compositional diversity within Mercury's mantle (Charlier et al., 2013; Namur et al., 2016a; Wang et al., 2022). Partial melting of certain chondritic precursors could also generate a wide variety of lava compositions, but this process alone cannot account for the full range of surface compositions observed on Mercury (Boujibar et al., 2025). Investigating the crystallization products of the Mercurian magma ocean (MMO) is thus crucial because its initial structure would have impacted convection and the thermal evolution of the mantle, setting the stage for mantle melt generation and effusive volcanism, which built the secondary crust until ca. 3.5 Ga (Brown and Elkins-Tanton, 2009; Byrne et al., 2016; McCoy et al., 2018; Mouser et al., 2021; Mouser and Dygert, 2023; Boukaré et al., 2019).

The MMO was unique among terrestrial planets: the MESSENGER spacecraft revealed the unusually high sulfur content and near FeO-free nature of Mercury's volcanic surface, which indicate highly reduced conditions (Nittler et al., 2011; McCubbin et al., 2012; Zolotov et al., 2013; Namur et al., 2016a). The high inferred bulk mantle S content (Namur et al., 2016a; Lark et al., 2022) has led authors to suggest that sulfide phases should have formed in the MMO, subsequently being stored in the mantle and/or primordial crust and potentially storing heat producing elements (HPEs; Boukaré et al., 2019; Boujibar et al., 2019; Pirotte et al., 2023). This process may have induced mantle overturn post-magma ocean crystallization (Mouser and Dygert, 2023). Vander Kaaden and McCubbin (2015) suggested that graphite would have been the only buoyant phase in such a FeO–depleted MMO, the flotation of which likely contributed to the formation of a graphite primordial crust. Investigating melt density and the specific effect of sulfur in the cooling and evolving magma ocean is thus crucial to quantitatively evaluate if other light phases such as sulfides, quartz, and plagioclase could have become buoyant during solidification. Moreover, if containing significant amounts of HPEs, the distribution of sulfide phases could have substantially impacted Mercury's thermal evolution (Boukaré et al., 2019; Boujibar et al., 2019; Pirotte et al., 2023).

In this study, we present crystallization experiments aimed at reconstructing the vertical structure of Mercury's primordial mantle as a direct consequence of the fractional crystallization of the putative MMO. By combining these and previous experiments, we develop a phase equilibria-based

crystallization model of the mineralogical and chemical evolution of the MMO from a range of BSMe compositions with different starting Mg/Si ratios. We further investigate the effect of sulfur content on the differentiation and density of the residual liquids, as well as the likelihood of crystalline phase flotation and its impact on the distribution of heat-producing elements. Our results refine our understanding of Mercury's early differentiation in terms of mantle mineralogy under reduced conditions.

4.2. Bulk Silicate Mercury (BSMe)

Enstatite chondrites (ECs) have commonly been considered as analogs of Mercury's building blocks due to their similar geochemical features, including FeO–free silicate phases and high abundances of sulfur and alkali metals (Na, K) (McCoy et al., 1999; Malavergne et al., 2010; Nittler et al., 2018; Fischer and Parman, 2025). The composition of the BSMe has been investigated by combining data from surface lavas with experiments simulating mantle melting (Namur et al., 2016a; Nittler et al., 2018) and by defining magmatic fractionation lines of surface and mantle compositions (Anzures et al., 2020; Fischer and Parman, 2025). Nittler et al. (2018) calculated the mantle source compositions of the high-Mg region and the North Volcanic Plains by considering the phase proportions and compositions of enstatite and forsterite reported by Namur et al. (2016a). Their results were similar to the silicate portion of enstatite chondrites and bencubbinites, adjusted to account for SiO_2 reduction to Si stored in the core under reduced conditions (e.g., Malavergne et al., 2010; Chabot et al., 2014). Recently, Fischer and Parman (2025) calculated a revised BSMe composition based on a new Mercury Fractionation Line (MFL) obtained by recalculating the Mg/Si and Al/Si ratios of X-Ray Spectrometer (XRS) data in McCoy et al. (2018). Because ECs are enriched in SiO_2 (Fig. 4.1.), they calculated the amount of Si being reduced and removed to the core for each published EC composition until the Si-depleted compositions fell along the MFL. Anzures et al. (2020) proposed a modified CH3 chondrite composition (ALH 85085) as the best approximation of the BSMe, due to its similar Mg/Si, Al/Si, Fe/Si, and Ni/Si ratios.

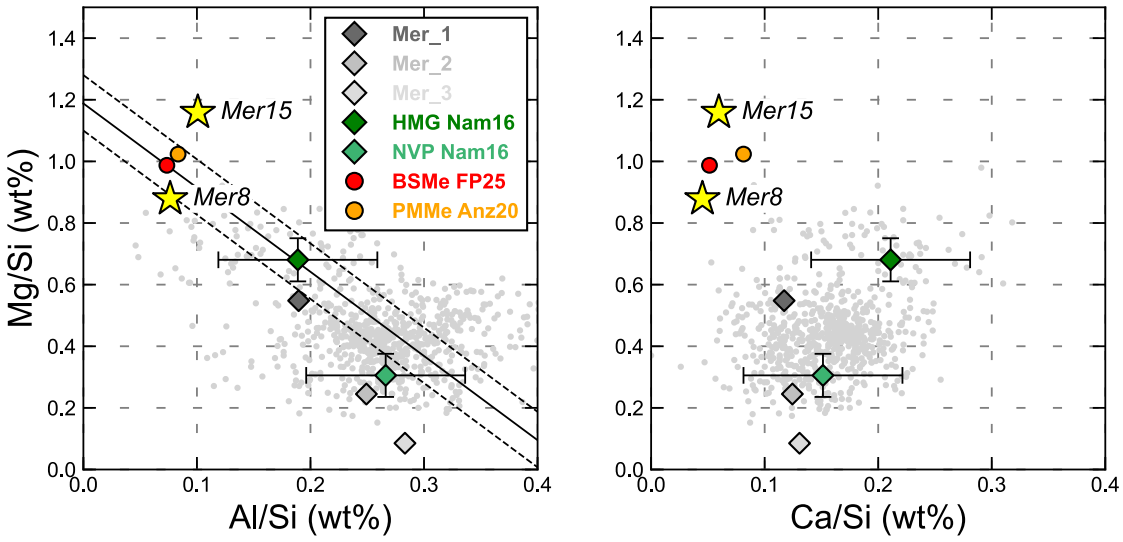

Figure 4.1. *Elemental ratios of major elements (wt%) of our starting compositions for (a) Al/Si versus Mg/Si and (b) Ca/Si versus Mg/Si. Also shown for comparison are the Bulk Silicate Mercury (BSMe) from Fischer and Parman (2025), the Primitive Mantle of Mercury (PMMe) from Anzures et al. (2020), and the Northern Volcanic Plains (NVP) and the High-Mg Intercrater Plains (HMG) from Namur et al. (2016b). Small grey circles are XRS measurements from Weider et al. (2015). The black solid line in (a) is the Mercury Fractionation Line (MFL), with relative upper and lower bounds (dashed lines) as calculated in Fischer and Parman (2025).*

The BSMe compositions considered in this study are inspired by the composition of the silicate fraction of enstatite chondrites (Fig. 4.1., Table 4.1.; Xu et al., 2024; Saracino et al., 2025). An average composition was obtained from chemical analyses of both high-iron (EH) and low-iron (EL) enstatite chondrites (Jarosewich, 1990; Berthet et al., 2009). We also decreased the P_2O_5 content to account for the markedly siderophile behaviour of P (Gu et al., 2019; Steenstra et al., 2020; Pirotte et al., 2023). Some Si was also removed from the original chondritic composition: two compositions with different Mg/Si ratios were selected, corresponding to the segregation of 8 wt% and 15 wt% Si from the silicate fraction into the core (named Mer8 and Mer15, respectively; Xu et al., 2024; Saracino et al., 2025). Assuming that the core of Mercury represents 67% of the planet's bulk mass (Hauck et al., 2013), these values reflect core Si contents of 2.9 wt% (Mer8) and 5.5 wt% Si (Mer15), spanning the lower range of estimated Si contents in the core of Mercury (Nittler et al., 2018). Our two compositions thus cover the BSMe compositional fields of Anzures et al. (2020) and Fischer and Parman (2025). Testing starting compositions with a range of different Mg/Si ratios is important because Mg/Si is known to promote the stability of enstatite or forsterite (Namur et al., 2016a; Anzures et al., 2020; Saracino et al., 2025).

Table 4.1. *Compositions of starting materials (expressed in wt%). Also shown are (a) pre-melting mantle compositions of the Northern Smooth Plains and Intercrater Highly cratered Terrains (Nittler et al., 2018); (b) PMM, the Primitive Mercurian Mantle (Anzures et al., 2020), (c) Bulk Silicate Mercury (Fischer and Parman, 2025), and (d) Bulk Silicate Earth (McDonough, 2025). Abbreviations: n.d., not determined.*

	Primitive compositions		**Pre-melting mantle (NSP)[a]**	**Pre-melting mantle (IcP HCT)[a]**	**Primitive Mantle Mercury[b]**	**Bulk Silicate Mercury[c]**	**Bulk Silicate Earth[d]**
	Mer8	**Mer15**					
SiO_2	54.82	47.91	53.67	51.98	51.32	52.06	44.92
TiO_2	0.14	0.16	0.24	0.21	0.21	0.13	0.20
Al_2O_3	3.70	4.26	4.57	4.24	3.78	3.38	4.19
Cr_2O_3	0.52	0.60	n.d.	n.d.	0.41	0.54	0.33
FeO_{tot}	n.d.	n.d.	0.02	0.03	0.54	0.20	8.05
MnO	0.28	0.33	n.d.	n.d.	0.09	0.31	0.14
MgO	37.32	43.04	36.89	37.64	40.72	39.84	37.81
CaO	1.62	1.87	2.26	3.84	2.73	1.75	3.27
Na_2O	1.37	1.58	1.97	1.29	0.08	1.62	0.36
K_2O	0.13	0.15	0.05	0.04	0.02	0.17	0.03
P_2O_5	0.10	0.10	n.d.	n.d.	n.d.	n.d	0.02
NiO	n.d.	n.d.	n.d.	n.d.	0.11	n.d	0.22
Total	100.00	100.00	99.67	99.27	100.01	100.00	99.54
Mg/Si	0.88	1.16	0.89	0.93	1.02	0.99	1.09
Ca/Al	1.18	1.18	1.34	2.45	1.95	1.40	2.11

4.3. Magma Ocean Modelling

4.3.1. Fractional Crystallization Modelling

We follow the modelling strategy of Elkins-Tanton et al. (2003) and Charlier et al. (2018), who developed a numerical code to simulate the crystallization of the Martian and lunar magma oceans,

respectively. Our code is rooted in experimentally determined phase equilibria and traces the solidification steps of the MMO through a stepwise approach in which we calculate the mineralogy, composition, and density of cumulates while tracking the compositional evolution of the residual silicate liquids. The initial compositions of the silicate liquid are the primitive compositions Mer8 and Mer15. Major elements and heat-producing elements (U, Th, K) were considered. FeO was excluded from the input compositions because MESSENGER data have demonstrated the paucity of FeO on the surface (Nittler et al., 2020). Fractional crystallization is described as (Namur et al., 2012; Charlier et al., 2018; Zhang et al., 2024a):

$$c^0_{i,\mathrm{Liq}} = (1-z)c^1_{i,\mathrm{Liq}} + z[(\sum_{j=1\rightarrow n} \quad X^j c^j_i)X^{\mathrm{Mush}}_{\mathrm{Sol}} + c^0_{i,\mathrm{Liq}}X^{\mathrm{Mush}}_{\mathrm{Liq}}] \qquad \text{(Eq. 4.1)}$$

where z is the crystallization increment (fixed at 1% of the residual liquid; i.e. z becomes increasingly small as crystallization proceeds), $c^1_{i,\mathrm{Liq}}$is the concentration of element i, bonded to oxygen, in the liquid at each step of fractionation, $c^0_{i,\mathrm{Liq}}$ is that during the previous step of fractionation, c^j_i is the concentration of element i in solid phase j, X^j is the proportion of phase j in the cumulate assemblage, and $X^{\mathrm{Mush}}_{\mathrm{Sol}}$ and $X^{\mathrm{Mush}}_{\mathrm{Liq}}$ are the bulk proportions of the solid phases and trapped liquid in the solidifying crystal mush.

To determine the density of the silicate liquid produced during MMO crystallization, we first calculated the density at zero pressure as:

$$\rho_{\mathrm{Liq}} = \sum \quad \frac{X_i M_i}{X_i V_i} \qquad \text{(Eq. 4.2)}$$

where X_i is the molar fraction of component i in the melt, M_i is its molar mass, and V_i is its partial molar volume. Density is then adjusted to account for the effect of pressure and temperature with a third order Birch-Murnaghan equation of state:

$$P = \frac{3}{2}k_T\left[\left(\frac{V_0}{V_\mathrm{f}}\right)^{\frac{7}{3}} - \left(\frac{V_0}{V_\mathrm{f}}\right)^{\frac{5}{3}}\right]\left\{1 - \left(\frac{3}{4}\right)(4 - k'_T)\left[\left(\frac{V_0}{V_\mathrm{f}}\right)^{\frac{2}{3}} - 1\right]\right\} \qquad \text{(Eq. 4.3)}$$

where P is pressure, k_T is Young's modulus, V_0 is the initial molar volume, V_f is the molar volume at pressure P, and k'_T is the pressure derivative of k_T. k_T and k'_T were determined via multiple linear regression of literature data as a function of major element melt compositions (Guillot and Sator, 2007; Ohtani and Maeda, 2001). The temperature dependence of the liquid density is calculated using the compositional expression of thermal expansion from Lange and Carmichael (1987). The parameters used to calculate the melt density are reported in the Appendix C (Section S4.1.). Other equations of state used for the calculation of the liquid density are shown for comparison in Fig. S4.1. The effect of

S on the density of the silicate liquid is poorly constrained in the literature, and a specific discussion of this aspect is presented in Section 6.4.

Magma oceans are considered to crystallize from the bottom up and to strongly convect, such that no chemical gradient is assumed (Walker et al., 1975; Brown and Elkins-Tanton, 2009). Starting from the density of the cumulus phases, the thickness of the different layers can be calculated as crystallization proceeds at each increment *z*. In our model, we allow crystallizing phases to float atop the magma ocean.

4.3.2. Depth of the Magma Ocean

The initial depth of the MMO was calculated using gravity models for Mercury. A smaller polar moment of inertia (MOI) (0.333 ± 0.005; Genova et al., 2019) yields a deeper core-mantle boundary (CMB), and therefore a deeper interface between the magma ocean and the metallic core (~485 ± 20 km depth in Goossens et al., 2022; ~463 km in Steinbrügge et al., 2021). Conversely, models with a higher MOI (0.346 ± 0.014; Margot et al., 2012) return a shallower CMB interface at ~430 km depth (Bertone et al., 2021). In this work, we simulate the crystallization of the MMO from an initial depth of 480 km, corresponding to the maximum possible CMB depth. Accordingly, we account for a higher volume of the silicate magma ocean, which is considered to have been ca. 17% greater than the present-day solid silicate shell.

4.3.3. Early Crystallization Stages

Literature data on near-liquidus experiments representative of the BSMe provide precious insights into the phase equilibria of early forming minerals (Anzures et al. 2020; Xu et al., 2024; Saracino et al., 2025). Xu et al. (2024) and Saracino et al. (2025) showed that enstatite is the liquidus phase in sulfide-saturated Mer8 (Mg/Si = 0.88) whereas forsterite is the liquidus phase in sulfide-saturated Mer15 (Mg/Si = 1.16) between 1 and 7 GPa. Interestingly, Saracino et al. (2025) showed that the residual melt compositions of sulfide-saturated Mer8 and Mer15 converge, eventually reaching a single cotectic curve after sufficient differentiation. The initial fractionation of the MMO can therefore be simulated by fractionating only enstatite for Mer8 and only forsterite for Mer15 until the residual MMO liquids reach the forsterite-enstatite cotectic (Fig. 4.2.). After reaching this cotectic curve, all Mercurian melts, including low- and high-Mg/Si melts, evolve towards the same eutectic where crystallization ends (Namur and Charlier, 2017). Accordingly, during the first stage of crystallization, the Mg/Si ratios of the Mer8 and Mer15 residual liquids converge until they cross at ~2.6 GPa (Fig. 4.3.). To further evolve the MMO, we consider an average of the two residual liquid compositions (Fig. 4.3.).

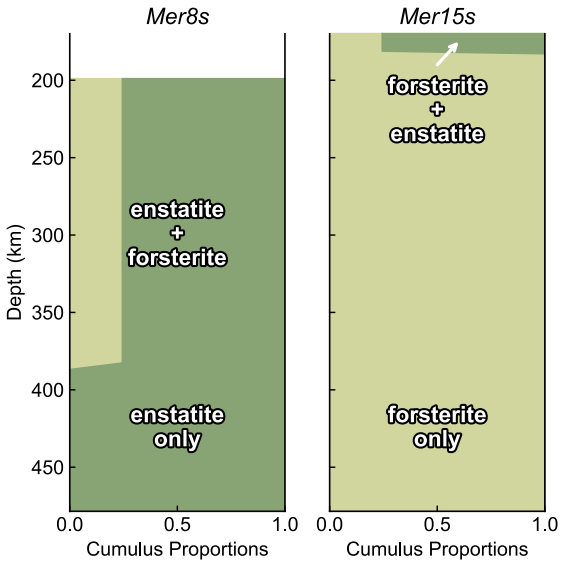

Figure 4.2. *The early crystallization sequence for S-bearing Mer8 and Mer15 compositions.*

The second stage of the forward model is the co-crystallization of forsterite and enstatite. The instantaneous relative proportions of forsterite and enstatite in the cumulate assemblage can be obtained from the tangent to the cotectic curve. We thus plotted experimental melts saturated with both forsterite and enstatite relevant to Mercury's mantle compositions (Saracino et al., 2025; Xu et al., 2024) in the diopside-SiO_2-forsterite ternary system (Fig. S4.2. in Section S.2). The plotted melts were produced from the same starting materials (Mer8 and Mer15) over a wide pressure range (1.5–7.0 GPa). Calculated mineral proportions from these experimental melts returned a range of relative proportions, from around $Fo_{42}En_{58}$ to $Fo_{10}En_{90}$, with higher pressures producing a higher Fo/En ratio due to the expansion of the enstatite stability field relative to that of forsterite with increasing pressure (Bowen, 1914; Kushiro, 1969; Chen and Presnall, 1975; Weng and Presnall, 2001; Falloon and Green, 1988; Fig. S4.2.). As an approximation, we therefore considered a rough average of the relative proportions: $Fo_{25}En_{75}$.

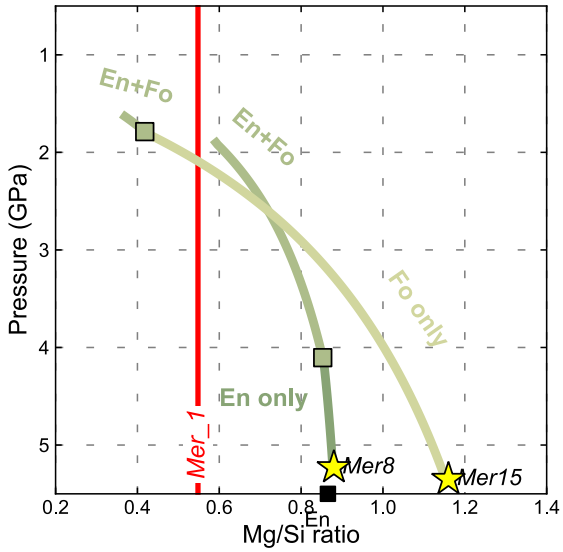

Figure 4.3. *Mg/Si ratio as a function of pressure (GPa) in the early crystallization sequence for both Mer8 and Mer15 compositions.*

4.4. Experimental and Analytical Methods

4.4.1. Experimental Strategy

Our experimental study aims to simulate the evolution of the silicate liquid in the MMO during cooling and with decreasing pressure as the cumulate pile thickens with the melt fraction (F) decreases. We used a stepwise approach to simulate the fractional crystallization of the BSMe. Starting composition Mer_1 corresponds to the cotectic composition at which forsterite and enstatite coexist, following the crystallization of forsterite from Mer15 and enstatite from Mer8 using the forward crystallization model described above (Fig. 4.3.). Experiments were performed with the Mer_1 composition until clinopyroxene joined the mineral assemblage with forsterite and enstatite. We then used the new residual melt composition in equilibrium with clinopyroxene, Mer_2, in further experiments until the appearance of quartz, which also corresponded to the destabilization of forsterite due to the high activity of SiO_2 (a_{SiO2}). Lastly, a final composition produced from the Mer_2 residual melts, Mer_3, was used to reach the most evolved stages of magma ocean solidification. These three starting compositions are reported in Table 4.2. Each new series of experiments pertaining to new starting materials were performed at progressively lower pressure-temperature conditions to simulate the incipient cooling and thinning of the residual MMO. The *P-T-F* profile and the complete crystallization sequence were obtained by combining the experimental results and the forward crystallization model. In total, our experiments span temperatures of 1525–1125 ℃ and pressures of 1.5–0.5 GPa (Fig. 4.4.).

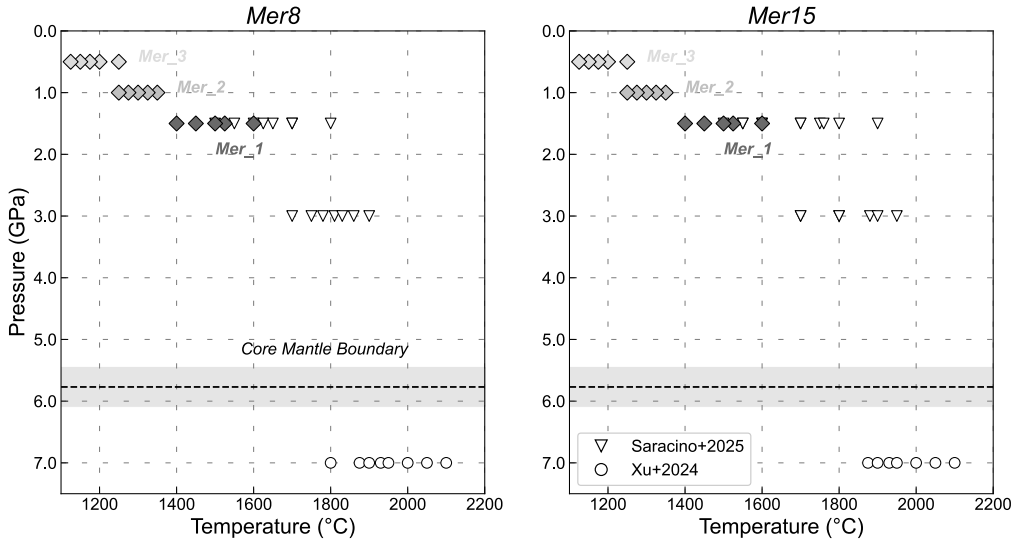

Figure 4.4. *Pressure and temperature conditions of our experimental runs representing the evolution of the residual MMO liquid. Experiments are from this study (diamonds with various shades of grey), Saracino et al. (2025; white downward inverted triangles), and Xu et al. (2024; white circles). The pressure estimate at the core-mantle boundary and relative upper and lower bounds are from Xu et al. (2024).*

Table 4.2. *Residual liquid compositions compared to the starting chondritic compositions Mer8 and Mer15. n.d., not determined.*

	Mer8	Mer15	Mer_1	Mer_1 FeS	Mer_1 FeS,S	Mer_1 S	Mer_2	Mer_2 FeS	Mer_3
SiO_2	54.82	47.91	56.53	45.22	45.22	48.05	62.91	52.22	66.48
TiO_2	0.14	0.16	0.38	0.30	0.30	0.32	0.17	0.14	0.16
Al_2O_3	3.70	4.26	9.46	7.57	7.57	8.04	13.85	11.49	16.62
Cr_2O_3	0.52	0.60	0.56	0.45	0.45	0.48	0.11	0.09	0.02
MnO	0.28	0.33	0.37	0.30	0.30	0.31	0.31	0.26	0.04
MgO	37.32	43.04	24.01	19.21	19.21	20.41	11.95	9.92	4.39
CaO	1.62	1.87	4.33	3.46	3.46	3.68	5.12	4.25	5.68
Na_2O	1.37	1.58	3.75	3.00	3.00	3.19	5.10	4.23	6.00
K_2O	0.13	0.15	0.36	0.28	0.28	0.30	0.49	0.41	0.60

	Mer8	Mer15	Mer_1	Mer_1 FeS	Mer_1 FeS,S	Mer_1 S	Mer_2	Mer_2 FeS	Mer_3
P_2O_5	0.10	0.10	0.26	0.20	0.20	0.22	n.d.	n.d.	n.d.
FeS				20.00	10.00			17.00	
S					10.00	15.00			
Total	100.00	100.00	100.00	100.00	100.00	100.00	100.00	100.00	100.00

4.4.2. Starting Materials

The starting materials (Table 4.2.) were produced from high-purity oxide powders: SiO_2, TiO_2, Al_2O_3, Cr_2O_3, MnO, MgO, $CaSiO_3$, Na_2SiO_3, $K_2Si_4O_9$, and $AlPO_4$. $CaSiO_3$, Na_2SiO_3, and $K_2Si_4O_9$ were produced by decarbonating mixtures of carbonates and SiO_2. Sulfur was added as FeS, FeS + S, or only as elemental S powder. Powders were mixed in an agate mortar with methanol and then stored in an oven at 120 °C. Different oxygen fugacity (fO_2) conditions were achieved by using different metallic Si/SiO_2 molar ratios in the starting materials: 0, 0.10, 0.20 (referred to as Mer(0), Mer(10), Mer(20)). Although fO_2 may not affect the stability of silicate phases in the Fe-free system, it affects S solubility in the melt and therefore the timing and nature of sulfide saturation (Namur et al., 2016b). With this approach, we were able to track the range of sulfides that can be produced using different Fe/S ratios. Neither S nor Si were added to Mer_3(0) because the solubility of S was observed to be low (<0.5 wt% S) in Mer_2 at temperatures below 1250 °C, in accordance with the decreasing solubility of S with decreasing T and increasing SiO_2 content (Namur et al., 2016b).

4.4.3. Experimental Methods

Experiments were conducted with a Voggenreiter Mavo LPC 250-300/50 end-loaded piston-cylinder apparatus at the University of Liège (Belgium). Half inch (1/2") assemblies were used in the pressure range 1.0–1.5 GPa, and 3/4" assemblies for runs at 0.5 GPa. For the 1/2" assembly, a graphite capsule with a MgO spacer was placed in a graphite furnace, and a $BaCO_3$ cell was used as the pressure medium. In the 3/4" assembly, a talc+pyrex cylinder was used as the pressure medium. Details on the cell assemblies employed in this study are reported in Appendix C (Fig. S4.3.). Temperature was monitored with a $W_{75}R_{25}/W_{97}R_3$ D-type thermocouple for both assemblies. A correction was applied for the temperature gradient between the tip of the thermocouple and the center of the capsule, which we estimate to be ~25 °C. The assemblies were first pressurized at room temperature to 0.7 GPa in the 1/2″ setup and 0.4 GPa in the 3/4″ setup. Then, temperature was increased to 865 °C at 100 °C/min while keeping the pressure constant. Temperature was then held for 6 min to pressurize to the target pressure.

Finally, temperature was increased again at 50 °C/min until the target temperature was attained. Friction correction coefficients of 9.3% for the 1/2" assembly and 20% for the 3/4" assembly were applied, respectively (Condamine et al., 2022). Experiments were quenched by switching off the power. Experimental samples were cut in half with a diamond wafer saw, mounted in epoxy, and polished to 1 µm.

4.4.4. Attainment of Equilibrium

We performed time-series experiments to test the attainment of equilibrium and the potential escape of volatiles (Na, S). Four experiments at 1300 °C and 1 GPa were run at different durations (30 min, 1 h, 3 h, 6 h) using Mer_2(20) as the starting material. In all these samples, enstatite, clinopyroxene, and quartz coexisted with the silicate melt, and these three crystalline phases produced small euhedral crystals regardless of the duration investigated. As commonly observed in experiments with Si/SiO_2 = 0.20, a slight excess of Si metal (~1 wt%) was observed in all four experiments. The compositions of the silicate glasses (Figs. S4.4. in Appendix C, see also Appendix D) show that sulfur was readily incorporated into the melt after 30 min and slightly decreased after one hour (from 3.4 to 2.7 wt%; Fig. S4.4.d). No substantial loss of Na was observed at durations up to 6 h (Fig. S4.4.c). We also observed that the concentration of Si in the silicate glass slightly increased at durations longer than 1 h (Fig. S4.4.a), explained by the likely oxidation of residual Si metal in longer duration runs. The progressive oxidation of the system is corroborated by the slight depletion of Si in the metallic phase (Fig. S4.5.) over durations longer than 1 h and the lower solubility of S in the silicate melt in longer experiments. Based on these results, we conclude that we reached thermodynamic equilibrium within ~1 h.

4.4.5. Analytical Methods

Imaging and phase identification were performed with the TESCAN MIRA 4th Generation Scanning Electron Microscope (SEM) at the Department of Geology, KU Leuven (Belgium). Quantitative analyses of our experimental products were conducted with the JEOL JXA-8530F electron probe micro-analyzer (EPMA) at the Department of Materials Engineering, KU Leuven. Silicate crystals and sulfide and metallic phases were measured with a 15 kV accelerating voltage and 10 nA beam current. Silicate melts (glass) were measured with a 15 kV accelerating voltage and a 15 nA beam current. Crystals were analyzed with a focused beam and glasses with a beam defocused to 5–20 µm depending on the size of the glass pool. Sulfides were measured with a focused beam and metals with either a focused or a defocused beam (5–10 µm) depending on the size of the metallic phase and the presence of heterogeneities and quench textures. Peak counting times were 10–30 s and background counting times on each side of the peak were 5–15 s for each element. We employed both natural and

synthetic standards. For silicate crystals we used albite for Na, orthoclase for K and Al, diopside for Ca, olivine for Si and Mg, rutile for Ti, MnO for Mn, Cr_2O_3 for Cr, and fayalite for Fe. For silicate glass we used albite for Na, obsidian for K and Al, olivine for Mg, diopside for Ca, rutile for Ti, rhodonite for Mn, Cr_2O_3 for Cr, hematite for Fe, and $BaSO_4$ for S. For sulfide and metallic phases we used albite for Na, Si metal for Si, diopside for Ca, olivine for Mg, obsidian for Al, rutile for Ti, Cr metal for Cr, Fe metal for Fe, Mn metal for Mn, and pyrite for S. Replicate measurements of international standards indicate analytical errors of less than 5% for major elements and 10–15 % for minor elements. For sulfur measurements in the silicate glass, reliability was attained through accurate calibration and reproducibility on $BaSO_4$, which suggest errors below 10-15%. Raw data were corrected for matrix effects with the CATZAF software.

4.4.6. Determination of Oxygen Fugacity

Under reduced conditions, the oxygen fugacity of the experimental charges can be calculated considering the equilibrium between Fe metal and FeO-bearing silicate melts as (Corgne et al., 2008):

$$Fe_{\text{Metal}} + \frac{1}{2}O_2 = FeO_{\text{Melt}} \qquad \text{(Eq. 4.4)}$$

The activity of Fe in the metal a_{Fe} is given by:

$$a_{\text{Fe}} = X_{\text{Fe}}\gamma_{\text{Fe}} \qquad \text{(Eq. 4.5)}$$

where X_{Fe} is the molar content of Fe in the Fe metal and γ_{Fe} is the activity coefficient of Fe. Analogously, the activity of FeO in the silicate melt a_{FeO} is given by:

$$a_{\text{FeO}} = X_{\text{FeO}}\gamma_{\text{FeO}} \qquad \text{(Eq. 4.6)}$$

where X_{FeO} is the molar content of FeO in the silicate melt and γ_{FeO} is the activity coefficient of FeO. However, typical Mercurian melt compositions have extremely low FeO contents (<1 wt%) and are close to or below the detection limit of analytical instruments. The activity coefficient of FeO at low Fe^{2+} concentrations is therefore poorly constrained (Cartier et al., 2014; Wykes et al., 2015; Namur et al., 2016a; Anzures et al., 2020; Pirotte et al., 2023), rendering fO_2 estimates using Eq. (4.4) unreliable. Nonetheless, under FeO-poor conditions, fO_2 can be determined using the equilibrium between Si-rich metal and SiO_2 in the silicate melt as (Cartier et al., 2014):

$$SiO_{2,\text{Melt}} = Si_{\text{Metal}} + O_2 \qquad \text{(Eq. 4.7)}$$

where $SiO_{2,\text{Melt}}$ is the SiO_2 concentration in the melt and Si_{Metal} is the Si concentration in the metal. The activity of Si in the metal is given by:

$$a_{Si} = X_{\mathrm{Si}}\gamma_{\mathrm{Si}} \qquad \text{(Eq. 4.8)}$$

with X_{Si} being the molar Si content in the metal and γ_{Si} the activity coefficient of Si. Here we use the Si activity coefficients calculated following Ma (2001). Similarly, the activity of SiO_2 in the silicate melt is calculated as:

$$a_{SiO_2} = X_{\mathrm{SiO_2}}\gamma_{\mathrm{SiO_2}} \qquad \text{(Eq. 4.9)}$$

where X_{SiO_2} is the molar SiO_2 content in the melt and γ_{SiO_2} is the activity coefficient of SiO_2. Because SiO_2 is the main component of the melt, which saturates quartz in most of our samples, a_{SiO_2} can be approximated as ~1 (Cartier et al., 2014). Only for runs in which no Si-bearing Fe metal was available (A461, A462, A469) did we calculate oxygen fugacity following the method of Namur et al. (2016b), where the oxygen fugacity can be calculated based on the sulfur content at sulfide saturation (SCSS) as:

$$\ln[S]_{\mathrm{SCSS}} = a + \frac{b}{T} + \frac{cP}{T} + d\log(fO_2) + \sum e_i \frac{X_i}{X_{\mathrm{SiO_2}}} \qquad \text{(Eq. 4.10)}$$

where $[S]_{SCSS}$ is the SCSS (in wt%), T is temperature (in K), P is pressure (in bar), fO_2 is the oxygen fugacity, X_i are the molar fractions of oxides in the silicate melt (renormalized to 100% on a S-free basis), and a, b, c, d, $e\mathrm{TiO_2}$, $e\mathrm{MgO}$, and $e\mathrm{Na_2O}$ are derived coefficients.

The fO_2 in experiments containing Si-bearing Fe metal spans the range from IW−5.6 to IW−8.4. The coexistence of excess Si metal and quartz suggests that some experiments are buffered at Si–SiO_2 equilibrium. For experiments that did not contain Si-bearing metal, we calculated the oxygen fugacity to be between IW−3.9 and IW−3.7.

4.5. Results

4.5.1. Experimental Textures and Phase Equilibria

Representative backscattered images of the experimental products are shown in Fig. 4.5. All experimental runs, P-T-fO_2 conditions, and phase assemblages are reported in Table 4.3. Mer_1 contained enstatite as the liquidus mineral at T = 1500 °C, so slightly offsets from the predicted enstatite-forsterite cotectic. Forsterite and clinopyroxene then appeared at T = 1450 °C. Enstatite and forsterite occurred as relatively large (5–50 μm) euhedral crystals (Fig. 4.5.a), and clinopyroxene as small (<10 μm), bright crystals often associated with enstatite. For Mer_1, we also ran experiments using a mix of different sulfur sources. Mer_1 + FeS,S still contained enstatite as the liquidus mineral at T = 1500 °C, and the melt later saturated with enstatite + forsterite + clinopyroxene at T = 1450 °C. Lastly, rounded quartz occurred at T = 1400 °C (Fig. 4.5.b). In contrast, Mer_1 + S contained silicate melt saturated with

enstatite + forsterite + clinopyroxene + quartz at T = 1500 ℃. In Mer_2(20), enstatite + forsterite + clinopyroxene + quartz co-crystallized at T = 1350 ℃. Forsterite later disappeared at T = 1325 ℃. Forsterite was small, rare, and usually surrounded by small (2–20 μm), euhedral crystals of enstatite (Fig. 4.5.d). Clinopyroxene was small and often displayed elongated, needle–like textures (Fig. 4.5.e). Quartz appeared as relatively large crystals (5–50 μm), always with rounded edges. In Mer_2(10), enstatite + forsterite + clinopyroxene + quartz was the cotectic assemblage at T = 1300 ℃. Forsterite was destabilized at T = 1250 ℃. Lastly, Mer_3 runs contained an assemblage of quartz, plagioclase, and clinopyroxene starting at T = 1250 ℃ (Table 4.3.). Quartz crystals were large (5–70 μm), whereas clinopyroxene crystals were small (<10 μm) (Fig. 4.5.e). Plagioclase crystals were small (<10 μm), tabular, and always found as clusters (Fig. 4.5.f). Our experimental samples also contained metal and sulfide phases. Mer_1 contained Si-bearing Fe metal (Fig. 4.5.a) surrounded first by a thick liquid FeS layer, then by a small (Mg,Fe,Ca)S veneer. Among experiments with different sulfur sources, Mer_1 + FeS,S mostly contained sulfide globules of unmixed FeS and (Mg,Fe,Ca) S. At 1400 ℃, we also observed pure Si metal. Conversely, Mer_1 + S only contained excess Si metal globules. We also identified some small euhedral Cr sulfide crystals at 1450 ℃ (Fig. 4.5.b). We are not aware of any other experimental work reporting this phase, although Cr-bearing sulfides have been reported in chondritic meteorites (Ma et al., 2011). Mer_2(20) mostly exhibited liquid FeS and (Mg,Fe,Ca)S droplets. Si-bearing Fe metal (Fig, 4.5d) and Si metal globules appeared at T = 1400 ℃. Mer_2(10) contained mostly Si metal and liquid FeS. Fe metal was very rare in our experiments, with only one small Si-free globule observed in only one sample (A462).

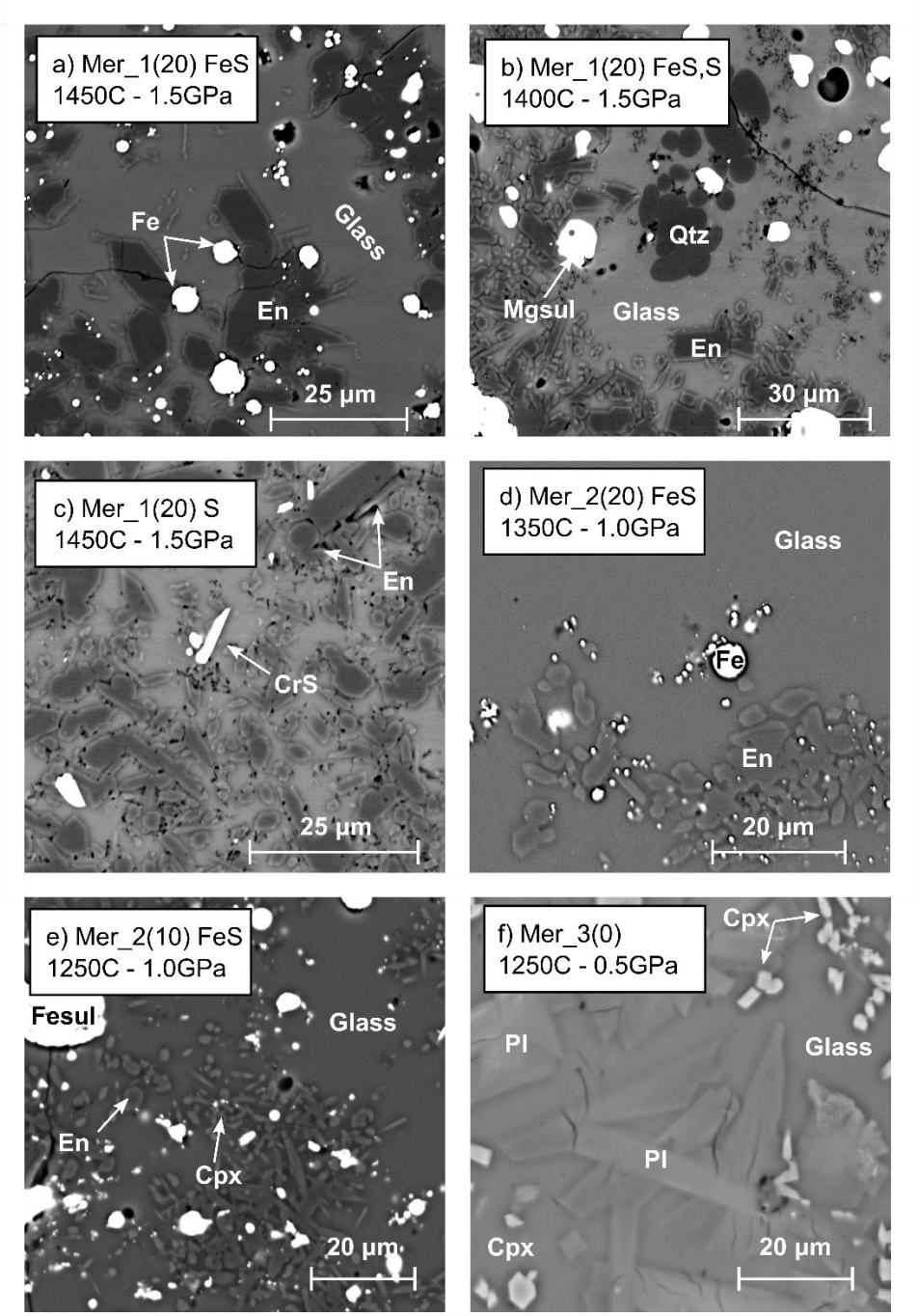

Figure 4.5. *Representative backscattered electron images of experimental runs. (a) A396. Orthopyroxene crystals and small needle–like clinopyroxene crystals surrounded by silicate glass. The bright rounded features are Fe metal globules. (b) A402. Orthopyroxene crystals (dark) and small bright CrS crystals surrounded by silicate glass. (c) A431. Small orthopyroxene crystals in silicate glass. The bright rounded features are FeS + (Mg,Fe)S globules. (d) A469. Small, elongated crystals of clinopyroxene surround darker orthopyroxene. The bright rounded features are FeS globules. (e) A477. Small tabular plagioclase crystals and small grains of clinopyroxene. Abbreviations: Fo, forsterite; En, enstatite; Cpx, clinopyroxene; Qtz, quartz; Pl, plagioclase; Fe, Fe metal; Mgsul, (Mg,Fe,Ca)S.*

Table 4.3. *Experimental run conditions and relative phase assemblages of the experiments. Oxygen fugacity was calculated after Cartier et al. (2014) and is expressed relative to the iron–wüstite (ΔIW) solid buffer. *For runs where no Si-bearing Fe metal is present, oxygen fugacity was calculated following the sulfur solubility model of Namur et al. (2016b). Abbreviations: Fo, forsterite; En, enstatite; Cpx, clinopyroxene; Qtz, quartz; Pl, plagioclase; Fe, Si–bearing Fe metal; Si, Si metal; Fesul, FeS; Mgsul, (Mg,Fe,Ca)S; Crsul, CrS.*

Run	T (˚C)	P (GPa)	Duration (hrs)	Silicate phases	Metals and sulfides	ΔIW[a]
Mer_1(20) + 20FeS						
A399	1525	1.5	02:00	Glass	Fe, Fesul, Mgsul	-5.6
A397	1500	1.5	02:30	Glass, En	Fe, Fesul, Mgsul	-5.7
A396	1450	1.5	03:00	Glass, En, Fo, Cpx	Fe, Fesul, Mgsul	-6.2
A404	1400	1.5	03:30	Glass, En, Fo, Cpx	Fe, Fesul, Mgsul	-6.6
Mer_1(20) + 10FeS,10S						
A401	1500	1.5	01:30	Glass, En	Fesul, Mgsul	
A400	1450	1.5	02:00	Glass, En, Fo, Cpx	Fesul, Mgsul	
A405	1400	1.5	02:30	Glass, En, Cpx, Qtz	Si, Fesul, Mgsul	
Mer_1(20) + 15S						
A403	1500	1.5	01:30	Glass, Fo, En, Cpx, Qtz	Si	
A402	1450	1.5	02:00	Glass, Fo, En, Cpx, Qtz	Si, Crsul	
Mer_2(20) + 20FeS						
A431	1350	1.0	00:30	Glass, En, Fo, Cpx, Qtz	Fe, Si, Fesul, Mgsul	-7.2
A444	1325	1.0	00:45	Glass, En, Cpx, Qtz	Fe, Si, Fesul, Mgsul	-7.9
A441	1300	1.0	01:00	Glass, En, Cpx, Qtz	Fe, Si, Fesul, Mgsul	-8.1
A445	1275	1.0	01:15	Glass, En, Cpx, Qtz	Fe, Si, Fesul, Mgsul	-8.4
A432	1250	1.0	01:30	Glass, En, Cpx, Qtz	Fe, Si, Fesul, Mgsul	-8.4
Mer_2(10) + 17FeS						
A462	1300	1.0	01:00	Glass, En, Fo, Cpx, Qtz	Fe, Si, Fesul	-3.7*
A461	1275	1.0	01:15	Glass, En, Fo, Cpx, Qtz	Si, Fesul	-3.9*
A469	1250	1.0	01:30	Glass, En, Cpx, Qtz	Si, Fesul	-3.7*
Mer_3(0)						
A477	1250	0.5	00:50	Glass, Cpx, Qtz, Pl		
A473	1200	0.5	01:00	Glass, Cpx, Qtz, Pl		
A475	1175	0.5	01:10	Glass, Cpx, Qtz, Pl		

Run	T (˚C)	P (GPa)	Duration (hrs)	Silicate phases	Metals and sulfides	ΔIW[a]
A486	1150	0.5	03:50	Glass, Cpx, Qtz, Pl		
A487	1125	0.5	04:00	Glass, Cpx, Qtz, Pl		

4.5.2. Chemical Composition of Silicate, Metal, and Sulfide phases

Quantitative analyses performed on the silicate glasses are shown in Table 4.4. with 1σ standard deviations reported in Appendix D. Experimental liquid lines of descent (LLDs) are shown in Figs. 4.6. and S4.6. The Si content constantly increased (26–37 wt%, Fig. 4.6.a) from 1550 to 1100 ℃, whereas the Mg content steadily dropped (15–0 wt%). Na was also progressively enriched in the glass (1–6 wt%, Fig. 4.6.d) with decreasing temperature. S content decreased from 1550 to 1250 ℃ (no S was added to experiments run at <1250 ℃, Fig. S4.6.f). The difference in temperature between the appearance of quartz when different S sources are added in Mer_1 (Table 4.3.) might be a cause of the differing Si content in the melt (Table 4.4.), which is affected by sulfur speciation. The glass in the more reduced experiment Mer_2(20) contained 2.0–4.5 wt% S, whereas that in the more oxidized experiment Mer_2(10) contained 0–1 wt% S. Both Al and Ca were enriched in the glass from 1550 to 1250 ℃ but were then depleted at lower temperatures (Figs. 4.6.b, c) due to the saturation of plagioclase and clinopyroxene. More Ca was present in Mer_2 when 10 wt% Si was added than when 20 wt% Si added (Fig. 4.6.c). This was likely the result of more Ca partitioning into the sulfide phases at the more reduced conditions in Mer_2(20). In all experiments, olivine and orthopyroxene matched their Mg endmember compositions (forsterite and enstatite, respectively). We only observed variations in CaO and Al_2O_3 contents in the enstatite composition over the range of starting materials investigated: both CaO (0.2–2.7 wt%) and Al_2O_3 contents (1.2–6.6 wt%) increased in enstatite with decreasing temperature (Appendix D). In Mer_1 and Mer_2, most clinopyroxene crystals were too small for compositional analysis, with the exception of a few crystals at 1250 ℃ (A469). In Mer_3, clinopyroxene crystals were larger and contained 3–10 wt% Al_2O_3, 11–19 wt% MgO, 20–22 wt% CaO, and 0.7–1.8 wt% Na_2O. The average clinopyroxene composition was $Wo_{48}En_{52}$ (Fig. S4.7.). Plagioclase was only observed in Mer_3(0) and became more sodic with decreasing temperature (An_{84} to An_{56}, where An = molar Ca/[Ca + Na]). The compositions of metals and sulfides are reported in Appendix D. Fe metallic alloys in Mer_1 + FeS contained 83–87 wt% Fe, 6–10 wt% Si, and 0.2–0.8 wt% S. Metal alloy in Mer_2(20) + FeS contained 82–87 wt% Fe, 13–20 wt% Si, and 0.1–0.3 wt% S. In Mer_2(10) + FeS we observed a single small Fe metal globule containing ~93 wt% Fe, 0 wt% Si, and ~1.7 wt% S in a single run at 1300 ℃. FeS in Mer_1 contained 51–57 wt% Fe, 36–42 wt% S, 2–6 wt% Cr, and 0.7–4.7 wt% Ti. Troilite in Mer_2 had a higher Fe content (60–64 wt%) and lower S (34–38 wt%), Cr (0.2–0.9 wt%), and Ti contents (<1.7 wt%).

Table 4.4. *Electron microprobe measurements of experimental glasses. Abbreviations: No, number of measurements; <dl, below detection limit. *Oxygen was calculated by stoichiometry. **An excess of O^{2-} is calculated as not all Mg^{2+} or Ca^{2+} being bonded with O^{2-}, but also with S^{2-} requiring correction of the total. *** Total corrected after removal of excess oxygen.*

1

Run	T (˚C)	P (GPa)	Composition of silicate glasses (wt%)												
			No	Si	Ti	Al	Fe	Mn	Mg	Ca	Na	K	S	O*	S=O**	Total***
Mer_1(20) + 20FeS																
A399	1525	1.5	11	26.20	< dl	4.85	0.23	0.21	13.99	3.09	2.34	0.25	5.23	45.70	2.61	99.48
A397	1500	1.5	10	26.36	< dl	5.51	0.30	0.16	12.67	3.51	2.57	0.30	5.65	45.86	2.82	100.08
A396	1450	1.5	10	26.86	< dl	6.59	0.32	< dl	9.78	4.17	3.36	0.38	5.74	45.98	2.86	100.31
A404	1400	1.5	10	28.38	< dl	7.28	0.26	< dl	6.62	4.47	3.80	0.46	5.08	46.48	2.54	100.28
Mer_1(20) + 10FeS,10S																
A401	1500	1.5	11	27.22	< dl	4.81	0.26	< dl	13.06	2.55	2.02	0.21	6.85	45.83	3.42	99.39
A400	1450	1.5	12	28.12	< dl	5.64	0.29	< dl	11.10	2.95	2.35	0.24	6.81	46.57	3.40	100.67
A405	1400	1.5	10	29.23	< dl	6.80	0.24	< dl	7.26	3.36	3.02	0.31	5.77	46.74	2.88	99.85
Mer_1(20) + 15S																
A403	1500	1.5	10	28.34	0.16	4.94	0.02	< dl	12.73	2.63	1.33	0.14	5.39	46.74	2.69	99.72
A402	1450	1.5	7	27.49	0.22	6.37	0.01	< dl	9.83	3.69	1.47	0.14	5.31	45.64	2.65	97.51
Mer_2(20) + 20FeS																
A431	1350	1.0	17	28.55	< dl	7.86	0.32	< dl	7.17	3.47	3.53	0.33	4.19	47.04	2.09	100.36
A444	1325	1.0	10	29.30	< dl	8.62	0.15	< dl	6.20	3.63	2.55	0.34	3.82	47.61	1.90	100.32
A441	1300	1.0	18	29.14	< dl	8.61	0.38	< dl	4.86	3.67	3.92	0.39	3.44	47.66	1.72	100.23
A445	1275	1.0	12	30.15	< dl	8.83	0.46	< dl	3.30	3.54	4.50	0.47	2.86	48.23	1.78	100.56
A432	1250	1.0	10	30.85	< dl	8.78	0.36	< dl	2.79	3.60	4.82	0.55	2.39	48.83	1.19	101.78

Run	T (˚C)	P (GPa)	Composition of silicate glasses (wt%)												
			No	Si	Ti	Al	Fe	Mn	Mg	Ca	Na	K	S	O*	S=O**	Total***
Mer_2(10) + 17FeS																
A462	1300	1.0	10	30.17	< dl	8.82	0.38	< dl	3.55	4.98	3.71	0.40	0.54	48.11	0.27	100.39
A461	1275	1.0	9	31.01	< dl	8.69	0.43	< dl	2.64	4.35	3.91	0.46	0.54	48.19	0.27	99.95
A469	1250	1.0	10	30.14	0.20	9.13	0.45	< dl	2.83	4.89	3.70	0.41	0.39	47.94	0.19	99.89
Mer_3(0)																
A477	1250	0.5	6	34.41	0.07	7.43		0.06	1.35	2.44	4.66	0.59		49.51		100.54
A473	1200	0.5	9	34.79	0.06	7.54		0.08	0.64	2.65	5.02	0.68		49.79		101.24
A475	1175	0.5	12	36.07	0.09	6.75		0.08	0.58	2.12	5.04	0.73		50.34		101.80
A486	1150	0.5	9	35.98	0.05	6.92		0.06	0.42	2.27	5.21	0.75		50.36		102.02
A487	1125	0.5	10	36.47	0.12	6.56		0.07	0.40	1.90	5.17	0.83		50.50		102.02

2

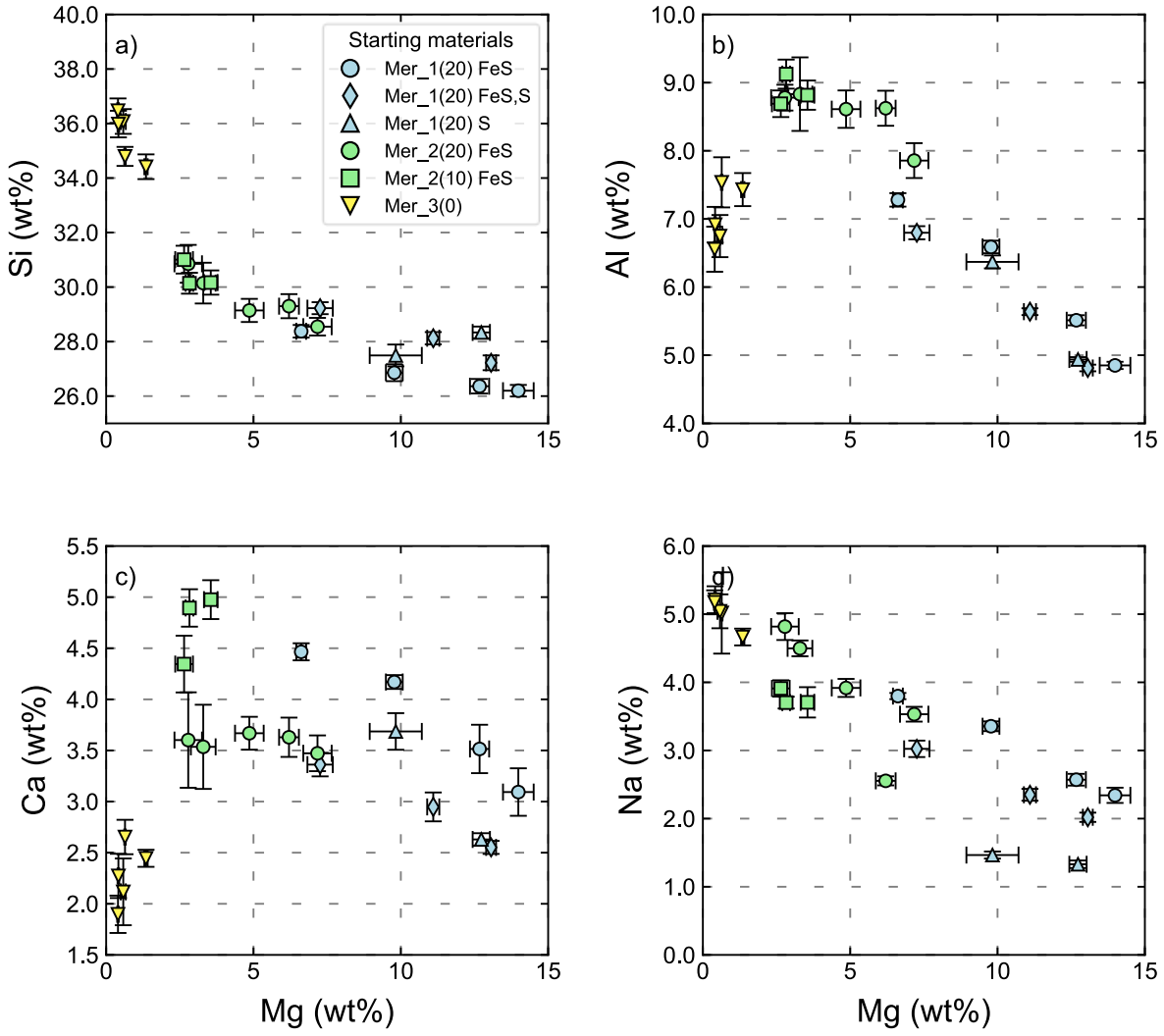

Figure 4.6. *Evolution of Si, Al, Ca, and Na concentrations (wt%) in the silicate glass as a function of the Mg content in the glass. Vertical and horizontal bars refer to 1σ standard deviations (the smallest 1σ values are smaller than the symbol size).*

4.5.3. Magma Ocean Modeling Parameterization

The experimentally determined phase relations (Table 4.3.) were used to mimic the fractional crystallization of the MMO. We calculated the cotectic proportions of mineral phases in order to model melt differentiation consistent with the experimental LLDs (Table 4.4.). The cotectic proportions of phases used in our modelling are listed in Appendix C (Table S4.2.). We used temperature as the main criterion to define the saturation or the destabilization of solid phases in the growing cumulate pile. We developed a S-free liquid thermometer based on experimental studies of Mercury-like mantle compositions (Charlier et al., 2013; Namur and Charlier, 2017; Namur et al., 2016a; Saracino et al., 2025) (Figs. S4.8., S4.9.) and applied a correction for the depression of the liquidus temperature in the

presence of sulfur (Saracino et al., 2025; Section S4.8). The phase assemblages considered in our magma ocean modelling as a function of temperature are reported in Section S4.9. (Fig. S4.10., Table S4.3.). The densities of crystals in the cumulate pile were determined at the solidus temperature derived by fitting the solidi of the evolving MMO liquid as determined using MAGEMin (Riel et al., 2022). The effects of temperature and pressure on mineral densities were calculated with a third-order Birch-Murnaghan equation of state. The parameters used in the calculation of mineral densities are reported in Appendix C (Section S4.1.). This procedure allows for the estimation of the thickness of the cumulate pile, and therefore the depth of the remaining MMO as a function of the fraction of residual melt.

4.6. Discussion

4.6.1. MMO Evolution and the Lithology of the Cumulate Pile

The evolution of the modelled MMO liquids for both Mer8 and Mer15 and a comparison with the experimental melts are reported in Fig. 4.7. As a first approximation, we assumed that no trapped liquid is present in the growing cumulate assemblage so that $X_{Liq}^{Mush} = 0$ in Eq. 4.1. The influence of Mg- and Ca-rich sulfides on the evolution of the MMO liquid is also shown (discussed further in Section 4.6.3.). The crystallization sequence of Mer8 and Mer15 as MMO bulk compositions is shown in Fig. 4.8. as a function of depth. In Mer8, the MMO solidification starts with the formation of a ~90-km-thick basal orthopyroxenitic layer (Fig. 4.8.a), whereas Mer15 forms a ~300-km-thick dunitic basal layer (Fig. 4.8.b). The residual melt of Mer8 becomes co-saturated in forsterite and enstatite at $F = 0.81$, whereas Mer15 reaches the forsterite-enstatite cotectic at $F = 0.38$. As also shown in Fig. 4.3. for Mer15, a thick dunite layer is produced before the MMO residual liquid saturates enstatite too. Here, the compositions of the residual melts from S-saturated Mer8 and Mer15 become similar (Fig. 4.7.). Over this range of F (1.00–0.81 for Mer8 and 1.00–0.38 for Mer15), Si, Al, and Ca contents increase in the melt, and the Mg content decreases due to the formation of enstatite and/or forsterite (Fig. 4.7.a, b). Clinopyroxene is the next phase to appear at $F = 0.40$ in Mer8 and $F = 0.35$ in Mer15. Forsterite-enstatite-clinopyroxene assemblages are then followed by the appearance of quartz at $F = 0.24$ in Mer8 and at $F = 0.28$ in Mer15. Forsterite is stable until $F = 0.15$ in Mer8 and until $F = 0.21$ in Mer15, after which it disappears. Plagioclase finally crystallizes at $F = 0.14$ in Mer8 and $F = 0.19$ in Mer15, when enstatite becomes unstable. The formation of plagioclase is accompanied by a depletion of both Ca and Al in the residual liquids of both Mer8 and Mer15 (Fig. 4.7.c, d).

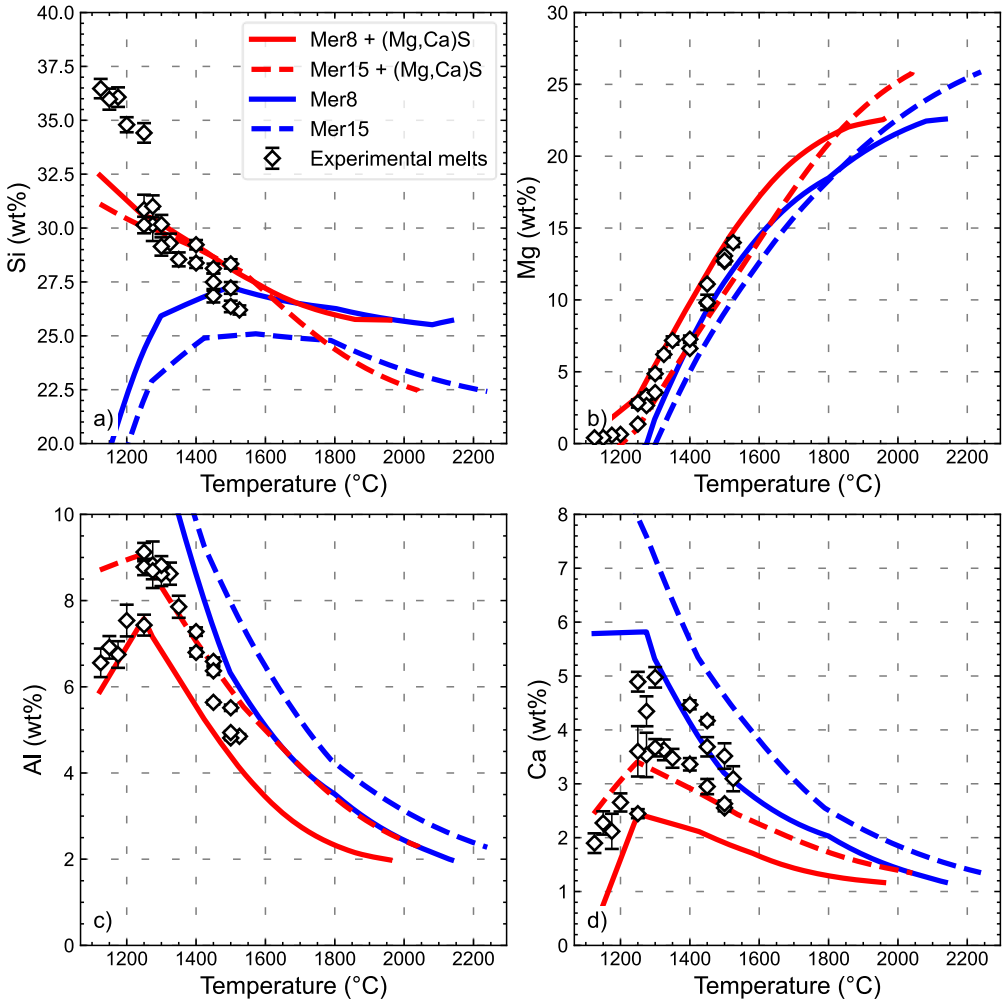

Figure 4.7. *Variations of major element contents (a) Si, (b) Mg, (c) Al, and (d) Ca (expressed in wt%) as a function of temperature (in °C), as obtained with our magma ocean model for both Mer8 (blue lines) and Mer15 (orange lines). Also shown for comparison are the experimentally determined silicate melt compositions (and relative errors; white diamonds) as listed in Table 4.4.*

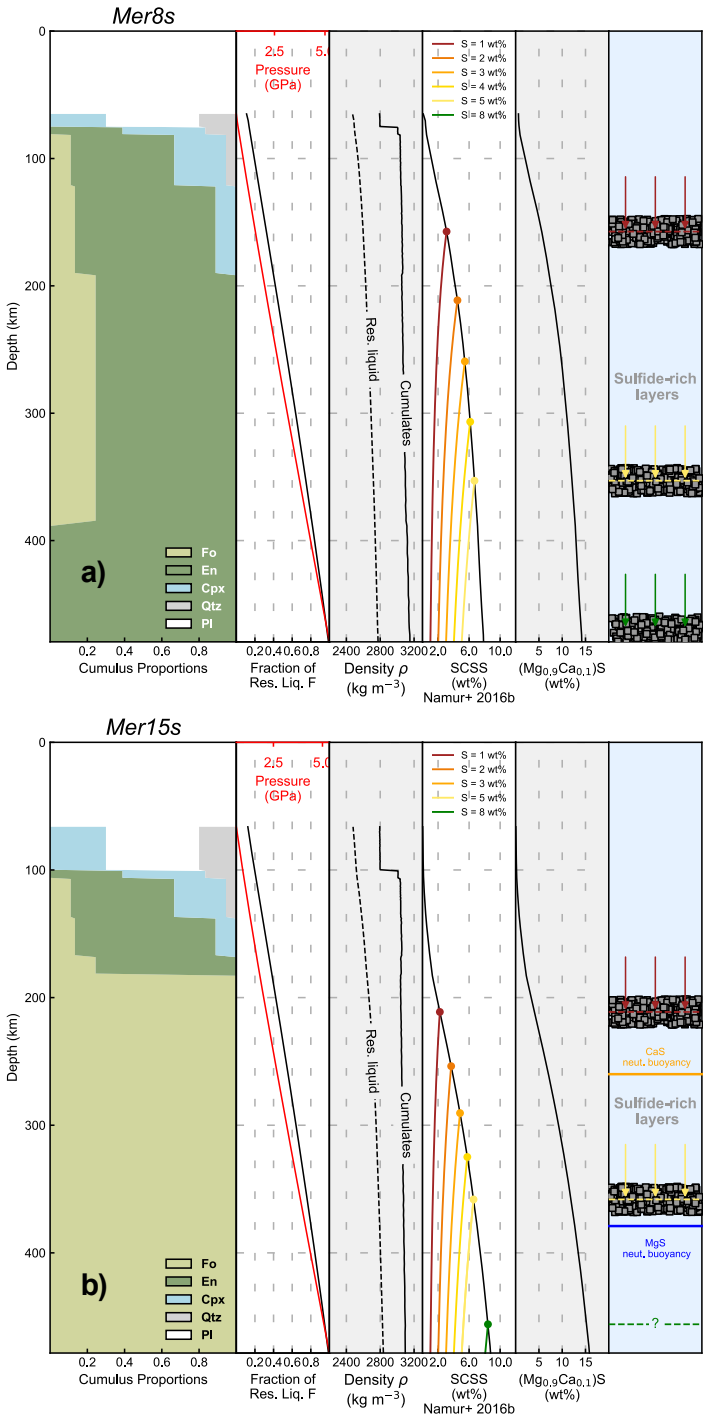

Figure 4.8. *Crystallization sequence of S-bearing (a) Mer8 and (b) Mer15 starting materials as a function of MMO depth (km). Also shown are the variations of the melt fraction F, pressure P, the densities of the cumulates (black) and the residual melt (grey), the sulfur content at sulfide saturation (SCSS), and the relative calculated amount of (Mg,Ca)S as a function of depth. Abbreviations : Fo, forsterite ; En, enstatite ; Cpx, clinopyroxene ; Qtz, quartz ; Pl, plagioclase.*

Here, we compare our models with the crystallization sequences modelled by Mouser and Dygert (2023) and Brown and Elkins-Tanton (2009). We rescaled their crystallization sequences to our updated MMO depths to directly compare the models (Fig. 4.9.; the unscaled figure is Fig. S4.11. in Appendix C).

The model of Mouser and Dygert (2023) shows a basal dunite layer, as we obtained for our Mer15 composition (Fig. 4.9.b, c). This is caused by the similar starting Mg/Si ratio of Mer15 and the modified silicate composition of the CH chondrite (Fig. 4.1.). The forsterite cumulate in Mer15 is nonetheless more than double the thickness of their basal layer. We also observe that the most evolved products differ substantially (Fig. 4.9.a–c). The lithologies that we obtained based on our experiments include quartz at depths shallower than ~140–120 km, whereas their model includes quartz-free assemblages at those depths. Our modeled sequence shows that a magma ocean composition with a high starting Mg/Si ratio (>0.8) can produce a large variety of residual liquid compositions (45–75 wt% SiO_2 and 40–0 wt% MgO) through fractional crystallization (Fig. 4.7.).

Although the models of Brown and Elkins-Tanton (2009) were based on an older estimate of the size of Mercury's core, a few considerations can be drawn from our comparison. First, none of their models produce a basal orthopyroxenite layer as produced from our Mer8 composition (Fig. 4.9.d–g), although the Mg/Si ratios of their starting compositions (0.9–1.1 with one exception) are comparable to ours (0.8–1.2). The only major difference is therefore the absence of S in their models, which allows olivine to appear in all their basal layers because sulfur tends to favor orthopyroxene over olivine (Namur et al., 2016a; Saracino et al., 2025). Second, clinopyroxene saturation occurs at around F = 0.50–0.40 in their models, similar to our clinopyroxene occurring at F = 0.40–0.35 in our models. Sulfur speciation has been shown to decrease the activity of CaO in silicate melts, delaying the formation of clinopyroxene (Anzures et al., 2020). Compared to S-free models from the literature, our S-bearing models indicate that this effect might not be as strong as previously suggested.

The different scenarios in the models of Brown and Elkins-Tanton (2009) also suggest that garnet and dense opaque phases (chromite, ilmenite) may have been stable in the MMO. Experiments at 7 GPa on the same compositions used herein (Xu et al., 2024) feature pyrope garnet at low melting fractions of F = 0.20–0.30. Garnet is thus a near-solidus phase and is not expected to fractionate from an evolving MMO near its liquidus. The production of high density, opaque minerals (ilmenite, chromite) at lower liquid fractions (Brown and Elkins-Tanton, 2009) is also not supported by our experiments. The paucity of Cr and Ti at the surface of Mercury (Nittler et al., 2011, 2018, 2023; Cartier et al., 2020; Peplowski et al., 2011), coupled with the more chalcophile behaviour displayed by both Cr and Ti in reduced conditions (Cartier et al., 2020), preclude those elements as being important to mineral formation in the MMO within the P-T-fO_2 range investigated herein.

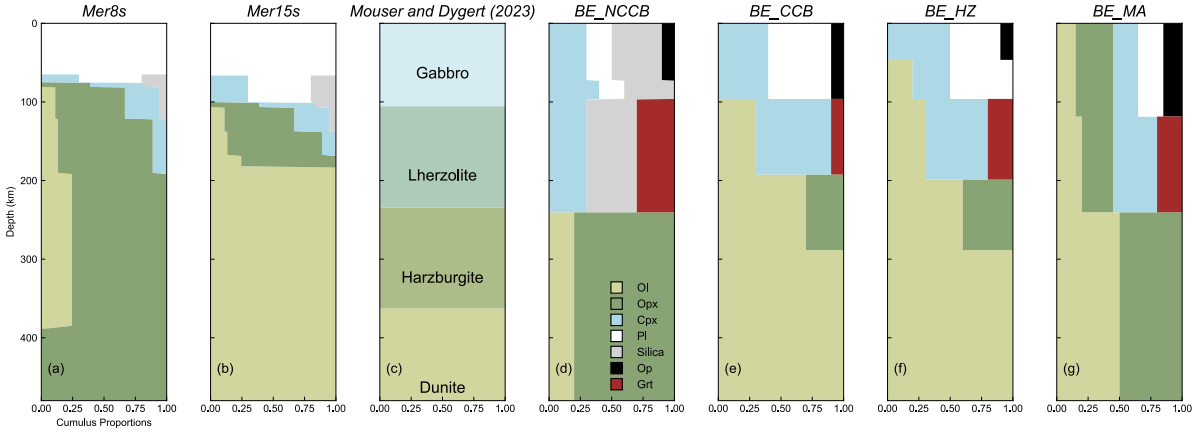

Figure 4.9. *Comparison of MMO crystallization sequence models. The depths have been scaled for comparison. (a) Mer8 and (b) Mer15 from this study. (c) Pre-mantle overturn crystallization sequence of Mouser and Dygert (2023). (d) Starting CB chondrite composition (Weisberg et al., 2000; Lauretta et al., 2007) with non-chondritic Si/Mg calculated by Brown and Elkins-Tanton (2009). (e) Starting CB chondrite (Weisberg et al., 2000, 2001; Lauretta et al., 2007) with chondritic Si/Mg calculated by Brown and Elkins-Tanton (2009). (f) Starting Earth mantle composition based on measurements of fertile lherzolites (Hart and Zindler, 1986) calculated by Brown and Elkins-Tanton (2009). (g) Model composition of Earth calculated from a nebular condensation model (Morgan and Anders, 1980) calculated by Brown and Elkins-Tanton (2009). The thicker mantles in the models of Brown and Elkins-Tanton (2009) were originally calculated for a ~1800-km core radius (Riner et al., 2008) but are scaled to the updated MMO stratigraphy determined herein for comparison. Abbreviations: Ol, olivine; Opx, orthopyroxene; Cpx, clinopyroxene; Silica, SiO_2 phases; Pl, plagioclase; Op, opaques; Grt, garnet.*

4.6.2. Refractory and Fertile Mantles: Implications for Crustal Production

The lithological evolution of Mercury's primordial mantle impacts mantle melting conditions and the production of partial melts, eventually influencing the compositions of surface lavas. Indeed, widespread volcanism on Mercury generated its diverse geochemical regions (Head et al., 2011; Weider et al., 2015). These regions have been shown to be the product of different degrees of partial melting of a heterogeneous mantle (Charlier et al., 2013; Namur et al., 2016b; Wang et al., 2022). Charlier et al. (2013) originally proposed different melting sources for two chemically distinct surface regions approximately in the southern hemisphere (termed the 'intercrater plains-highly cratered terrains' or IcP-HCT) based on the first XRS data from the MESSENGER spacecraft. They suggested that the two geochemically distinct units G1 (low Al_2O_3 and high CaO, MgO) and G2 (high Al_2O_3 and low CaO, MgO) were the product of low-pressure (<10 kbar) partial melting of lherzolitic and harzburgitic mantle sources, respectively. As new geochemical data became available (Weider et al., 2015), Namur et al.

(2016a) proposed that the geochemical terrains had equilibrated at low pressure (<15 kbar) following adiabatic decompression of lherzolitic mantles differing by their clinopyroxene fraction. In particular, they found that MgO-rich lavas were generated by a high degree of partial melting (F = 0.35 ± 0.03) starting deeper in the mantle (~360 km depth, corresponding to ~4.5 GPa) and at higher temperatures (~1720 ℃) compared to Northern Volcanic Plain lavas (F = 0.27 ± 0.04) that formed at shallower depths (~160 km) and lower temperatures (~1435 ℃). Similarly, Wang et al. (2022) showed that the geochemical region characterized by high Mg/Si (the 'high Mg region' or HMR) may have originated from multiple mantle sources characterized by jagged, irregular boundaries, whose melting was likely favored by local thermal anomalies early in the planet's history (>4.1 Ga). Melting experiments on a synthetic EH4 composition at 0.5–5.0 GPa (relevant to the petrogenesis of Mercury's surface lavas) showed that melting of a single enstatite-rich chondritic composition can produce a variety of silicate melt compositions, from high-Mg melts at high pressure (2–5 GPa) to silica-rich silicate melts at low pressure (0.5–1.0 GPa) (Boujibar et al., 2025). They also argued that Mercury's mantle is mainly pyroxenitic in composition due to the large stability field of orthopyroxene in sulfur-bearing systems.

Studying the primordial mantle of Mercury as produced from a fractionating magma ocean is paramount to understanding the melting sources responsible for the formation of the surface lavas. Importantly, previous melting studies overlooked that certain portions of the primordial mantle would have been more refractory to melting. Our results show that a refractory mantle is produced in the lower cumulate pile, which could be uniquely forsterite, uniquely enstatite, or include both phases. In the upper-MMO sequence, a fertile mantle forms when clinopyroxene becomes part of the cumulus assemblage. The formation of clinopyroxene-bearing mantle lithologies starts at around 160–190 km depth (Fig. 4.10.). Experimental studies have shown that a refractory mantle made of an olivine + orthopyroxene assemblage would melt congruently between 1680 °C at 1.2 GPa and 1780 °C at 2.5 GPa (Chen and Presnall, 1975). Conversely, a mantle containing olivine + orthopyroxene + clinopyroxene would start melting between 1310–1320 °C at 1.2 GPa and 1520 °C at 2.5 GPa (Walter and Presnall, 1994).

Because of the contrasting fusibility of the refractory and fertile mantles, it is expected that the fertile mantle was the dominant contributor to crustal production via partial melting. Here, we evaluate if the fertile mantle produced by MMO crystallization can actually produce the relatively thick volcanic surface of Mercury by partial melting alone. We consider the thickness of the fertile mantle to be ~ 140 km. We then calculate the volume of the silicate shell corresponding to the fertile reservoir as:

$$V_{\text{fertile mantle}} = \frac{4}{3}\pi\left(R^3_{\text{Mercury}} - R^3_{\text{core+refractory mantle}}\right) \quad \text{(Eq. 4.12)}$$

where $V_{\text{fertile mantle}}$ is the volume of the fertile mantle, R_{Mercury} is the radius of Mercury (2439 km), and $R_{\text{core + refractory mantle}}$ is the radius of the core plus the refractory reservoir of Mercury (2300 km). From this, we can calculate the volume of melt produced at a fixed melt fraction F, and the relative thickness it

would produce as lavas after extraction and cooling at the surface. We first consider a minimum degree of partial melting (F = 0.30) among estimated values in the literature (Namur et al., 2016a; Beuthe et al., 2020; Wang et al., 2022; Boujibar et al., 2025). Then we can calculate the volume of partial melt produced, and therefore the thickness of the layer that such a melt would produce at the surface (or within the crust, i.e., intrusive magmatism). We find the thickness of the volcanic crust to be 40 km, in good agreement with the estimated crustal thickness of 35 ± 17 km of Padovan et al. (2015). Higher degrees of partial melting (up to 0.70 for the HMR region; Boujibar et al., 2025) have also been suggested. Higher values of F (0.50–0.60) in our models would indeed yield a crustal thickness in the range 60–80 km. The range of crustal thicknesses produced by low degrees of partial melting are well within the various estimates of the extent of the Mercurian crust (Padovan et al., 2015; Beuthe et al., 2020). Our results therefore suggest that Mercury's volcanic crust may have originated from the partial melting of the fertile mantle portion alone. It is important to note, however, that the mantle of Mercury, as formed post-MMO crystallization, might have undergone one or multiple episodes of density-driven mantle overturn (Brown and Elkins-Tanton, 2009; Mouser and Dygert, 2023), which may have refertilized deeper mantle sources capable of producing partial melts by adiabatic decompression melting (Namur et al., 2016a).

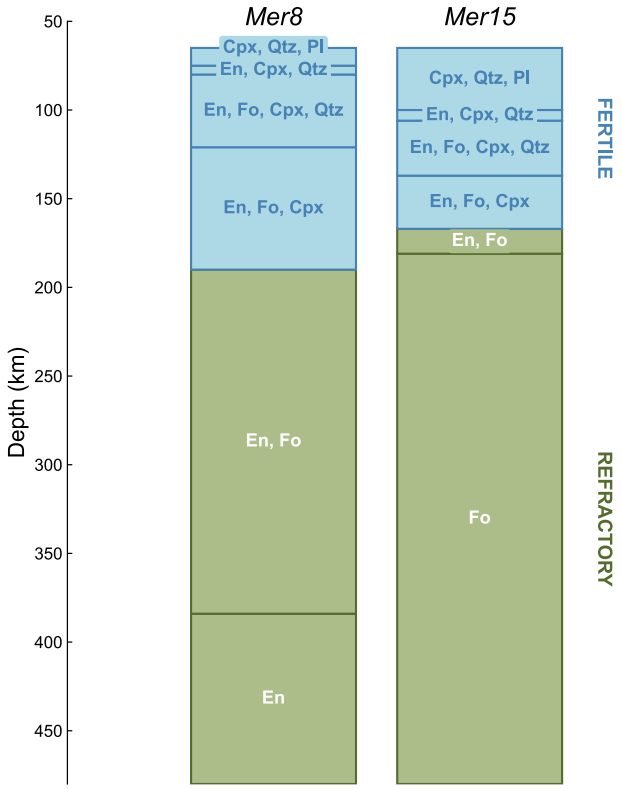

Figure 4.10. *Refractory (green) and fertile (light blue) mantle reservoirs for Mer8 and Mer15, respectively.*

4.6.3. Sulfides in the Mantle of Mercury

SCSS can be calculated at each incremental step of our crystallization model to track the formation of Mg- and Ca-rich sulfides. Studies investigating the MgS-CaS system show that a (Mg,Ca)S solid solution is stable over the MMO's temperature range (Pitsch et al., 2025). Under reduced conditions, SCSS sensibly decreases with temperature and is affected by the composition of the silicate melt (Namur et al., 2016b). Two end-member scenarios are usually considered when investigating the fate of sulfur in early differentiation processes on Mercury (e.g., Boukaré et al., 2019; Pirotte et al., 2023). In the first, the magma ocean was initially saturated with sulfides, allowing for sulfide phases to form at the CMB, perhaps together with an FeS layer atop the core. In the second, the MMO reached sulfide saturation later (at lower temperature) during crystallization, preventing sulfides from forming during the early stages.

To explore the potential sulfur content of the cumulate pile, we calculated SCSS using the model of Namur et al. (2016b), assuming an average mantle oxygen fugacity of $\log(fO_2)$ = IW−5.4 (Namur et al., 2016b) for both Mer8 and Mer15 (Fig. 4.8.). At CMB conditions, Mer15 (SCSS ≈ 8.8 wt% at 2040 ℃) has a higher SCSS than Mer8 (SCSS ≈ 7.8 wt% at 1960 ℃) due to the higher temperatures and MgO concentrations of Mer15 melts. We use a range of BSMe S concentrations (1–8 wt% S) and track the onset (fraction of residual liquid) of sulfide crystallization. We treat sulfur as a fully incompatible element in the silicate melt ($D_S^{crystal/melt} = 0$). The concentration of sulfur in the melt can therefore be determined as:

$$C_{S,Liq} = C_{S,0} F^{-1} \qquad \text{(Eq. 4.13)}$$

where $C_{S,Liq}$ is the concentration of sulfur in the residual liquid and $C_{S,0}$ is the starting concentration of sulfur in BSMe. When the path of increasing sulfur content with decreasing depth (or the fraction of residual liquid) reaches the modelled SCSS, the magma ocean becomes saturated with sulfide. We observe that for 1 wt% S in the starting BSMe, sulfide saturation is attained at a F = 0.33 (~160 km depth) for Mer8 and F = 0.45 (~210 km depth) for Mer15. At 5 wt% S in the BSMe, sulfide saturation occurs closer to the CMB (~350 km depth for Mer8 and ~360 km depth for Mer15). At 8 wt% S, the Mer8 MMO would be saturated with S at the onset of crystallization, whereas the Mer15 MMO would only reach sulfide saturation at ~450–460 km depth (Fig. 4.8.b). At >8.8 wt% S, the Mer15 MMO would be saturated with S at the CMB.

In Fig. 4.8.a,b, we show the potential sulfide content in the cumulate pile. As an approximation, $(Mg_{0.9}Ca_{0.1})S$ is considered as the stable sulfide phase that would form in this fO_2 range ($\Delta IW < -4.5$; Anzures et al., 2020, 2025). Different starting BSMe S contents would affect the amount of (Mg,Ca)S

in Mercury's primordial mantle. For example, in Mer8, 1 wt% S in the starting silicate magma ocean would produce ~5.5 wt% (Mg,Ca)S at 160 km depth, whereas 5 wt% S in the magma ocean would crystallize ~12.0 wt% sulfides at 350 km depth. Lark et al. (2022) calculated the abundance of Mg- and Ca-rich sulfides in Mercury's mantle based on the inferred mantle S content of Namur et al. (2016b). They found that 13–20 wt% (Mg,Ca)S would crystallize from the MMO.

We also evaluate the role that 10 wt% (Mg,Ca)S could play on the evolution of the residual MMO liquid in Fig. 4.7. Sulfide-free residual liquids (blue lines in Fig. 4.7.), after an initial slight increase in Si (up to 25–28 wt%), become depleted in silica with progressive crystallization in both the Mer8 and Mer15 cases (with Si down to 20–15 wt%). In contrast, due to decreased proportions of crystallizing silicate minerals, sulfide-bearing liquids (red lines) show enrichments of up to ~32–33 wt% Si under the investigated conditions (Fig. 4.7.a). This is supported by the composition of the experimentally determined S-bearing silicate melts (Fig. 4.7.a). Importantly, the fate of Al and Ca changes dramatically depending on the presence or absence of sulfides (Fig. 4.7.c, d). In accordance with our experiments, Al and Ca concentrations in sulfide-bearing liquids will first increase (up to 7–10 wt% Al and 2–4 wt% Ca) because they are hardly consumed by early forming phases (enstatite, forsterite). Then, once plagioclase crystallizes, their concentrations decrease (down to 5–9 wt% Al and 0–3 wt% Ca). Conversely, in sulfide-free liquids, we observe an enhanced enrichment of Al and Ca before plagioclase formation (>10 wt% Al and >5 wt% Ca). In addition, we also observe that Mg behaves similarly in the sulfide-free MMO as in its sulfide-bearing counterparts (Fig. 4.7.b).

4.6.4. MMO Density and Potential Mineral Flotation

Determining the density of silicate melts containing sulfur requires knowledge of the nature of bonding between S and typical silicate melt cations, for which the uncertainties remain large. Silicate melts are considered to dissolve ionic S (e.g., O'Neill, 2021), although several studies have demonstrated the bonding of S with cations like Mg, Ca, Si, and Na in silicate glasses using a variety of analytical approaches (Namur et al., 2016b; Anzures et al., 2020, 2025; Pommier et al., 2023). Some of these analyses, however, were performed on quenched products, which may show differences in speciation and elemental distributions compared to silicate melts (Mysen, 1983). Under reduced conditions, anionic oxygen is partly replaced by sulfur (Fincham and Richardson, 1954); therefore, in terms of molar mass, the density of a silicate liquid containing dissolved S is slightly higher than that of a S-free silicate liquid because sulfur has roughly twice the mass of oxygen (32 vs. 16 g mol^{-1}). However, the ionic radius of S^{2-} (1.84 Å) is larger than that of O^{2-} (1.41 Å), implying a greater molar volume and thus a lower specific density of sulfur-bearing melt components. Indeed, S has a lower specific density than other typical melt components. At room temperature, the partial specific density

(M_i / V_i, with M_i being the molar mass and V_i the molar volume of melt component i) of S (~2060 kg m^{-3}) is within the range of the specific densities of other melt components like SiO_2 or K_2O (2000–2200 kg m^{-3}), and higher than those of common volatiles (H_2O, CO_2 at 900–1400 kg m^{-3}) (Lesher and Spera, 2015). In contrast, if we assume MgS and CaS as melt species in sulfur-bearing silicate melts, the bonding of S with Mg and Ca would decrease the activities, and therefore the molar fractions, of MgO and CaO species in the silicate melt, which have higher specific densities (3300–3600 kg m^{-3}) compared to S and other sulfides. Furthermore, the occurrence of MgS and CaS melt species will increase, which have specific densities of ~2500–2700 kg m^{-3} in their solid form (Lark et al., 2022). The densities of these species are higher than dominant melt components like SiO_2 (2200 kg m^{-3}) but lower than the specific densities of MgO and CaO.

Therefore, the densities of silicate liquids containing dissolved S should, in principle, slightly decrease. We therefore calculated the effect of sulfur on the density of the MMO liquid (details on the procedure are reported in Appendix C, Section S4.12.). The resulting densities of the MMO calculated for Mer8 and Mer15 are shown in Fig. 4.11.

To our knowledge, this study is the first attempt to explore the impact of S on the density of reduced, Mg-rich silicate melts, although we stress that further studies specifically dedicated to understanding the volumetric properties of S and other sulfides at high temperatures and pressures are needed. Nonetheless, we importantly find that sulfur plays a major role in decreasing the density of silicate liquids. For example, around 10 wt% S dissolved in a silicate liquid would decrease the density by ca. 210 kg m^{-3}. This effect may have serious consequences on the ability of newly formed solid phases to float in a vast magma ocean.

To investigate the possibility that minerals formed in the MMO could become buoyant, we compare the densities of the S-bearing residual liquids for both the Mer8 and Mer15 BSMe compositions with the density of solid phases as a function of depth (Fig. 4.11.). Mineral phase densities are calculated with third-order Birch-Murnaghan equations of state in terms of density (Birch, 1947; Vander Kaaden and McCubbin, 2015) using parameters for graphite, quartz, and sulfides from Colonna et al. (2011), Kosinski et al. (1992), Frondel (1962), Lark et al. (2022), Peiris et al. (1994), and Baldwin and Tompson (1964). We confirm that graphite has a lower density than any residual MMO melt and may have thus continuously contributed to the formation of the primordial graphite crust. We also observe that quartz, appearing at F = 0.24–0.28, is denser than the residual melts. We also plot potential sulfide minerals (niningerite, MgS; oldhamite, CaS) that could have segregated from the MMO (Boukaré et al., 2019; Mouser and Dygert, 2023). For Mer8, since the beginning of MMO crystallization, the density of the MMO liquid is lower than the densities of the sulfides. If the MMO was initially sulfide saturated, we would then expect the sulfides to sink into the cumulate pile with the early formed silicates like enstatite

and/or forsterite (last panel in Fig. 4.8.a). Even in the case that sulfide saturation was attained later during MMO crystallization, the newly formed sulfides would still have been denser than the residual liquid (Fig. 4.8.a). As for Mer15, we observe that at CMB conditions, sulfides are slightly positively buoyant with respect to the MMO liquid ($\Delta\rho^{\text{sulfides, MMO}}$ = 3–13 kg m^{-3}; last panel of Fig. 4.8.b). Nonetheless, gravitational phase segregation depends on crystal size (Solomatov, 2015), and sulfide flotation may have been hindered by turbulent convection in the magma ocean (Schmidt and Kraettli, 2022). In the case of Mer15, the density contrast between the sulfides and the magma ocean is too small to effectively segregate sulfides; in this case, sulfides would be trapped amongst the co-crystallizing forsterite minerals.

Considering a MMO of Mer15 composition saturated with sulfides at the onset of crystallization, the sulfides, whether formed before or after the sulfide density crossover, would be stored in the lower and intermediate sections of the mantle. In the alternative case where the MMO Mer15 composition is not saturated with sulfides from the onset of crystallization, sulfides would likely start forming at intermediate depths in the mantle.

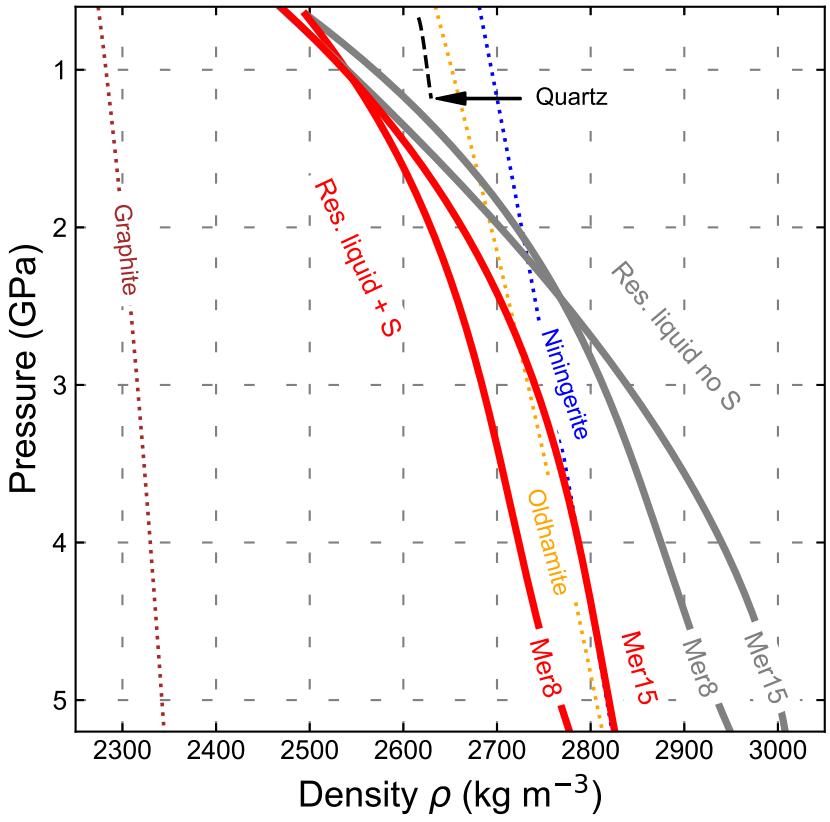

Figure 4.11. *The densities of evolving residual MMO liquids as compared to quartz, graphite, and sulfides.*

4.6.5. Implications for the Storage of Heat-Producing Elements

The primordial structure of the Mercurian mantle affected the distribution of HPEs like U, Th, and K. The partitioning of these elements between the silicate, metallic, and sulfide phases may have also been influenced by the reduced conditions during Mercury's differentiation (Boujibar et al., 2019; Pirotte et al., 2023). Elements tend to become more chalcophile and siderophile at increasingly reduced conditions (McCubbin et al., 2012; Boujibar et al., 2019; Pirotte et al., 2023). A FeS layer atop the metallic core may also affect the HPE distribution and heat production (Boujibar et al., 2019; Boukaré et al., 2019), although the existence of such a layer remains debated (Smith et al., 2012; Cartier et al., 2020; Pirotte et al., 2023). Oxygen fugacity and the initial S content of the MMO have been shown to affect the storage of U in the Mercurian mantle (Boukaré et al., 2019). At low initial S contents (~1 wt%) and relatively oxidizing conditions (IW−4 to IW−2), sulfides remain in sufficiently abundances that HPEs could be preferentially hosted in a sort of KREEPy (K, REE, and P-rich) layer in the upper mantle or, if present, in the FeS layer at the CMB. Under more reducing conditions (IW−6), sulfides are segregated in the shallow mantle of Mercury (<96 km depth), making this region richer in HPEs. At higher initial S contents (~5 wt% S) and oxidizing conditions (>IW−4), SCSS is low, and an FeS layer would form at the CMB, storing important amounts of HPEs (Boukaré et al., 2019). At high S contents and reduced conditions, HPEs would mostly be concentrated in the intermediate and upper mantle (<220 km depth; see Fig. 2. in Boukaré et al., 2019).

Importantly, large uncertainties surround the HPE distribution between Mg- and Ca-rich sulfides and the silicate melt (e.g., Boukaré et al. 2019). Only Pirotte et al. (2023) recently determined the partition coefficients of HPEs between MgS and the silicate melt under reduced conditions (IW−8.5). Using their estimates, we here quantify HPE partitioning in the MMO for both Mer8 and Mer15 compositions. The partitioning of element *i* between a solid phase and the silicate melt is expressed by the partition coefficient D_i, as:

$$D_i^{\text{crystal/melt}} = C_i^{\text{crystal}} / C_i^{\text{melt}} \qquad \text{(Eq. 4.14)}$$

where C_i^{crystal} is the concentration of element *i* in a given crystal phase, and C_i^{melt} is the concentration of element *i* in the melt. The concentrations of trace elements, like HPEs, in the MMO are calculated following Rayleigh's equation for fractional crystallization (Eq. 4.1). We calculate the distribution of HPEs based on the estimated (Mg,Ca)S content as shown in Fig. 4.8.a, b. Partition coefficients for the silicate minerals are from White (2013). The starting U, Th, and K concentrations in the BSMe are from Pirotte et al. (2023). The concentrations of U, Th, and K in the MMO as a function of depth are reported in panel a) of Fig. 4.12. Furthermore, after calculating the concentration of HPEs in the evolving MMO liquid, we could also determine the HPE abundances in the cumulate assemblages. The results are reported in Fig. 12.b. For clarity, we only show Mer8 (Fig. 4.12.). Plots for Mer15 are shown in

Appendix C (Fig. S4.13.). U, Th, and K are all incompatible, and their concentrations increase in the silicate liquid as the cumulate grows in thickness (red lines in Fig. 4.12.a). We also show sulfide-free magma ocean models for comparison (black lines in Fig. 4.12.). The residual sulfide-bearing liquids are slightly more depleted than the corresponding sulfide-free liquids, given the more compatible behaviour displayed by U and Th (Fig. S4.14.). Silicate liquids trapped in the growing cumulate might affect the trace element budget of the residual magma ocean liquid (Snyder et al., 1992; Elkins-Tanton et al., 2011). We therefore modelled the HPE budget considering 5% trapped liquid in the cumulate assemblages (green lines in Fig. 4.12.). HPEs are still enriched in the residual MMO liquid as crystallization proceeds. We only observe slightly lower HPE abundances compared to sulfide-bearing liquids with no trapped melt. In general, considering both S-free and S-bearing scenarios, we observe that the residual liquid of the MMO would likely contribute to forming a shallow layer that is rich in incompatible elements. A KREEP layer in the upper mantle of Mercury is therefore hypothesized, similar to the Moon (Warren and Wasson, 1979; Warren, 1988; Zhang et al., 2024a). On Mercury, such a layer would be found between the late cumulates and the primary graphite crust. As regards the cumulates-, we notice that the presence of sulfides combined with that of trapped melt has an effect on HPE distribution in the cumulates (Fig. 4.12.b). Although we observe that sulfides alone will only cause a small U, Th enrichment in early cumulates (roughly a 2-5 ppb difference), the presence of trapped liquid will cause a steeper U, Th enrichment, especially in the late cumulate sequence (< 200 km depth). K is almost absent in early formed cumulates (only trapped liquid has a minor effect), and it will only be stored when plagioclase saturates.

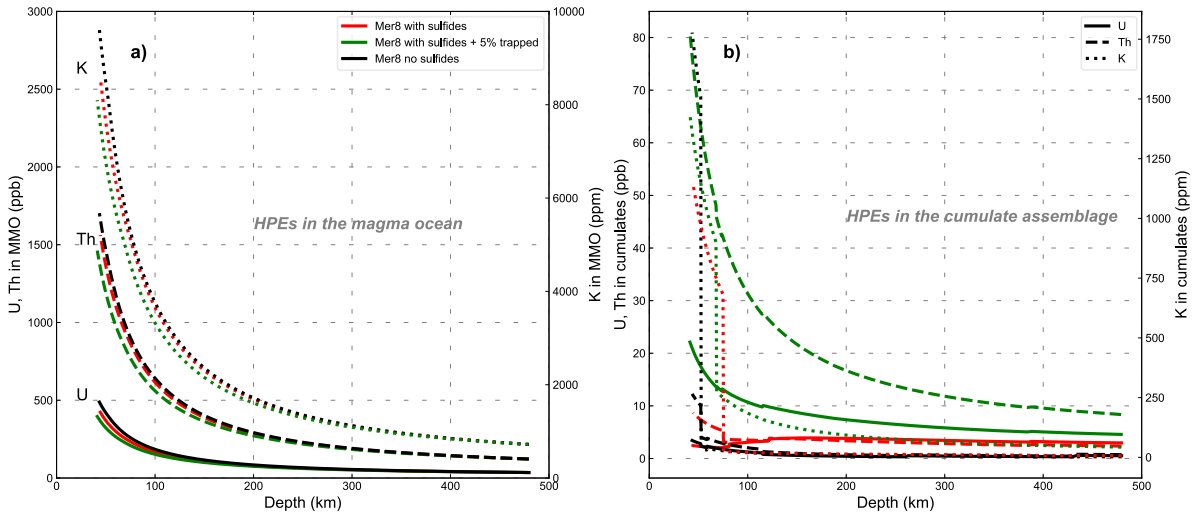

Figure 4.12. *(a) Uranium, thorium (both ppb), and potassium (ppm) distributions in the MMO as a function of depth (km) in Mer8. Black lines refer to sulfide-free Mer8, red lines refer to sulfide-bearing Mer8, and green lines refer to sulfide-bearing Mer8 with 5% trapped melt in the cumulate pile. (b)*

Uranium, thorium (both ppb), and potassium (ppm) distributions in the growing cumulates as a function of depth (km) in Mer8. Solid lines refer to uranium (U), dashed lines refer to thorium (Th), and dotted lines refer to potassium (K). Black lines refer to sulfide-free Mer8, red lines refer to sulfide-bearing Mer8, and green lines refer to sulfide-bearing Mer8 with 5% trapped liquid in the cumulate pile.

4.7. Conclusions

We investigated early differentiation processes occurring during the first evolutionary stages of planet Mercury. In detail, we studied the crystallization products of a S-rich Mercurian Magma Ocean (MMO) under reduced conditions. Our major findings and their implications are summarized as follows:

- The lithology of the primordial mantle of Mercury relies heavily on the Bulk Silicate Mercury (BSMe) composition and the presence of sulfur. A BSMe with a low Mg/Si ratio and a high S content will favor the formation of an orthopyroxenite layer at the base of the primordial mantle, whereas an S-saturated BSMe with a high Mg/Si ratio will crystallize a thick forsterite basal layer.
- Sulfur strongly impacts silicate phase equilibria. S in the MMO decreases the activity of MgO and CaO in the residual liquid, delaying the formation of clinopyroxene and plagioclase. In contrast, S increases the activity of SiO_2, allowing quartz to form early in the crystallization sequence.
- Due to the delayed formation of clinopyroxene and plagioclase, we showed that only a small portion of the primordial Mercurian mantle would have contributed to forming a fertile mantle reservoir.
- Sulfur plays a critical role in the chemical evolution of the MMO liquid. We showed that S-bearing silicate liquids have LLDs that are dramatically different from their S-free counterparts. Particularly, we showed that even primitive compositions with high Mg/Si will produce silica-rich, MgO-poor residual liquids.
- Sulfur also affects the density of the MMO. S-bearing silicate liquids are less dense than S-free liquids. However, further detailed studies are necessary to investigate the volumetric properties of sulfur and sulfides at high temperatures and pressures in magmatic systems.
- Graphite is likely the main mineral to float in the MMO and contribute to the formation of the primordial crust. Mg- and Ca-rich sulfides are generally denser than the MMO and are likely stored in the Mercurian mantle. Their distribution also depends on the bulk sulfur content of the BSMe.
- Heat-producing elements behaved incompatibly in the MMO and likely accumulated in the upper primordial mantle of Mercury. We highlight the effect of trapped liquid coupled with the presence of sulfides on the storage of HPE in the growing cumulate sequence. We suggest that a sulfide-

bearing KREEP layer, similar to that on the Moon, formed on Mercury. The presence of sulfides and trapped silicate liquid in the cumulate causes a small depletion of HPEs in the uppermost layers.

The upcoming ESA and JAXA BepiColombo mission (Benkhoff et al., 2021), and particularly the compositional and mineralogical data returned by the MERTIS, MGNS, MIXS, and SYMBYO-SIS instruments (Bunce et al., 2020; Cremonese et al., 2020; Hiesinger et al., 2020; Mitrofanov et al., 2021; Rothery et al., 2020), will be able to test our scenarios, therefore providing a revised model of Mercury's internal differentiation and crustal formation. We believe that our study represents a starting point for investigating the early differentiation processes of Mercury, and it may be also extended to exploring the early evolution of reduced, S-rich exoplanets with high core-to-mantle ratios (e.g., Santerne et al., 2018; Barros et al., 2022; Cioria et al., 2024; Zhang et al., 2024b).

CRedit authorship contribution statement

Fabrizio Saracino: Writing - original draft; Writing - review and editing, Data Curation, Investigation, Visualization, Formal analysis, Software, Conceptualization, Funding Acquisition. **Bernard Charlier:** Writing – review & editing, Supervision, Software, Conceptualization, Funding Acquisition. **Yishen Zhang:** Writing – review & editing, Software **Olivier Namur:** Writing – review & editing, Software, Formal analysis, Funding Acquisition, Conceptualization.

Declaration of competing interest

None.

Disclosure of generative AI assistance

Generative AI was employed for code refinement and illustration purposes.

Acknowledgements

FS wishes to thank Thomas Van Gerve (KU Leuven) for his help in the use of the SEM and the EPMA. We are grateful to Robert Dennen for his careful editing of the manuscript. This article was possible thanks to the support of the National Fund for Scientific Research (FNRS, Belgium) grant FRIA 40021515 (Fund for Research Training in Industry and Agriculture). BC is a Research Associate of the Belgian Fund for Scientific Research-FNRS and acknowledges funding from the ESA PRODEX Program (Grant 4000142722). ON acknowledges support from the European Research Council (ERC)

for a Consolidator Grant (IronHeart) under the European Union's Horizon (grant agreement no. 101125126).

Data and code availability

All data and codes are available in the main manuscript and relative online repository.

References

Anzures, B.A., Parman, S.W., Milliken, R.E., Namur, O., Cartier, C., McCubbin, F.M., Vander Kaaden, K.E., Prissel, K., Iacovino, K., Lanzirotti, A., Newville, M., 2025. An oxygen fugacity-temperature-pressure-composition model for sulfide speciation in Mercurian magmas. Geochim. Cosmochim. Acta 388, 61–77. https://doi.org/10.1016/j.gca.2024.11.012

Anzures, B.A., Parman, S.W., Milliken, R.E., Namur, O., Cartier, C., Wang, S., 2020. Effect of sulfur speciation on chemical and physical properties of very reduced Mercurian melts. Geochim. Cosmochim. Acta 286, 1–18. https://doi.org/10.1016/j.gca.2020.07.024

Baldwin, T.O., Tompson, C.W., 1964. X-ray characteristic temperatures of some II-VI ionic compounds. J. Chem. Phys., 41 (5), 1420-1426. https://doi.org/10.1063/1.1726083

Barros, S.C.C., Demangeon, O.D.S., Alibert, Y., Leleu, A., Adibekyan, V., Lovis, C., Bossini, D., Sousa, S.G., Hara, N., Bouchy, F., Lavie, B., Rodrigues, J., Da Silva, J.G., Lillo-Box, J., Pepe, F.A., Tabernero, H.M., Osorio, M.R.Z., Sozzetti, A., Mascareño, A.S., Micela, G., Prieto, C.A., Cristiani, S., Damasso, M., Di Marcantonio, P., Ehrenreich, D., Faria, J., Figueira, P., Hernández, J.I.G., Jenkins, J., Lo Curto, G., Martins, C.J.A.P., Micela, G., Nunes, N.J., Pallé, E., Santos, N.C., Rebolo, R., Seager, S., Twicken, J.D., Udry, S., Vanderspek, R., Winn, J.N., 2022. HD 23472: a multi-planetary system with three super-Earths and two potential super-Mercuries. Astron. Astrophys. 665, A154. https://doi.org/10.1051/0004-6361/202244293

Benkhoff, J., Murakami, G., Baumjohann, W., Besse, S., Bunce, E., Casale, M., Cremonese, G., Glassmeier, K.-H., Hayakawa, H., Heyner, D., Hiesinger, H., Huovelin, J., Hussmann, H., Iafolla, V., Iess, L., Kasaba, Y., Kobayashi, M., Milillo, A., Mitrofanov, I.G., Montagnon, E., Novara, M., Orsini, S., Quemerais, E., Reininghaus, U., Saito, Y., Santoli, F., Stramaccioni, D., Sutherland, O., Thomas, N., Yoshikawa, I., Zender, J., 2021. BepiColombo - Mission overview and science goals. Space Sci. Rev. 217, 90. https://doi.org/10.1007/s11214-021-00861-4

Berthet, S., Malavergne, V., Righter, K., 2009. Melting of the Indarch meteorite (EH4 chondrite) at 1GPa and variable oxygen fugacity: Implications for early planetary differentiation processes. Geochim. Cosmochim. Acta 73, 6402–6420. https://doi.org/10.1016/j.gca.2009.07.030

Bertone, S., Mazarico, E., Barker, M.K., Goossens, S., Sabaka, T.J., Neumann, G.A., Smith, D.E., 2021. Deriving Mercury geodetic parameters with altimetric crossovers from the Mercury laser altimeter (MLA). J. Geophis. Res. Planets 126, e2020JE006683. https://doi.org/10.1029/2020JE006683

Beuthe, M., Charlier, B., Namur, O., Rivoldini, A., Van Hoolst, T., 2020. Mercury's crustal thickness correlates with lateral variations in mantle melt production. Geophys. Res. Lett. 47, e2020GL087261.https://doi.org/10.1029/2020GL087261

Birch, F., 1947. Finite elastic strain of cubic crystals. Phys. Rev. 71, 809–824. DOI: https://doi.org/10.1103/PhysRev.71.809

Boujibar, A., Habermann, M., Righter, K., Ross, D.K., Pando, K., Righter, M., Chidester, B.A., Danielson, L.R., 2019. U, Th, and K partitioning between metal, silicate, and sulfide and implications for Mercury's structure, volatile content, and radioactive heat production. Am. Min. 104, 1221–1237. https://doi.org/10.2138/am-2019-7000

Boujibar, A., Righter, K., Fontaine, E., Collinet, M., Lambart, S., Nittler, L.R., Pando, K.M., 2025. A pyroxenite mantle on Mercury? Experimental insights from enstatite chondrite melting at pressures up to 5 GPa. Icarus 437, 116602. https://doi.org/10.1016/j.icarus.2025.116602

Boukaré, C.-E., Parman, S.W., Parmentier, E.M., Anzures B.A., 2019. Production and Preservation of Sulfide Layering in Mercury's Mantle. J. Geophys. Res. Planets 124, 3354–3372. https://doi.org/10.1029/2019JE005942

Bowen, N.L., 1914. The ternary system: diopside-forsterite-silica. Am. J. Sci. 38, 207-264. https://doi.org/10.2475/ajs.s4-38.225.207

Brown, S.M., Elkins-Tanton, L.T., 2009. Compositions of Mercury's earliest crust from magma ocean models. Earth Planet. Sci. Lett. 286, 446–455. https://doi.org/10.1016/j.epsl.2009.07.010

Bunce, E.J., Martindale, A., Lindsay, S., Muinonen, K., Rothery, D.A., Pearson, J., McDonnell, I., Thomas, C., Thornhill, J., Tikkanen, T., Feldman, C., Huovelin, J., Korpela, S., Esko, E., Lehtolainen, A., Treis, J., Majewski, P., Hilchenbach, M., Väisänen, T., Luttinen, A., Kohout, T., Penttilä, A., Bridges, J., Joy, K.H., Alcacera-Gil, M.A., Alibert, G., Anand, M., Bannister, N., Barcelo-Garcia, C., Bicknell, C., Blake, O., Bland, P., Butcher, G., Cheney, A., Christensen, U., Crawford, T., Crawford, I.A., Dennerl, K., Dougherty, M., Drumm, P., Fairbend, R., Genzer, M., Grande, M., Hall, G.P., Hodnett, R., Houghton, P., Imber, S., Kallio, E., Lara, M.L., Balado Margeli, A., Mas-Hesse, M.J., Maurice, S., Milan, S., Millington-Hotze, P., Nenonen, S., Nittler, L., Okada, T., Ormö, J., Perez-Mercader, J., Poyner, R., Robert, E., Ross, D., Pajas-Sanz, M., Schyns, E., Seguy, J., Strüder, L., Vaudon, N., Viceira-Martín, J., Williams, H., Willingale, D., Yeoman, T., 2020. The BepiColombo Mercury Imaging X-Ray Spectrometer: Science goals, instrument performance, and operations. Space Sci. Rev. 216, 126, https://doi.org/10.1007/s11214-020-00750-2

Byrne, P.K., Ostrach, L.R., Fassett, C.I., Chapman, C.R., Denevi, B.W., Evans, A.J., Klimczak, C., Banks, M.E., Head, J.W., Solomon, S.C., 2016. Widespread effusive volcanism on Mercury likely ended by about 3.5 Ga. Geophys. Res. Lett. 43, 7408–7416. https://doi.org/10.1002/2016GL069412

Cartier, C., Hammouda, T., Doucelance, R., Boyet, M., Devidal, J.-L., Moine, B., 2014. Experimental study of trace element partitioning between enstatite and melt in enstatite chondrites at low oxygen fugacities and 5 GPa. Geochim. Cosmochim. Acta 130, 167-187.http://dx.doi.org/10.1016/j.gca.2014.01.002

Cartier, C., Namur, O., Nittler, L.R., Weider, S.Z., Crapster-Pregont, E., Vorburger, A., Frank, E.A. and Charlier, B., 2020. No FeS layer in Mercury? Evidence from Ti/Al measured by MESSENGER. Earth Planet. Sci. Lett. 534, 116108. https://doi.org/10.1016/j.epsl.2020.116108

Chabot, N.L., Wollack, E.A., Klima, R.L., Minitti, M.E. (2014). Experimental constraints on Mercury's core composition. Earth Planet Sci. Lett. 390(0):199-208 http://dx.doi.org/10.1016/j.epsl.2014.01.004

Charlier, B., Grove, T.L., Namur, O., Holtz, F. (2018). Crystallization of the lunar magma ocean and the primordial mantle-crust differentiation of the Moon. Geochim. Cosmochim. Acta 234, 50–69.

Charlier, B., Grove, T.L., Zuber, M.T., 2013. Phase equilibria of ultramafic compositions on Mercury and the origin of the compositional dichotomy. Earth Planet Sci. Lett. 363, 50–60. https://doi.org/10.1016/j.gca.2018.05.006

Charlier, B., Namur, O., 2019. The origin and differentiation of planet Mercury, Elements 15, 9-14. 10.2138/gselements.15.1.9

Chen, C.-H., Presnall. D.C., 1975. The system Mg_2SiO_4-SiO_2 at pressures up to 25 kilobars. Am. Min. 60(5-6_Part_1):398-406

Cioria, C., Mitri, G., Connolly, J.A.D., Perrillat, J., Saracino, F., 2024. Mantle mineralogy of reduced sub-Earths exoplanets and exo-Mercuries. J. Geophys. Res. Planets 129, e2023JE008234. https://doi.org/10.1029/2023JE008234

Colonna, F., Fasolino, A., Meijer, E.J., 2011. High-pressure high-temperature equation of state of graphite from Monte Carlo simulations. Carbon 49, 364–368. https://doi.org/10.1016/j.carbon.2010.09.029

Condamine, P., Tournier, S., Charlier, B., Médard, E., Triantafyllou, A., Dalou, C., Tissandier, L., Lequin, D., Cartier, C., Füri, E., Burnard, P.G., Demouchy, S., Marrocchi, Y., 2022. Influence of intensive parameters and assemblies on friction evolution during piston-cylinder experiments. Am. Min. 107, 1575–1581. https://doi.org/10.2138/am-2022-7958

Corgne, A., Keshav, S., Wood, B.J., McDonough, W.F., Fei, Y., 2008. Metal-silicate partitioning and constraints on core composition and oxygen fugacity during Earth accretion. Geochim. Cosmochim. Acta 72, 574-589. 10.1016/j.gca.2007.10.006

Cremonese, G., Capaccioni, F., Capria, M.T., Doressoundiram, A., Palumbo, P., Vincendon, M., Massironi, M., Debei, S., Zusi, M., Altieri, F., Amoroso, M., Aroldi, G., Baroni, M., Barucci, A., Bellucci, G., Benkhoff, J., Besse, S., Bettanini, C., Blecka, M., Borrelli, D., Brucato, J.R., Carli, C., Carlier, V., Cerroni, P., Cicchetti, A., Colangeli, L., Dami, M., Da Deppo, V., Della Corte, V., De Sanctis, M.C., Erard, S., Esposito, F., Fantinel, D., Ferranti, L., Ferri, F., Ficai Veltroni, I., Filacchione, G., Flamini, E., Forlani, G., Fornasier, S., Forni, O., Fulchignoni, M.,

Galluzzi, V., Gwinner, K., Ip, W., Jorda, L., Langevin, Y., Lara, L., Leblanc, F., Leyrat, C., Li, Y., Marchi, S., Marinangeli, L., Marzari, F., Mazzotta Epifani, E., Mendillo, M., Mennella, V., Mugnuolo, R., Muinonen, K., Naletto, G., Noschese, R., Palomba, E., Paolinetti, R., Perna, D., Piccioni, G., Politi, R., Poulet, F., Ragazzoni, R., Re, C., Rossi, M., Rotundi, A., Salemi, G., Sgavetti, M., Simioni, E., Thomas, N., Tommasi, L., Turella, A., Van Hoolst, T., Wilson, L., Zambon, F., Aboudan, A., Barraud, O., Bott, N., Borin, P., Colombatti, G., El Yazidi, M., Ferrari, S., Flahaut, J., Giacomini, L., Guzzetta, L., Lucchetti, A., Martellato, E., Pajola, M., Slemer, A., Tognon, G. and Turrini, D., 2020. SIMBIO-SYS: Scientific cameras and spectrometer for the BepiColombo mission. Space Sci. Rev. 216, 75. https://doi.org/10.1007/s11214-020-00704-8

Elkins-Tanton, L.T, Parmentier, E.M., Hess, P.C., 2003. Magma ocean fractional crystallization and cumulate overturn in terrestrial planets: Implications for Mars. Meteorit. Planet. Sci. 38(12):1753-1771 https://doi.org/10.1111/j.1945-5100.2003.tb00013.x

Elkins-Tanton, L.T., Burgess, S., Yin, Q.-Z., 2011. The lunar magma ocean: Reconciling the solidification process with lunar petrology and geochronology. Earth Planet. Sci. Lett. 304, 326-336. 10.1016/j.epsl.2011.02.004

Falloon, T.J., Green, D.H., 1988. Anhydrous partial melting of peridotite from 8 to 35 kb and the petrogenesis of MORB. J. Petrol. Special_Volume (1):379-414 https://doi.org/10.1093/petrology/Special_Volume.1.379

Fincham, C., Richardson, F.D., 1954. The behaviour of sulphur in silicate and aluminate melts. Proc. R. Soc. Lond. A 223 (1152), 40–62. https://doi.org/10.1098/rspa.1954.0099

Fischer, E.L., Parman, S.W., 2025. The bulk composition and initial size of Mercury. Icarus 439, 116664. https://doi.org/10.1016/j.icarus.2025.116664

Frondel, C., 1962. The system of mineralogy: Vol. III Silica minerals, John Wiley and Sons Inc.

Genova, A., Goossens, S., Mazarico, E., Lemoine, F.G., Neumann, G.A., Kuang, W., Sabaka, T.J., Hauck, S.A., Smith, D.E., Solomon, S.C., Zuber, M.T., 2019. Geodetic evidence that Mercury has a solid inner core. Geophys. Res. Lett. 46, 3625–3633. https://doi.org/10.1029/2018GL081135

Goossens, S., Renaud, J.P., Henning, W.G., Mazarico, E., Bertone, S., Genova, A., 2022. Evaluation of recent measurements of Mercury's moments of inertia and tides using a comprehensive Markov Chain Monte Carlo method. Planet. Sci. J. 3, 37. 10.3847/PSJ/ac4bb8

Gu T., Stagno V. and Fei Y., 2019. Partition coefficient of phosphorus between liquid metal and silicate melt with implications for the Martian magma ocean. Phys. Earth Planet. Inter. 295, 106298. https://doi.org/10.1016/j.pepi.2019.106298

Guillot, B., Sator, N., 2007. A computer simulation study of natural silicate melts. Part I: Low pressure properties. Geochim. Cosmochim. Acta 71, 1249–1265. https://doi.org/10.1016/j.gca.2006.11.015

Hart, S.R., Zindler, A., 1986. In search of a bulk-Earth composition. Chem. Geol. 57, 247–267. https://doi.org/10.1016/0009-2541(86)90053-7

Hauck, S.A., Margot, J., Solomon, S.C., Phillips, R.J., Johnson, C.L., Lemoine, F.G., Mazarico, E., McCoy, T.J., Padovan, S., Peale, S.J., Perry, M.E., Smith, D.E. and Zuber, M.T., 2013. The curious case of Mercury's internal structure. J. Geophys. Res. Planets 118, 1204–1220. https://doi.org/10.1002/jgre.20091

Head, J.W., Chapman, C. ., Strom, R.G., Fassett, C.I., Denevi, B.W., Blewett, D.T., Ernst, C.M., Watters, T.R., Solomon, S.C., Murchie, S.L., Prockter, L.M., Chabot, N.L., Gillis-Davis, J.J., Whitten, J.L., Goudge, T.A., Baker, D.M.H., Hurwitz, D.M., Ostrach, L.R., Xiao, Z., Merline, W.J., Kerber, L., Dickson, J.L., Oberst, J., Byrne, P.K., Klimczak, C., Nittler, L.R., 2011. Flood Volcanism in the Northern High Latitudes of Mercury Revealed by MESSENGER. Science 333, 1853–1856. DOI: 10.1126/science.1211997

Hiesinger, H., Helbert J., Alemanno, G., Bauch, K.E., D'Amore, M., Maturilli, A., Morlok, A., Reitze, M.P., Stangarone, C., Stojic, A.N., Varatharajan, I., Weber, I., the MERTIS Co-I Team, 2020. Studying the composition and mineralogy of the Hermean surface with the Mercury Radiometer and Thermal Infrared Spectrometer (MERTIS) for the BepiColombo mission: An update. Space Sci. Rev. 216:110. https://doi.org/10.1007/s11214-020-00732-4

Jarosewich, E., 1990. Chemical analyses of meteorites: A compilation of stony and iron meteorite analyses. Meteoritics 25, 323–337. https://doi.org/10.1111/j.1945-5100.1990.tb00717.x

Kosinski, J.A., Gualtieri, J.G., Ballato, A., 1992. Thermoelastic coefficients of alpha quartz. IEEE Trans. Ultrason. Ferroelectr. Freq. Control, 39, 502–507. 10.1109/58.148541

Kushiro, I. (1969). The system forsterite-diopside-silica with and without water at high pressures. Am. J. Sci., 267-A, 269-294. https://doi.org/10.2475/001c.125224

Lange, R., Carmichael, I.S.E., 1987. Densities of Na_2O-K_2O-MgO-MgO-FeO-Fe_2O_3-Al_2O_3-TiO_2-SiO_2 liquids: New measurements and derived partial molar properties. Geochim. Cosmochim. Acta 51, 2931–2946. https://doi.org/10.1016/0016-7037(87)90368-1

Lark, L.H., Parman, S., Huber, C., Parmentier, E.M., Head, J.W., 2022. Sulfides in Mercury's Mantle: Implications for Mercury's Interior as Interpreted From Moment of Inertia. Geophys. Res. Lett. 49, e2021GL096713. https://doi.org/10.1029/2021GL096713

Lauretta, D.S., Goreva, J.S., Hill, D.H., Killgore, M., 2007. Bulk compositions of the CB Chondrites Bencubbin, Fountain Hills, MAC 02675, and MIL 05082. LPSC Abstracts 38, 2236.

Lesher, C.E., Spera, F.J., 2015. Thermodynamic and Transport Properties of Silicate Melts and Magma, in: The Encyclopedia of Volcanoes. Elsevier, pp. 113–141. https://doi.org/10.1016/B978-0-12-385938-9.00005-5

Ma, C., Beckett, J.R., Rossman, G.R., 2011. Murchisite, Cr_5S_6, a new mineral from the Murchison meteorite. Am. Min. 96, 1905-1908. https://doi.org/10.2138/am.2011.3858

Ma, Z., 2001. Thermodynamic description for concentrated metallic solutions using interaction parameters. Metall. Mater. Trans. 32B, 87-103. https://doi.org/10.1007/s11663-001-0011-0

Malavergne, V., Toplis, M.J., Berthet, S., Jones, J., 2010. Highly reducing conditions during core formation on Mercury: Implications for internal structure and the origin of a magnetic field. Icarus 206, 199–209. https://doi.org/10.1016/j.icarus.2009.09.001

Margot, J., Peale, S.J., Solomon, S.C., Hauck, S.A., Ghigo, F.D., Jurgens, R.F., Yseboodt, M., Giorgini, J.D., Padovan, S., Campbell, D.B., 2012. Mercury's moment of inertia from spin and gravity data. J. Geophys. Res. Planets 117, 2012JE004161. https://doi.org/10.1029/2012JE004161

McCoy, T.J., Dickinson, T.L., Lofgren, G.E., 1999. Partial melting of the Indarch (EH4) meteorite: A textural, chemical, and phase relations view of melting and melt migration. Meteorit. Planet. Sci. 34, 735-746. https://doi.org/10.1111/j.1945-5100.1999.tb01386.x

McCoy, T.J., Peplowski, P.N., McCubbin, F.M., Weider, S.Z., 2018. The Geochemical and Mineralogical Diversity of Mercury. In Mercury (eds. S. C. Solomon, L. R. Nittler, and B. J. Anderson). Cambridge University Press. pp. 176–190. https://doi.org/10.1017/9781316650684.008

McCubbin, F.M., Riner, M.A., Vander Kaaden, K.E., Burkemper, L.K., 2012. Is Mercury a volatile-rich planet? Geophys. Res. Lett., 39, L09202. https://doi.org/10.1029/2012GL051711

McDonough, W.F., 2025. Earth's composition: origin, evolution, and energy budget. ArXiv. https://doi.org/10.48550/arXiv.2505.02641

Mitrofanov, I.G., Kozyrev, A.S., Lisov, D.I., Litvak, M.L., Malakhov, A.A., Mokrousov, M.I., Benkhoff, J., Owens, A., Schulz, R., Quarati, F., 2021. The Mercury Gamma-Ray and Neutron Spectrometer (MGNS) Onboard the Mercury Planetary Orbiter of the BepiColombo mission: Design updates and first measurements in space. Space Sci. Rev. 217. https://doi.org/10.1007/s11214-021-00842-7

Morgan, J.W., Anders, E., 1980. Chemical composition of Earth, Venus, and Mercury. Proc. Natl. Acad. Sci. USA, 77, 6973–6977. https://doi.org/10.1073/pnas.77.12.6973

Mouser, M. D., Dygert, N., 2023. On the potential for cumulate mantle overturn in Mercury. J. Geophys. Res. Planets 128, e2023JE007739. https://doi.org/10.1029/2023JE007739

Mouser, M.D., Dygert, N., Anzures, B.A., Grambling, N.L., Hrubiak, R., Kono, Y., Shen, G., Parman, S.W., 2021. Experimental investigation of Mercury's magma ocean viscosity: Implications for the formation of Mercury's cumulate mantle, its subsequent dynamic evolution, and crustal petrogenesis. J. Geophys. Res. Planets 126, e2021JE006946. https://doi.org/10.1029/2021JE006946

Mysen, B.O., 1983. The structure of silicate melts. Annu. Rev. Earth Planet. Sci., 11, 75-97.

Namur, O., Charlier, B., 2017. Silicate mineralogy at the surface of Mercury. Nat. Geosci.10, 9–13. https://doi.org/10.1038/ngeo2860

Namur, O., Charlier, B., Holness, M.B., 2012. Dual origin of Fe-Ti-P gabbros by immiscibility and fractional crystallization of evolved tholeiitic basalts in the Sept Iles layered intrusion. Lithos, 154, 100-114. https://doi.org/10.1016/j.lithos.2012.06.034

Namur, O., Charlier, B., Holtz, F., Cartier, C., and McCammon, C., 2016b. Sulfur solubility in reduced mafic silicate melts: Implications for the speciation and distribution of sulfur on Mercury. Earth Planet Sci. Lett. 448, 102–114. https://doi.org/10.1016/j.epsl.2016.05.024

Namur, O., Collinet, M., Charlier, B., Grove, T.L., Holtz, F., and McCammon, C., 2016a. Melting processes and mantle sources of lavas on Mercury. Earth Planet Sci. Lett. 439, 117–128. https://doi.org/10.1016/j.epsl.2016.01.030

Nittler, L.R., Boujibar, A., Crapster-Pregont, E., Frank, E.A., McCoy, T.J., McCubbin, F.M., Starr, R.D., Vorburger, A., Weider, S.Z., 2023. Chromium on Mercury: New Results From the MESSENGER X-Ray Spectrometer and Implications for the Innermost Planet's Geochemical Evolution. J. Geophys. Res. Planets 128, e2022JE007691. https://doi.org/10.1029/2022JE007691

Nittler, L.R., Chabot, N.L., Grove, T.L., and Peplowski, P.N., 2018. The Chemical Composition of Mercury. In Mercury (eds. S. C. Solomon, L. R. Nittler, and B. J. Anderson). Cambridge University Press. pp. 30–51. https://doi.org/10.1017/9781316650684.003

Nittler, L.R., Frank, E.A., Weider, S.Z., Crapster-Pregont, E., Vorburger A., Starr, R.D., and Solomon S.C., 2020. Global major-element maps of Mercury from four years of MESSENGER X-Ray Spectrometer observations. Icarus 345, 113716. https://doi.org/10.1016/j.icarus.2020.113716

Nittler, L.R., Starr, R.D., Weider, S.Z., McCoy, T.J., Boynton, W.V., Ebel, D.S., Ernst, C.M., Evans, L.G., Goldsten, J.O., Hamara, D.K., Lawrence, D.J., McNutt, R.L., Schlemm, C.E., Solomon, S.C., Sprague, A.L., 2011. The major-element composition of Mercury's surface from MESSENGER X-ray Spectrometry. Science 333, 1847–1850. DOI: 10.1126/science.1211567

O'Neill, H.S.C., 2021. The thermodynamic controls on sulfide saturation in silicate melts with application to ocean floor basalts. In: Moretti, R., Neuville, D.R. (Eds.), Magma Redox Geochemistry. John Wiley and Sons. https://doi.org/10.1002/9781119473206.ch10

Ohtani, E., Maeda, M., 2001. Density of basaltic melt at high pressure and stability of the melt at the base of the lower mantle. Earth Planet Sci. Lett. 193, 69–75. https://doi.org/10.1016/S0012-821X(01)00505-2

Padovan, S., Wieczorek, M.A., Margot, J.-L., Tosi, N., Solomon. S.C., 2015. Thickness of the crust of Mercury from geoid-to-topography ratios. Geophys. Res. Lett. 42, 1029-1038. https://doi.org/10.1002/2014GL062487

Peiris, S. M., Campbell, A. J., & Heinz, D. L., 1994. Compression of MgS to 54 GPa. J. Phys. Chem. Sol., 55 (5), 413-419. https://doi.org/10.1016/0022-3697(94)90166-X

Peplowski, P.N., Evans, L.G., Hauck, S.A., McCoy, T.J., Boynton, W.V., Gillis-Davis, J.J., Ebel, D.S., Goldsten, J.O., Hamara, D.K., Lawrence, D.J., McNutt, R.L., Nittler, L.R., Solomon, S.C., Rhodes, E.A., Sprague, A.L., Starr, R.D., Stockstill-Cahill, K.R, 2011. Radioactive elements on Mercury's surface from MESSENGER: Implications for the planet's formation and evolution. Science 333, 1850–1852. https://doi.org/10.1126/science.1211576

Pirotte, H., Cartier, C., Namur, O., Pommier, A., Zhang, Y., Berndt, J., Klemme, S., Charlier, B., 2023. Internal differentiation and volatile budget of Mercury inferred from the partitioning of heat-producing elements at highly reduced conditions. Icarus 405, 115699. https://doi.org/10.1016/j.icarus.2023.115699

Pitsch, S., Connolly, J.A.D., Schmidt, M.W., Sossi, P.A., Liebske, C., 2025. Solids and liquids in the (Fe, Mg, Ca) S-system: experimentally determined and thermodynamically modelled phase relations. Phys. Chem. Miner. 52, 12. https://doi.org/10.1007/s00269-025-01313-z

Pommier, A., Tauber, M.J., Pirotte, H., Cody, G.D., Steele, A., Bullock, E.S., Charlier, B., Mysen, B.O., 2023. Experimental investigation of the bonding of sulfur in highly reduced silicate glasses and melts. Geochim. Cosmochim. Acta 363, 114-128. https://doi.org/10.1016/j.gca.2023.10.027

Riel, N., Kaus, B.J.P., Green, E.C.R., Berlie, N., 2022. MAGEMin, an efficient Gibbs energy minimizer: Application to igneous systems. Geochem. Geophys. Geosyst. 23, e2022GC010427. https://doi.org/10.1029/2022GC010427

Riner, M.A., Bina, C.R., Robinson, M.S., Desch, S.J., 2008. Internal structure of Mercury: Implications of a molten core. J. Geophys. Res. Planets 113, 2007JE002993. https://doi.org/10.1029/2007JE002993

Rothery, D. A., Massironi, M., Alemanno, G., Barraud, O., Besse, S., Bott, N., Brunetto, R., Bunce, E., Byrne, P., Capaccioni, F., Capria, M. T., Carli, C., Charlier, B., Cornet, T., Cremonese, G., D'Amore, M., De Sanctis, M. C., Doressoundiram, A., Ferranti, L., Filacchione, G., Galluzzi, V., Giacomini, L., Grande, M., Guzzetta, L.G., Helbert, J., Heyner, D., Hiesinger, H., Hussmann, H., Hyodo, R., Kohout, T., Kozyrev, A., Litvak, M., Lucchetti, A., Malakhov, A., Malliband, C., Mancinelli, P., Martikainen, J., Martindale, A., Maturilli, A., Milillo, A., Mitrofanov, I., Mokrousov, M., Morlok, A., Muinonen, K., Namur, O., Owens, A., Nittler, L.R., Oliveira, J.S., Palumbo, P., Pajola, M., Pegg, D.L., Penttilä, A., Politi, R., Quarati, F., Re, C., Sanin, A., Schulz, R., Stangarone, C., Stojic, A., Tretiyakov, V., Väisänen, T., Varatharajan, I., Weber, I., Wright, J., Wurz, P., Zambon, F., 2020. Rationale for BepiColombo Studies of Mercury's Surface and Composition. Space Sci. Rev., 216(4), 66. https://doi.org/10.1007/s11214-020-00694-7

Santerne, A., Brugger, B., Armstrong, D.J., Adibekyan, V., Lillo-Box, J., Gosselin, H., Aguichine, A., Almenara, J.-M., Barrado, D., Barros, S.C.C., Bayliss, D., Boisse, I., Bonomo, A.S., Bouchy, F., Brown, D.J.A., Deleuil, M., Delgado Mena, E., Demangeon, O., Díaz, R.F., Doyle, A., Dumusque, X., Faedi, F., Faria, J.P., Figueira, P., Foxell, E., Giles, H., Hébrard, G., Hojjatpanah, S., Hobson, M., Jackman, J., King, G., Kirk, J., Lam, K.W.F., Ligi, R., Lovis, C., Louden, T., McCormac, J., Mousis, O., Neal, J.J., Osborn, H.P., Pepe, F., Pollacco, D., Santos, N.C., Sousa, S.G., Udry, S., Vigan, A., 2018. An Earth-sized exoplanet with a Mercury-like composition. Nat. Astron. 2, 393–400. https://doi.org/10.1038/s41550-018-0420-5

Saracino, F., Charlier, B., Zhang, Y., Lécaille, M., Lin, Y., Namur, O., 2025. The role of sulfur on the liquidus temperature and olivine-orthopyroxene equilibria in highly reduced magmas. Chem. Geol. 683, 122777. https://doi.org/10.1016/j.chemgeo.2025.122777

Schaefer, L., Elkins-Tanton, L.T., 2018. Magma oceans as a critical stage in the tectonic development of rocky planets. Phil. Trans. R. Soc. A 376, 20180109. https://doi.org/10.1098/rsta.2018.0109

Schmidt, M.W., Kraettli, G., 2022. Experimental crystallization of the lunar magma ocean, initial selenotherm and density stratification, and implications for crust formation, overturn, and the bulk silicate Moon composition. J. Geophys. Res. Planets 127, 5. https://doi.org/10.1029/2022JE007187

Schubert, G., Ross, M.N., Stevenson, D.J., Spohn, T., 1988. Mercury's thermal history and the generation of its magnetic field, in Mercury (Eds. Vilas, F., Chapman, C.R., Shapley Matthews, M.), The University of Arizona Press, Tucson AZ, USA.

Smith, D.E., Zuber, M.T., Phillips, R.J., Solomon, S.C., Hauck, S.A., Lemoine, F.G., Mazarico, E., Neumann, G.A., Peale, S.J., Margot, J.-L., Johnson, C.L., Torrence, M.H., Perry, M.E., Rowlands, D.D., Goossens, S., Head, J.W., Taylor, A.H., 2012. Gravity field and internal structure of Mercury from MESSENGER. Science 80 (336), 214–217. DOI: 10.1126/science.1218809

Snyder, G.A., Taylor, L.A., Neal, C.R., 1992. A chemical model for generating the sources of mare basalts: Combined equilibrium and fractional crystallization of the lunar magmasphere. Geochim. Cosmochim. Acta 56, 3809-3823. https://doi.org/10.1016/0016-7037(92)90172-F

Solomatov, V., 2015. Magma oceans and primordial mantle differentiation. In: Schubert, G. (ed) Treatise on Geophysics (Second Edition), vol. 9, Elsevier, Amsterdam, pp 81-104. http://dx.doi.org/10.1016/B978-0-444-53802-4.00155-X

Steenstra, E.S., Seegers., A.X., Putter, R., Berndt, J., Klemme, S., Matveev, S., Bullock, E.S. and Van Westrenen, W., 2020. Metal-silicate partitioning systematics of siderophile elements at reducing conditions: A new experimental database. Icarus 335, 113391. https://doi.org/10.1016/j.icarus.2019.113391

Steinbrügge, G., Dumberry, M., Rivoldini, A., Schubert, G., Cao, H., Schroeder, D. M., Soderlund, K. M., 2021. Challenges on Mercury's interior structure posed by the new measurements of its obliquity and tides. Geophys. Res. Lett. 48, e2020GL089895. https://doi.org/10.1029/2020GL089895

Vander Kaaden, K.E., McCubbin, F.M., 2015. Exotic crust formation on Mercury: Consequences of a shallow, FeO-poor mantle. J. Geophys. Res. Planets 120, 195–209. https://doi.org/10.1002/2014JE004733

Walker, D., Longhi, J., Hays, J.F., 1975. Differentiation of a very thick magma body and implications for the source region of mare basalts. Proc. Lunar Sci. Conf. 6, 1103-1120, Lunar and Planetary Institute, Houston TX, USA.

Walter, M.J., Presnall, D.C., 1994. Melting behavior of simplified lherzolite in the system CaO-MgO-Al_2O_3-SiO_2-Na_2O from 7 to 35 kbar. J. Petrol. 35, 329-359. https://doi.org/10.1093/petrology/35.2.329

Wang, Y., Xiao, Z., Xu, R., 2022. Multiple Mantle Sources of High-Magnesium Terranes on Mercury. J. Geophys. Res. Planets 127, e2022JE007218. https://doi.org/10.1029/2022JE007218

Warren, P.H., 1988. The origin of pristine KREEP: effects of mixing between UrKREEP and the magmas parental to the Mg-rich cumulates. In: Lunar Planet. Sci. Conf. Proc., 233-241.

Warren, P.H., Wasson, J.T., 1979. The origin of KREEP. Rev. Geophys. 17, 73–88. https://doi.org/10.1029/RG017i001p00073.

Weider, S.Z., Nittler, L.R., Starr, R.D., Crapster-Pregont, E.J., Peplowski, P.N., Denevi, B.W., Head, J.W., Byrne, P.K., Hauck, S.A., Ebel, D.S., Solomon, S.C., 2015. Evidence for geochemical terranes on Mercury: Global mapping of major elements with MESSENGER's X-Ray Spectrometer. Earth Planet Sci. Lett. 416, 109–120. https://doi.org/10.1016/j.epsl.2015.01.023

Weisberg, M.K., Prinz, M., Clayton, R.N., Mayeda, T.K., Sugiura, N., Zashu, S., Ebihara, M., 2001. A new metal-rich chondrite grouplet. Meteorit. Planet. Sci. 36, 401–418. https://doi.org/10.1111/j.1945-5100.2001.tb01882.x

Weisberg, M.K., Prinz, M., Humayun, M., Campbell, A.J., 2000s. Origin of metal in the CB (Bencubbinite) chondrites. Lunar and Planetary Institute Conference Abstracts 31,1466.

Weng, Y.-H., Presnall, D.C., 2001. The system diopside forsterite enstatite at 5.1 GPa: a ternary model for melting of the mantle. Can. Min. 39, 299–308. https://doi.org/10.2113/gscanmin.39.2.299

White, W.M., 2013. Geochemistry. Wiley-Blackwell, John Wiley & Sons.

Wykes, J.L., O'Neill, H.St.C., Mavrogenes, J.A., 2015. The Effect of FeO on the sulfur content at sulfide saturation (SCSS) and the selenium content at selenide saturation of silicate melts. J. Petrol. 56, 1407-1424. https://doi.org/10.1093/petrology/egv041

Xu, Y., Lin, Y., Wu, P., Namur, O., Zhang, Y., Charlier, B., 2024. A diamond-bearing core-mantle boundary on Mercury. Nat. Commun. 15, 5061. https://doi.org/10.1038/s41467-024-49305-x

Zhang, Y., Charlier, B., Krein, S.B., Grove, T.L., Namur, O., and Holtz, F., 2024a. The very late-stage crystallization of the lunar magma ocean and the composition of immiscible urKREEP. Earth Planet Sci. Lett. 646, 118989. https://doi.org/10.1016/j.epsl.2024.118989

Zhang, Y., Namur, O., Hakim, K., Dasgupta, R., Shorttle, O., 2024b. Forming Mercury-analog planets in the solar neighborhood. 2024 Goldschmidt Conference.

Zolotov, M.Yu., Sprague, A.L., Hauck, S.A., Nittler, L.R., Solomon, S.C., Weider, S.Z., 2013. The redox state, FeO content, and origin of sulfur-rich magmas on Mercury. J. Geophys. Res. Planets 118, 138–146. https://doi.org/10.1029/2012JE004274

Chapter 5: Perspectives for BepiColombo

5.1. BepiColombo

As briefly discussed in Chapter 1 (Section 1.1.2.), BepiColombo represents the new joint effort of ESA and JAXA to place a spacecraft in orbit around Mercury with the goal of exploring comprehensively the innermost planet (Benkhoff et al., 2021). BepiColombo is equipped with two orbiters, the Mercury Magnetosphere Orbiter (Mio, previously MMO), and the Mercury Planet Orbiter (MPO). The Mio and MPO are carried on top of the Mercury Transfer Module (MTM), which is the element providing power, attitude, and orbit control (Benkhoff et al., 2021). The Mio is led by JAXA and will study Mercury's environment, including its exosphere and magnetic field. The MPO is led by ESA and will provide a global characterization of Mercury, by investigating the surface, interior, exosphere, and magnetosphere (Benkhoff et al., 2021). Starting from the characterization of the surface of the planet, three spectrometers onboard MPO will provide never-before-seen insight into the surface geochemistry and mineralogy. The Mercury Thermal Infrared Spectrometer (MERTIS) instrument (Hiesinger et al., 2020) will globally map the spectral emittance at high spectral resolution to investigate the surface composition, identify major rock forming minerals (mainly plagioclase endmembers, pyroxenes, elemental sulfur, plus other unusual phases), map the surface mineralogy, and study the thermal properties of surface materials. The Mercury Gamma Ray and Neutron Spectrometer (MGNS) instrument (Mitrofanov et al., 2021) will measure the elemental composition (Si, O, C, Al, Na, Fe, Ca, S, Cl, K, Th, U) of the surface and sub-surface of Mercury with a surface resolution of 400 km, characterize the distribution of volatile-rich polar deposits, by globally mapping the surface hydrogen distribution. The Mercury Imaging X-Ray Spectrometer (MIXS) instrument (Bunce et al. 2020) will measure fluorescent X-ray emissions from the surface of the planet at high spectral and spatial resolutions. The X-rays emitted by the planet are characteristic of the elemental species present on the surface. They will therefore provide a global coverage of the regolith composition in both hemispheres of key elements (Na, Mg, Al, Si, P, S, K, Ca, Ti, Cr, Mn, Fe, Ni). Also, surface imaging and chemical investigation will be performed by the Spectrometers and Imagers for BepiColombo-Integrated Observatory SYStem (SIMBIO-SYS) instrument (Cremonese et al., 2020). SIMBIO-SYS will investigate topographic, geomorphologic, volcanic, and tectonic features on Mercury's surface. It will also study surface age (crater population), composition, and geophysics. As for the interior of the planet, MESSENGER radar observations have been used to place constraints on the properties of the core (h_{core} ~ 2000 km; ρ_{core} ~ 7000 kg m^{-3}), mantle (h_{mantle} ~ 420 km; ρ_{mantle} ~ 3200 kg m^{-3}), and crust (h_{crust} = 35 – 53 km; ρ_{crust} = 2700 – 3100 kg m^{-3}) (Margot et al., 2018). Uncertainties, especially regarding the inner core size, are nonetheless still large (Benkhoff et al., 2021). The instruments onboard BepiColombo will

help refine these measurements and will provide a new model of its interior structure. In detail, the Mercury Orbiter Radio Science Experiment (MORE) (Iess et al., 2021) will help refine the determination of the gravity field of Mercury (with implications for mass distribution), allowing to better place constraints on the core state and properties.

5.2. Testing our results with BepiColombo

It would be legitimate to ask how this research, which is centered on the investigation of reducing, sulfur-rich magmatic systems and the early differentiation of Mercury, could contribute to the interpretation of the observations that will be provided by the BepiColombo mission. Further related questions may emerge, for which exhaustive answers may prove tricky to find. These issues can be grouped in three main paragraphs, which are summarized here below:

Mercury's interior configuration: The surface of Mercury was shaped by both impacts and extensive volcanism (Charlier and Namur, 2019). The northern hemisphere of Mercury is geochemically heterogeneous (Weider et al., 2015). This variety has been explained by partial melting-driven extrusion of magmas from a heterogeneous mantle (Charlier et al., 2013; Namur et al., 2016a). As the surface composition of Mercury serves as a proxy for its interior (Hiesinger et al., 2020), investigating the surface volcanic products proves crucial to get a glimpse on mantle sources and processes (e.g., Namur et al., 2016a; Boujibar et al., 2025). Importantly, due to MESSENGER's highly eccentric orbit, the southern hemisphere was not as resolved as the northern hemisphere (McCoy et al., 2018). BepiColombo is now set to provide the most up-to-date view of Mercury's surface configuration, by also covering the southern hemisphere. This will likely be characterized by the same geochemical variability that can be seen in the northern hemisphere (see Section 1.1.3.), and potentially new geochemical units might be discovered, which might add complexity to the picture. In addition to the insights derived from the analysis of the southern hemisphere, impact craters may also provide crucial information on planetary interiors. Impact structures on the surface of Mercury indeed represent surface 'windows' to its interior makeup (e.g. McCoy et al., 2018). Upon impacts, excavation of material from the surface may have indeed exposed portions of layers which would be otherwise hidden. In the case of Mercury, parts of the lower secondary crust, or remnants of the graphite-dominated primary crust, or even the upper mantle may be exposed to the surface. Studying such units represents a unique opportunity to investigate Mercury's mantle. Importantly, the composition and inferred mineralogy of such units be directly compared to our modelled mineral assemblages of the upper crystallization sequence (Chapter 4) to test whether they are the direct product of Mercury's magma ocean crystallization, or whether they have been modified afterwards as a consequence of mantle processes, like density-driven overturn, mantle re-melting. In addition, as hypothesised in Chapter 4, Mercury

might host a Moon-like KREEPy layer in the upper mantle. Analysing the surface of these geologic windows might also help us verify the presence of KREEPy surface material.

Sulfur speciation: as discussed in Chapters 3 and 4, large uncertainties surround the speciation of sulfur in reduced melts relevant to the petrogenesis of Mercury's volcanic crust. In reducing conditions, sulfur is considered to be dissolved as ionic (S^{2-}) in silicate melts, as S^{2-} replaces onto the anionic sublattice (O'Neill, 2021). On the other hand, multiple studies suggest that S bonds with cations like Si, Ca, Mg, Na, Ti using a variety of analytical techniques such as Raman, and XANES (Fogel, 2005; Métrich et al., 2009; Namur et al., 2016a; Anzures et al., 2020, 2025; Pommier et al., 2023). In the case of Mg and Ca, S^{2-} is considered to replace O^{2-} in $[SiO_4]^{4-}$ tetrahedra and bonding with Mg^{2+} and Ca^{2+} (Namur et al., 2016a). Detailed thermodynamic considerations coupled with in situ measurements of reduced melts are needed to shed more light on the subject, as this was not the scope of this doctoral thesis. In Chapter 1, a brief paragraph on the geochemical diversity displayed by Mercury's surface has been presented. Positive correlations between the abundance of S and elements like Mg, Ca have been found (Weider et al., 2015; Nittler et al., 2018, 2020). Sulfides are therefore likely present on the surface of the planet in non-negligible amounts (Vander Kaaden et al., 2017). The instruments onboard BepiColombo will measure the abundance of S and other elements that may bond with S under reducing conditions (e.g. Bunce et al., 2020). The positive correlation between these elements and sulfur might allow us to get a glimpse on the sulfur species that could form in S-bearing magmatic systems under low fO_2. BepiColombo's compositional data will therefore test the possibility for the formation of Mg-, Ca-bearing sulfides such as those assumed in this doctoral thesis, or whether other forms of sulfur-bearing phases might be present on the surface.

Mercury's redox state: Mercury, as we have seen, is considered an endmember planet in terms of redox conditions of formation (e.g. Cartier and Wood, 2019). The innermost planet differentiated under reducing conditions (Zolotov et al., 2013; Namur et al., 2016a; Nittler et al., 2023). The experiments featured in this work were performed in an oxygen fugacity range (from IW-3 to IW-9) which is within that hypothesised for Mercury's mantle (e.g. Namur et al., 2016a; Cartier and Wood, 2019; Nittler et al., 2023; Fischer and Parman, 2025). We modelled the crystallization of the magma ocean of Mercury considering the magma ocean's oxygen fugacity of IW-5.4 based on the estimates of Namur et al. (2016a). Relatively more oxidized oxygen fugacities have also been proposed (from IW-2 to IW-4.5, Anzures et al., 2020; Fischer and Parman, 2025). Importantly, highly reducing conditions (< IW-5.5) would preclude the formation of sulfides in Mercury's interior, whether under the form of a FeS layer at the CMB or as Ca-, Mg-sulfides in the mantle (Nittler et al., 2023). As explained in Chapter 3 and in the point above, sulfide speciation is sensitive to the redox conditions of magmas (Namur et al., 2016b; Anzures et al., 2020; 2025). For example, Mg sulfides are dominant under lower fO_2 (< IW-4), while Ca sulfides are dominant under relatively higher fO_2 (> IW-4) (Anzures et al., 2020, 2025). Therefore, the abundance correlations between sulfur and potential sulfide-forming elements provided

by the instruments onboard BepiColombo will enable us to place tighter constraints on the redox conditions of the magmas in Mercury's interior.

5.3. Concluding remarks

We investigated the early evolutionary processes of planet Mercury, in particular the crystallization of a putative, global scale S-rich, reduced magma ocean, in order to reconstruct the structure of the primordial mantle of the planet. In parallel, we investigated the role of sulfur, such an important element in Mercury's interior, on phase equilibria, the liquidus temperature, liquid density, HPE distribution in a vast range of compositions, oxygen fugacity, and physical conditions. Although we think that this contribution will be the basis for understanding the early stage of evolution of reduced, high core-to-mantle ratio planets like Mercury, future research efforts will need to tackle several issues that we could not address in higher detail.

First, given the large uncertainties regarding the effect of sulfur in silicate melts as discussed in Chapter 3, new contributions will need to tackle the thermodynamic behaviour of sulfur, with a focus on its speciation and the nature of bonding of sulfur with melt components. The potential dual nature of sulfur, as both network modifier and network former (e.g. Anzures et al., 2020; Pommier et al., 2023) makes it indeed complex to assess its effect on melt properties. Additionally, volumetric properties of sulfur and sulfide phases (liquids and solids) will need to be studied more in depth, as this might help us get a better, sharper picture on the effect of sulfur on the density of silicate liquids, which in turn might sensibly affect the possibility for crystals to float in the MMO (Chapter 4). Furthermore, we demonstrated that sulfur is as important as other volatiles in affecting the liquidus temperature of silicate melts. While we focused on the liquidus, new studies will need to explore its effect on the solidus temperature. This would have serious implications for the genesis of partial melts, and thus the formation of the secondary crust on the planet. As concerns the structure of the primordial mantle as obtained in our contribution (Chapter 4), more in-depth studies will need to focus on the uppermost part of the primordial mantle, and the primary crust. As the residual MMO liquid is strongly enriched in SiO_2, the crust-mantle interface would be likely rich in quartz. As for the primary crust, although our study confirms graphite as the main contributor to the crust, new efforts should turn their interest into the possibility of sulfides to be able to reach positive buoyancy conditions. In conclusion, we highlighted the importance of oxygen fugacity in the early differentiation of Mercury, particularly in affecting element partitioning and sulfide speciation. Future experimental work should focus on isolating the effect of oxygen fugacity on the melting behavior of silicate compositions, which remains a matter of debate (e.g., Lin et al., 2021; Walker et al., 2022).

References

Anzures, B.A., Parman, S.W., Milliken, R.E., Namur, O., Cartier, C., McCubbin, F.M., Vander Kaaden, K.E., Prissel, K., Iacovino, K., Lanzirotti, A., Newville, M., 2025. An oxygen fugacity-temperature-pressure-composition model for sulfide speciation in Mercurian magmas. Geochim. Cosmochim. Acta 388, 61–77. https://doi.org/10.1016/j.gca.2024.11.012

Anzures, B.A., Parman, S.W., Milliken, R.E., Namur, O., Cartier, C., Wang, S., 2020. Effect of sulfur speciation on chemical and physical properties of very reduced mercurian melts. Geochim. Cosmochim. Acta 286, 1–18. https://doi.org/10.1016/j.gca.2020.07.024

Benkhoff, J., Murakami, G., Baumjohann, W., Besse, S., Bunce, E., Casale, M., Cremonese, G., Glassmeier, K.-H., Hayakawa, H., Heyner, D., Hiesinger, H., Huovelin, J., Hussmann, H., Iafolla, V., Iess, L., Kasaba, Y., Kobayashi, M., Milillo, A., Mitrofanov, I.G., Montagnon, E., Novara, M., Orsini, S., Quemerais, E., Reininghaus, U., Saito, Y., Santoli, F., Stramaccioni, D., Sutherland, O., Thomas, N., Yoshikawa, I., Zender, J., 2021. BepiColombo - Mission overview and science goals. Space Sci. Rev. 217. https://doi.org/10.1007/s11214-021-00861-4

Boujibar, A., Righter, K., Fontaine, E., Collinet, M., Lambart, S., Nittler, L.R., Pando, K.M., 2025. A pyroxenite mantle on Mercury? Experimental insights from enstatite chondrite melting at pressures up to 5 GPa. Icarus 437, 116602. https://doi.org/10.1016/j.icarus.2025.116602

Bunce, E.J., Martindale, A., Lindsay, S., Muinonen, K., Rothery, D.A., Pearson, J., McDonnell, I., Thomas, C., Thornhill, J., Tikkanen, T., Feldman, C., Huovelin, J., Korpela, S., Esko, E., Lehtolainen, A., Treis, J., Majewski, P., Hilchenbach, M., Väisänen, T., Luttinen, A., Kohout, T., Penttilä, A., Bridges, J., Joy, K.H., Alcacera-Gil, M.A., Alibert, G., Anand, M., Bannister, N., Barcelo-Garcia, C., Bicknell, C., Blake, O., Bland, P., Butcher, G., Cheney, A., Christensen, U., Crawford, T., Crawford, I.A., Dennerl, K., Dougherty, M., Drumm, P., Fairbend, R., Genzer, M., Grande, M., Hall, G.P., Hodnett, R., Houghton, P., Imber, S., Kallio, E., Lara, M.L., Balado Margeli, A., Mas-Hesse, M.J., Maurice, S., Milan, S., Millington-Hotze, P., Nenonen, S., Nittler, L., Okada, T., Ormö, J., Perez-Mercader, J., Poyner, R., Robert, E., Ross, D., Pajas-Sanz, M., Schyns, E., Seguy, J., Strüder, L., Vaudon, N., Viceira-Martín, J., Williams, H., Willingale, D., Yeoman, T., 2020. The BepiColombo Mercury Imaging X-Ray Spectrometer: Science goals, instrument performance, and operations. Space Sci. Rev. 216. https://doi.org/10.1007/s11214-020-00750-2

Cartier, C., Wood, B.J., 2019. The role of reducing conditions in building Mercury. Elements 15, 39–45. https://doi.org/10.2138/gselements.15.1.39

Charlier, B., Grove, T.L., Zuber, M.T., 2013. Phase equilibria of ultramafic compositions on Mercury and the origin of the compositional dichotomy. Earth Planet. Sci. Lett. 363, 50–60. https://doi.org/10.1016/j.epsl.2012.12.021

Charlier, B., Namur, O., 2019. The Origin and Differentiation of Planet Mercury, Elements 15, 9-14. https://doi.org/10.2138/gselements.15.1.9

Cremonese, G., Capaccioni, F., Capria, M.T., Doressoundiram, A., Palumbo, P., Vincendon, M., Massironi, M., Debei, S., Zusi, M., Altieri, F., Amoroso, M., Aroldi, G., Baroni, M., Barucci, A., Bellucci, G., Benkhoff, J., Besse, S., Bettanini, C., Blecka, M., Borrelli, D., Brucato, J.R., Carli, C., Carlier, V., Cerroni, P., Cicchetti, A., Colangeli, L., Dami, M., Da Deppo, V., Della Corte, V., De Sanctis, M.C., Erard, S., Esposito, F., Fantinel, D., Ferranti, L., Ferri, F., Ficai Veltroni, I., Filacchione, G., Flamini, E., Forlani, G., Fornasier, S., Forni, O., Fulchignoni, M., Galluzzi, V., Gwinner, K., Ip, W., Jorda, L., Langevin, Y., Lara, L., Leblanc, F., Leyrat, C., Li, Y., Marchi, S., Marinangeli, L., Marzari, F., Mazzotta Epifani, E., Mendillo, M., Mennella, V., Mugnuolo, R., Muinonen, K., Naletto, G., Noschese, R., Palomba, E., Paolinetti, R., Perna, D., Piccioni, G., Politi, R., Poulet, F., Ragazzoni, R., Re, C., Rossi, M., Rotundi, A., Salemi, G., Sgavetti, M., Simioni, E., Thomas, N., Tommasi, L., Turella, A., Van Hoolst, T., Wilson, L., Zambon, F., Aboudan, A., Barraud, O., Bott, N., Borin, P., Colombatti, G., El Yazidi, M., Ferrari, S., Flahaut, J., Giacomini, L., Guzzetta, L., Lucchetti, A., Martellato, E., Pajola, M., Slemer, A., Tognon, G., Turrini, D., 2020. SIMBIO-SYS: Scientific cameras and spectrometer for the BepiColombo mission. Space Sci. Rev. 216. https://doi.org/10.1007/s11214-020-00704-8

Fischer, E.L., Parman, S.W., 2025. The bulk composition and initial size of Mercury. Icarus 439, 116664. https://doi.org/10.1016/j.icarus.2025.116664

Fogel, R.A., 2005. Aubrite basalt vitrophyres: The missing basaltic component and high-sulfur silicate melts. Geochim. Cosmochim. Acta 69, 1633–1648. https://doi.org/10.1016/j.gca.2003.11.032

Hiesinger, H., Helbert, J., Alemanno, G., Bauch, K.E., D'Amore, M., Maturilli, A., Morlok, A., Reitze, M.P., Stangarone, C., Stojic, A.N., Varatharajan, I., Weber, I., the MERTIS Co-I Team, 2020. Studying the composition and mineralogy of the Hermean surface with the Mercury Radiometer and Thermal Infrared Spectrometer (MERTIS) for the BepiColombo Mission: An update. Space Sci. Rev. 216. https://doi.org/10.1007/s11214-020-00732-4

Iess, L., Asmar, S.W., Cappuccio, P., Cascioli, G., De Marchi, F., Di Stefano, I., Genova, A., Ashby, N., Barriot, J.P., Bender, P., Benedetto, C., Border, J.S., Budnik, F., Ciarcia, S., Damour, T., Dehant, V., Di Achille, G., Di Ruscio, A., Fienga, A., Formaro, R., Klioner, S., Konopliv, A., Lemaître, A., Longo, F., Mercolino, M., Mitri, G., Notaro, V., Olivieri, A., Paik, M., Palli, A., Schettino, G., Serra, D., Simone, L., Tommei, G., Tortora, P., Van Hoolst, T., Vokrouhlický, D., Watkins, M., Wu, X., Zannoni, M., 2021. Gravity, geodesy, and fundamental physics with BepiColombo's MORE investigation. Space Sci. Rev. 217, 21. https://doi.org/10.1007/s11214-021-00800-3

Lin, Y., van Westrenen, W., Mao, H.-K., 2021. Oxygen controls on magmatism in rocky exoplanets. Proc. Natl. Acad. Sci. USA 118, No 45 e2110427118 https://doi.org/10.1073/pnas.2110427118

Margot, J.-L., Hauck, S.A., Mazarico, E., Padovan, S., Peale, S.J., 2018. Mercury's Internal Structure, in: Solomon, S.C., Nittler, L.R., Anderson, B.J. (Eds.), Mercury. Cambridge University Press, pp. 85–113. https://doi.org/10.1017/9781316650684.005

McCoy, T.J., Peplowski, P.N., McCubbin, F.M., Weider, S.Z., 2018. The geochemical and mineralogical diversity of Mercury, in: Solomon, S.C., Nittler, L.R., Anderson, B.J. (Eds.), Mercury. Cambridge University Press, pp. 176–190. https://doi.org/10.1017/9781316650684.008

Métrich, N., Berry, A.J., O'Neill, H.St.C., Susini, J., 2009. The oxidation state of sulfur in synthetic and natural glasses determined by X-ray absorption spectroscopy. Geochim. Cosmochim. Acta 73, 2382–2399. https://doi.org/10.1016/j.gca.2009.01.025

Mitrofanov, I.G., Kozyrev, A.S., Lisov, D.I., Litvak, M.L., Malakhov, A.A., Mokrousov, M.I., Benkhoff, J., Owens, A., Schulz, R., Quarati, F., 2021. The Mercury Gamma-Ray and Neutron Spectrometer (MGNS) onboard the Mercury Planetary Orbiter of the BepiColombo mission: Design updates and first measurements in space. Space Sci. Rev. 217. https://doi.org/10.1007/s11214-021-00842-7

Namur, O., Charlier, B., Holtz, F., Cartier, C., McCammon, C., 2016a. Sulfur solubility in reduced mafic silicate melts: Implications for the speciation and distribution of sulfur on Mercury. Earth Planet. Sci. Lett. 448, 102–114. https://doi.org/10.1016/j.epsl.2016.05.024

Namur, O., Collinet, M., Charlier, B., Grove, T.L., Holtz, F., McCammon, C., 2016b. Melting processes and mantle sources of lavas on Mercury. Earth Planet. Sci. Lett. 439, 117–128. https://doi.org/10.1016/j.epsl.2016.01.030

Nittler, L.R., Boujibar, A., Crapster-Pregont, E., Frank, E.A., McCoy, T.J., McCubbin, F.M., Starr, R.D., Vorburger, A., Weider, S.Z., 2023. Chromium on Mercury: New results from the MESSENGER X-Ray Spectrometer and implications for the innermost planet's geochemical evolution. J. Geophys. Res. Planets 128, e2022JE007691. https://doi.org/10.1029/2022JE007691

Nittler, L.R., Chabot, N.L., Grove, T.L., Peplowski, P.N., 2018. The chemical composition of Mercury, in: Solomon, S.C., Nittler, L.R., Anderson, B.J. (Eds.), Mercury. Cambridge University Press, pp. 30–51. https://doi.org/10.1017/9781316650684.003

Nittler, L.R., Frank, E.A., Weider, S.Z., Crapster-Pregont, E., Vorburger, A., Starr, R.D., Solomon, S.C., 2020. Global major-element maps of Mercury from four years of MESSENGER X-Ray Spectrometer observations. Icarus 345, 113716. https://doi.org/10.1016/j.icarus.2020.113716

O'Neill, H.S.C., 2021. The thermodynamic controls on sulfide saturation in silicate melts with application to ocean floor basalts, in: Moretti, R., Neuville, D.R. (Eds.), Magma Redox Geochemistry. John Wiley and Sons. https://doi.org/10.1002/9781119473206.ch10

Pommier, A., Tauber, M.J., Pirotte, H., Cody, G.D., Steele, A., Bullock, E.S., Charlier, B., Mysen, B.O., 2023. Experimental investigation of the bonding of sulfur in highly reduced silicate glasses and melts. Geochim. Cosmochim. Acta 363, 114–128. https://doi.org/10.1016/j.gca.2023.10.027

Vander Kaaden, K.E., McCubbin, F.M., Nittler, L.R., Peplowski, P.N., Weider, S.Z., Frank, E.A., McCoy, T.J., 2017. Geochemistry, mineralogy, and petrology of boninitic and komatiitic rocks on the mercurian surface: insights into the mercurian mantle. Icarus 285, 155–168. https://doi.org/10.1016/j.icarus.2016.11.041

Walker, D., Ding. S., Moussallam, Y., 2022. Does fO_2 influence reversible silicate melting without redox-active cations? Proc. Natl. Acad. Sci. USA 119, No41, e2211358119. https://doi.org/10.1073/pnas.2211358119

Weider, S.Z., Nittler, L.R., Starr, R.D., Crapster-Pregont, E.J., Peplowski, P.N., Denevi, B.W., Head, J.W., Byrne, P.K., Hauck, S.A., Ebel, D.S., Solomon, S.C., 2015. Evidence for geochemical terranes on Mercury: Global mapping of major elements with MESSENGER's X-Ray Spectrometer. Earth Planet. Sci. Lett. 416, 109–120. https://doi.org/10.1016/j.epsl.2015.01.023

Zolotov, M.Yu., Sprague, A.L., Hauck, S.A., Nittler, L.R., Solomon, S.C., Weider, S.Z., 2013. The redox state, FeO content, and origin of sulfur-rich magmas on Mercury. J. Geophys. Res. Planets 118, 138–146. https://doi.org/10.1029/2012JE004274

Appendix A

The role of sulfur on the liquidus temperature and olivine-orthopyroxene equilibria in highly reduced magmas

Fabrizio Saracino, Bernard Charlier, Yishen Zhang, Manon Lécaille, Yanhao Lin, Olivier Namur

S3.1. Experimental methods

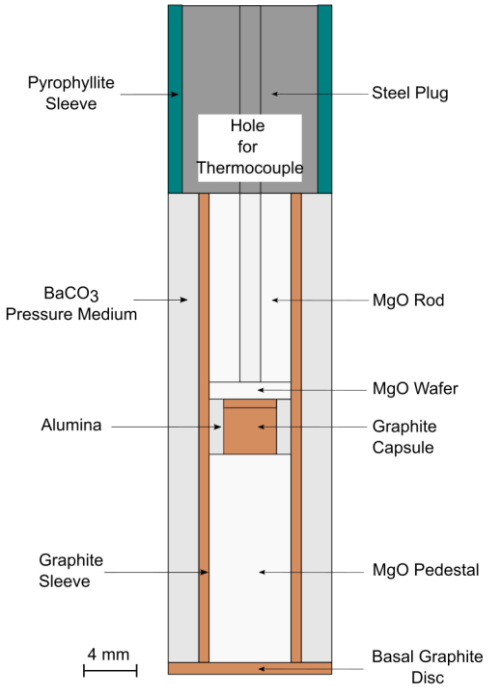

Figure S3.1. *Schematic of the cell assembly design employed in our experiments. The sample is placed in the graphite capsule (centre).*

S3.2. Oxygen fugacity calculations

At equilibrium, the Gibbs energy of the reaction can be written as

$$\Delta G = 0 = \Delta G^0 + RTlnK_{eq}$$

with K_{eq} being equilibrium constant as

$$K_{eq} = \frac{a_{Si} fO_2}{a_{SiO_2}}$$

$$\Delta G^0 = \Delta_r H^0 - T\Delta_r S^0 + \int \quad \Delta V dP = -RT\, ln \frac{a_{Si} fO_2}{a_{SiO_2}}$$

yielding

$$fO_2 = \frac{-\Delta G^0}{RT} \frac{a_{SiO_2}^{Sil}}{a_{Si}^{Met}}$$

Where $a_{SiO_2}^{Sil}$ is the activity of SiO_2 in the silicate melt. a_{Si}^{Met} is the activity of Si in the Fe metal, ΔG^0 is the free energy change at standard conditions, $\Delta_r H^o$ is the enthalpy change of the reaction, $\Delta_r S^o$ is the entropy change of the reaction, ΔV is the volume change, R is the gas constant, T is the temperature

(K), P is the pressure (in bar). $\Delta_r H^o$, $\Delta_r S^o$, ΔV were calculated using the compiled data from Robie and Hemingway (1995). fO_2 can be calculated relative to the IW buffer, as follows:

$$log\ fO_2\ (sample)\ = log\ fO_{2\ (IW)}\ +\ \Delta IW$$

where

$$log\ fO_{2\ (IW)} = 6.57 - \frac{27215}{T\ (K)} + 0.055\frac{P\ (bar)-1}{T\ (K)}$$ (Cartier et al., 2014)

Due to coexisting olivine and orthopyroxene in several of our samples, the activity of SiO_2 in the silicate melt was calculated from the following reaction:

$$Mg_2SiO_4(Fo) + SiO_2 = Mg_2Si_2O_6(En)$$

Where

$$K_{eq} = \frac{a_{En}}{a_{Fo}a_{SiO_2}}$$

And

$$K_{eq} = e^{-\Delta G_r^0/RT}$$

where ΔG^0_r is the Gibbs free energy of reaction. K_{eq} was calculated using the compiled data of Holland and Powell (1998).

S3.3. Textures and phase equilibria

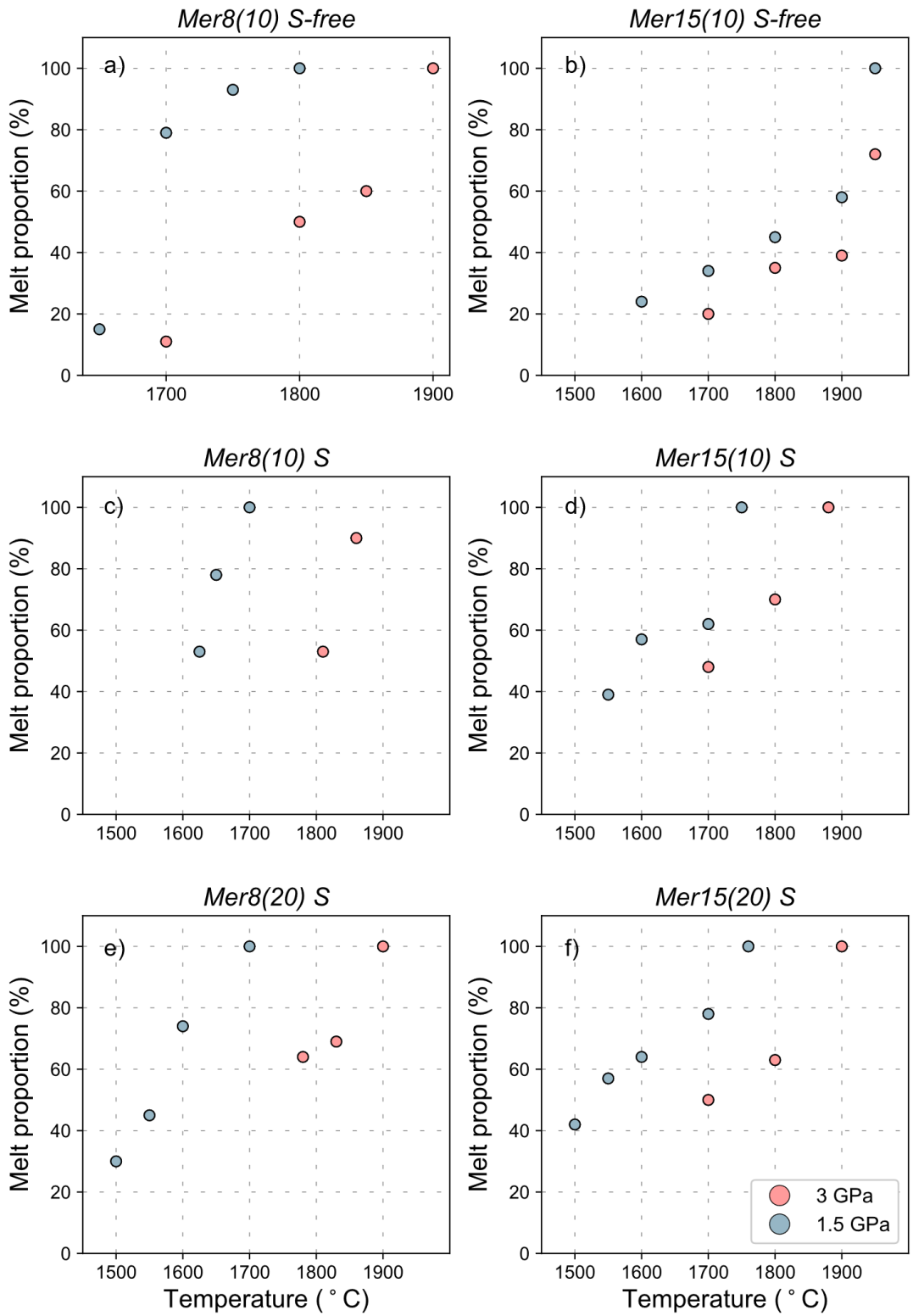

Figure S3.2. *Melt proportion (%) as a function of temperature (in °C) for all our S-free and S-saturated experiments.*

Liquidus curves and major phase transitions were calculated using Theriak/Domino (de Capitani and Brown, 1987; de Capitani and Petrakakis, 2010). Starting compositions were converted from wt% oxide to mole % and stored in the THERIN file. Next, three main commands were run: *domino* (selection of thermodynamic database, definition of axes limits, type of calculation); *guzzler* (style of curve labels, creation of graphic file); *explot* (conversion from graphic file to postscript file). We used the thermodynamic database of Jennings and Holland (2015), which is suitable for mafic and ultramafic liquids. Selected solid and liquid phases, and solid solutions were removed to make the plot clearer to visualize (Phases: Kalsilite, Leucite, Rutile, Geikielite, Spinel, Leucite_liq, Rutile_liq; solution models: spinel). Liquidus curves for the two sulfur-free compositions are shown in Fig. S3.3.

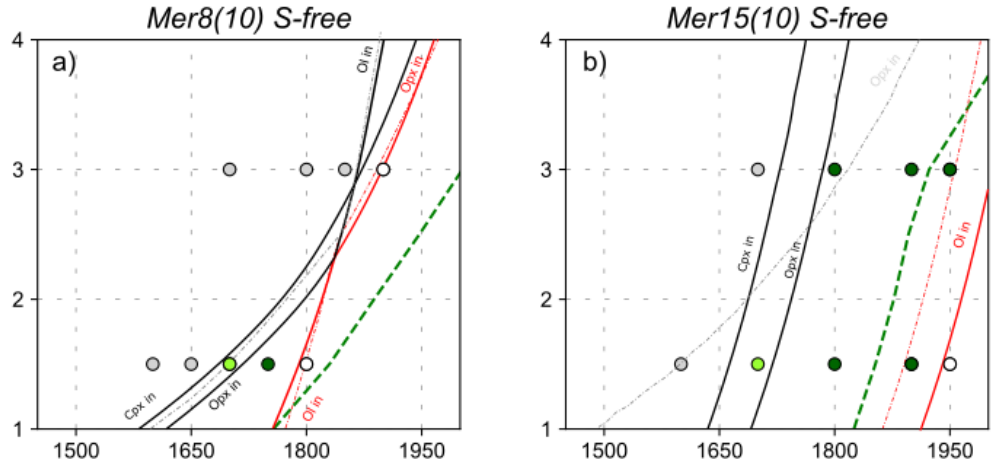

Figure S3.3. *Inferred liquidus curves, and major phase boundaries of S-free Mer8 and Mer15 experiments from this study (solid red and black lines, respectively). Also shown as comparison are the liquidi, and major phase boundaries as modelled by Theriak-Domino (dashed red and black, respectively; de Capitani and Brown, 1987; de Capitani and Petrakakis, 2010), and the liquidi as modelled with pMELTS (green dashed lines; Ghiorso et al., 2002). White circles are super-liquidus experiments; dark green circles are olivine-only experiments; bright green circles are olivine+orthopyroxene experiments; grey circles are olivine+orthopyroxene+clinopyroxene experiments.*

S3.4. Composition of phases

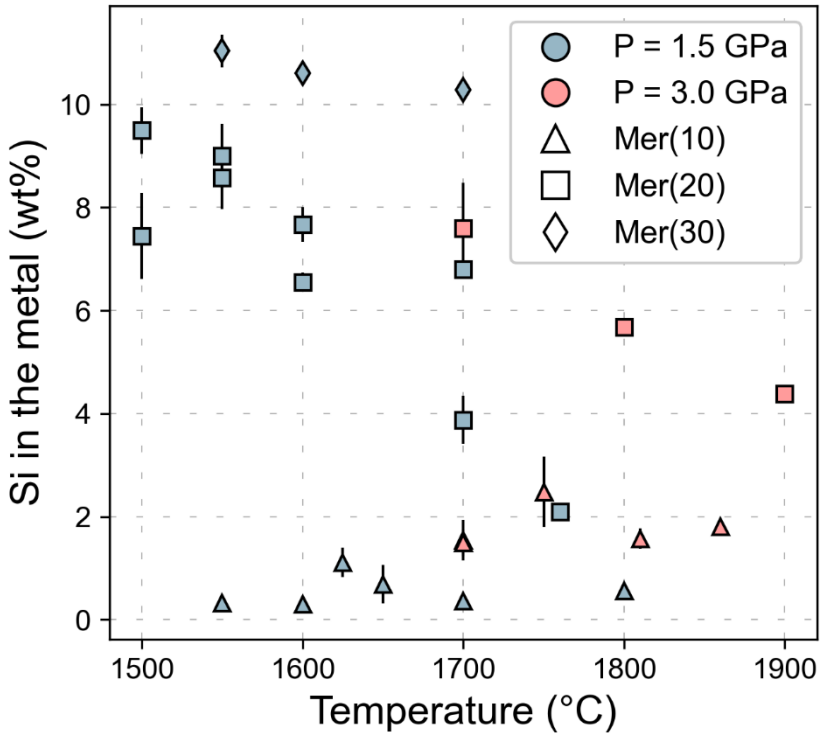

Figure S3.4. *Si content in the metal (wt%) as a function of temperature (expressed in °C).*

S3.5. Attainment of equilibrium and time series

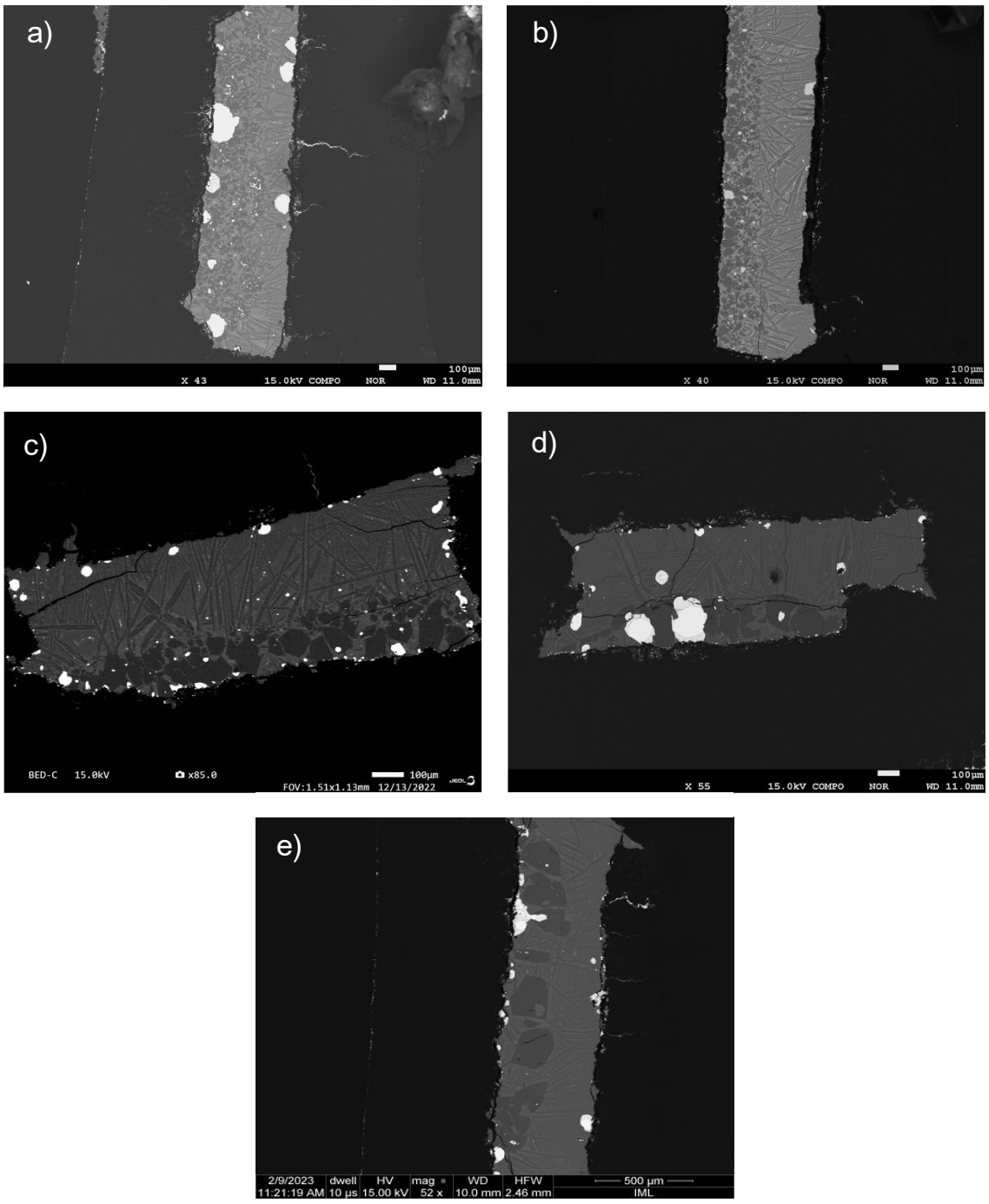

Figure S3.5. *Backscattered images of time series experiments. All experimental runs were run at the same temperature, pressure conditions (T = 1700 °C, P = 1.5 GPa) using the same starting compositions (Mer15(20) S). (a) A354 – Duration 00:15 hours; (b) A352 – Duration – 00:30 hours; (c) A339 – Duration – 01:10 hours; (d) A356 – Duration 03:00 hours; (e) A368 – Duration 06:00 hours.*

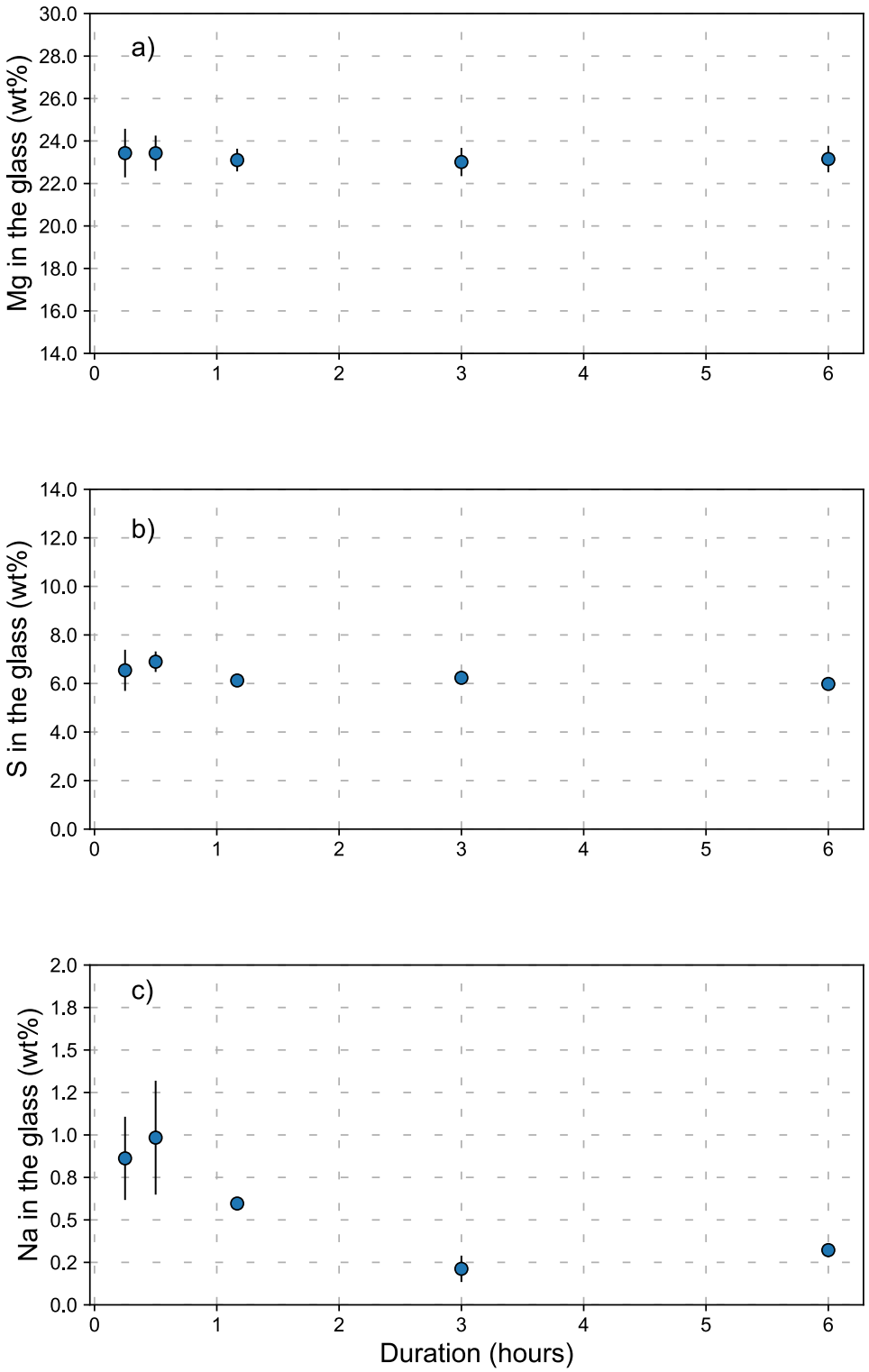

Figure S3.6. *Mg, S, and Na content in the glass (in wt%) as a function of the experimental duration (expressed in hours) of our five time series experiments. Vertical bars represent 1σ standard deviation.*

S3.6. The role of sulfur on the olivine and orthopyroxene stability

Data reduction was done according to O'Hara (1976). Only TiO_2 and Cr_2O_3 were ignored (Sorbadere et al., 2013):

$$C = \frac{CaO + 2\,Na_2O + 2\,K_2O}{Sum} \cdot 100$$

$$M = \frac{MgO + FeO + MnO}{Sum} \cdot 100$$

$$A = \frac{Al_2O_3 + Na_2O + K_2O}{Sum} \cdot 100$$

$$S = \frac{SiO_2 - 2\,Na_2O - 2\,K_2O}{Sum} \cdot 100$$

where Sum = CaO + Na_2O + K_2O + MgO + FeO + MnO + Al_2O_3 + SiO_2 and where all concentrations are expressed in mol%. The projection on the Ol-CaTs-Qz plane was performed using the following matrix (Médard, 2004):

	Ol	**CaTs**	**Qz**	**Di**
C	-1.5	0	-1.5	4
M	1.5	0	-0.5	0
A	1.5	3	0.5	-4
S	0	0	1	0

of which only the Ol, CaTs and Qz components have been considered and summed to 100%. This matrix is obtained by inverting the matrix showing the composition of olivine, Ca-Tschermak molecule, quartz and diopside in terms of CaO, MgO, Al_2O_3 and SiO_2 components and multiplying each column by the number of these components in each phase.

	C	**M**	**A**	**S**
Ol	0	2	0	1
CaTs	1	0	1	1
Qz	0	0	0	1
Di	1	1	0	2

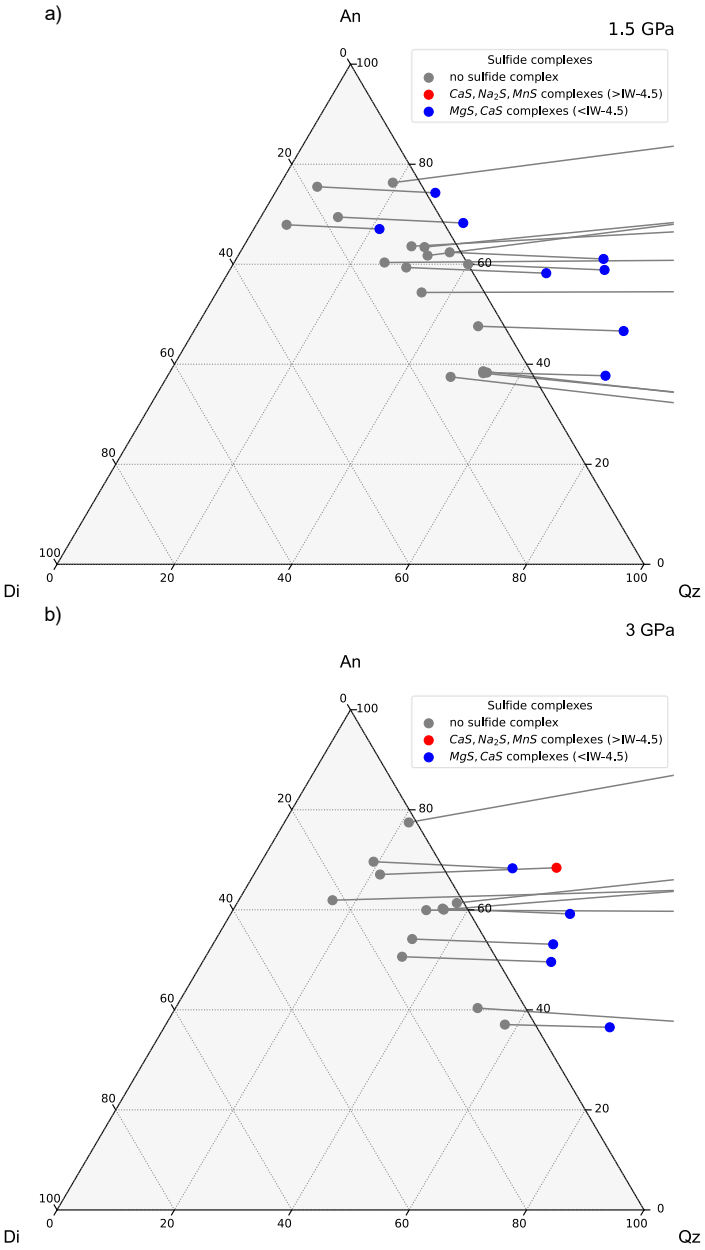

Figure S3.7. *Molecular normative projection from olivine of the major element compositions of our experimental glasses on the plane diopside-anorthite-quartz (Médard, 2004; Sorbadere et al., 2013). Grey circles are S-bearing melts without considering the effect of sulfide speciation on the silicate melt. Red circles are recalculated glass compositions by considering the formation of CaS, Na_2S, and MnS complexes. Blue circles represent recalculated melt compositions by considering the formation of MgS, CaS complexes (see also Fig. S8 Namur et al., 2016a; Anzures et al., 2020, 2025).*

References

Anzures, B.A., Parman, S.W., Milliken, R.E., Namur, O., Cartier, C., McCubbin, F.M., Vander Kaaden, K.E., Prissel, K., Iacovino, K., Lanzirotti, A., Newville, M., 2025. An oxygen fugacity-temperature-pressure-composition model for sulfide speciation in Mercurian magmas. Geochim. Cosmochim. Acta 388, 61–77. https://doi.org/10.1016/j.gca.2024.11.012

Anzures, B.A., Parman, S.W., Milliken, R.E., Namur, O., Cartier, C., Wang, S., 2020. Effect of sulfur speciation on chemical and physical properties of very reduced mercurian melts. Geochim. Cosmochim. Acta 286, 1–18. https://doi.org/10.1016/j.gca.2020.07.024

Cartier, C., Hammouda, T., Doucelance, R., Boyet, M., Devidal, J.-L., Moine, B., 2014. Experimental study of trace element partitioning between enstatite and melt in enstatite chondrites at low oxygen fugacities and 5GPa. Geochim. Cosmochim. Acta 130, 167–187. https://doi.org/10.1016/j.gca.2014.01.002

de Capitani, C., Brown, T.H., 1987. The computation of chemical equilibrium in complex systems containing non-ideal solutions. Geochim. Cosmochim. Acta 51, 2639–2652. https://doi.org/10.1016/0016-7037(87)90145-1

de Capitani, C., Petrakakis, K., 2010. The computation of equilibrium assemblage diagrams with Theriak/Domino software. Am. Mineral. 95, 1006–1016. https://doi.org/10.2138/am.2010.3354

Ghiorso, M.S., Hirschmann, M.M., Reiners, P.W., Kress III, V.C., 2002. The pMELTS: A revision of MELTS for improved calculation of phase relations and major element partitioning related to partial melting of the mantle to 3 GPa. Geochem. Geophys. Geosyst. 3, N5. https://doi.org/10.1029/2001GC000217

Holland, T.J.B., Powell, R., 1998. An internally consistent thermodynamic data set for phases of petrological interest. J. metamorphic Geol. 16, 309–343. https://doi.org/10.1111/j.1525-1314.1998.00140.x

Jennings, E.S., Holland, T.J.B., 2015. A simple thermodynamic model for melting of peridotite in the system NCFMASOCr, J. Petrol. 56, 869-892. https://doi.org/10.1093/petrology/egv020

Médard, E., 2004. Genèse de magmas riches en calcium dans les zones de subduction et sous les rides médio-océaniques : approche expérimentale. Université Blaise Pascal, Clermont-Ferrand.

Namur, O., Charlier, B., Holtz, F., Cartier, C., McCammon, C., 2016a. Sulfur solubility in reduced mafic silicate melts: Implications for the speciation and distribution of sulfur on Mercury. Earth Planet. Sci. Lett. 448, 102–114. https://doi.org/10.1016/j.epsl.2016.05.024

O'Hara, M.J., 1976. Data reduction and projection schemes for complex compositions. Progress in experimental petrology, N.E.R.C. Publication Series D 6, 103–126.

Robie, R.A., Hemingway, B.S., 1995. Thermodynamic properties of minerals and related substances at 298.15K and 1 bar (10^5 Pascals) pressure and at higher temperatures, US Geological Survey Bulletin 2131.

Sorbadere, F., Schiano, P., Métrich, N., 2013. Constraints on the Origin of Nepheline-Normative Primitive Magmas in Island Arcs Inferred from Olivine-hosted Melt Inclusion Compositions. J. Petrol. 54, 215–233. https://doi.org/10.1093/petrology/egs063

Appendix B

The role of sulfur on the liquidus temperature and olivine-orthopyroxene equilibria in highly reduced magmas

Fabrizio Saracino, Bernard Charlier, Yishen Zhang, Manon Lécaille, Yanhao Lin, Olivier Namur

Composition of silicate glass (gl in Chapter 3) (and relative 1σ standard deviation in *italic*). Abbreviations: No – Number of analyses. * Calculated by stoichiometry

Run	No	Si	Ti	Al	Fe	Mn	Mg	Ca	Na	K	S	Cr	O*	Total
A247	12	26.2	0.09	2.01	0.29	0.18	21.8	1.20	0.81	0.10	3.14	< dl	47.0	102.8
		0.2	*0.02*	*0.11*	*0.04*	*0.03*	*0.5*	*0.07*	*0.08*	*0.01*	*0.20*			
A249	8	26.1	0.10	2.02	0.43	0.18	21.7	1.25	0.78	0.10	2.81	< dl	46.9	102.4
		0.2	*0.02*	*0.09*	*0.06*	*0.02*	*0.5*	*0.09*	*0.04*	*0.01*	*0.16*			
A257	8	27.0	0.20	5.08		0.34	17.4	3.07	0.14	0.13		0.11	48.3	101.8
		0.3	*0.04*	*0.44*		*0.03*	*1.0*	*0.31*	*0.06*	*0.04*		*0.08*		
A259	5	24.9	0.14	3.94	0.37	0.18	20.0	2.28	1.16	0.14	2.93	< dl	46.9	103.0
		0.4	*0.05*	*0.28*	*0.19*	*0.05*	*1.2*	*0.11*	*0.42*	*0.05*	*0.10*			
A262	10	26.0	0.11	2.16		0.21	22.5	1.31	0.57	0.11		< dl	47.3	100.3
		0.0	*0.02*	*0.05*		*0.02*	*0.2*	*0.02*	*0.02*	*0.01*				
A263	11	27.0	0.14	2.45		0.22	20.9	1.57	0.39	0.12		0.19	47.8	100.7
		0.2	*0.04*	*0.35*		*0.05*	*0.5*	*0.27*	*0.08*	*0.03*		*0.18*		
A265	7	27.1	0.23	6.33		0.37	12.8	4.18	1.06	0.20		< dl	47.5	99.8
		0.5	*0.03*	*0.26*		*0.03*	*1.0*	*0.60*	*0.12*	*0.03*				
A268	8	26.2	0.12	2.51	0.56	0.18	20.9	1.40	0.85	0.13	2.66	< dl	47.2	102.7
		0.3	*0.02*	*0.35*	*0.25*	*0.05*	*0.5*	*0.23*	*0.19*	*0.03*	*0.39*			
A273	5	25.2	0.15	4.27		0.28	21.5	2.39	0.09	0.14		0.11	47.9	102.1
		0.4	*0.04*	*0.20*		*0.05*	*0.6*	*0.12*	*0.00*	*0.01*		*0.11*		
A279	5	26.9	0.14	5.70	0.32	0.13	13.1	3.86	1.84	0.23	3.84	< dl	47.0	103.0
		0.1	*0.01*	*0.2*	*0.04*	*0.05*	*0.7*	*0.16*	*0.22*	*0.03*	*0.23*			
A282	9	25.5	0.17	4.42	0.66	0.18	17.4	2.66	1.22	0.16	2.28	< dl	46.5	101.1
		0.2	*0.02*	*0.22*	*0.31*	*0.03*	*1.0*	*0.20*	*0.19*	*0.02*	*0.36*			

Run	No	Si	Ti	Al	Fe	Mn	Mg	Ca	Na	K	S	Cr	O*	Total
A290	7	26.6	0.12	2.19		0.20	22.3	1.31	0.33	0.10		0.20	47.9	101.2
		0.2	*0.02*	*0.08*		*0.03*	*0.4*	*0.05*	*0.03*	*0.01*		*0.17*		
A294	5	27.1	0.17	8.37		0.30	11.6	5.95	0.13	0.37		< dl	48.6	102.6
		0.7	*0.04*	*0.52*		*0.04*	*0.7*	*0.29*	*0.03*	*0.05*				
A303	6	28.2	0.22	6.79		0.34	12.1	4.25	0.87	0.30		0.14	48.7	101.9
		0.6	*0.06*	*0.32*		*0.06*	*0.9*	*0.16*	*0.07*	*0.05*		*0.08*		
A304	5	24.2	0.21	8.19		0.30	13.3	6.42	0.88	0.31		0.10	47.0	100.9
		0.5	*0.10*	*0.58*		*0.04*	*1.2*	*1.56*	*0.32*	*0.40*		*0.08*		
A305	8	26.0	0.14	3.16		0.21	20.6	1.99	0.57	0.14		0.10	47.4	100.4
		0.3	*0.04*	*0.27*		*0.02*	*0.3*	*0.21*	*0.11*	*0.04*		*0.05*		
A306	5	25.7	< dl	6.04	0.36	< dl	15.0	4.03	1.58	0.19	2.10	< dl	47.1	102.2
		0.9		*0.4*	*0.20*		*0.8*	*0.82*	*0.29*	*0.07*	*0.63*			
A307	7	26.6	0.12	2.27		0.20	22.8	1.35	0.38	0.08		< dl	48.2	102.0
		0.3	*0.01*	*0.12*		*0.03*	*0.5*	*0.06*	*0.02*	*0.01*				
A308	5	27.7	0.22	5.89		0.29	14.9	3.57	0.52	0.17		< dl	48.6	101.9
		0.3	*0.03*	*0.23*		*0.02*	*0.9*	*0.15*	*0.04*	*0.01*				
A309	9	25.0	0.09	3.18	0.42	0.15	20.1	1.96	1.12	0.18	3.79	< dl	46.1	102.0
		0.5	*0.03*	*0.45*	*0.12*	*0.06*	*0.8*	*0.47*	*0.32*	*0.05*	*0.77*			
A311	7	24.3	< dl	10.5		0.09	8.16	8.79	1.32	0.87		< dl	46.8	100.9
		0.3		*0.3*		*0.07*	*0.5*	*0.24*	*0.05*	*0.03*				
A322	13	25.5	0.12	1.95	0.39	0.19	22.0	1.17	0.58	0.08	5.12	< dl	46.2	103.3
		0.1	*0.02*	*0.09*	*0.06*	*0.03*	*0.3*	*0.06*	*0.07*	*0.01*	*0.09*			
A323	6	22.6	0.10	2.47	0.48	0.22	24.7	1.35	0.54	0.11	5.50	< dl	45.3	103.4
		0.2	*0.03*	*0.17*	*0.08*	*0.03*	*0.6*	*0.10*	*0.06*	*0.02*	*0.43*			

Run	No	Si	Ti	Al	Fe	Mn	Mg	Ca	Na	K	S	Cr	O*	Total
A328	10	24.4	< dl	2.53	0.47	0.21	21.8	1.50	0.64	0.12	6.92	< dl	45.6	104.2
		0.1		*0.17*	*0.07*	*0.05*	*0.4*	*0.20*	*0.11*	*0.02*	*0.12*			
A329	12	23.6	0.08	3.40	0.47	0.20	21.3	1.93	0.59	0.17	6.42	< dl	45.3	103.4
		0.1	*0.02*	*0.09*	*0.11*	*0.03*	*0.3*	*0.11*	*0.10*	*0.02*	*0.19*			
A331	6	25.6	< dl	7.71	0.39	0.15	11.8	4.41	1.81	0.36	4.28	< dl	46.8	103.4
		0.3		*0.3*	*0.17*	*0.10*	*0.9*	*0.63*	*0.25*	*0.04*	*0.19*			
A334	11	25.0	0.09	1.92	0.37	0.17	21.8	1.22	0.65	0.09	5.71	< dl	45.5	102.5
		0.1	*0.03*	*0.01*	*0.08*	*0.02*	*0.2*	*0.03*	*0.04*	*0.01*	*0.22*			
A339	6	23.1	0.09	2.88	0.46	0.25	23.1	1.69	0.60	0.14	6.12	0.10	45.4	103.9
		0.2	*0.03*	*0.20*	*0.06*	*0.05*	*0.5*	*0.12*	*0.03*	*0.01*	*0.11*	*0.03*		
A343	10	24.1	0.12	3.31		0.19	24.8	1.86	0.06	0.10		< dl	47.6	102.1
		0.3	*0.05*	*0.27*		*0.04*	*0.8*	*0.14*	*0.01*	*0.01*				
A344	7	24.5	0.12	3.70	0.52	0.18	21.5	2.13	0.99	0.18	3.05	< dl	47.0	103.9
		0.5	*0.01*	*0.26*	*0.11*	*0.03*	*0.9*	*0.18*	*0.07*	*0.02*	*0.20*			
A349	6	21.5	0.09	1.20	0.58	0.12	26.6	1.27	0.30	0.04	1.73	< dl	44.0	97.4
		0.4	*0.03*	*0.16*	*0.17*	*0.04*	*1.0*	*0.21*	*0.04*	*0.01*	*0.17*			
A351	5	23.8	0.10	3.72		0.21	23.5	2.06	0.32	0.13		< dl	47.1	101.0
		0.6	*0.03*	*0.30*		*0.04*	*1.0*	*0.19*	*0.02*	*0.01*				
A352	7	22.6	0.10	2.80	0.45	0.27	23.4	1.62	0.98	0.12	6.90	0.10	45.2	104.6
		0.4	*0.02*	*0.24*	*0.06*	*0.04*	*0.8*	*0.13*	*0.34*	*0.04*	*0.42*	*0.05*		
A354	6	22.8	0.10	2.79	0.52	0.22	23.4	1.66	0.86	0.12	6.54	0.10	45.3	104.4
		0.4	*0.03*	*0.29*	*0.14*	*0.04*	*1.1*	*0.20*	*0.24*	*0.03*	*0.85*	*0.03*		
A356	9	22.9	< dl	2.86	0.46	0.19	23.0	1.75	0.21	0.12	6.23	< dl	44.8	102.6
		0.3		*0.19*	*0.14*	*0.04*	*0.7*	*0.11*	*0.08*	*0.02*	*0.16*			

Run	No	Si	Ti	Al	Fe	Mn	Mg	Ca	Na	K	S	Cr	O*	Total
A361	11	23.8	< dl	3.81	0.43	0.08	19.0	2.56	0.97	0.22	8.00	< dl	44.7	103.6
		0.1		*0.14*	*0.05*	*0.03*	*0.6*	*0.35*	*0.09*	*0.02*	*0.13*			
A362	7	22.6	0.09	4.33	0.51	0.09	18.0	2.72	1.77	0.22	7.59	< dl	43.7	101.7
		0.6	*0.02*	*0.15*	*0.10*	*0.02*	*0.3*	*0.13*	*0.22*	*0.02*	*0.13*			
A364	7	23.7	0.11	3.44	0.29	0.24	20.8	2.00	0.83	0.13	6.34	< dl	45.2	103.1
		0.3	*0.04*	*0.10*	*0.05*	*0.02*	*0.6*	*0.10*	*0.22*	*0.04*	*0.35*			
A367	9	22.4	0.09	4.17	0.43	0.18	19.6	2.78	1.02	0.17	7.27	< dl	44.1	102.2
		0.4	*0.03*	*0.14*	*0.19*	*0.04*	*0.4*	*0.24*	*0.19*	*0.04*	*0.33*			
A368	13	23.1	0.10	2.89	0.56	0.21	23.1	1.72	0.32	0.11	5.98	< dl	45.3	103.5
		0.3	*0.02*	*0.19*	*0.16*	*0.03*	*0.6*	*0.12*	*0.04*	*0.02*	*0.18*			
A372	11	22.3	0.09	2.52	0.62	0.21	24.4	1.54	0.58	0.11	6.35	< dl	45.0	103.7
		0.2	*0.02*	*0.17*	*0.13*	*0.03*	*0.6*	*0.11*	*0.04*	*0.01*	*0.39*			
A373	6	23.8	0.10	3.15	0.53	0.15	22.7	1.84	0.74	0.10	2.24	0.10	46.3	101.8
		0.4	*0.03*	*0.20*	*0.29*	*0.03*	*1.3*	*0.14*	*0.20*	*0.03*	*0.52*	*0.06*		
A375	9	24.4	< dl	5.30	0.31	< dl	14.5	4.10	2.45	0.36	7.50	< dl	45.1	104.1
		0.2		*0.08*	*0.04*		*0.4*	*0.31*	*0.19*	*0.02*	*0.10*			
A376	10	23.2	< dl	5.00	0.45	< dl	17.0	3.17	1.99	0.27	7.72	< dl	44.5	103.3
		0.2		*0.10*	*0.04*		*0.4*	*0.21*	*0.19*	*0.03*	*0.14*			
A377	6	24.0	0.09	2.78	0.40	0.21	21.0	1.76	1.08	0.14	7.18	< dl	45.2	103.8
		0.3	*0.01*	*0.35*	*0.09*	*0.06*	*0.6*	*0.17*	*0.21*	*0.02*	*0.96*			
A378	7	23.3	0.14	3.03	0.44	0.24	21.0	2.31	1.40	0.21	4.76	< dl	45.0	101.9
		0.6	*0.02*	*0.42*	*0.07*	*0.06*	*0.5*	*0.33*	*0.51*	*0.08*	*0.70*			
A379	7	23.7	0.12	2.46	0.46	0.21	21.4	1.77	0.99	0.14	7.28	< dl	44.8	103.4
		0.4	*0.02*	*0.36*	*0.06*	*0.07*	*0.8*	*0.23*	*0.22*	*0.03*	*0.78*			

Run	No	Si	Ti	Al	Fe	Mn	Mg	Ca	Na	K	S	Cr	O*	Total
A380	7	25.3	0.08	2.09	0.58	0.16	21.7	1.32	0.74	0.10	2.62	0.10	46.2	100.9
		0.2	*0.02*	*0.21*	*0.31*	*0.05*	*0.3*	*0.12*	*0.23*	*0.03*	*0.23*	*0.02*		
A381	5	26.9	0.16	2.99		0.15	21.1	1.56	0.17	0.07		< dl	48.1	101.3
		0.8	*0.05*	*1.01*		*0.09*	*1.2*	*0.82*	*0.11*	*0.08*				
A456	10	24.1	< dl	1.89	0.64	0.17	21.5	1.09	0.61	0.10	9.01	< dl	44.3	103.5
		0.3		*0.04*	*0.37*	*0.05*	*0.2*	*0.08*	*0.04*	*0.01*	*0.30*			
A466	10	24.7	< dl	1.90	0.54	0.14	21.1	1.12	0.62	0.10	8.61	< dl	44.7	103.5
		0.2		*0.04*	*0.06*	*0.03*	*0.1*	*0.07*	*0.06*	*0.01*	*0.13*			
A468	13	26.0	< dl	2.51	0.53	< dl	19.3	1.24	1.07	0.15	6.86	< dl	45.8	103.4
		0.4		*0.14*	*0.09*		*0.5*	*0.15*	*0.15*	*0.02*	*0.48*			

Composition of silicate crystals. Abbreviations: No – Number of analyses, ol – olivine, opx – orthopyroxene, cpx – clinopyroxene.

Run	Crystals	No	SiO_2	TiO_2	Al_2O_3	FeO	MnO	MgO	CaO	Na_2O	Total
A257	ol	5	42.4		0.14	< dl	0.12	56.9	0.04		99.6
A259	ol	6	42.6		0.07	0.34	< dl	57.2	0.06		100.3
A263	ol	8	42.6		0.11	< dl	0.16	56.2	0.10		99.2
	opx	8	59.3		0.52	< dl	0.14	40.7	0.24		100.9
A265	ol	5	42.7		0.08	< dl	0.21	57.2	0.10		100.3
	opx		Not measured								
A268	ol		Not measured								
	opx	7	59.5		0.35	0.30	< dl	39.8	0.16		100.1
A273	ol	5	43.2		0.15	< dl	0.14	56.9	0.13		100.5
A279	ol	6	42.3		0.07	0.33	< dl	57.0	0.07		99.8
A282	ol	4	42.5		0.12	0.39	< dl	56.4	0.09		99.5
A290	ol	6	43.1		0.10	< dl	0.14	56.2	0.07		99.8
A294	ol	3	42.9		0.10	< dl	0.23	55.1	0.13		98.5
	opx	4	58.9		1.80	< dl	0.21	38.7	0.67		100.3
	cpx		Not measured								
A296	ol	3	42.8		0.10	< dl	0.24	55.3	0.12		98.6
	opx	4	59.8		0.87	< dl	0.08	39.2	0.58		100.5
	cpx		Not measured								
A297	ol		Not measured								
	opx	5	59.1		1.59	0.22	< dl	38.8	0.39		100.1
A302	ol	1	41.9		0.11	< dl	0.22	55.9	0.08		98.2
	opx	8	58.6		2.53	< dl	0.20	37.6	1.15		100.1
	cpx	2	51.4	0.70	12.9						

Run	Crystals	No	SiO_2	TiO_2	Al_2O_3	FeO	MnO	MgO	CaO	Na_2O	Total
A303	ol	6	42.4		0.15	< dl	0.17	56.8	0.11		99.6
A304	ol	6	42.6		0.25	< dl	0.25	56.5	0.20		99.8
	opx	4	57.6		2.97	< dl	0.21	37.1	1.12		99.0
	cpx	4	50.2	0.37	15.6	< dl	0.34	22.4	11.4	0.83	101.2
A305	ol	8	41.7		0.12	< dl	0.17	55.6	0.09		97.7
	opx	6	58.5		3.20	< dl	0.20	38.0	0.98		100.9
	cpx		Not measured								
A306	ol	6	42.6		0.14	0.41	< dl	56.9	0.09		100.1
	opx	6	58.9		1.92	0.36	0.04	38.7	0.49		100.4
A308	ol	5	42.5		0.15	< dl	0.13	56.2	0.10		99.2
A309	ol	1	43.1		< dl	0.20	< dl	56.9	0.04		100.2
	opx	5	59.8		0.47	0.19	< dl	39.3	0.20		100.0
A311	ol	2	42.9		0.09	< dl	0.12	55.8	0.08		99.0
	opx	10	59.4		0.65	< dl	< dl	39.3	0.32		99.7
	cpx		Not measured								
A328	opx	4	59.6		0.39	0.15	< dl	39.9	0.15		100.2
A329	ol	5	42.9		0.05	0.22	< dl	55.9	0.05		99.1
A331	ol	6	42.7		0.19	0.43	< dl	57.2	0.12		100.6
	opx	4	58.8		1.39	0.27	< dl	39.1	0.42		100.0
A339	ol	5	42.8		0.06	0.15	< dl	57.4	0.04		100.5
A344	ol	4	42.8		0.06	0.36	< dl	57.2	0.06		100.5
A351	ol	4	42.2		0.14	< dl	0.14	56.7	0.11		99.3
A352	ol	5	42.6		0.06	0.20	< dl	57.2	0.04		100.1
A354	ol	5	42.8		0.06	0.21	< dl	57.3	0.05		100.4

Run	Crystals	No	SiO_2	TiO_2	Al_2O_3	FeO	MnO	MgO	CaO	Na_2O	Total
A356	ol	5	42.4		0.06	0.18	< dl	57.0	0.05		99.7
A359	ol		Not measured								
	opx	4	58.8		1.32	0.20	< dl	38.7	0.36		99.4
A361	ol		Not measured								
	opx		59.6		0.76	0.23	< dl	39.3	0.18		100.1
A362	ol	3	42.3		0.08	0.14	< dl	56.3	0.05		98.9
	opx	3	59.0		1.16	0.22	< dl	39.0	0.26		99.6
A364	ol	6	42.7		0.10	0.12	< dl	56.6	0.05		99.6
A367	ol	5	42.7		0.13	0.20	< dl	57.2	0.07		100.3
	opx		Not measured								
A368	ol	7	42.5		0.05	0.11	< dl	56.9	0.04		99.6
A373	ol	4	42.5		0.12	0.29	< dl	56.7	0.07		99.7
A375	ol		Not measured								
	opx	5	59.5		0.92	0.21	< dl	39.3	0.32		100.3
A376	ol	5	42.7		0.07	0.27	< dl	56.9	0.06		100.0
	opx		Not measured								
A377	opx	6	59.1		0.82	0.19	< dl	39.3	0.19		99.6
A378	opx	5	59.0		0.95	0.23	< dl	39.2	0.25		99.6
A379	opx	4	59.7		0.66	0.25	< dl	39.9	0.18		100.7
A380	opx	5	58.9		0.90	0.30	< dl	39.0	0.33		99.4
A381	ol	5	42.5		0.17	< dl	0.15	56.7	0.09		99.6
	opx	6	58.5		1.63	< dl	0.15	38.9	0.45		99.6
	cpx		Not measured								
A466	opx	7	60.4		0.43	0.47	< dl	40.7	0.11		102.2

Run	Crystals	No	SiO_2	TiO_2	Al_2O_3	FeO	MnO	MgO	CaO	Na_2O	Total
A468	ol		Not measured								
	opx	5	59.3		0.32	0.19	< dl	39.9	0.12		99.9

Composition of Si-bearing Fe metal (mm in Chapter 3). Abbreviations: No – Number of analyses. Mm * C calculated with Eq. 20 in Xu et al. (2024) ** Corrected total considering calculated C

Run	No	Si	Cr	Fe	P	S	Total	C calc*	Ctotal**
A247	7	1.54	0.12	95.2	0.70	1.21	98.8	4.81	103.6
		0.40	*0.02*	*1.5*	*0.23*	*0.96*			
A249	4	0.57	0.14	91.9	1.85	1.62	96.1	5.23	101.3
		0.10	*0.06*	*2.1*	*1.05*	*1.20*			
A259	8	0.36	0.18	93.5	2.33	1.27	97.6	5.32	103.0
		0.08	*0.08*	*1.3*	*1.42*	*1.43*			
A268	4	0.69	0.11	92.6	1.34	0.64	95.4	5.17	100.6
		0.37	*0.05*	*2.1*	*0.54*	*0.41*			
A279	6	0.30	0.08	91.1	1.50	4.25	97.2	5.35	102.6
		0.10	*0.03*	*1.3*	*0.44*	*0.96*			
A297	7	1.50	0.12	92.8	0.76	2.52	97.7	4.83	102.5
		0.25	*0.03*	*0.9*	*0.15*	*0.80*			
A309	7	1.11	0.13	94.3	1.02	0.83	97.4	4.99	102.4
		0.29	*0.07*	*1.0*	*0.79*	*0.78*			
A322	7	10.5	0.63	85.9	0.37	0.31	97.7	1.75	99.5
		0.2	*0.08*	*0.4*	*0.02*	*0.08*			
A323	6	4.38	0.50	89.8	0.47	0.62	95.8	3.68	99.5
		0.15	*0.11*	*0.7*	*0.06*	*0.17*			
A328	6	7.67	0.17	88.2	0.48	0.30	96.8	2.56	99.4
		0.33	*0.10*	*0.4*	*0.05*	*0.03*			
A329	9	6.55	0.33	88.7	0.43	0.26	96.3	2.92	99.2
		0.18	*0.15*	*0.7*	*0.03*	*0.10*			

Run	No	Si	Cr	Fe	P	S	Total	C calc*	Ctotal**
A331	9	0.32	< dl	91.0	1.35	4.57	97.2	5.34	102.6
		0.14		*0.8*	*0.47*	*1.24*			
A334	9	6.80	0.61	88.0	0.36	0.22	96.0	2.84	98.8
		0.17	*0.09*	*0.4*	*0.08*	*0.04*			
A339	10	3.88	0.35	90.8	0.54	0.64	96.2	3.87	100.1
		0.46	*0.06*	*0.5*	*0.18*	*0.38*			
A352	10	4.21	0.34	89.9	0.50	0.22	95.2	3.75	98.9
		0.98	*0.17*	*1.0*	*0.17*	*0.06*			
A354	10	3.43	0.48	90.7	0.32	0.66	95.6	4.04	99.6
		0.06	*0.04*	*0.3*	*0.02*	*0.04*			
A356	10	4.24	0.32	90.1	0.43	0.48	95.6	3.73	99.3
		0.94	*0.08*	*1.1*	*0.18*	*0.22*			
A359	7	2.48	0.11	92.5	1.14	1.36	97.6	4.42	102.0
		0.68	*0.02*	*0.9*	*0.41*	*0.92*			
A361	7	9.00	< dl	88.1	0.34	0.33	97.8	2.16	99.9
		0.63		*0.4*	*0.05*	*0.12*			
A362	9	8.57	0.27	88.2	0.42	0.29	97.8	2.28	100.0
		0.61	*0.22*	*0.8*	*0.09*	*0.11*			
A364	10	5.68	0.32	88.8	0.54	1.10	96.4	3.21	99.7
		0.10	*0.11*	*0.5*	*0.03*	*0.15*			
A367	8	7.59	0.12	88.2	0.63	0.40	96.9	2.58	99.5
		0.89	*0.04*	*0.9*	*0.06*	*0.13*			
A368	8	2.89	0.15	91.1	0.91	1.24	96.3	4.25	100.5
		0.56	*0.04*	*0.7*	*0.24*	*0.52*			

Run	No	Si	Cr	Fe	P	S	Total	C calc*	Ctotal**
A372	11	2.09	0.42	91.3	0.44	0.87	95.1	4.58	99.7
		0.11	*0.10*	*0.5*	*0.09*	*0.12*			
A375	8	9.49	< dl	87.8	0.32	0.27	97.9	2.02	99.9
		0.46		*0.3*	*0.11*	*0.05*			
A376	8	7.44	0.21	88.7	0.50	0.25	97.1	2.63	99.7
		0.83	*0.16*	*0.8*	*0.42*	*0.11*			
A377	10	8.92	0.19	87.0	0.39	0.56	97.1	2.18	99.2
		0.29	*0.04*	*0.2*	*0.10*	*0.05*			
A378	6	1.57	0.16	90.8	1.43	3.16	97.1	4.80	101.9
		0.19	*0.04*	*1.1*	*0.43*	*0.98*			
A379	8	10.5	0.18	85.8	0.36	0.47	97.3	1.75	99.1
		0.2	*0.13*	*0.6*	*0.05*	*0.47*			
A380	8	1.81	0.13	90.8	1.09	2.71	96.5	4.69	101.2
		0.16	*0.06*	*0.7*	*0.22*	*0.65*			
A456	11	10.3	0.13	87.4	0.17	0.43	98.4	1.80	100.2
		0.1	*0.02*	*0.3*	*0.02*	*0.06*			
A466	14	10.6	0.21	86.9	0.18	0.33	98.3	1.72	100.0
		0.2	*0.04*	*0.3*	*0.03*	*0.16*			
A468	10	11.0	0.07	87.0	0.20	0.36	98.7	1.61	100.3
		0.3	*0.02*	*0.3*	*0.02*	*0.11*			

Composition of sulfides phases. Abbreviations: No – Number of analyses, s1m – Troilite (FeS), s3m – (Mg,Fe)S

Run		No	Si	Ti	Cr	Fe	Mn	Mg	Ca	Na	S	Total
A247	s1m	7	< dl	0.27	3.98	58.0	0.74	0.09			36.2	99.3
A249	s1m		Not measured									
A259	s1m	4	< dl	0.63	5.46	55.9	1.02	0.09			37.4	100.5
A268	s1m	8	< dl	0.41	3.04	60.3	0.75	0.09			34.4	99.0
A279	s1m	6	0.07	0.56	3.59	57.2	0.99	0.14			36.9	99.5
A282	s1m	8	< dl	0.12	2.18	62.5	0.76	0.06			32.7	98.3
A297	s1m	4	< dl	1.08	3.54	57.5	0.62	0.10			37.1	99.9
A306	s1m	5	0.05	0.85	3.87	57.1	0.91	0.08			37.1	100.0
A309	s1m	3	< dl	0.86	3.79	57.8	0.59	0.11			36.9	100.1
A322	s1m		Not measured									
A323	s1m		Not measured									
A328	s1m		Not measured									
A329	s1m	6	0.06	0.64	4.14	55.4	1.24	0.61			35.9	98.0
A331	s1m	7	< dl	0.56	2.81	59.5	1.26	0.39			33.8	98.3
A334	s1m		Not measured									
A339	s1m	3	< dl	0.94	7.07	52.1	0.93	0.19			36.8	98.0
A344	s1m	8	< dl	0.08	2.11	63.9	0.66	0.07			32.0	98.8
A349	s1m	6	0.06	0.09	3.66	58.7	0.75	< dl			36.5	99.8
A352	s1m	3	0.05	0.44	8.31	51.5	0.74	0.28			37.5	98.8
A354	s1m	5	< dl	0.55	8.53	52.3	0.78	0.25			37.5	99.9
A356	s1m	5	0.05	0.49	5.21	55.9	0.75	0.13			37.3	99.8
A359	s1m	5	< dl	1.09	4.25	56.1	0.69	0.11			36.9	99.1
A361	s1m	6	< dl	2.04	3.81	56.6	0.23	0.20			37.3	100.2

Run		No	Si	Ti	Cr	Fe	Mn	Mg	Ca	Na	S	Total
	s3m	7	< dl	0.53	2.28	18.6	3.29	24.4	1.34	0.17	48.1	98.7
A362	s1m	3	< dl	1.32	4.86	55.5	0.67	0.32			37.1	99.8
	s3m	3	0.06	0.65	3.73	17.2	4.34	23.0	1.66	0.37	47.3	98.3
A364	s1m	6	< dl	0.73	5.55	55.1	0.90	0.13			37.1	99.5
A367	s1m	4	0.05	1.53	5.71	54.4	0.57	0.16			37.0	99.4
	s3m	5	0.45	0.58	2.69	15.3	7.64	22.3	1.78	0.42	45.9	97.1
A368	s1m	8	0.11	0.81	5.14	54.2	1.02	0.29			36.8	98.4
A372	s1m	5	0.06	0.27	5.23	56.1	0.76	0.16			36.7	99.3
A373	s1m	5	0.05	0.17	4.20	57.6	0.94	0.05			36.4	99.4
A375	s1m	6	0.05	1.81	2.99	57.5	0.12	0.20			36.9	99.6
	s3m	6	0.05	0.51	2.17	19.9	2.48	23.3	2.33	0.29	47.6	98.6
A376	s1m	5	< dl	2.11	4.92	55.1	0.26	0.16			37.4	100.0
	s3m	5	< dl	0.54	2.79	18.1	3.74	23.0	2.00	< dl	47.9	98.1
A377	s1m	5	0.23	0.94	5.56	54.9	0.75	0.17			36.5	99.1
A378	s1m	5	< dl	0.78	4.49	56.2	0.78	0.06			37.2	99.5
A379	s1m	2	0.06	0.81	6.84	52.8	0.44	0.12			37.4	98.5
A380	s1m	4	< dl	0.66	5.47	55.6	0.79	0.07			37.0	99.6
A456	s1m	4	< dl	1.14	4.15	56.7	0.44	0.27			37.9	100.6
A466	s1m	5	< dl	1.52	4.13	56.4	0.23	0.22			37.4	99.9
	s3m	3	< dl	0.43	3.90	33.1	2.41	15.1	0.33	0.12	43.9	99.3
A468	s1m	4	< dl	1.82	3.41	56.8	0.19	0.29			37.4	99.9
	s3m	4	< dl	0.38	1.77	19.6	2.55	25.3	0.70	0.14	48.7	99.1

Appendix C

The crystallization of the Mercury's magma ocean and the formation of its primordial mantle

Fabrizio Saracino, Bernard Charlier, Yishen Zhang, Olivier Namur

S4.1. Parameters for the calculation of density of S-free liquids and minerals

Here below is a list with all the partial molar volumes, thermal expansion, Young modulus, and pressure derivative of the Young modulus of the MMO liquid. V_i values are from Lange and Carmichael (1987), Bottinga et al. (1983), Warren (1995). dV_i/dT data are from Lange and Carmichael (1987), Warren (1995).

[SiO_2, TiO_2, Al_2O_3, Cr_2O_3, FeO, MnO, MgO, CaO, Na_2O, K_2O]

V_i = [26.90, 24.60, 37.63, 31.40, 14.23, 14.13, 11.98, 17.15, 30.26, 48.22 [m^3mol^{-1}]

dV_i/dT = [0.00, 7.24, 2.62, 4.40, 2.92, 2.62, 2.62, 2.92, 7.41, 11.91] [$x10^9$ $m^3mol^{-1}K^{-1}$]

K = [5.1485, 29.518, 0.28658, 1.0456, -0.20818, -1.3441, -4.4982] [GPa]

dK/dP = [3.387, -4.3588, -0.049056, -0.28022, 0.13524, 0.47933, 1.3291]

Table S4.1. *List of physical and volumetric parameters for the solid phases as modelled in our MMO crystallization code. (a)Bertka and Fei (1998) (b) Holland and Powell (1998) (c) Lange and Carmichael (1987) (d) Toplis et al. (1994) (e) Fei et al. (1990) (f) Niu and Batiza (1991) (g) Kosinski (1992) (h) Frondel (1962) (i) Peiris et al. (1994) (j) Baldwin and Tompson (1964).*

	ρ (1atm, 298K)	α_0 (/K)	α_1 ($x10^{-5}$) (/K)	α_2 ($x10^{-9}$) (/K)	Ref.
Forsterite	3223	3.034	7.422	-0.5381	a,b,c,d
Enstatite	3204	2.947	2.694	-0.5588	c,d,e
Diopside	3272	3.330	2.694	-0.5588	a,c,d
Plagioclase	2762	4.560	-	-	b,c,d,f
Quartz	2671	1.310	0.002	-0.0606	b,g,h
MgS	2661	6.00E-05	-	-	i,j

	K_T (298K) (GPa)	δK / δP	δK / δT (GPa/K)	V0 (cm^3/mol)	Ref.
Forsterite	127.1	5.39	-0.0239	43.60	a,b,c,d
Enstatite	107.0	5.00	-0.0270	62.67	c,d,e
Diopside	113.0	4.50	-0.0200	66.04	a,c,d
Plagioclase	94.3	4.00	-0.0200	100.43	b,c,d,f
Quartz	96.0	8.40	-0.0200	20.64	b,g,h
MgS	78.9	3.71	-0.0200	21.18	i,j

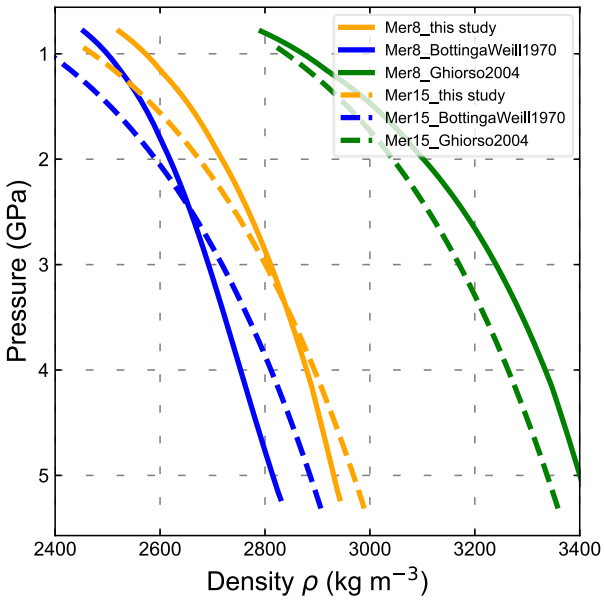

Figure S4.1. *Density of the residual liquid of the MMO for both Mer8 (solid lines) and Mer15 (dashed lines) using different equations of state (EoS) from this study (orange), Bottinga and Weill (1970) (blue) and Ghiorso (2004) (green). All density calculations here displayed do not consider the effect of sulfur on the liquid density.*

S4.2. The forsterite-enstatite cotectic

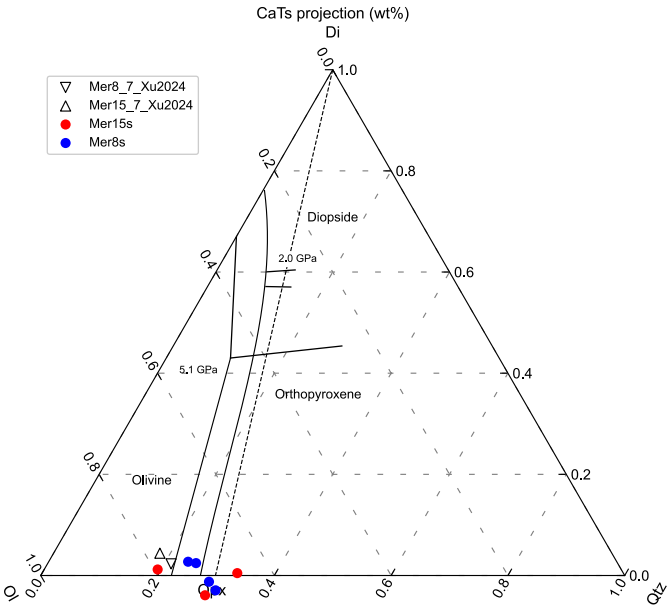

Figure S4.2. *Diopside-SiO_2-olivine system showing the experimental melts of Mercury's mantle compositions from Saracino et al. (2025) (circles) and Xu et al. (2024) (triangles). The silicate melts were renormalized considering the effect of S on the distribution of MgO, and CaO between silicate and sulfide melts (more details are in Saracino et al., 2025). Also shown are the olivine-orthopyroxene boundaries at 5.1 GPa (Weng and Presnall, 2001), and 2 GPa (Kushiro, 1969).*

S4.3. Cell assemblies

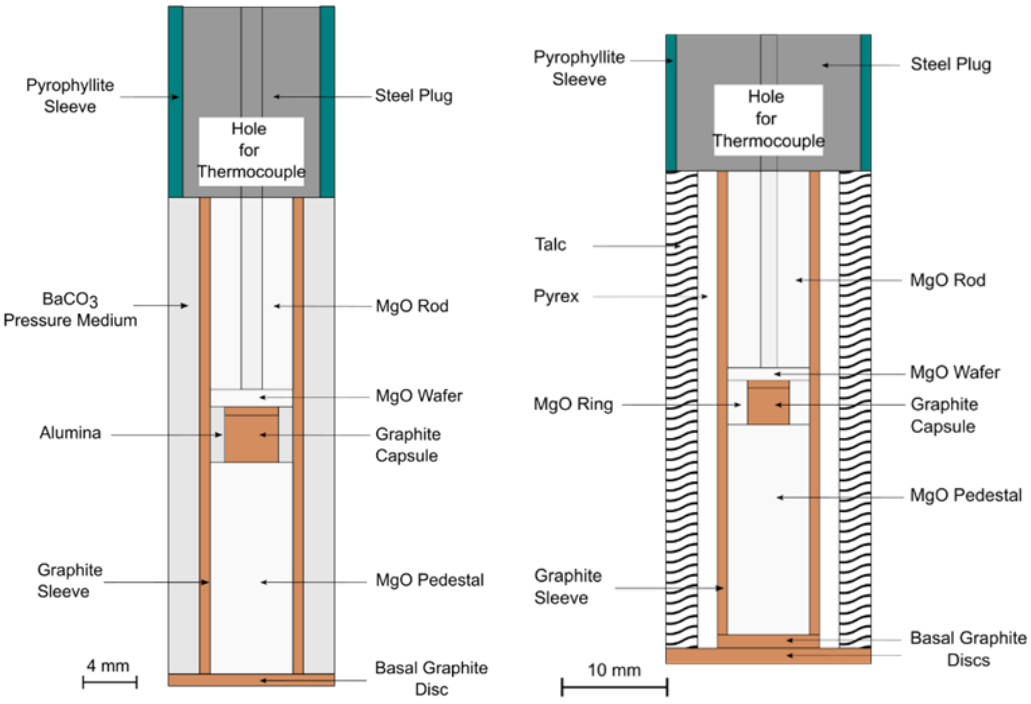

Figure S4.3. *Two-dimensional sketch of the ½ " and the ¾" experimental assemblies employed in this study.*

S4.4. Composition of silicate melt and metals in time series experiments

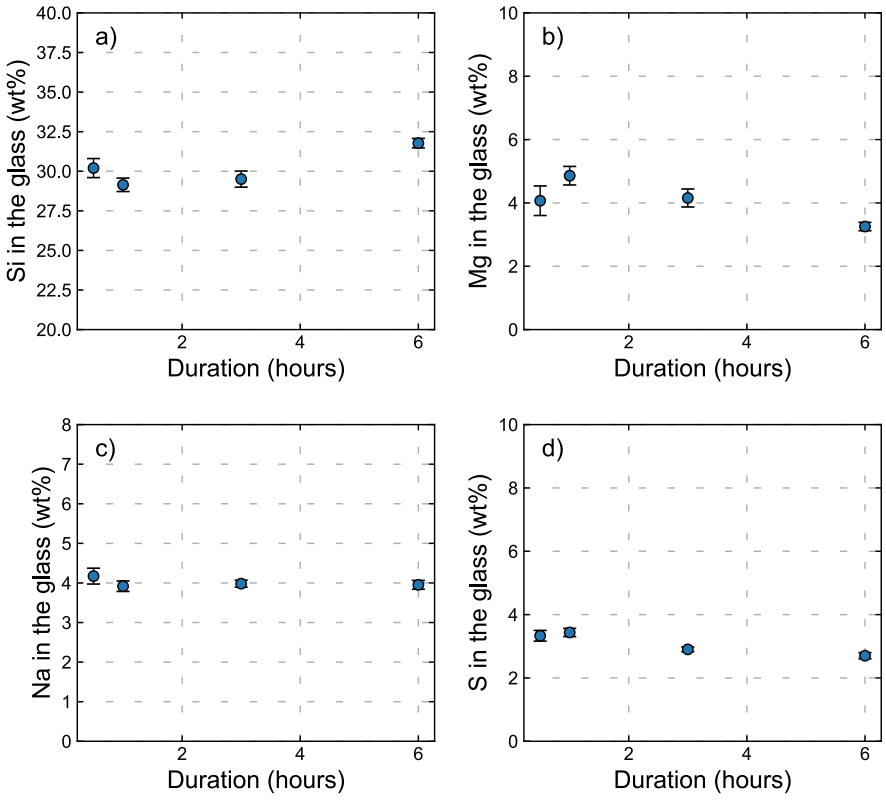

Figure S4.4. *Major element variation (in wt%) in time series experiments as a function of the experimental duration (in hours).*

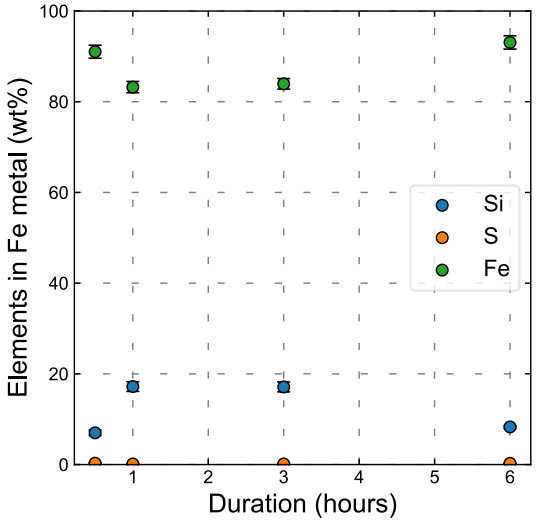

Figure S4.5. *Variation of Fe, S, and Si in Fe metal (expressed in wt%) in time series experiments as a function of the experimental duration (in hours).*

S4.5. Composition of experimentally determined silicate melts

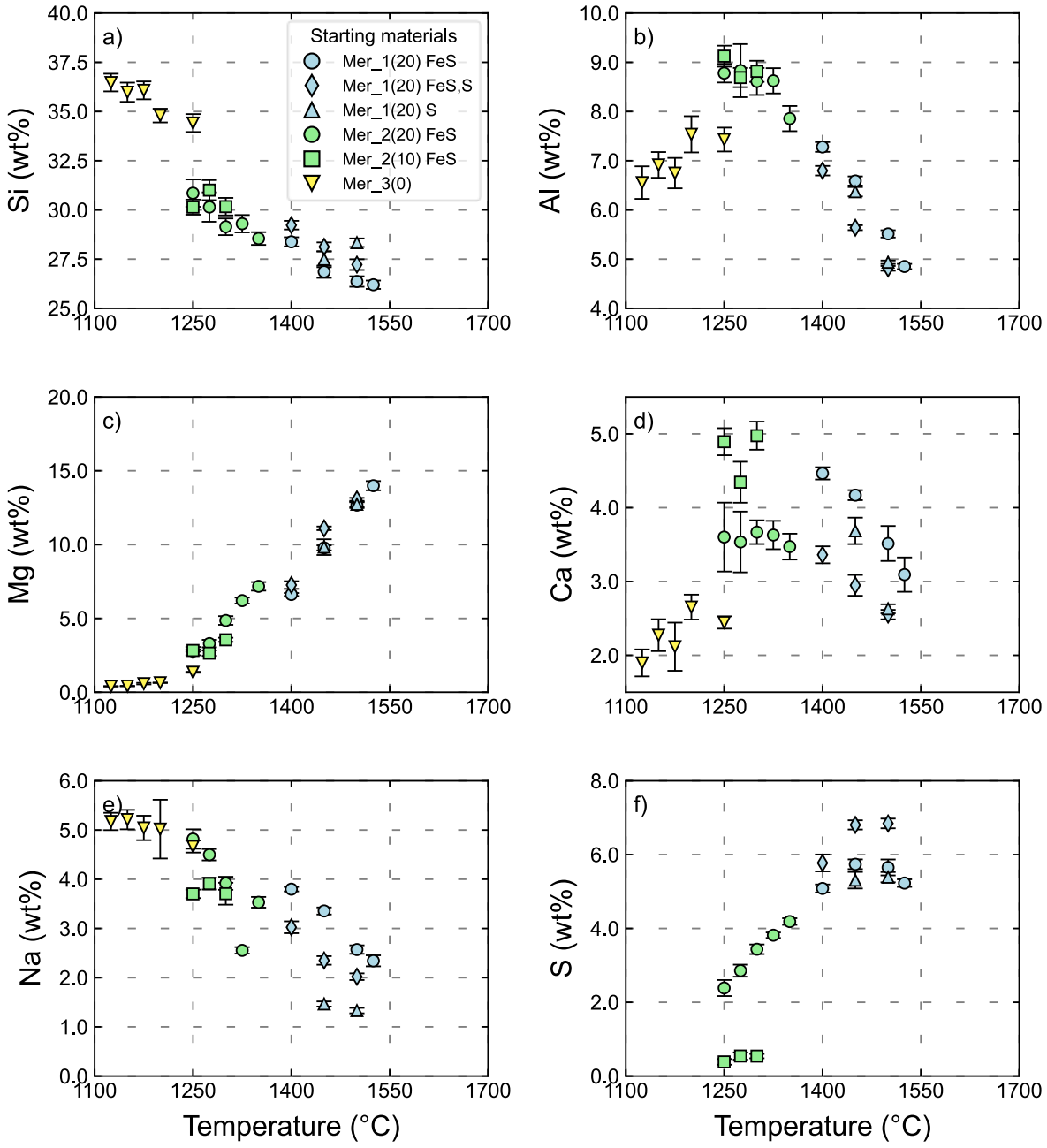

Figure S4.6. *Evolution of element concentrations (wt%) in the silicate glass as a function of temperature (in °C). Vertical bars refer to the 1σ standard deviation of analyses (small 1σ values are hidden by symbols).*

S4.6. Composition of experimental pyroxenes

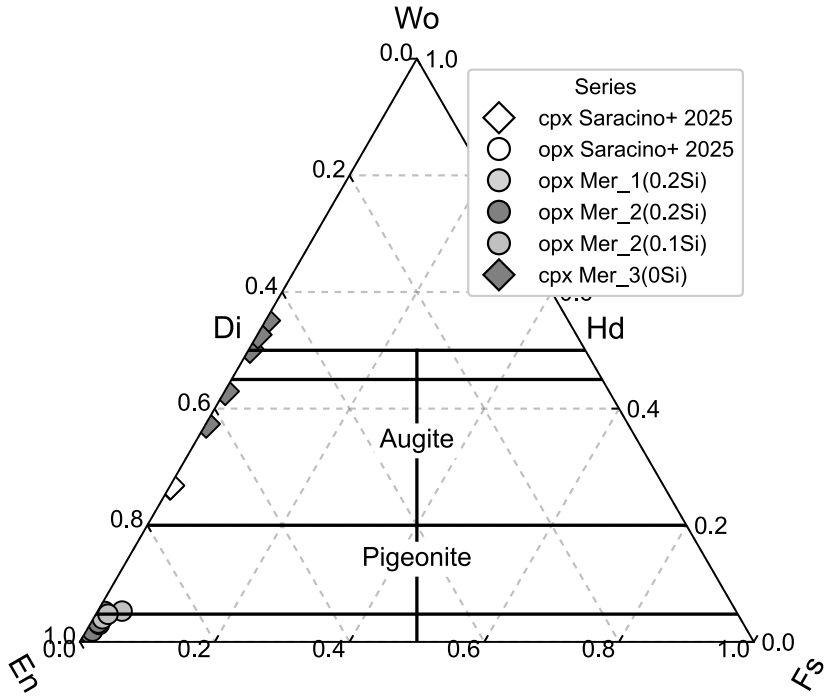

Figure S4.7. *Pyroxene ternary system (in wt%) showing the composition of orthopyroxene and clinopyroxene crystals in our suite of experiments. Also shown as comparison are the orthopyroxene and clinopyroxene crystals measured in 1.5 GPa and 3.0 GPa experiments on Mer8 and Mer15 compositions in Saracino et al. (2025). Abbreviations: opx – orthopyroxene, cpx – clinopyroxene.*

S4.7. Equations for the calculation of the liquidus, solidus temperatures

The thermometer used to calculate the temperature of the MMO at each incremental step of crystallization is based on S-free experimental runs featured in Charlier et al. (2013), Namur and Charlier (2017), Namur et al. (2016a), and Saracino et al. (2025) (N=89). The resulting equation is the following (Fig. S4.2.):

$$T_{\text{Liquidus,S-free}} = 858.78 + 105.43\ P\ (GPa) + 18.42\ [MgO] + 13.23\ [Al_2O_3] + 3.71[Na_2O + K_2O]$$

Where T is the temperature expressed in °C, P is the pressure in GPa, and the oxide concentrations are expressed as wt%. The fit achieves an R^2 of 0.95 (adjusted R^2 = 0.95) and the SEE is 45 °C. After calculating the S-free liquidus temperature at each increment, we applied a correction to account for the influence of S as in Eq. 10 of Saracino et al. (2025):

$$\Delta T_{\text{Liquidus}}(°C) = 8.65\ [S]_{\text{Melt}} + 4.89\ [S]^2_{\text{Melt}} - 0.39\ [S]^3_{\text{Melt}}$$

Where ΔT (°C) is the liquidus temperature depression, and $[S]_{melt}$ is the concentration of sulfur in the melt (in wt%). The corrected liquidus temperature can now be calculated as such:

$$T_{\text{Liquidus,S-bearing}}(°C) = T_{\text{Liquidus,S-free}}(°C) - \Delta T_{\text{Liquidus}}(°C)$$

A comparison between the uncorrected (S-free) and the corrected (S-bearing) temperatures is shown in Fig. S4.3. The solidus temperature was derived by fitting the solidus temperatures of our S-free evolving MMO liquid as determined with MAGEMin (Riel et al., 2022) using the 'igneous' database of Holland et al. (2018). The temperature is calculated as follows:

$$T_{Solidus}(°C) = 864.30 + 222.41\ P(GPa) - 7.77\ P\ (GPa)^2$$

Where P is the pressure (in GPa). The fit achieves an R^2 of 0.99 and the SEE is 34 °C. To retrieve the actual solidus temperature, the effect of S on the solidus temperature is needed. To our knowledge, no study focused on quantitatively determining the solidus depression as a function of the sulfur content in reduced silicate melts relevant to Bulk Silicate Mercury (BSMe). As a first approximation, we can therefore apply the same ΔT for the liquidus temperature following the approach of Katz et al. (2003) for H_2O (Fig. S4.3.).

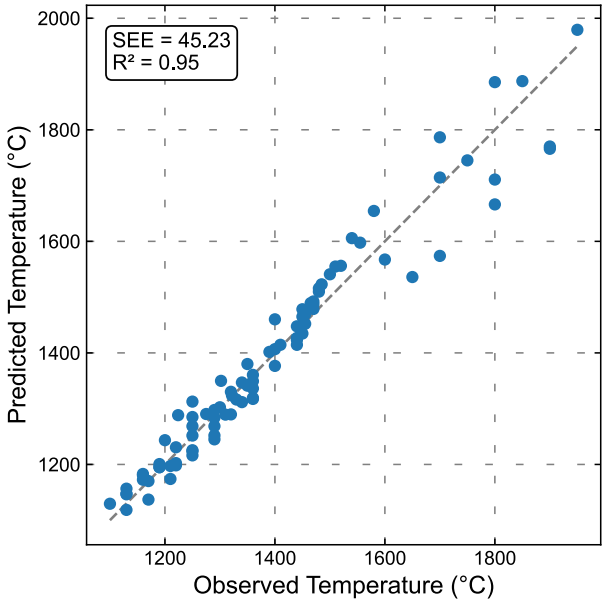

Figure S4.8. *Calculated versus measured temperatures of Mercury-like mantle compositions. The dataset is from Saracino et al. (2025), Charlier et al. (2013), Namur and Charlier (2017), Namur et al. (2016a). The fit achieves an R^2 of 0.95 and a Standard Error of Estimate (SEE) of 45 °C (N=89). The oxide concentrations are expressed in wt%.*

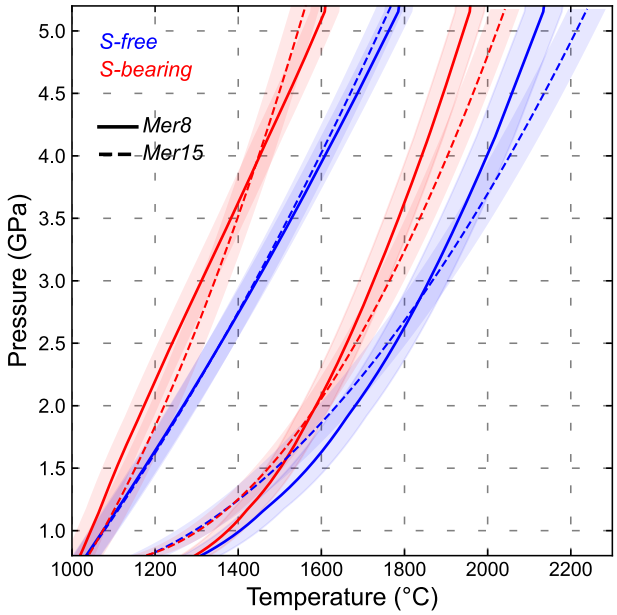

Figure S4.9. *Comparison between uncorrected, S-free liquidus temperature (blue line) calculated with Mercury's mantle thermometer, and the corrected, S-bearing liquidus temperature (red line). Also shown as comparison is the S-free and S-bearing solidus temperature. The colored areas alongside the curves represent the Standard Errors of Estimate (SEE) of each expression as estimated in this study ($T_{liquidus,\ S\text{-}free}$) and in Saracino et al. (2025) ($\Delta T_{liquidus}$).*

S4.8. Cotectic proportions

Table S4.2. *Cotectic proportions used for the MMO crystallization modelling with sulfide-bearing (a) Mer8 and (b) Mer15 starting compositions, respectively.*

(a) Mer8 + (Mg,Ca)S

Cumulus assemblage (wt%)	Fo	En	Cpx	Qtz	Pl	(Mg,Ca)S
En		90				10
En, Fo	22	68				10
En, Fo, Cpx	12	68	10			10
En, Fo, Cpx, Qtz	10	50	25	5		10
En, Cpx, Qtz		35	40	15		10
Cpx, Qtz, Pl			27	18	45	10

(b) Mer15 + (Mg,Ca)S

Cumulus assemblage (wt%)	Fo	En	Cpx	Qtz	Pl	(Mg,Ca)S
Fo	90					10
En, Fo	22	68				10
En, Fo, Cpx	12	68	10			10
En, Fo, Cpx, Qtz	10	50	25	5		10
En, Cpx, Qtz		35	40	15		10
Cpx, Qtz, Pl			27	18	45	10

S4.9. Crystallization sequence as a function of temperature

Table S4.3. *Input range of temperature (in °C) used to compute the MMO evolution for Mer8 and Mer15, respectively. Abbreviations : Fo – forsterite, En– enstatite, Cpx – clinopyroxene, Qtz – quartz, Pl – plagioclase.*

Cumulus assemblage	Mer8	Mer15
En / Fo	> 1850 (En)	> 1540 (Fo)
En, Fo	1850 < T < 1575	1540 < T < 1500
En, Fo, Cpx	1575 < T < 1425	1500 < T < 1375
En, Fo, Cpx, Qtz	1425 < T < 1275	1375 < T < 1275
En, Cpx, Qtz	1275 < T < 1250	1275 < T < 1250
Cpx, Qtz, Pl	T < 1250	T < 1250

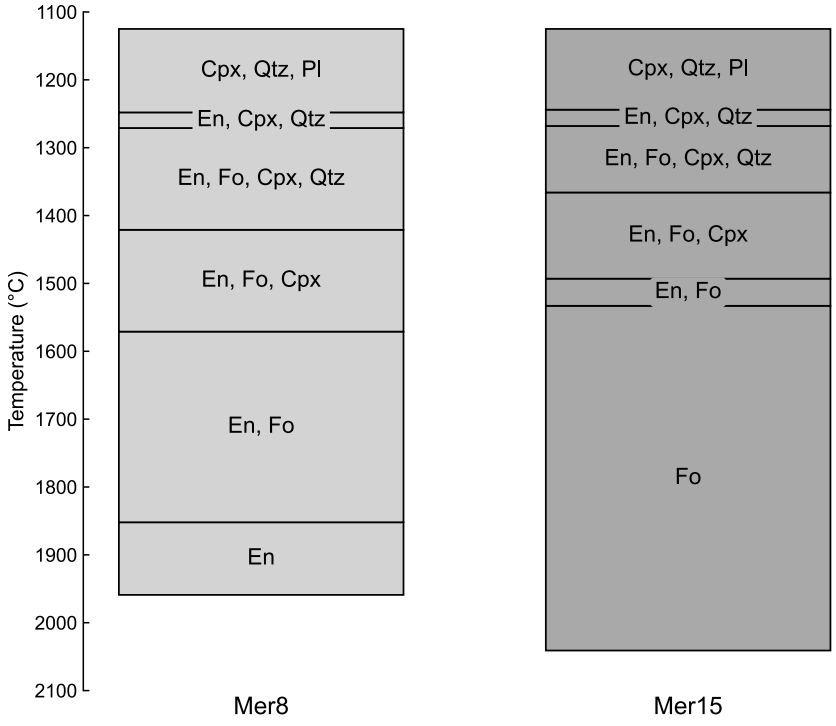

Figure S4.10. *Crystallization sequence as a function of temperature (°C) for our two sulfide-bearing Mer8 and Mer15. Abbreviations : Fo – forsterite, En– enstatite, Cpx – clinopyroxene, Qtz – quartz, Pl – plagioclase.*

S4.10. Equations for the calculation of mineral compositions

Olivine

- Fo = 1
- $Al_2O_{3\ ol}$ = -0.198 + 0.00009**T* + 0.02398**P* + 0.01221*$Al_2O_{3\ liq}$ (R^2 = 0.81; SEE = 0.019)
- CaO_{ol} = -0.09 + 0.00006**T* + 0.00181**P* + 0.01183*CaO_{liq} (R^2 = 0.83; SEE = 0.006)
- MnO_{ol} = 0.05

Orthopyroxene

- En = 1
- Na_2O, K_2O, P_2O_5 = 0
- CaO_{opx} = 1.871 + 0.29504*CaO_{liq} - 0.00128**T* + 0.20994**P* (R^2 = 0.80; SEE = 0.06)
- TiO_{2opx} = 0.05
- Al_2O_{3opx} = 17.482 - 0.00404*$Al_2O_{3\ liq}$ + 1.87433**P* – 0.01236**T* (R^2 = 0.90; SEE = 0.35)
- MnO_{opx} = 0.07

Clinopyroxene

- FeO, Na_2O, K_2O, P_2O_5 = 0
- MgO = 15.46 wt%
- SiO_2 = 50.00 wt%
- CaO_{cpx} = 4.00 wt%
- $TiO_{2\ cpx}$ = 0.09 wt%
- $Al_2O_{3\ cpx}$ = 7.12 wt%
- MnO_{cpx} = 0.33 wt%

Quartz

- SiO_2 = 100 wt%

Plagioclase

- SiO2 = 50.03 wt%
- Al_2O_3 = 33.49 wt%
- CaO = 10.49 wt%
- Na_2O = 5.00 wt%

S4.11. Lithology of the cumulate pile

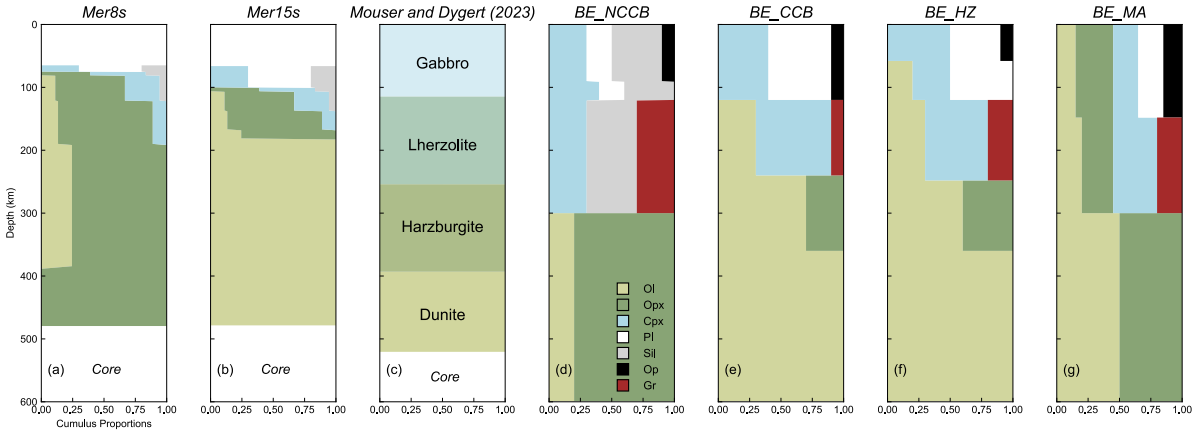

Figure S4.11. *Comparison of MMO crystallization sequence models (depths are not scaled). (a) Mer8 and (b) Mer15 are from this study; (c) pre-mantle overturn crystallization sequence of Mouser and Dygert (2023) (d) Starting CB chondrite composition (Weisberg et al., 2000; Lauretta et al., 2007) with non-chondritic Si/Mg from Brown and Elkins-Tanton (2009) (e) Starting CB chondrite (Weisberg et al., 2000, 2021; Lauretta et al., 2007) with chondritic Si/Mg from Brown and Elkins-Tanton (2009) (f) Starting Earth's mantle composition based on measurements of fertile lherzolites (Hart and Zindler, 1986) from Brown and Elkins-Tanton (2009) (g) Model composition of Earth calculated from nebular condensation model (Morgan and Anderson, 1980) from Brown and Elkins-Tanton (2009). The thicker mantle in the models of Brown and Elkins-Tanton (2009) is based on an old configuration of the interior where a ~ 1800 km-core radius is considered (Riner et al., 2008). Abbreviations: ol – olivine, opx – orthopyroxene, cpx – clinopyroxene, Sil – silica phases, pl – plagioclase, op – opaques, gr – garnet.*

S4.12. Calculation of S-bearing liquid densities

To investigate the effect of sulfur on the density of silicate liquids, first we calculated the density of the MMO both in S-free and S-bearing conditions following the method of Bottinga and Weill (1970). Volumetric properties of both elemental S and sulfide phases are not well constrained in the literature, so some approximations were necessary. At room temperature, solid S has a molar volume of ~ 15.5 $cm^3\ mol^{-1}$ (Singman, 1984; Robie and Hemingway, 1995). Sulfides like troilite (FeS), alabandite (MnS), niningerite (MgS), and oldhamite (CaS) have molar volumes in the range 18 - 28 $cm^3\ mol^{-1}$ (Robie and Hemingway, 1995; Lark et al., 2022).

As concerns the S-bearing liquid density calculation, sulfur was considered with M_i = 32.065 g mol^{-1} and with V_i = 20 $cm^3\ mol^{-1}$, although we do not exclude larger volumes. MMO liquid densities were computed considering different S contents (0, 1, 3, 5, 10 wt%) at an interval of 0.10 in the melt fraction F. Next, we determine the difference in density between the S-free and S-bearing MMO silicate liquids calculated as follows:

$$\Delta\rho_{\mathrm{MMOs}} = \rho_{\mathrm{MMO,S-free}} - \rho_{\mathrm{MMO,S-bearing}}$$

Where $\rho_{\mathrm{MMO,S\text{-}free}}$ is the density of the MMO liquid in S-free conditions and $\rho_{\mathrm{MMO,S\text{-}bearing}}$ is the density of the MMO liquid in S-bearing conditions (all expressed in kg m^{-3}). The $\Delta\rho_{\mathrm{MMOs}}$ values that we obtained are then plotted as a function of the S content in the MMO liquid (Fig. S4.12.), where a linear relation was found:

$$\Delta\rho_{\mathrm{MMOs}} = 21.38\,[S]_{\mathrm{Melt}} \qquad (R^2 = 0.99)$$

Where $\Delta\rho_{\mathrm{MMOs}}$ is the density difference expressed in kg m^{-3}, and $[S]_{\mathrm{melt}}$ is the concentration of sulfur in the melt expressed in wt%. As a first approximation, we assumed $\Delta\rho_{\mathrm{MMOs}} = 0$ when no S is dissolved in the melt. We apply this correction to the S-free liquid density calculated with the EoS described in Section 3.1.

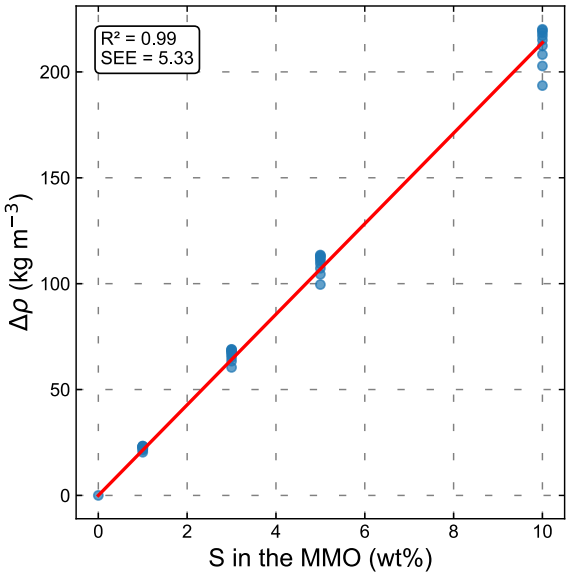

Figure S4.12. *Density difference between calculated S-free and S-bearing MMO liquids ($\Delta\rho_{MMOs}$) as a function of the S content in the melt (expressed as wt%). The R^2 is 0.99 and the standard error of estimate (SEE) is 5.33 kg m^{-3}.*

S4.13. HPE partitioning in the MMO

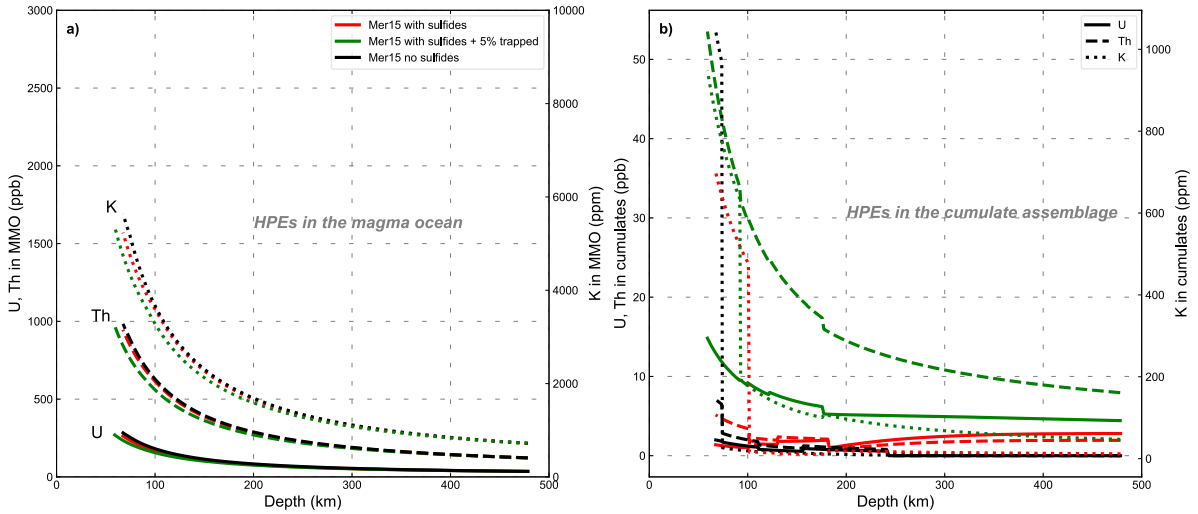

Figure S4.13. (a) *Uranium, thorium (ppb) and potassium (ppm) distribution in sulfide-bearing (red lines), sulfide-bearing with 5% trapped melt (green), and sulfide-free (black lines) Mer15 MMO as a function of depth (km). (b) Uranium, thorium (both ppb), and potassium (ppm) distributions in the growing cumulates as a function of depth (km) in Mer15. Solid lines refer to uranium (U), dashed lines refer to thorium (h), and dotted lines refer to potassium (K). Black lines refer to sulfide-free Mer15, red lines refer to sulfide-bearing Mer15, and green lines refer to sulfide-bearing Mer15 with 5% trapped melt in the cumulate pile.*

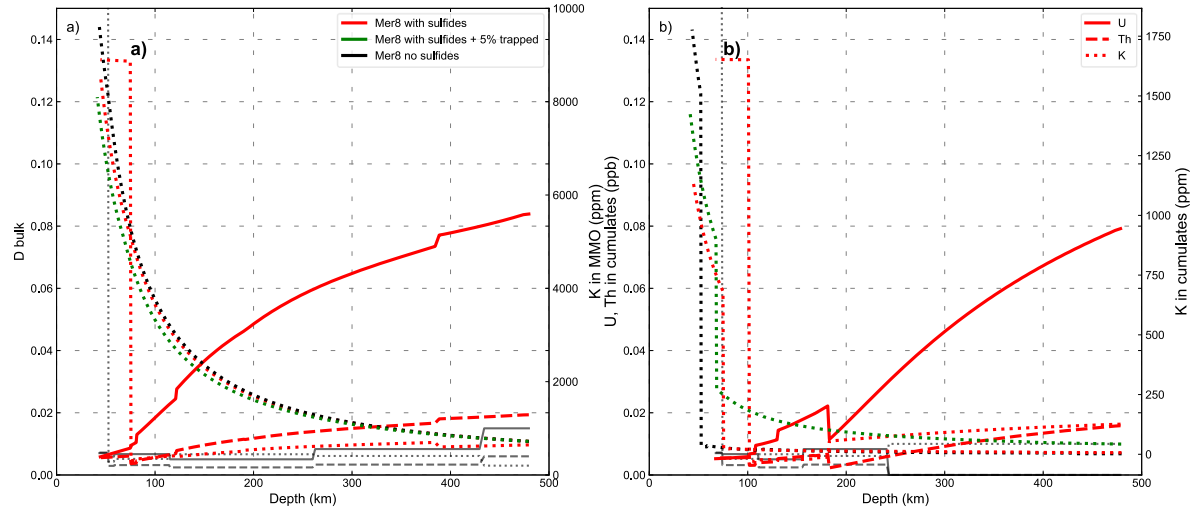

Figure S4.14. *Bulk partitioning coefficients D_{bulk} of U, Th, and K as a function of depth (km) for sulfide-free (black lines) and sulfide-bearing (red lines) for both (a) Mer8 and (b) Mer15.*

References

Baldwin, T. O., Tompson, C. W., 1964. X-ray characteristic temperatures of some II-VI ionic compounds. The J. Chem. Phys., 41(5), 14201426. https://doi.org/10.1063/1.1726083

Bertka, C.M., Fei, Y., 1998. Density profile of an SNC model Martian interior and the moment-of-inertia factor of Mars. Earth Planet Sci. Lett. 157, 79-88. https://doi.org/10.1016/S0012-821X(98)00030-2

Bottinga, Y., Richet, P., Weill, D.F., 1983. Calculation of the density and thermal expansion coefficient of silicate liquid. Bull. Mineral., 106, 129-138.

Bottinga, Y., Weill, D.F., 1970. Density of liquid silicate systems calculated from partial molar volumes of oxide components. Am. J. Sci.269, 169-182. https://doi.org/10.2475/ajs.269.2.169

Brown, S.M., Elkins-Tanton, L.T., 2009. Compositions of Mercury's earliest crust from magma ocean models. Earth Planet. Sci. Lett. 286, 446–455. https://doi.org/10.1016/j.epsl.2009.07.010

Charlier, B., Grove, T.L., Zuber, M.T., 2013. Phase equilibria of ultramafic compositions on Mercury and the origin of the compositional dichotomy. Earth Planet Sci. Lett. 363, 50–60. https://doi.org/10.1016/j.epsl.2012.12.021

Fei, Y., Saxena, S.K., Navrotsky, A., 1990. Internally consistent thermodynamic data and equilibrium phase relations for compounds in the system MgO-SiO2 at high pressure and high temperature. J. Geophys. Res. Solid Earth 95, 6915-6928. https://doi.org/10.1029/JB095iB05p06915

Frondel, C., 1962. The system of mineralogy. Volume III, Silica minerals, John Wiley, and Sons.

Ghiorso, M.S., 2004. An equation of state for silicate melts. I. Formulation of a general model. Am. J. Sci.304, 637–678. https://doi.org/10.2475/ajs.304.8-9.637

Hart, S.R., Zindler, A., 1986. In search of a bulk-Earth composition. Chem. Geol. 57, 247–267. https://doi.org/10.1016/0009-2541(86)90053-7

Holland, T.J.B., Green, E.C.R., Powell, R., 2018. Melting of Peridotites through to Granites: A Simple Thermodynamic Model in the System KNCFMASHTOCr. J. Petrol. 59, 881–900. https://doi.org/10.1093/petrology/egy048

Holland, T.J.B., Powell, R., 1998. An internally consistent thermodynamic data set for phases of petrological interest. J. Metamorph. Geol.16, 309-343. https://doi.org/10.1111/j.1525-1314.1998.00140.x

Katz, R.F., Spiegelman, M., Langmuir, C.H., 2003. A new parameterization of hydrous mantle melting. Geochem. Geophys. Geosyst. 4. https://doi.org/10.1029/2002GC000433

Kosinski, J.A., 1992. Thermoelastic coefficients of alpha quartz. IEEE Trans. ultrasonics, ferroelectrics, frequency control, 39, 4. 10.1109/58.148541

Kress, V.C., Carmichael, I.S.E., 1991. The compressibility of silicate liquids containing Fe2O3 and the effect of composition, temperature, oxygen fugacity, and pressure on their redox states. Contrib. to Mineral. Petrol. 108, 82-92. https://doi.org/10.1007/BF00307328

Kushiro, I., 1969. The system forsterite-diopside-silica with and without water at high pressures. Am. J. Sci., 267-A, 269-294. https://doi.org/10.2475/001c.125224

Lange, R., Carmichael, I.S.E., 1987. Densities of Na2O-K2O-MgO-MgO-FeO-Fe2O3-Al2O3-TiO2-SiO2 liquids: New measurements and derived partial molar properties. Geochim. Cosmochim. Acta 51, 2931–2946. https://doi.org/10.1016/0016-7037(87)90368-1

Lark, L.H., Parman, S., Huber, C., Parmentier, E.M., Head, J.W., 2022. Sulfides in Mercury's Mantle: Implications for Mercury's Interior as Interpreted From Moment of Inertia. Geophys. Res. Lett. 49, e2021GL096713. https://doi.org/10.1029/2021GL096713

Lauretta, D.S., Goreva, J.S., Hill, D.H., Killgore, M., 2007. Bulk compositions of the CB Chondrites Bencubbin, Fountain Hills, MAC 02675, and MIL 05082. LPSC Abstracts 38, 2236.

Meyer, B., 1977. Properties, in: Sulfur, Energy, and Environment. Elsevier, pp. 38–116. https://doi.org/10.1016/B978-0-444-41595-0.50006-1

Morgan, J.W., Anders, E., 1980. Chemical composition of Earth, Venus, and Mercury. Proc. Natl. Acad. Sci. USA, 77, 6973–6977. https://doi.org/10.1073/pnas.77.12.6973

Namur, O., Charlier, B., 2017. Silicate mineralogy at the surface of Mercury. Nat. Geosci.10, 9–13. https://doi.org/10.1038/ngeo2860

Namur, O., Collinet, M., Charlier, B., Grove, T.L., Holtz, F., McCammon, C., 2016. Melting processes and mantle sources of lavas on Mercury. Earth Planet Sci. Lett. 439, 117–128. https://doi.org/10.1016/j.epsl.2016.01.030

Niu, Y.L., Batiza, R., 1991. In situ densities of MORB melts and residual mantle - Implications for buoyancy forces beneath midocean ridges. J. Geol. 99, 767-775. https://doi.org/10.1086/629538

Peiris, S. M., Campbell, A. J., & Heinz, D. L., 1994. Compression of MgS to 54 GPa. J. Phys. Chem. Sol., 55(5), 413419. https://doi.org/10.1016/0022-3697(94)90166-X

Riel, N., Kaus, B.J.P., Green, E.C.R., Berlie, N., 2022. MAGEMin, an Efficient Gibbs Energy Minimizer: Application to Igneous Systems. Geochem. Geophys. Geosyst. 23. https://doi.org/10.1029/2022GC010427

Riner, M.A., Bina, C.R., Robinson, M.S., Desch, S.J., 2008. Internal structure of Mercury: Implications of a molten core. J. Geophys. Res. Planets 113, 2007JE002993. https://doi.org/10.1029/2007JE002993

Robie, R.A., Hemingway, B.S., 1995. Thermodynamic properties of Minerals and Related Substances at 298.15 K and 1 Bar (105 Pascals) Pressure and at Higher Temperatures. U.S. Geological Survey Bulletin 2131.

Saracino, F., Charlier, B., Zhang, Y., Lécaille, M., Lin, Y., Namur, O., 2025. The role of sulfur on the liquidus temperature and olivine-orthopyroxene equilibria in highly reduced magmas. Chem. Geol. 683, 122777. https://doi.org/10.1016/j.chemgeo.2025.122777

Singman, C.N., 1984. Atomic volume and allotropy of the elements. J. Chem. Educ. 61, 137. https://doi.org/10.1021/ed061p137

Toplis, M.J., Dingwell, D., Libourel, G., 1994. The effect of phosphorus on the iron redox ratio, viscosity, and density of an evolved ferrobasalt. Contrib. Mineral. Petrol. 117, 293-304. https://doi.org/10.1007/BF00310870

Warren, P.H., 1995. Extrapolated partial molar densities of $S0_3$, P_20_5, and other oxides in silicate melts. Am. Min., 80, 1085-1088. https://doi.org/10.2138/am-1995-9-1027

Weisberg, M.K., Prinz, M., Clayton, R.N., Mayeda, T.K., Sugiura, N., Zashu, S., Ebihara, M., 2001. A new metal-rich chondrite grouplet. Meteorit. Planet. Sci. 36, 401–418. https://doi.org/10.1111/j.1945-5100.2001.tb01882.x

Weisberg, M.K., Prinz, M., Humayun, M., Campbell, A.J., 2000. Origin of metal in the CB (Bencubbinite) chondrites. Lunar and Planetary Institute Conference Abstracts 31,1466.

Weng, Y.-H., Presnall, D.C., 2001. The system diopside forsterite enstatite at 5.1 GPa: a ternary model for melting of the mantle. Can. Mineral. 39, 299–308. https://doi.org/10.2113/gscanmin.39.2.299

Xu, Y., Lin, Y., Wu, P., Namur, O., Zhang, Y., Charlier, B., 2024. A diamond-bearing core-mantle boundary on Mercury. Nat. Commun. 15. https://doi.org/10.1038/s41467-024-49305-x

Appendix D

The crystallization of the Mercury's magma ocean and the formation of its primordial mantle

Fabrizio Saracino, Bernard Charlier, Yishen Zhang, Olivier Namur

Composition of silicate glass (and relative 1σ standard deviation in *italic*). Abbreviations: No – Number of analyses. * Calculated by stoichiometry

Run	No	Si	Ti	Al	Fe	Mn	Mg	Ca	Na	K	S	O*	Tot
A396	10	26.86	< dl	6.59	0.32	< dl	9.78	4.17	3.36	0.38	5.74	46.46	103.66
		0.31		*0.09*	*0.04*		*0.17*	*0.07*	*0.07*	*0.02*	*0.13*		
A397	10	26.36	< dl	5.51	0.30	0.16	12.67	3.51	2.57	0.30	5.65	46.22	103.25
		0.27		*0.07*	*0.06*	*0.05*	*0.20*	*0.24*	*0.09*	*0.02*	*0.22*		
A399	11	26.20	< dl	4.85	0.23	0.21	13.99	3.09	2.34	0.25	5.23	46.03	102.42
		0.21		*0.05*	*0.04*	*0.05*	*0.31*	*0.23*	*0.11*	*0.03*	*0.10*		
A400	12	28.12	< dl	5.64	0.29	< dl	11.10	2.95	2.35	0.24	6.81	46.90	104.40
		0.23		*0.05*	*0.06*		*0.12*	*0.14*	*0.09*	*0.01*	*0.13*		
A401	11	27.22	< dl	4.81	0.26	< dl	13.06	2.55	2.02	0.21	6.85	46.11	103.09
		0.27		*0.05*	*0.03*		*0.10*	*0.06*	*0.07*	*0.03*	*0.13*		
A402	7	27.49	0.22	6.37	0.01	< dl	9.83	3.69	1.47	0.14	5.31	45.84	100.37
		0.40	*0.03*	*0.09*	*0.02*		*0.53*	*0.18*	*0.05*	*0.02*	*0.22*		
A403	10	28.34	0.16	4.94	0.02	< dl	12.73	2.63	1.33	0.14	5.39	46.92	102.60
		0.22	*0.05*	*0.03*	*0.02*		*0.18*	*0.06*	*0.06*	*0.02*	*0.14*		
A404	10	28.38	< dl	7.28	0.26	< dl	6.62	4.47	3.80	0.46	5.08	47.02	103.37
		0.23		*0.10*	*0.03*		*0.10*	*0.08*	*0.05*	*0.03*	*0.11*		
A405	10	29.23	< dl	6.80	0.24	< dl	7.26	3.36	3.02	0.31	5.77	47.16	103.15
		0.22		*0.10*	*0.05*		*0.26*	*0.11*	*0.12*	*0.02*	*0.23*		
A431	17	28.55	< dl	7.86	0.32	< dl	7.17	3.47	3.53	0.33	4.19	47.54	102.96
		0.32		*0.26*	*0.09*		*0.29*	*0.17*	*0.11*	*0.02*	*0.09*		
A432	10	30.85	< dl	8.78	0.36	< dl	2.79	3.60	4.82	0.55	2.39	48.83	102.97
		0.69		*0.19*	*0.07*		*0.28*	*0.47*	*0.20*	*0.04*	*0.22*		
A441	18	29.14	< dl	8.61	0.38	< dl	4.86	3.67	3.92	0.39	3.44	47.66	102.07
		0.42		*0.27*	*0.20*		*0.29*	*0.16*	*0.13*	*0.03*	*0.13*		
A444	10	29.30	< dl	8.62	0.15	< dl	6.20	3.63	2.55	0.34	3.82	47.97	102.58
		0.44		*0.26*	*0.10*		*0.20*	*0.19*	*0.07*	*0.01*	*0.07*		
A445	12	30.15	< dl	8.83	0.46	< dl	3.30	3.54	4.50	0.47	2.86	48.23	102.34

Run	No	Si	Ti	Al	Fe	Mn	Mg	Ca	Na	K	S	O*	Tot
		0.75		*0.54*	*0.15*		*0.25*	*0.41*	*0.12*	*0.03*	*0.16*		
A451	8	30.20	< dl	8.43	0.35	< dl	4.07	3.45	4.17	0.45	3.33	48.23	102.68
		0.60		*0.45*	*0.07*		*0.47*	*0.37*	*0.20*	*0.02*	*0.17*		
A452	10	29.50	< dl	9.21	0.26	< dl	4.16	3.87	3.98	0.39	2.90	48.22	102.49
		0.51		*0.29*	*0.07*		*0.28*	*0.22*	*0.09*	*0.03*	*0.08*		
A453	12	31.77	< dl	8.33	0.34	< dl	3.25	3.14	3.95	0.44	2.70	49.15	103.07
		0.30		*0.18*	*0.11*		*0.13*	*0.16*	*0.11*	*0.02*	*0.10*		
A461	9	31.01	< dl	8.69	0.43	< dl	2.64	4.35	3.91	0.46	0.54	48.19	100.22
		0.51		*0.20*	*0.15*		*0.18*	*0.28*	*0.12*	*0.04*	*0.10*		
A462	10	30.17	< dl	8.82	0.38	< dl	3.55	4.98	3.71	0.40	0.54	48.11	100.66
		0.44		*0.21*	*0.04*		*0.14*	*0.19*	*0.22*	*0.03*	*0.06*		
A469	10	30.14	0.20	9.13	0.45	< dl	2.83	4.89	3.70	0.41	0.39	47.94	100.08
		0.38	*0.05*	*0.21*	*0.09*		*0.08*	*0.18*	*0.09*	*0.04*	*0.08*		
A473	9	34.79	0.06	7.54		0.08	0.64	2.65	5.02	0.68		50.49	101.95
		0.35	*0.09*	*0.37*		*0.02*	*0.02*	*0.17*	*0.60*	*0.02*			
A475	12	36.07	0.09	6.75		0.08	0.58	2.12	5.04	0.73		51.04	102.50
		0.45	*0.09*	*0.31*		*0.01*	*0.05*	*0.33*	*0.25*	*0.03*			
A477	6	34.41	0.07	7.43		0.06	1.35	2.44	4.66	0.59		50.17	101.18
		0.45	*0.05*	*0.24*		*0.01*	*0.03*	*0.08*	*0.12*	*0.02*			
A486	9	35.98	0.05	6.92		0.06	0.42	2.27	5.21	0.75		51.09	102.75
		0.49	*0.03*	*0.26*		*0.02*	*0.02*	*0.22*	*0.20*	*0.01*			
A487	10	36.47	0.12	6.56		0.07	0.40	1.90	5.17	0.83		51.22	102.74
		0.45	*0.10*	*0.33*		*0.02*	*0.02*	*0.18*	*0.18*	*0.02*			

Composition of silicate crystals. Abbreviations: No – Number of analyses. Fo – Forsterite, En – Enstatite, Cpx – Clinopyroxene, Pl – Plagioclase.

Run		No	SiO_2	TiO_2	Al_2O_3	FeO	MnO	MgO	CaO	Na_2O	K_2O	Cr_2O_3	Tot
A396	Fo	1	42.30	< dl	0.15	0.35	< dl	56.40	0.12				99.32
	En	5	57.96	0.08	2.87	0.37	< dl	38.80	0.52	0.08			100.68
	Cpx		Not measured										
A397	En	5	58.56	< dl	1.20	0.24	< dl	38.89	0.41	0.05			99.35
A400	Fo		Not measured										
	En	3	59.52	0.10	2.43	0.19	< dl	39.38	0.37	0.05			102.04
	Cpx		Not measured										
A401	En	3	59.45	< dl	1.82	0.14	< dl	39.38	0.36	0.04			101.19
A402	Fo		Not measured										
	En	5	58.59	0.07	2.55	< dl	< dl	38.46	0.39	< dl			100.06
	Cpx		Not measured										
A403	Fo		Not measured										
	En	4	59.58	< dl	1.53	< dl	< dl	39.30	0.27	0.04			100.72
	Cpx		Not measured										
A404	Fo		Not measured										
	En	5	58.09	< dl	2.10	0.47	< dl	37.78	1.23	0.15			99.82
	Cpx		Not measured										
A405	En	5	58.51	< dl	3.03	0.18	< dl	37.99	0.44	0.10			100.25
	Cpx		Not measured										
A431	Fo		Not measured										
	En	7	57.10	< dl	6.64	0.42	< dl	36.25	0.80	0.47			101.73
	Cpx		Not measured										
A432	En	5	59.41	< dl	3.10	0.70	< dl	35.06	2.72	0.67			101.82
	Cpx		Not measured										
A441	En	4	58.46	< dl	4.53	0.93	< dl	35.96	1.56	0.47			102.04
	Cpx		Not measured										
A444	En	3	57.76	< dl	5.43	0.63	< dl	37.01	0.98	0.33			102.20

Run		No	SiO_2	TiO_2	Al_2O_3	FeO	MnO	MgO	CaO	Na_2O	K_2O	Cr_2O_3	Tot
	Cpx		Not measured										
A445	En	2	59.56	< dl	3.41	0.75	< dl	36.53	1.72	0.53			102.60
	Cpx		Not measured										
A451	En	4	57.67	< dl	5.78	0.67	< dl	35.06	1.83	0.54			101.68
	Cpx		Not measured										
A452	En	10	58.54	< dl	2.97	0.44	< dl	36.64	1.77	0.34			100.84
	Cpx		Not measured										
A453	En	4	55.42	< dl	8.90	0.58	< dl	35.56	0.98	0.30			101.81
	Cpx		Not measured										
A461	En	2	55.89	0.22	3.74	0.92	0.13	36.19	2.11	0.25			99.45
	Cpx		Not measured										
	Fo	2	42.32	< dl	0.23	1.07	0.10	55.94	0.19				
A462	En	1	54.29	0.11	3.29	0.37	0.18	39.50	1.05	0.07			98.86
	Cpx		Not measured										
	Fo		Not measured										
A469	En	2	58.09	0.06	1.76	1.23	0.19	36.33	2.57	0.16			100.47
	Cpx	2	62.75	0.10	10.66	0.47	0.08	19.02	4.29	2.76	0.35		100.48
A473	Cpx	4	56.47	0.08	3.22		0.45	15.58	21.90	0.84	0.12		98.66
	Pl	5	51.35	0.15	31.65			0.32	12.28	4.37	0.07		100.19
A475	Cpx	2	52.75	0.09	9.17		0.43	12.64	21.95	1.73	0.08		98.76
	Pl	2	51.72	0.22	31.38			0.40	11.87	4.57	0.07		100.23
A477	Cpx	5	53.80	0.10	3.96		0.37	18.35	20.27	0.75	0.04		97.55
	Pl	5	48.50	0.06	34.21			0.44	13.95	3.00	0.06		100.22
A486	Cpx	2	54.69	0.08	8.59		0.34	11.73	20.47	1.62	0.16		97.68
	Pl	3	53.00	< dl	31.61			0.30	8.97	6.19	0.12		100.19
A487	Cpx		Not measured										
	Pl	2	50.12	< dl	36.44			0.94	7.19	6.23	0.17		101.09

Composition of Fe metal (and relative 1σ standard deviation in *italic*). Abbreviations: No – Number of analyses.

Run	No	Si	Cr	Fe	P	S	Tot
A396	9	8.61	0.17	86.48	0.78	0.28	96.32
		0.25	*0.04*	*0.64*	*0.08*	*0.10*	
A397	7	7.33	0.16	88.02	0.91	0.31	96.73
		0.57	*0.07*	*0.90*	*0.09*	*0.09*	
A399	12	6.85	0.17	83.35	1.17	0.75	92.29
		0.16	*0.02*	*0.69*	*0.02*	*0.16*	
A404	10	9.57	0.10	86.43	0.63	0.23	96.96
		0.32	*0.03*	*0.46*	*0.09*	*0.03*	
A431	9	13.25		86.98		0.26	100.49
		1.14		*1.62*		*0.07*	
A432	5	18.17		81.84		0.16	100.17
		0.12		*0.67*		*0.04*	
A441	7	17.20		83.22		0.12	100.54
		1.07		*1.25*		*0.04*	
A444	4	17.22		82.80		0.12	100.14
		0.31		*1.55*		*0.03*	
A445	7	18.30		82.25		0.13	100.68
		1.30		*1.49*		*0.03*	
A451	4	7.00		91.03		0.30	98.33
		0.59		*1.43*		*0.05*	
A452	7	17.11		83.95		0.13	101.19
		1.09		*1.16*		*0.02*	
A453	5	8.29		93.08		0.27	101.64
		0.30		*1.47*		*0.05*	
A462		Not measured					

Composition of troilite (FeS) (and relative 1σ standard deviation in *italic*). Abbreviations: No – Number of analyses.

Run	No	Si	Ti	Cr	Fe	Mn	Mg	Ca	S	Total
A396	4	0.07	4.06	3.43	52.75	0.37	0.17	0.06	37.44	98.35
		0.04	*0.77*	*0.30*	*0.76*	*0.02*	*0.04*	*0.00*	*0.01*	
A397	6	0.06	3.29	5.07	51.82	0.89	0.42	0.08	37.75	99.38
		0.02	*0.82*	*0.32*	*0.90*	*0.32*	*0.63*	*0.13*	*0.15*	
A399	2	< dl	0.73	4.16	56.12	1.15	0.23	< dl	36.65	99.04
			0.41	*0.59*	*0.85*	*0.26*	*0.03*		*0.05*	
A400	6	0.09	1.71	2.88	51.34	0.26	0.21	0.10	41.17	97.76
		0.09	*0.20*	*0.23*	*0.56*	*0.06*	*0.34*	*0.07*	*0.91*	
A401	4	0.04	1.20	3.22	52.84	0.37	0.13	0.05	41.17	99.02
		0.02	*0.02*	*0.07*	*0.25*	*0.04*	*0.13*	*0.02*	*0.27*	
A404	3	0.04	4.66	3.35	52.67	0.20	0.14	0.06	37.81	98.93
		0.02	*1.03*	*0.30*	*0.42*	*0.08*	*0.01*	*0.03*	*0.18*	
A405	3	0.05	1.99	2.15	52.33	0.16	0.05	0.05	41.82	98.60
		0.02	*0.06*	*0.10*	*1.05*	*0.01*	*0.01*	*0.00*	*0.29*	
A431	8	0.13	1.69	0.86	60.57	0.48	0.14	0.08	35.92	99.87
		0.04	*0.93*	*0.25*	*1.17*	*0.10*	*0.04*	*0.12*	*0.92*	
A432	5	0.13	< dl	0.33	63.31	0.26	0.09	0.05	35.80	99.97
		0.03		*0.21*	*0.97*	*0.05*	*0.03*	*0.03*	*0.33*	
A441	8	0.18	< dl	0.63	62.58	0.23	0.07	0.06	34.89	98.64
		0.11		*0.15*	*0.66*	*0.04*	*0.04*	*0.02*	*0.48*	
A444	8	0.12	0.34	0.66	62.23	0.32	0.08	0.05	35.50	99.30
		0.02	*0.21*	*0.12*	*0.64*	*0.06*	*0.02*	*0.03*	*0.33*	
A445	4	0.11	< dl	0.52	62.36	0.33	0.10	0.05	35.43	98.90
		0.01		*0.21*	*1.29*	*0.08*	*0.02*	*0.02*	*0.64*	
A451	4	0.12	< dl	0.52	63.45	0.46	0.10	0.07	36.33	101.05
		0.01		*0.07*	*0.20*	*0.07*	*0.02*	*0.05*	*0.24*	
A452	6	0.10	< dl	0.57	62.79	0.35	0.11	0.05	36.10	100.07

Run	No	Si	Ti	Cr	Fe	Mn	Mg	Ca	S	Total
		0.03		*0.09*	*1.15*	*0.08*	*0.03*	*0.03*	*0.58*	
A453	5	0.10	0.15	0.53	63.95	0.25	0.12	0.05	35.51	100.66
		0.01	*0.08*	*0.05*	*0.32*	*0.02*	*0.02*	*0.01*	*0.47*	
A461	6	< dl	0.25	0.23	61.95	0.79		0.05	36.73	100.00
			0.14	*0.06*	*0.44*	*0.12*		*0.01*	*0.20*	
A462	7	< dl	0.20	0.39	60.54	1.20		0.06	36.47	98.86
			0.07	*0.15*	*0.98*	*0.16*		*0.02*	*1.28*	
A469	6	< dl	0.45	0.36	60.79	1.11		0.19	37.12	100.02
			0.51	*0.14*	*1.04*	*0.09*		*0.37*	*0.70*	

Appendix E

Here listed in chronological order are the backscattered (BSE) images of all the experimental charges, together with temperature, pressure conditions, phase assemblages, and glass compositions featured in my doctoral project and scientific papers. All the samples were the result of piston-cylinder experiments conducted at the Laboratoire de Pétrologie, Géochimie et Pétrophysique (Department of Geology, University of Liege). The BSE images show large scale charges (where available) portraying glass and crystal textures, metallic and sulfide blob features. Numbers in parentheses shown in the starting composition refer to the percentage of metallic Si with respect to Si. The experimental duration (expressed in hours) is considered after the target temperature has been reached. All the experiments here were performed with graphite capsules. The BSE images here shown were captured with the FEI QEMSCAN 650 F electron microscope at the University of Aachen (Institute of Advanced Mining Technology, RWTH Aachen), and with the TESCAN MIRA 4th Generation at the Department of Geology in KU Leuven (Belgium). The chemical compositions (expressed in element wt%) were obtained with the CAMECA Sx Five Tactis electron probe micro analyzer at Laboratoire Magmas et Volcans, Universite Clermont Auvergne (Clermont-Ferrand, France), and with the JEOL JXA-8530F at the Department of Material Engineering at KU Leuven. Oxygen was calculated by stoichiometry. Abbreviations: Gl – Silicate glass, Ol – Olivine, Opx – Orthopyroxene, Cpx – Clinopyroxene, Qtz – Quartz, Pl – Plagioclase. *Oxygen was calculated by stoichiometry, < dl – below detection limits.

A247

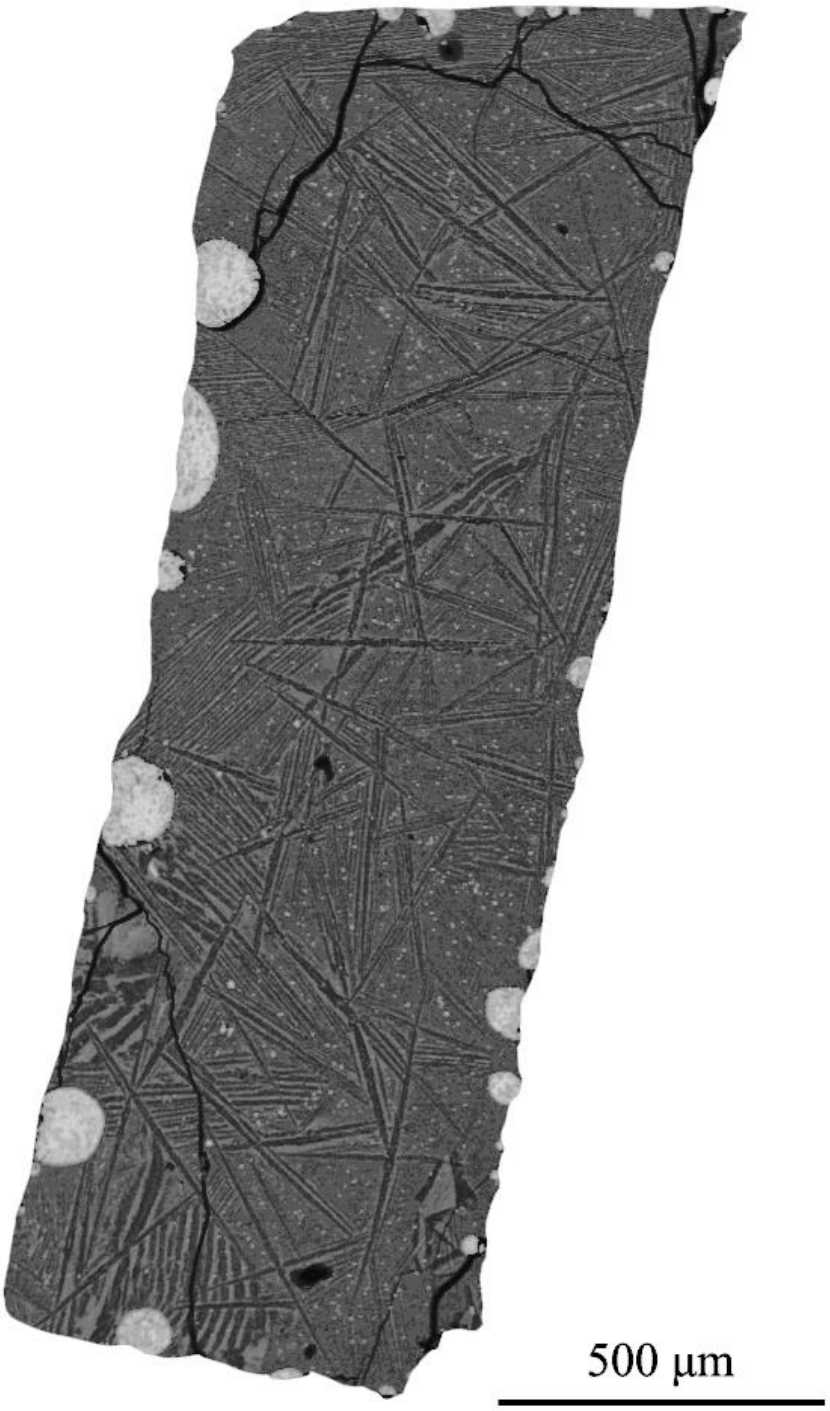

T (°C)	1700	**Run**	**A247**
P (GPa)	1.5	**Si**	26.15
Starting composition	Mer8(10) + 16.7% FeS	**Ti**	0.09
Duration (hrs)	00:30	**Al**	2.01
Silicate Phases (wt%)	Gl (100)	**Fe**	0.29
		Mn	0.18
		Mg	21.82
		Ca	1.20
		Na	0.81
		K	0.10
		S	3.14
		Cr	< dl
		O*	47.04
		Tot	102.83

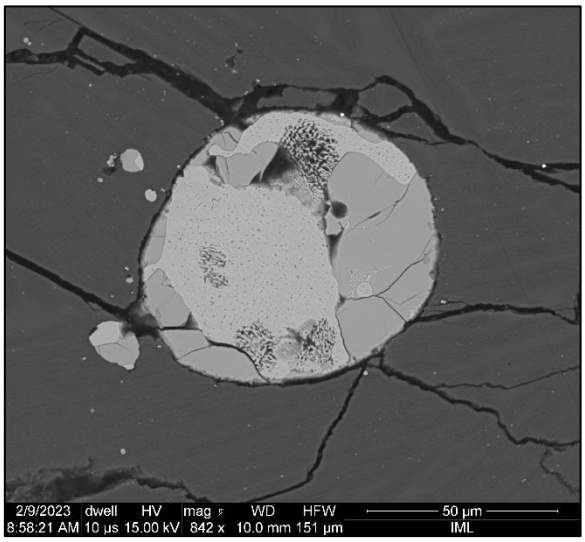

A249

T (°C)	1800	**Run**	**A249**
P (GPa)	1.5	**Si**	26.08
Starting composition	Mer15(10) + 16.7% FeS	**Ti**	0.10
Duration (hrs)	00:30	**Al**	2.02
Silicate Phases (wt%)	Gl (100)	**Fe**	0.43
		Mn	0.18
		Mg	21.69
		Ca	1.25
		Na	0.78
		K	0.10
		S	2.81
		Cr	< dl
		O*	46.94
		Tot	102.39

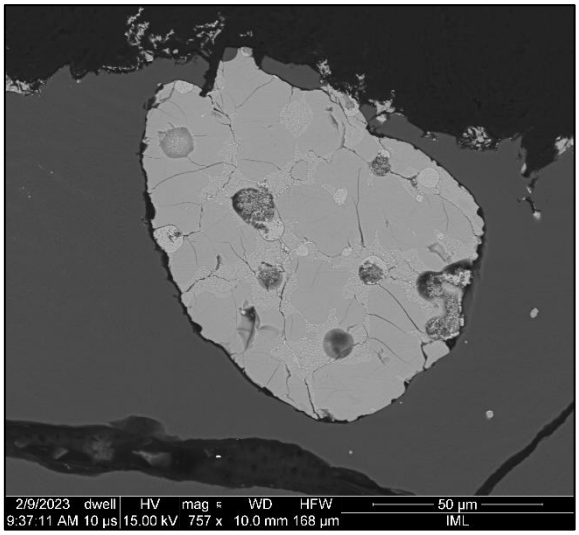

A257

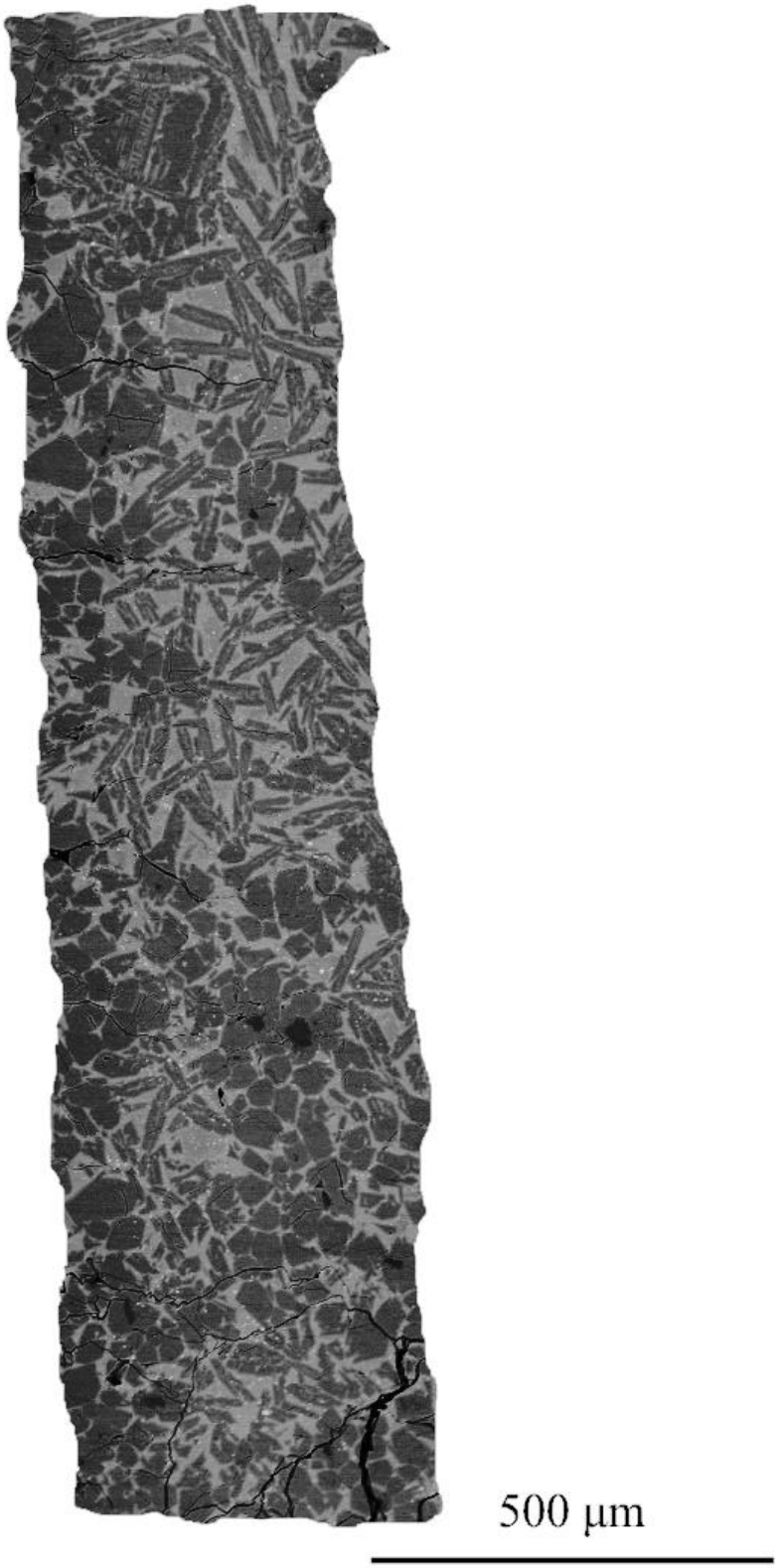

T (°C)	1800	**Run**	**A257**
P (GPa)	1.5	**Si**	27.01
Starting composition	Mer15(10)	**Ti**	0.20
Duration (hrs)	00:30	**Al**	5.08
Silicate Phases (wt%)	Gl (45) Ol (55)	**Fe**	
		Mn	0.34
		Mg	17.36
		Ca	3.07
		Na	0.14
		K	0.13
		S	
		Cr	0.11
		O*	48.32
		Tot	101.76

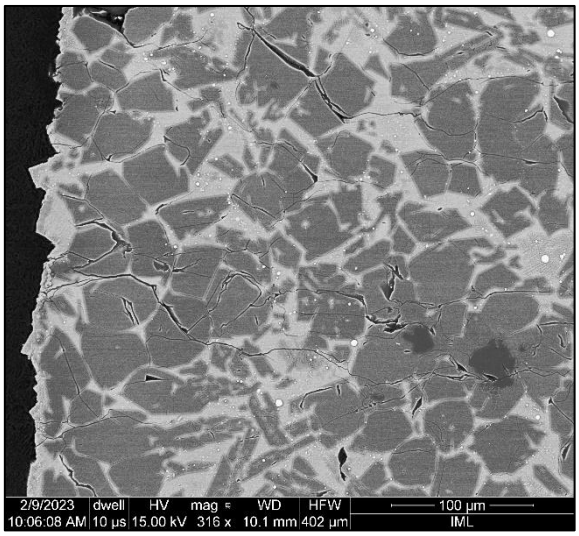

A259

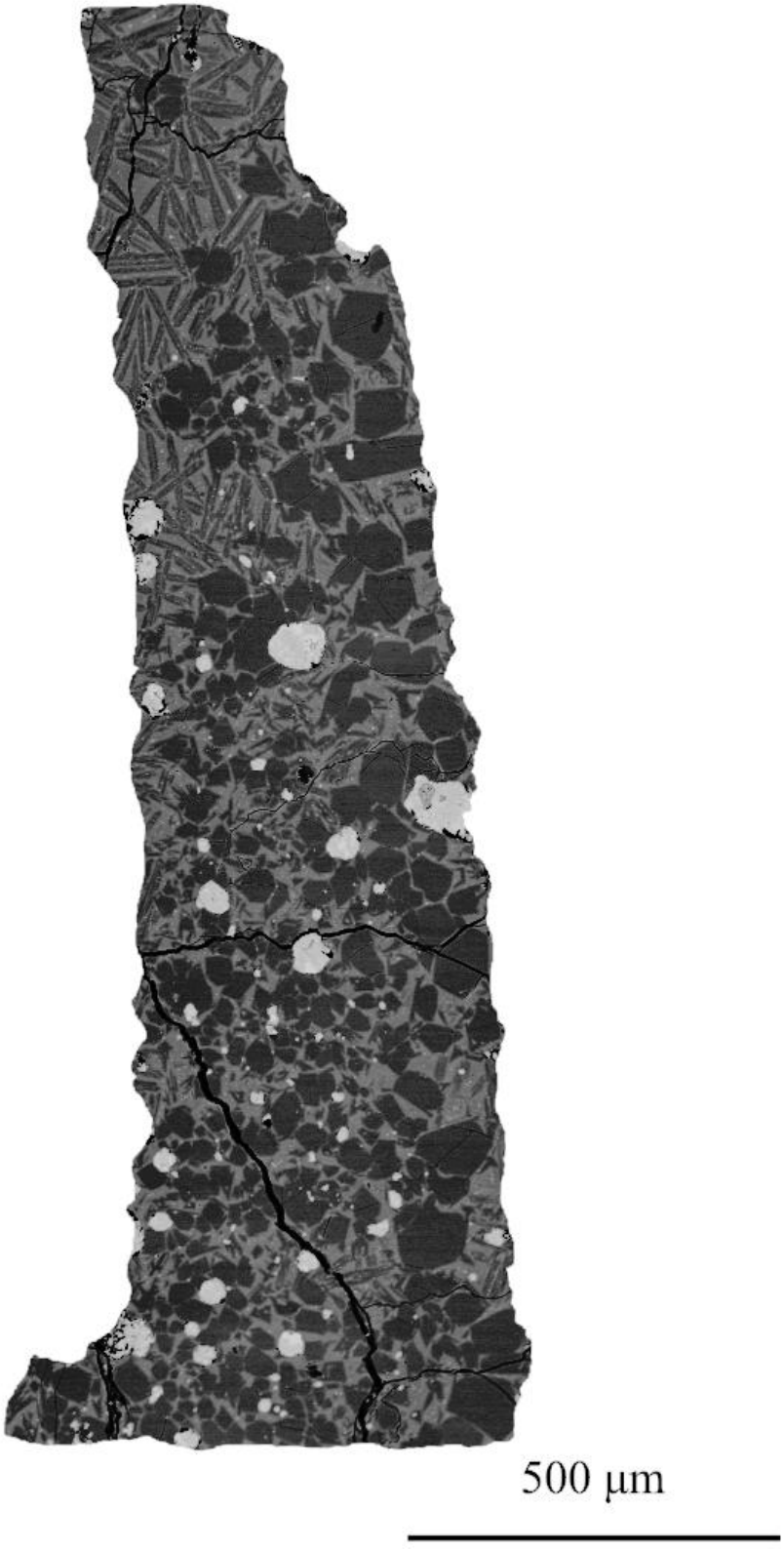

T (°C)	1700	**Run**	**A259**
P (GPa)	1.5	**Si**	24.92
Starting composition	Mer15(10) + 16.7% FeS	**Ti**	0.14
Duration (hrs)	01:00	**Al**	3.94
Silicate Phases (wt%)	Gl (57) Ol (43)	**Fe**	0.37
		Mn	0.18
		Mg	20.04
		Ca	2.28
		Na	1.16
		K	0.14
		S	2.93
		Cr	< dl
		O*	46.86
		Tot	102.98

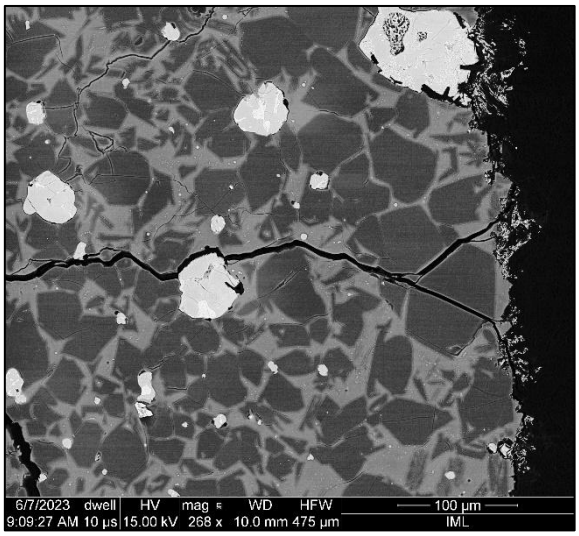

A262

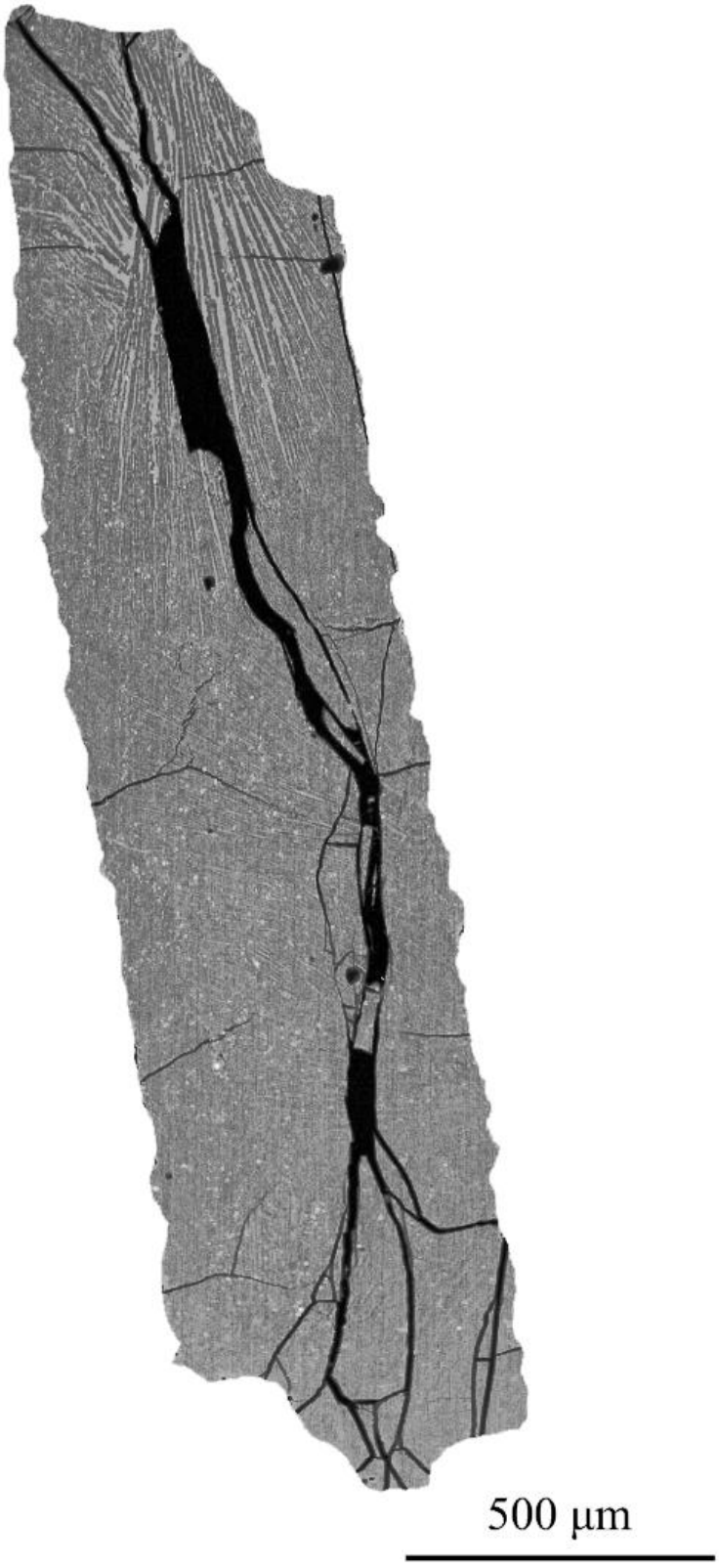

T (°C)	1800	**Run**	**A262**
P (GPa)	1.5	**Si**	26.02
Starting composition	Mer8(10)	**Ti**	0.11
Duration (hrs)	00:30	**Al**	2.16
Silicate Phases (wt%)	Gl (100)	**Fe**	
		Mn	0.21
		Mg	22.49
		Ca	1.31
		Na	0.57
		K	0.11
		S	
		Cr	< dl
		O*	47.34
		Tot	100.32

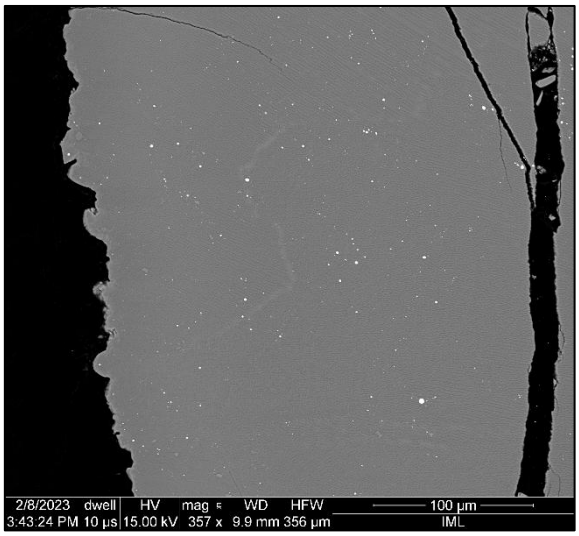

A263

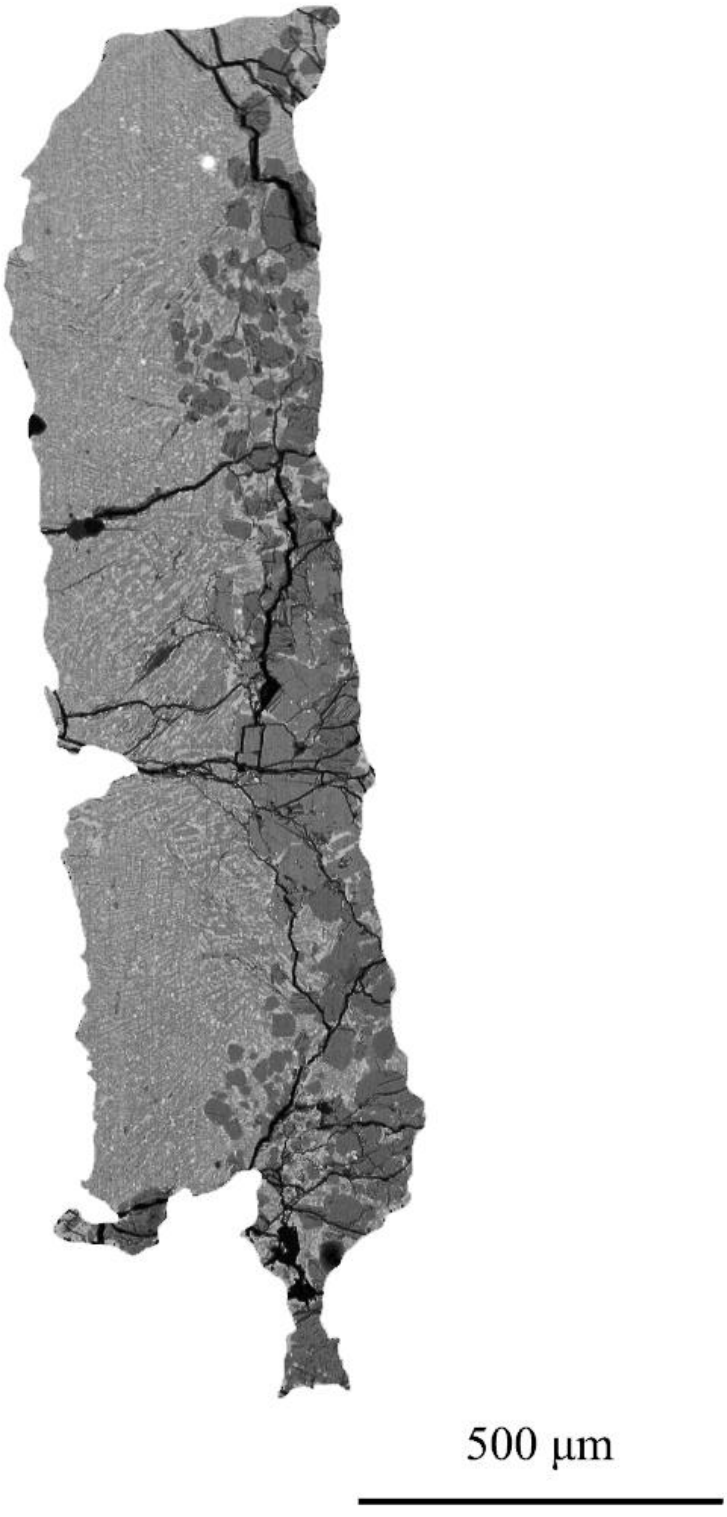

T (°C)	1700	**Run**	**A263**
P (GPa)	1.5	**Si**	27.00
Starting composition	Mer8(10)	**Ti**	0.14
Duration (hrs)	01:00	**Al**	2.45
Silicate Phases (wt%)	Gl (79) Ol (13) Opx (8)	**Fe**	

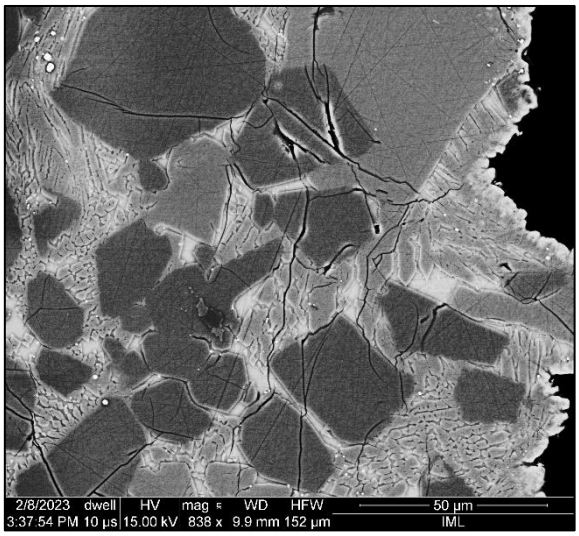

Mn	0.22
Mg	20.90
Ca	1.57
Na	0.39
K	0.12
S	
Cr	0.19
O*	47.80
Tot	100.70

A265

T (°C)	1700	**Run**	**A265**
P (GPa)	1.5	**Si**	27.14
Starting composition	Mer15(10)	**Ti**	0.23
Duration (hrs)	01:00	**Al**	6.33
Silicate Phases (wt%)	Gl (34) Ol (61) Opx (5)	**Fe**	
		Mn	0.37
		Mg	12.83
		Ca	4.18
		Na	1.06
		K	0.20
		S	
		Cr	< dl
		O*	47.49
		Tot	99.81

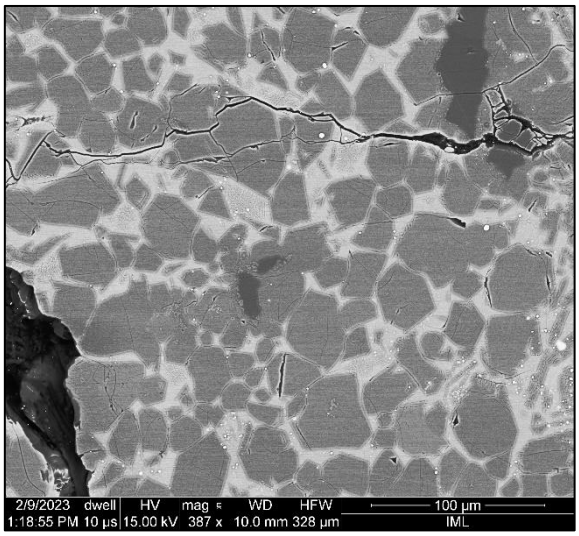

A268

T (°C)	1650	**Run**	**A268**
P (GPa)	1.5	**Si**	26.20
Starting composition	Mer8(10) + 16.7% FeS	**Ti**	0.12
Duration (hrs)	02:30	**Al**	2.51
Silicate Phases (wt%)	Gl (78) Ol (10) Opx (12)	**Fe**	0.56
		Mn	0.18
		Mg	20.94
		Ca	1.40
		Na	0.85
		K	0.13
		S	2.66
		Cr	< dl
		O*	47.17
		Tot	102.73

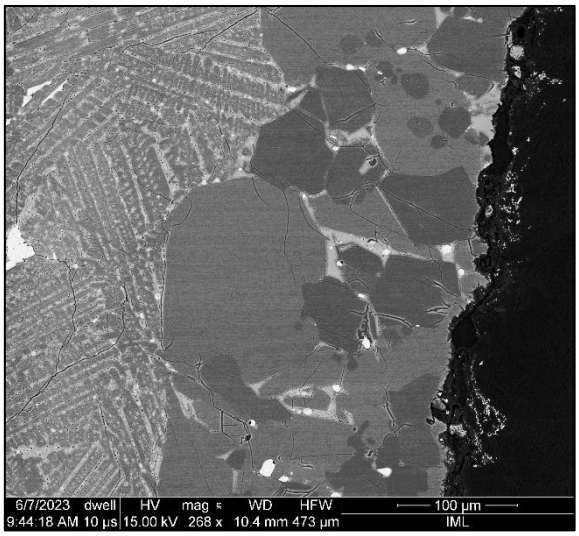

A273

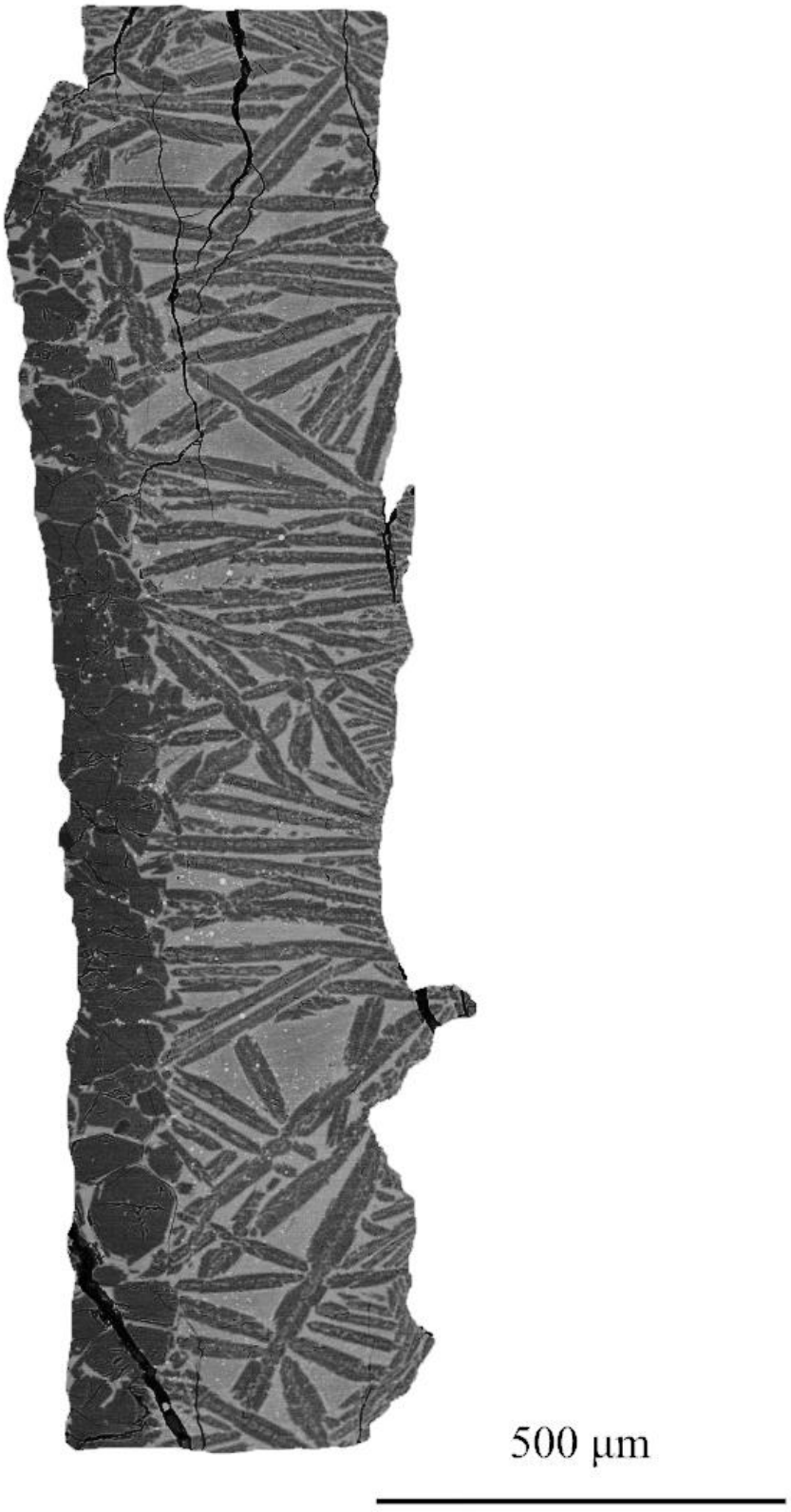

T (°C)	1900	**Run**	**A273**
P (GPa)	1.5	**Si**	25.18
Starting composition	Mer15(10)	**Ti**	0.15
Duration (hrs)	00:30	**Al**	4.27
Silicate Phases (wt%)	Gl (58) Ol (42)	**Fe**	
		Mn	0.28
		Mg	21.51
		Ca	2.39
		Na	0.09
		K	0.14
		S	
		Cr	0.11
		O*	47.92
		Tot	102.05

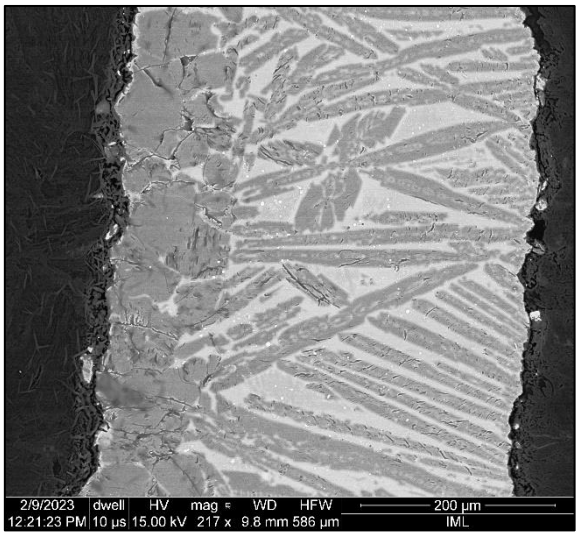

A279

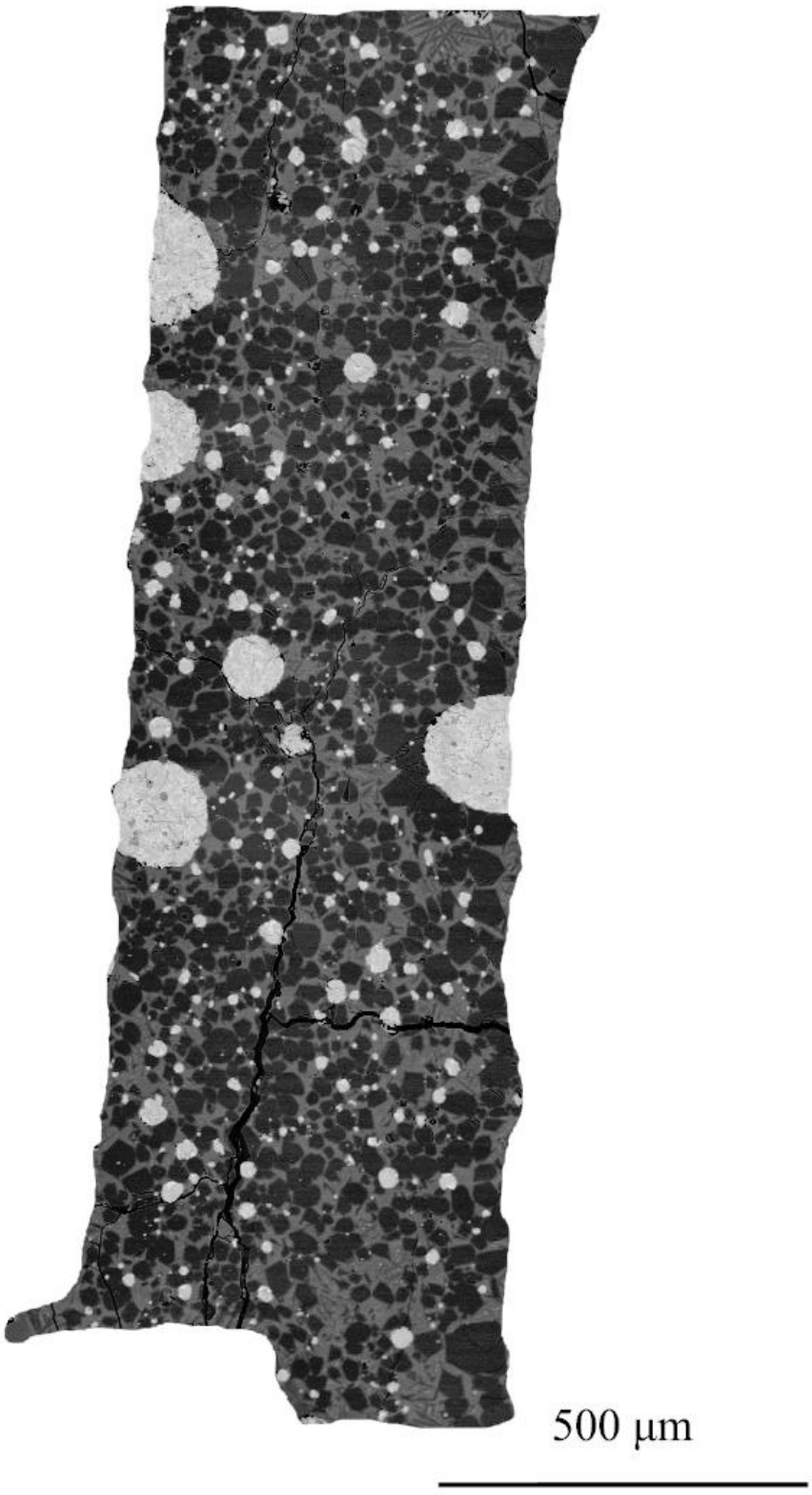

T (°C)	1600	**Run**	**A279**
P (GPa)	1.5	**Si**	26.87
Starting composition	Mer15(10) + 16.7% FeS	**Ti**	0.14
Duration (hrs)	03:00	**Al**	5.70
Silicate Phases (wt%)	Gl (39) Ol (61)	**Fe**	0.32
		Mn	0.13
		Mg	13.06
		Ca	3.86
		Na	1.84
		K	0.23
		S	3.84
		Cr	< dl
		O*	47.01
		Tot	103.02

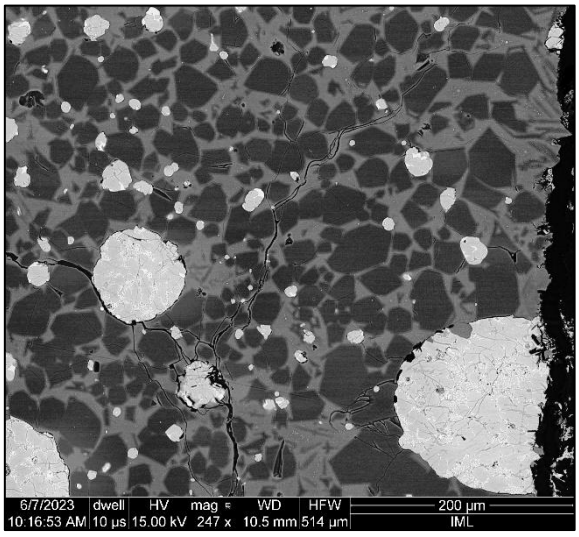

A282

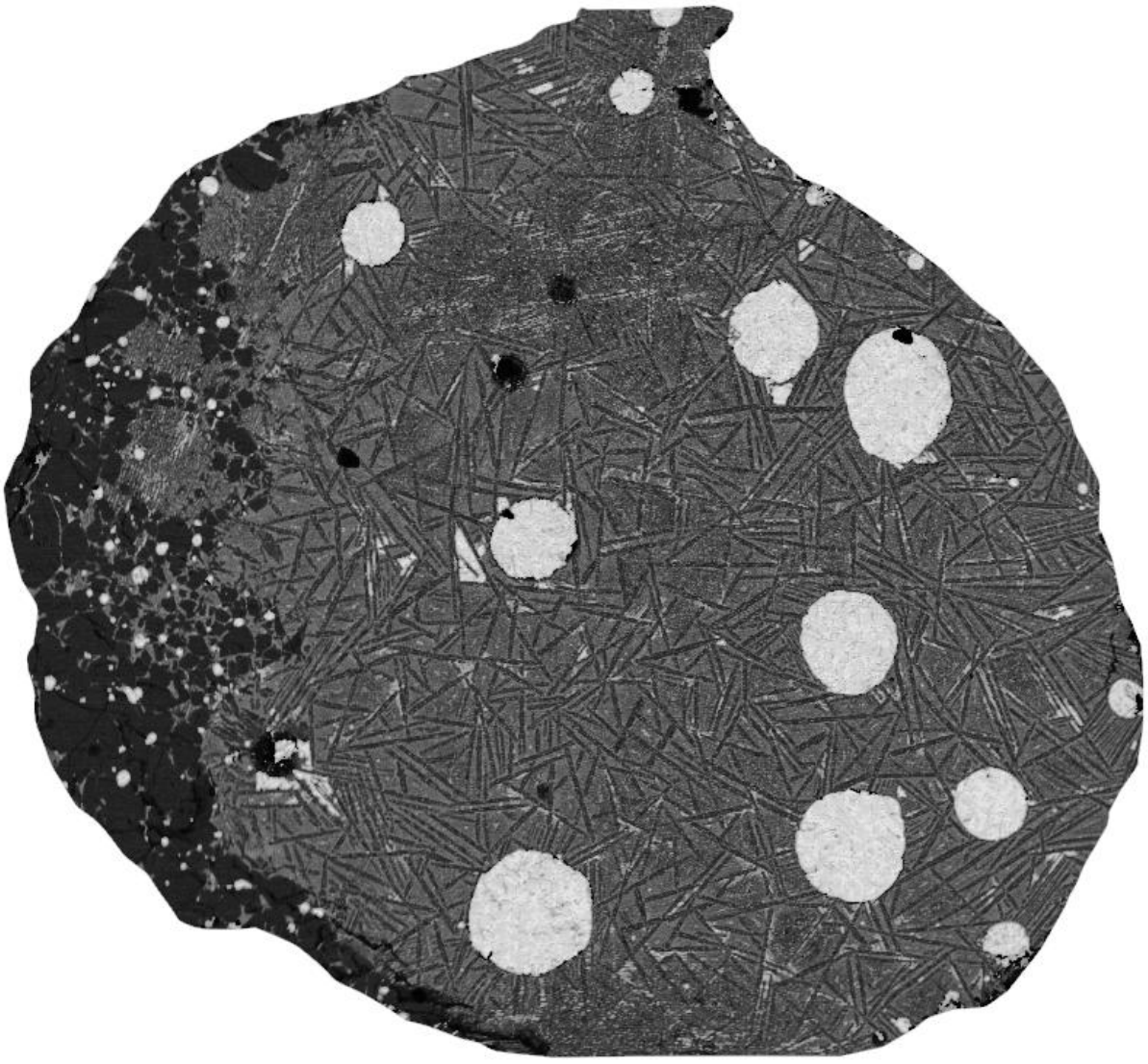

500 μm

T (°C)	1800	**Run**	**A282**
P (GPa)	3.0	**Si**	25.45
Starting composition	Mer15(10) + 16.7% FeS	**Ti**	0.17
Duration (hrs)	01:20	**Al**	4.42
Silicate Phases (wt%)	Gl (48) Ol (52)	**Fe**	0.66
		Mn	0.18
		Mg	17.43
		Ca	2.66
		Na	1.22
		K	0.16
		S	2.28
		Cr	< dl
		O*	46.45
		Tot	101.07

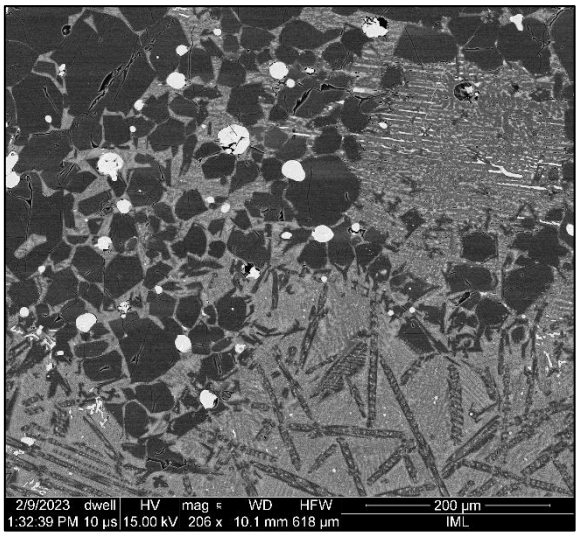

A290

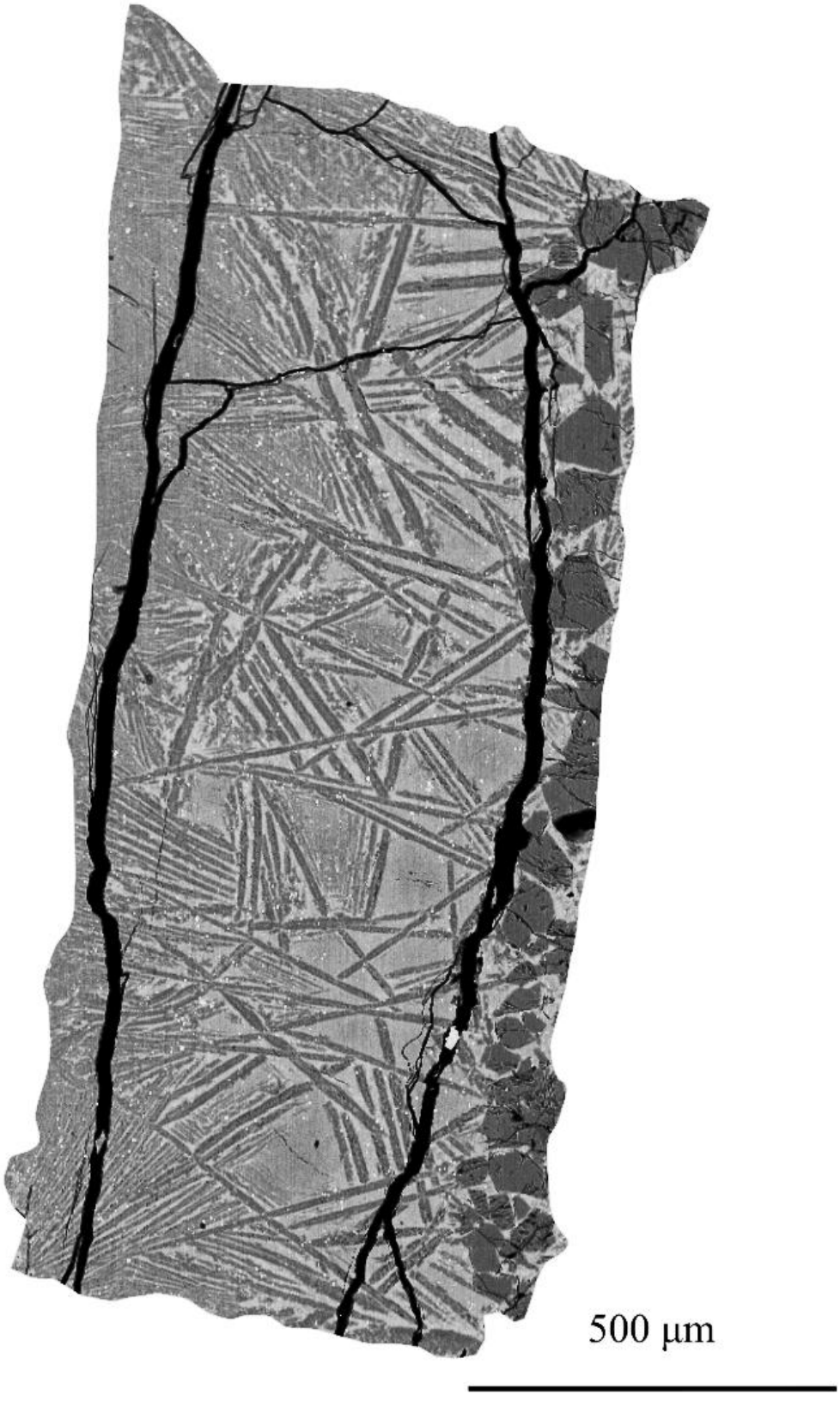

T (°C)	1750	**Run**	**A290**
P (GPa)	1.5	**Si**	26.60
Starting composition	Mer8(10)	**Ti**	0.12
Duration (hrs)	01:00	**Al**	2.19
Silicate Phases (wt%)	Gl (93) Ol (7)	**Fe**	
		Mn	0.20
		Mg	22.30
		Ca	1.31
		Na	0.33
		K	0.10
		S	
		Cr	0.20
		O*	47.90
		Tot	101.20

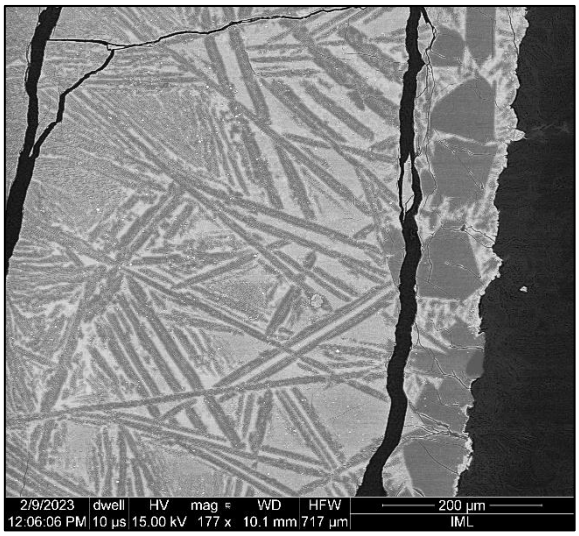

A294

T (°C)	1600	**Run**	**A294**
P (GPa)	1.5	**Si**	27.06
Starting composition	Mer15(10)	**Ti**	0.17
Duration (hrs)	06:00	**Al**	8.37
Silicate Phases (wt%)	Gl (24) Ol (61) Opx (15) Cpx (x)	**Fe**	

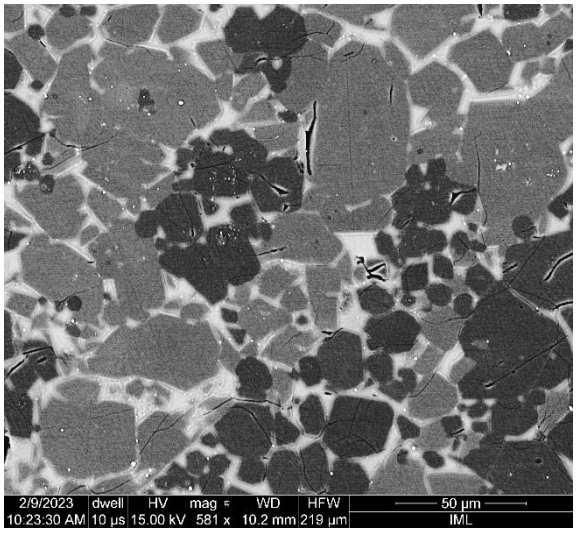

Mn	0.30
Mg	11.57
Ca	5.95
Na	0.13
K	0.37
S	
Cr	< dl
O*	48.62
Tot	102.55

A296

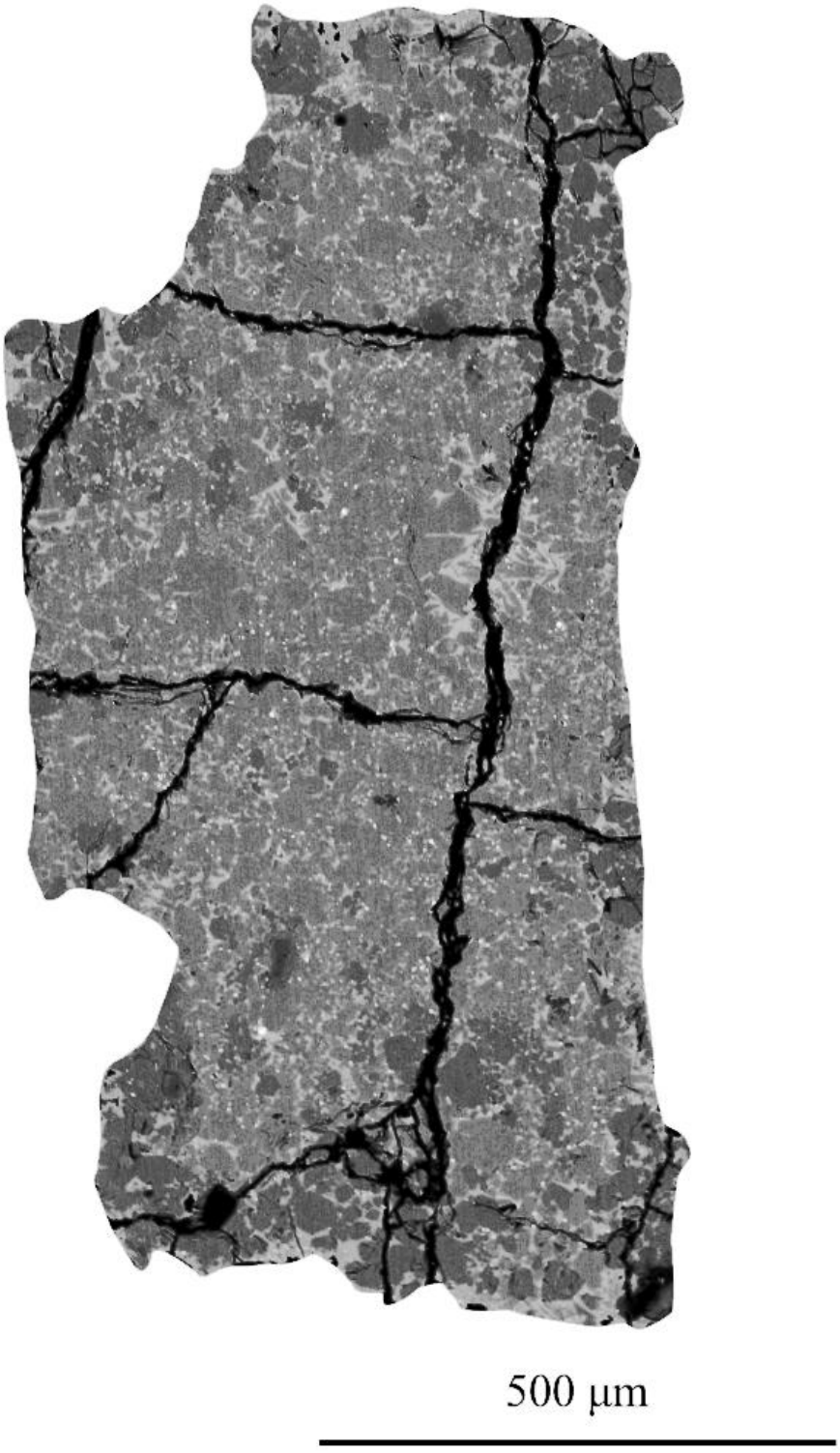

T (°C)	1600	**Run**	**A296**
P (GPa)	1.5	**Si**	
Starting composition	Mer8(10)	**Ti**	
Duration (hrs)	03:00	**Al**	
Silicate Phases (wt%)	Gl (<15) Ol () Opx () Cpx ()	**Fe**	
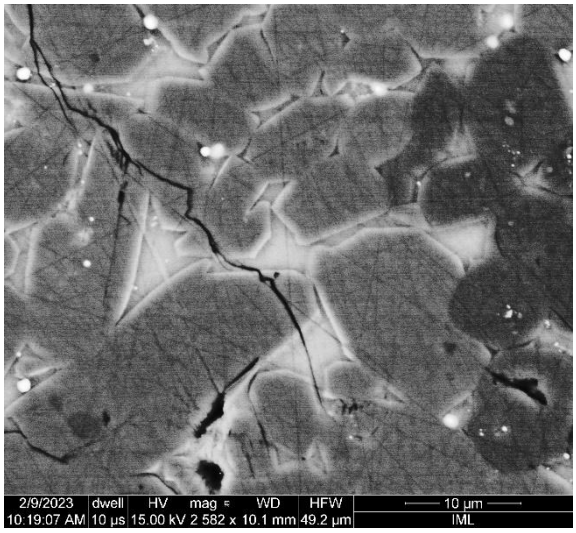		**Mn**	
		Mg	
		Ca	
		Na	
		K	
		S	
		Cr	
		O*	
		Tot	

A297

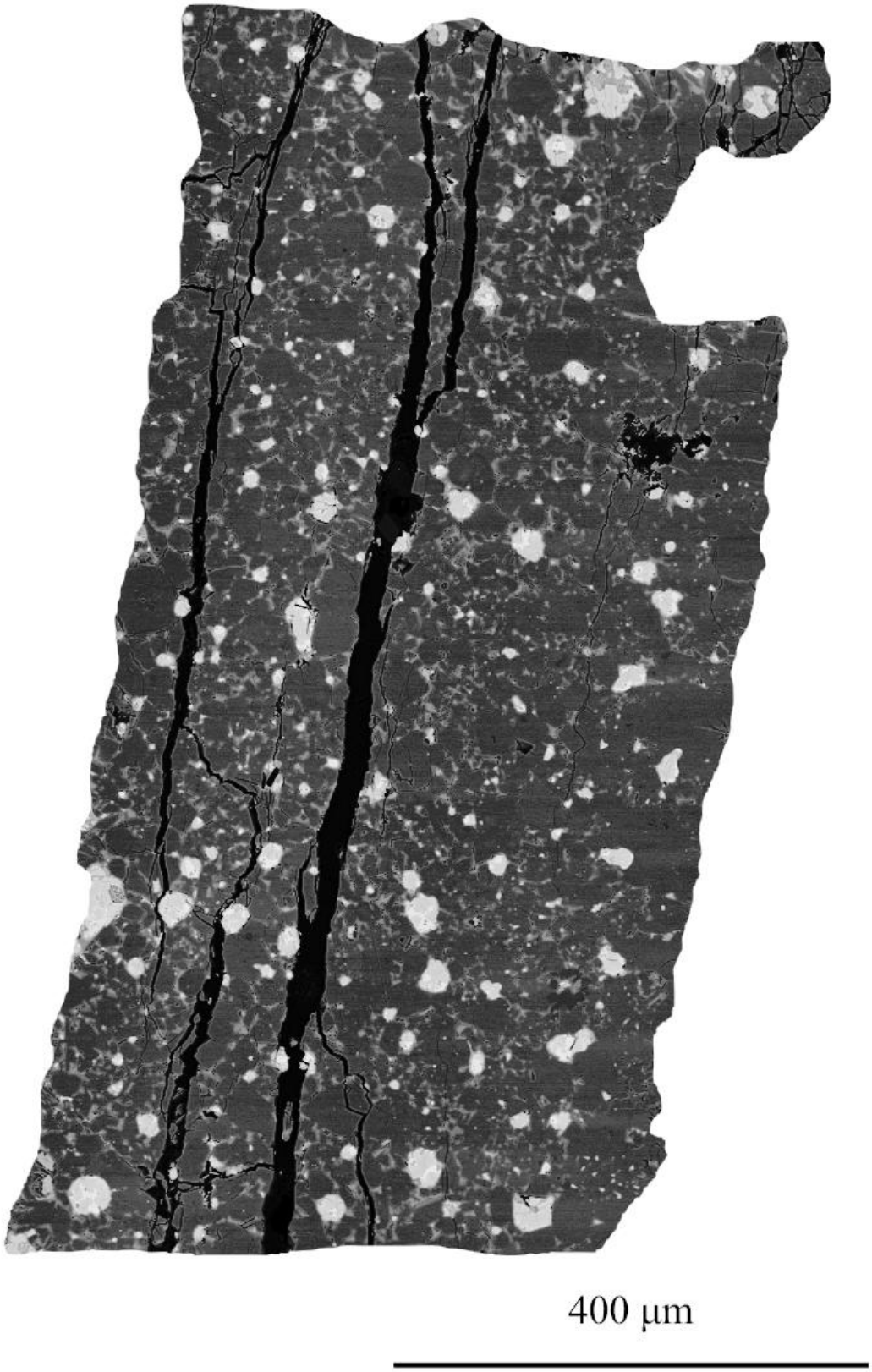

T (°C)	1700	**Run**	**A297**
P (GPa)	3.0	**Si**	
Starting composition	Mer8(10) + 16.7% FeS	**Ti**	
Duration (hrs)	01:50	**Al**	
Silicate Phases (wt%)	Gl (<20) Ol () Opx ()	**Fe**	
		Mn	
		Mg	
		Ca	
		Na	
		K	
		S	
		Cr	
		O*	
		Tot	

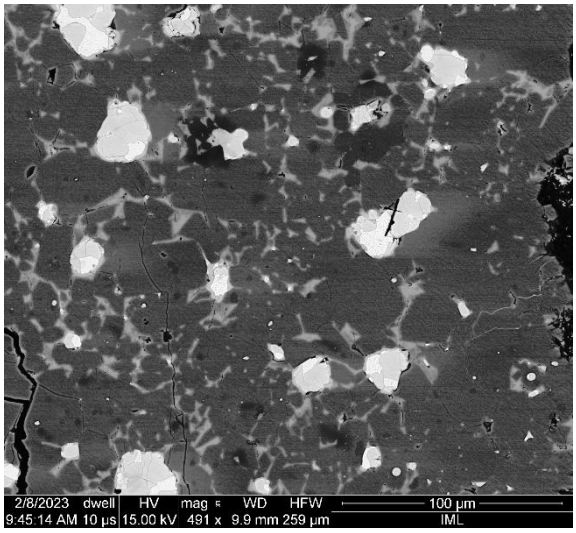

A302

T (°C)	1700	**Run**	**A302**
P (GPa)	3.0	**Si**	
Starting composition	Mer8(10)	**Ti**	
Duration (hrs)	01:50	**Al**	
Silicate Phases (wt%)	Gl () Ol () Opx () Cpx ()	**Fe**	
		Mn	
		Mg	
		Ca	
		Na	
		K	
		S	
		Cr	
		O*	
		Tot	

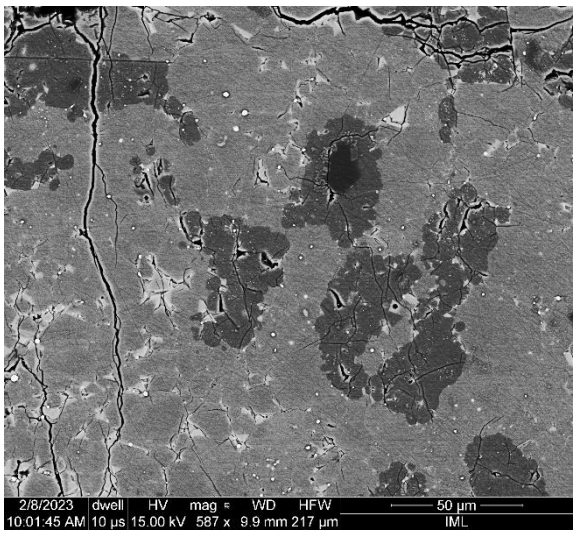

A303

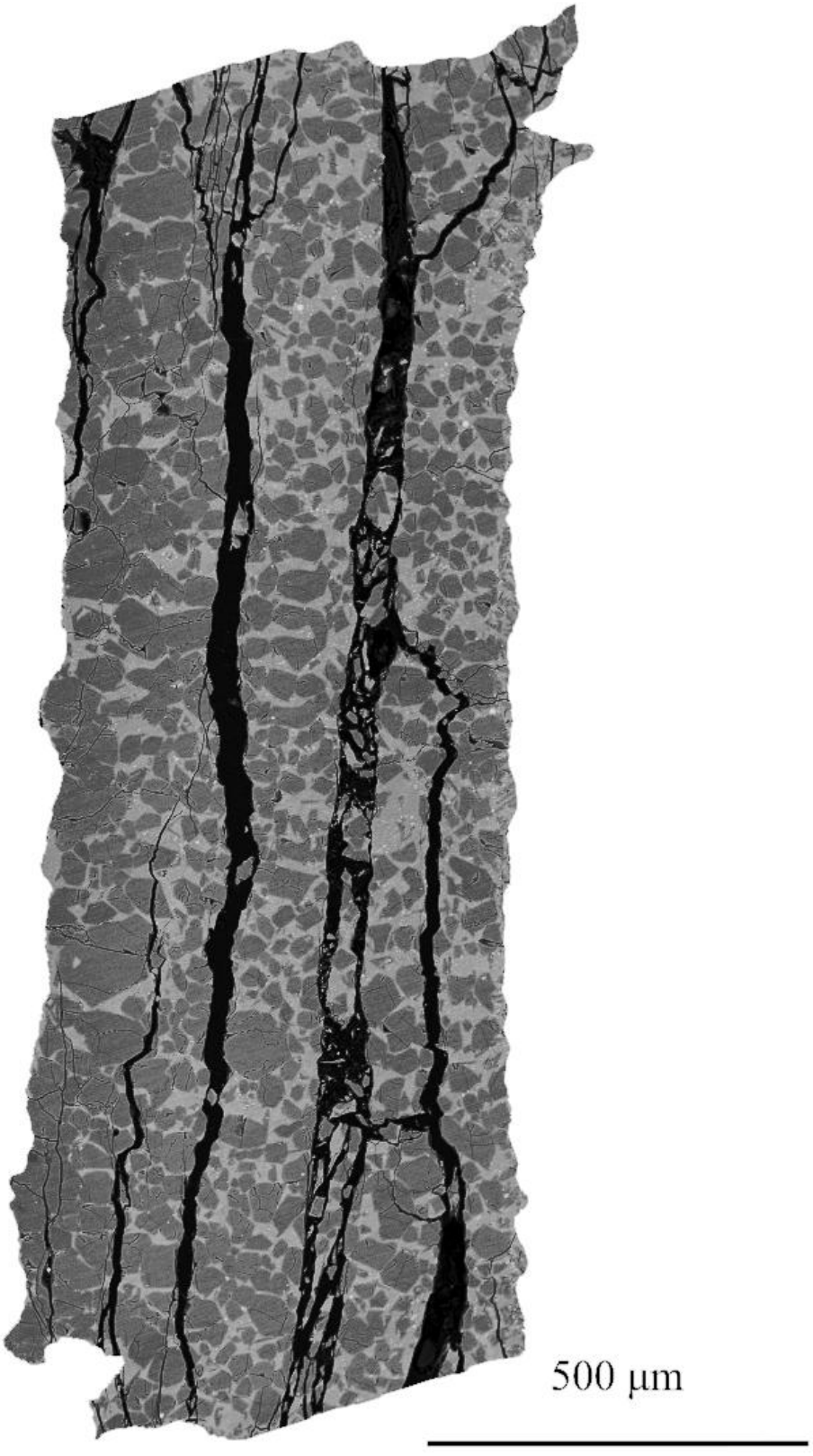

T (°C)	1800	**Run**	**A303**
P (GPa)	3.0	**Si**	28.22
Starting composition	Mer15(10)	**Ti**	0.22
Duration (hrs)	01:20	**Al**	6.79
Silicate Phases (wt%)	Gl (35) Ol (65)	**Fe**	
		Mn	0.34
		Mg	12.11
		Ca	4.25
		Na	0.87
		K	0.30
		S	
		Cr	0.14
		O*	48.66
		Tot	101.88

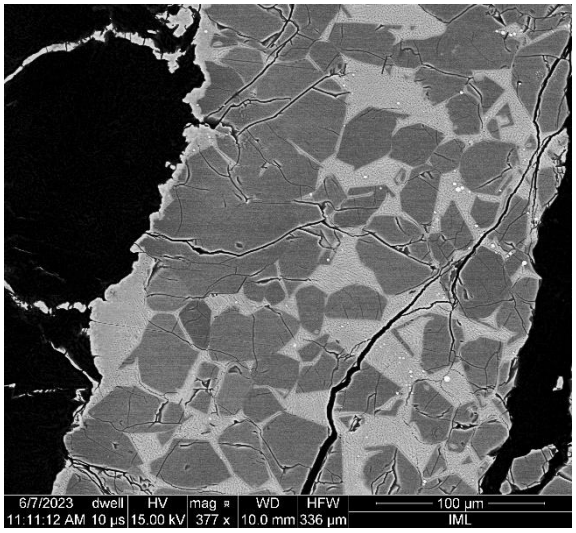

A304

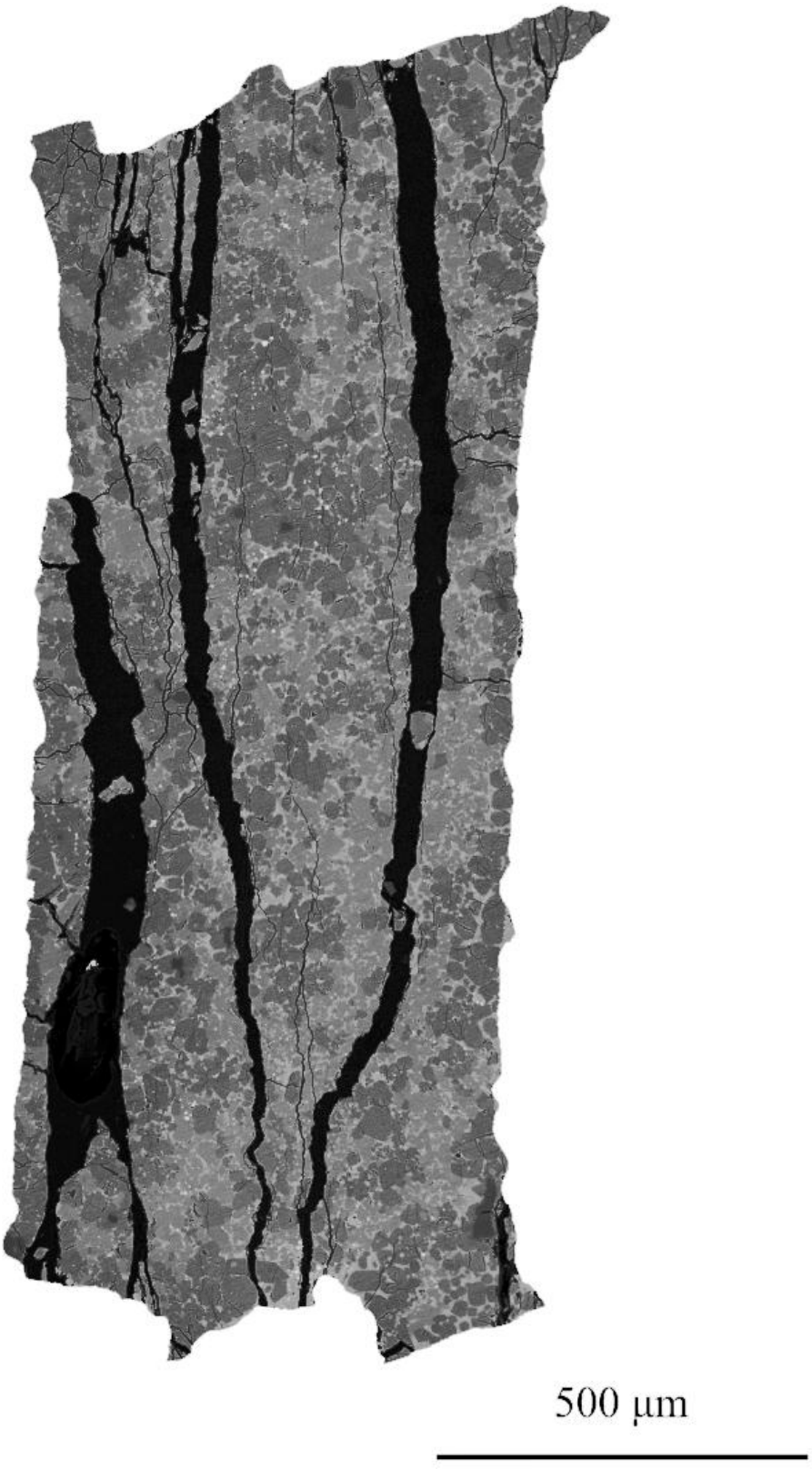

T (°C)	1700	**Run**	**A304**
P (GPa)	3.0	**Si**	24.23
Starting composition	Mer15(10)	**Ti**	0.21
Duration (hrs)	01:50	**Al**	8.19
Silicate Phases (wt%)	Gl (20) Ol (51) Opx (29) Cpx (x)	**Fe**	
		Mn	0.30
		Mg	13.27
		Ca	6.42
		Na	0.88
		K	0.31
		S	
		Cr	0.10
		O*	46.96
		Tot	100.86

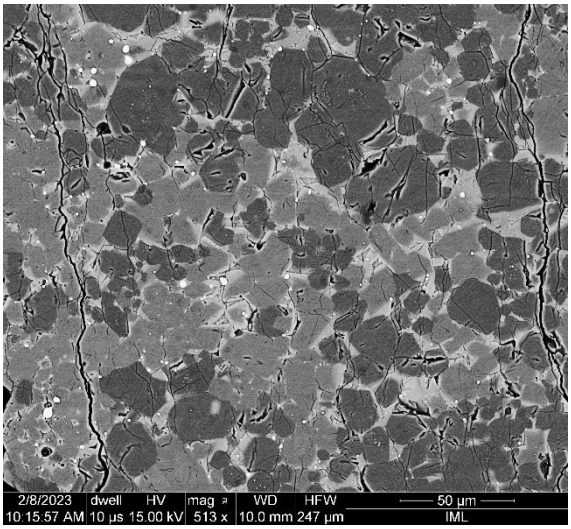

A305

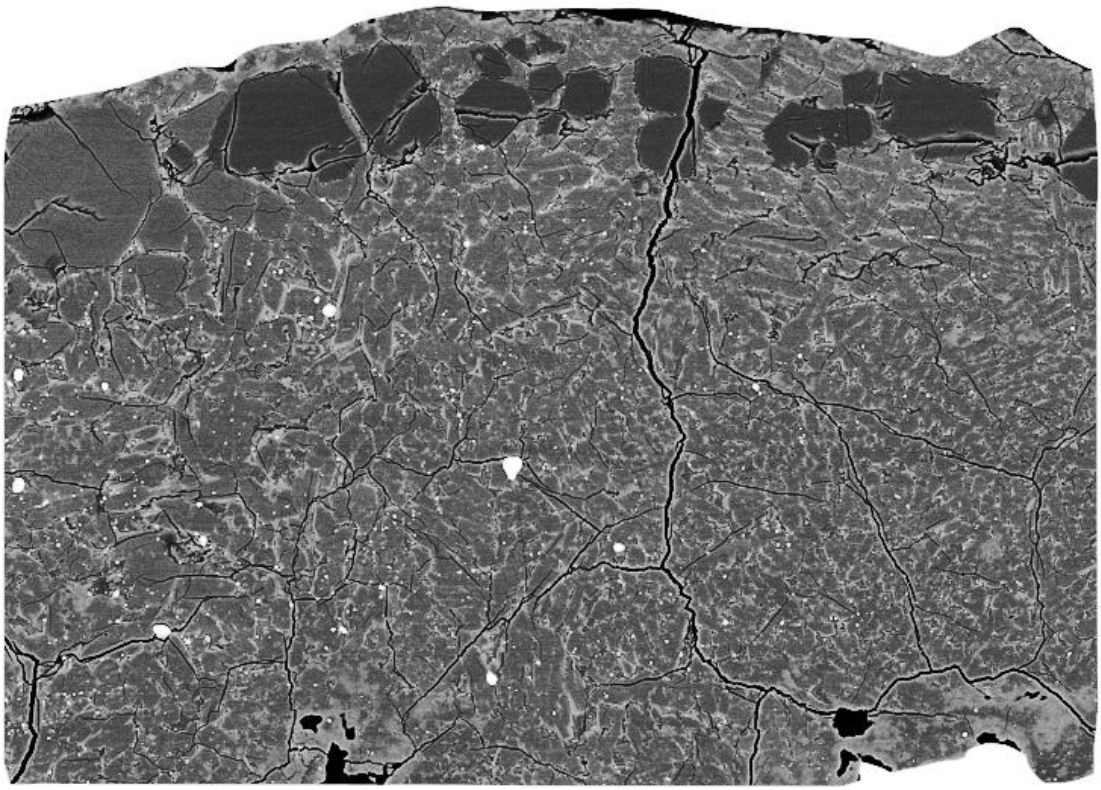

100 μm

T (°C)	1800	**Run**	**A305**
P (GPa)	3.0	**Si**	26.05
Starting composition	Mer8(10)	**Ti**	0.14
Duration (hrs)	01:20	**Al**	3.16
Silicate Phases (wt%)	Gl (50) Ol (10) Opx (41) Cpx (x)	**Fe**	
		Mn	0.21
		Mg	20.63
		Ca	1.99
		Na	0.57
		K	0.14
		S	
		Cr	0.10
		O*	47.37
		Tot	100.37

A306

T (°C)	1700	**Run**	**A306**
P (GPa)	3.0	**Si**	25.66
Starting composition	Mer15(10) + 16.7% FeS	**Ti**	< dl
Duration (hrs)	01:55	**Al**	6.04
Silicate Phases (wt%)	Gl (35) Ol (54) Opx (12)	**Fe**	0.36
		Mn	< dl
		Mg	15.05
		Ca	4.03
		Na	1.58
		K	0.19
		S	2.10
		Cr	< dl
		O*	47.11
		Tot	102.21

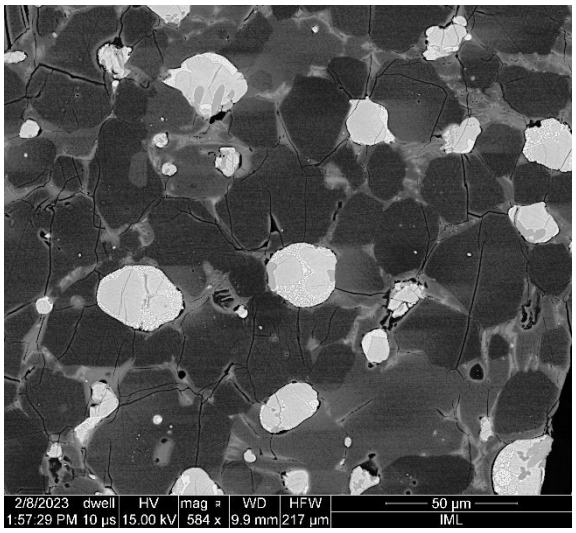

A307

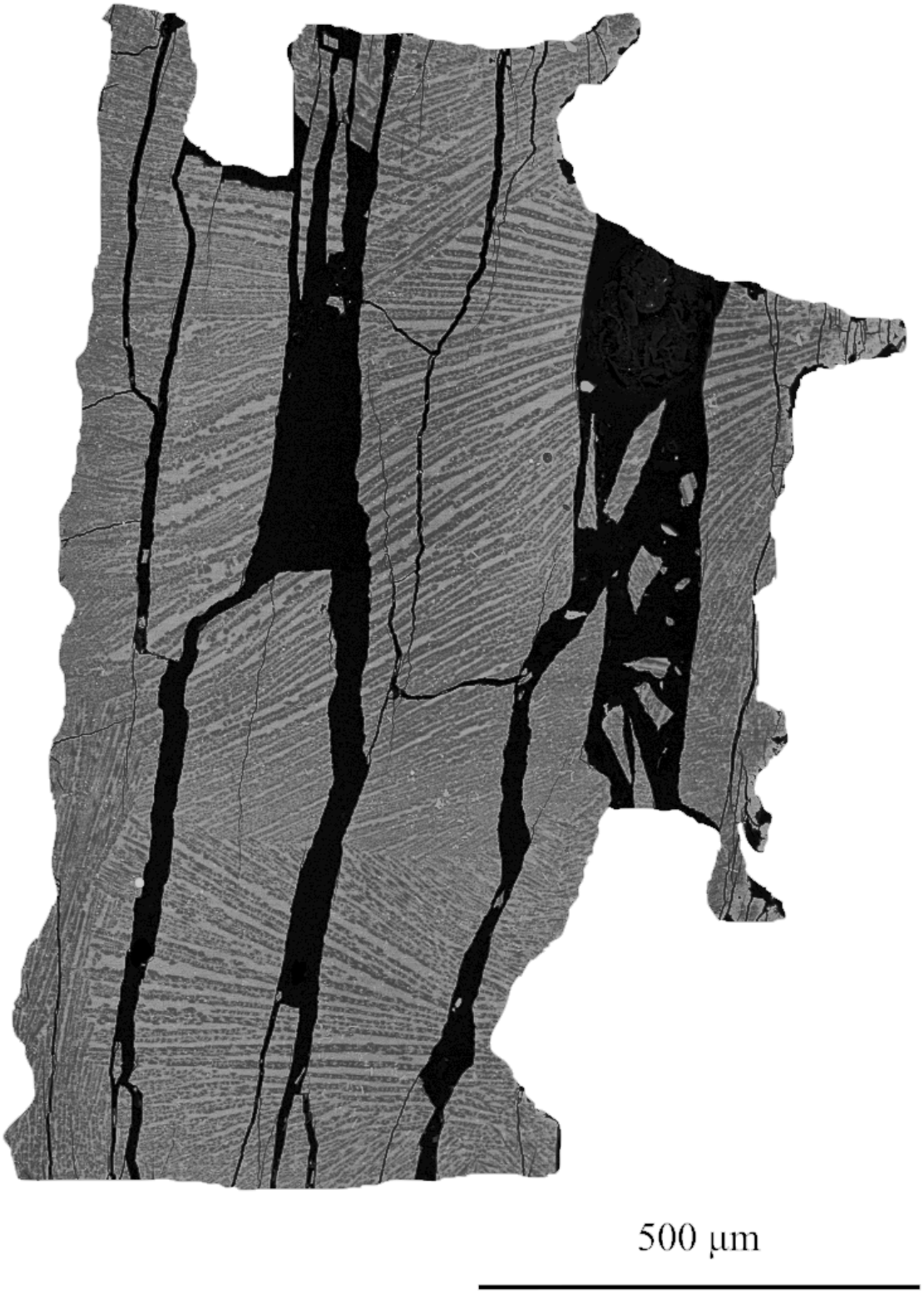

T (°C)	1900	**Run**	**A307**
P (GPa)	3.0	**Si**	26.58
Starting composition	Mer8(10)	**Ti**	0.12
Duration (hrs)	01:00	**Al**	2.27
Silicate Phases (wt%)	Gl (100)	**Fe**	
		Mn	0.20
		Mg	22.79
		Ca	1.35
		Na	0.38
		K	0.08
		S	
		Cr	< dl
		O*	48.20
		Tot	101.98

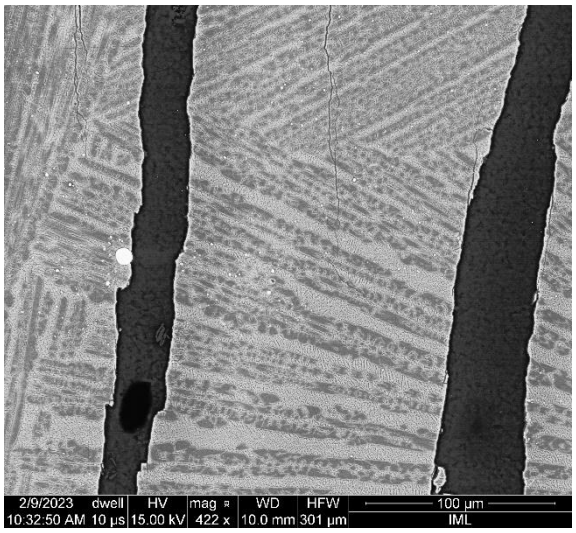

A308

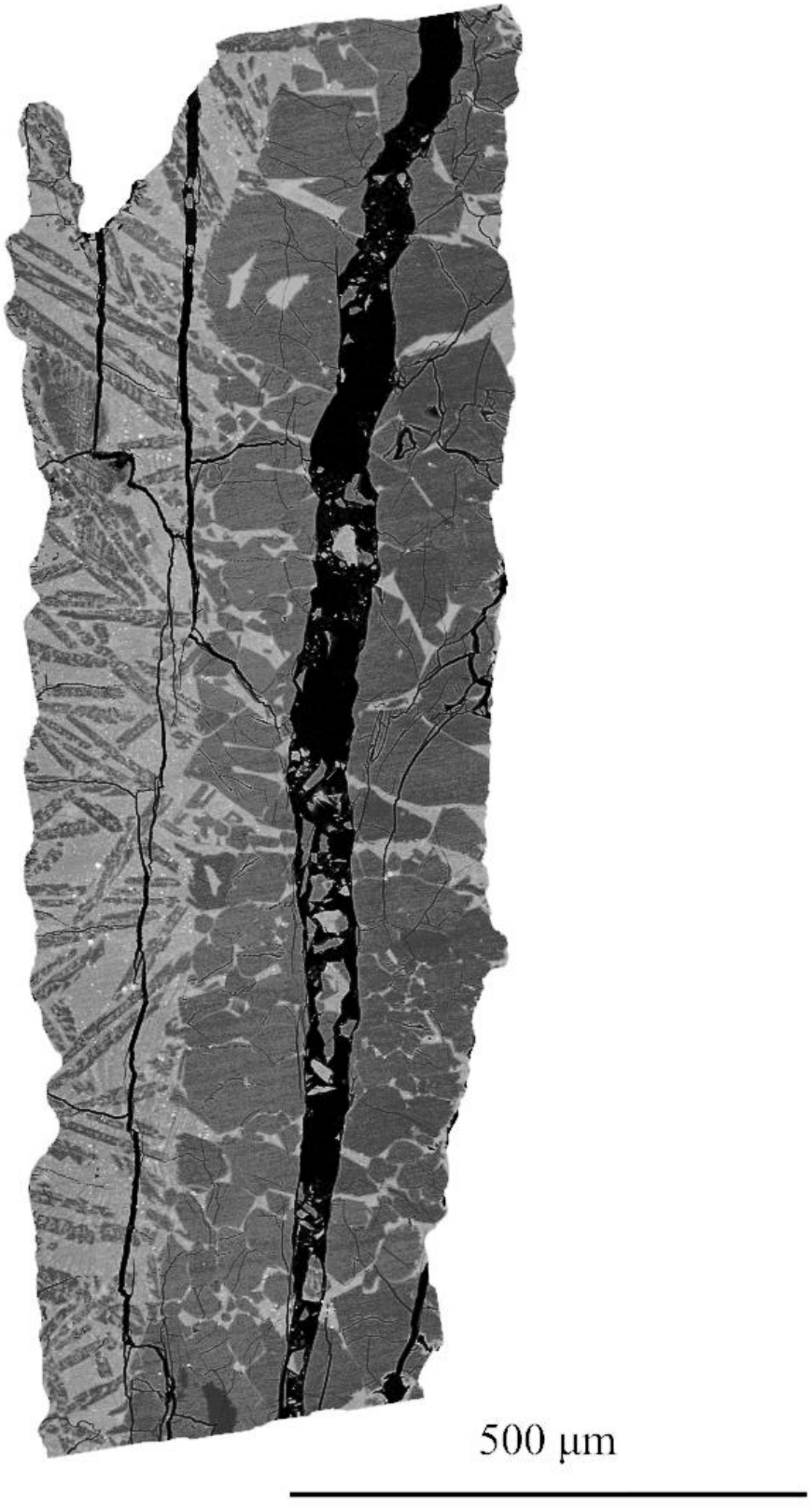

T (°C)	1900	**Run**	**A308**
P (GPa)	3.0	**Si**	27.70
Starting composition	Mer15(10)	**Ti**	0.22
Duration (hrs)	01:00	**Al**	5.89
Silicate Phases (wt%)	Gl (39) Ol (61)	**Fe**	
		Mn	0.29
		Mg	14.93
		Ca	3.57
		Na	0.52
		K	0.17
		S	
		Cr	< dl
		O*	48.58
		Tot	101.87

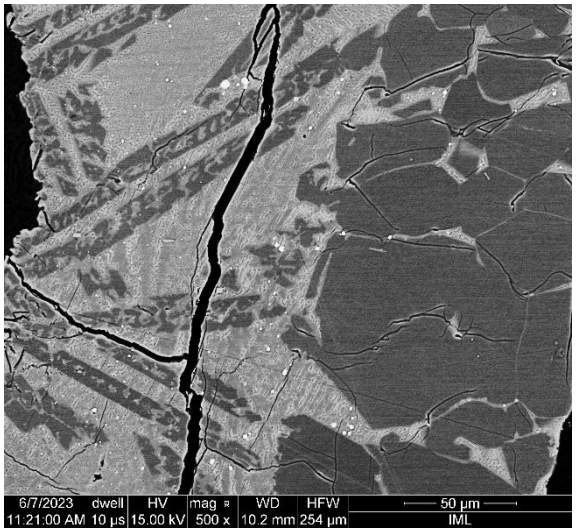

A309

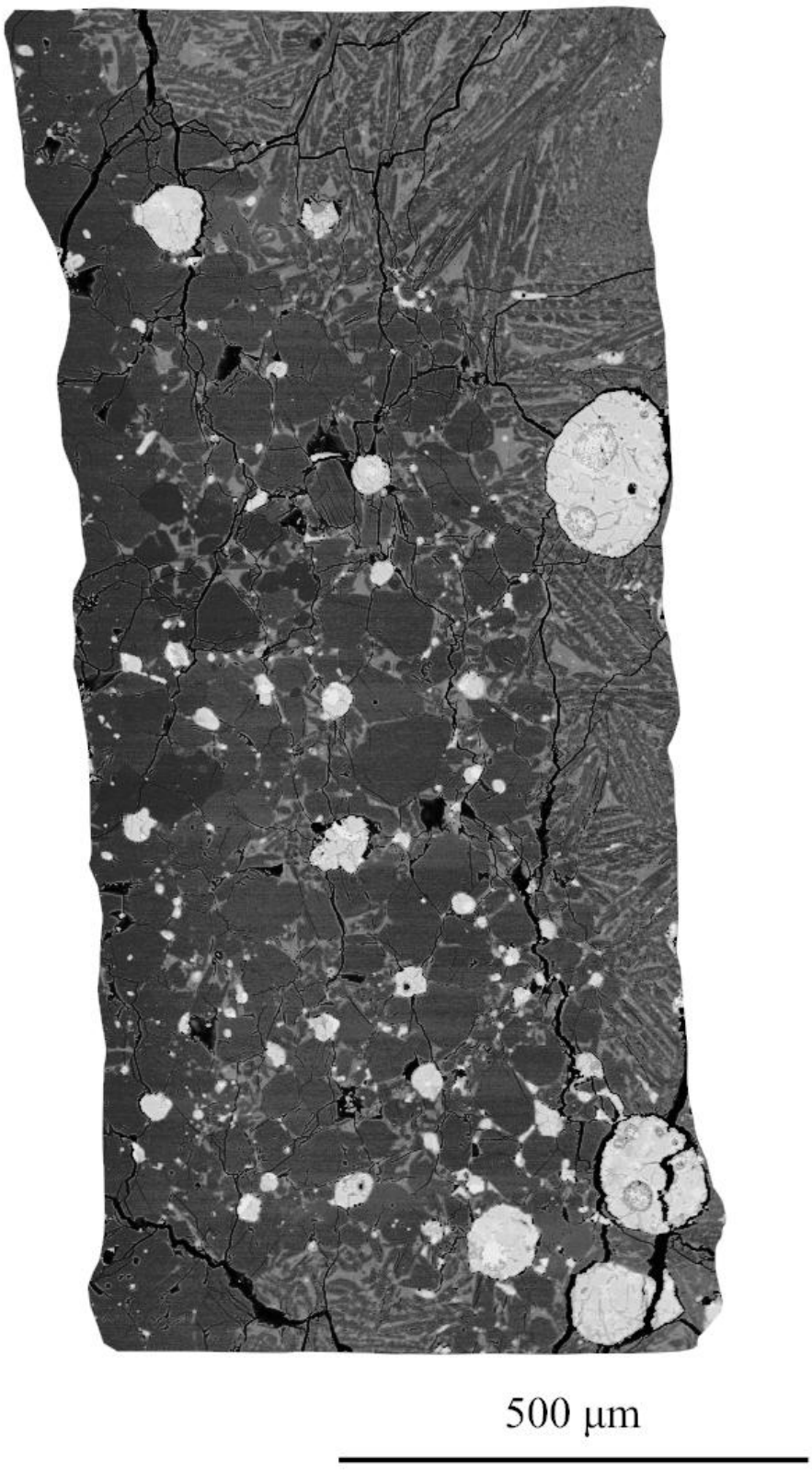

T (°C)	1625	**Run**	**A309**
P (GPa)	1.5	**Si**	24.95
Starting composition	Mer8(10) + 16.7% FeS	**Ti**	0.09
Duration (hrs)	02:45	**Al**	3.18
Silicate Phases (wt%)	Gl (53) Ol (8) Opx (39)	**Fe**	0.42
		Mn	0.15
		Mg	20.05
		Ca	1.96
		Na	1.12
		K	0.18
		S	3.79
		Cr	< dl
		O*	46.06
		Tot	101.96

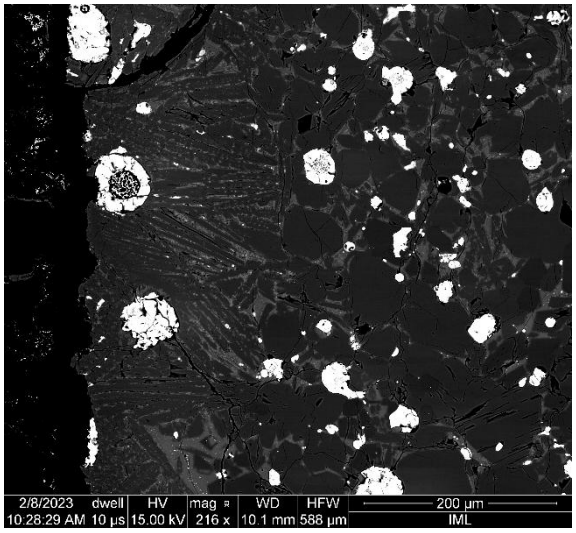

A311

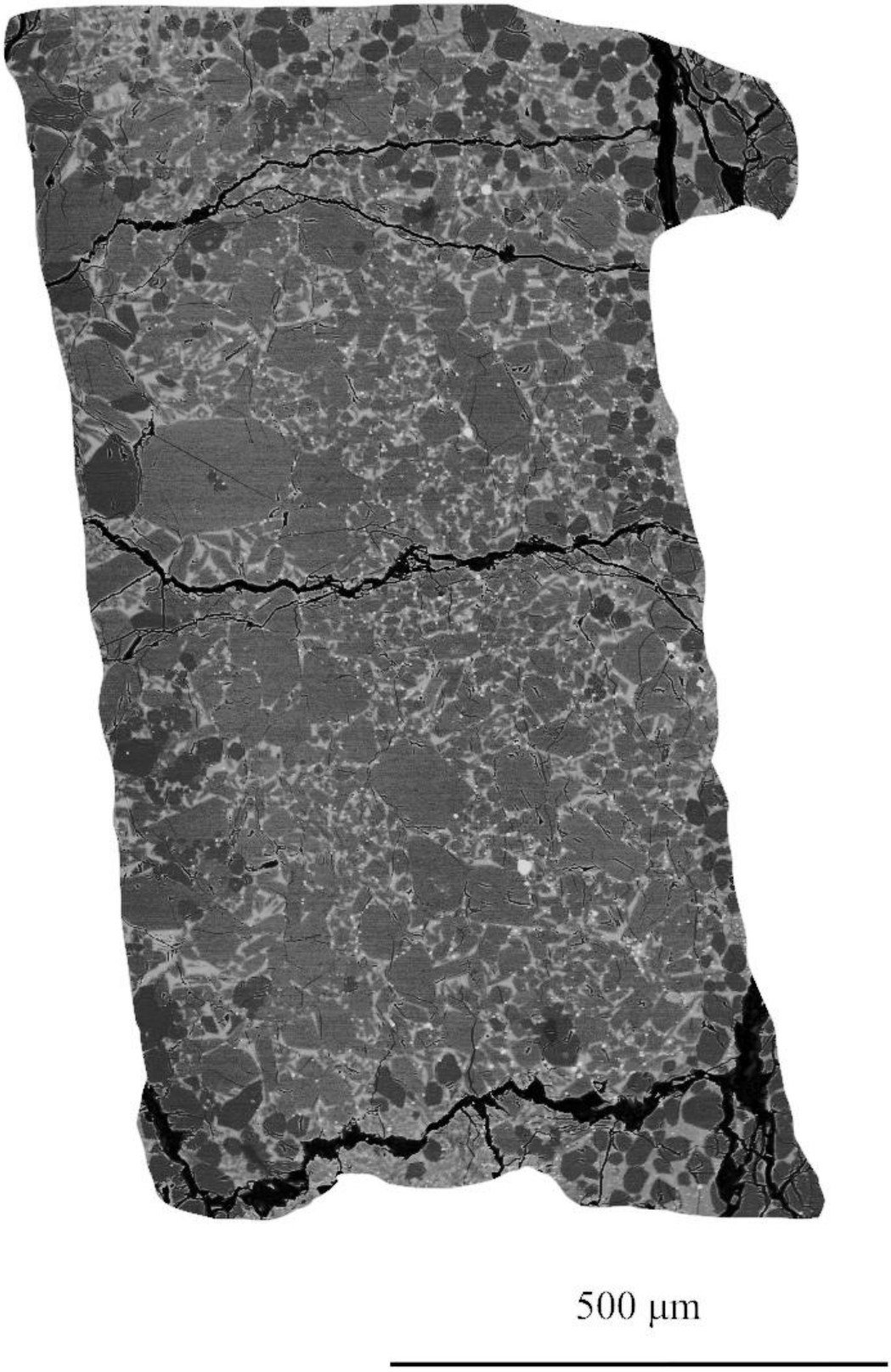

T (°C)	1650	**Run**	**A311**
P (GPa)	1.5	**Si**	24.27
Starting composition	Mer8(10)	**Ti**	< dl
Duration (hrs)	02:00	**Al**	10.53
Silicate Phases (wt%)	Gl (15) Ol (16) Opx (69) Cpx (x)	**Fe**	
		Mn	0.09
		Mg	8.16
		Ca	8.79
		Na	1.32
		K	0.87
		S	
		Cr	< dl
		O*	46.80
		Tot	100.89

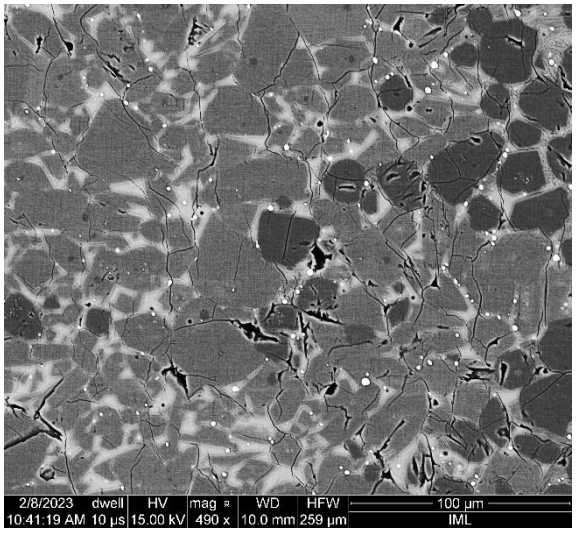

A322

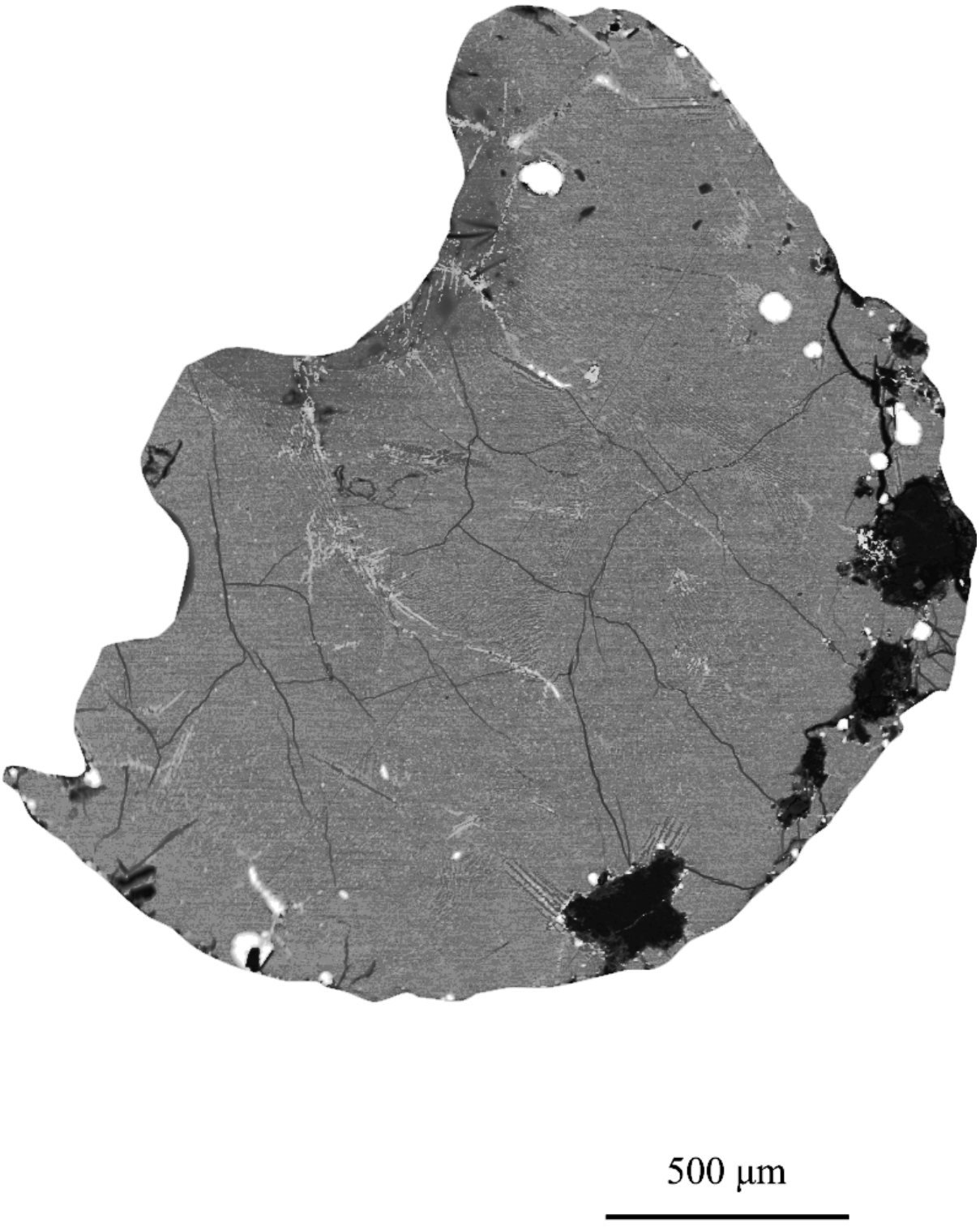

T (°C)	1900	**Run**	**A322**
P (GPa)	3.0	**Si**	25.46
Starting composition	Mer8(20) + 20% FeS	**Ti**	0.12
Duration (hrs)	00:40	**Al**	1.95
Silicate Phases (wt%)	Gl (100)	0.39	0.39
		Mn	0.19
		Mg	21.99
		Ca	1.17
		Na	0.58
		K	0.08
		S	5.12
		Cr	< dl
		O*	46.25
		Tot	103.31

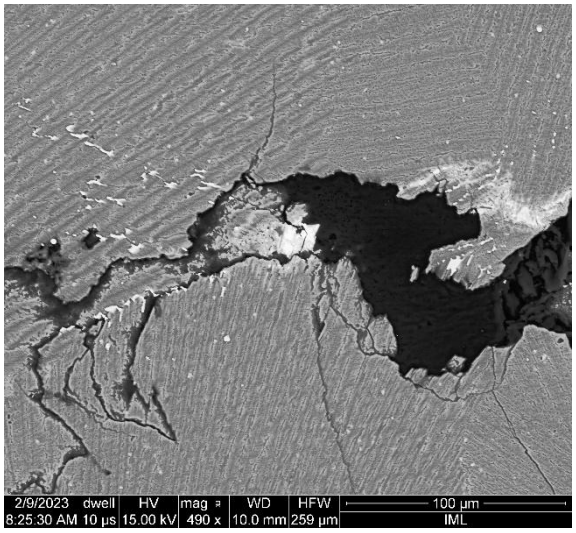

A323

T (°C)	1900	**Run**	**A323**
P (GPa)	3.0	**Si**	22.60
Starting composition	Mer15(20) + 20% FeS	**Ti**	0.10
Duration (hrs)	00:40	**Al**	2.47
Silicate Phases (wt%)	Gl (100)	**Fe**	0.48
		Mn	0.22
		Mg	24.68
		Ca	1.35
		Na	0.54
		K	0.11
		S	5.50
		Cr	< dl
		O*	45.30
		Tot	103.37

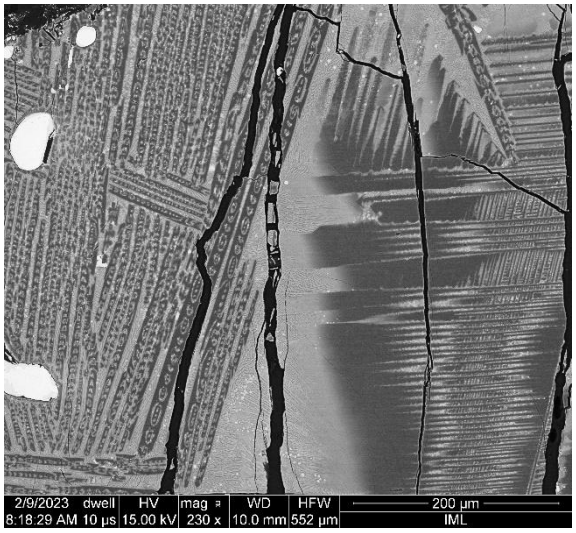

A328

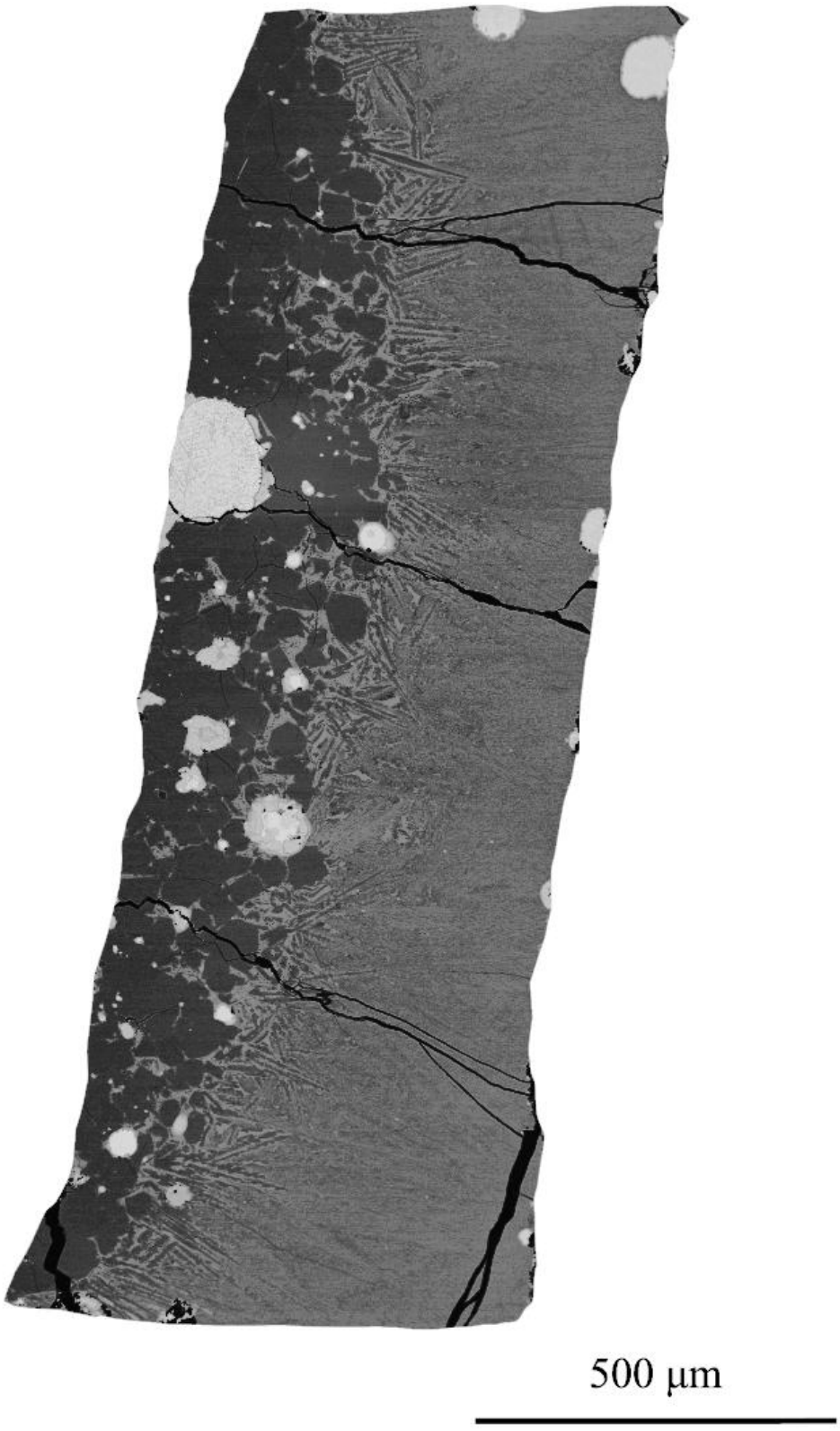

T (°C)	1600	**Run**	**A328**
P (GPa)	1.5	**Si**	24.41
Starting composition	Mer8(20) + 20% FeS	**Ti**	< dl
Duration (hrs)	03:00	**Al**	2.53
Silicate Phases (wt%)	Gl (74) Opx (26)	**Fe**	0.47
		Mn	0.21
		Mg	21.75
		Ca	1.50
		Na	0.64
		K	0.12
		S	6.92
		Cr	< dl
		O*	45.57
		Tot	104.19

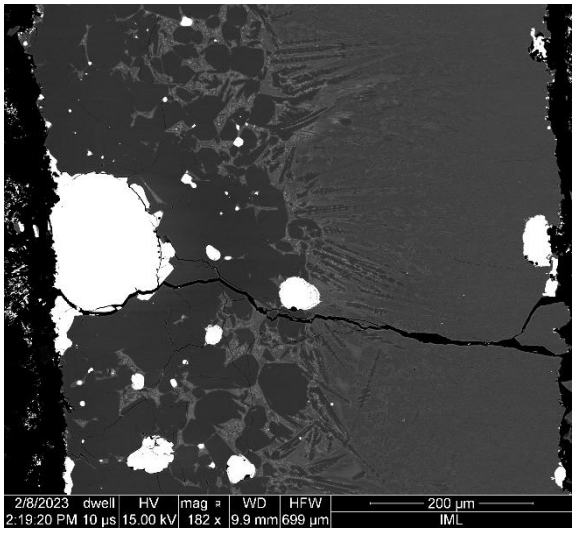

A329

T (°C)	1600	**Run**	**A329**
P (GPa)	1.5	**Si**	23.55
Starting composition	Mer15(20) + 20% FeS	**Ti**	0.08
Duration (hrs)	03:00	**Al**	3.40
Silicate Phases (wt%)	Gl (64) Ol (36)	**Fe**	0.47
		Mn	0.20
		Mg	21.33
		Ca	1.93
		Na	0.59
		K	0.17
		S	6.42
		Cr	< dl
		O*	45.25
		Tot	103.39

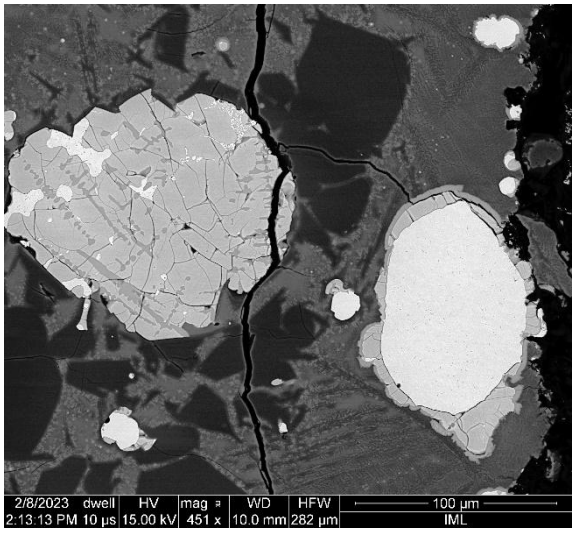

A331

T (°C)	1550	**Run**	**A331**
P (GPa)	1.5	**Si**	25.64
Starting composition	Mer15(10) + 16.7% FeS	**Ti**	< dl
Duration (hrs)	03:30	**Al**	7.71
Silicate Phases (wt%)	Gl (28) Ol (56) Opx (17)	**Fe**	0.39
		Mn	0.15
		Mg	11.82
		Ca	4.41
		Na	1.81
		K	0.36
		S	4.28
		Cr	< dl
		O*	46.78
		Tot	103.42

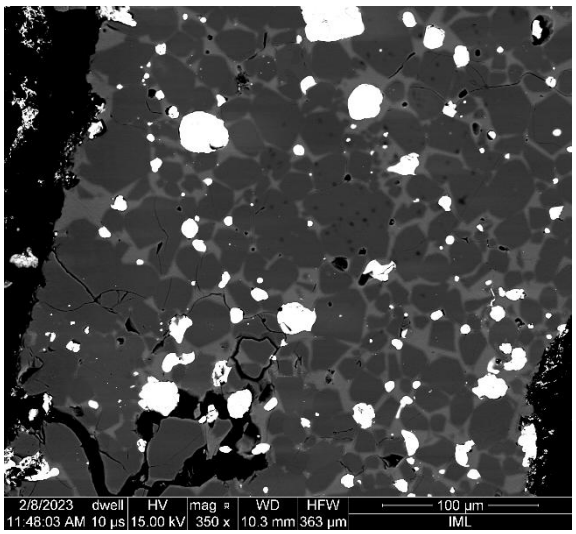

A334

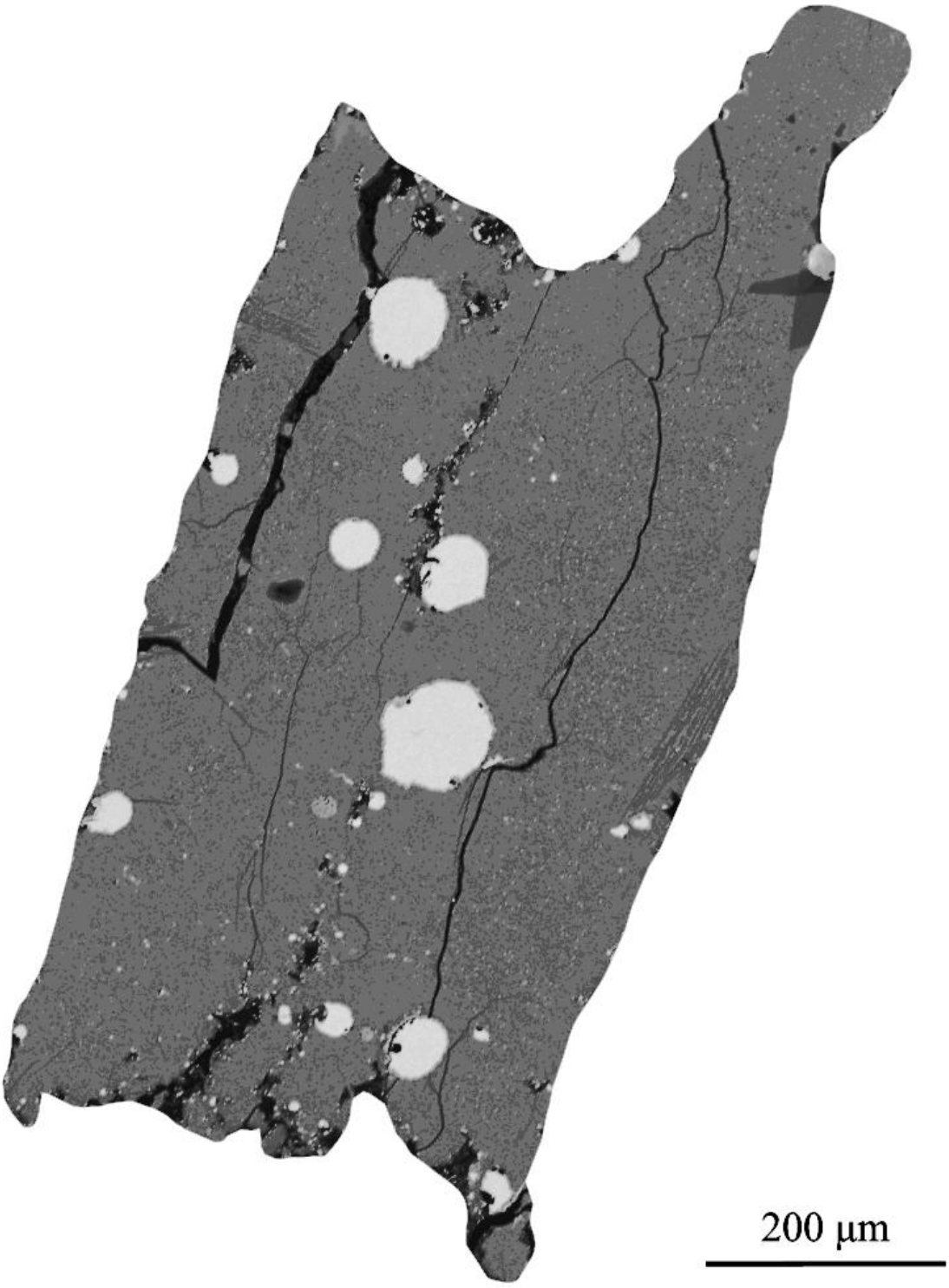

T (°C)	1700	**Run**	**A334**
P (GPa)	1.5	**Si**	24.96
Starting composition	Mer8(20) +20% FeS	**Ti**	0.09
Duration (hrs)	01:10	**Al**	1.92
Silicate Phases (wt%)	Gl (100)	**Fe**	0.37
		Mn	0.17
		Mg	21.79
		Ca	1.22
		Na	0.65
		K	0.09
		S	5.71
		Cr	< dl
		O*	45.53
		Tot	102.50

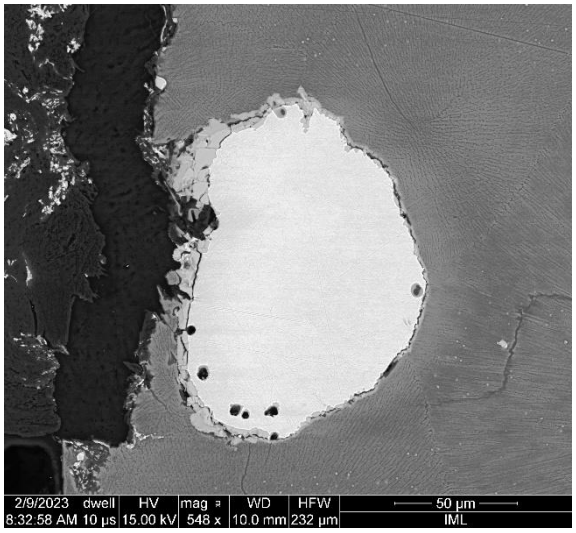

A339

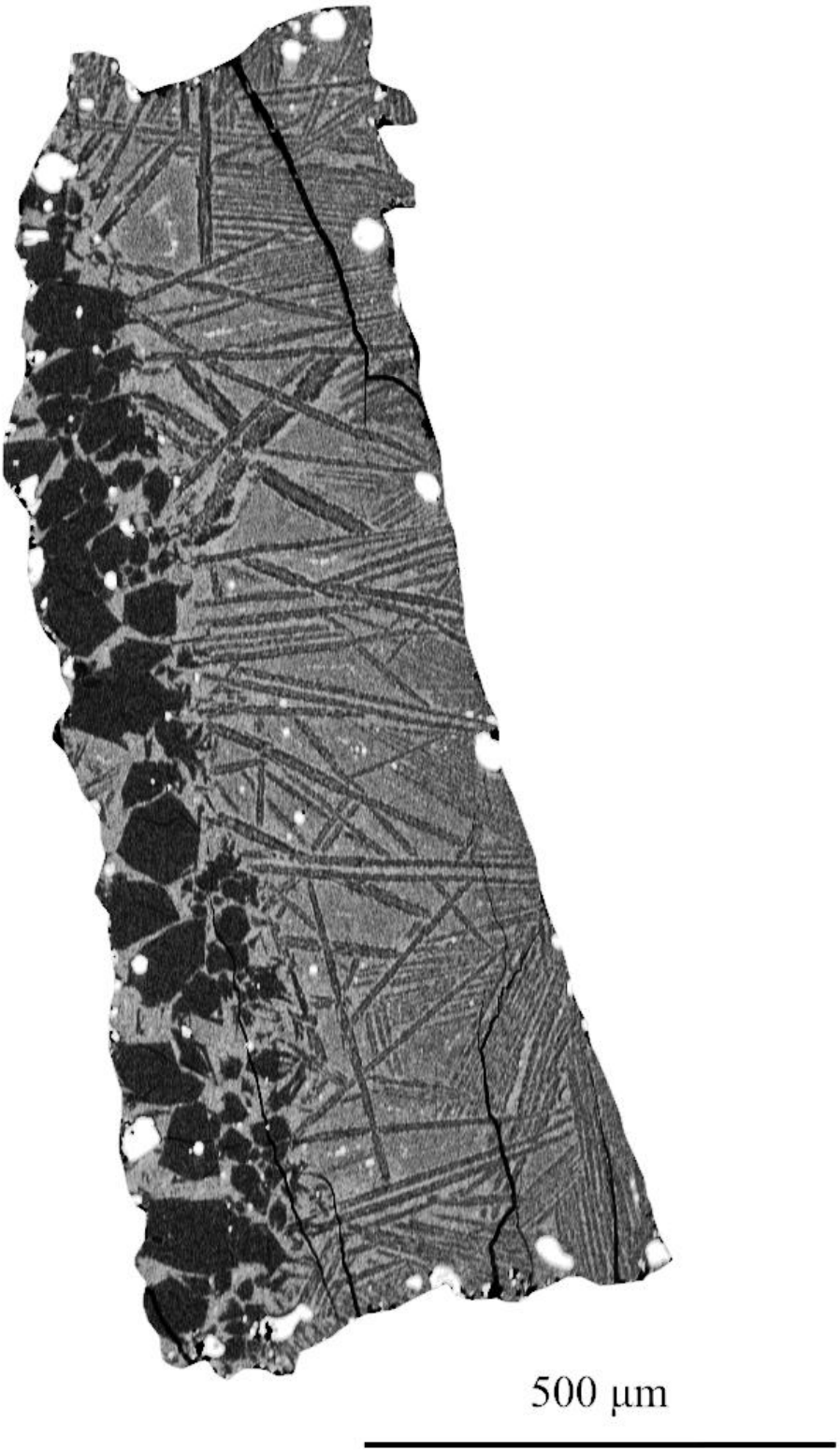

T (°C)	1700	**Run**	**A339**
P (GPa)	1.5	**Si**	23.11
Starting composition	Mer15(20) + 20% FeS	**Ti**	0.09
Duration (hrs)	01:10	**Al**	2.88
Silicate Phases (wt%)	Gl (78) Ol (22)	**Fe**	0.46
		Mn	0.25
		Mg	23.10
		Ca	1.69
		Na	0.60
		K	0.14
		S	6.12
		Cr	0.10
		O*	45.41
		Tot	103.95

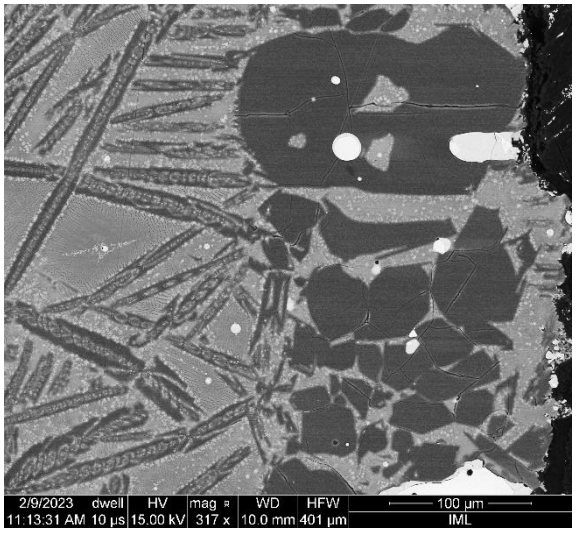

A343

T (°C)	1950	**Run**	**A343**
P (GPa)	1.5	**Si**	24.10
Starting composition	Mer15(10)	**Ti**	0.12
Duration (hrs)	00:20	**Al**	3.31
Silicate Phases (wt%)	Gl (100)	**Fe**	
		Mn	0.19
		Mg	24.76
		Ca	1.86
		Na	0.06
		K	0.10
		S	
		Cr	< dl
		O*	47.62
		Tot	102.11

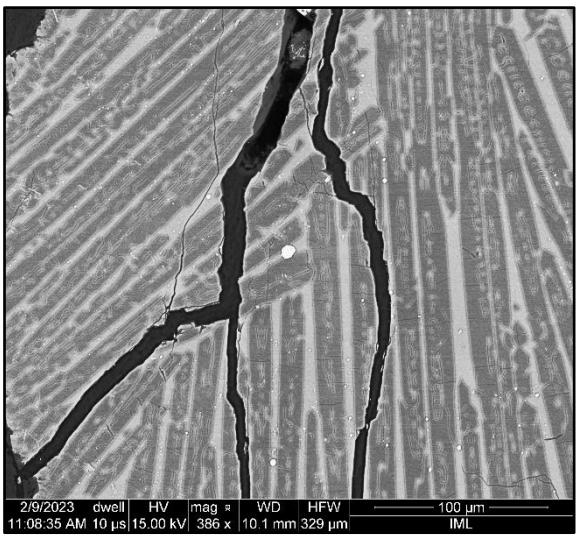

A344

T (°C)	1750	**Run**	**A344**
P (GPa)	1.5	**Si**	24.51
Starting composition	Mer15(10) + 16.7% FeS	**Ti**	0.12
Duration (hrs)	00:45	**Al**	3.70
Silicate Phases (wt%)	Gl (62) Ol (38)	**Fe**	0.52
		Mn	0.18
		Mg	21.46
		Ca	2.13
		Na	0.99
		K	0.18
		S	3.05
		Cr	< dl
		O*	47.02
		Tot	103.87

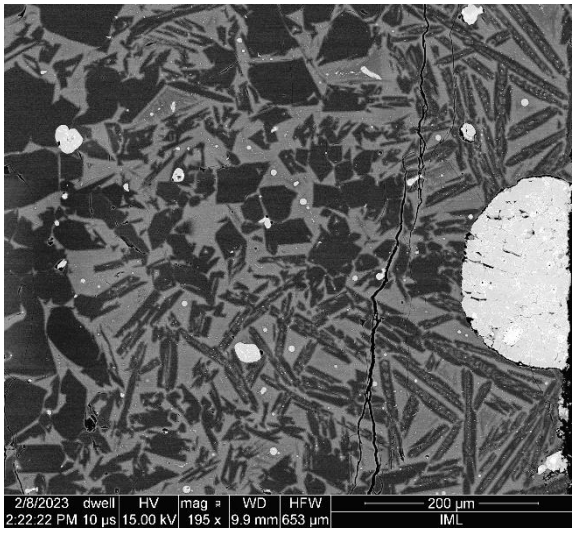

A349

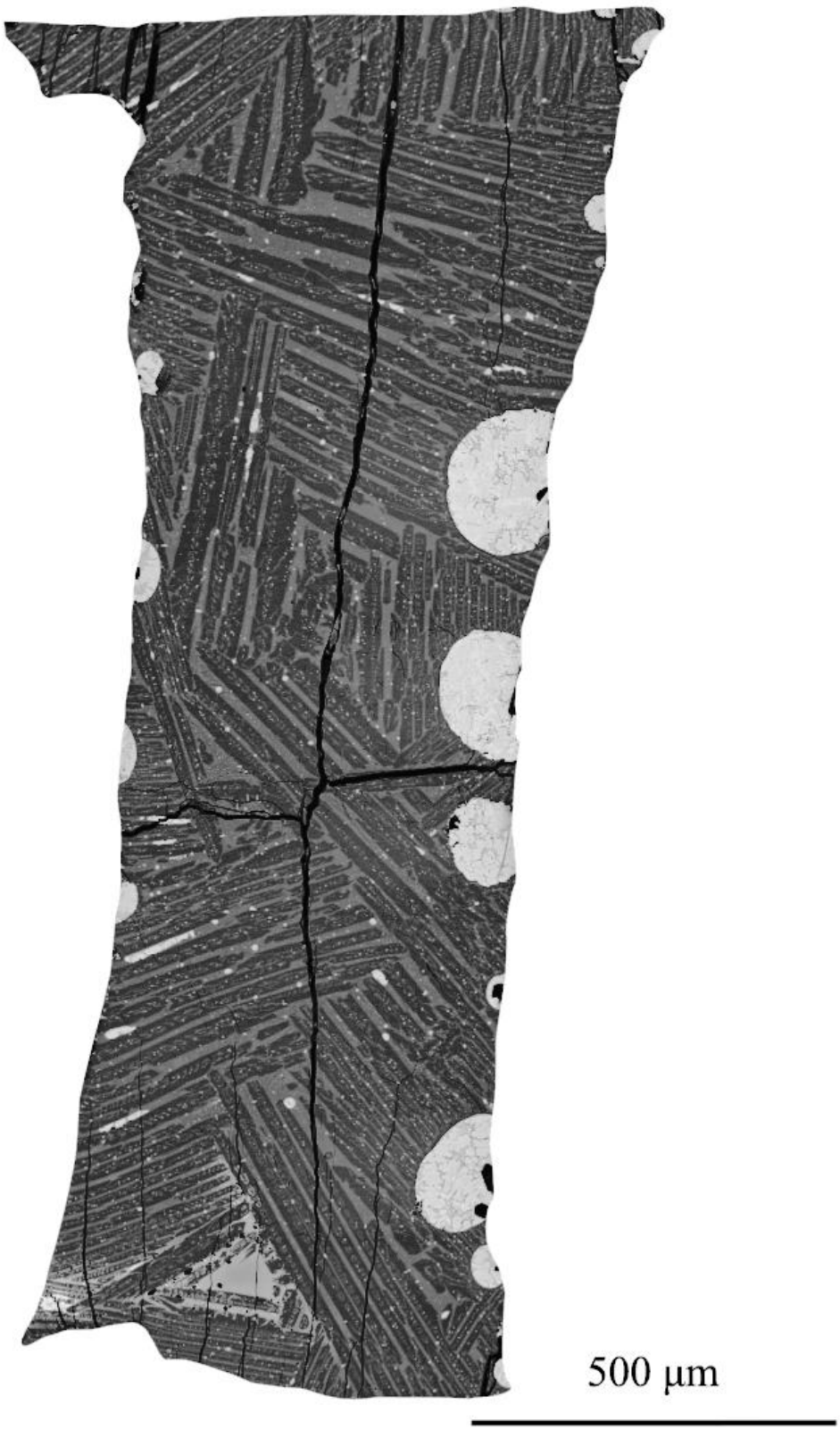

T (°C)	1950	**Run**	**A349**
P (GPa)	3.0	**Si**	21.47
Starting composition	Mer15(10) + 16.7% S	**Ti**	0.09
Duration (hrs)	00:35	**Al**	1.20
Silicate Phases (wt%)	Gl (100)	**Fe**	0.58
		Mn	0.12
		Mg	26.60
		Ca	1.27
		Na	0.30
		K	0.04
		S	1.73
		Cr	< dl
		O*	43.98
		Tot	97.38

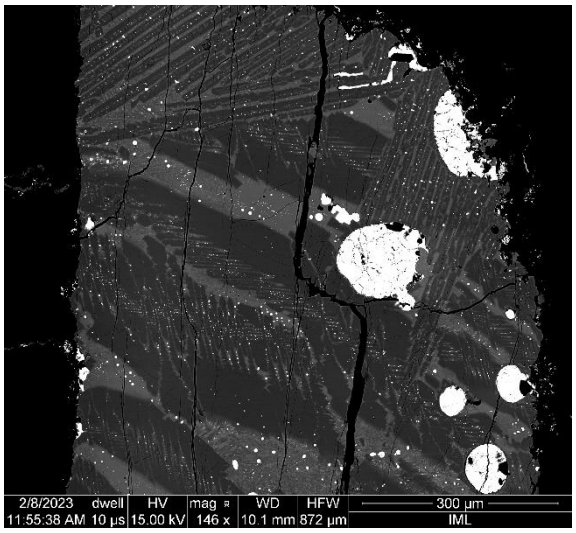

A351

T (°C)	1950	**Run**	**A351**
P (GPa)	3.0	**Si**	23.83
Starting composition	Mer15(10)	**Ti**	0.10
Duration (hrs)	00:35	**Al**	3.72
Silicate Phases (wt%)	Gl (72) Ol (28)	**Fe**	
		Mn	0.21
		Mg	23.51
		Ca	2.06
		Na	0.32
		K	0.13
		S	
		Cr	< dl
		O*	47.08
		Tot	100.97

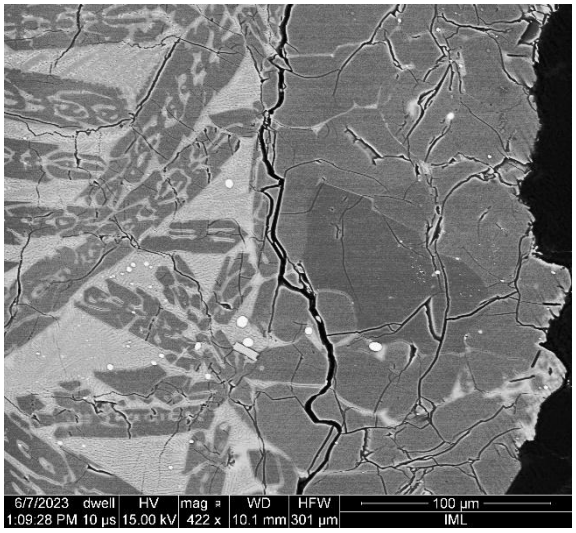

A352

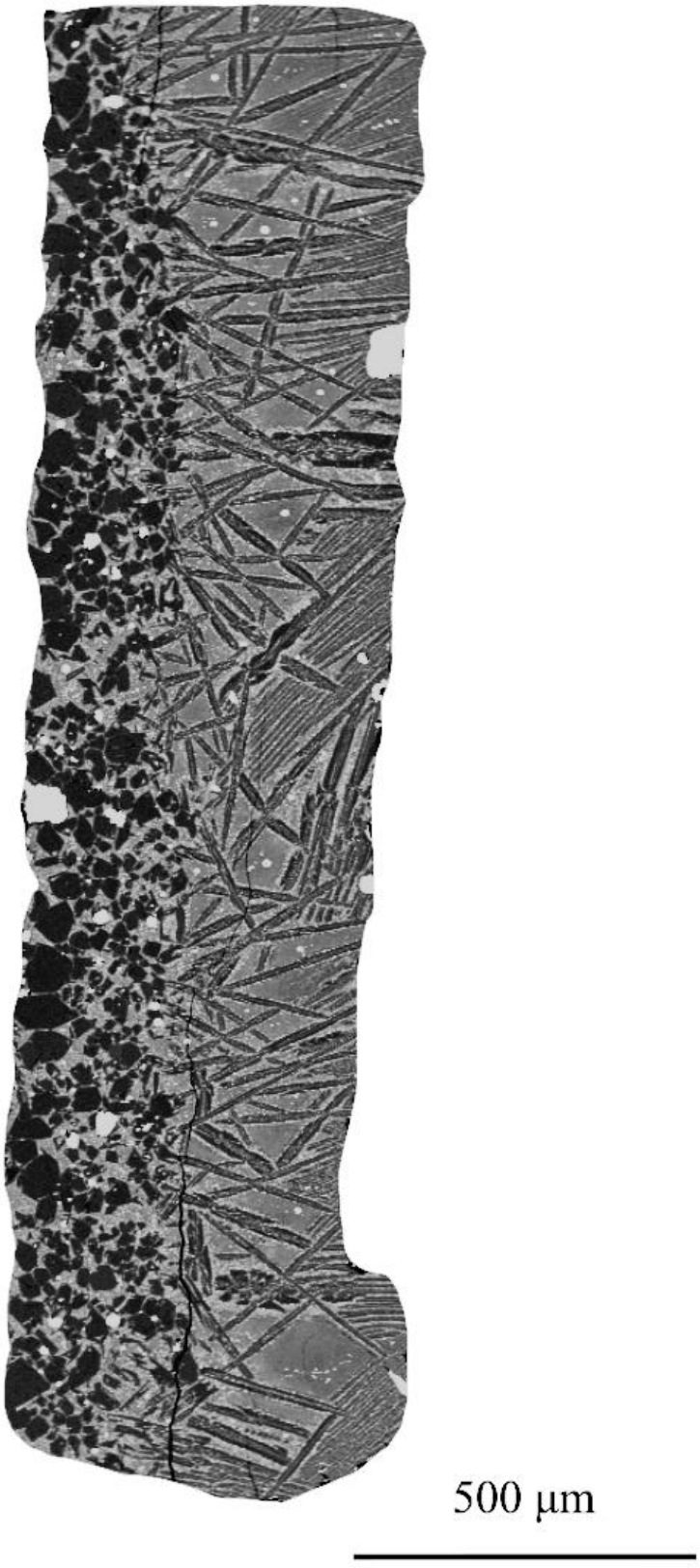

T (°C)	1700	**Run**	**A352**
P (GPa)	1.5	**Si**	22.62
Starting composition	Mer15(20) + 20% FeS	**Ti**	0.10
Duration (hrs)	00:30	**Al**	2.80
Silicate Phases (wt%)	Gl (79) Ol (21)	**Fe**	0.45
		Mn	0.27
		Mg	23.43
		Ca	1.62
		Na	0.98
		K	0.12
		S	6.90
		Cr	0.10
		O*	45.17
		Tot	104.56

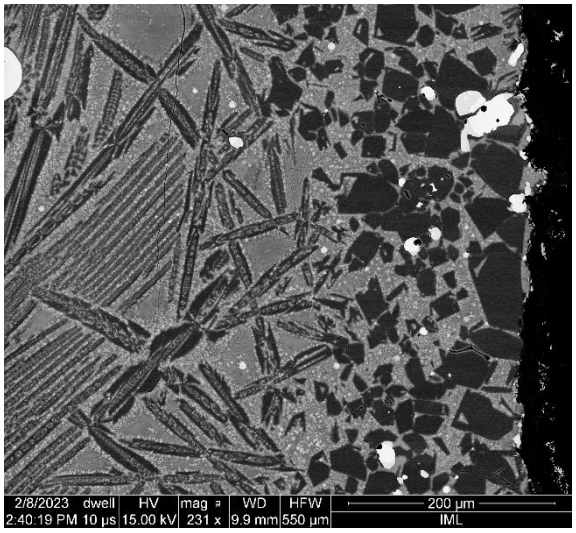

A354

T (°C)	1700	**Run**	**A354**
P (GPa)	1.5	**Si**	22.77
Starting composition	Mer15(20) + 20% FeS	**Ti**	0.10
Duration (hrs)	00:15	**Al**	2.79
Silicate Phases (wt%)	Gl (82) Ol (18)	**Fe**	0.52
		Mn	0.22
		Mg	23.43
		Ca	1.66
		Na	0.86
		K	0.12
		S	6.54
		Cr	0.10
		O*	45.29
		Tot	104.41

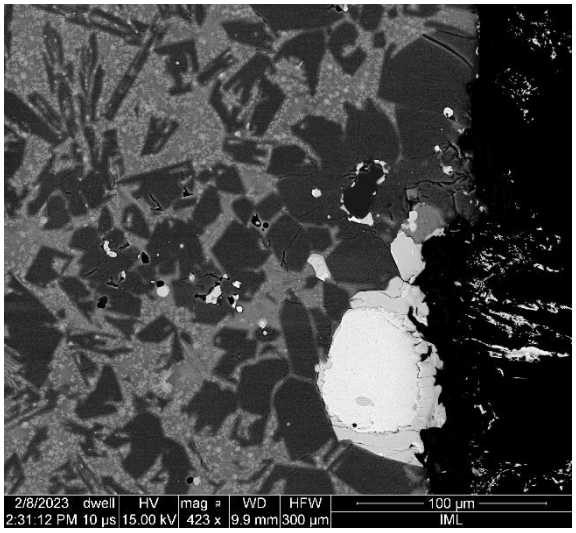

A356

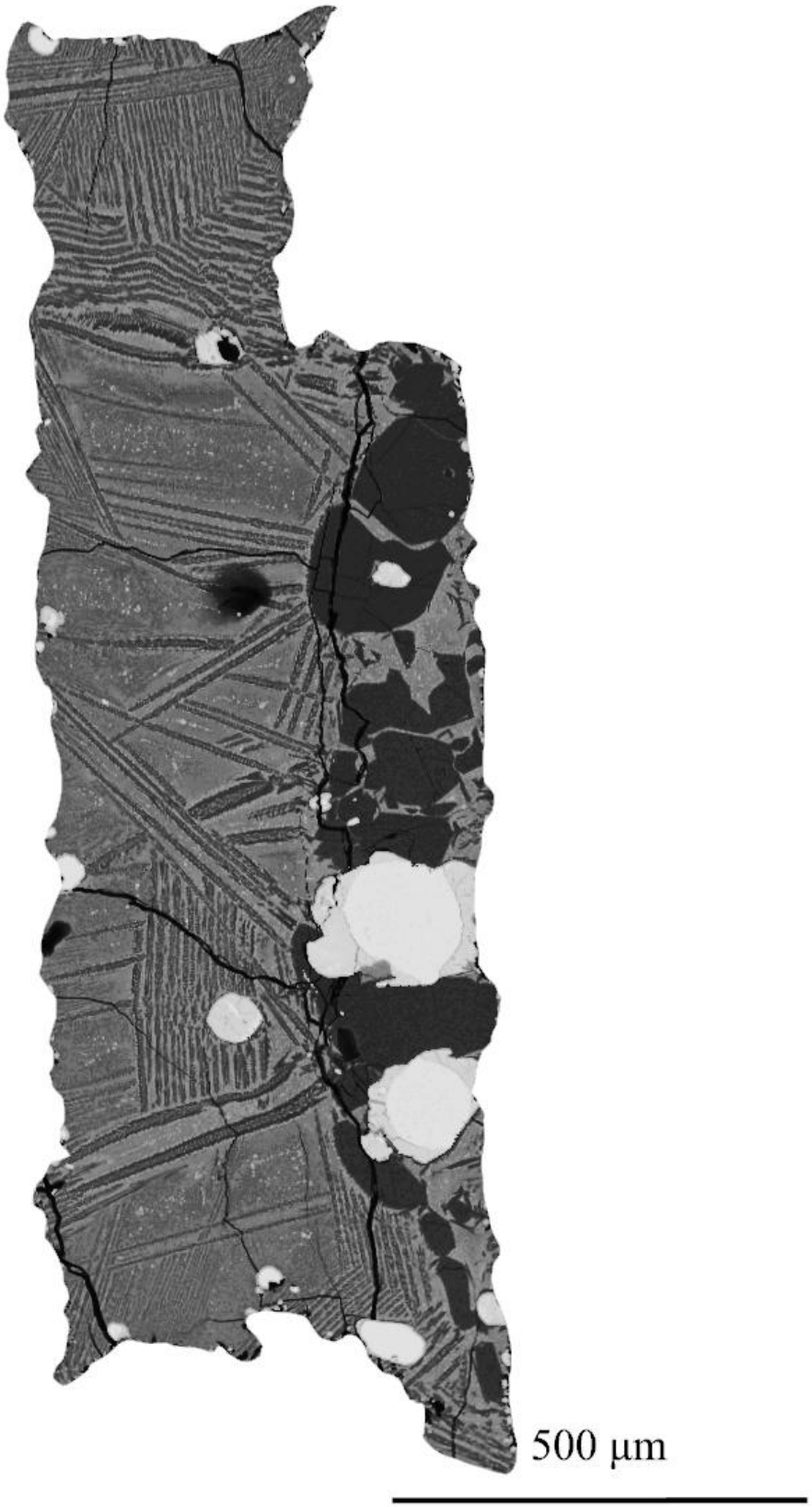

T (°C)	1700	**Run**	**A356**
P (GPa)	1.5	**Si**	22.93
Starting composition	Mer15(20) + 20% FeS	**Ti**	< dl
Duration (hrs)	03:00	**Al**	2.86
Silicate Phases (wt%)	Gl (76) Ol (24)	**Fe**	0.46
		Mn	0.19
		Mg	23.01
		Ca	1.75
		Na	0.21
		K	0.12
		S	6.23
		Cr	< dl
		O*	44.84
		Tot	102.60

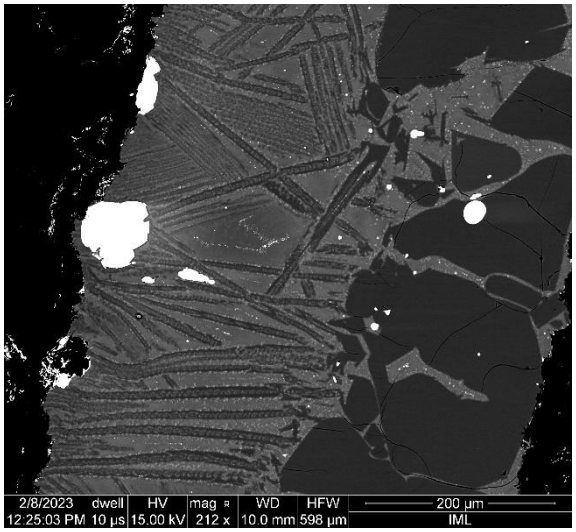

A359

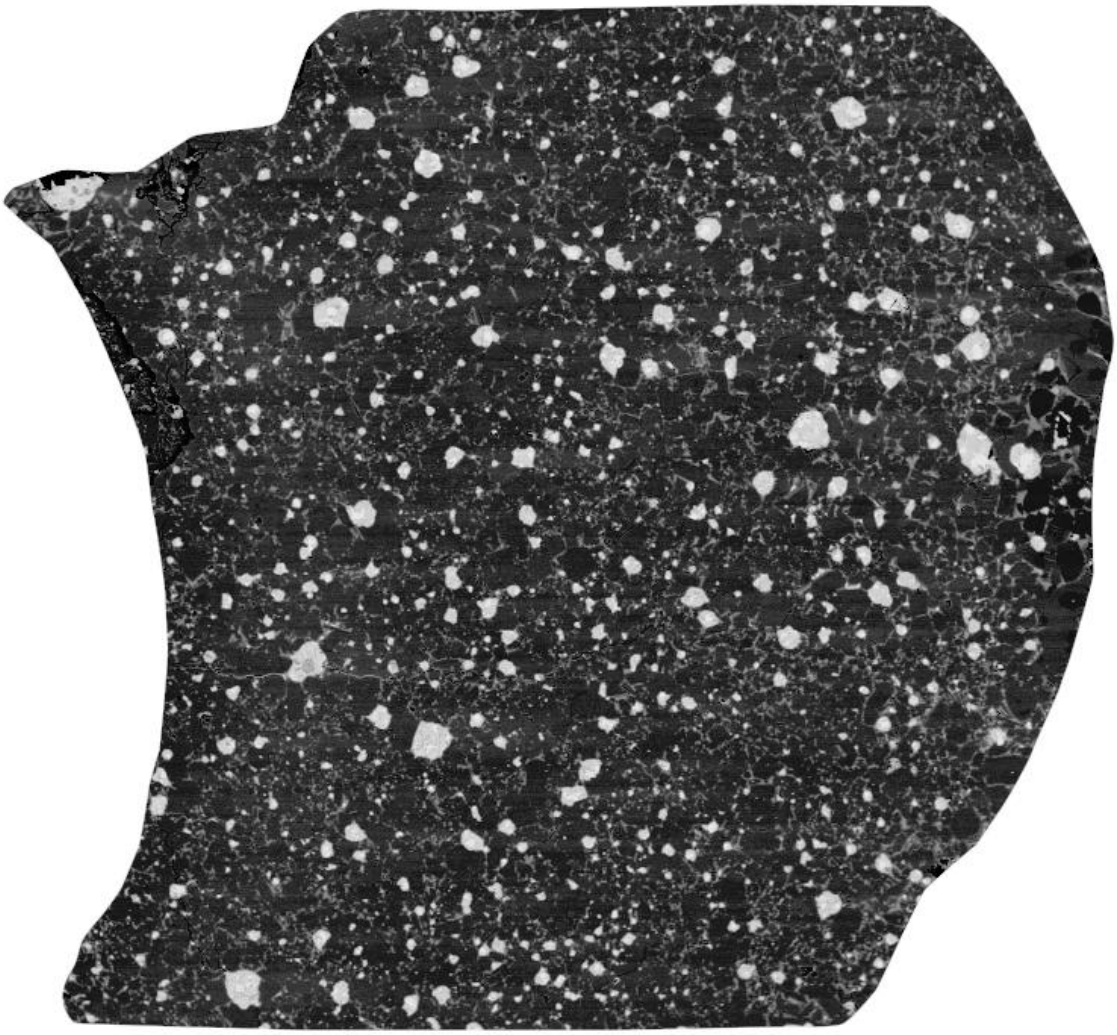

T (°C)	1750	**Run**	**A359**
P (GPa)	3.0	**Si**	
Starting composition	Mer8(10) + 16.7% FeS	**Ti**	
Duration (hrs)	01:35	**Al**	
Silicate Phases (wt%)	Gl (<20) Ol () Opx ()	**Fe**	
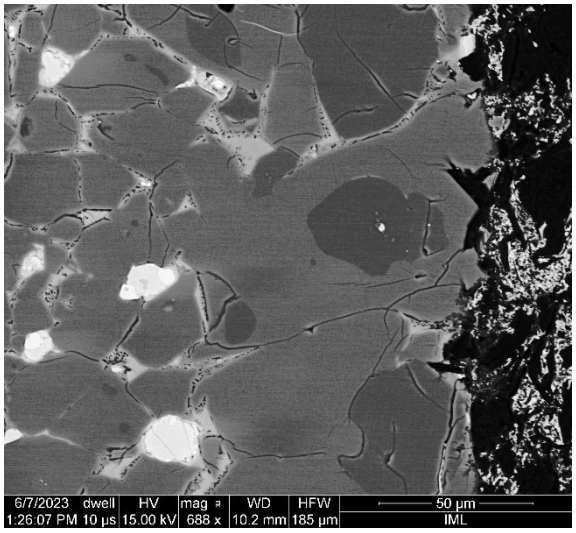		**Mn**	
		Mg	
		Ca	
		Na	
		K	
		S	
		Cr	
		O*	
		Tot	

A361

T (°C)	1550	**Run**	**A361**
P (GPa)	1.5	**Si**	23.78
Starting composition	Mer8(20) + 20% FeS	**Ti**	< dl
Duration (hrs)	03:30	**Al**	3.81
Silicate Phases (wt%)	Gl (45) Ol (7) Opx (47)	**Fe**	0.43
		Mn	0.08
		Mg	18.95
		Ca	2.56
		Na	0.97
		K	0.22
		S	8.00
		Cr	< dl
		O*	44.70
		Tot	103.57

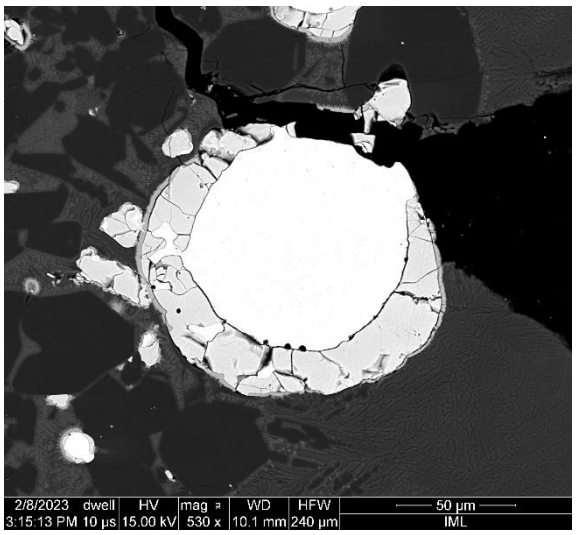

A362

T (°C)	1550	**Run**	**A362**
P (GPa)	1.5	**Si**	22.62
Starting composition	Mer15(20) + 20% FeS	**Ti**	0.09
Duration (hrs)	03:30	**Al**	4.33
Silicate Phases (wt%)	Gl (57) Ol (39) Opx (4)	**Fe**	0.51
		Mn	0.09
		Mg	18.05
		Ca	2.72
		Na	1.77
		K	0.22
		S	7.59
		Cr	< dl
		O*	43.74
		Tot	101.74

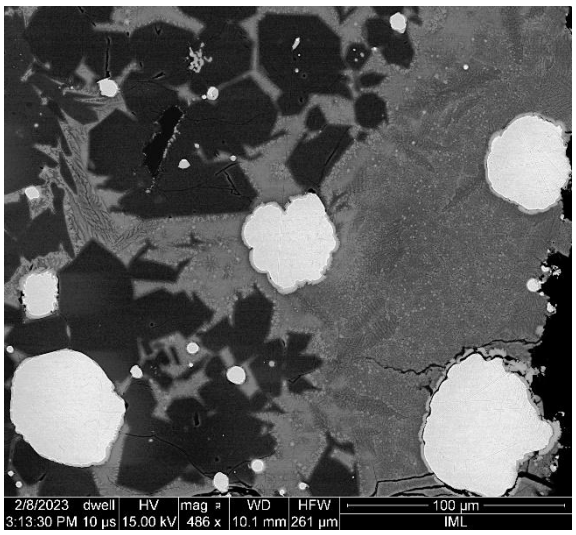

A364

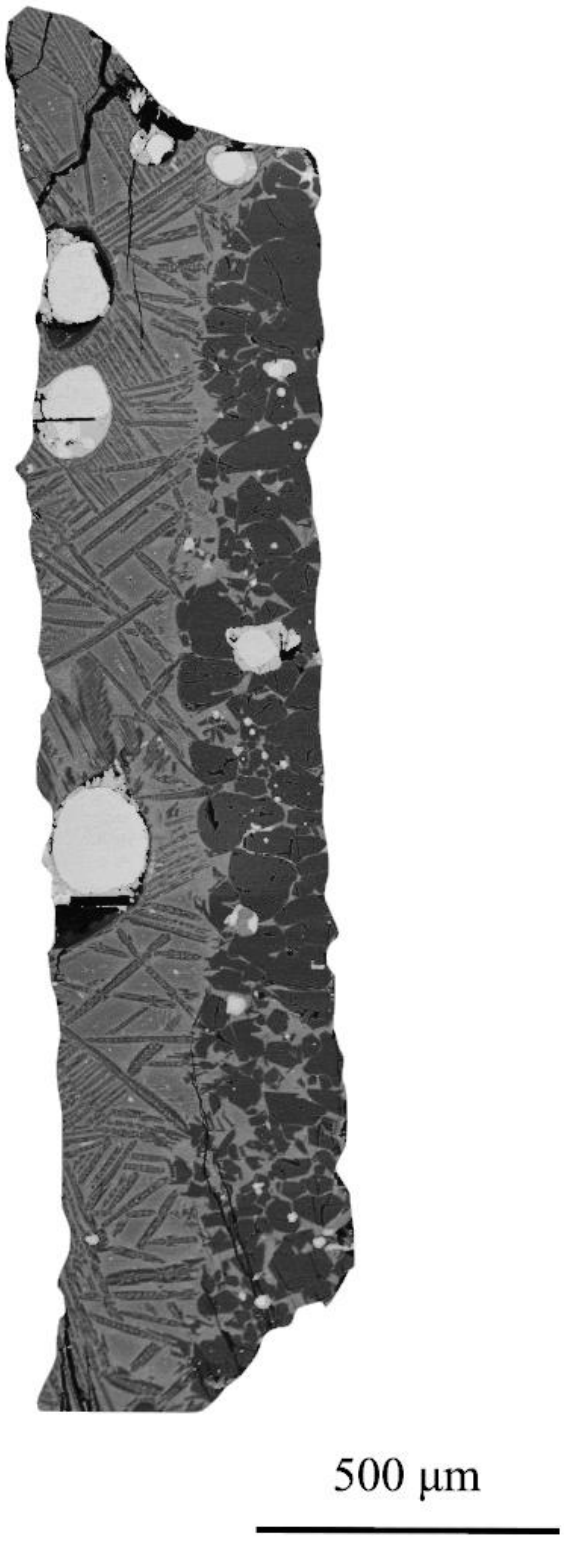

T (°C)	1800	**Run**	**A364**
P (GPa)	3.0	**Si**	23.69
Starting composition	Mer15(20) + 20% FeS	**Ti**	0.11
Duration (hrs)	01:00	**Al**	3.44
Silicate Phases (wt%)	Gl (63) Ol (37)	**Fe**	0.29
		Mn	0.24
		Mg	20.81
		Ca	2.00
		Na	0.83
		K	0.13
		S	6.34
		Cr	< dl
		O*	45.21
		Tot	103.08

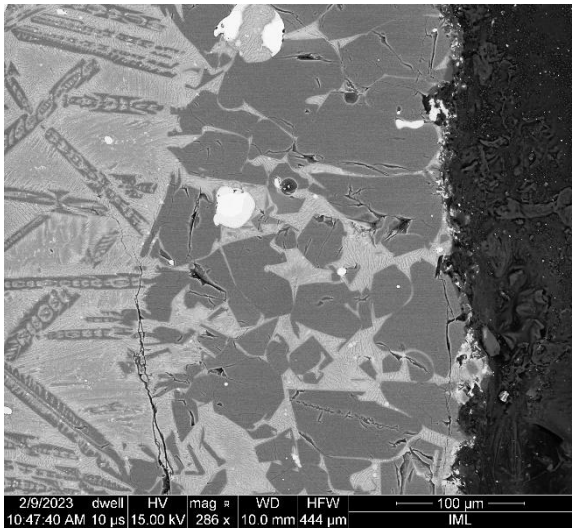

A367

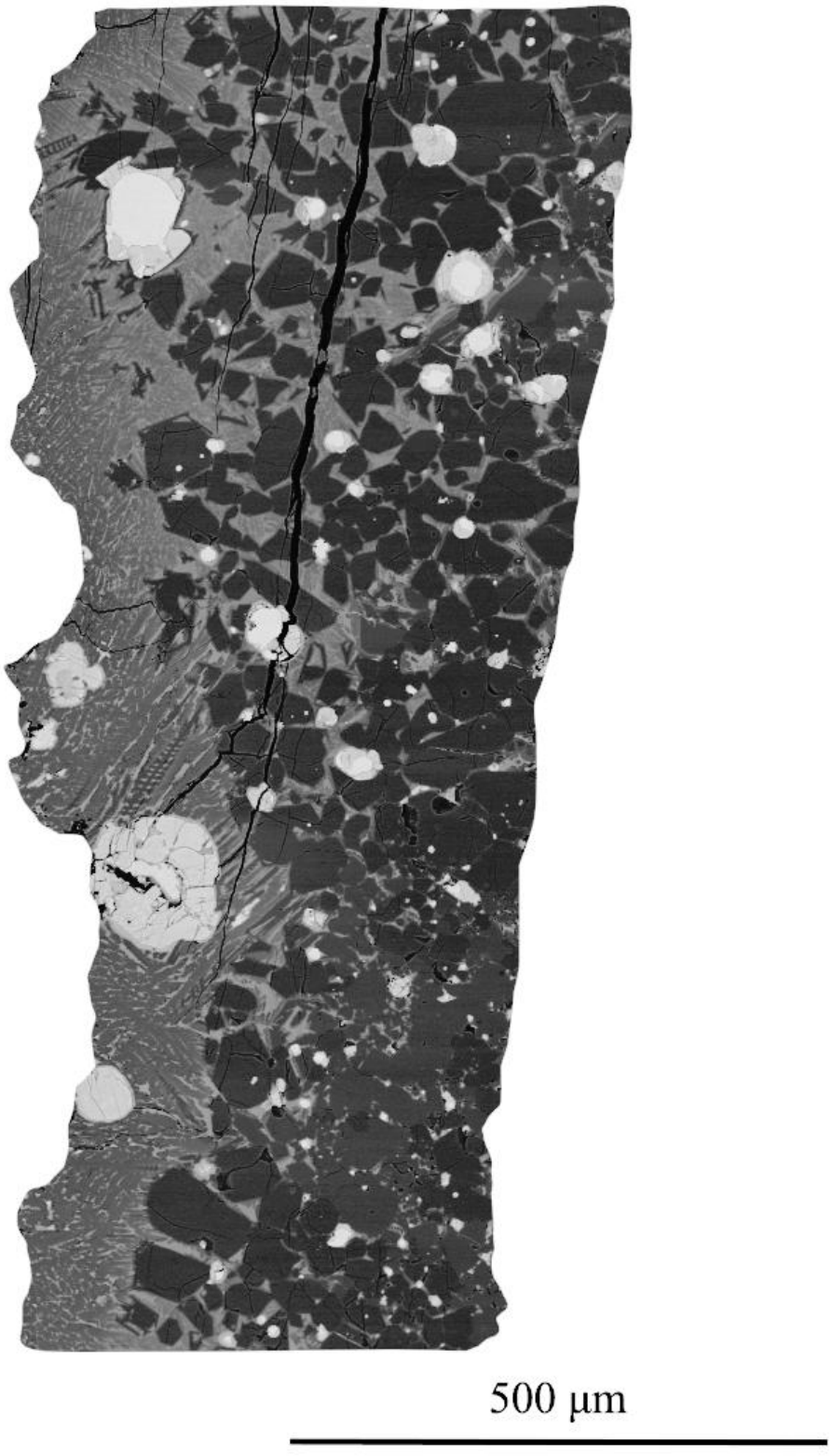

T (°C)	1700	**Run**	**A367**
P (GPa)	3.0	**Si**	22.42
Starting composition	Mer15(20) + 20% S	**Ti**	0.09
Duration (hrs)	01:30	**Al**	4.17
Silicate Phases (wt%)	Gl (50) Ol (37) Opx (13)	**Fe**	0.43
		Mn	0.18
		Mg	19.61
		Ca	2.78
		Na	1.02
		K	0.17
		S	7.27
		Cr	< dl
		O*	44.05
		Tot	102.19

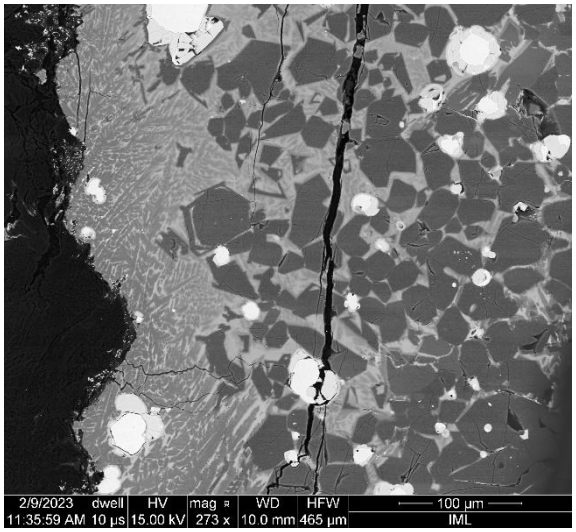

A368

T (°C)	1700	**Run**	**A368**
P (GPa)	1.5	**Si**	23.14
Starting composition	Mer15(20) + 20% FeS	**Ti**	0.10
Duration (hrs)	06:00	**Al**	2.89
Silicate Phases (wt%)	Gl (76) Ol (24)	**Fe**	0.56
		Mn	0.21
		Mg	23.15
		Ca	1.72
		Na	0.32
		K	0.11
		S	5.98
		Cr	< dl
		O*	45.34
		Tot	103.53

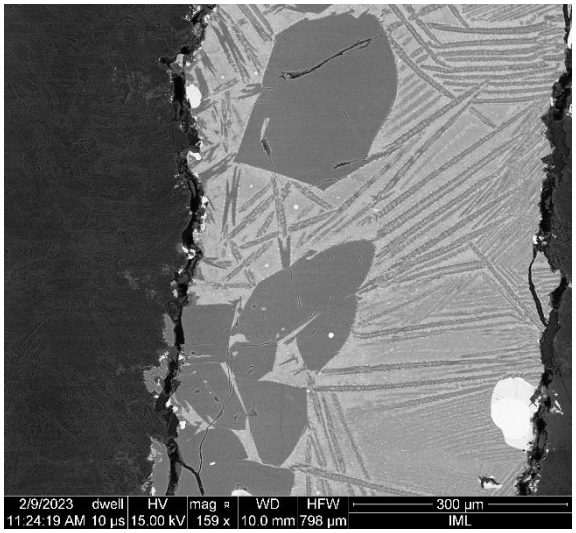

A372

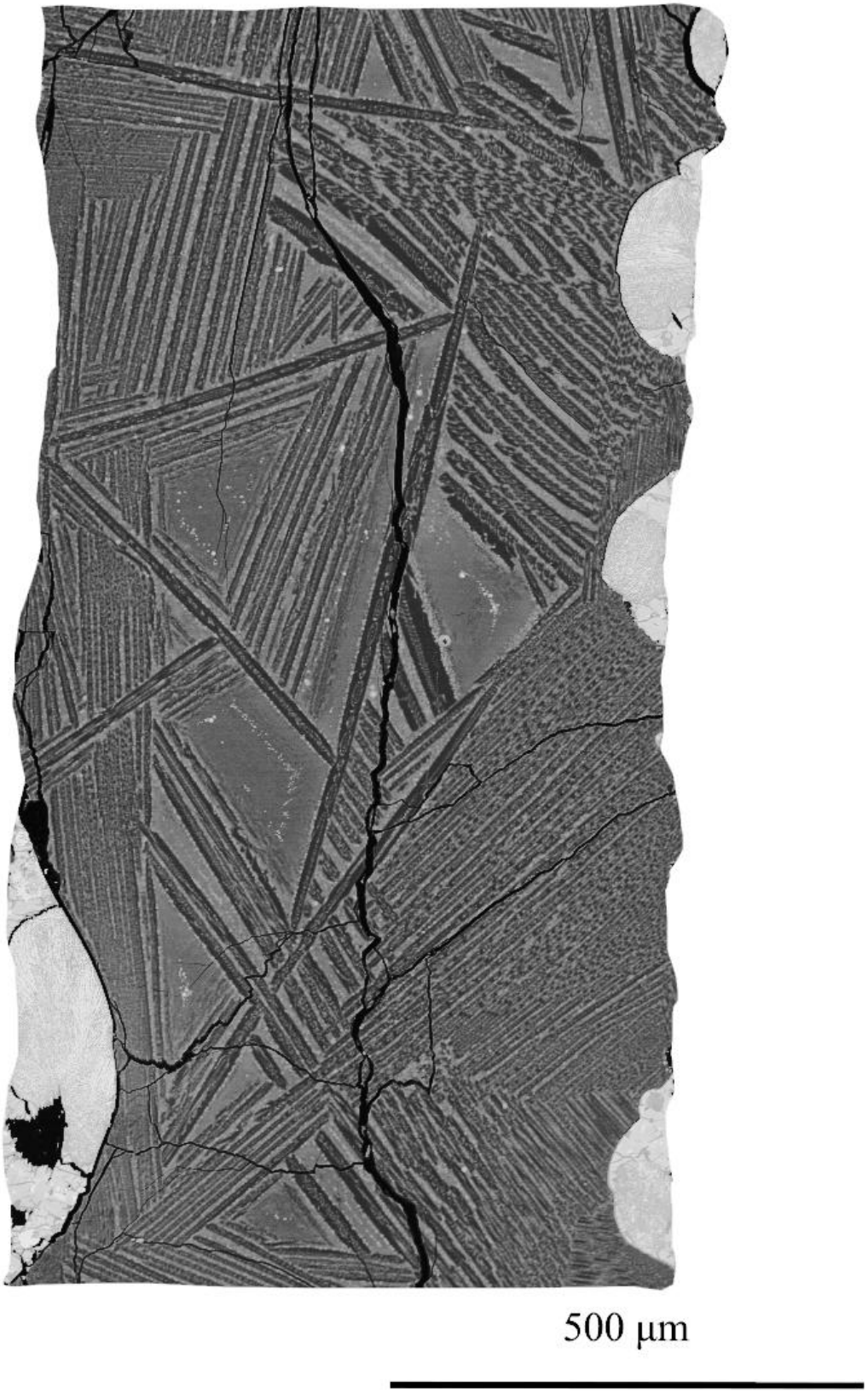

T (°C)	1760	**Run**	**A372**
P (GPa)	1.5	**Si**	22.32
Starting composition	Mer15(20) + 20% FeS	**Ti**	0.09
Duration (hrs)	00:40	**Al**	2.52
Silicate Phases (wt%)	Gl (100)	**Fe**	0.62
		Mn	0.21
		Mg	24.39
		Ca	1.54
		Na	0.58
		K	0.11
		S	6.35
		Cr	< dl
		O*	44.96
		Tot	103.69

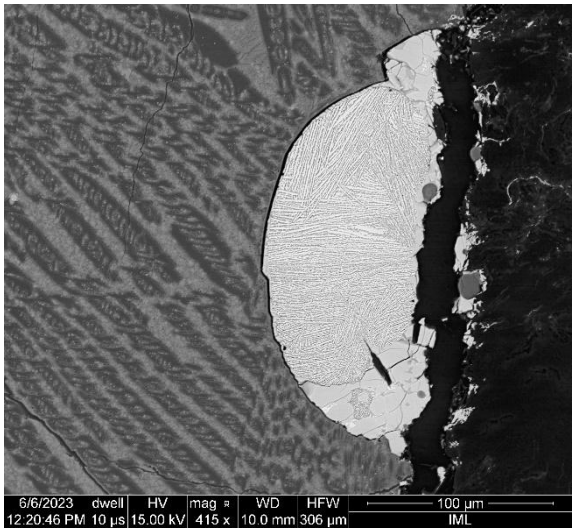

A373

T (°C)	1880	**Run**	**A373**
P (GPa)	3.0	**Si**	23.84
Starting composition	Mer15(10) + 16.7% S	**Ti**	0.10
Duration (hrs)	01:00	**Al**	3.15
Silicate Phases (wt%)	Gl (70) Ol (30)	**Fe**	0.53
		Mn	0.15
		Mg	22.69
		Ca	1.84
		Na	0.74
		K	0.10
		S	2.24
		Cr	0.10
		O*	46.34
		Tot	101.84

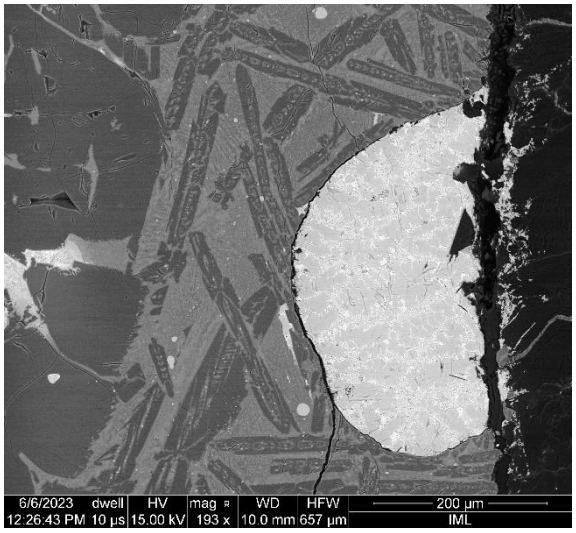

A375

T (°C)	1500	**Run**	**A375**
P (GPa)	1.5	**Si**	24.41
Starting composition	Mer8(20) + 20% FeS	**Ti**	< dl
Duration (hrs)	04:00	**Al**	5.30
Silicate Phases (wt%)	Gl (30) Ol (15) Opx (55)	**Fe**	0.31
		Mn	< dl
		Mg	14.47
		Ca	4.10
		Na	2.45
		K	0.36
		S	7.50
		Cr	< dl
		O*	45.10
		Tot	104.06

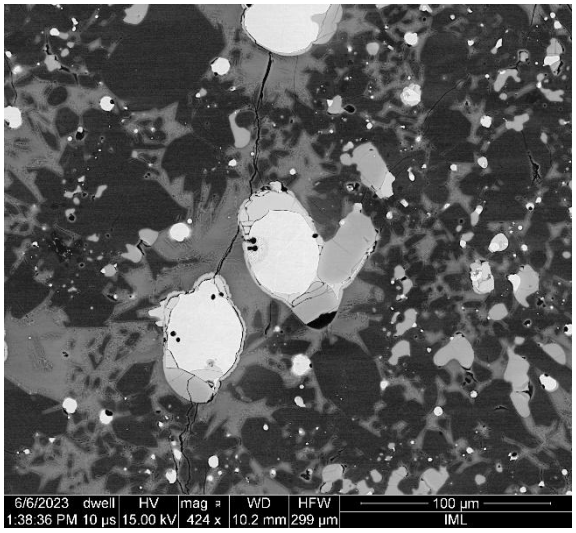

A376

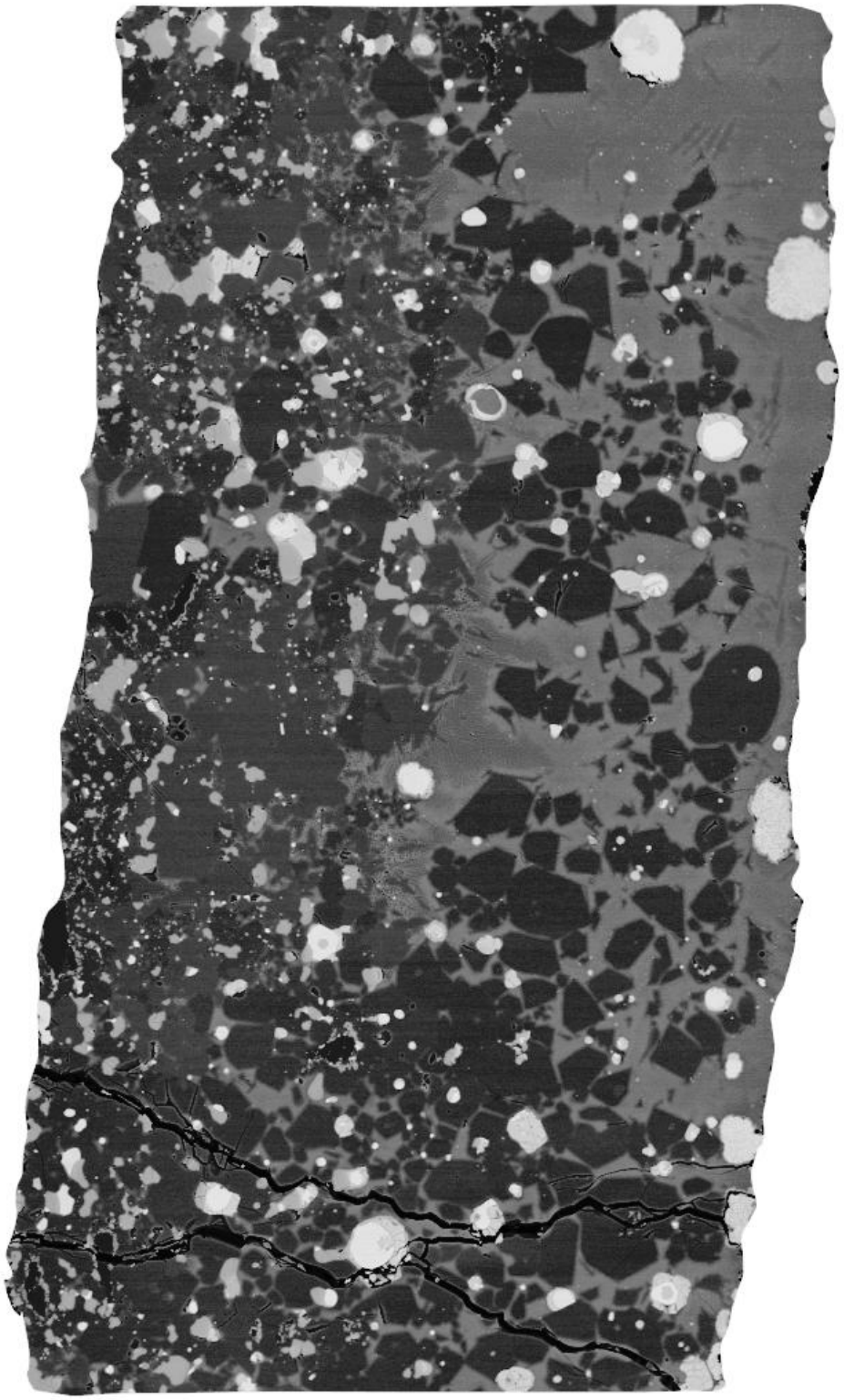

T (°C)	1500	**Run**	**A376**
P (GPa)	1.5	**Si**	23.19
Starting composition	Mer15(20) + 20% FeS	**Ti**	< dl
Duration (hrs)	04:00	**Al**	5.00
Silicate Phases (wt%)	Gl (42) Ol (46) Opx (11)	**Fe**	0.45
		Mn	< dl
		Mg	17.03
		Ca	3.17
		Na	1.99
		K	0.27
		S	7.72
		Cr	< dl
		O*	44.51
		Tot	103.33

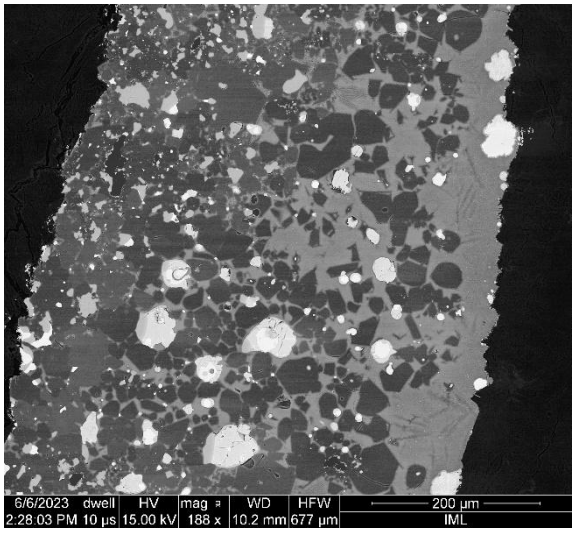

A377

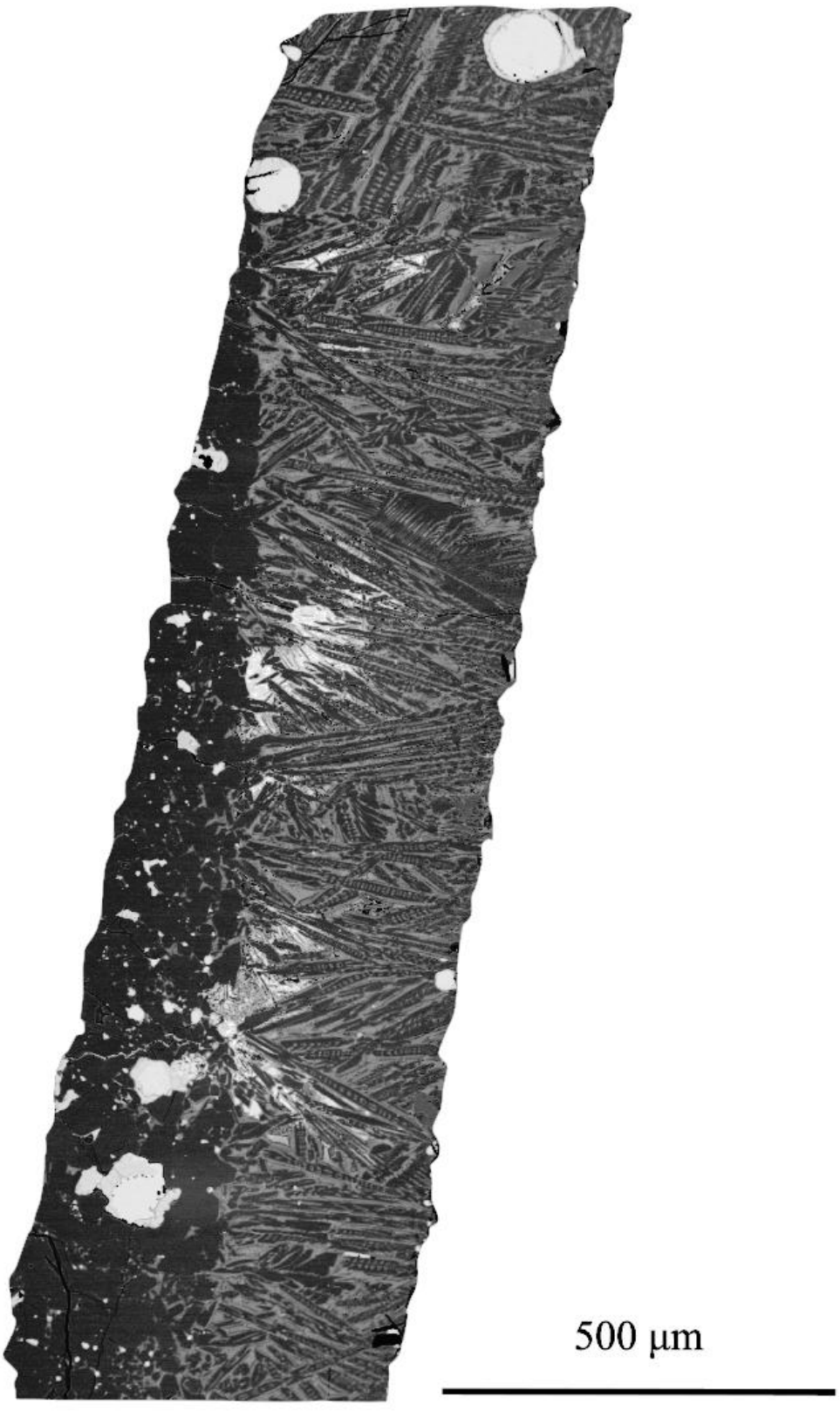

T (°C)	1780	**Run**	**A377**
P (GPa)	3.0	**Si**	24.05
Starting composition	Mer8(20) + 20% FeS	**Ti**	0.09
Duration (hrs)	01:00	**Al**	2.78
Silicate Phases (wt%)	Gl (64) Opx (36)	**Fe**	0.40
		Mn	0.21
		Mg	20.96
		Ca	1.76
		Na	1.08
		K	0.14
		S	7.18
		Cr	< dl
		O*	45.17
		Tot	103.80

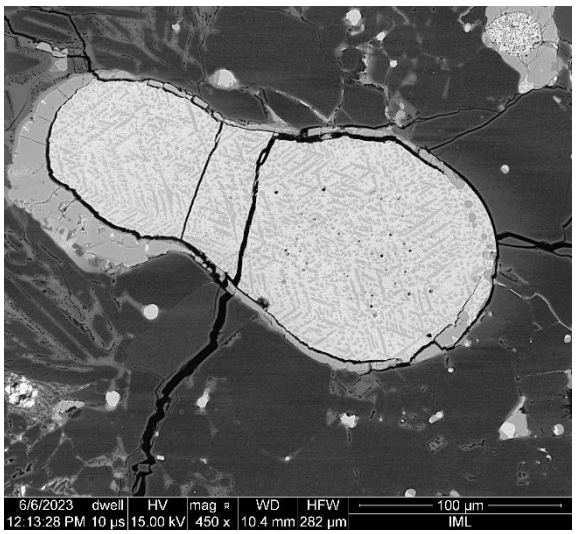

A378

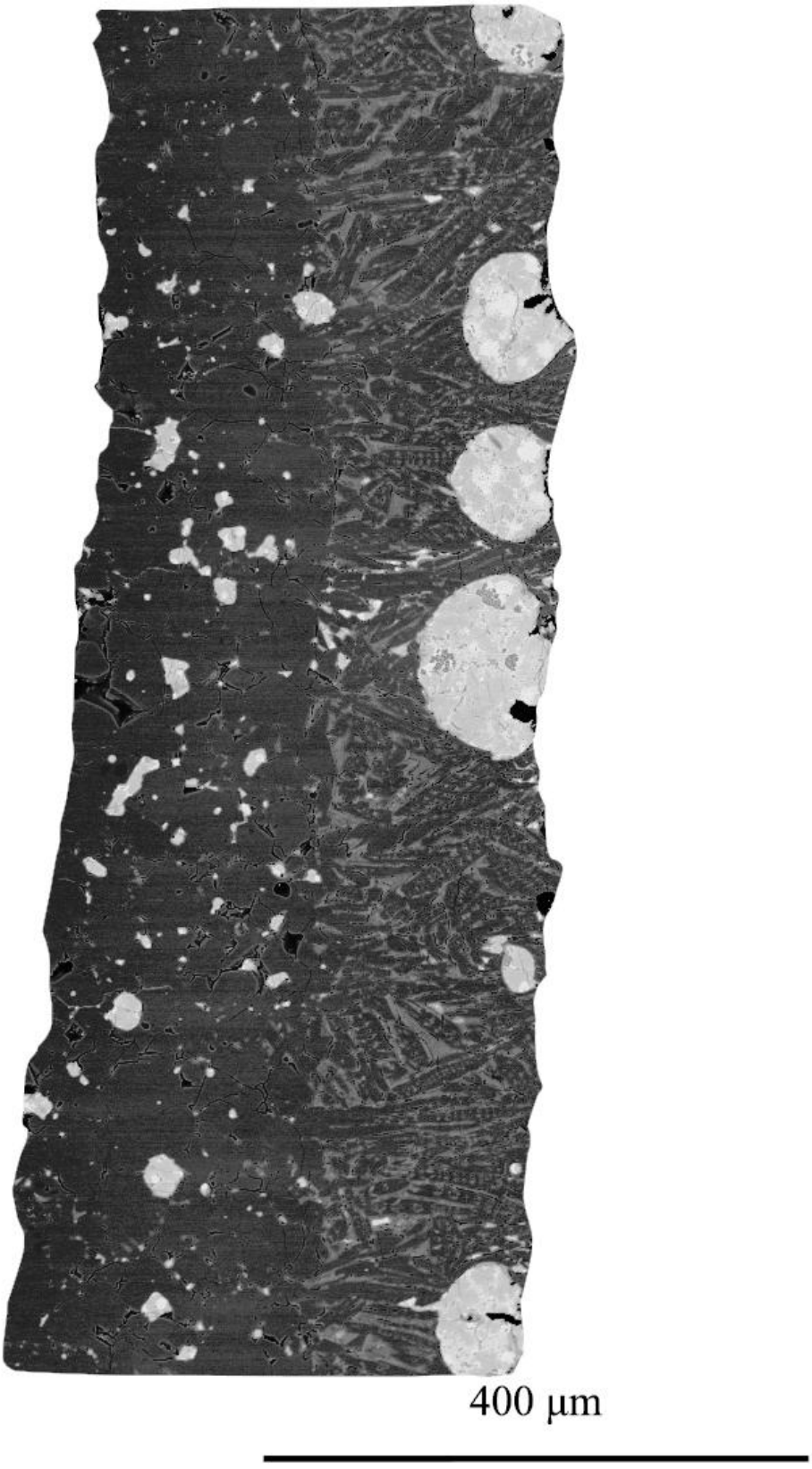

T (°C)	1810	**Run**	**A378**
P (GPa)	3.0	**Si**	23.33
Starting composition	Mer8(20) + 20% FeS	**Ti**	0.14
Duration (hrs)	01:10	**Al**	3.03
Silicate Phases (wt%)	Gl (53) Opx (47)	**Fe**	0.44
		Mn	0.24
		Mg	20.97
		Ca	2.31
		Na	1.40
		K	0.21
		S	4.76
		Cr	< dl
		O*	45.03
		Tot	101.87

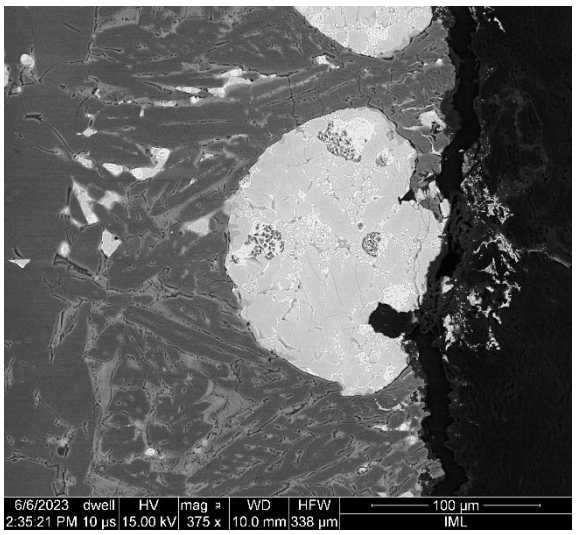

A379

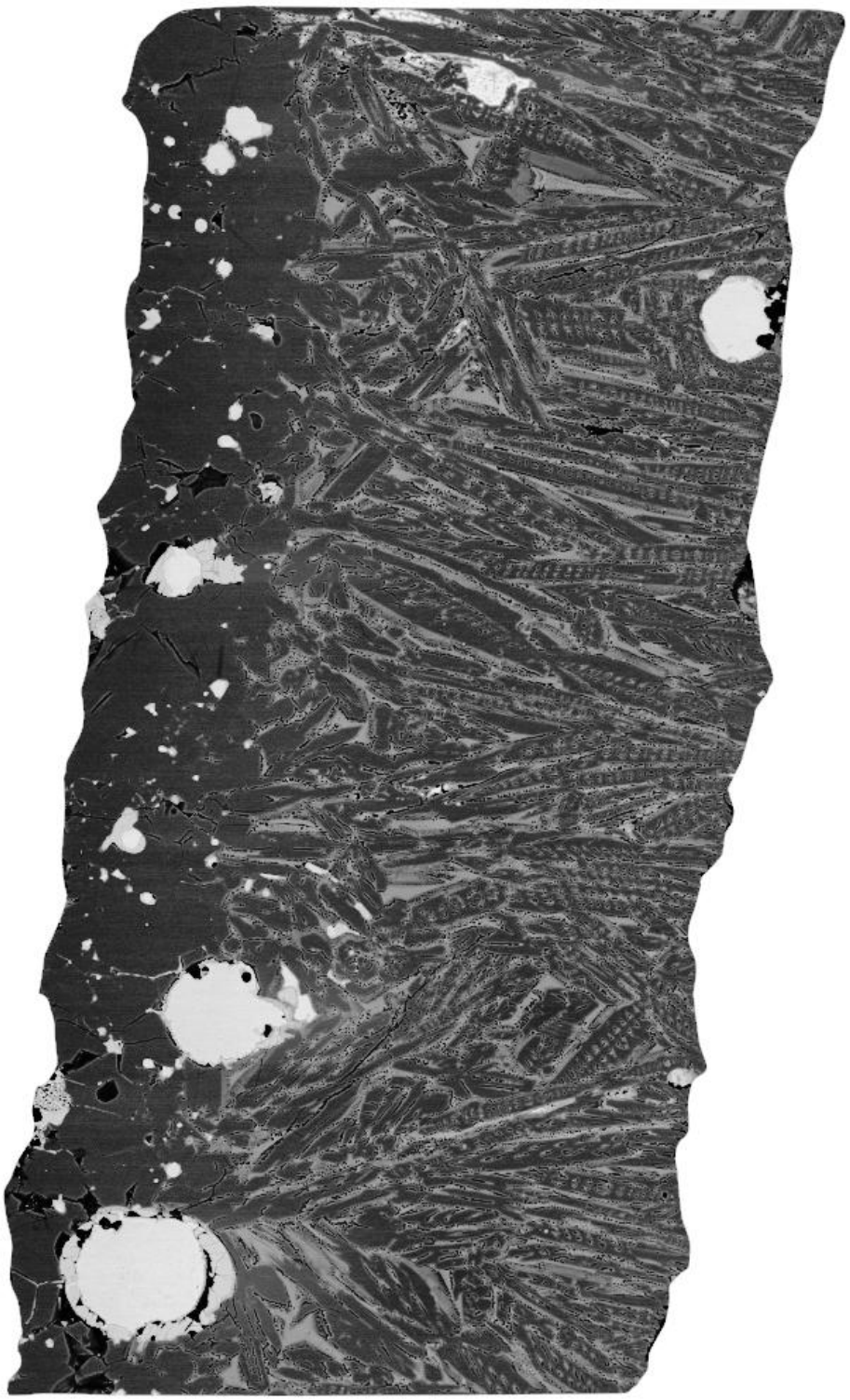

T (°C)	1830	**Run**	**A379**
P (GPa)	3.0	**Si**	23.73
Starting composition	Mer8(20) + 20% FeS	**Ti**	0.12
Duration (hrs)	00:45	**Al**	2.46
Silicate Phases (wt%)	Gl (69) Opx (31)	**Fe**	0.46
		Mn	0.21
		Mg	21.43
		Ca	1.77
		Na	0.99
		K	0.14
		S	7.28
		Cr	< dl
		O*	44.83
		Tot	103.41

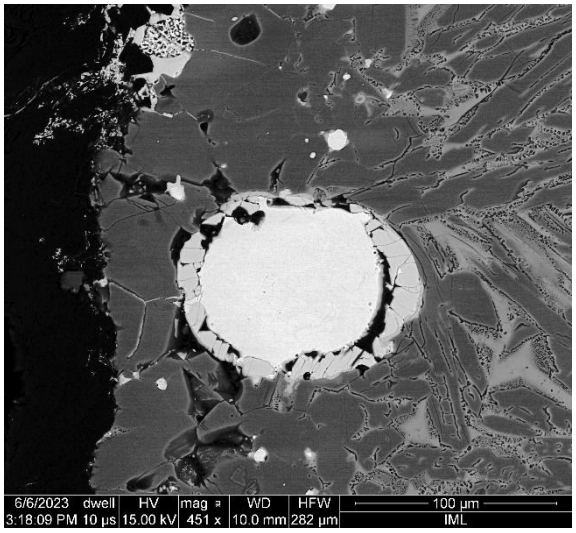

A380

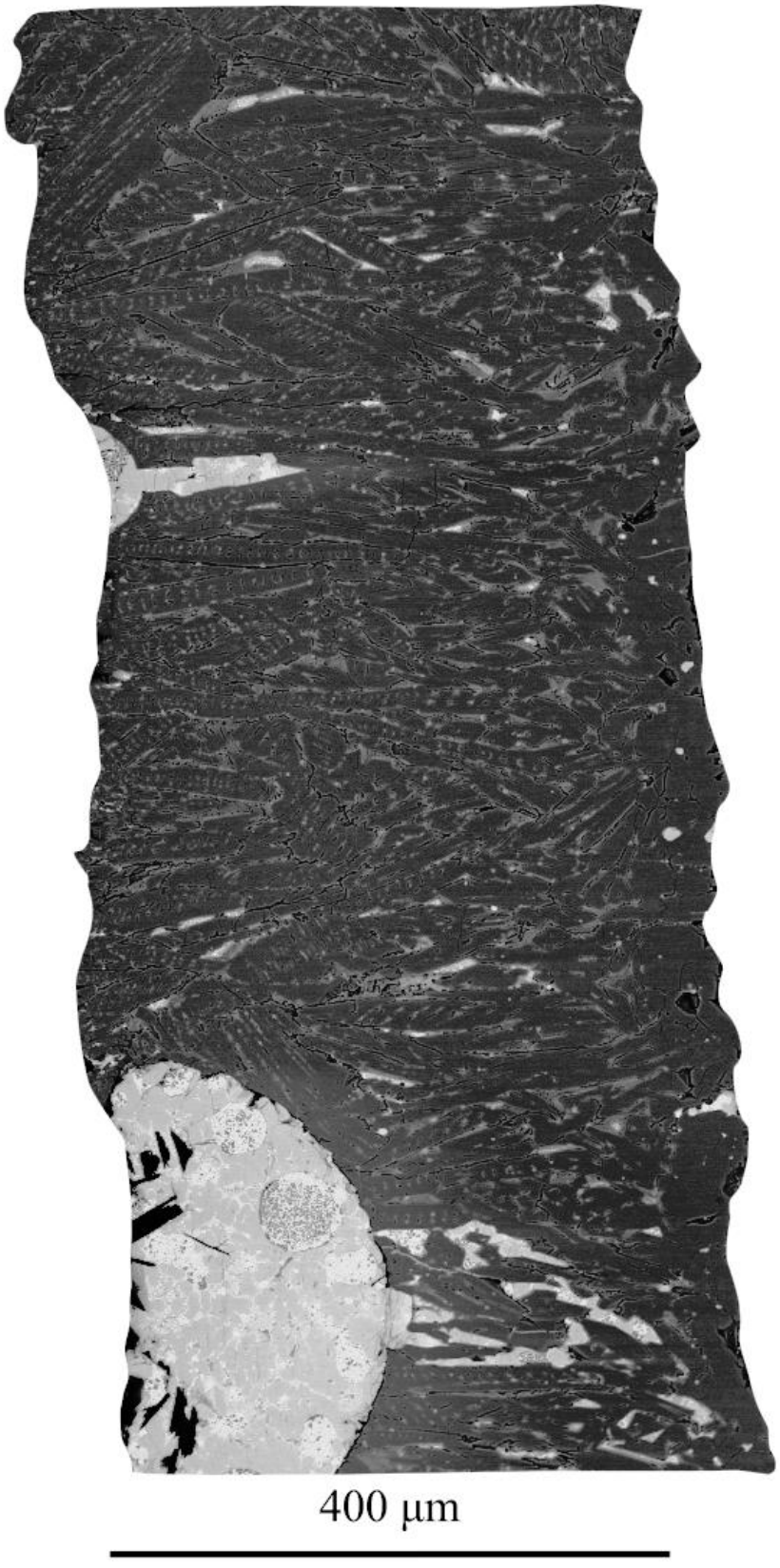

T (°C)	1860	**Run**	**A380**
P (GPa)	3.0	**Si**	25.31
Starting composition	Mer8(20) + 20% FeS	**Ti**	0.08
Duration (hrs)	00:20	**Al**	2.09
Silicate Phases (wt%)	Gl (90) Opx (10)	**Fe**	0.58
		Mn	0.16
		Mg	21.66
		Ca	1.32
		Na	0.74
		K	0.10
		S	2.62
		Cr	0.10
		O*	46.19
		Tot	100.94

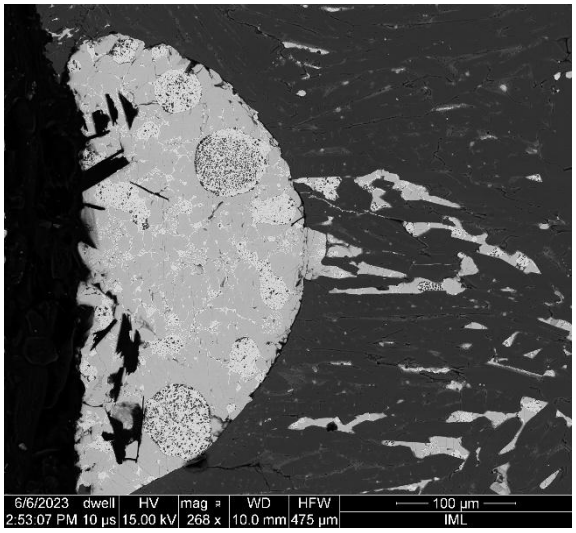

A381

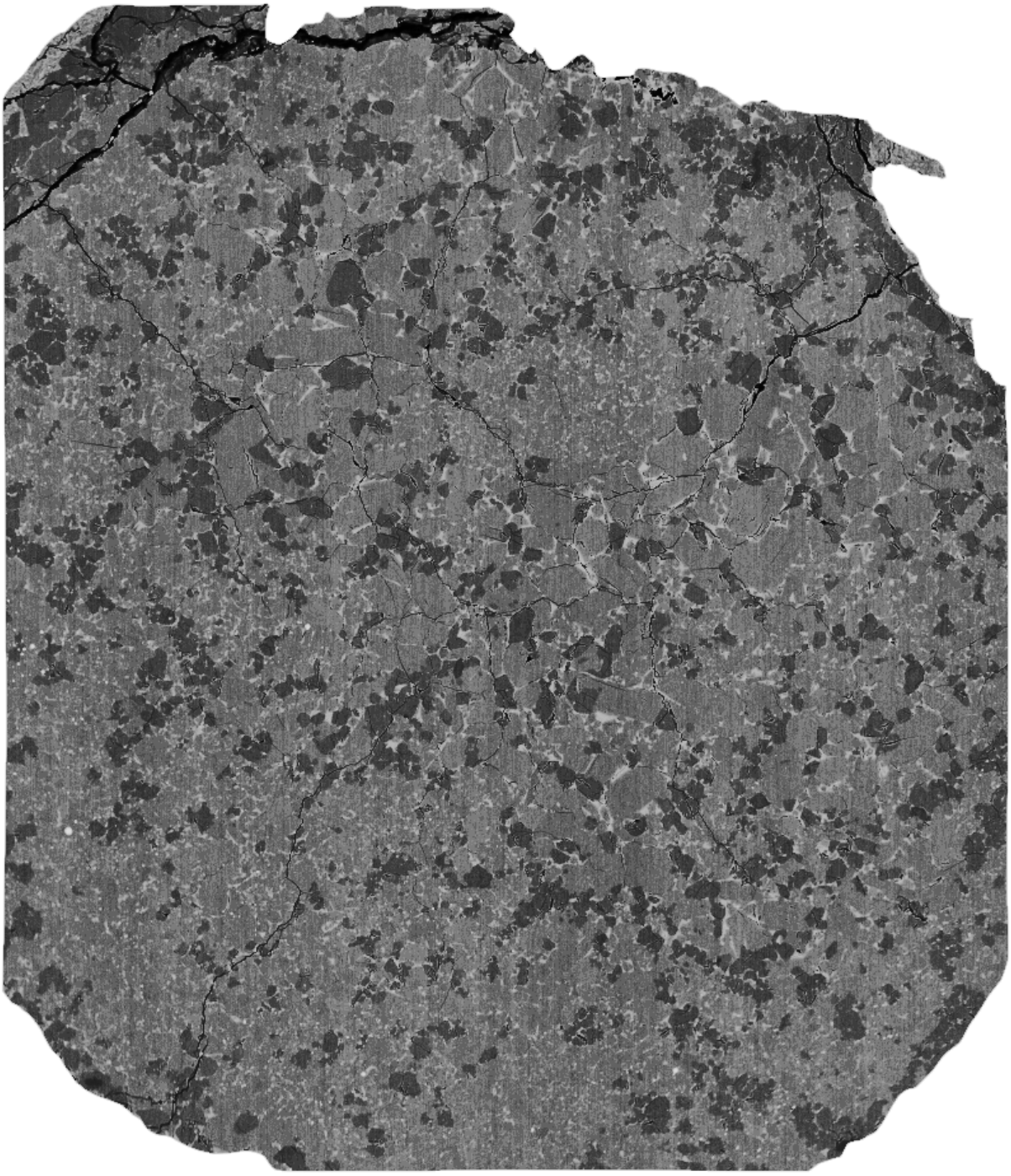

T (°C)	1850	**Run**	**A381**
P (GPa)	3.0	**Si**	26.92
Starting composition	Mer8(10)	**Ti**	0.16
Duration (hrs)	01:10	**Al**	2.99
Silicate Phases (wt%)	Gl (60) Ol (10) Opx (30) Cpx (x)	**Fe**	

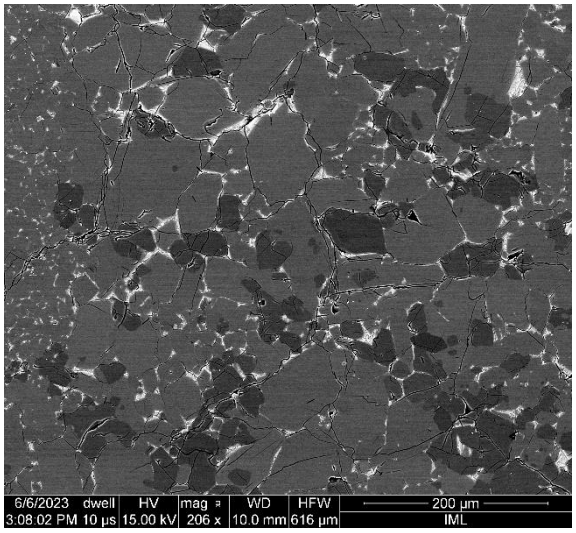

Mn	0.15
Mg	21.15
Ca	1.56
Na	0.17
K	0.07
S	
Cr	< dl
O*	48.13
Tot	101.30

A396

T (°C)	1450	**Run**	**A396**
P (GPa)	1.5	**Si**	26.86
Starting composition	Mer_1(20) + 20% FeS	**Ti**	< dl
Duration (hrs)	03:00	**Al**	6.59
Silicate Phases (wt%)	Gl () Ol () Opx () Cpx ()	**Fe**	0.32
		Mn	< dl
		Mg	9.78
		Ca	4.17
		Na	3.36
		K	0.38
		S	5.74
		Cr	
		O*	46.46
		Tot	103.65

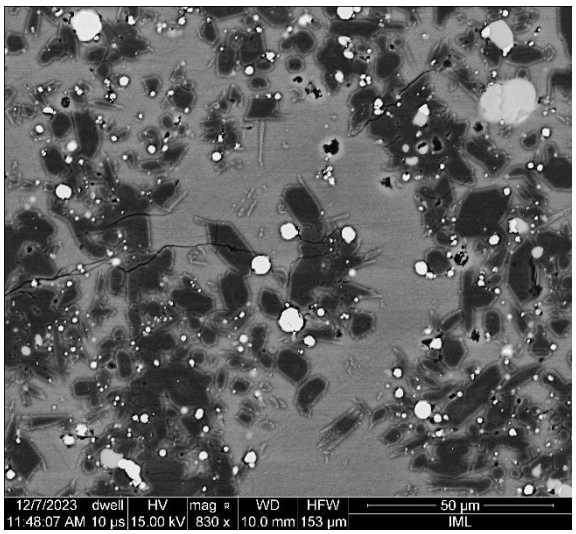

A397

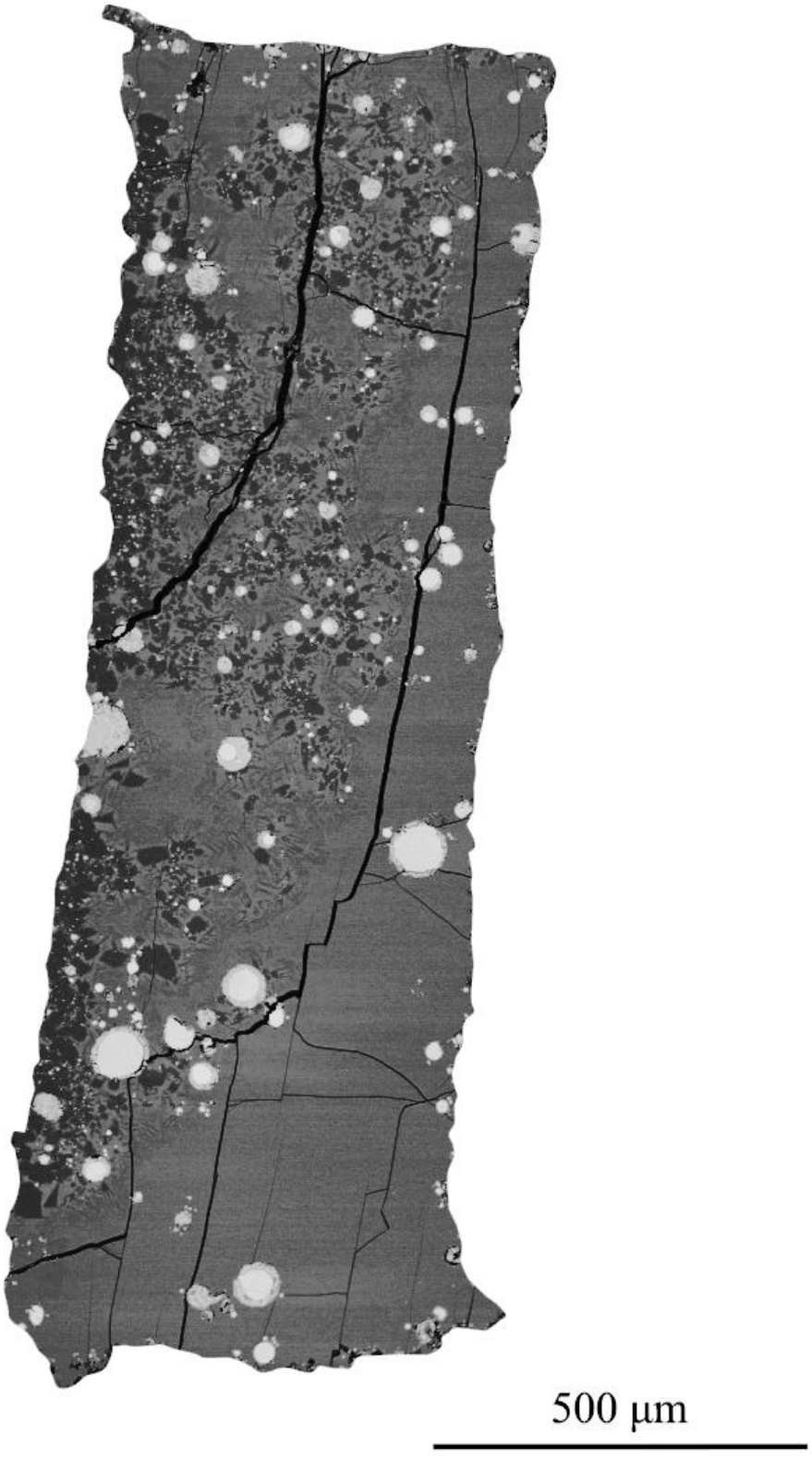

T (°C)	1500	**Run**	**A397**
P (GPa)	1.5	**Si**	26.36
Starting composition	Mer_1(20) + 20% FeS	**Ti**	< dl
Duration (hrs)	02:30	**Al**	5.51
Silicate Phases (wt%)	Gl () Opx ()	**Fe**	0.30
		Mn	0.16
		Mg	12.67
		Ca	3.51
		Na	2.57
		K	0.30
		S	5.65
		Cr	
		O*	46.22
		Tot	103.27

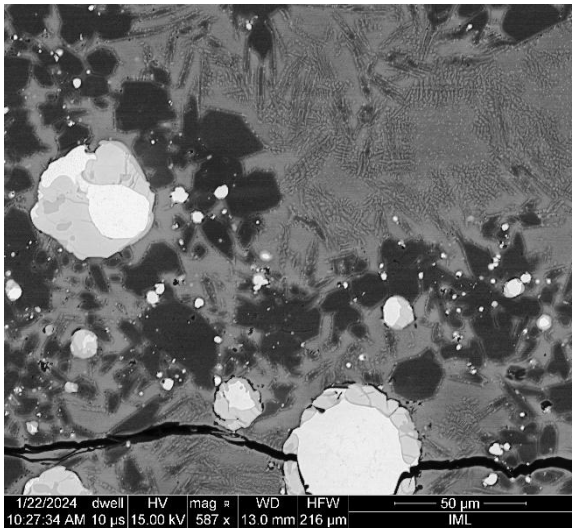

A399

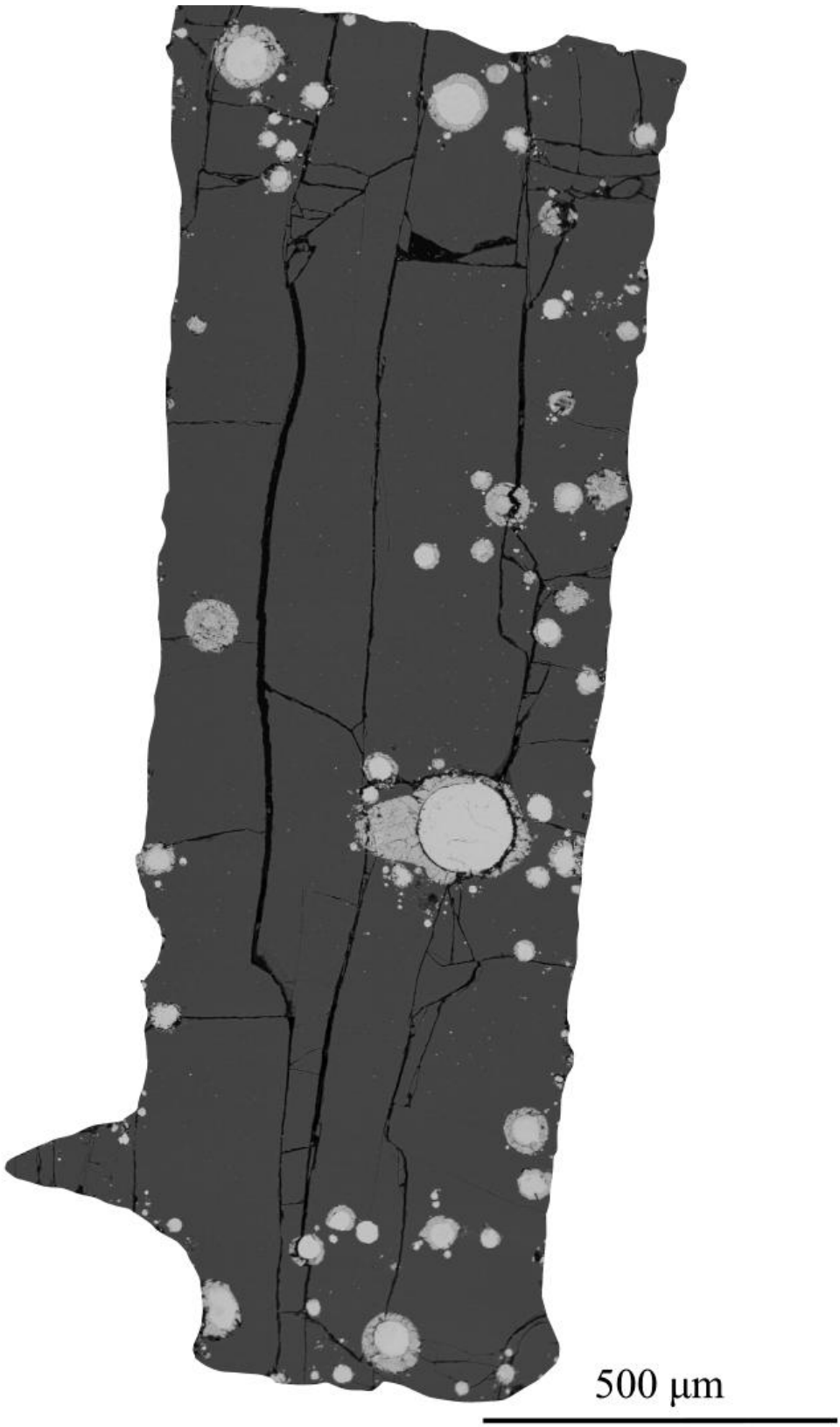

T (°C)	1525	**Run**	**A399**
P (GPa)	1.5	**Si**	26.20
Starting composition	Mer_1(20) + 20% FeS	**Ti**	< dl
Duration (hrs)	02:00	**Al**	4.85
Silicate Phases (wt%)	Gl (100)	**Fe**	0.23
		Mn	0.21
		Mg	13.99
		Ca	3.09
		Na	2.34
		K	0.25
		S	5.23
		Cr	
		O*	46.03
		Tot	102.42

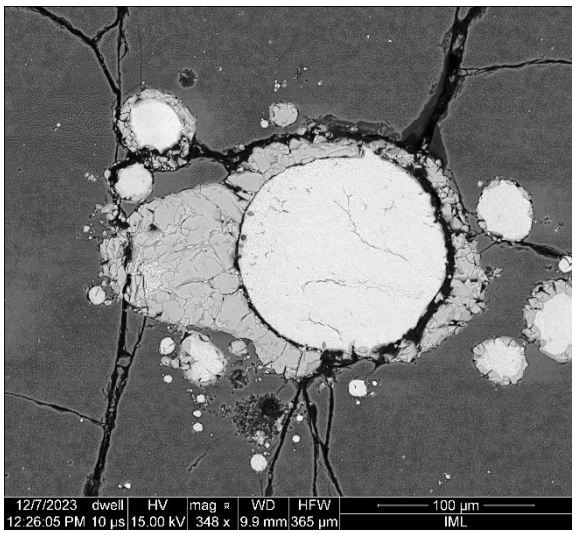

A400

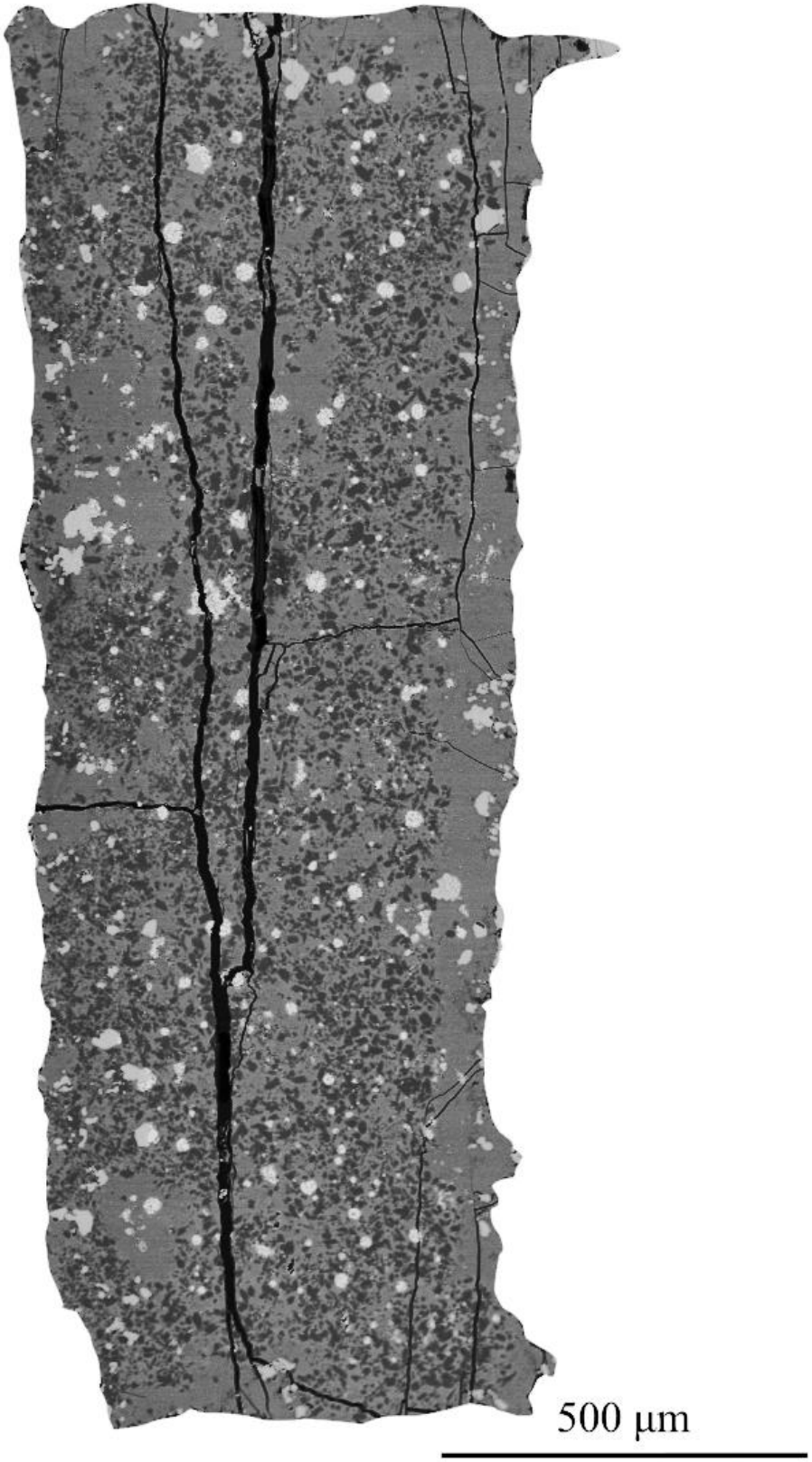

T (°C)	1450	**Run**	**A400**
P (GPa)	1.5	**Si**	28.12
Starting composition	Mer_1(20) + 10% FeS. 10% S	**Ti**	< dl
Duration (hrs)	02:00	**Al**	5.64
Silicate Phases (wt%)	Gl () Ol () Opx () Cpx ()	**Fe**	0.29
		Mn	< dl
		Mg	11.10
		Ca	2.95
		Na	2.35
		K	0.24
		S	6.81
		Cr	
		O*	46.90
		Tot	104.39

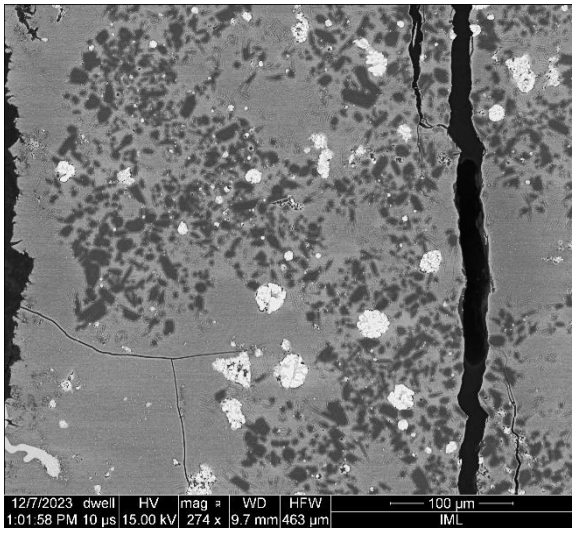

A401

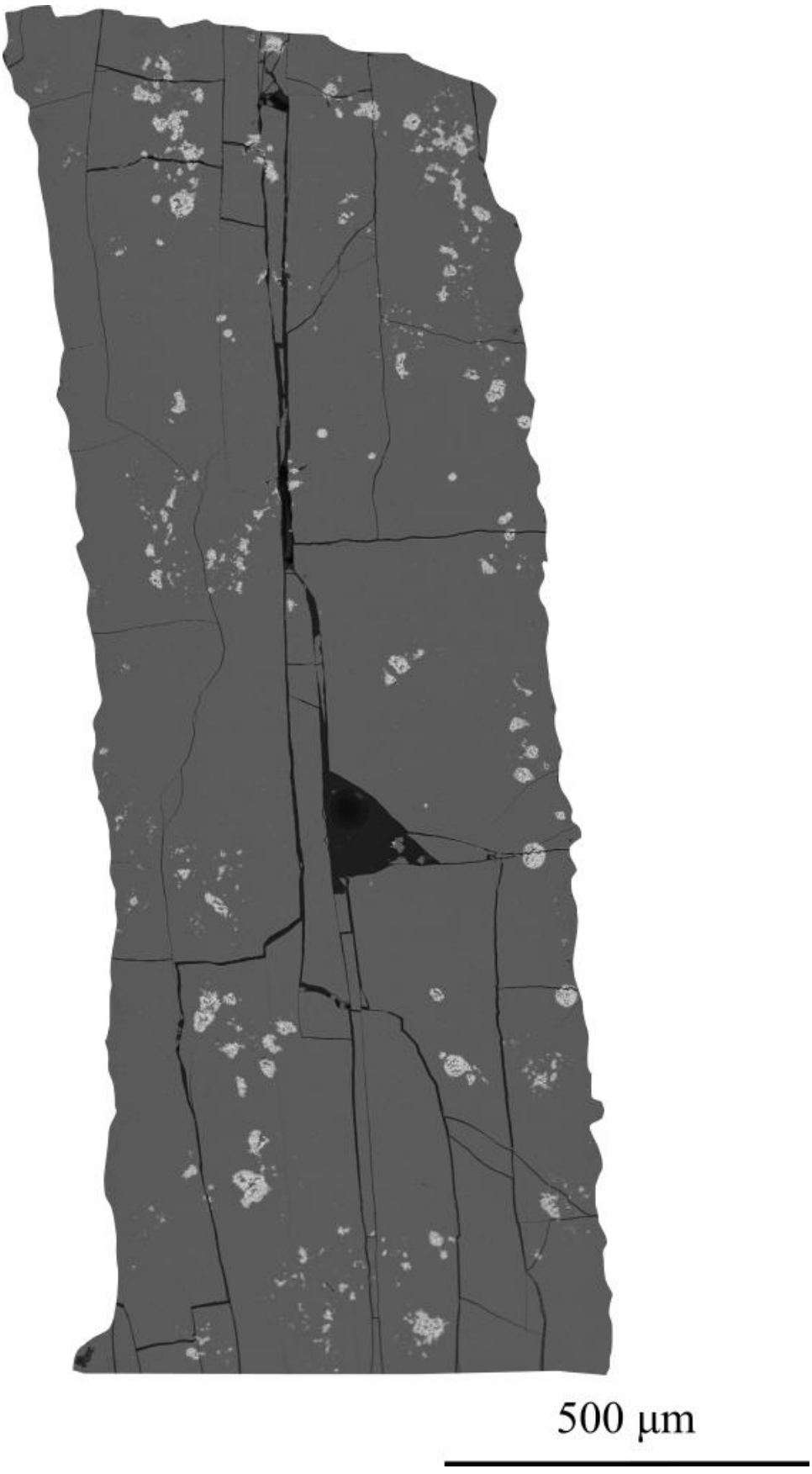

T (°C)	1500	**Run**	**A401**
P (GPa)	1.5	**Si**	27.22
Starting composition	Mer_1(20) + 10% FeS. 10% S	**Ti**	< dl
Duration (hrs)	01:30	**Al**	4.81
Silicate Phases (wt%)	Gl () Opx ()	**Fe**	0.26
		Mn	< dl
		Mg	13.06
		Ca	2.55
		Na	2.02
		K	0.21
		S	6.85
		Cr	
		O*	46.11
		Tot	103.09

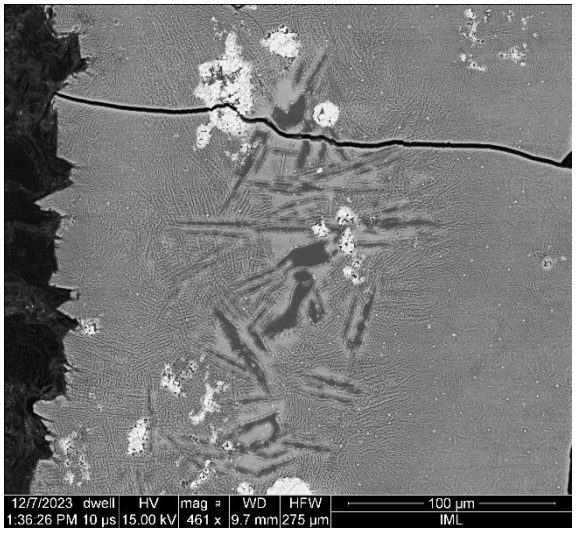

A402

T (°C)	1450	**Run**	**A402**
P (GPa)	1.5	**Si**	27.49
Starting composition	Mer_1(20) + 15% S	**Ti**	0.22
Duration (hrs)	02:00	**Al**	6.37
Silicate Phases (wt%)	Gl () Ol () Opx () Cpx () Qtz ()	**Fe**	

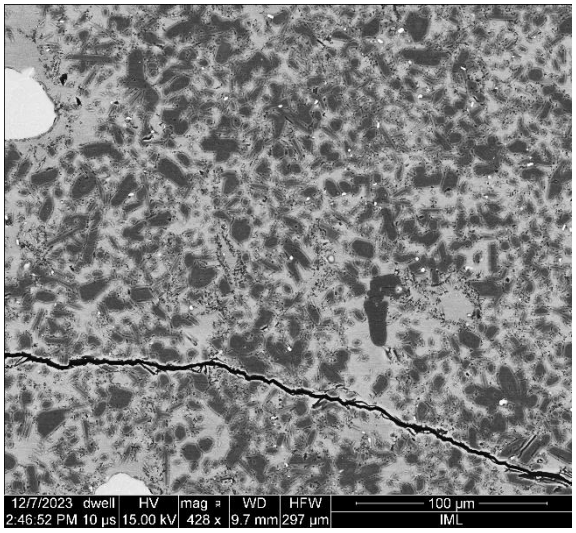

Mn	< dl
Mg	9.83
Ca	3.69
Na	1.47
K	0.14
S	5.31
Cr	
O*	45.84
Tot	100.36

A403

T (°C)	1500	**Run**	**A403**
P (GPa)	1.5	**Si**	28.34
Starting composition	Mer_1(20) + 15% S	**Ti**	0.16
Duration (hrs)	01:30	**Al**	4.94
Silicate Phases (wt%)	Gl () Ol () Opx () Cpx () Qtz ()	**Fe**	
		Mn	< dl
		Mg	12.73
		Ca	2.63
		Na	1.33
		K	0.14
		S	5.39
		Cr	
		O*	46.92
		Tot	102.60

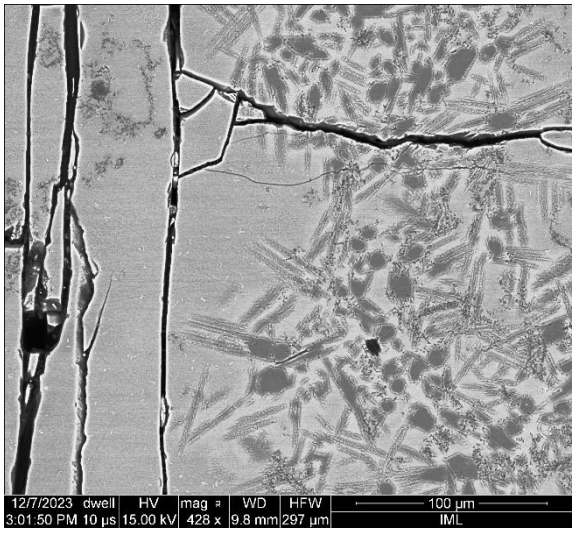

A404

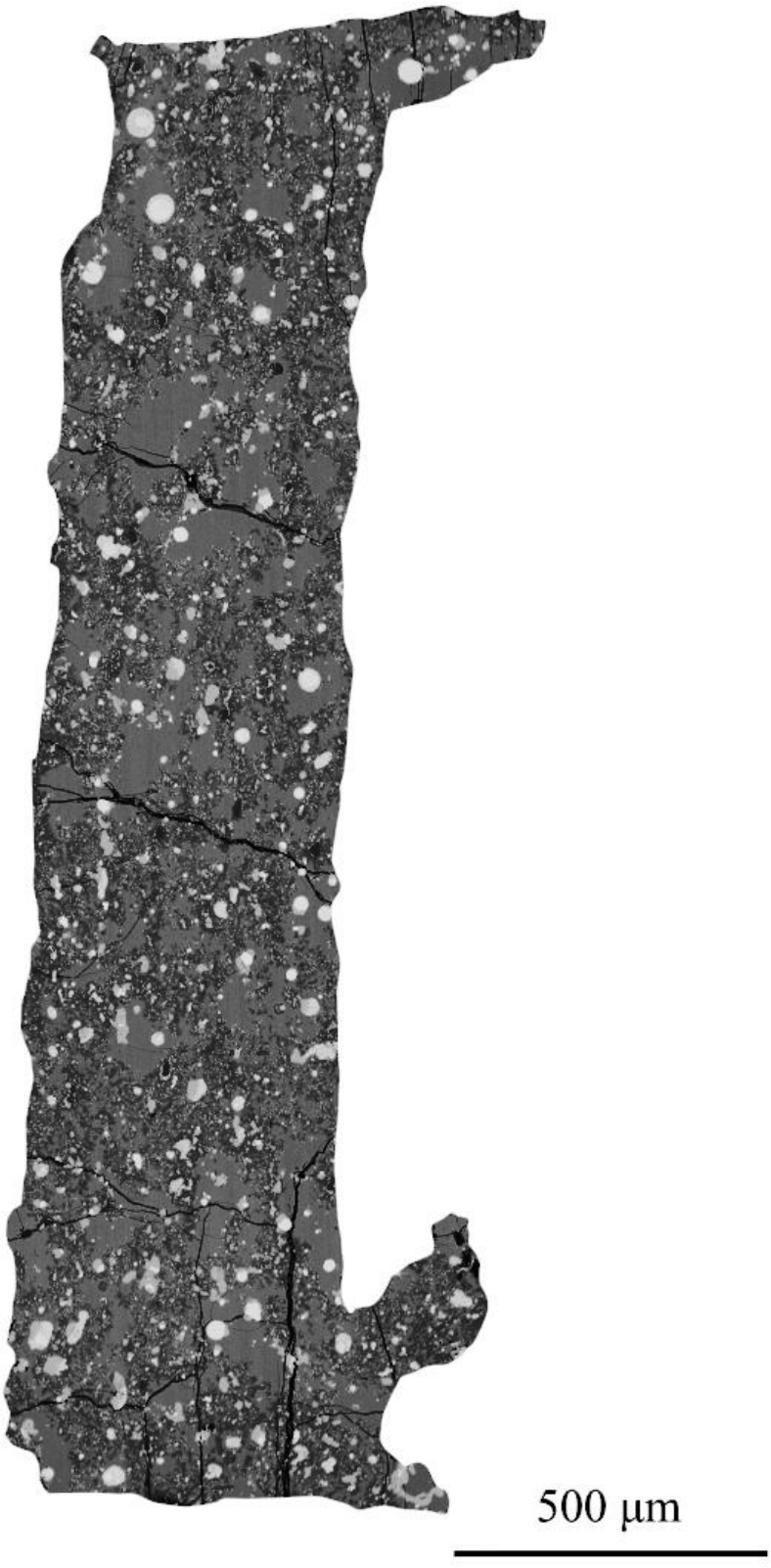

T (°C)	1400	**Run**	**A404**
P (GPa)	1.5	**Si**	28.38
Starting composition	Mer_1(20) + 20% FeS	**Ti**	< dl
Duration (hrs)	03:30	**Al**	7.28
Silicate Phases (wt%)	Gl () Ol () Opx () Cpx ()	**Fe**	0.26
		Mn	< dl
		Mg	6.62
		Ca	4.47
		Na	3.80
		K	0.46
		S	5.08
		Cr	
		O*	47.02
		Tot	103.36

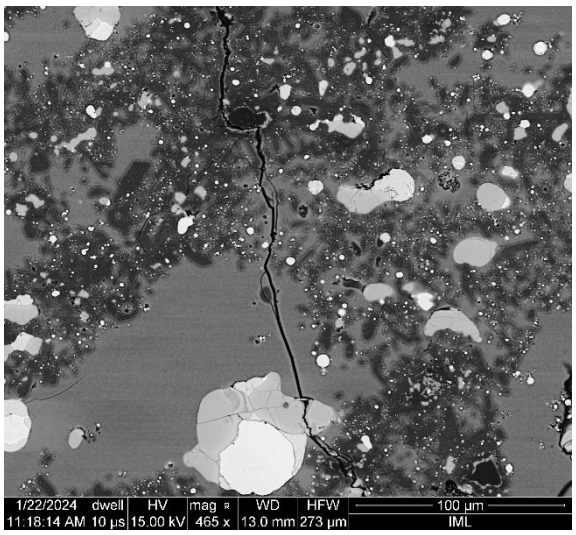

A405

T (°C)	1400	**Run**	**A405**
P (GPa)	1.5	**Si**	29.23
Starting composition	Mer_1(20) + 10% FeS. 10% S	**Ti**	< dl
Duration (hrs)	02:30	**Al**	6.80
Silicate Phases (wt%)	Gl () Ol () Cpx () Qtz ()	**Fe**	0.24
		Mn	< dl
		Mg	7.26
		Ca	3.36
		Na	3.02
		K	0.31
		S	5.77
		Cr	
		O*	47.16
		Tot	103.15

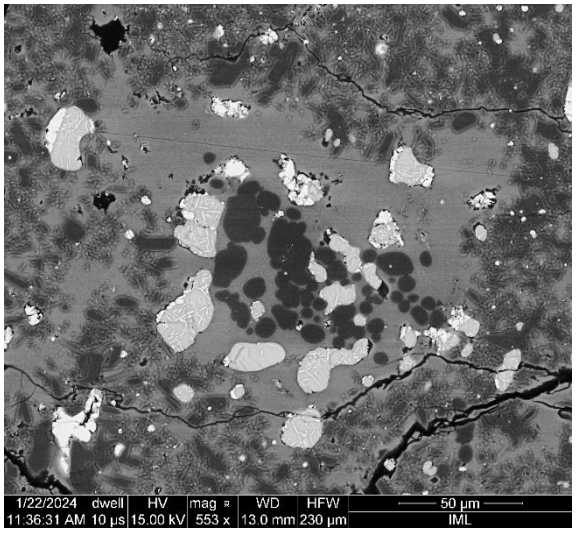

A431

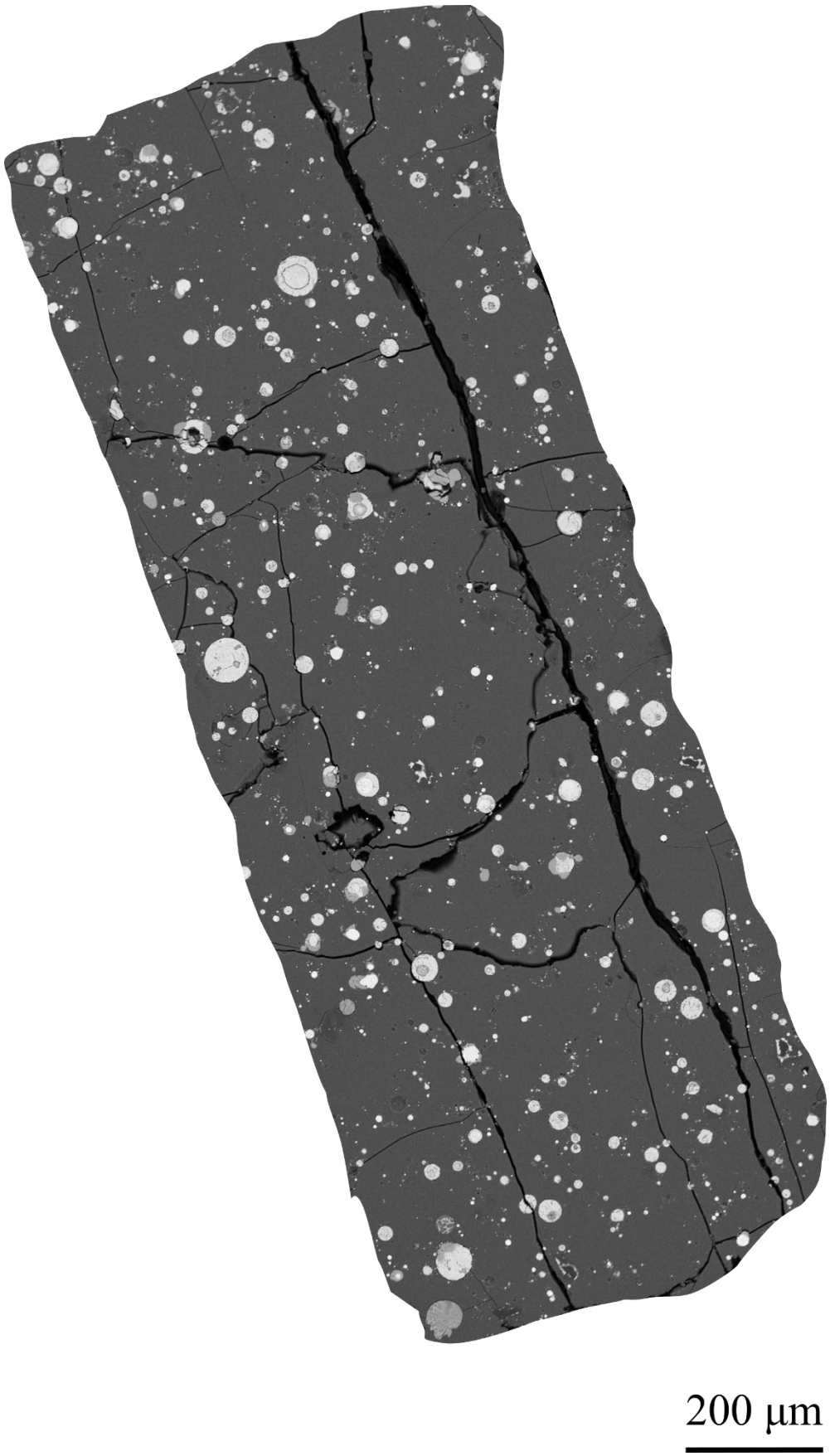

T (°C)	1350	**Run**	**A431**
P (GPa)	1.0	**Si**	28.55
Starting composition	Mer_2(20) + 20% FeS	**Ti**	< dl
Duration (hrs)	00:30	**Al**	7.86
Silicate Phases (wt%)	Gl () Ol () Opx () Cpx() Qtz ()	**Fe**	0.32
		Mn	< dl
		Mg	7.17
		Ca	3.47
		Na	3.53
		K	0.33
		S	4.19
		Cr	
		O*	47.54
		Tot	102.95

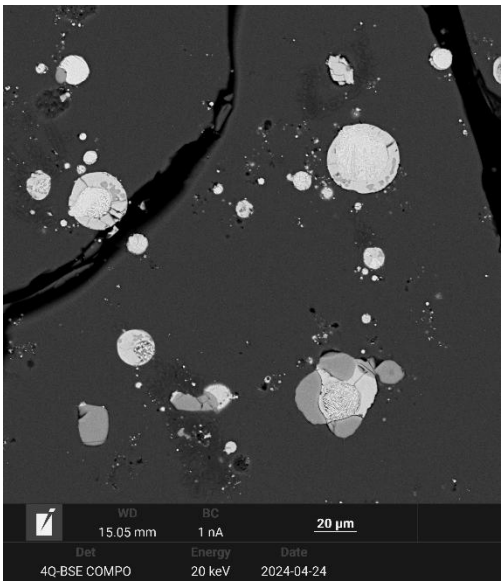

A432

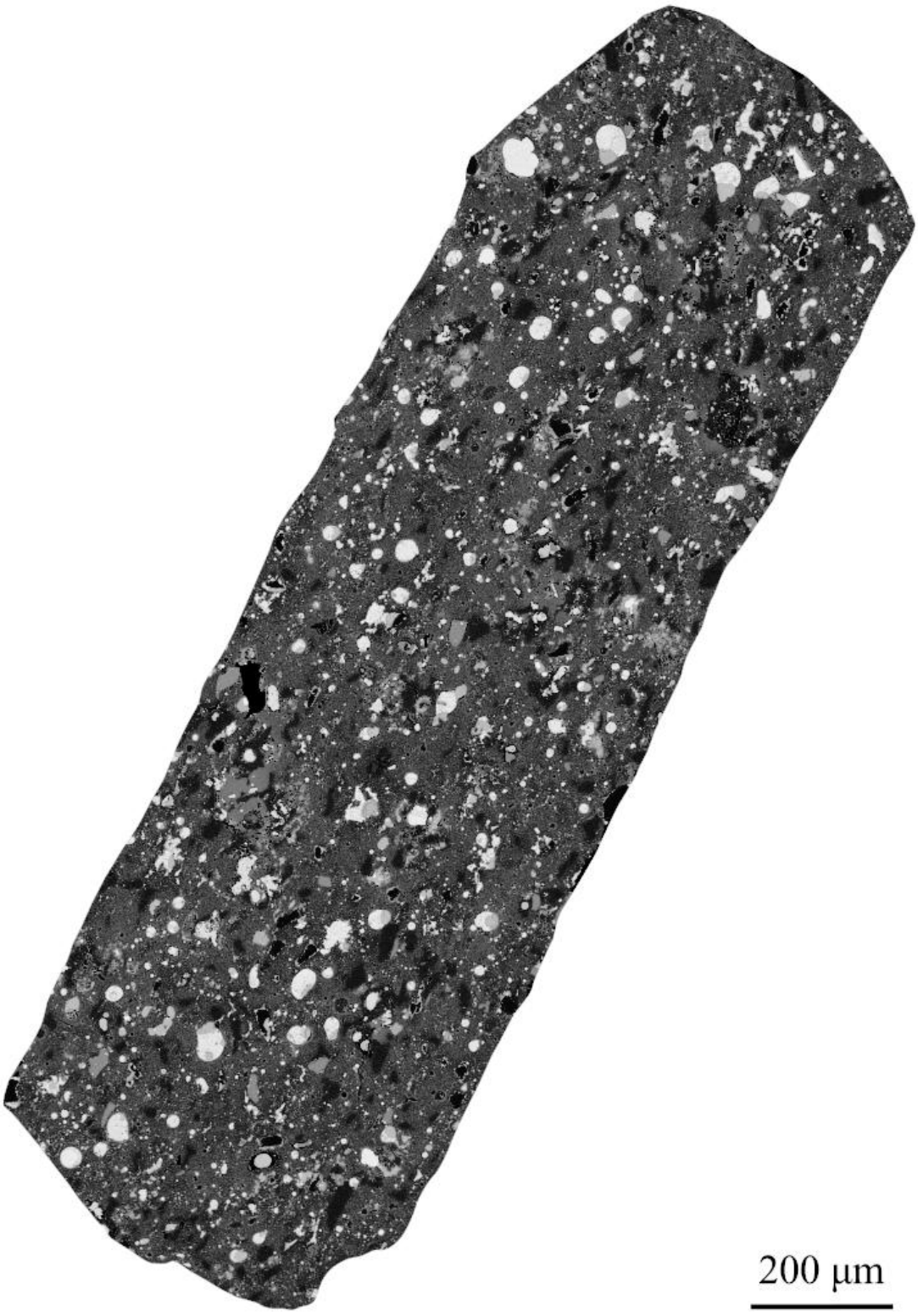

T (°C)	1250	**Run**	**A432**
P (GPa)	1.0	**Si**	30.85
Starting composition	Mer_2(20) + 20% FeS	**Ti**	< dl
Duration (hrs)	01:30	**Al**	8.78
Silicate Phases (wt%)	Gl () Opx () Cpx() Qtz ()	**Fe**	0.36
		Mn	< dl
		Mg	2.79
		Ca	3.60
		Na	4.82
		K	0.55
		S	2.39
		Cr	
		O*	48.83
		Tot	102.97

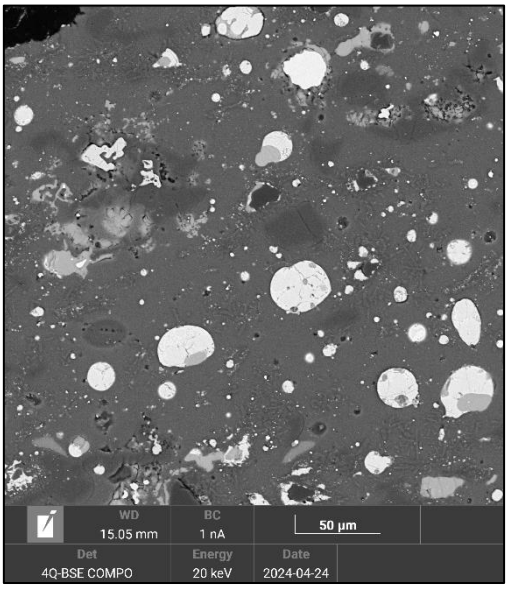

A441

T (°C)	1300	**Run**	**A441**
P (GPa)	1.0	**Si**	29.14
Starting composition	Mer_2(20) + 20% FeS	**Ti**	< dl
Duration (hrs)	01:00	**Al**	8.61
Silicate Phases (wt%)	Gl () Opx () Cpx() Qtz ()	**Fe**	0.38
		Mn	< dl
		Mg	4.86
		Ca	3.67
		Na	3.92
		K	0.39
		S	3.44
		Cr	
		O*	47.66
		Tot	102.07

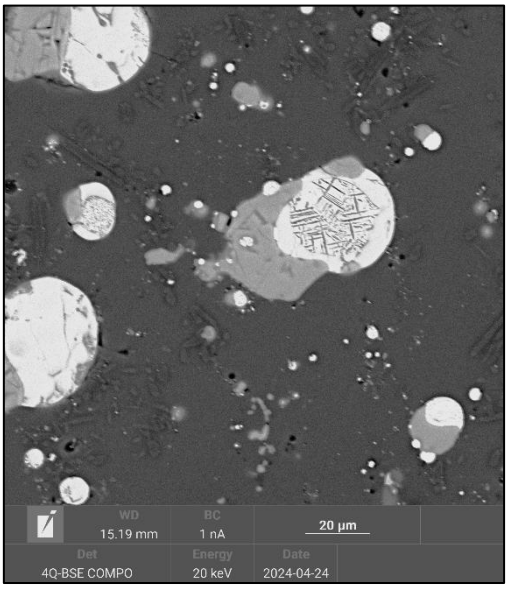

A444

T (°C)	1325	**Run**	**A444**
P (GPa)	1.0	**Si**	29.30
Starting composition	Mer_2(20) + 20% FeS	**Ti**	< dl
Duration (hrs)	00:45	**Al**	8.62
Silicate Phases (wt%)	Gl () Opx () Cpx() Qtz ()	**Fe**	0.15
		Mn	< dl
		Mg	6.20
		Ca	3.63
		Na	2.55
		K	0.34
		S	3.82
		Cr	
		O*	47.97
		Tot	102.59

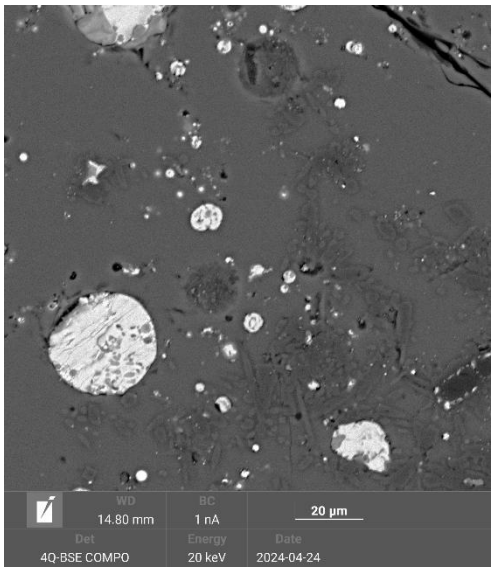

A445

T (°C)	1275	**Run**	**A445**
P (GPa)	1.0	**Si**	30.15
Starting composition	Mer_2(20) + 20% FeS	**Ti**	< dl
Duration (hrs)	01:15	**Al**	8.83
Silicate Phases (wt%)	Gl () Opx () Cpx() Qtz ()	**Fe**	0.46
		Mn	< dl
		Mg	3.30
		Ca	3.54
		Na	4.50
		K	0.47
		S	2.86
		Cr	
		O*	48.23
		Tot	102.34

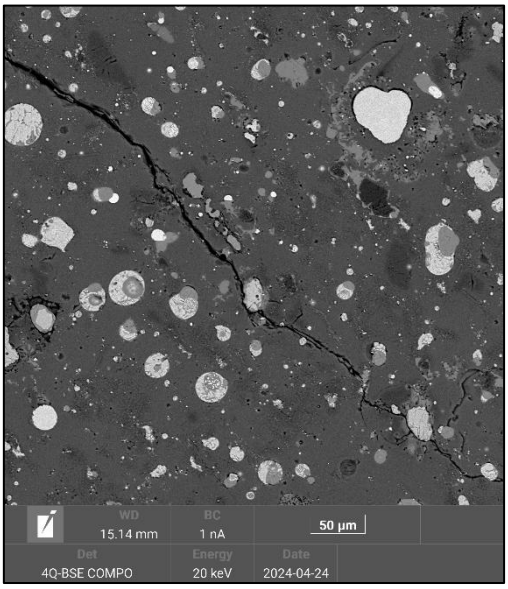

A451

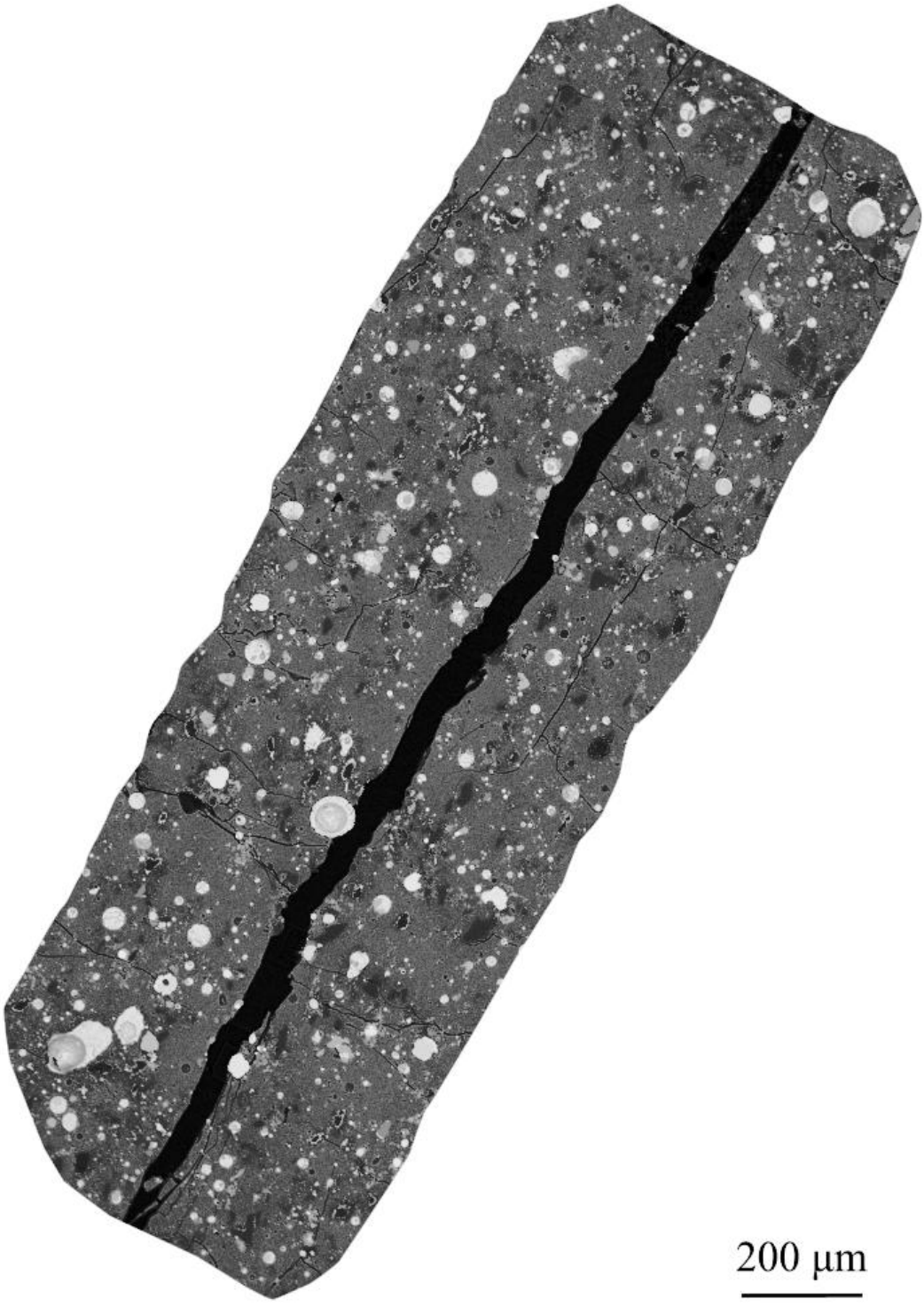

T (°C)	1300	**Run**	**A451**
P (GPa)	1.0	**Si**	30.20
Starting composition	Mer_2(20) + 20% FeS	**Ti**	< dl
Duration (hrs)	00:30	**Al**	8.43
Silicate Phases (wt%)	Gl () Opx () Cpx() Qtz ()	**Fe**	0.35
		Mn	< dl
		Mg	4.07
		Ca	3.45
		Na	4.17
		K	0.45
		S	3.33
		Cr	
		O*	48.23
		Tot	102.68

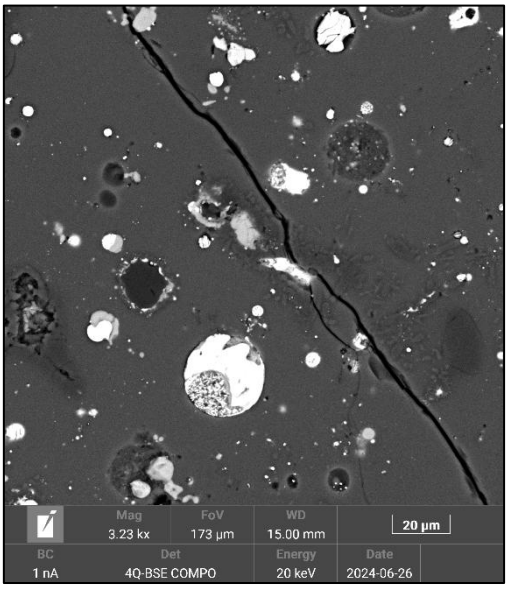

A452

T (°C)	1300	**Run**	**A452**
P (GPa)	1.0	**Si**	29.50
Starting composition	Mer_2(20) + 20% FeS	**Ti**	< dl
Duration (hrs)	03:00	**Al**	9.21
Silicate Phases (wt%)	Gl () Opx () Cpx() Qtz ()	**Fe**	0.26
		Mn	< dl
		Mg	4.16
		Ca	3.87
		Na	3.98
		K	0.39
		S	2.90
		Cr	
		O*	48.22
		Tot	102.50

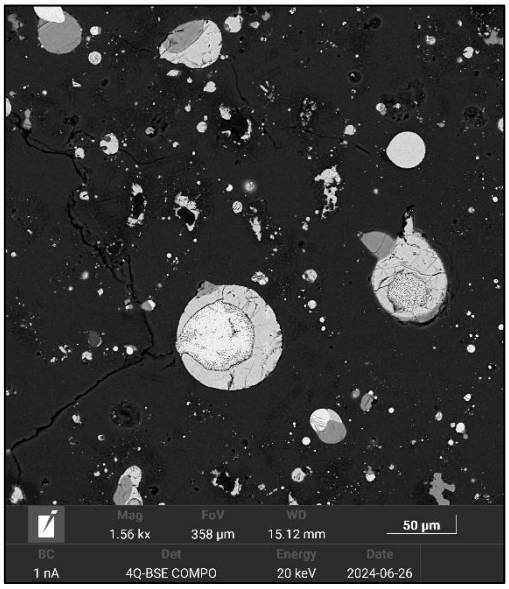

A453

T (°C)	1300	**Run**	**A453**
P (GPa)	1.0	**Si**	31.77
Starting composition	Mer_2(20) + 20% FeS	**Ti**	< dl
Duration (hrs)	06:00	**Al**	8.33
Silicate Phases (wt%)	Gl () Opx () Cpx() Qtz ()	**Fe**	0.34
		Mn	< dl
		Mg	3.25
		Ca	3.14
		Na	3.95
		K	0.44
		S	2.70
		Cr	
		O*	49.15
		Tot	103.09

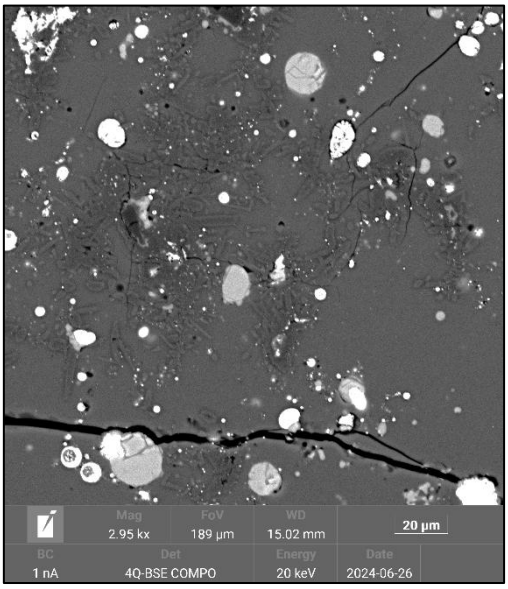

A456

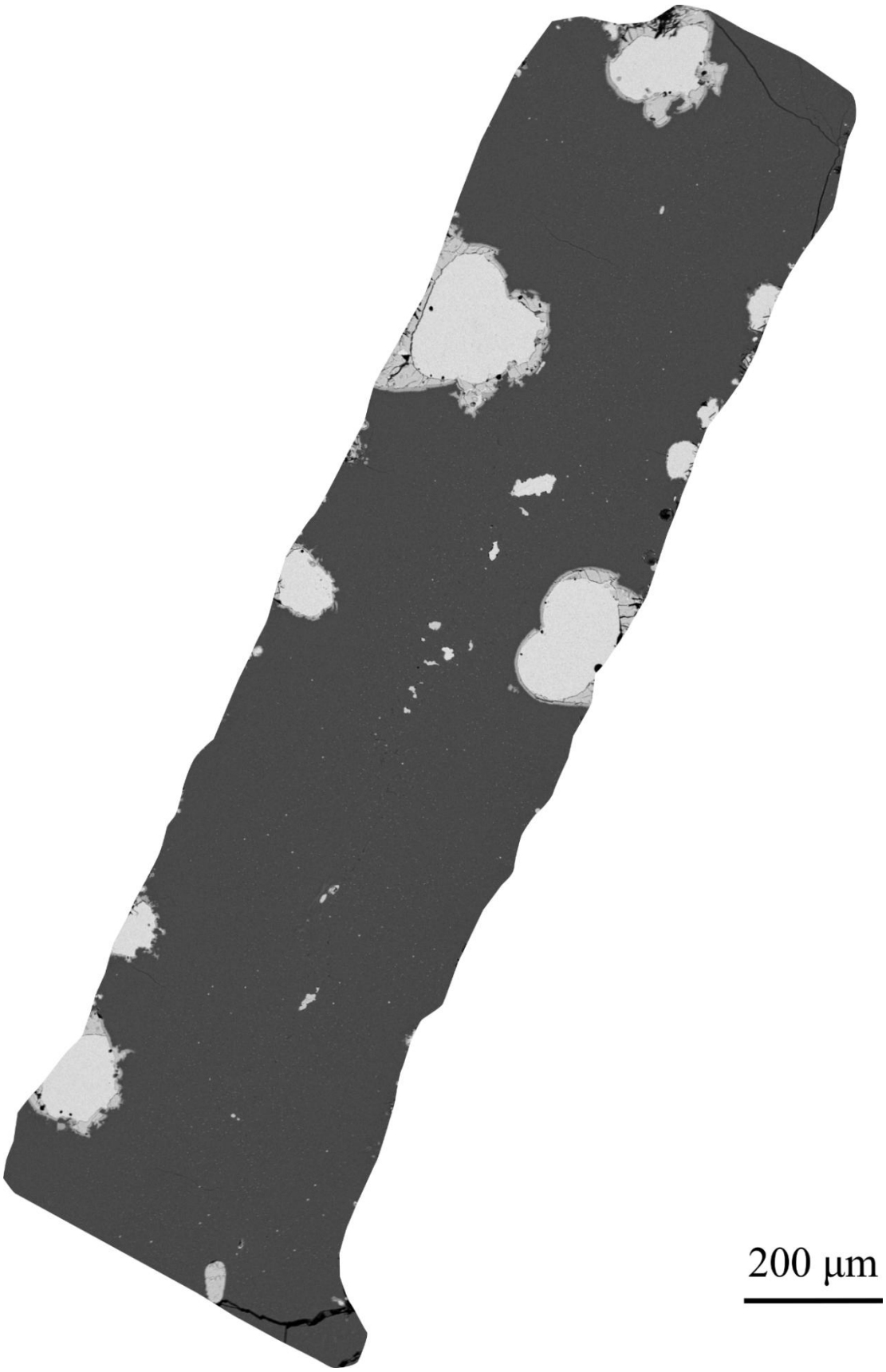

T (°C)	1700	**Run**	**A456**
P (GPa)	1.5	**Si**	24.13
Starting composition	Mer8(30) + 30% FeS	**Ti**	< dl
Duration (hrs)	00:30	**Al**	1.89
Silicate Phases (wt%)	Gl (100)	**Fe**	0.64
		Mn	0.17
		Mg	21.47
		Ca	1.09
		Na	0.61
		K	0.10
		S	9.01
		Cr	< dl
		O*	44.35
		Tot	103.53

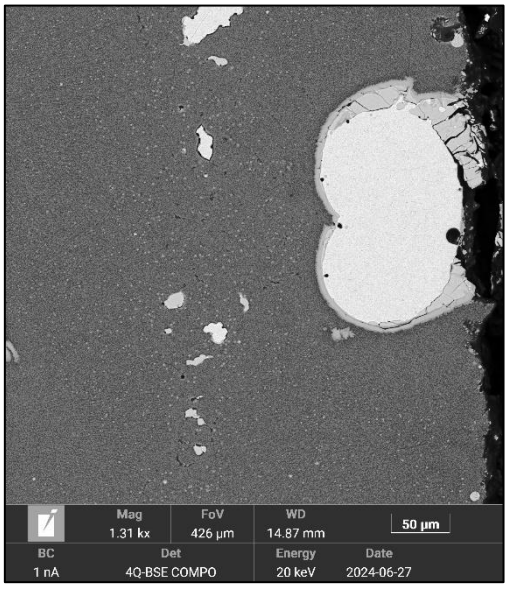

A461

T (°C)	1275	**Run**	**A461**
P (GPa)	1.0	**Si**	31.01
Starting composition	Mer_2(10) + 16.7 % FeS	**Ti**	< dl
Duration (hrs)	01:15	**Al**	8.69
Silicate Phases (wt%)	Gl () Opx () Ol () Cpx() Qtz ()	**Fe**	0.43
		Mn	< dl
		Mg	2.64
		Ca	4.35
		Na	3.91
		K	0.46
		S	0.54
		Cr	
		O*	48.19
		Tot	100.22

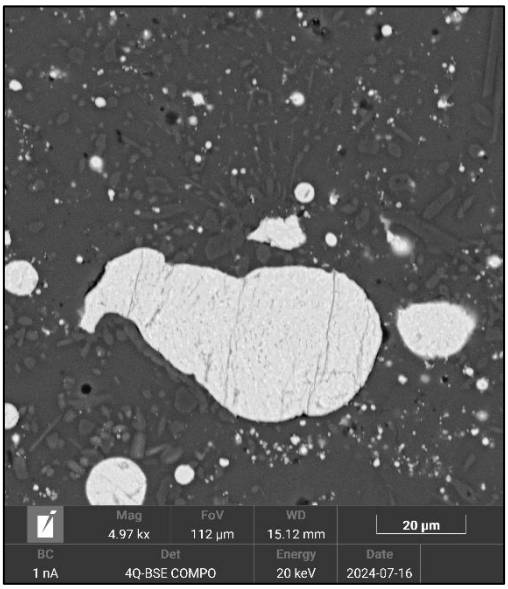

A462

T (°C)	1300	**Run**	**A462**
P (GPa)	1.0	**Si**	30.17
Starting composition	Mer_2(10) + 16.7% FeS	**Ti**	< dl
Duration (hrs)	01:00	**Al**	8.82
Silicate Phases (wt%)	Gl () Opx () Ol () Cpx() Qtz ()	**Fe**	0.38
		Mn	< dl
		Mg	3.55
		Ca	4.98
		Na	3.71
		K	0.40
		S	0.54
		Cr	
		O*	48.11
		Tot	100.66

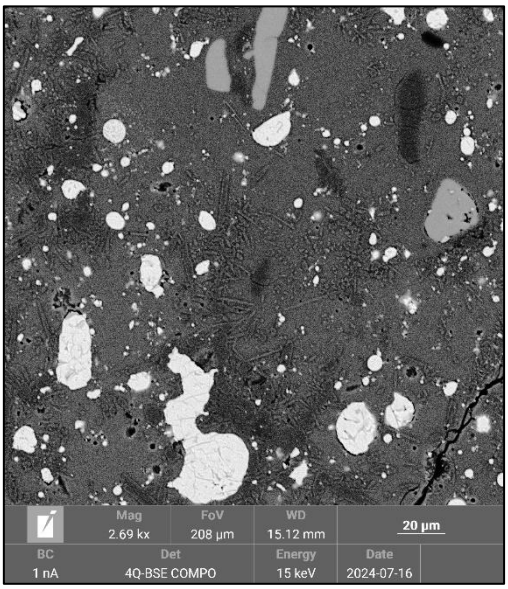

A466

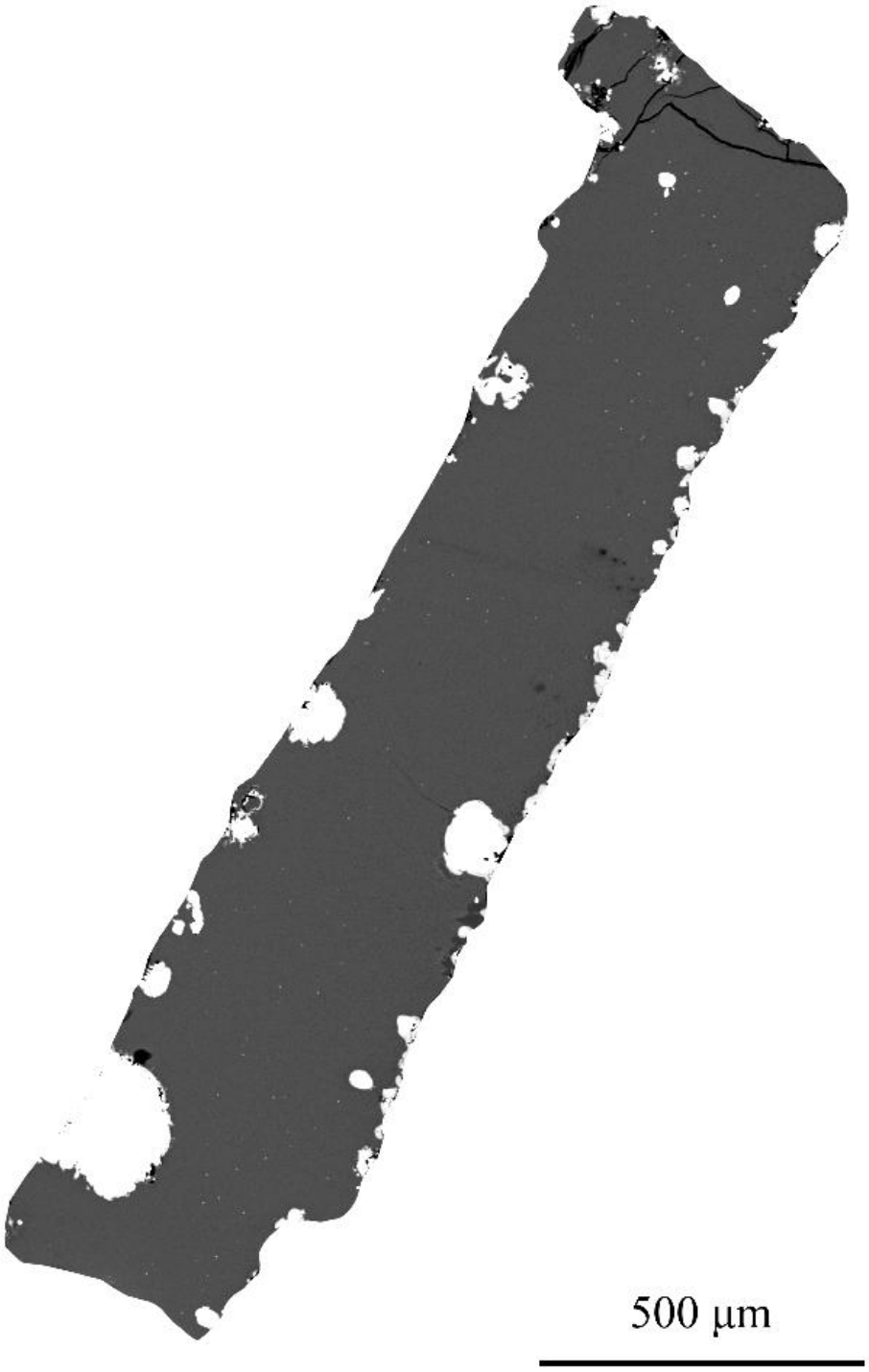

T (°C)	1600	**Run**	**A466**
P (GPa)	1.5	**Si**	24.66
Starting composition	Mer8(30) + 30% FeS	**Ti**	< dl
Duration (hrs)	00:50	**Al**	1.90
Silicate Phases (wt%)	Gl (99) Opx (1)	**Fe**	0.54
		Mn	0.14
		Mg	21.07
		Ca	1.12
		Na	0.62
		K	0.10
		S	8.61
		Cr	< dl
		O*	44.66
		Tot	103.45

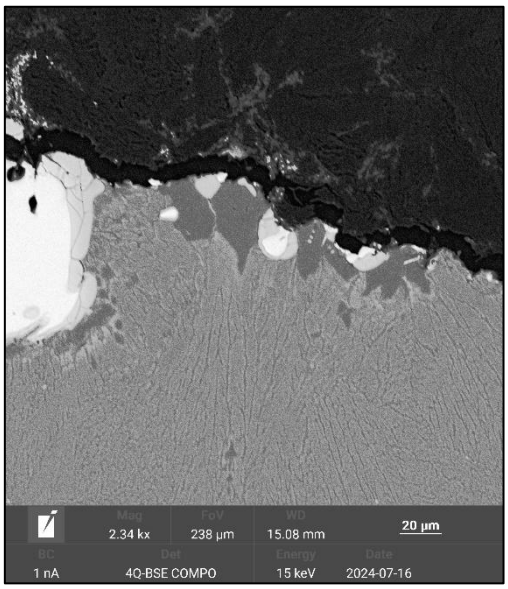

A468

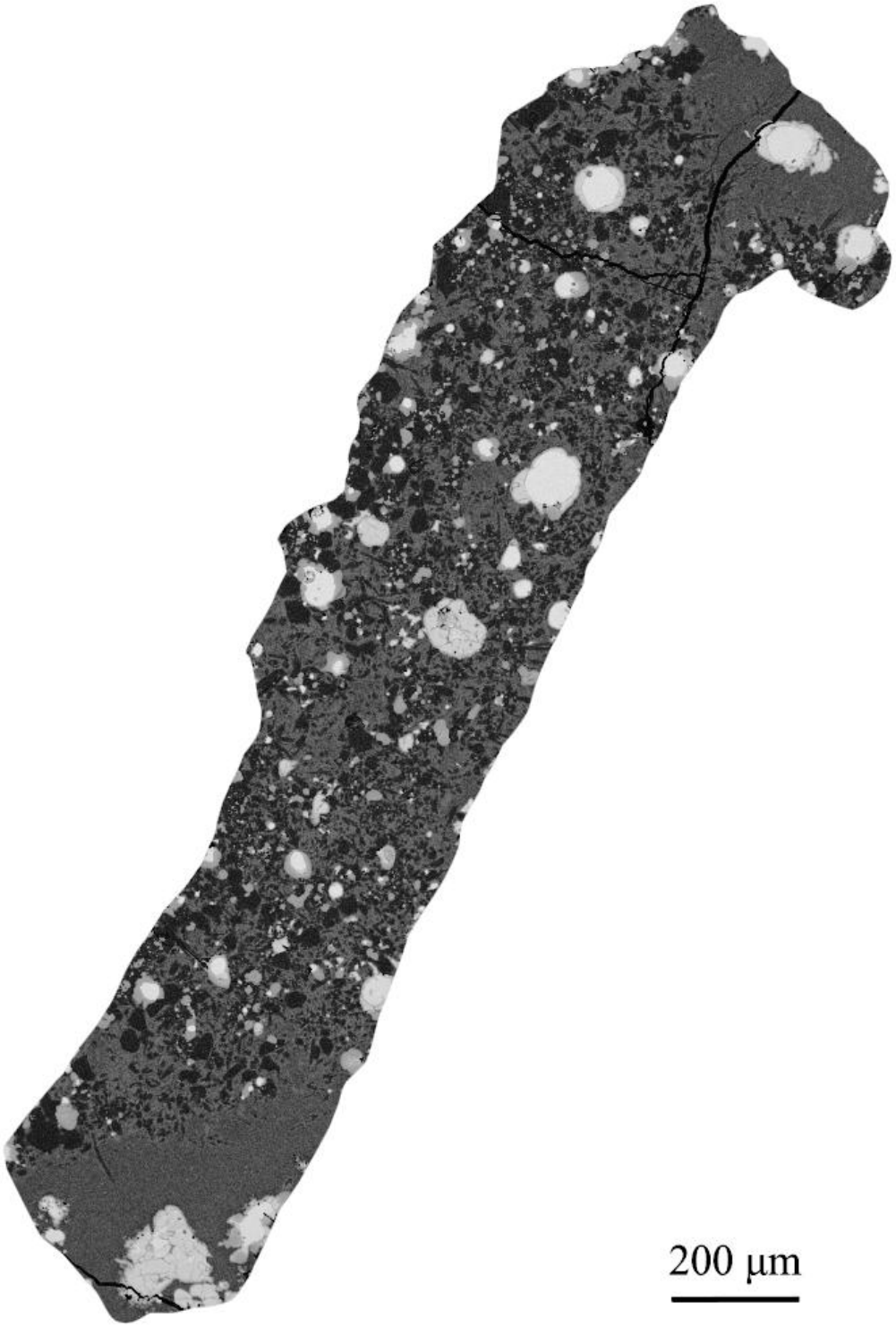

T (°C)	1550	**Run**	**A468**
P (GPa)	1.5	**Si**	25.97
Starting composition	Mer8(30) + 30% FeS	**Ti**	< dl
Duration (hrs)	00:55	**Al**	2.51
Silicate Phases (wt%)	Gl (77) Ol (16) Opx (6)	**Fe**	0.53
		Mn	< dl
		Mg	19.27
		Ca	1.24
		Na	1.07
		K	0.15
		S	6.86
		Cr	< dl
		O*	45.76
		Tot	103.43

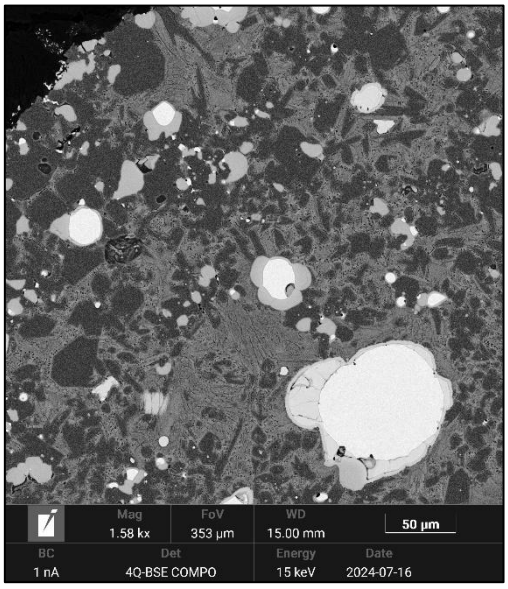

A469

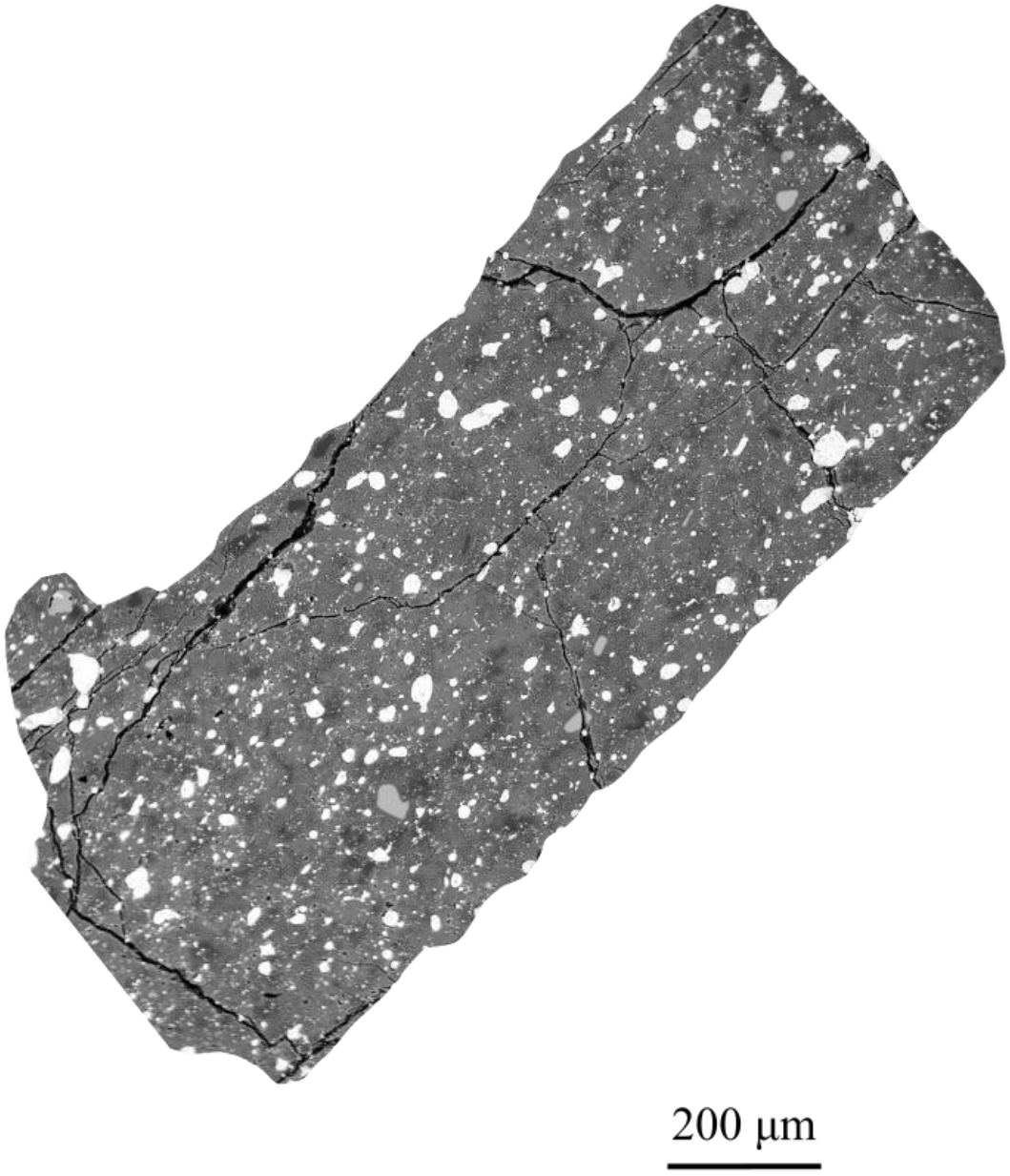

T (°C)	1250	**Run**	**A469**
P (GPa)	1.0	**Si**	30.14
Starting composition	Mer_2(10) + 16.7% FeS	**Ti**	0.20
Duration (hrs)	01 :30	**Al**	9.13
Silicate Phases (wt%)	Gl () Opx () Cpx() Qtz ()	**Fe**	0.45
		Mn	< dl
		Mg	2.83
		Ca	4.89
		Na	3.70
		K	0.41
		S	0.39
		Cr	
		O*	47.94
		Tot	100.08

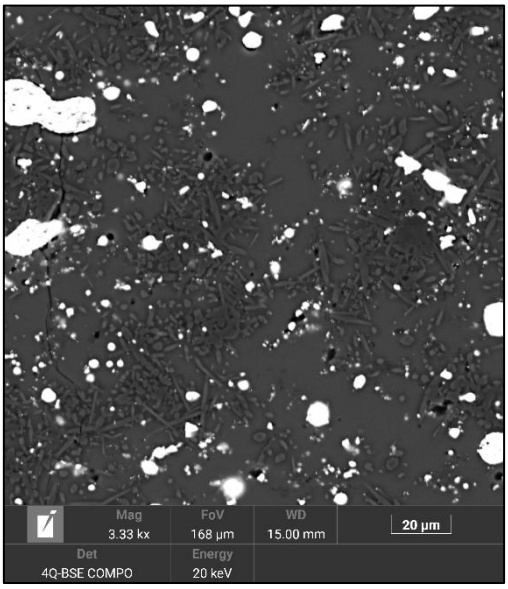

A473

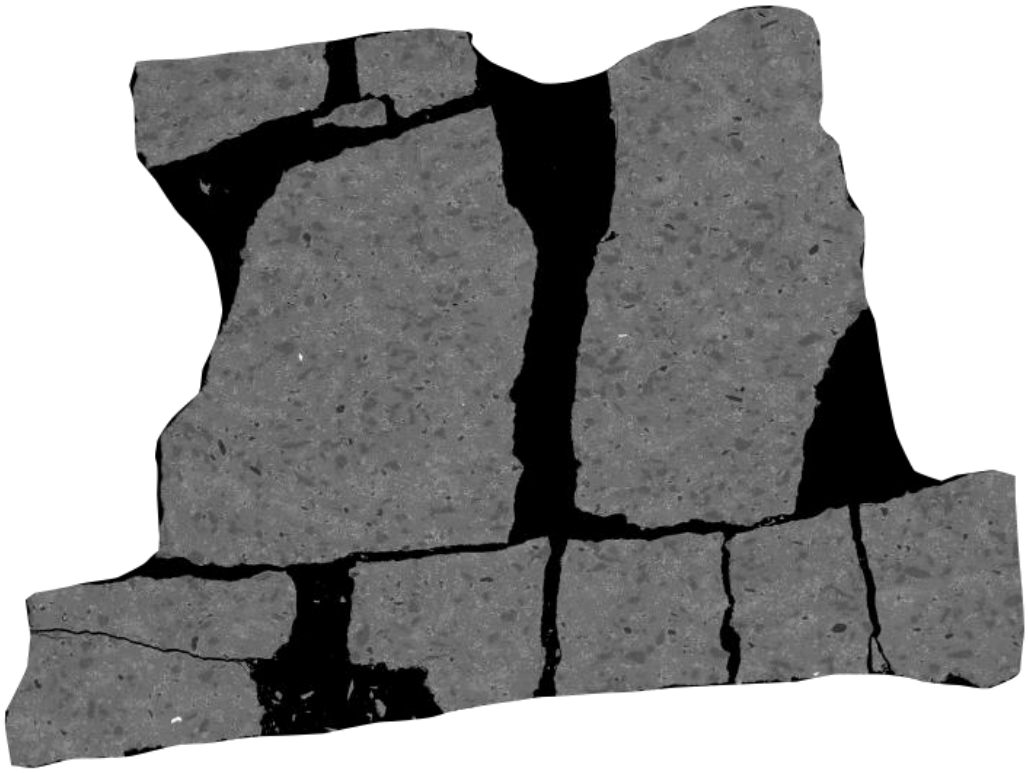

T (°C)	1200	**Run**	**A473**
P (GPa)	0.5	**Si**	34.79
Starting composition	Mer_3(0)	**Ti**	0.06
Duration (hrs)	01:00	**Al**	7.54
Silicate Phases (wt%)	Gl () Cpx () Qtz () Pl ()	**Fe**	
		Mn	0.08
		Mg	0.64
		Ca	2.65
		Na	5.02
		K	0.68
		S	
		Cr	
		O*	50.49
		Tot	101.95

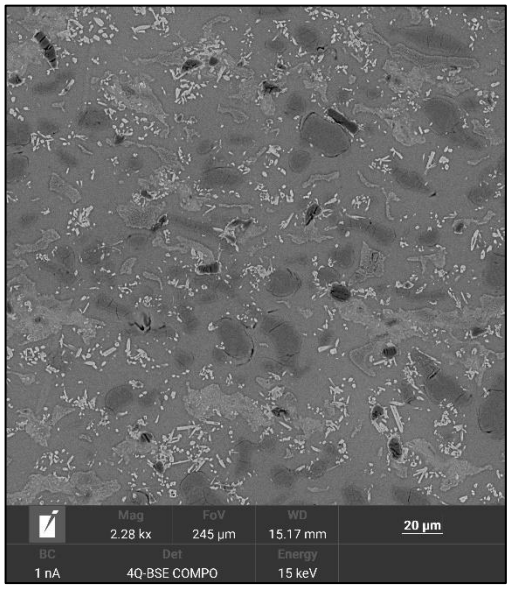

A475

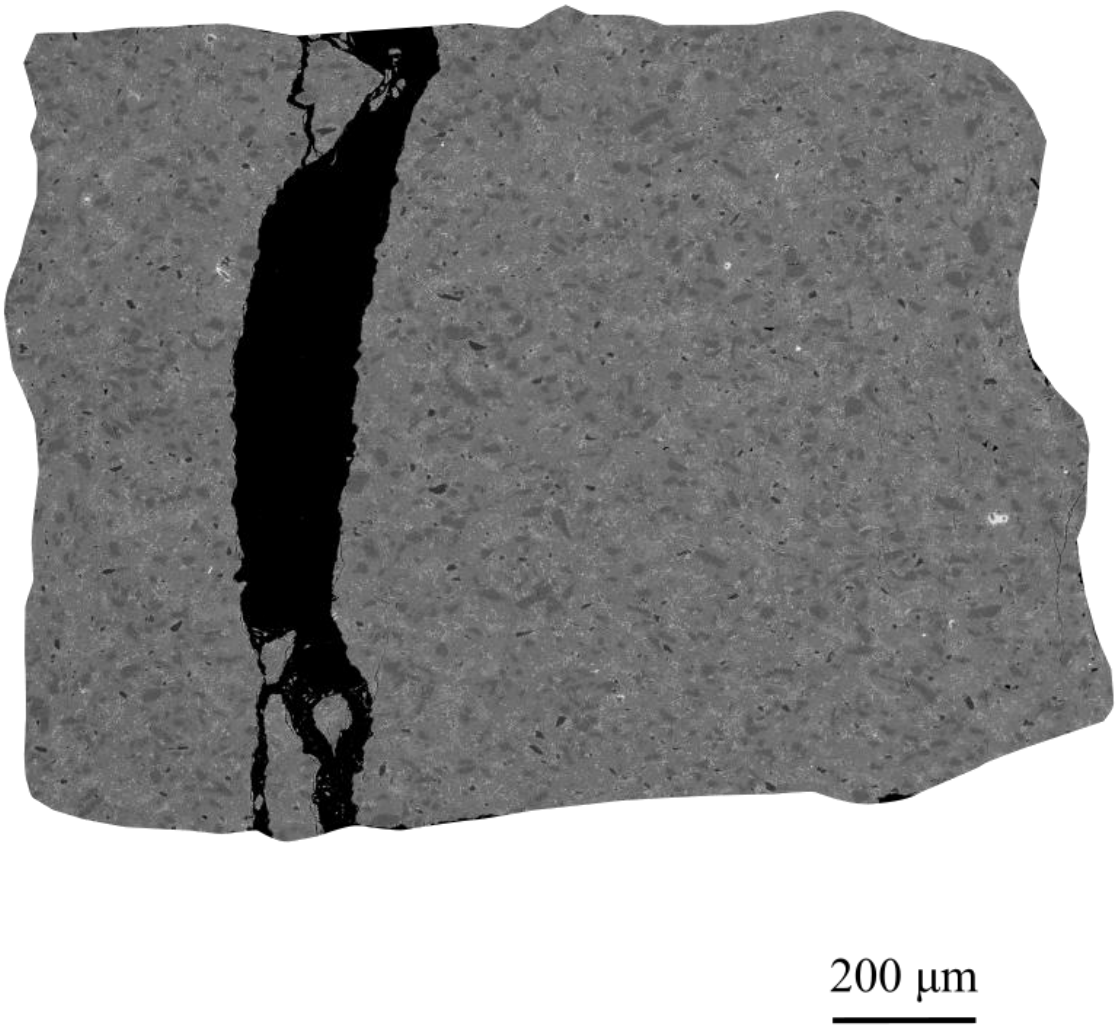

T (°C)	1175	**Run**	**A475**
P (GPa)	0.5	**Si**	36.07
Starting composition	Mer_3(0)	**Ti**	0.09
Duration (hrs)	01:10	**Al**	6.75
Silicate Phases (wt%)	Gl () Cpx () Qtz () Pl ()	**Fe**	
		Mn	0.08
		Mg	0.58
		Ca	2.12
		Na	5.04
		K	0.73
		S	
		Cr	
		O*	51.04
		Tot	102.51

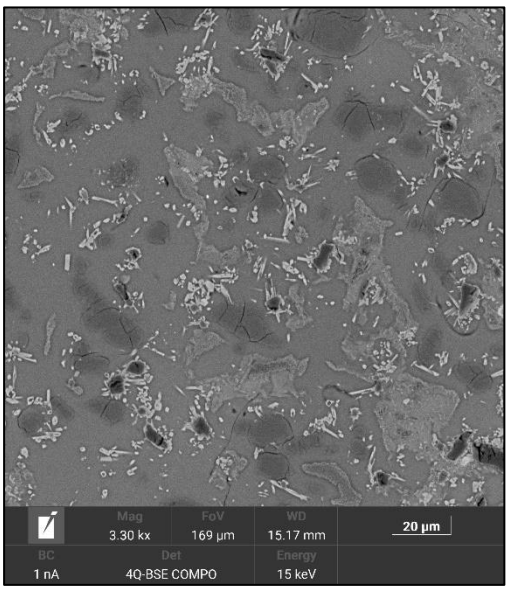

A477

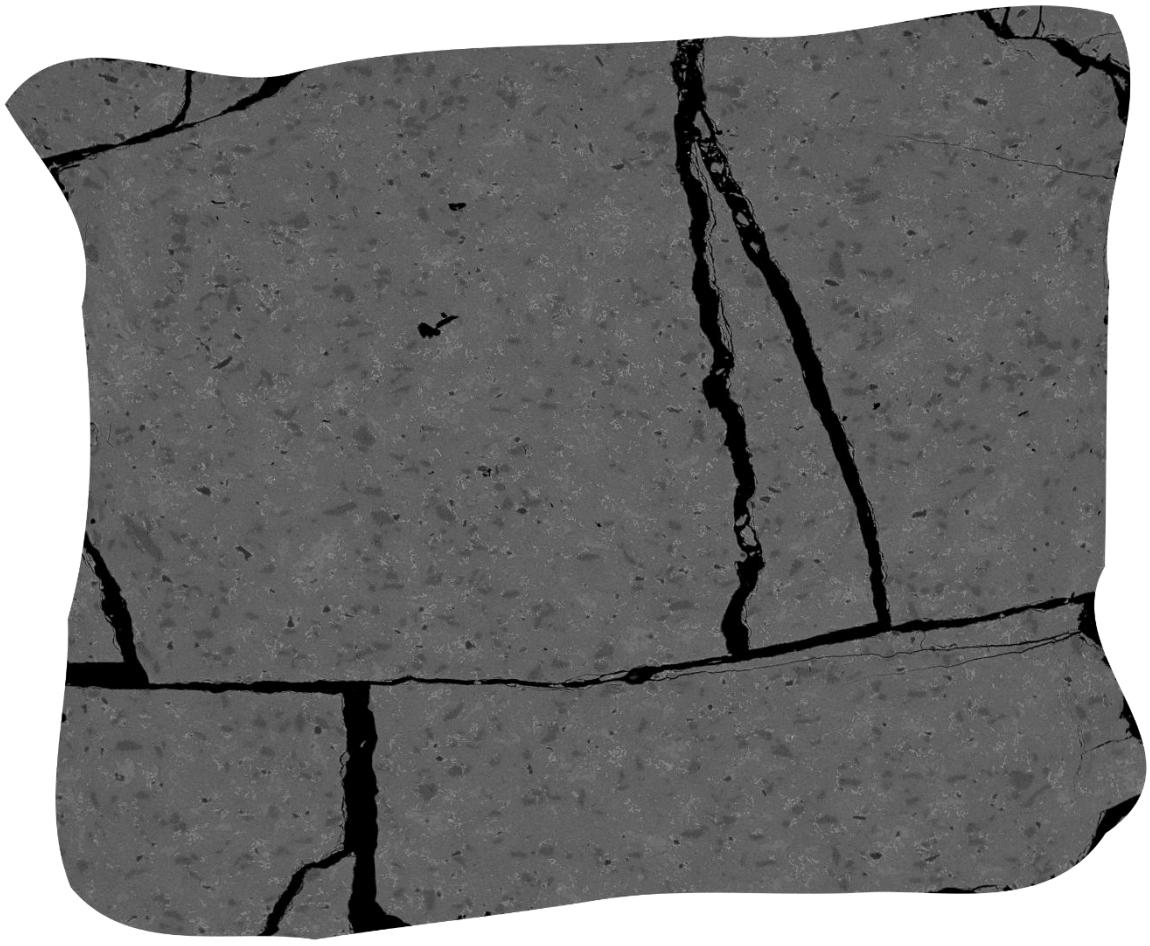

T (°C)	1250	**Run**	**A477**
P (GPa)	0.5	**Si**	34.41
Starting composition	Mer_3(0)	**Ti**	0.07
Duration (hrs)	00:50	**Al**	7.43
Silicate Phases (wt%)	Gl () Cpx () Qtz () Pl ()	**Fe**	
		Mn	0.06
		Mg	1.35
		Ca	2.44
		Na	4.66
		K	0.59
		S	
		Cr	
		O*	50.17
		Tot	101.19

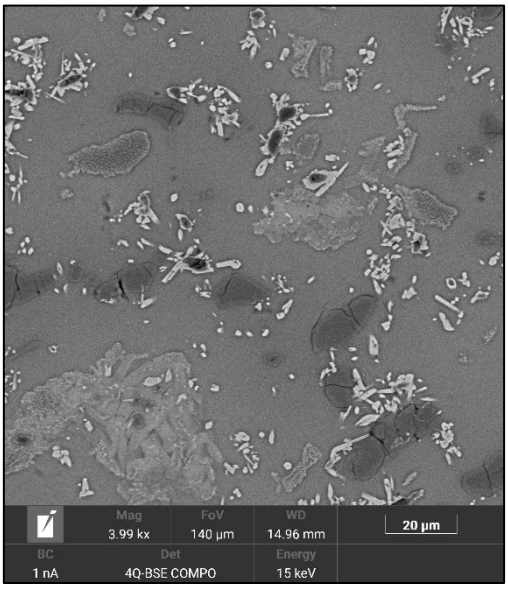

A486

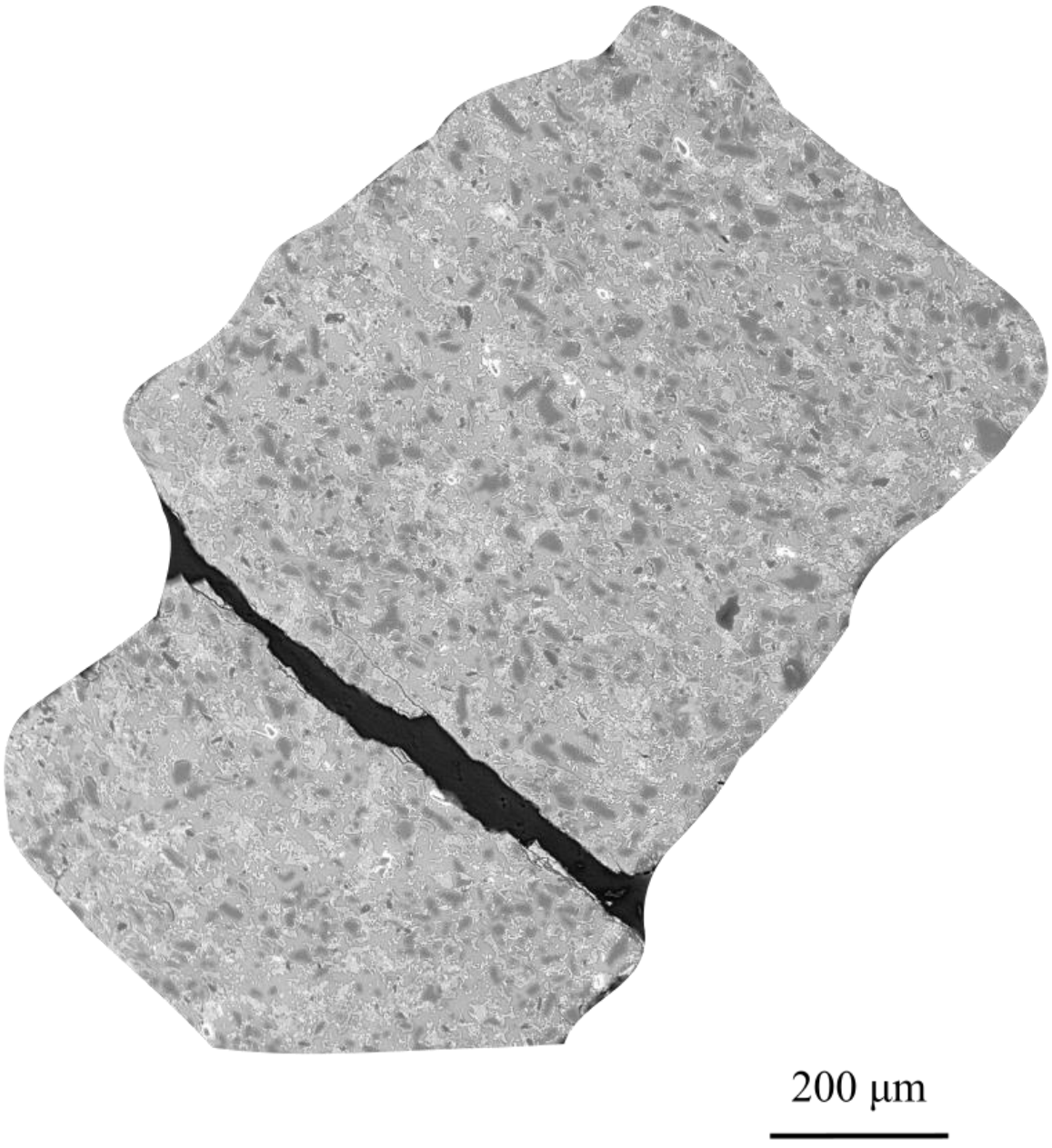

T (°C)	1150	**Run**	**A486**
P (GPa)	0.5	**Si**	35.98
Starting composition	Mer_3(0)	**Ti**	0.05
Duration (hrs)	03:50	**Al**	6.92
Silicate Phases (wt%)	Gl () Cpx() Qtz () Pl ()	**Fe**	

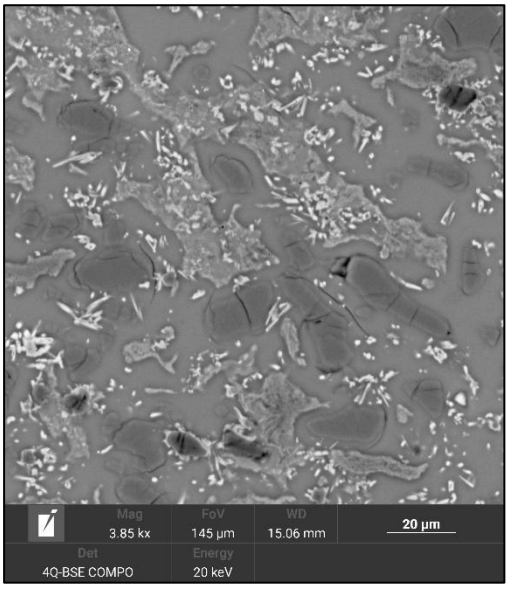

Mn	0.06
Mg	0.42
Ca	2.27
Na	5.21
K	0.75
S	
Cr	
O*	51.09
Tot	102.75

A487

T (°C)	1125	**Run**	**A487**
P (GPa)	0.5	**Si**	36.47
Starting composition	Mer_3(0)	**Ti**	0.12
Duration (hrs)	04:00	**Al**	6.56
Silicate Phases (wt%)	Gl () Cpx() Qtz () Pl ()	**Fe**	
		Mn	0.07
		Mg	0.40
		Ca	1.90
		Na	5.17
		K	0.83
		S	
		Cr	
		O*	51.22
		Tot	102.75